University of Southampton

Faculty of Engineering and the Environment

Eddy Currents applied to Space Debris Objects

by

Natalia Ortiz Gómez

Thesis for the degree of Doctor of Philosophy

Supervisors: Dr. Scott J.I. Walker
Dr. Angelo Grubisic

September 2017

University of Southampton

Faculty of Engineering and the Environment

ABSTRACT

Doctor of Philosophy

EDDY CURRENTS APPLIED TO SPACE DEBRIS OBJECTS

by Natalia Ortiz Gómez

The increasing population of space debris in the near-Earth region poses a serious threat to operational satellites in-orbit. This situation has led to the development of numerous guidelines in order to mitigate the potential danger of in-orbit collisions, fragmentations and uncontrolled re-entries. Among the various recommendations, active debris removal is considered as a possible solution to help decrease the chance of the aforementioned risks. However, active debris removal has never been done in space and it still requires further development of various technologies and orbit testing before it can become a reality. One of the major challenges to overcome is how to capture rotating space debris objects. Some of these objects may have high rotational speeds which hampers their capture and subsequent controlled re-entry.

This research focuses on the analysis of the eddy current phenomenon on space debris objects by the Earth magnetic field as well as its practical application to develop a de-tumbling method for active debris removal based on the generation of eddy currents.

The first part of the project focuses on the development of a new mathematical approach which generalises the existing analytical models and simplifies the numerical methods typically employed to analyse the eddy current phenomenon. This mathematical approach, referred to as the magnetic tensor theory, is validated both numerically and experimentally. The theory is based on the discovery of a symmetric Cartesian tensor of second order with no negative eigenvalues, named the magnetic tensor. A method to evaluate this tensor based on a generic finite element method is provided as well as a particularization for a specific F.E.M. which leads to a direct formula to evaluate this tensor. This way, the eddy current torque solution may be found without the necessity to solve the classical Poisson equation with Neumann boundary conditions in each time step of the integration process of Euler's equation. This breakthrough greatly reduces the complexity and computational time of the classical approach commonly adopted in the past.

The second part of the project focuses on the design of a contactless de-tumbling method based on the generation of eddy currents named the eddy brake method. This design delves deeper into the idea first suggested by Kadaba and Naishadham in 1995 which consists in subjecting a space debris object to an enhanced magnetic field in order to damp its rotation. The advances in high temperature superconducting materials as well as spacecraft sensors and actuators has allowed for a compelling new design to be reached within this research which may serve as a stepping stone for future ADR missions.

A thorough systems engineering design of the eddy brake is presented with special attention to the thermal and guidance, navigation and control subsystems. These subsystems have been identified as the two most relevant ones to support the operation of the eddy brake. The results show that the eddy brake is a promising solution to reduce the rotation of metallic space debris and allow for their subsequent capture.

CONTENTS

LIST OF FIGURES

LIST OF TABLES

DECLARATION OF AUTHORSHIP

I, Natalia Ortiz Gómez, declare that the thesis entitled:

Eddy Currents applied to Space Debris Objects

and the work presented in it are my own and has been generated by me as the result of my own original research.

I confirm that:

1. This work was done wholly or mainly while in candidature for a research degree at this University;

2. Where any part of this thesis has previously been submitted for a degree or any other qualification at this University or any other institution, this has been clearly stated;

3. Where I have consulted the published work of others, this is always clearly attributed;

4. Where I have quoted from the work of others, the source is always given. With the exception of such quotations, this thesis is entirely my own work;

5. I have acknowledged all main sources of help;

6. Where the thesis is based on work done by myself jointly with others, I have made clear exactly what was done by others and what I have contributed myself;

7. Parts of this work have been published as: [please list references below]:

   - Journal paper and book publications

     - N. Ortiz Gómez and S.J. Walker, *'Earth's Gravity Gradient and Eddy Currents Effects on the Rotational Dynamics of Space Debris Objects: Envisat Case Study'*, Advances in Space Research, January 2015, doi:10.1016/j.asr.2014.12.031,

     - N. Ortiz Gómez and S.J. Walker, *'Eddy Currents applied to De-tumbling of Space Debris: Analysis and Validation of Approximate Proposed Methods'*, volume 114, pages 34-53, Acta Astronautica, April 2015, doi: 10.1016/j.actaastro.2015.04.012,

     - N. Ortiz Gómez and S.J. Walker, *'Guidance, navigation and control for the Eddy Brake method'*, volume 40, issue 1, pages 52-68, Journal of Guidance, Control, and Dynamics, December 2016, doi:10.2514/1.G002081,

   - Conference proceedings

     - N. Ortiz Gómez and S.J. Walker, *'Eddy currents applied to de-tumbling of space debris: feasibility analysis, design and optimization aspects'*, Proceedings of the 40th COSPAR Scientific Assembly PEDAS.1-0030-14, Moscow, August 2014.

     - N. Ortiz Gómez and S.J. Walker, *'Eddy currents applied to de-tumbling of space debris: analysis and validation of approximate proposed methods'*, Proceedings of the 65th International Astronautical Congress IAC-14,A6,6,2x22528, Toronto, September 2014.

- M. Jankovic, K. Kumar, N. Ortiz Gómez, J. Romero Martín, F. Kirchner, F. Topputo, S. Walker and M. Vasile, *'Spacecraft concept for active de-tumbling and robotic capture of Ariane rocket bodies'*, 13th Symposium on Advanced Space Technologies in Robotics and Automation (ASTRA), ESTEC The Netherlands, May 2015.

- Jankovic, M., Kumar, K., Romero Martín, J., Ortiz Gómez, N., Kirchner, F., Topputo, F., Vasile, M., Walker, S., *'Autonomous robotic system for active debris removal: requirements, state-of-the-art and concept architecture of the rendezvous and capture (RVC) control system'*, 5th CEAS Air & Space Conference (Council of European Aerospace Societies), The Netherlands, September 2015.

- K. Kumar, N. Ortiz Gómez, M. Jankovic, J. Romero Martín, F. Topputo, S.J. Walker, F. Kirchner and M. Vasile, *'Agora: Mission to demonstrate technologies to actively remove Ariane rocket bodies'*, 66th International Astronautical Congress IAC-15,A6,6,1,x28851, Jerusalem, October 2015.

- N. Ortiz Gómez and S.J. Walker, M. Jankovic, J. Romero Martín, F. Kirchner and M. Vasile, *'Control analysis for a contactless de-tumbling method based on eddy currents: problem definition and approximate proposed solutions'*, AIAA Guidance, Navigation, and Control Conference, AIAA SciTech, San Diego, CA, January 2016.

- N. Ortiz Gómez and S.J. Walker, M. Jankovic and J. Paul, *'Pose estimation and control for the eddy brake de-tumbling method'*, Stardust 2nd Global Virtual Workshop on asteroids and space debris, Southampton, UK, January 2016.

- N. Ortiz Gómez and S.J. Walker, *'The eddy brake method. A contactless de-tumbling method for space debris objects'*, Final Stardust Conference, European Space Agency (ESTEC), The Netherlands, November 2016.

Signed:

Date:

ACKNOWLEDGEMENTS

ACRONYMS

Acronym	Expansion
AIAA	American Institute of Aeronautics and Astronautics
ACS	Attitude and Control System
ADR	Active Debris Removal
AGORA	Active Grabbing & Orbital Removal of Ariane
CAM	Collision Avoidance Manoeuvre
CFRP	Carbon Fibre Reinforced Plastics
CMG	Control Moment Gyro
COG	Centre of Gravity
COM	Centre of Mass
COP	Centre of Pressure
COPUOS	Committee on the Peaceful Uses of Outer Space
ESA	European Space Agency
FEM	Finite Element Method
GEO	Geostationary orbit
GNC	Guidance, Navigation and Control
GTO	Geostationary Transfer Orbit
HTS	High Temperature Superconducting
IADC	Inter-Agency Space Debris Coordination Committee
IMU	Inertial Measurement Unit
ISS	International Space Station
IGRF	International Geomagnetic Reference Field
JGM	Joint Gravity Model
LEO	Low Earth Orbit
LHP	Loop Heat Pipe
LIDAR	Light Detection And Radar
LTS	Low Temperature Superconducting
MEO	Medium Earth Orbit
MTT	Magnetic Tensor Theory
NASA	National Aeronautics and Space Administration
OBC	On-Board Computer
PMD	Post Mission Disposal
RAAN	Right Ascension of the Ascending Node
S/C	Spacecraft
SDM	Separation and Distancing Module
SRP	Solar Radiation Pressure
R/B	Rocket Body
TRL	Technology Readiness Level

Table 1: Acronyms.

NOMENCLATURE

Symbol	Quantity	Unit	Symbol	Quantity	Unit
A	Area	m^2	$\boldsymbol{\Lambda}$	Jacobian of magnetic field	T·m^{-1}
$\vec{B}$	Magnetic induction	T	$\vec{v}$	Velocity vector	m·s
C	Damping coefficient	s^{-1}	V	Volume	m^3
$\vec{E}$	Electric field vector	V m^{-1}	W	Energy	J
e	Thickness	m	α	Absorptivity	-
f	Force	N	γ	Surface tension	N·m^{-1}
G	Shear modulus	Pa	δ	Skin depth	m
$\vec{H}$	Angular momentum	N·m·s	ϵ	Electric permittivity	F·m^{-1}
$\vec{\mathcal{H}}$	Magnetic field	A·m^{-1}	ε	Emissivity	-
$\mathbf{I}$	Inertia tensor	kg m^2	$\mathcal{E}$	Electromotive force	V
$\boldsymbol{\mathcal{I}}$	Identity matrix	-	ζ	Damping ratio	-
I	Electric intensity	A	κ	Torsion coefficient	N·m·rad^{-1}
$\vec{j}$	Electric current density vector	A·m^{-2}	μ	Magnetic permeability	H·m^{-1}
$\mathbf{K}$	Stiffness matrix	N·V^{-1}	ξ	Magnetic scalar potential	A
k	Thermal conductivity	W·m^{-1}·K^{-1}	ρ	Density	kg·m^{-3}
L	Length	m	ϱ	Charge density	A·s·m^{-3}
$\mathbf{M}$	Magnetic tensor	S·m^4	σ	Conductivity	S·m^{-1}
$\vec{m}$	Magnetic moment	A·m^2	σ^{stress}	Tensile stress	Pa
m	Mass	kg	τ	Characteristic time	s
P	Power	W	τ^{shear}	Shear stress	Pa
Q	Heat rate	W	ϕ	Electric potential	V
R	Radius	m	φ	Magnetic flux	V·s
$\mathcal{R}$	Resistance	Ohm	χ_m	Magnetic susceptibility	-
$\vec{r}$	Position vector	m	ψ	Potential	V
T	Temperature	K	$\vec{\omega}$	Angular velocity vector	rad·s^{-1}
$\vec{T}$	Torque	N·m			
t	Time	s			

Table 2: Nomenclature.

Symbol	Expansion
c	chaser
t	target

Table 3: Common subscripts.

PHYSICAL UNITS

Unit symbol	Name	SI derived unit
A	Ampere	
C	Coulomb	A·s
°C	Degrees Celsius	273.15 K
deg	Degrees	$\pi/180$ rad
F	Farad	s^4·A^2·m^{-2}·kg^{-1}
J	Joule	N·m or kg·m^2·s^{-2}
K	Kelvin	
kg	Kilogram	
l	Litre	0.001 m^3
m	Metre	
N	Newton	kg·m·s^{-2}
Pa	Pascal	N·m^{-2} or kg·m^{-1}·s^{-2}
rad	Radian	
S	Siemens	m^{-2}·kg^{-1}·s^3·A^2
s	Second	
T	Tesla	kg·s^{-2}·A^{-1}
Torr	Torr	101325/760 Pa
V	Volt	m^2·kg·s^{-3}·A^{-1}
W	Watt	J·s^{-1} or m^2·kg·s^{-3}

Table 4: Physical units.

PHYSICAL CONSTANTS

Constant	Symbol	Value	Units
Speed of light in free space	c	$2.9979 \cdot 10^8$	m·s^{-1}
Gravitational constant	G	$6.6726 \cdot 10^{-11}$	m^3·s^{-1}·kg^{-1}
Gravitational acceleration	g	9.81	m·s^{-2}
Permittivity of free space	ϵ_0	$8.854 \cdot 10^{-12}$	F·m^{-1}
Permeability of free space	μ_0	$4\pi \cdot 10^{-7}$	N·A^{-2}
Mean Earth's radius	R_E	6371	km
Stefan-Boltzmann constant	σ_{sb}	5.67×10^{-8}	W·m^{-2}·K^{-4}

Table 5: Physical constants.

Science is about what is.
Engineering is about what can be.

- Neil Armstrong

INTRODUCTION

1.1 Motivation

The space debris population has drastically grown since the first launch of an artificial satellite in 1957 and it has become a serious threat to the security, safety and sustainability of space activities [33, 34]. At present, operational satellites located in the most densely populated regions receive numerous collision warnings which may result in the need to conduct collision avoidance manoeuvres (CAMs) [35]. This has resulted in the need to monitor operational satellites continuously and to allocate a certain amount of propellant in every mission to perform the aforementioned CAMs. However, there are several detrimental events which are unavoidable and are unfortunately becoming more frequent such as in-orbit fragmentation of space debris, in-orbit collisions or uncontrolled re-entries of non-cooperative objects [36].

This threatening environment has fostered worldwide cooperation to tackle this problem. In this context, space mitigation guidelines have been developed by national space agencies which include the systematic passivation of every discarded stage, the depletion of the batteries at the end of the satellite's life and the compliance with a maximum post-mission lifetime of 25 years in the low Earth orbit (LEO) region [1, 37–40]. However, a study initiated in 2009 by the Inter-Agency Space Debris Coordination Committee (IADC) showed that the proposed mitigation measures may not be enough to stabilise the future orbital debris environment and that more aggressive remediation techniques such as active debris removal (ADR) should be adopted [41]. All in all, there is a broad consensus within the scientific community that the combination of post mission disposal (PMD) measures with ADR processes is an effective solution to stop the population from growing, assuming some reasonable assumptions in terms of future number of launches, in-orbit explosions, level of compliance with post-mission disposal and solar cycle projections [42, 43].

Nevertheless, ADR has never been done in space and it still requires further development of various technologies and orbit testing before it can become a reality. Currently proposed ADR methods may be classified into contact and contactless methods [44]. At present, the European Space Agency requires a controlled re-entry for those objects that have a casualty risk on ground higher than 0.0001 [45]. This can only be achieved with contact ADR methods based on chemical propulsive devices [45, 46]. Therefore, the challenges derived from the proximity operations and capturing process within a contact ADR method need to be addressed. One of the most critical issues is the capturing process of a tumbling object. All contact ADR methods have a physical limit depending on the maximum angular momentum that can be absorbed. Consequently, a de-tumbling phase may be necessary prior to the capturing phase.

The strong limitations of contact ADR methods with respect to the angular velocity of the target

show the necessity to acquire a precise knowledge of its rotational parameters in order to predict accurately its long term evolution. The total time required from the initial conception of an ADR mission until its launch can extend over a period of 10 years [25]. This means that reliable and accurate predictions on the rotational motion of the defunct object are necessary in order to select the most suitable ADR method in the early phases. This analysis will determine the feasibility of a given ADR method and whether it is necessary or not to employ a de-tumbling system. Otherwise, a wrong decision at an early stage in the mission design can jeopardise the completion of the mission. All these arguments have motivated the need to carry out research on the rotational dynamics of space debris objects and in particular, analyse and design a contactless de-tumbling method based on eddy currents to serve as a stepping stone for future ADR missions.

1.2 Report outline

This document presents a detailed account of this research which is split into a further 7 chapters. The following chapter provides the reader with a detailed overview of the space debris environment and the various challenges that must be addressed in ADR processes. Special attention is given to the ground observations made of the attitude of space debris and the existing theoretical understanding of spacecraft attitude dynamics, emphasising the identified gaps. The chapter concludes with a detailed description of the current de-tumbling technologies for ADR and the advantages and disadvantages of a de-tumbling method based on the generation of eddy currents.

Chapter 3 presents a novel electromagnetic theory referred to as *magnetic tensor theory* (MTT) which generalises the existing mathematical processes to analyse the eddy current phenomenon. Typical numerical methods employed to solve the eddy current problem need to apply the classical Poisson equation with Neumann conditions, resulting in complex and computationally expensive processes. However, the magnetic tensor theory provides a direct formula to evaluate the magnetic forces and torques. The theory is based on the computation of a new tensor called the *'magnetic tensor'*, which gives an insight of how the conductive material is distributed throughout a body. This chapter describes this theory starting from basic fundamentals of electromagnetism and reaches a direct analytical formula to evaluate both the eddy current torque and force for any kind of body.

Experimental testing performed to validate the MTT is then presented in Chapter 4. The experimental tests were carried out at Airbus Defence & Space in Stevenage (UK) during a three-month secondment conducted at this location. A comprehensive description of the experimental set-up together with a detailed description of the experimental procedures and results are provided in this chapter.

Concurrently a contactless active de-tumbling method called the *eddy brake* is described in Chapters 5 and 6. The eddy brake method is based on the generation of eddy currents on a rotating metallic object subject to an enhanced magnetic field and the process is carried out actively by a chaser spacecraft which has an electromagnetic coil on-board based on high temperature superconducting wires. Chapter 5 focuses on the systems engineering design, including a thorough analysis of the coil materials and sizing as well as the key chaser subsystems that must support the operation of the eddy brake.

Subsequently, Chapter 6 deals with the dynamics of the chaser-target system. The 3D numerical integration process of the chaser-target system is a complex problem as it includes a set of non-linear differential equations where the translational and rotational dynamics of the two objects are coupled. The complexity of the problem increases when adding inaccuracies and delays in the control derived from the sensors and actuators which can easily lead to instabilities unless proper control manoeuvres are included. A generalised 3D control strategy based on a proportional-derivative control is presented and tested in various case studies.

The thesis closes with a summary and conclusions of the project in Chapter 7 where key research results and future research areas are highlighted.

STATE OF THE ART

2.1   Space debris overview

Orbital debris are defined by the Inter-Agency Space Debris Coordination Committee (IADC) as *'all man-made objects, including fragments and elements thereof, in Earth orbit or re-entering the atmosphere, that are non-functional'* [47].

As of February 2017, the number of space debris objects tracked and monitored by the US Space Surveillance Network is approximately 18000 [48]. This data is currently acquired by ground-based radars and optical telescopes and space-based telescopes which are able to track objects on the order of 10 cm in low-Earth orbits (LEO) and objects on the order of 1 m in geostationary orbits (GEO) [34]. However, only 4% of these objects are active satellites while the rest are qualified as space debris [36]. In addition to the aforementioned catalogued objects, the number of particles between 1 and 10 cm in size is estimated to be around 670000 and estimates suggest that there are over 170 million particles smaller than 1 cm [49]. Due to the space debris proliferation, the IADC and the Committee on the Peaceful Uses of Outer Space (UN-COPUOS) declared two protected near-Earth regions depicted in Figure 2.1 [1, 37]. These are the *LEO Region* which covers all altitudes below 2000 km and the *Geosynchronous region* located between the altitudes 35768 ± 200 km and inclinations $[-15, 15]$ degrees [47]. Currently, the most densely populated area is the LEO region where 40% of the overall mass resides (not including the International Space Station) and the highest mass concentrations are found at 600, 800 and 1000 km of altitude [42].
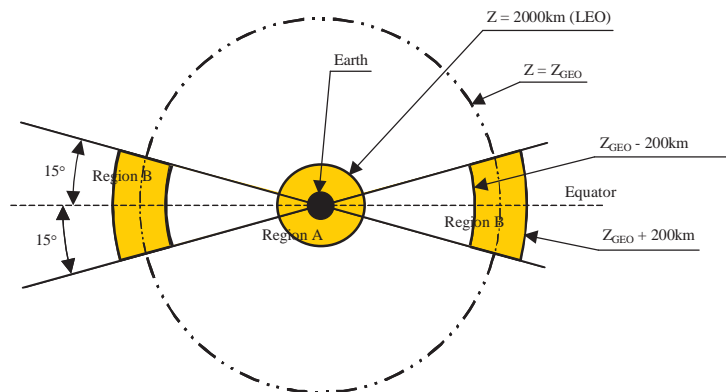
Figure 2.1: Protected regions defined by the IADC (note that the diagram is not to scale) [1].

After the launch of the first artificial satellite, Sputnik-1, in 1957, the first space debris object was created. However, space debris objects are created not only due to the appearance of defunct satellites or upper stages but also due to the occurrence of in-orbit collisions, fragmentations or break-ups. For instance, only four years after the launch of Sputnik-1, an Ablestar rocket body exploded in LEO generating 300 traceable fragments. After this event, explosions in the near-Earth region have taken place on a yearly basis [36] up to and including 2016. The most recent satellite break-ups have taken place in the year 2016. The first event in 2016 took place on the 16th of January when a Briz-M upper stage fragmented near the geosynchronous region creating 10 traceable pieces. The second event happened on 26 March 2016 when a ullage motor from a Proton Block DM fourth stage fragmented into 21 pieces in a highly elliptical orbit that passes through the LEO region [50].

Various detrimental consequences are currently taking place due to the proliferation of space debris such as in-orbit fragmentations and collisions or the uncontrolled re-entry of objects into the Earth's atmosphere. This has, in turn, unwanted adverse effects on the ground-based and space-based infrastructures [35, 36].

- On-ground permanent surveillance and tracking of the active satellites is necessary in order to provide the satellite operators with conjunction warnings which leads to the necessity to allocate man-hours for the use of ground sensors and operation centres.

- Additional fuel needs to be considered in the design of new space missions for potential collision avoidance manoeuvres (CAMs) which increases the weight of the satellite.

- The spacecraft performance is degraded by the impact of small space debris which deteriorates, for instance, the solar panels.

- The potential impact of space debris pose a threat to the ISS and the astronauts.

- The uncontrolled re-entry of big satellites that do not disintegrate in the atmosphere pose a threat to human beings and ground-based infrastructure.

As mentioned above, the space debris population growth has also led to the necessity to allocate a certain amount of propellant for CAMs in every new mission [35]. Nowadays, satellites in popular orbits receive collision warnings on a weekly basis which may result in the need to conduct CAMs [36]. For instance, the International Space Station (ISS) had to carry out 5 CAMs throughout the year 2014, which is the highest number to date for the ISS [51]. However, collisions between defunct objects can not be prevented from taking place. In mid-2013, the average estimated collision rate per year was estimated to be 0.24 (i.e. 1 collision every 5 years) [52] and this rate is likely to increase unless precautionary measures are taken.

In-orbit fragmentations and collisions are unfortunately becoming more frequent and there is a growing sense within the space science community that there is a tangible threat of a collision cascade becoming a reality [33]. This collision cascade effect typically referred to as the *'Kessler syndrome'* could render certain regions of near-Earth space unusable in the future.

In order to mitigate this problematic situation, new guidelines in the design of space missions have been developed by several national space agencies [37, 38, 53, 54]. Within these guidelines, it is recommended to carry out a systematic passivation of every stage, to deplete the batteries at the end of the satellite's life and to comply with a maximum post-mission lifetime of 25 years in the LEO region. However, a study initiated in 2009 by the IADC showed that the proposed mitigation measures may not be enough to stabilise the future orbital debris environment and that more aggressive remediation techniques such as active debris removal (ADR) should be adopted [41]. Active debris removal is defined as the deliberate process of removing an existing debris object from orbit above and beyond the currently-adopted mitigation measures [42].

The combination of post mission disposal (PMD) measures with ADR processes is considered to be an effective solution to stop the population from growing, assuming some reasonable assumptions in terms of future number of launches, in-orbit explosions, level of compliance with post-mission disposal and solar cycle projections [42, 43]. In these studies, it was concluded that a removal

rate in the order of five objects per year should be enough to stabilise the future orbital debris environment over a 200-year period.

Nevertheless, if the hypotheses made in terms of the launch rate, the explosion rate, PMD compliance or the solar cycle predictions are modified, the results can drastically change [55]. Some of the results obtained include scenarios where ADR is not necessary and only PMD measures are sufficient to stabilise the space debris population or scenarios in which the combination of ADR and PMD measures are not enough to stop the growth of the space debris population [55]. In order to take into account the uncertainties in these parameters, an adaptive strategy for ADR has also been proposed that selects the most adequate number of removals per year depending on the evolution of the space debris population [56]. This strategy has proven to increase the probability of reaching a stable space debris population with an average removal rate of 3.1 objects per year [56].

2.2 Active debris removal challenges

The vast majority of the studies carried out foresee the need to perform ADR in the future to remove those objects that pose the biggest risk in orbit and help in the stabilisation of the space debris environment.

An active debris removal mission consists of the following phases [57, 58]:

- Launch and Early Orbit Phase (LEOP),

- orbit phasing,

- far-range rendezvous phase,

- close-range rendezvous phase,

- capturing phase (if a contact method is employed) and

- removal phase.

The first four stages can be characterised as more conventional as they have already been addressed in the past for rendezvous and formation flying missions while the capturing and removal phases are the least mature and most challenging stages.

2.2.1 Debris characterisation

In order to track and characterise the space debris objects, optical and radar measurements are employed from ground and/or from space [57, 59, 60]. Debris characterisation requires obtaining the 3D translation and rotation of the target, referred to as 3D pose estimation. The pose estimation of a non-cooperative object is a complex process that is still under investigation. It entails various difficulties due to the lack of cooperativeness of the space debris object. First of all, the target does not have any operating navigation sensors or dedicated interfaces (e.g. reflectors) that can help during the process. Secondly, the physical properties of the target (shape, COG, inertias, etc.) may be uncertain or unknown depending on the availability of previous 3D models. In addition, the derelict may also be deteriorated or damaged and it will have unknown internal physical properties (e.g. fuel left on-board). These conditions can modify the surface properties, mass distribution and inertias with respect to the available initial data which would lead to uncertainties in the pose estimation process [61].

Available sensors may be divided into the following groups [57, 59, 60]:

- Optical sensors: these sensors measure the reflected light on the surface of the object which can be illuminated either passively or actively or measure the thermal radiation of the target.

– Passive visual methods: visual methods are based on the measurement of the brightness variation of the object due to the specular reflection of sunlight and this is represented by light curves. This technique may be used with telescopes from ground or visual cameras from space. Their major disadvantage is that they are very sensitive to the illumination conditions. Ground-based telescopes can only be used during night-time and they are strongly affected by adverse meteorological conditions. Moreover, passive visual cameras in-orbit can not be used during eclipse. The use of active illumination systems to light up the target's surface is usually suggested for improving the visibility of passive cameras. Passive visual cameras may be used not only to determine the relative distance to the object but also measure its size, shape and attitude [62].

– Passive infrared methods: these passive sensors measure the thermal radiation emitted by the target. They are less affected by the illumination conditions and may be used during eclipse. This type of sensors may be carried on-board spacecraft and can be used to estimate the pose of the target object [63].

– Active methods: these sensors actively illuminate the scene with a laser and measure the reflected signal. Light Detection and Ranging Sensors (LIDARs) may be carried on-board spacecraft. They emit a pulse of light and measure the time interval between when the pulse is emitted and when the reflected pulse is detected. This way the distance to the target object is determined. Furthermore, by scanning the surface of the target, advanced range finders can determine the target's 3D pose in addition to its distance [64]. Active optical sensors are also used in ground stations primarily to track space debris objects which have retroreflectors. This methodology is referred to as Satellite Laser Ranging (SLR) and it provides very accurately range measurements from ground.

• Radar sensors: these active sensors measure the travel time of a radar pulse emitted from a ground station and reflected from the target which provides range measurements. It has the advantage that it can be used both during day-time and night-time and it is not affected by the meteorological conditions. Radar measurements from ground have been classically limited to the analysis of space objects in LEO due to the power necessary to get a return signal.

In general, in-orbit sensors such as passive cameras (visual or infrared), active LIDAR sensors or a combination of both are employed in the process of 3D pose estimation.

Passive camera-based sensors used in spacecraft have lower hardware complexity than the LIDARs, they are cheaper and their mass and power consumption is lower [64, 65]. However, their resolution is usually poorer than the one provided by LIDARs.

LIDARs are robust sensors with respect to the illumination conditions and they usually have a better resolution than the one provided by passive sensors [64]. However, it should be noted that both active and passive sensors experience problems in the detection of very reflective materials (e.g. MLI) in the short range and low-reflective materials in the long range [61].

2.2.2 Removal process

A wide variety of removal methods have been proposed for ADR [44, 45]. Space debris can be either re-orbited into a graveyard orbit or de-orbited to burn up into the atmosphere [46]. In addition, the de-orbit option may be controlled or uncontrolled.

• Re-orbiting: this option is preferred for geosynchronous satellites (altitude 35785 km). Space debris within the geosynchronous protected region must be moved into a graveyard orbit as indicated in the IADC guidelines [1].

• De-orbiting: this option is preferred for low Earth orbit satellites (< 2000 km).

– Controlled disposal: a controlled re-entry is required when the casualty risk on ground is greater than 10^{-4} and it should achieve a re-entry over non-inhabited areas [45]. In

order to achieve a controlled re-entry at a targeted impact location, it is necessary to have a sufficiently steep flight path angle at the atmospheric interface. By convention, the flight path angle at an altitude of 120 km should be between 1.5 and 2.5 degrees depending on the initial orbit altitude [66]. The classical re-entry method consists in applying two or three apogee boosts to transfer the vehicle into a 60 km perigee orbit or lower [66] and this results in high $\Delta V s$ that can only be achieved by means of chemical propellant [45, 46]. As a rule of thumb, targets with a mass higher than 1000 kg will require a controlled re-entry [36].

– Uncontrolled disposal: an uncontrolled re-entry is only allowed if the casualty risk is lower than 10^{-4} [45]. An uncontrolled re-entry consists in a gradual perigee decrease allowing atmospheric re-entry in a limited time (at least less than 25 years to comply with international regulations) without any control of the impact footprint [44]. This type of re-entry method usually tries to benefit from natural forces acting on the target to decrease its altitude more rapidly (e.g. drag augmentation devices or the use of an electrodynamic tether). As a rule of thumb, targets with a mass lower than 200 kg will have a lower risk of casualty on ground than 10^{-4}. For satellites in between 200 and 1000 kg, a rigorous analysis is required in order to choose the best re-entry option.

Furthermore, ADR methods can be divided into contact and contactless methods for complete removal [44].

- Contact methods: These methods need to capture the target in order to either attach a de-orbit device or de-orbit the compound chaser-target together. The attachment of a de-orbit kit allows the potentiality of a multi-target mission to be carried out and these may be again divided into propulsive and non-propulsive methods. Contact methods are usually classified into two big groups depending on the type of connection (stiff or flexible) between the chaser and the target [44]. An example of a rigid connection systems is the robotic arm [58]. Examples of flexible capture systems are nets [66] or a harpoon [67] which connect both objects with a tether. Other techniques such as the tentacles or the clamp may generate a semi-rigid contact depending on the materials employed [68]. Figure 2.2 shows two contact ADR methods by means of a rigid and a flexible connection.
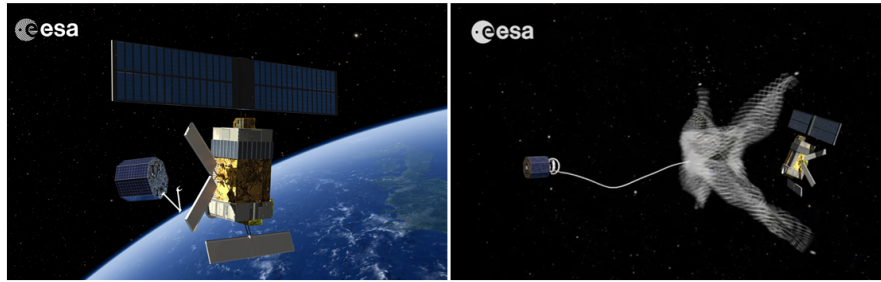
Figure 2.2: Capturing with a robotic arm (left) and a net (right) (courtesy of European Space Agency).

- Contactless methods: These methods modify the target's orbit without any physical contact. Among these methods, the ion-beam shepherd [69], the COBRA concept [70] and the laser [71] transfer the momentum remotely using the exhaust of an ion thruster, a chemical thruster or a laser, respectively, pointed at the target from a nearby chaser satellite. Figure 2.3 shows an ADR method based on plume impingement. Another proposed contactless method is the foam projection, which consists of ejecting foam from a nearby chaser that will adhere to the target's surface and increase its area to mass ratio such that the atmospheric drag can exert a significant influence to decelerate the debris [72]. In addition, a contactless electrostatic disposal has also been proposed which consists in remotely charging the target object by using an electron beam so that electrostatic forces can be induced and therefore, modify the

target's orbit [73]. The main advantage of the non-contact methods is the avoidance of the hazards associated with grabbing a non-cooperative target which is explained below in more detail. However, none of the contactless methods have been proven to achieve a controlled re-entry [45].
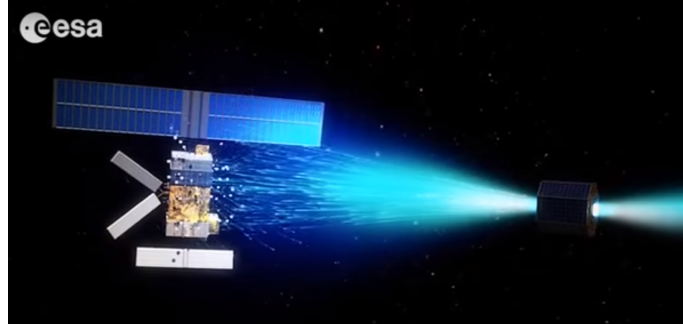
Figure 2.3: Plume impingement (courtesy of European Space Agency).

As it has been previously highlighted, in order to perform a controlled re-entry using current technology, a contact method based on chemical propulsive devices is necessary. Therefore, the challenges derived from the capture of a non-cooperative object need to be addressed. The first difficulty found by the chaser is that the target will not have dedicated surfaces for capture. Therefore, a structural feature that can serve as capture interface must be found or the complete body must be embraced. Moreover, if the target has appendages mounted out from its surface (e.g. solar panels, booms, antennae), the capturing process becomes more complex and the collision risk increases. Once the target has been captured, the new combined system will have a new centre of gravity (COG) and new inertia properties which, in general, are not known a priori as it will depend on the current state of the target object and how the debris is caught. Therefore, the chaser spacecraft must have a robust guidance, navigation and control (GNC) subsystem that can control and stabilise the compound [46].

2.2.3 De-orbiting phase

Finally, the de-orbiting phase requires an accurate knowledge of the COG and inertias of the two-body system. The generated thrust must pass through the COG of the compound in order to avoid offset torques that will spin up the system. Moreover, the type of connection (stiff or flexible) between the two objects plays an important role in the dynamics of the system during the stabilisation phase and the final de-orbiting phase. Ideally, this connection should be stiff enough to allow for attitude and trajectory control during the re-entry.

The disposal phase is particularly challenging if tethers are involved. In this case, it is necessary to deal with multi-body dynamics in order to model the flexible link between the two objects. The chaser must control the oscillations of the system during the burn phase that will continuously stretch and release the tether and it may result in a collision between the two objects. Furthermore, possible lateral oscillations may take place that will turn into a pendulum motion of the target around the orbit path [66]. Additional potential risks are the resonances of the elastic oscillations of the tether with the tank sloshing or the deployable structures, the resonances between the elastic motion and the lateral target oscillations or the tether rupture [74]. The tether's material is of paramount importance for the frequency and amplitude of these oscillations and the avoidance of the aforementioned resonances [74].

2.2.4 Communications, autonomy and illumination conditions

On top of the difficulties previously described, the communication windows, level of autonomy of the chaser and the illumination conditions have an important effect on the mission risk [75].

Communications for a non-cooperative rendezvous are expected to be very demanding. However, the communication windows in Low Earth Orbit (LEO) are short, in the order of 10 minutes, which leads to the necessity of increasing the level of autonomy of the mission and/or using relay communications satellites to ease the operations.

In addition, the illumination conditions may not be optimal due to the possible periodical eclipses or the shadows caused by the target during the final approach and the navigation system must be able to cope with these conditions.

2.2.5 Tumbling

So far, numerous challenges have been addressed that will arise in ADR missions. Nevertheless, there is one additional issue that is critical in all contact ADR methods regarding the rotational motion of the target. An object is said to be spinning when it has a stable cyclic rotation, usually around an inertia axis, whilst it is said to be tumbling when it has a more complicated irregular rotation, about any inertia axis or a combination of them [76]. Space debris is the collection of uncontrolled objects that may be tumbling with a wide variety of spinning rates. All contact ADR methods have a physical limit depending on the maximum angular momentum that can be absorbed and therefore, a de-tumbling phase may be necessary prior to the capturing phase.

For example, rigid capture systems such as a robotic arm have a structural limit which translates to a maximum rotational speed that can be stopped for a certain body. When the manipulator grabs the target, an interaction torque will appear that should be constrained in order to avoid any mechanical damage to either the target or the robotic arm. Extensive research is ongoing as to how to minimise the loads generated during the capture and the braking phases [8, 77]. A commonly suggested strategy is to synchronise the chaser and the target motion before the capture (i.e. achieve a zero relative linear and angular velocity). This process already imposes a limitation on the maximum target's speed that can be stopped based on the maximum achievable speed during the synchronisation. Then, the chaser needs to reach the grasping point while avoiding collisions with possible existing appendages on the target's surface. Once the derelict is grabbed, the robotic arm is slowed down with a certain joint force/torque control law and it transfers momentum from the target to the servicer. It is claimed that the robotic manipulator can de-tumble large space debris objects (e.g. Envisat, Cosmos upper stage) that are rotating between 3 to 10 deg/s [8, 45, 58].

Moreover, numerous experimental tests have been conducted at the Spacecraft Robotics Laboratory of the Naval Postgraduate School to test guidance, navigation and control strategies for planar docking trajectories between a chaser spacecraft and a non-cooperative rotating object, including uncertainties derived from the navigation sensors and actuators [78]. The results show that the tested GNC subsystem could only provide robust performance for target's rotation rates below 4 deg/s.

Therefore, limitations on the maximum absorbed angular momentum not only come from structural limitations but also from limitations on the robustness and accuracy of the real-time on-board guidance, navigation and control [79]. It should also be noted that even if the target is rotating at a low speed, it could have a very complex tumbling motion (e.g. rotation about the three inertia axes), making the synchronisation phase very challenging. This aspect is not thoroughly addressed in the literature given that the analyses are normally limited to objects rotating around one of the principal inertia axes.

The viability of capturing rotating objects by means of flexible contact methods is still an open question. Once the target is captured, the tether must be tensioned as fast as possible to avoid entanglement around the rotating debris. The free motion phase before the tensioning is extremely critical if the derelict is a fast rotator because the wrapping of the tether around the target would

be hard to avoid. Moreover, if the tether contact point is misaligned with respect to the target's COG, torques will be generated during the pulling phase which can again lead to an entanglement. A multi-burn strategy is usually proposed to retain control authority and achieve a stable pulling phase [74, 80].

2.3   Space debris attitude observations

So far, the scientific community has made a great effort to observe and predict the orbital evolution of space debris. Nowadays, there are various public catalogues and databases which provide information on the two-line element set (TLE) of each object in orbit. This information is essential to be able to carry out collision avoidance manoeuvres or to predict the evolution of the space debris population. However, little information is available regarding the rotational state of space debris. At present, there are no public databases that provide the attitude parameters of space debris objects. The only available information can be found in a few tens of publications that describe the optical and radar measurements carried out from ground which shed some light on the rotational state of uncontrolled objects.

2.3.1   Observations in MEO and GEO

The Astronomical Institute of the University of Bern (AIUB) has conducted numerous optical observations of defunct spacecraft [81]. For instance, the observations made for the decommissioned GLONASS constellation at 19100 km of altitude showed a wide variety of spin rates, the fastest being the object 89001B rotating at 38.9 deg/s and the slowest being the object 94021B rotating at 3.1 deg/s. The measurements also showed that the rotation rates of these objects hardly changed between the observations made in the years 2000 and 2015 [81]. Another observation campaign was carried out for the defunct spacecraft PAKSAT 1 (19960-06A) in GEO between 2013 and 2014 which exhibited alternating accelerations and decelerations between 0.5 deg/s and 1.5 deg/s.

In addition an observation campaign was carried out in 2011 for two upper stages; CZ-3B and SL-12 rocket bodies (R/Bs) [82]. The object CZ-3B R/B resided in a highly elliptical GTO orbit and the results concluded that it was rotating in a flat spin motion (about the maximum axis of inertia) at 211.76 deg/s. The rocket body SL-12, which was located at an altitude of about 20000 km, has a spin velocity of 37 deg/s.

The Maui Research and Technology Centre (MRTC) in Hawaii tracked a decommissioned subset of the Geostationary Operational Environmental Satellite (GOES) between December 2013 and July 2014 [83]. GOES-8 decreased its angular velocity from 21.4 deg/s to 4.8 deg/s in just a few months, GOES-10 and GOES-12 exhibited a mean rotation period of 12 deg/s and 32 deg/s respectively and GOES-9 and GOES-11, which could only be observed for a few hours, were rotating at 15.9 deg/s and 17.2 deg/s respectively. It was also noticed that GOES-8 and GOES-10 had simple rotations while GOES-9, GOES-11, and GOES-12 exhibited more complicated, multi-axial tumbling modes.

Researchers at the Magdalena Ridge Observatory (MRO) in New Mexico have tracked defunct spacecraft in GEO since 2007 and their results demonstrate the existence of stable fast rotators in GEO [84]. The lightcurves obtained for the spacecraft BSAT-1A between April 2014 and September 2015 show that its rotation period remains unchanged at approximately 115 deg/s. Another observation accomplished in March 2015 of the spacecraft Brazilsat-B1 unveiled that its rotation period is equal to 120 deg/s.

From the observations of uncontrolled artificial satellites in MEO and GEO, it has been derived that satellites which were once spin-stabilised now have rotation periods ranging from 50 deg/s to 150 deg/s, objects such as empty launch vehicles now have rotation periods between 24 deg/s to 72 deg/s and satellites which were 3-axis-stabilised now have periods ranging from 0.1 deg/s to 24 deg/s [85–87]. It was also concluded that symmetrical objects exhibit a more stable spin rate than those objects that are highly asymmetric and contain various appendages.

However, spasmodic variations in the rotational period have also been observed in GEO and their cause remains unknown. This is the case of the observations made between 1994 and 1999 for the spacecraft Raduga 14 which showed chaotic changes in the range of 6.7 to 7.7 deg/s [85]. In addition, in March 1998 the defunct spacecraft experienced a sudden deceleration up to a complete stop with the following re-acceleration of the rotation to the original parameter during one day. Abnormal decelerations and accelerations have also been observed for the uncontrolled objects Cosmos 1897, Raduga 23, Raduga 12 and Raduga 31 [85]. This behaviour is attributed to a spontaneous switching-on and off of the on-board gyroscopes or a reaction force of a micro jet, arising from a micro hole in the hermetic pressurised cabin of the satellite.

2.3.2 Observations in LEO

Publications related to observations in LEO are more scarce. One of the first publications on photometric measurements of disposed objects dates from 1978 which describes the observations made for several Cosmos rocket bodies in LEO [88]. The measurements were carried out in the years 1973 and 1974 and they show a deceleration of the spin rate for all the bodies, attributed to the effect of the Earth's magnetic field. In addition, the Rocket Intercosmos 11 was tracked from June 1974 until June 1976 which orbited at an altitude of 500 km [89]. This object first showed a spin acceleration for two months, which is attributed to a propellant outgassing, followed by a gradual deceleration of the spin period again attributed to the effect of the Earth's magnetic field.

In addition, the Belgian Working Group for Satellites (BWGS) co-ordinates the observations made by amateur observers of rocket bodies in LEO. The data has been collected in the database Photometric Periods of Artificial Satellites (PPAS) since 1989 [90]. Most of these observations are done with modest observing equipment (naked eye or binoculars) and therefore, measurements may have a low degree of precision ($> 10\%$ uncertainty). The database provides the apparent flash periods of the objects which correspond to the number of flashes per second seen by an observer. The computation of the real inertial rotation rate of the object, called the *sidereal period*, from the apparent flash period, called the *synodic period*, is not straight-forward as one needs to take into account the varying geometry of the observer-satellite-Sun angle during the observations, called the *synodic effect*. The average value of the apparent flash period leads to a certain number of possible sidereal periods. This ambiguity is resolved by analysing the possible orientations of the body together with the changing observer-satellite-Sun geometry. Although the sidereal period is not provided in the database, some qualitative analyses can be derived from the observations. For instance, two R/Bs were observed during a long observation campaign, Cosmos 54 (65-11D) and Cosmos 1320-1327 (81-116J), which were tracked for 1.5 years and for almost 4 years respectively. Both objects show gradual decelerations, which are attributed to the eddy currents phenomenon, as well as multiple rapid accelerations, which have puzzled the observers and were attributed to collisions with some sort of space debris or a fuel leak.

In January 2004, the JAXAs Innovative Technology Research Centre carried out an observation campaign on the rocket body Cosmos 2082, launched in 1990, located at an altitude of approximately 850 km [91]. The observations demonstrated that the object had a rotation rate of 8.8 deg/s combined with a precession motion of 0.2 deg/s and an amplitude of 30.5 deg. This result showed that rocket bodies in LEO can have non-negligible spin rates even several decades after launch.

More recently, the AIUB Institute obtained several light curves of the rocket upper stage N-1 R/B (1978-018B) [92]. This object is currently in a LEO orbit which has a perigee of 977 km, an apogee of 1221 kmand an inclination of 69 degrees. Three spin period measurements were accomplished over 5 months including values of 31.6 deg/s in February 2014, 35.2 deg/s in March 2014 and 34.9 deg/s in June 2014. These results highlight that the object is subject to alternating accelerating and decelerating periods. The causes for this behaviour are not yet well understood.

In addition, the Satellite Laser Ranging (SLR) techniques have also been used to study non-operational satellites equipped with Corner Cube Reflectors. This is the case of the Envisat spacecraft which has been tracked since contact was lost in April 2012 [2, 93]. Figure 2.4 depicts

the evolution of the observed synodic period in seconds (blue dots) and the sidereal period. In this case, there is an ambiguity between the clockwise (CW) and the counterclockwise (CCW) rotation of the object which leads to two possible solutions for the sidereal period. For the first two months of observation, Envisat increased its rotational spin from 2 deg/s up to approximately 3.2 deg/s. As stated for previous occasions, this acceleration remains unexplained [93]. After this initial acceleration period, the angular velocity started to decrease monotonically until the latest observations in mid-2015 which show a final spin of 2.5 deg/s.
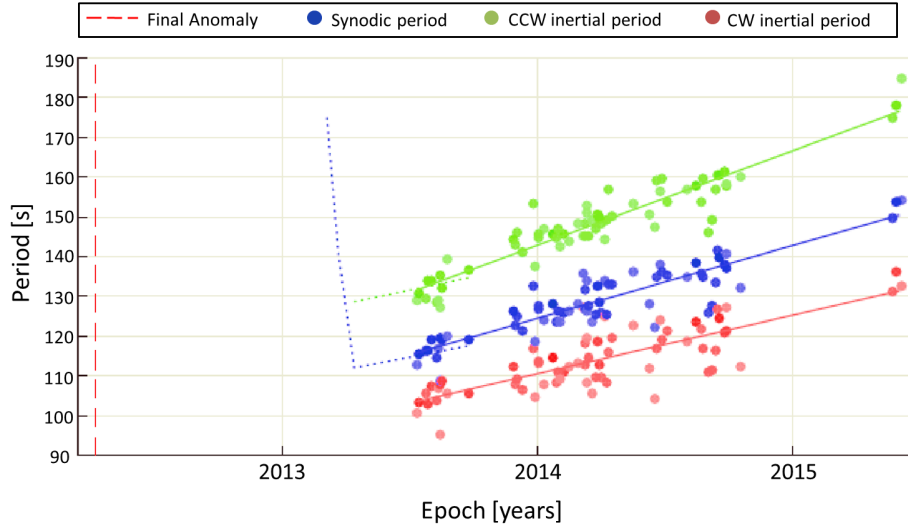
Figure 2.4: Envisat Spin Period [2].

The outlined optical and radar observations reveal a wide variety of spin motions of derelict objects in space. The causes of many of the observed spin rate evolutions are still unexplained which underscores the lack of knowledge of the scientific community on this matter. However, the measurements point out the relevance of the orbit, the shape, the surface materials and the end of life conditions on the rotational dynamics of space debris objects.

2.4 Space debris attitude modelling

In the past, spacecraft rotational dynamics were studied with the main purpose of analysing the attitude stability achieved passively and/or actively. However, only in the past few decades have the long term propagations of the attitude of disposed satellites been of interest.

The total time required from the initial conception of a new mission until its launch can extend over a period of 10 years [25]. For an ADR mission, the removal method should be selected during the early phases of the design, between the feasibility study (Phase 0) and the detailed definition phase (Phase B). The subsequent phases, which include the development, manufacture, integration, testing and final launch campaign, may last from 3 to 6 years [25]. This means that reliable and accurate predictions on the rotational motion of the target are necessary in order to select the most adequate ADR method in the early phases. This analysis will determine the feasibility of a given ADR method to capture the target and whether it is necessary or not to employ a de-tumbling system. Otherwise, a wrong decision at an early stage in the mission design can jeopardise the completion of the mission.

The fundamental quantity that governs the attitude dynamics of a body is its angular momentum

$\vec{H}$ defined as the integral (2.1) extended over the whole volume of the body V,

$$\vec{H} = \int_V \rho \vec{r} \times \vec{v} dV, \tag{2.1}$$

where ρ, $\vec{r}$ and $\vec{v}$ are the density, position and velocity vectors of each volume element dV.

A rigid body is defined as a system of particles such that the distances between the particles do not vary, that is, no deformation within the object takes place [94]. The angular momentum of a rigid body may be expressed in terms of its angular velocity $\vec{\omega}$ and it takes the form provided in Equation (2.2) when referred to the centre of mass of the body [25],

$$\vec{H} = \mathbf{I}\vec{\omega}, \tag{2.2}$$

where $\mathbf{I}$ is the inertia matrix based upon the centre of mass. This tensor is a 3×3 symmetric matrix that indicates how the mass is distributed throughout the rigid body and it is computed as outlined in Equation (2.3),

$$I_{ik} = \int_V \rho(x_l^2 \delta_{ik} - x_i x_k) dV. \tag{2.3}$$

Like any symmetrical tensor of rank two, it can be reduced to its diagonal form by appropriately choosing the direction of the axes x_1, x_2, x_3 [94]. These directions are called the *principal axes of inertia* and the diagonal components of the tensor are the *principal moments of inertia* denoted by I_1, I_2, I_3 in Equation (2.4),

$$\mathbf{I} = \begin{bmatrix} I_1 & 0 & 0 \\ 0 & I_2 & 0 \\ 0 & 0 & I_3 \end{bmatrix}. \tag{2.4}$$

Finally, the *torque*, denoted by the symbol $\vec{T}$, is the primary magnitude used to characterise the rotational dynamics of any given object. It represents the tendency of a force to rotate an object about an axis and it can be divided into *internal* and *external* torques.

2.4.1 Internal Torques

In the absence of any external torques, a rigid body will oscillate in a free precession motion with an amplitude depending on the initial conditions. This problem has an analytical solution and it can be found in reference [94].

However, no real physical body is truly a rigid body due to the presence of relative motion between constituent elements of the satellite. These effects can generate conservative or elastic internal torques and dissipative internal torques which can have a profound influence on attitude stability and control [95].

The major sources of internal torques are [95],

- Fuel sloshing

- Crew motions in manned vehicles

- Operating attitude on-board equipment without any mass ejection (e.g. reaction wheels)

- Internal stresses due to material deformations

- Geometrical changes of units which are not fixed or are flexible devices

By definition, internal torques, denoted by $\vec{T}_{int}$, do not modify the total momentum of a body but it can be redistributed [94]. This statement is valid both for rigid and non-rigid bodies. For a differential element ρdV of the body, Newton's Law applies as follows:

$$\rho \frac{d\vec{v}}{dt} = \vec{f}_{ext} + \vec{f}_{int}, \tag{2.5}$$

where $\vec{f}_{ext}$ and $\vec{f}_{int}$ are the external and internal forces per unit volume respectively. Moreover, employing Equation (2.1), the derivative of the angular momentum is:

$$\frac{d\vec{H}}{dt} = \int_V \rho \overbrace{\vec{v} \times \vec{v}}^{=\vec{0}} dV + \int_V \rho \vec{r} \times \frac{d\vec{v}}{dt} dV = \int_V \vec{r} \times \vec{f}_{ext} \, dV + \overbrace{\int_V \vec{r} \times \vec{f}_{int} \, dV}^{=\vec{0}} \tag{2.6}$$

and therefore,

$$\frac{d\vec{H}}{dt} = \vec{T}_{ext}. \tag{2.7}$$

Equation (2.7) indicates that the angular momentum is conserved, in an inertial reference system, for a body not subjected to external forces and this statement is valid both for rigid and non-rigid bodies.

Now assuming that the spacecraft may be considered to behave as a quasi-rigid body, this results in a slow internal dissipation (slow energy sink). Therefore, if the geometry of the quasi-rigid body varies slowly, the concept of an inertia tensor may be employed and Equation (2.2) may be assumed to be applicable. Under these assumptions, the dissipative torques will reduce the angular velocity of the object and the satellite will reorient itself to end-up spinning about its maximum axis of inertia. This state is referred to as *flat spin* and it coincides with the state of minimum energy of the spacecraft [96]. In order to comply with the condition given by (2.8),

$$\vec{H} = \mathbf{I}\vec{\omega} = constant \overset{\omega\downarrow}{\rightarrow} \vec{H} = I_{max} \cdot \omega_{min}, \tag{2.8}$$

the body must change its attitude and end up rotating about the maximum axis of inertia.

This phenomenon has been observed immediately after the launch of Explorer I [97] and ATS-5 [98]. The Explorer I satellite was launched in 1958 and it had a long cigar-shape configuration. It was designed to spin about its longitudinal axis or minimum axis of inertia. However, the satellite had four flexible whip telemetry antennas which dissipated the energy until the system reached its minimum energy state by rotating about the maximum axis of inertia. The ATS-5 satellite was launched in 1969 and shortly after it reached its final orbit it went into a flat spin motion. The cause was attributed to excessive fuel slosh.

As a first approximation, dissipative torques can be modelled as a vector proportional to the angular momentum of the body $\vec{T}\alpha\vec{H}$ [99, 100],

$$\vec{T}_{fr} = -\frac{\vec{H}}{\tau_{fr}} = -\frac{\mathbf{I}\vec{\omega}}{\tau_{fr}}, \tag{2.9}$$

where τ_{fr} is the characteristic time of the dissipative phenomenon. This parameter can be in the order of months or even days for fuel slosh or in the order of hundreds to thousands of years for solid internal friction of metallic structures [101].

Moreover, there are additional internal processes which are unpredictable for defunct satellites and can modify abruptly the attitude and spin rate of objects in-orbit. This is the case of sudden switching on and off of internal attitude and control system (ACS) devices like gyroscopes or geometrical changes of specific units such as solar panels or antenna modules [85].

2.4.2 External torques

External torques, denoted by $\vec{T}_{ext}$, command the rate of change of the angular momentum given by Equation (2.10). Note that this expression is only valid when $\vec{H}$ is referred to the centre of mass of the body or an inertially fixed point [25].

$$\frac{d\vec{H}}{dt} = \sum \vec{T}_{ext}. \tag{2.10}$$

Moreover, Equation (2.10) reduces to Equation (2.11) for a rigid body,

$$\frac{d}{dt}(\mathbf{I}\vec{\omega}) = \sum \vec{T}_{ext}. \tag{2.11}$$

In general, it is more convenient to express Equation (2.11) in a fixed frame to the body ('Body Reference Frame') because the inertia tensor is constant within this frame. This change leads to Equation (2.12), also referred to as the 'Euler Equations'.

$$\mathbf{I}\dot{\vec{\omega}} + (\vec{\omega} \times \mathbf{I}\vec{\omega}) = \sum \vec{T}_{ext}. \tag{2.12}$$

The main sources of external torques can be of environmental and non-environmental origin [95],

- Environmental sources
  - Gravity gradient
  - Atmospheric Drag
  - Solar Radiation Pressure
  - YORP effect
  - Earth Magnetic Field
  - Micrometeoroid impact
- Non-environmental sources
  - Leaks, venting or exhaust plume
  - Space debris impact

2.4.2.1 Environmental external torques

Objects in-orbit are also subject to environmental perturbations that affect their rotational dynamics. The degree of importance of each environmental perturbation depends on the type of orbit, the geometry and the materials of the spacecraft.

Gravity Gradient Torque:

The gravity gradient torque follows the expression given by (2.13) [102, 103],

$$\vec{T}_{grav} = \frac{3k}{R^3} \left(\vec{u}_R \times \mathbf{I}\vec{u}_R \right), \tag{2.13}$$

where k is given by Equation (2.14),

$$\frac{3k}{R^3} = \omega_0^2 \left(\frac{1 + e\cos(\nu)}{1 - e^2} \right)^3 \tag{2.14}$$

and where ω_0 is the mean orbital angular velocity, e is the orbit eccentricity, ν is the eccentric anomaly, R is the distance from the satellite's COG to the Earth and $\vec{u}_R$ is a unit vector in the direction of the line joining the centre of mass of both the satellite and the Earth.

The gravity gradient torque is inversely proportional to the cube of the geocentric distance and therefore, it will decrease rapidly with orbit height. This perturbation is usually dominant between altitudes of 500 and 10000 km, although it depends on the inertias of the object. For instance, it is inferred from Equation (2.13) that a spacecraft with all the principal moments of inertia equal to each other will have no torques due to the gravity gradient.

When computing the Earth's gravity gradient torque, it is generally assumed that the Earth possesses a spherical symmetrical mass distribution. The second order term in the expansion of the Earth's gravitational potential corresponds to the oblateness of the Earth given by the term J_2

[95]. The gravity gradient torque due to this term diminishes with the distance from the Earth's centre ($\sim R^5$) much faster than the main term ($\sim R^3$). Therefore, the correction for oblateness and further terms in the expansion can be neglected [95].

A stability analysis of the rotational dynamics of a spacecraft under the effect of the gravity gradient torque shows that the stable equilibrium is achieved when the minimum axis of inertia is parallel to the local vertical and the maximum axis of inertia is perpendicular to the orbital plane [76]. Moreover, gravity gradient torques are conservative torques which generate periodic oscillations around the stable equilibrium and the mechanical energy of the system is conserved. The amplitude of these oscillations will depend on the initial attitude conditions [104].

The gravity gradient torques generated by the Sun and the Moon on Earth-orbiting spacecraft are of the same order of magnitude for an Earth-orbiting satellite and they can both be neglected. The ratio between the torque arising from the secondary celestial bodies to that arising from Earth is equal to 10^{-5} in GEO and equal to 10^{-8} in LEO [95].

Atmospheric Drag Torque:

The atmospheric drag usually predominates at orbital altitudes below 500 km [25]. In LEO, the rarefied atmosphere can be characterised by the free-molecular flow regime and therefore, the air drag torque can be represented by (2.15) [103],

$$\vec{T}_{aero} = \int_S \vec{r} \times d\vec{F}_{aero}, \quad d\vec{F}_{aero} = -\frac{1}{2}\rho C_D V^2 (\vec{u}_N \cdot \vec{u}_V)\vec{u}_V dS, \qquad (2.15)$$

where ρ is the atmospheric density, C_D is the drag coefficient, $\vec{V}$ is the translational velocity of the vehicle with respect to the atmosphere, $\vec{r}$ is the position vector of each incremental area with respect to the centre of mass, $\vec{u}_N$ is the outward unit normal of each incremental area dS and $\vec{u}_V$ is a unit vector in the direction of $\vec{V}$. The integral extends over the spacecraft surface for which $\vec{u}_N \cdot \vec{u}_V > 0$.

Moreover, the translational velocity of each surface element dA for a spacecraft spinning with an angular velocity $\vec{\omega}$ is given by Equation (2.16).

$$\vec{V} = \vec{V}_0 + \vec{\omega} \times \vec{r}, \qquad (2.16)$$

where $\vec{V}_0$ is the velocity of the centre of mass relative to the atmosphere. Then, Equations (2.15) and (2.16) can be combined to yield,

$$\vec{T}_{aero} = \frac{1}{2}\rho C_D V_0^2 \int_S (\vec{u}_N \cdot \vec{u}_{V0})(\vec{u}_{V0} \times \vec{r})dS +$$

$$\frac{1}{2}\rho C_D V_0 \int_S \left\{ \vec{u}_N \cdot (\vec{\omega} \times \vec{r})(\vec{u}_{V0} \times \vec{r}) + (\vec{u}_N \cdot \vec{u}_{V0})((\vec{\omega} \times \vec{r}) \times \vec{r}) \right\} dS. \qquad (2.17)$$

The first term in Equation (2.17) appears due to the displacement of the spacecraft's centre of pressure (COP) and the COG. The COP is defined as the average location of the overall pressure acting upon a body and the relative distance between the COP and COG is called *aerodynamic eccentricity* [4]. The second term in Equation (2.17) is proportional to the spacecraft's angular velocity $\vec{\omega}$ and therefore, it is a dissipative torque. However, for a spacecraft in Earth orbit $\omega << V_0$ and the second term may be neglected [103]. Consequently, the aerodynamic torque acting on spacecraft is a conservative torque which will cause periodic oscillations of the satellite's attitude.

The stabilizing or destabilizing character of this torque depends primarily on the vehicle's configuration and the aerodynamic eccentricity [105, 106]. An appropriate symmetric design of the spacecraft together with a COP located slightly behind the COG can lead to a marginally stable system, which would generate small and slow oscillations due to the atmospheric torques. However, the combined interaction of the gravity gradient and the air drag torques generate stable and unstable regimes depending on the relative attitude of the object in orbit [105, 106].

Solar Radiation Pressure Torque:

The sources of electromagnetic radiation that cause forces on objects in orbit are direct solar photon radiation, Earth-reflected sunlight and the infrared emission from Earth [107]. Among these effects, the most important cause of radiation force is direct solar illumination while the other sources are usually at least an order of magnitude smaller. While the Earth's gravity, the Earth's magnetic field and the atmospheric drag diminish rapidly with increasing altitude, the radiation forces are nearly constant for near-Earth orbits. Therefore, this effect may surpass the rest of the perturbations at altitudes above 1000 km and it is dominant in GEO orbits. The solar radiation pressure (SRP) torque can be formulated as shown in Equation (2.18) [25],

$$\vec{T}_{SRP} = \int_S \vec{r} \times d\vec{F}_{SRP}, \quad d\vec{F}_{SRP} = -P\left((1-f_s)\vec{u}_S + 2(f_s\cos\theta + \frac{1}{3}f_d)\vec{u}_N\right)\cos\theta dS, \qquad (2.18)$$

where $P = 4.7 \cdot 10^{-6}$ N·m^{-2} is the mean radiation flux in the vicinity of the Earth, $\vec{u}_S$ is the unit vector from the spacecraft to the Sun, $\vec{u}_N$ is the outward unit normal of each incremental area dS, θ is the angle of incidence of the radiation and f_s and f_d are the coefficients of specular and diffuse reflection respectively [25]. This perturbation may lead to the spin-up of objects and it can change the rotational state significantly in a few orbital periods [108].

YORP Torque:

In addition to the angular momentum transfer, the sunlight can generate an additional effect which will result in a torque. This effect is based on the absorption and re-emission of sunlight where the photons that are re-emitted create a net force on the body [109]. This phenomenon, called the YORP (YarkovskyO'KeefeRadzievskiiPaddack) effect, is well known in the study of long term rotational dynamics of asteroids and it has been recently studied for space debris objects [110]. This phenomenon has a characteristic time of actuation in the order of years, which is much higher than the characteristic time of the most significant environmental torques, usually in the order of days or months [101, 108]. However, the YORP effect is non-negligible in the long term rotational dynamics of space debris and it is also believed that this effect together with the SRP torques could be the reason for the existence of fast rotators [110].

Earth's Magnetic Field Torque:

The Earth's magnetic field is also a significant source of environmental torques on space debris objects. The magnetic moment of an object, $\vec{m}$, is a vector quantity used to measure the tendency of an object to interact with an external magnetic field, $\vec{B}$. By definition, the magnetic moment is equal to the integral,

$$\vec{m} = \frac{1}{2}\int_V \vec{r} \times \vec{j}dV, \qquad (2.19)$$

where $\vec{j}$ is the electric current density vector inside the volume of the object V [111, 112]. This interaction generates a torque given by Equation (2.20),

$$\vec{T}_{mag} = \vec{m} \times \vec{B}. \qquad (2.20)$$

The materials employed in the manufacture of spacecraft play an important role on the generation of magnetic torques. Materials can be classified by their response to an external magnetic field in three groups:

- Diamagnetic,

- paramagnetic and

- ferromagnetic.

This response is quantified by the magnetic susceptibility χ_m and the permeability μ of the material. The susceptibility indicates whether a material is attracted into or repelled out of a magnetic field. The permeability measures the ability of a material to support the formation of a magnetic field within itself (degree of magnetisation). This parameter is sometimes provided in the form $\mu_r =$

μ/μ_0 where μ_r is the relative permeability and μ_0 is the permeability of free space $\mu_0 = 4\pi \cdot 10^{-7}$ N·A^{-2}. In addition the susceptibility and the relative permeability are related by the mathematical relationship (2.21),

$$\chi_m = \mu_r - 1. \tag{2.21}$$

Diamagnetic materials, such as copper and silver, have a weak negative susceptibility to magnetic fields and they are slightly repelled by them. Paramagnetic materials, such as aluminium or titanium, have a small positive susceptibility and they are slightly attracted by a magnetic field. However, ferromagnetic materials possess a large positive susceptibility to external magnetic fields and they are strongly attracted to magnetic fields.

In addition, non-ferromagnetic materials have a relative permeability close to 1 and they can not be magnetised. However, ferromagnetic materials possess relative permeabilities far larger than 1 and they can retain the magnetic properties even when the magnetic field disappears. Several values of susceptibilities and permeabilities of materials employed in spacecraft structures and components are provided in Table 2.1. Typical structural materials used for spacecraft are non-ferromagnetic

Material	Magnetic susceptibility	Relative permeability	Type
Aluminium	$2.2 \cdot 10^{-5}$	1.000022	Paramagnetic
Titanium	$1.8 \cdot 10^{-4}$	1.000050	Paramagnetic
Copper	$-1 \cdot 10^{-5}$	0.999994	Diamagnetic
Iron	$2 \cdot 10^{5}$	5000-200000	Ferromagnetic
Nickel	600	100-600	Ferromagnetic

Table 2.1: Examples of magnetic susceptibility values [24].

(aluminium, titanium). The presence of ferromagnetic materials on a spacecraft generates a residual magnetic dipole. The existence of this residual dipole generates a disturbance torque that would try to align the magnetic moment of the spacecraft with the Earth's magnetic field lines. Although ferromagnetic materials are usually avoided in spacecraft design, their use is unavoidable in some functional components such as travelling-wave tubes, batteries, magnetorquers, etc. [113]. Components with a large dipole moment are usually paired to produce cancellation or even shielded. Average residual magnetic moments of spacecraft range between 0.1 and 10 A·m^2 [3, 113].

A second type of magnetic torque appears on metallic rotating objects subject to an external magnetic field. This interaction will lead to the appearance of 'Eddy Currents' within the metallic parts of the object which, in turn, will induce a magnetic moment on the target that will generate a magnetic torque [114]. Eddy currents, also called Foucault currents, are electric current loops induced within conductors subject to a time-varying magnetic field ('Faraday law of induction' [112]). Similarly, eddy current loops will appear on a rotating metallic object subject to a constant magnetic field because this field is seen as a time-varying magnetic field from a reference frame fixed to the rotating object. In contrast to the previous magnetic interaction, the eddy current torques are dissipative and they will tend to decrease the angular velocity of the object [114].

The eddy current torques can be significant for altitudes lower than 1000 km [101] and past observations have confirmed the existence of this effect [88, 89, 115]. The first papers that analyse the generation of eddy currents on spacecraft were published in 1956 [116] and 1957 [117]. These two documents analyse the torque induced on a spherical shell deriving the following formula for the induced magnetic moment,

$$\vec{m} = \frac{2\pi}{3}\sigma R^4 e(\vec{\omega} \times \vec{B}), \tag{2.22}$$

where R is the radius of the spherical shell, e its thickness, σ its electrical conductivity, $\vec{\omega}$ corresponds to the angular velocity of the object and $\vec{B}$ is the external magnetic field. In 1962 Smith published some analytical solutions of the torques induced in bodies of revolution for a certain orientation between the rotational velocity vector and the magnetic field [118]. Additional analyses on the dissipative effects in LEO were done between 1965 and 1978 [88, 114, 119].

At present, the generalised analytical formulation currently employed for the eddy current torques

is given by Equation (2.23) [95, 103],

$$\vec{m} = k(\vec{\omega} \times \vec{B}), \tag{2.23}$$

where k is defined as a constant dependant on the geometry and electromagnetic properties of the object. However, for a non-spherical object, the parameter $k = k(t)$ will also vary depending on the relative attitude of the object with respect to the external magnetic field [118, 120]. For instance, given an open cylinder rotating in the presence of a magnetic field $\vec{B}$, the k parameter needed to evaluate the induced magnetic moment will not be the same if the object is rotating about the minimum or the maximum axis of inertia [118].

Therefore, the generalised form of the induced magnetic torque (Eq. 2.23) is only valid for spherical objects where all axis are principal axis of inertia of equal magnitude and the relative orientation of the object does not alter the generation of the eddy currents. This fact underscores the absence of a generalised analytical solution of the eddy current torque.

Nowadays, numerical methods are utilised in order to evaluate the eddy current torque on spacecraft [120]. A generic finite element method (FEM) is used to describe the geometry of the object and Maxwell's equations are solved for each element of the grid. This process needs to be repeated in each time step of the integration process because the attitude of the object will vary with respect to the external magnetic field, which generates, in turn, new eddy current loops. This is a complex and computationally expensive process.

In the case of ferromagnetic materials, there is an additional dissipative effect that takes place on top of the eddy current phenomenon caused by the hysteresis. When a ferromagnetic material rotates in the presence of a magnetic field, it will experience a time-varying magnetic field and the periodic magnetisation and demagnetisation results in hysteretic energy losses [113]. In contrast to the eddy current torque, the hysteresis energy losses are independent of the spin rate. Therefore, hysteresis damping is linear instead of exponential and its relative importance increases with decreasing spin rate. The hysteresis torque over a complete period of rotation can be approximated by (2.24),

$$T_{hysteresis} = \frac{1}{2\pi} V \left(\oint H dB_i \right), \tag{2.24}$$

where V is the volume of ferromagnetic material and $(\oint H dB_i)$ is the area of the hysteresis loop, being H the intensity of the external magnetic field and B_i the induced magnetic flux.

Magnetic hysteresis rods have been used in the past for attitude stabilisation [95]. However, for reasonable rod lengths, this effect is rather weak and this attitude stabilisation method requires high masses and volumes compared to other techniques [95]. Ferromagnetic materials may be found in very low quantities in space debris objects unless the spacecraft contained magnetic hysteresis rods. Therefore, this effect should be small compared to other environmental perturbations.

2.4.2.2 Non-environmental external torques

Leaks, venting or an exhaust plume:

Non-environmental external torques can take place due to unintentional mass ejections such as leaks, venting or exhaust plume [95].

External torques due to mass ejection can also be deliberate for passivation purposes. Commonly, intentional leaks are not applicable as it would entail that the object is still functional and thus should not be considered debris. However, these leaks are highlighted here due to the fact that functional spacecraft experience a controlled outgassing at the end of life which results in a rotational motion as they become space debris.

Current space debris mitigation guidelines recommend emptying the fuel tanks of satellites and upper stages at the end of life to reduce the risk of explosions due to overpressure. In the case

of upper stages, the typical passivation sequence after spacecraft separation takes place as follows [121],

1. the stage is reoriented towards a safe direction with respect to the spacecraft orbits,

2. the stage is spun up to 45 deg/s for stabilisation purposes,

3. the outgassing of tanks through valves is carried out.

This process will lead to high rotational rates for spent upper stages in orbit which must be taken into account for ADR processes.

Space debris and micrometeoroid impact:

The impact of small space debris and micrometeoroids results in a momentum transfer which may generate a perturbing external torque. Even though the impact of micrometeoroids in reality belongs to the group of environmental torques, they are typically studied alongside space debris impacts as they produce similar effects.

Figure 2.5 depicts the probability of impact of meteoroids and space debris for different diameter sizes at low Earth altitudes (500-1000 km). The figure shows that the average fluxes of both sources are similar. The relative velocity of meteoroids with respect to objects in Earth orbit lies between 10-70 km/s while average relative velocities of orbital debris is 10 km/s in LEO and 250 m/s in GEO. This results in a more aggressive environment in low Earth orbit.
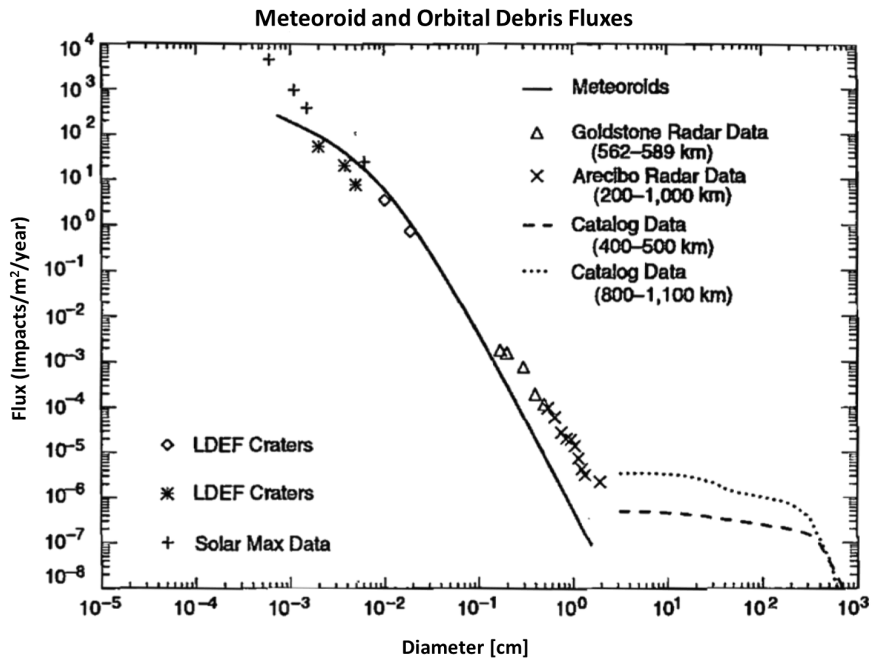
Figure 2.5: Impact probability of meteoroids and orbital debris at low altitude orbits [3].

2.4.3 Comparison of common torques in space debris objects

Figure 2.6 depicts the environmental torques in LEO generated on an active cylindrical spacecraft of 1.52 metres in diameter and 9.14 metres in length [4]. The following perturbations were analysed:

- Aerodynamic torque: The aerodynamic eccentricity considered to evaluate this torque is 1.1 m. It may be observed that this perturbation is dominant for low altitudes as predicted by the mathematical models.

- Earth's gravity gradient torque: the gravity gradient was evaluated for an angle of 1 deg between the symmetry axis of the cylinder and the Earth radius vector. It may be observed that the gravity gradient torque surpasses the aerodynamic torque above 400 km of altitude.

- Magnetic torque: The magnetic torque was computed assuming that the spacecraft has a residual magnetic dipole equal to the magnetic moment generated by a 1 A current in a single loop of wire around the length of the cylinder. Although, this is a very simplified model, it gives a first insight into the expected values of the magnetic torque. In this example, the magnetic torques are of the same order of magnitude as the gravity gradient torque. No eddy current torques are considered here due to the fact that the spacecraft is operational and 3-axis stabilised.

- Solar radiation pressure torque: A lever arm of 0.36 m was considered in order to evaluate this torque. The results show that this perturbation is two orders of magnitude lower than the gravity gradient in LEO. Moreover, for altitudes higher than 700 km, the SRP torque surpasses the air drag torque.

- Cosmic dust: The lever arm considered for this perturbation is equal to 0.36 m. The computed torque is several orders of magnitude lower than the SRP and therefore, its effect can be neglected.

It should be noted that the effects of the various environmental torques depend to a large extent on the shape, materials, orbit type and end-of-life conditions which makes it difficult to extrapolate generalised conclusions from a single object. Three different targets have been selected and are analysed throughout this dissertation which are potential candidates for an ADR mission; the Ariane-4 H-10 rocket body (R/B), the Ariane-5 EPS R/B and the Envisat spacecraft.

Within this section, the environmental perturbations on these targets are studied at different altitudes to quantify their respective effects. It should be emphasised that even though Envisat has a defined orbit, it has been analysed here for various altitudes in order to acquire a broader insight of the environmental torques.

Table 2.2 includes the physical properties assumed for each object and Figures 2.7, 2.8 and 2.9 indicate the dimensions of each object. Currently, there are more than 120 Ariane rocket bodies in orbit, primarily in Geostationary Transfer Orbit (GTO) and LEO, which pose a sizable risk to other objects in space. Both spent upper stages and the Envisat spacecraft are among the highest priority targets for ADR [42].

Parameter	Ariane-4 H-10 [6, 122]	Ariane-5 EPS [7]	Envisat [5, 123]
Dry mass [kg]	2154.0	2550.5	7827.9
COG (Ref. exit plane of the engine) [m]	[0.004, 0.028,4]	-	[0.003,0.009,3.905]
Ppal. Inertias [kg·m^2]	$I_{xx} = 28000$, $I_{yy} = 28000$, $I_{zz} = 3000$	$I_{xx} = 11148$, $I_{yy} = 8058$, $I_{zz} = 6479$	$I_{xx} = 129180$, $I_{yy} = 124801$, $I_{zz} = 16979$
Size [m]	Length 11.2, Max. diameter 3.9	Length 4.6 Max. diameter 5.4	Service mod. 10×4×4, Solar panel 5×14
C_D	2.3	2.3	2.3
Angular vel. [deg/s]	10	10	10

Table 2.2: Physical properties of the Envisat spacecraft and the Ariane-4 H-10 and Ariane-5 EPS upper stages.
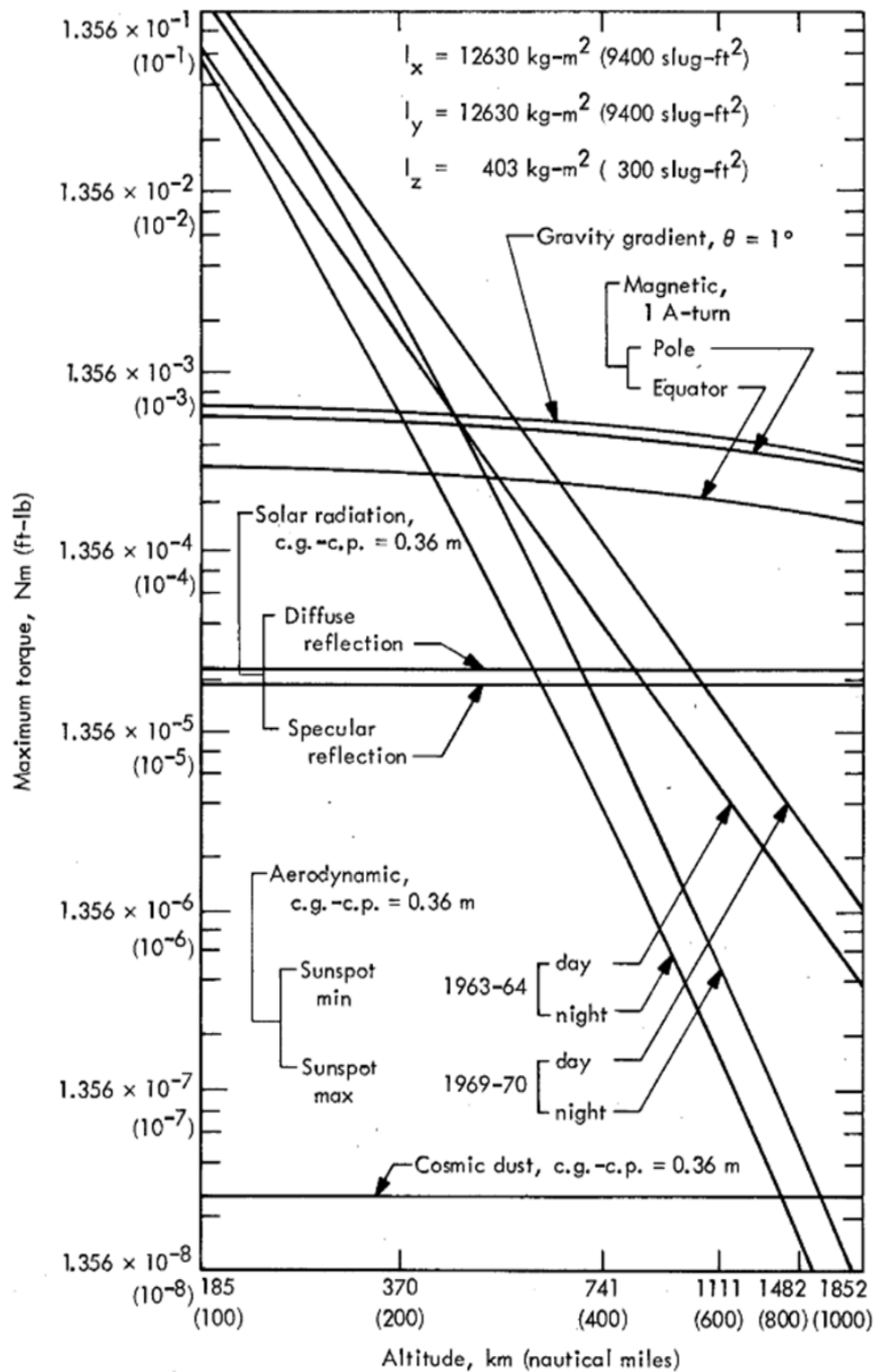
Figure 2.6: Relative magnitudes of the environmental torques for a cylindrical satellite in LEO [4].
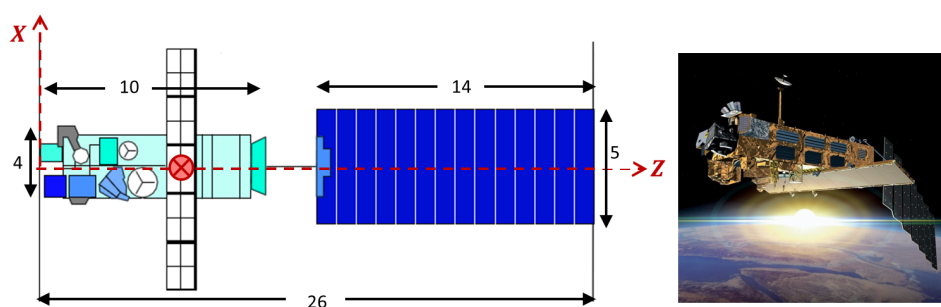
Figure 2.7: Envisat spacecraft dimensions (in metres) [5].
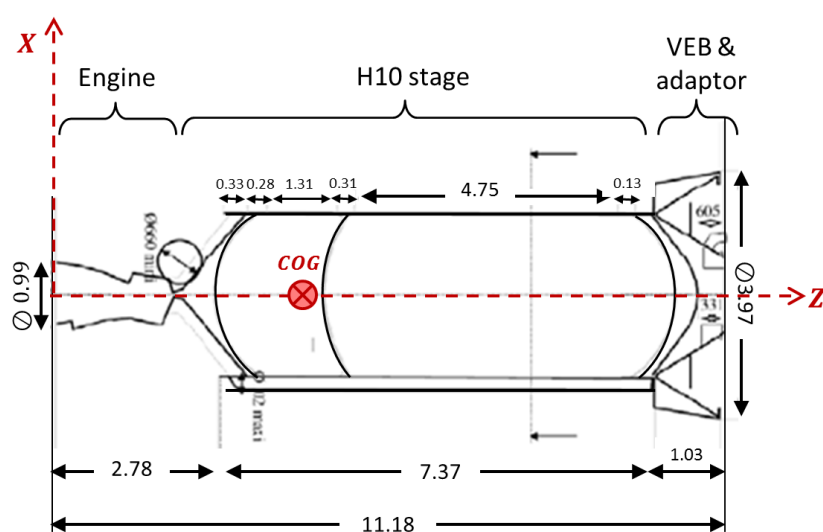
Figure 2.8: Ariane-4 H-10 upper stage dimensions (in metres) [6].
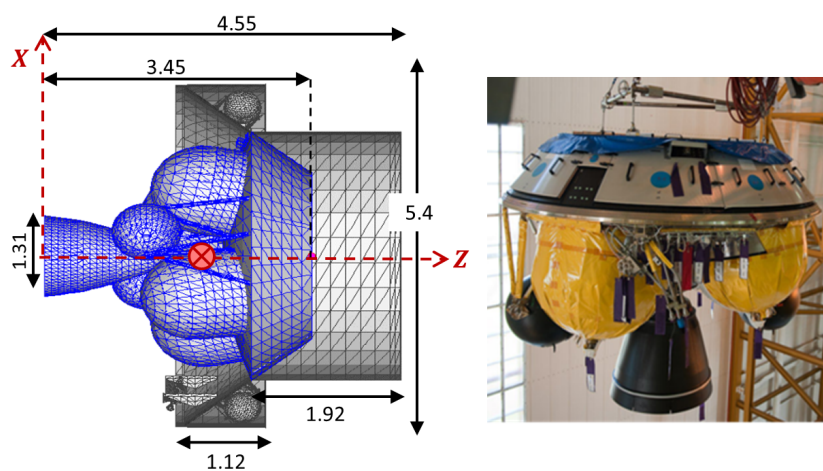
Figure 2.9: Ariane-5 EPS upper stage dimensions (in metres) [7].

Figures 2.10 and 2.11 depict the major environmental torques that affect the Ariane R/Bs and the Envisat spacecraft at different altitudes. All the assumptions made in order to model each environmental torque are explained subsequently.

- Aerodynamic torque: With respect to the aerodynamic torques, typical drag coefficients range between 2 and 2.6 [4, 95] and a value of $C_D = 2.3$ has been adopted. For the computation of the projected area of the object incident to the air flow, an average value between the maximum and the minimum exposed surfaces has been taken into account. In addition, the air drag lever arm for the Ariane-4 R/B and Envisat has been modelled as the distance between the COG of each spacecraft and the geometrical centre of the object [4, 95]. In the absence of this specific information (i.e. for the Ariane-5 R/B), it is recommended to approximate the aerodynamic eccentricity as one third of the spacecraft's maximum dimension [4]. Moreover, the atmospheric density has been computed using the Jacchia 1970 model for low solar activity (F10=70, Ap=0) and high solar activity (F10=250, Ap=25) [124].

- Earth's gravity gradient torque: The gravity gradient torque was computed assuming a certain deviation from stable equilibrium. To this end, two different angles between the local vertical and the minimum axis of inertia have been considered equal to 1 and 10 degrees.

- Solar radiation pressure torque: In order to analyse the SRP, a different approach has been taken for each object. For the Ariane-4 and the Ariane-5 R/Bs, the projected area exposed to the Sun and the SRP lever arm have been computed using the same approach that was performed for the air drag. For the Envisat S/C, it has been assumed that the SRP torques are caused primarily by the solar panel. The ASAR antenna is approximately located at the COG of Envisat and therefore, its contribution to the torque is neglected. The area exposed to the Sun has been taken as the overall area of the solar panel and the lever arm has been computed as the distance between the geometrical centre of the solar panel and the COG of the S/C. Furthermore, two different cases have been analysed, a full specular reflection ($f_s = 2$, $f_d = 0$) and a full diffuse reflection ($f_s = 0$, $f_d = 1.3$) [25].

- Eddy current torque: The eddy current torques have been modelled using the Magnetic Tensor Theory (MTT) developed in Chapter 3. The magnetic tensor for Envisat is obtained in Section 3.5 and the magnetic tensors for the Ariane-4 and the Ariane-5 upper stages are obtained in Sections 5.8.4.2 and 6.3.3 respectively. In addition, an average angular velocity of 10 deg/s has been adopted for all the objects and the torques have been evaluated at the Equator and the poles which are the most favourable and adverse cases. The Earth's magnetic field has been modelled based on the International Geomagnetic Reference Field IGRF-11 [125].

- Residual magnetic moment: Moreover, the magnetic torque caused by the existence of a residual magnetic moment has been computed. In this case, the magnetic field has been considered at the poles and two different residual magnetic dipoles have been analysed; 0.1 and 10 A·m^2.

The subsequent analysis is inspired by the results provided in Figure 2.6 [4]. However, the following results shown in Figures 2.10 and 2.11 are improved by analysing three different representative space debris objects instead of a metallic cylinder which is a very simplified spacecraft model. Moreover, a more in depth analysis is done for the magnetic torques as they are divided into the eddy current torque and the residual magnetic dipole torque. In addition, the torque caused by the cosmic dust is not included hereinafter because its effect is negligible in the near-Earth region compared to other environmental torques [4].

The results obtained for low Earth orbits (see Fig. 2.10) show that the gravity gradient torque is likely to be the dominant perturbation for altitudes above 600 km. Between 400 to 600 km, the air drag torques and the gravity gradient torques may be of the same order of magnitude while the atmospheric drag is usually the dominant effect below 400 km.

In the case of the Ariane-4 R/B, the eddy current torques are one order of magnitude higher than the SRP torques in LEO while the opposite happens for the Ariane-5 and Envisat. The Ariane-4 contains a larger amount of metallic material than the other two objects which explains this

difference.

The importance of the perturbations derived from the existence of a residual magnetic moment show a high degree of uncertainty although the average value tends to be lower than the rest of the perturbations.
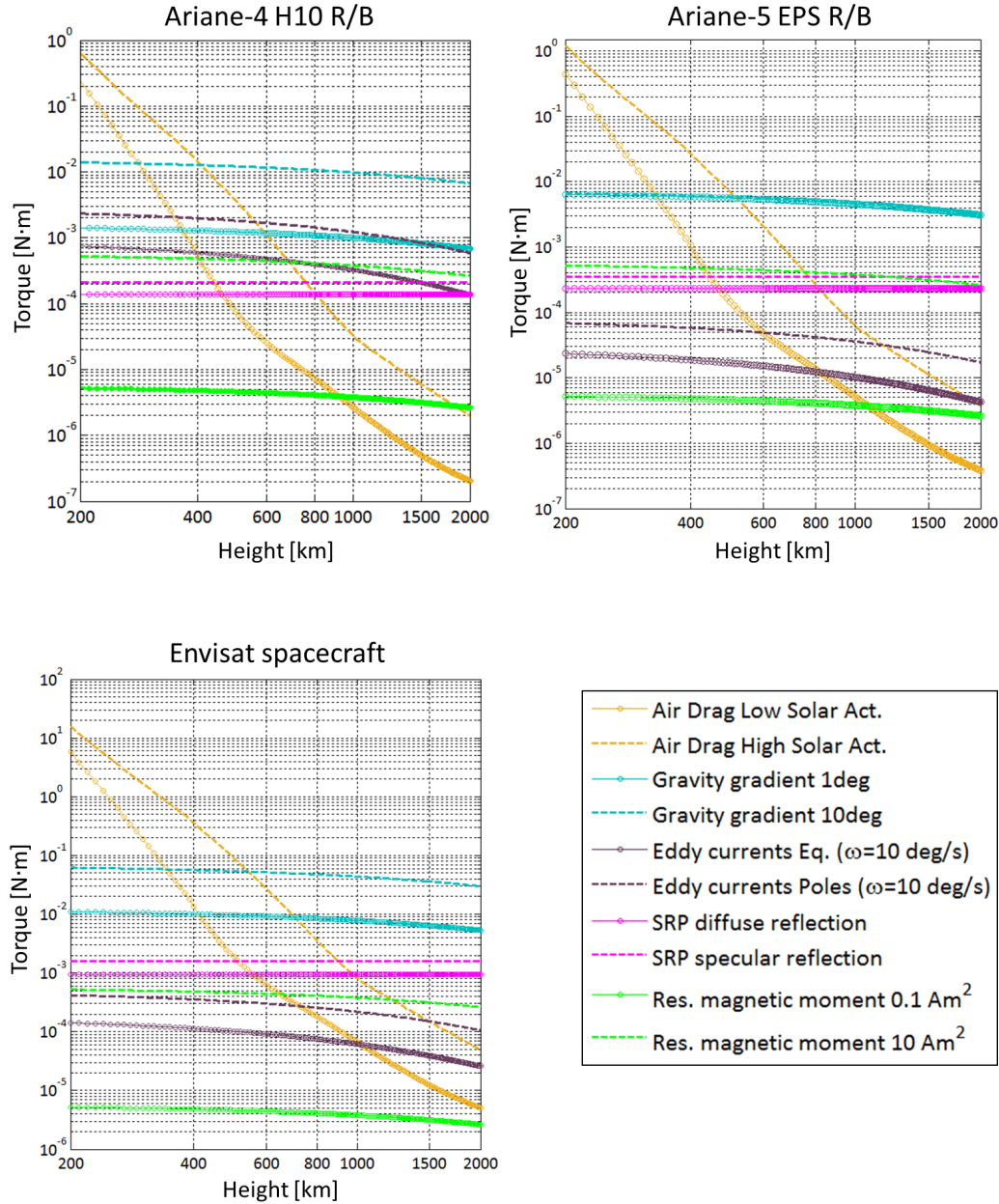
Figure 2.10: Major environmental torques on the Ariane-4, Ariane-5 R/Bs and Envisat in LEO.

The results obtained for higher altitudes are shown in Figure (2.11). Above 2000 km, the effect of the atmospheric drag can be neglected and the effect of the Earth's magnetic field also decreases very fast with the increasing height. At geosynchronous altitudes, the effect of the SRP gains importance and it can become the dominant perturbation. Again, the effect of a possible residual magnetic moment shows a great degree of uncertainty but, in general, it will be several orders of magnitude lower than the gravity gradient and the solar radiation torque.
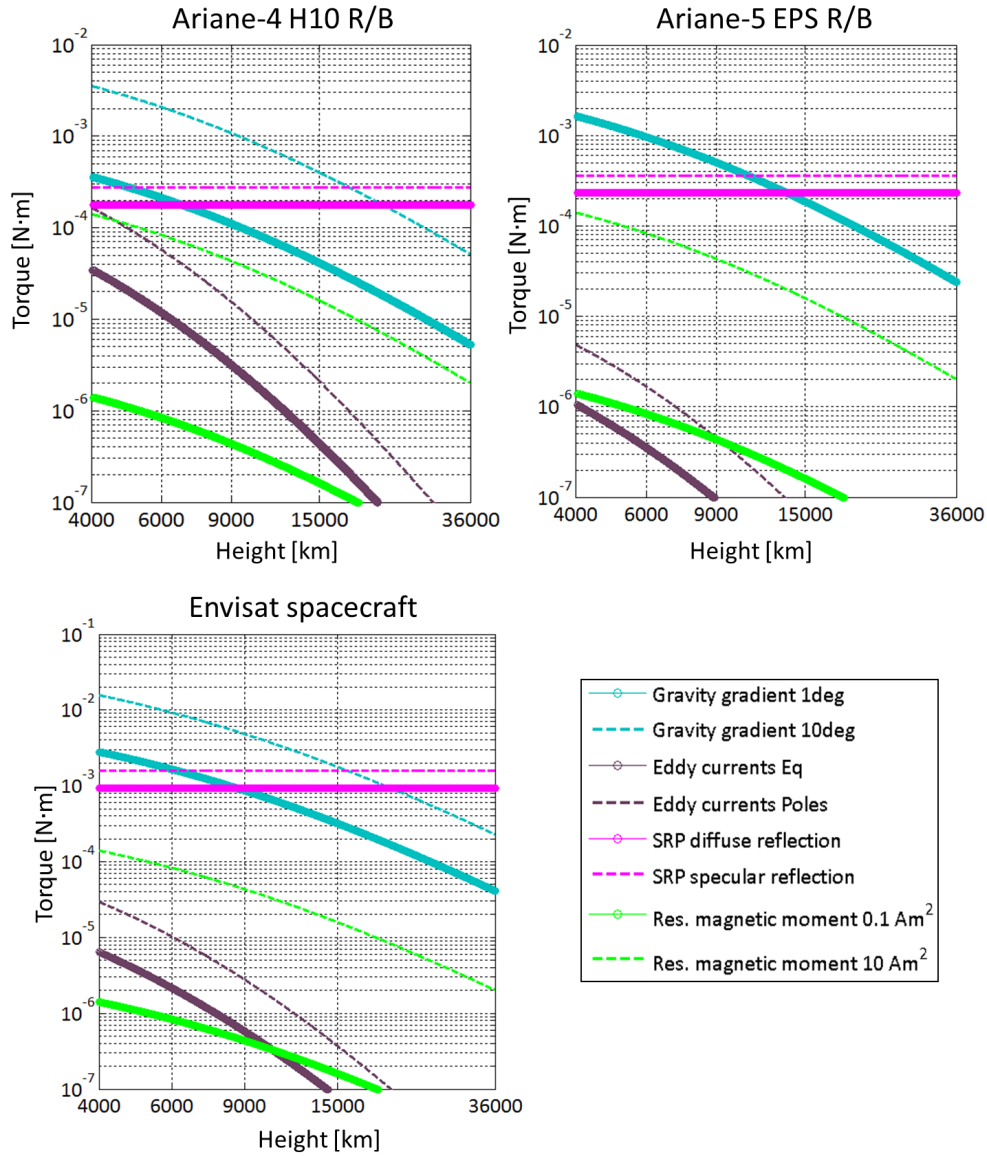
Figure 2.11: Major environmental torques on the Ariane-4, Ariane-5 R/Bs and Envisat in MEO and GEO.

2.5 De-tumbling methods

As explained in Section 2.1 contact ADR methods have poor robustness with respect to the rotational dynamics of the debris object. The observed spin rates of objects in orbit range between few deg/s up to many tens of deg/s while contact ADR methods are able to control objects that have a maximum spin rate of a few degrees per second or even lower depending on the capturing process [8, 45, 58]. Moreover, further research is needed in the modelling of the internal and external torques that affect space debris objects in order to explain many of the unresolved attitude observations and to be able to predict accurately their future evolution. However, there are various effects which are difficult to model and predict such as unexpected leaks, venting, sudden switching on and off of ACS equipment on-board, uncertainties in the existence of fuel inside the propellant tanks which would generate sloshing effects, geometrical changes of units which are not fixed or have flexible components or the impact of micrometeoroids and orbital debris.

The high degree of uncertainty in the attitude long term predictions necessitates the development of a robust ADR process that can handle potentially high rotation rates. A de-tumbling phase prior to the capturing phase may be necessary for this purpose.

Existing de-tumbling options can be divided into *contact* and *contactless* methods.

2.5.1 Contact de-tumbling methods

Contact de-tumbling methods may be based on the application of repeated mechanical impulses. These impulses can be achieved with projectiles propelled from a service satellite [126]. Both numerical and ground experiments have been carried out to prove the feasibility of the method [127]. However, this process poses some challenges. First of all, these impulses need to be very accurate in terms of the position of the application force as well as the transmitted impulse and this is difficult to model due to uncertainties in the friction and collision effect [126]. Secondly, the impulse received by the target will modify its orbit and the service satellite will also move backward as a reaction of propelling projectile. Therefore, the distance between the target and the service satellite needs to be controlled. In addition, the target's angular velocity can not be reduced below a certain limit due to the inaccuracies of the process and there exists the risk of increasing it due to misalignments of the off-axis forces. Finally, there is a risk of damaging the target due to the impact and the ejected projectiles will turn into new orbital debris unless they stay attached to the object after the impact [126].

A different contact de-tumbling method consists in the use of a 'brush type contactor' placed at the tip of the robotic arm [8]. A prototype of this brush contactor is shown in Figure 2.12. This device decelerates the target by tapping its surface until its angular velocity is low enough to be captured by the robotic arm. Simulated results show that an object of 500 kg rotating at 3 deg/s can be slowed down by a 10% within 7 seconds using this method [8].
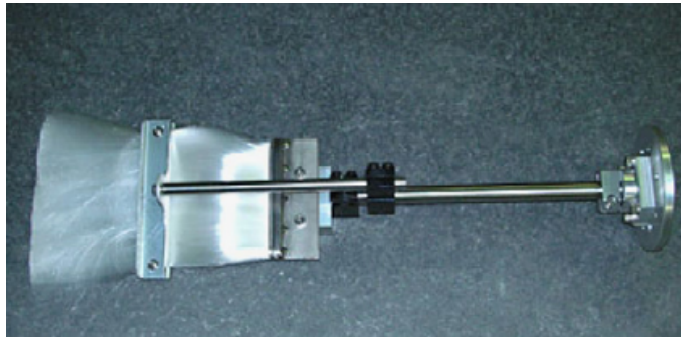
Figure 2.12: Prototype of brush contactor [8].

Additional contact de-tumbling methods are based upon the attachment of a de-tumbling kit [128, 129]. The kit could consist in a propulsive device that once attached would generate torques thanks to the forces exerted by the thrusters [128, 130]. It has also been proposed that the kit could interact with the Earth's magnetic field by generating a magnetic moment that will tend to align itself with the magnetic field lines of the Earth. The device should have its own power source and it could consist of magnetorquers [129] or electromagnetic coils [128]. In this case, the de-tumbling process could only take place in LEO where the Earth's magnetic field is noticeable. The main challenge of these methods is actually the attachment process which could be achieved by using harpoons or by the kit itself which should dock with the target object. For instance, the de-tumbling kit could be a propulsive module which flies autonomously from the chaser to the target and attaches itself to the target [129]. The major threat of contact de-tumbling methods is the risk of collision during the challenging proximity operations with a non-cooperative rotating object. Thus, this issue has incentivised the research on alternative de-tumbling methods that avoid these operations.

2.5.2 Contactless de-tumbling methods

Contactless de-tumbling methods avoid complex proximity operations and therefore, reduce the hazards of collision.

2.5.2.1 Plume impingement

One of the proposed methods is based on the interaction of a thruster's plume with the surface of the target (see Figure 2.13). This could be done by means of a chemical propulsion system [9, 131, 132] or an electrical propulsion system [9, 69]. It is important to take into account that the servicer needs to add a balance thruster on the opposite side to compensate for the effect of the blowing thruster. This method has the advantage that it has a high Technology Readiness Level (TRL) as both chemical an electrical thrusters are conventional equipment used in space missions. Various simulations carried out by GMV S.L. show that a large object such as Envisat can be decelerated from 5 deg/s to 0.5 deg/s in terms of hours with chemical propellant, by placing the chaser at a distance of 20 meters from the target and consuming approximately $\Delta V = 50$ m/s [132]. Nonetheless, it should be noted that a favourable rotation was assumed so that the thruster could be pointed at the solar panel [132]. Electrical propellant has a higher specific impulse and therefore, the propellant consumption would be lower at the expense of increasing the de-tumbling time. In this case, the de-tumbling process could last for a few days [9].

The success or failure of this de-tumbling method is based upon the ability to be able to generate adequate off axis forces in order to produce damping torques. This requires an accurate knowledge of the physical properties of the object (e.g. mass, COG and inertias). Moreover, the efficiency of this method will rely upon the geometry of the surfaces (e.g. flat, curved) and the inertias of the object [132]. Adequate objects for this method are highly asymmetrical objects with flat surfaces (e.g. solar panels) whereas the process is less efficient for symmetrical objects with curved surfaces.
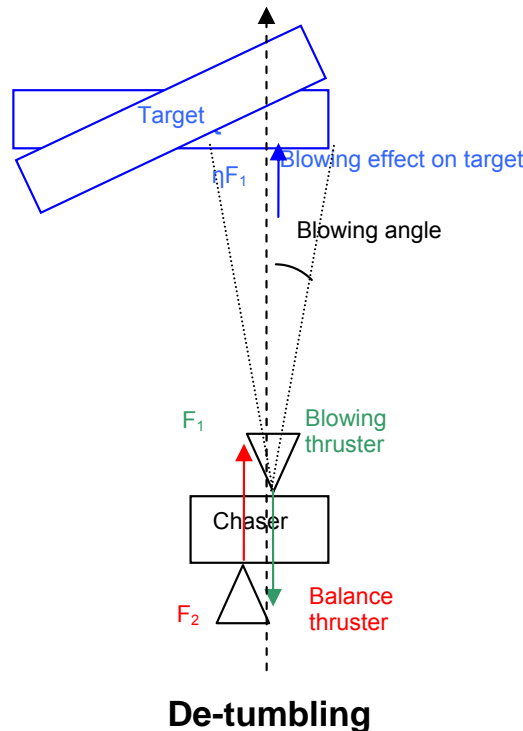
Figure 2.13: De-tumbling by plume interaction [9].
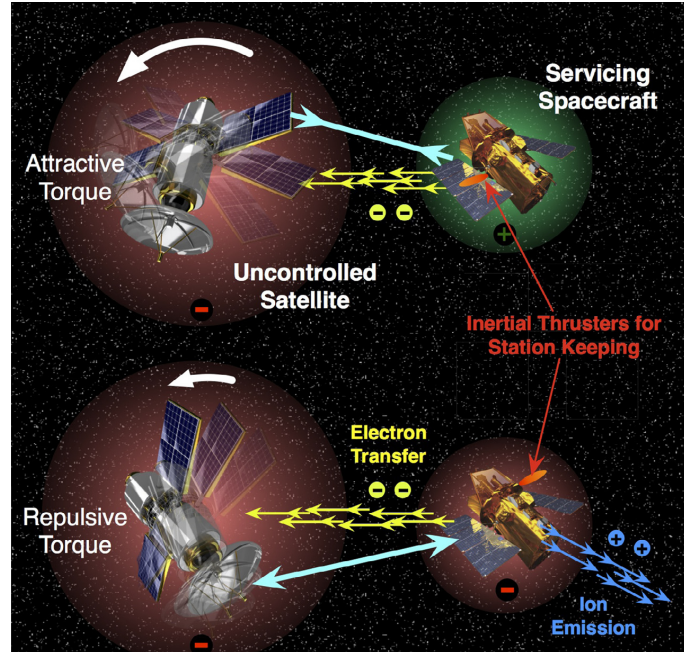
Figure 2.14: Contactless electrostatic de-tumbling [10].

2.5.2.2 Electrostatic torques

Furthermore, a touchless de-tumbling concept based on electrostatic forces has been investigated [10, 133]. The interaction arises from Coulomb forces between electrically charged spacecraft (see Figure 2.14). This is achieved by actively charging the target with an electron or an ion gun [10]. The de-tumbling process can take place at a relative distance of 3-4 spacecraft radii ($\sim 10 - 20$ metres) and the de-spinning of a large spacecraft (~ 1000 kg) initially rotating at 5 deg/s can be achieved over a period several weeks [10].

However, this de-tumbling process has several disadvantages. First of all, its application is restricted to geostationary orbits where the Debye length is in the order of tens of meters. The Debye length indicates how far the electrostatic effects of a charged object immersed in a plasma environment persist. Every Debye-length, the electric potential of a charged object will decrease by a factor of $1/e$ [134]. In LEO, the Debye length is in the order of centimetres which unfortunately impedes the use of this method at those altitudes.

Secondly, the de-spin concept is based on the generation of off-axes forces which will, in turn, generate torques. These forces are generated assuming a varying charge distribution throughout the body. This way the chaser spacecraft will attract the closest receding feature of the target and repel the closest approaching feature [133]. However, the analyses carried out assume that the debris object is fully conducting, thus ensuring a uniform potential throughout the object. In addition, if the target contains an axis of symmetry, the electrostatic torques about this axis are impossible [10] which results in an incomplete reduction of the object's total momentum. Consequently, spherical objects can not be de-tumbled with this method unless differential potentials across the surface can be generated.

Meanwhile, a net attractive or repulsive force will appear between the two objects and it must be continuously counteracted throughout the process. Finally, the potential difference between the chaser and target can not exceed a certain limit to avoid electron backflux to the chaser. This creates a limit in the maximum de-tumbling torques that can be generated.

2.5.2.3 Laser ablation

Another contactless de-tumbling method, studied in the past to de-spin asteroids, is based on laser ablation techniques [135, 136]. This process consists in irradiating a certain area of the debris with a high intensity light source. The illuminated spot sublimates and generates an ejecta plume. This ejecta acts as a propulsive force. The rotational motion of the debris can be controlled by off-setting the generated force with respect to its centre of mass.

The main disadvantage of this method is the generation of additional space debris particles due to the ablation. Moreover, the ejecta plume can contaminate the solar panels on the chaser spacecraft and reduce the efficiency of the method. For the nominal selected distance of 50 metres and characteristic time of the process in the order of days/weeks, the contamination effects are assumed to be negligible.

Furthermore, an off-axis force with respect to the targets COG will generate not only a torque used to de-tumble the object but also a force that accelerates the target. Thus, the chaser will experience the same acceleration in opposite direction and adequate control manoeuvres are necessary.

The method is very effective for targets with flat surfaces but the efficiency of the method decreases for curved surfaces. A simulation carried out to control a Envisat-like satellite of parallelepiped shape rotating initially at 3.5 deg/s, could be de-spun to 1 deg/s in 2 days while the same satellite with cylindrical shape could be de-spun in 14 days [136].

2.5.2.4 Magnetic torques

Additional contactless de-tumbling methods have been proposed which exploit the interaction of a magnetic field with the target.

In 2012, a new method was suggested that is based on the interaction of a induced magnetic field created by the chaser with the residual magnetic dipole of the target object, referred to as NOMAD concept [137]. The main idea is to generate off-axis forces thanks to the dipole to dipole interaction. However, several assumptions have been made which are too optimistic. First of all, average residual magnetic moments of objects in orbit range between 0.1 and 10 A·m^2 [3, 113] while a value of 300 A·m^2 has been assumed in the NOMAD study [137]. Moreover, the magnetic dipole moment is a vector inherent to the object and it will have a fixed direction with respect to the defunct satellite. Therefore, the directions to the dipole to dipole forces and the torques are a priori unknown and it may be difficult to generate torques that will oppose the angular velocity vector of the target object.

Another concept that exploits the external magnetic fields is based on the generation of eddy currents. A metallic rotating object immersed in an external magnetic field will induce an electromotive force (EMF) which in turn, leads to the appearance of electric current loops named as '*Eddy Currents*'; explained by Faraday's law of induction [111, 112]. In addition, these currents will generate a secondary magnetic field that opposes the external magnetic field and this creates a drag force that opposes the movement of the object (Lenz's law [111, 112]). The consumed kinetic energy in overcoming this drag force is dissipated as heat due to Joule's law.

This process can be done actively by a chaser spacecraft which has a magnetic coil on-board. This idea was first introduced by Kadaba and Naishadham in 1995 [11, 138]. Within this work, two possible designs were investigated. The first option consists in placing a large diameter current loop around the target and the second option uses a U-shape permanent magnet placed closed to the target (see Figure 2.15). The first design tries to take advantage of the fact that the magnetic field generated by an electromagnetic coil is highest at its centre. The coil has a diameter of ten metres and it is made of aluminium. However, the power requirements drives the necessity to employ a cooling jacket with liquid nitrogen to decrease the resistivity of the aluminium and the overall weight and power requirements of this first design are 362 kg and 1.1 kW. The U-shaped electromagnet total weight is 365 kg and it requires a power of 1 kW. For this second design, the target is placed at a relative distance of 0.5 metres which is very challenging. The de-tumbling

system is able to decrease the angular velocity of the fully conductive cylinder from 60 deg/s to 2 deg/s within 1 hour. However, the mass and power requirements are extremely demanding for a payload subsystem on-board a spacecraft [3].
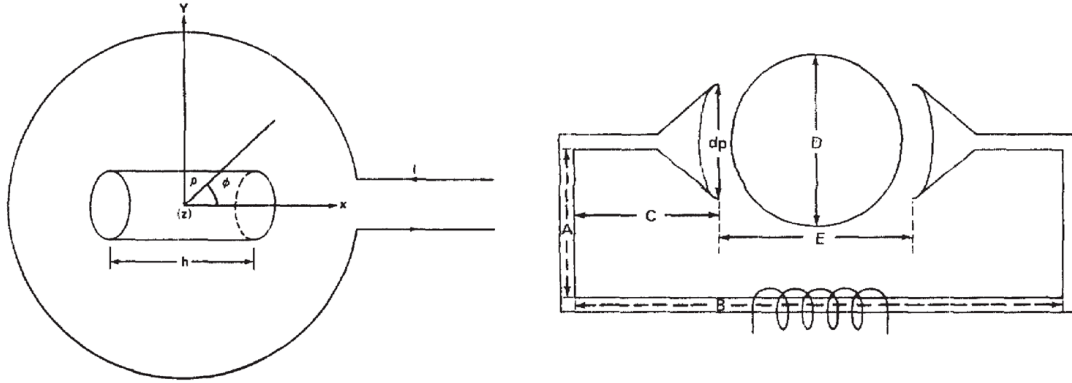
Figure 2.15: First designs for a de-tumbling method based on eddy currents [11].

Little work has been carried out since this concept was initially introduced. An article published in 2012 by Sugai et al. [12, 139] recovered this idea and presented a new design of a chaser spacecraft with two robotic arms and two small magnetic coils attached at the tip of the robotic manipulators (see Figure 2.16). The coils are placed on opposite sides of the space debris object in order to generate forces in opposite directions that will cancel each other and only generate a reaction torque.

The first challenge that appears is the fact that the robotic manipulators may need to continuously move for complex nutational motions in order to keep a constant distance between the target surface and the coil [12]. Secondly, very long robotic manipulators would be needed for large targets such as Envisat. Furthermore, the relative distances considered between the target and the coil are in the order of a few millimetres which poses very stringent requirements for the proximity operations [12].

1, Detumbling   2, Reducing spin rate   3, Capturing
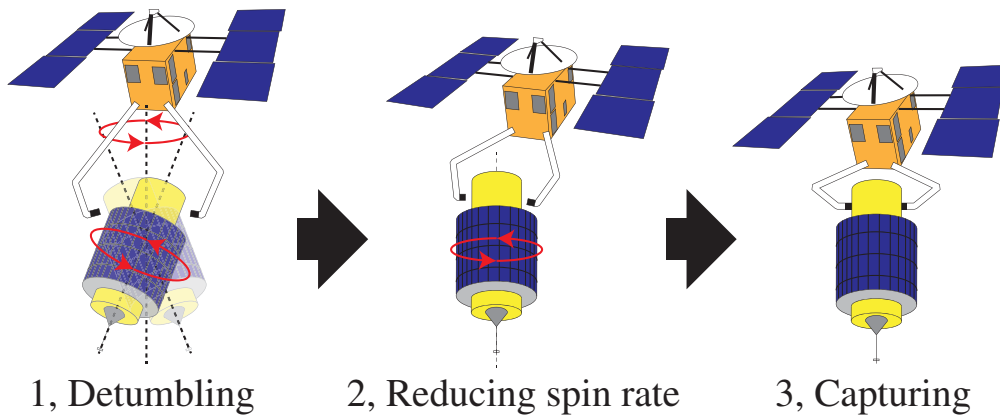
Figure 2.16: Proposed de-tumbling method based on the generation of eddy currents [12].

A de-tumbling method based on the generation of eddy currents seems promising but the amount of research carried out on this topic is very scarce.

The most important advantages are:

- <u>Contactless method</u>: this eliminates the hazards associated with complicated proximity operations and docking/grabbing of a non-cooperative rotating object.

- <u>Non-invasive technique</u>: the risk of generating new debris is very low. The decrease of the angular velocity occurs gradually thanks to Joule's effect that dissipates the kinetic energy of the object into heat. Therefore, this method is less aggressive for the target object than other de-tumbling methods which generate impulsive forces that can damage the object or that are based on the sublimation of the surface material.

- <u>Target's angular velocity control</u>: The eddy current torques will always oppose the angular velocity of the object, thus, there is no risk of increasing its spin rate. Moreover, the control of the target's angular velocity is easier with this method than those based on the generation of off-axis forces which need to know precisely the angular velocity vector, the target's COG and inertias.

However, there are some constraints in the former magnetic de-tumbling methods which hamper their implementation:

- <u>Mathematical models</u>: There is not a generic analytical formulation to evaluate the eddy current torque and the exiting numerical models are complex to implement and computationally expensive. This issue hinders the analysis of the de-tumbling process. The geometries and materials considered in previous analyses are too simple and not representative of the wide variety of materials and shapes of space debris objects.

- <u>Mass requirements</u>: The previous designs of the coil employ conventional materials which require high masses, in the order of hundreds of kg [11], in order to design a compelling system.

- <u>Power consumption</u>: A coil design based on conventional materials also leads to high power consumptions, in the order of kW [11], which makes this de-tumbling method less attractive than other de-tumbling methods.

- <u>Relative distance</u>: The eddy current torque is inversely proportional to the square of the distance, therefore, the efficiency of this method decreases with the chaser-target distance. The proposed designs consider very small relative distances which are in line with the performance of their coil designs; half a metre in the first design (Figure 2.15) and in the order of millimetres in the subsequent design [12]. These distances are very challenging to implement in orbit and lead to high collision risks.

2.5.3 De-tumbling methods comparison

Table 2.17 summarises the existing de-tumbling methods for ADR. A colour code is used to indicate if the specified property is bad (red), medium (orange) or good (green).

Every method has its restrictions and limitations depending on the target's shape, materials, orbital altitude and rotational motion and there is not a single method that clearly stands out as the best solution.

Method	Angular velocity limit	Rotation control	Time	Relative motion	Relative distance	Risk of damaging target	Risk of collision	Orbit	Target type
Robotic arm	Upper limit few degrees per second	Good	Minutes	Zero relative angular velocity needed	Direct contact	Risk of fracture depends on grabbing point	Risks associated with the docking or grabbing phase	All	All
Projectiles impact	Lower limit due to inaccuracy of the impulse	Difficult	Minutes	Target will change position due to the impulse and chaser will receive a reaction force	No limits	The impact could damage the target. The projectiles may turn into new debris	Low	All	All
Attach propulsion device	Limit given by the amount of propellant	Good	Minutes	Complicated proximity operations to attach device	Direct contact needed	It will depend on the attachment process	Risks associated with the docking or grabbing phase	All	All
Attach magnetic rod	Component parallel to the Earth's magnetic field is not damped. (at least two perpendicular devices needed)	Good	Days/ weeks	Complicated proximity operations to attach device	Direct contact needed	It will depend on the attachment process	Risks associated with the docking or grabbing phase	Only in LEO	All
Plume impingement	No upper or lower limits	Control off-axis forces needed	Hrs/Days	Balance thruster needed on chaser	Nominal distance 5-50 m depending on the object	Low	Low	All	Less efficient curve surfaces
Laser	No upper or lower limits	Control off-axis forces needed	Days/ weeks	Relative forces of repulsion need to be counteracted	Large distances needed to avoid contamination (nominal 50 m)	Laser ablation generates additional debris particles	Low	All	Less efficient curve surfaces
Touchless electrostatic	Electrostatic torques about an axis of symmetry are impossible.	Good	Days/ weeks	Relative forces of attraction/repulsion need to be counteracted	Efficiency decreases with distance (10-20 m)	Low	Low	Not in LEO	Fully conducting object. Non-symmetrical
Former magnetic de-tumbling	No upper or lower limits	Good	Minutes/ hours	Relative forces need to be counteracted.	Millimetres - 0.5 metres	High for such low relative distances	High for such low relative distances	All	Conducting material needed

Figure 2.17: Comparison of de-tumbling methods.

2.6 Chapter summary

At present, various detrimental consequences are taking place due to the proliferation of space debris which affect both ground-based and the space-based infrastructures. In 2009, the IADC concluded that the combination of mitigation techniques to reduce the risk of explosions and collisions together with post mission disposal measures are not enough to prevent the space debris population from growing and that more aggressive remediation techniques such as ADR processes should to be adopted. Consequently, the challenges of removing a non-cooperative target from its orbit need to be addressed. Among them, there are the strong limitations of contact ADR methods with respect to the angular velocity of the target. This constraint implies the need for accurate measurements and reliable long term predictions of the rotational motion of space debris objects. These analyses will determine the feasibility of a given ADR method to capture a specific object and whether it is necessary or not to employ a de-tumbling system.

The observations carried out in LEO, MEO and GEO show a wide variety of spin rates that range from < 1 deg/s up to few hundreds of deg/s. In spite of the fact that the metallic objects are expected to be decelerated by the induced eddy currents in LEO, some of the objects exhibit high spin rates in this orbital region several decades after their launch. The causes of many of the observed spin rate evolutions are still unknown, such as occasionally observed multiple rapid accelerations, which underscores the lack of knowledge of the scientific community on this matter.

The existing mathematical models used to characterise the rotational dynamics of space debris objects distinguish between internal and external torques. There are numerous consolidated models that characterise the main environmental external perturbations. The degree of importance of each environmental perturbation depends on the type of orbit, the geometry and the materials of the spacecraft as well as its end-of-life conditions. Nevertheless, the unresolved attitude observations are typically attributed to various effects which are difficult to model and predict such as unexpected leaks, venting, sudden switching on and off of ACS equipment on-board, uncertainties in the existence of fuel inside the propellant tanks, geometrical changes of units which are not fixed or have flexible components or the impact of micrometeoroids and orbital debris.

Moreover, special attention was given to the eddy current torque induced by the Earth's magnetic field. At present, a generalised analytical formulation for the eddy current torque does not exist and the current numerical methods are long-winded and computationally expensive. The motivation to find a simpler way to analyse the eddy current phenomenon together with the current need to better model the long term rotational evolution of space debris is the first driver for this research.

In addition, the high degree of uncertainty in the long term predictions necessitates the development of a robust ADR process that can handle potentially high rotation rates. A de-tumbling phase prior to the capturing phase may be necessary for this purpose and various de-tumbling options have been proposed. Nevertheless, each option exhibits various restrictions depending on the shape, materials, orbital altitude and rotational motion resulting in the fact that no de-tumbling method outstands in terms of simplicity of versatility with respect to the others.

An active contactless de-tumbling method based on eddy currents seems promising but the amount of research carried out on this topic is very scarce. The main advantages of this method stem from its contactless non-invasive nature, which allows the target's angular velocity to be easily controlled compared to other methods. However, the past designs require a high mass, high power consumption and a low relative distance which makes this de-tumbling process less attractive.

Great progress has been made since 1995 in space sensors and actuators as well as materials employed for electromagnetic coils which facilitate the design of a more compelling magnetic de-tumbling system. In order to investigate this method, a suitable mathematical model must be first developed in order to outcome the weaknesses of the current analytical and numerical methods and this is tackled in Chapters 3 and 4. Furthermore, its applicability to satellites must be addressed, including a proper systems engineering design and a thorough analysis of the dynamics of the chaser-target system which are addressed in Chapters 5 and 6 respectively. The gap in this line of research together with the current need for investigating new de-tumbling methods for ADR has been the second driver for this research.

THREE

MAGNETIC TENSOR THEORY: FUNDAMENTAL THEORY

3.1 Introduction

Active debris removal methods will become a reality in the coming decades. Measurements and predictions of the rotational dynamics of defunct objects is of paramount importance to design an appropriate ADR method than can handle the target's spin rate. However, some of the rotational behaviours observed from ground remain unexplained which highlight our lack of knowledge in this domain.

One of the fundamental perturbations that affect objects in orbit is the Earth's magnetic field which generates torques and, therefore, modifies their rotational motion. When a conductive body moves in the presence of a magnetic field, electric currents appear on the conductive body which describe close loops. These currents are known as *eddy currents*. Current numerical models used for the analysis of eddy current require complex and computationally expensive processes which are usually replaced by existing analytical formulations of the eddy current torque. However, these analytical formulations exist for very few geometries and they are only valid for specific orientations of the object with respect to the magnetic field and its angular velocity vector. In addition, many references present a generic analytical formulation of the eddy current torque from one obtained for a spherical shell [95, 103] which is not valid for other geometries. In order to address these limitations and derive an improved method it is first necessary to present the fundamental laws and equations that govern eddy current induction.

3.2 General theory

In 1830, Faraday discovered that electricity and magnetism are two aspects of the same phenomenon, referred to as electromagnetism [140]. Prior to 1830, the only known way to generate an electric current flow was to connect the ends of a conducting wire to the positive and negative terminals of a battery. The electromotive force, e.m.f or voltage, denoted by $\mathcal{E}$, is the ability of the battery to push current down the wire. The e.m.f is the difference in electric potential energy between two points per unit electric charge and it admits the representation given by Equation (3.1),

$$\mathcal{E} = \int \vec{E}\vec{dl}, \tag{3.1}$$

where $\vec{E}$ is the electric field and $\vec{dl}$ is the displacement vector along the conductor. If a closed loop wire C (with no battery) is considered, then the electromotive force is zero,

$$\mathcal{E} = \oint_C \vec{E}\vec{dl} = 0. \tag{3.2}$$

However, Faraday discovered that a close loop of wire subject to a time-varying magnetic field would cause a current to flow around the wire. He also found out that an electric current appeared when the magnetic field was kept constant and the loop of wire was moved inside the field. These electric currents are called *'eddy currents'* or *'Foucault currents'*. Thanks to his experiments he could postulate that;

- when the magnetic flux changes through a conductive circuit, an electromotive force (e.m.f) is induced,

- the magnitude of the e.m.f. is proportional to the variation of the flux.

In addition, according to *Lenz's law* (3.3), postulated in 1834, the direction of the induced e.m.f. $\mathcal{E}$ is such that the induced current opposes the variation of the magnetic flux φ [140],

$$\mathcal{E} = \oint_C \vec{E}\vec{dl} = -\frac{\partial}{\partial t} \int_S \vec{B}d\vec{S} = -\frac{d\varphi}{dt}, \tag{3.3}$$

where $\vec{B}$ is the external magnetic field and S is a generic surface attached to the close loop C.

Applying Stokes' theorem to Equation (3.3), we reach Maxwell's generalisation of Faraday's law (3.4):

$$\nabla \times \vec{E} = -\frac{\partial \vec{B}}{\partial t}, \tag{3.4}$$

Faraday's law (3.4) is valid whatever the reason for the change in the magnetic flux. It can be a variation of the field itself or a motion of the conductor through a constant magnetic field [111].

In general, the laws of electromagnetism can be written as four field equations, named as *Maxwell's equations* [140]:

$$\nabla \cdot \vec{E} = \frac{\varrho}{\epsilon_0}, \tag{3.5}$$

$$\nabla \cdot \vec{B} = 0, \tag{3.6}$$

$$\nabla \times \vec{E} = -\frac{\partial \vec{B}}{\partial t}, \tag{3.7}$$

$$\nabla \times \frac{\vec{B}}{\mu_0} = \vec{j} + \epsilon_0 \frac{\partial \vec{E}}{\partial t}, \tag{3.8}$$

where $\epsilon_0 = 8.854 \cdot 10^{-12}$ F·m^{-1} is the vacuum permittivity, $\mu_0 = 4\pi \cdot 10^{-7}$ N·A^{-2} is the vacuum permeability, ϱ is the charge density and $\vec{j}$ is the current density vector. Equation (3.5) is derived from *Gauss's law* which postulates that the flux of the electric field through a closed surface equals the total enclosed charge, divided by vacuum permittivity. Equation (3.6), sometimes referred to as Gauss's law for magnetism, simply expresses that the flux of the magnetic field through any closed surface is zero and it can also be inferred from it that magnetic monopoles do not exist. Equation (3.7) relates the induced electric field $\vec{E}$ with the variation of the external magnetic field $\vec{B}$ as explained by Faraday's and Lenz's laws. Finally, Equation (3.8), known as the *Ampère-Maxwell law*, indicates that changing electric fields give rise to circulating magnetic fields [140].

Furthermore, the charge is a conserved quantity and it complies with the continuity equation (3.9). Note that this equation can be derived from Equations (3.5) and (3.8) [111]. It indicates that the net rate of charge flow out of the closed surface S is equal to the rate of decrease of charge in the

volume inside the closed surface S.

$$\nabla \cdot \vec{j} = -\frac{\partial \varrho}{\partial t}. \tag{3.9}$$

An additional important equation is the *Lorentz force* [141]. This corresponds to the force acting on a particle of charge q moving at a speed $\vec{v}_q$ with respect to an external electrical field $\vec{E}$ and magnetic field $\vec{B}$. Maxwell's equations (3.5, 3.6, 3.7, 3.8) together with the Lorentz force form the foundation of classical electrodynamics. The Lorentz force is given by the formula,

$$\vec{F} = q(\vec{E} + \vec{v}_q \times \vec{B}). \tag{3.10}$$

As the interest of this research resides in the analysis of man-made objects in orbit, from now on, an electrically neutral conductor will be considered. For this case, Maxwell's equations as well as the Lorentz force are employed at a macroscopic level and the physical quantities are averaged over elements of volume [111]. A solid conductor is composed of free charges (e.g. electrons) as well as ions which form the lattice of the conductor. If the conductor is electrically neutral then the total density charge must be equal to zero,

$$\varrho = \varrho_e + \varrho_l = 0, \tag{3.11}$$

where ϱ_e is the charge density of the electrons and ϱ_l is the charge density of the ions that make up the lattice. In the absence of an electromotive force, the electrons will just have a thermal velocity, $\vec{v}_t$, with random directions and average to zero [141]. The ions in the lattice also have a thermal velocity $\vec{v}_t'$ which make them vibrate. When the conductor is subject to an electric field, the electrons will be accelerated in the direction opposite to the field. However, during their motion, the electrons collide with the ions of the lattice of the conductor, dissipating kinetic energy into heat. This phenomenon is known as *Joule's heating effect*. The balance between the interaction forces of the medium and the accelerating force of the electric field, leads the electric current to reach a steady state motion of a constant drift velocity, $\vec{u}$ [111, 140].

The current density vector $\vec{j}$ is the electric current per unit area of cross section and it is measured in Amperes per square metre. For a solid conductor, the macroscopic current density field is defined as the product of the charge density and the average velocity of the particles [141]. For an electrically neutral conductor moving at a velocity $\vec{v}$, the current density vector reduces to the product of the charge density of the electrons and the drift velocity of the charges with respect to the conductor as shown in Equation (3.12),

$$\vec{j} = \varrho_e(\vec{v} + \overbrace{\vec{v}_t}^{=\vec{0}} + \vec{u}) + \varrho_l(\vec{v} + \overbrace{\vec{v}_t'}^{=\vec{0}}) = (\overbrace{\varrho_e + \varrho_l}^{=0})\vec{v} + \varrho_e\vec{u} = \varrho_e\vec{u}, \tag{3.12}$$

where $\overline{\vec{v}_t}$ and $\overline{\vec{v}_t'}$ are the mean values of the thermal velocities of the electrons and the ions respectively and whose averaged value is equal to zero.

In addition, the constitutive relationship between an electric field and the generated electric current density vector depends on the properties of the conductor. For most solid conductors, the current density $\vec{j}$ is proportional to the force per unit charge $\vec{f}$ [141],

$$\vec{j} = \sigma\vec{f} = \sigma(\vec{E} + (\vec{v} + \vec{u}) \times \vec{B}), \tag{3.13}$$

where $\vec{f} = \vec{F}/q$ follows from Equation (3.10) when averaging $\vec{v}_q = \vec{v} + \vec{u} + \vec{v}_t'$. The proportionality factor σ is an empirical constant that varies from one material to another and it is called the *conductivity* of the body [141]. This law is usually referred to as *Ohm's law*.

For a conductor at rest ($\vec{v} = \vec{0}$), the mean velocity of the particles in Equation (3.13) corresponds to the drift velocity. Ordinarily, this velocity is very small. For instance, for a 12-gauge copper wire carrying a 10 Ampere DC current, the average electron drift velocity is about 8 centimetres per hour [141]. Therefore, for a conductor at rest Ohm's law can be simplified to,

$$\vec{j} = \sigma\vec{E}. \tag{3.14}$$

For a conductor moving at a given velocity $\vec{v}$ with respect to a general inertial reference frame K, we define a reference frame K' fixed to an inertial observer instantaneously at rest with respect to a point in the moving conductor. It must be taken into account that the electric and magnetic fields are not the same in each reference frame [111]. Einstein's first paper on special relativity in 1905 explains how to transform Maxwell's equations between the two frames. The relationship between the electric field expressed both frames K and K' is given by [111, 114],

$$\vec{E}' = \gamma(\vec{E} + \vec{v} \times \vec{B}) - (\gamma - 1)(\vec{E} \cdot \vec{\hat{v}})\vec{\hat{v}}, \tag{3.15}$$

where $\gamma = \frac{1}{\sqrt{1 - \frac{v^2}{c^2}}}$, $\vec{\hat{v}}$ is the velocity unit vector and c is the speed of light in free space. For $v << c$ we get

$$\vec{E}' \approx \vec{E} + \vec{v} \times \vec{B}. \tag{3.16}$$

In addition, the relationship between the magnetic field expressed in each reference frame K and K' is given by,

$$\vec{B}' = \gamma(\vec{B} - \frac{\vec{v} \times \vec{E}}{c^2}) - (\gamma - 1)(\vec{B} \cdot \vec{\hat{v}})\vec{\hat{v}}. \tag{3.17}$$

For $v << c$ we get,

$$\vec{B}' \approx \vec{B}. \tag{3.18}$$

Moreover, the electric current density vector is not the same for a charged body when expressed in the general inertial frame K and the instantaneous fixed frame to the conductor K' as seen in Equation (3.19). However, for an electrically neutral conductor $\varrho = 0$ and therefore, $\vec{j} = \vec{j}'$ [111, 114].

$$\vec{j} = \vec{j}' + \varrho\vec{v} \overset{\varrho=0}{\Rightarrow} \vec{j} = \vec{j}'. \tag{3.19}$$

Then, Equations (3.14) and (3.16) can be combined to yield,

$$\vec{j} = \sigma(\vec{E} + \vec{v} \times \vec{B}), \tag{3.20}$$

which is obviously consistent with Equation (3.13), assuming that $|\vec{u}| << |\vec{v}|$. In addition, the conductive body may have both a linear velocity $\vec{v}$ and/or angular velocity $\vec{\omega}$, therefore, Ohm's Law for a rigid conductive body should be generalised as,

$$\vec{j} = \sigma(\vec{E} + \vec{v} \times \vec{B} + (\vec{\omega} \times \vec{r}) \times \vec{B}), \tag{3.21}$$

where $\vec{r}$ is the position vector of each incremental volume of the object with respect to its COG.

Finally, the Lorentz force that appears on a moving conductor subject to an external electrical field $\vec{E}$ and magnetic field $\vec{B}$ is equal to,

$$\vec{F} = \int \left[\varrho_e(\vec{E} + (\vec{v} + \vec{v}_t + \vec{u}) \times \vec{B}) + \varrho_l(\vec{E} + (\vec{v} + \vec{v}'_t) \times \vec{B}) \right] dV. \tag{3.22}$$

Taking into account that the average value of the thermal velocities is zero and that the conductor is electrically neutral, Equation (3.22) reduces to,

$$\vec{F} = \int \varrho_e \vec{u} \times \vec{B} dV = \int \vec{j} \times \vec{B} dV. \tag{3.23}$$

In addition to the induced force, the conductor will also be subject to a torque given by the formula (3.24),

$$\vec{T} = \int \vec{r} \times (\vec{j} \times \vec{B}) dV = \vec{m} \times \vec{B}. \tag{3.24}$$

The classic formula in electromagnetism that provides the resulting body torque is typically expressed as the cross product of the magnetic moment $\vec{m}$ and the magnetic field vector [95, 111, 112]

where the magnetic moment is defined as,

$$\vec{m} = \frac{1}{2} \int \vec{r} \times \vec{j} \, dV. \tag{3.25}$$

Table (3.1) summarises the key formulas explained in this section.

Glossary of equations	
Lenz's law	$\mathcal{E} = -\frac{d\varphi}{dt}$
Gauss's law	$\nabla \cdot \vec{E} = \frac{\varrho}{\epsilon_0}$
Gauss's law for magnetism	$\nabla \cdot \vec{B} = 0$
Faraday's law	$\nabla \times \vec{E} = -\frac{\partial \vec{B}}{\partial t}$
Ampère-Maxwell law	$\nabla \times \frac{\vec{B}}{\mu_0} = \vec{j} + \epsilon_0 \frac{\partial \vec{E}}{\partial t}$
Continuity equation	$\nabla \cdot \vec{j} = -\frac{\partial \varrho}{\partial t}$
Electric current density vector	$\vec{j} = \varrho_e \vec{u}$
Generalised Ohm's law	$\vec{j} = \sigma(\vec{E} + \vec{v} \times \vec{B} + (\vec{\omega} \times \vec{r}) \times \vec{B})$
Lorentz force	$\vec{F} = \int \vec{j} \times \vec{B} \, dV$
Magnetic moment	$\vec{m} = \frac{1}{2} \int \vec{r} \times \vec{j} \, dV$
Magnetic torque	$\vec{T} = \vec{m} \times \vec{B}$

Table 3.1: Glossary of equations.

3.3 Eddy currents induced in a rotating object

In this section, it will be assumed that the rotating body is a rigid body which is subject to a constant and uniform magnetic field $\vec{B}(\vec{r}, t) = constant$. In addition, the conductive materials considered have a relative permeability close to 1. This is the case of typical metallic materials used on spacecraft such as aluminium, titanium or copper.

3.3.1 Differential equations

First of all, the continuity equation (3.26) is employed, assuming that there is no accumulation of charge. The term $\frac{\partial \varrho}{\partial t}$ accounts for a transient state of charge building on the conductive object (charge relaxation) before the currents form closed loops. The characteristic time of this state is equal to the ratio between the electrical permittivity and the electrical conductivity of the material $\tau_c = \frac{\epsilon}{\sigma}$. This characteristic time is $1.5 \cdot 10^{-19}$ seconds for copper and $0.2 \cdot 10^{-18}$ seconds for aluminium so this effect can be neglected for the metallic materials considered [114, 142] and the continuity equation reduces to,

$$\nabla \cdot \vec{j} = 0. \tag{3.26}$$

The second equation for $\vec{j}$ is obtained by combining Maxwell's Equation (3.4) with Ohm's Law (3.21) for a conductor rotating with an angular velocity $\vec{\omega}$,

$$\nabla \times \vec{j} = \sigma(\nabla \times ((\vec{\omega} \times \vec{r}) \times \vec{B}) = \sigma(\vec{\omega} \times \vec{B}) = \sigma\vec{\Omega}, \tag{3.27}$$

where $\vec{\omega}$ is the angular velocity of the conductor, $\vec{r}$ is the position vector of each incremental volume of the object with respect to its COG and the magnitude $\vec{\Omega}$ is defined as,

$$\vec{\Omega} = \vec{\omega} \times \vec{B}. \tag{3.28}$$

Finally, the boundary condition for the current density vector states that the current must stay inside the volume,

$$\vec{j} \cdot \vec{n}_v = 0 \;\; \forall P \in \partial V, \tag{3.29}$$

where $\vec{n}_v$ is the vector normal to the contour surface ∂V.

All in all, the differential equations that allow for the computation of $\vec{j}$ are,

$$\nabla \cdot \vec{j} = 0 \;\; \forall P \in V, \tag{3.30}$$

$$\nabla \times \vec{j} = \sigma\vec{\Omega} \;\; \forall P \in V, \tag{3.31}$$

$$\vec{j} \cdot \vec{n}_v = 0 \;\; \forall P \in \partial V, \tag{3.32}$$

The solution to this system of linear differential Equations (3.30, 3.31, 3.32) can be expressed as the sum of a particular solution and a homogeneous solution as shown in (3.33), where ψ is an unknown scalar function [143].

$$\vec{j} = \vec{j}_{part} - \sigma \cdot \nabla\psi. \tag{3.33}$$

3.3.2 Particular solutions for the current density vector

3.3.2.1 First particular solution. Classical formulation.

The classical way to express the current density vector is by choosing the particular solution [94, 114],

$$\vec{j}_{part}^{(1)} = \sigma(\vec{\omega} \times \vec{r}) \times \vec{B} \tag{3.34}$$

and therefore, the general solution to Equations (3.30, 3.31, 3.32) is,

$$\vec{j} = \sigma(\vec{\omega} \times \vec{r}) \times \vec{B} - \sigma\nabla\phi. \tag{3.35}$$

Looking closer at Equation (3.34), it is deduced that it coincides with Ohm's Law and the scalar function ϕ corresponds to the electric potential $\vec{E} = -\nabla\phi$. Introducing solution (3.34) in the continuity Equation (3.30) and the boundary conditions (3.32), the following Poisson equation with Neumann conditions is obtained for ϕ [120],

$$\nabla^2\phi = \frac{2}{\sigma}\vec{\omega} \cdot \vec{B} \;\; \forall P \in V, \tag{3.36}$$

$$\frac{\partial\phi}{\partial n_v} = ((\vec{\omega} \times \vec{r}) \times \vec{B}) \cdot \vec{n}_v \;\; \forall P \in \partial V, \tag{3.37}$$

3.3.2.2 Second particular solution.

In some cases, it may be more convenient to choose a different particular solution. Looking closer at Equation (3.31), it is observed that the curl of the vector field $\vec{j}$ is equal to the constant vector

$\sigma\vec{\Omega}$. This is analogous to the vector field that describes the velocity field of a rotating body $\vec{v} = \vec{\omega} \times \vec{r}$. The curl of this velocity field is equal to $\nabla\vec{v} = 2\vec{\omega}$, that is, the rotation axis points in the direction of the curl of the field and the angular speed of rotation is half the magnitude of the curl [140]. Therefore, in (3.31), $\sigma\vec{\Omega}$ indicates the magnitude and direction of rotation of the eddy current loops described by the vector field $\vec{j}$. Following this analogy, a solution of the kind $\vec{j}(\vec{r}) = constant \cdot (\vec{\Omega} \times \vec{r})$ can be found which complies with Equation (3.31) and it is equal to,

$$\vec{j}_{part}^{(2)} = \frac{\sigma}{2}\vec{\Omega} \times \vec{r}. \tag{3.38}$$

In this case, the general solution for $\vec{j}$ has the form,

$$\vec{j} = \frac{\sigma}{2}\vec{\Omega} \times \vec{r} - \sigma \cdot \nabla\psi. \tag{3.39}$$

Moreover, this solution has the advantage of leading to a Laplace Equation (3.40) instead of the non-homogeneous equation in partial derivatives (3.36). Introducing (3.39) in the continuity Equation (3.30) and the boundary conditions (3.32), the following Laplace equation with Neumann boundary conditions is obtained for ψ:

$$\nabla^2\psi = 0 \ \ \forall P \in V, \tag{3.40}$$

$$\frac{\partial\psi}{\partial n_v} = -\frac{1}{2}(\vec{r} \times \vec{\Omega}) \cdot \vec{n}_v \ \ \forall P \in \partial V, \tag{3.41}$$

where V and ∂V are the volume and the contour surface of the conductor.

It must be highlighted that the scalar function ψ of the second particular solution does not correspond anymore to the conventional electric potential ϕ. Therefore, it will be called the 'effective potential'.

Note that if the Neumann boundary conditions are null, then the Laplace equation leads to the solution $\psi = constant \ \forall P \in V$ and therefore, the particular solution $\vec{j}_{part}^{(2)}$ corresponds to the exact solution, that is, $\vec{j} = \vec{j}_{part}^{(2)}$. For instance, this situation takes place for a spherical shell $\forall\vec{\Omega}$ [114], a cylindrical shell with $\vec{\Omega}$ along its axis and a flat circular plate with $\vec{\Omega}$ perpendicular to its plane.

Consequently, this particular solution *may* approximate better to the real distribution of electric currents and it corresponds to the exact solution for certain geometrical bodies.

Finally, this formulation introduces naturally the parameter $\vec{\Omega} = \vec{\omega} \times \vec{B}$. Equations (3.30, 3.31, 3.32) and (3.40, 3.41) show the linearity of the solution of ψ and $\vec{j}$ with respect to this parameter $\vec{\Omega}$. This will be the key to prove the existence of the magnetic tensor in Section 3.3.3 and the particular solution $\vec{j}_{part}^{(2)}$ will help to find a direct formula for the magnetic tensor in Section 3.3.4.2.

3.3.3 The magnetic tensor

The general formula of the eddy current torque and the magnetic moment are given by Equations (3.24) and (3.25) respectively.

One general way to evaluate this torque would be to use a finite element method (FEM) in order to divide the volume into a grid and solve the Laplace equation with Neumann boundary conditions (3.40, 3.41) for each element in the grid. Once the scalar function ψ is known, the current density vector $\vec{j}$ and therefore, the magnetic moment (3.25) and the torque (3.24) can be evaluated. The next step would be to integrate Euler Equations (2.12) in order to obtain the evolution of the angular velocity vector $\vec{\omega}$. It must be highlighted that the whole process would have to be repeated in each time step during the integration process of Euler equations, unless explicit direct formulae for the eddy current torque were obtained.

The fact that it is impractical to solve the Neumann problem at each time step has already been

shown in previous articles [114, 118, 120], where specific formulae were obtained for the eddy current torque in some particular cases. As it will be proved in this section, the torque can be expressed in a general way by means of a tensor which will be called the *'magnetic tensor'* $\mathbf{M}$. The concept of the magnetic tensor provides us with a general strategy to solve the problem for any body type. As it will be explained below, this tensor only depends on the physical properties of the body and it only needs to be computed once. When the magnetic tensor is known, the evaluation of the torque due to the eddy currents consists of a direct formula given by (3.45).

As it was explained in the previous section, the general solution for $\vec{j}$ is linear in $\vec{\Omega}$. If a physical phenomenon is governed by a set of linear equations, it admits the superposition principle. This principle states the following: when two stimuli ($\vec{\Omega}_1$ and $\vec{\Omega}_2$) lead to two different responses ($\vec{j}_1$ and $\vec{j}_2$), the simultaneous effect of the stimuli ($\vec{\Omega}_1 + \vec{\Omega}_2$) is equal to the sum of effects ($\vec{j}_1 + \vec{j}_2$) produced by each stimulus individually [144].

If Equations (3.30, 3.31, 3.32) are solved for the three different cases, $\vec{\Omega}^{(i)}$ ($i = 1, 3$),

$$\vec{\Omega}^{(1)} = \begin{bmatrix} 1 \\ 0 \\ 0 \end{bmatrix} , \ \vec{\Omega}^{(2)} = \begin{bmatrix} 0 \\ 1 \\ 0 \end{bmatrix} , \ \vec{\Omega}^{(3)} = \begin{bmatrix} 0 \\ 0 \\ 1 \end{bmatrix} , \tag{3.42}$$

a set of solutions $\vec{j}^{(1)}(\vec{r}), \vec{j}^{(2)}(\vec{r}), \vec{j}^{(3)}(\vec{r})$ is obtained.

Taking into account the linearity with respect to $\vec{\Omega}$, the solution for $\vec{j}$ can be expressed for a given $\vec{\Omega} = \begin{bmatrix} \Omega_1 \\ \Omega_2 \\ \Omega_3 \end{bmatrix} = \sum_{i=1}^{n} \Omega_i \vec{\Omega}^{(i)}$ as,

$$\vec{j}(\vec{r}) = \Omega_1 \vec{j}^{(1)} + \Omega_2 \vec{j}^{(2)} + \Omega_3 \vec{j}^{(3)} = \sum_{k=1}^{3} \Omega_k \cdot \vec{j}^{(k)}(\vec{r}). \tag{3.43}$$

In addition, introducing (3.43) in (3.25), it is derived that the magnetic moment $\vec{m}$ is also linear in $\vec{\Omega}$ and it acquires the general form,

$$m_i = \sum_{j=1}^{3} M_{ij} \Omega_j, \quad 1 \leq j \leq 3 \rightarrow \vec{m} = \mathbf{M}\vec{\Omega}. \tag{3.44}$$

Note that $\vec{j}(\vec{r})$ depends on $\vec{B}$ and $\vec{\omega}$ only through $\vec{\Omega} = \vec{\omega} \times \vec{B}$. Therefore, the components M_{ij} should be considered as proportionality 'constants' of the i-component of $\vec{m}$ with respect to the three components of $\vec{\Omega}$ and these components M_{ij} only depend on the geometry and conductivity of the body. The parameter $\mathbf{M}$ will be called the *'magnetic tensor'*.

Combining Equations (3.24) and (3.44), the torque induced by the eddy currents is equal to,

$$\vec{T} = (\mathbf{M}\vec{\Omega}) \times \vec{B}. \tag{3.45}$$

Next, various properties of the magnetic tensor are proved:

3.3.3.1 M is a Cartesian tensor of second order

$\vec{m}$ and $\vec{\Omega}$ are two vectors which can be transformed from an arbitrary Cartesian reference frame to another using the corresponding rotation matrix $\mathbf{R}$. These transformations can be expressed as,

$$\begin{cases} \vec{m}' = \mathbf{R}\vec{m} & \forall \vec{m}, \\ \vec{\Omega}' = \mathbf{R}\vec{\Omega} & \forall \vec{\Omega}. \end{cases} \tag{3.46}$$

Entering into (3.44) $\vec{m}' = \mathbf{M}'\vec{\Omega}' \Rightarrow \mathbf{R}\vec{m} = \mathbf{M}'\mathbf{R}\vec{\Omega} \Rightarrow \vec{m}' = \mathbf{R}^\mathbf{T}\mathbf{M}'\mathbf{R}\vec{\Omega}' = \mathbf{M}\vec{\Omega}'$. As the previous relationship holds $\forall\vec{\Omega}$ and its corresponding variable $\vec{m}$, it can be inferred that $\mathbf{M} = \mathbf{R}^\mathbf{T}\mathbf{M}'\mathbf{R}$ or $\mathbf{M}' = \mathbf{R}\mathbf{M}\mathbf{R}^\mathbf{T}$. Therefore, it can be concluded that $\mathbf{M}$ transforms as a Cartesian tensor of second order.

3.3.3.2 M has dimensions of [S·m^4] where S the Siemens unit

The units of the magnetic tensor can be derived from Equation (3.44) as the magnetic moment $\vec{m}$ is measured in ampere-square metre [A·m^2] and $\vec{\Omega}$ is measured in Tesla-radians per second [T·rad/s]. Therefore the units of the magnetic tensor are,
$$[\text{s}^3 \cdot \text{A}^2 \text{m}^2 \text{kg}^{-1} = \text{S} \cdot \text{m}^4].$$

3.3.3.3 The dissipated energy per unit time due to the eddy currents has the form $\dot{W} = -\vec{\Omega}^T \mathbf{M} \vec{\Omega}$

The dissipated energy per unit time due to the eddy current phenomenon is $\dot{W} = \vec{T} \cdot \vec{\omega}$. Using Equation (3.45), it can be found that,

$$\dot{W} = ((\mathbf{M}\vec{\Omega}) \times \vec{B}) \cdot \vec{\omega} = (\mathbf{M}\vec{\Omega}) \cdot (\vec{B} \times \vec{\omega}) = -\vec{\Omega}^T \mathbf{M} \vec{\Omega}. \tag{3.47}$$

3.3.3.4 The magnetic tensor is symmetric

The symmetry of $\mathbf{M}$ is an important property because it will allow for its subsequent derivation from the energy dissipation balance. In order to proof that the magnetic tensor is symmetric, two different proofs are provided. Proof number 1 is more mathematical and proof number 2 is more physical based on the dissipative behaviour of the eddy current phenomenon.

Proof 1:

The current density vector can be written in a general way as the sum of a particular and a homogeneous solution,
$$\vec{j} = \vec{j}^{(part)} + \vec{j}^{(hom)} = \frac{\sigma}{2}\vec{\Omega} \times \vec{r} - \sigma \cdot \nabla\psi. \tag{3.48}$$

Based on Equation (3.48), the magnetic moment can be expressed as the sum of a particular solution and homogeneous solution,

$$\vec{m} = \frac{1}{2}\int_V \vec{r} \times \vec{j}\,dV = \vec{m}^{(part)} + \vec{m}^{(hom)} = (\mathbf{M^{(part)}} + \mathbf{M^{(hom)}})\vec{\Omega}. \tag{3.49}$$

The general equations for ψ are,
$$\Delta\psi = 0 \ \ \forall P \in \ V, \tag{3.50}$$

$$\frac{\partial\psi}{\partial n_v} = -\frac{1}{2}(\vec{r} \times \vec{\Omega}) \cdot \vec{n}_v = -\frac{1}{2}\vec{\Omega} \cdot \vec{t} \ \forall P \in \ \partial V, \quad \vec{t} = (\vec{n}_v \times \vec{r}). \tag{3.51}$$

The particular solution of the magnetic moment is,

$$\vec{m}^{(part)} = \mathbf{M^{(part)}}\vec{\Omega} = \frac{\sigma}{4}\int_V \vec{r} \times (\vec{\Omega} \times \vec{r})dV = \frac{\sigma}{4}(\int_V (r^2\boldsymbol{\mathcal{I}} - \vec{r}\vec{r}^T)dV)\vec{\Omega}, \tag{3.52}$$

where $\boldsymbol{\mathcal{I}}$ is the identity matrix. Note that the integral $\int_V (r^2\boldsymbol{\mathcal{I}} - \vec{r}\vec{r}^T)dV$ shows a great similarity with respect to the general expression of the inertia tensor. This aspect is further discussed in Subsection 3.3.4.5.

Therefore, the particular solution of the Magnetic Tensor is derived from Equation (3.52) and it

is symmetric,

$$\mathbf{M^{(part)}} = \frac{\sigma}{4}(\int_V (r^2\boldsymbol{\mathcal{I}} - \vec{r}\vec{r}^T)dV) \Rightarrow \mathbf{M^{(part)}} = (\mathbf{M^{(part)}})^{\mathbf{T}}. \tag{3.53}$$

Moreover, the homogeneous solution of the magnetic moment is,

$$\vec{m}^{(hom)} = \mathbf{M^{(hom)}}\vec{\Omega} = -\frac{\sigma}{2}\int_V \vec{r} \times \nabla\psi \, dV. \tag{3.54}$$

The solution of Equations (3.50, 3.51) can be expressed as,

$$\forall \vec{r} \in V : \psi(\vec{r}) = \psi_0 + \int_{\vec{s}\in\partial V} G_N(\vec{r},\vec{s})\frac{\partial\psi(\vec{s})}{\partial n_v}dS, \tag{3.55}$$

$$\forall \vec{s} \in V : \psi(\vec{s}) = \psi_0 + \int_{\vec{s}'\in\partial V} G_N(\vec{s},\vec{s}')\frac{\partial\psi(\vec{s}')}{\partial n_v}dS', \tag{3.56}$$

where ψ_0 is an arbitrary constant and $G_N(\vec{s},\vec{s}')$ is a Green function of the Neumann problem.

The constant $\psi_0 = \int_{\vec{s}'\in\partial V} F(\vec{s}')\frac{\partial\psi(\vec{s}')}{\partial n_v}dS'$ can be chosen in such a way that $G(\vec{s},\vec{s}') = G_N(\vec{s},\vec{s}') + F(\vec{s}')$ is symmetric, that is, $G(\vec{s},\vec{s}') = G(\vec{s}',\vec{s})$ [145]. Below, the convention of summation over repeated indices is used.

$$\frac{(\partial e_{ijk}x_j\psi)}{\partial x_k} = \overbrace{e_{ijk}\delta_{jk}\psi}^{=0} + e_{ijk}x_j\frac{\partial\psi}{\partial x_k} \Rightarrow m_i^{(hom)} = -\frac{\sigma}{2}\int_V \frac{\partial(e_{ijk}x_j\psi)}{\partial x_k}dV, \tag{3.57}$$

where δ_{jk} is the Kronecker delta and e_{ijk} is the Levi-Cevita function, whose terms are equal to $e_{123} = e_{231} = e_{312} = 1$, $e_{321} = e_{213} = e_{132} = -1$ and the rest are equal to zero.

Applying the divergence theorem to Equation (3.57),

$$m_i^{(hom)} = -\frac{\sigma}{2}\int_{\partial V} e_{ijk}x_j n_k \psi dS \Rightarrow \vec{m}^{(hom)} = \frac{\sigma}{2}\int_{\vec{s}\in\partial V} \vec{t}(\vec{s}) \cdot \psi(\vec{s})dS, \tag{3.58}$$

Now making use of Equation (3.56) first and then the boundary conditions (3.56), $\vec{m}^{(hom)}$ results in,

$$m_i^{(hom)} = \frac{\sigma}{2}\int_{\vec{s}\in\partial V} t_i(\vec{s}) \cdot \int_{\vec{s}'\in\partial V} G(\vec{s},\vec{s}')\frac{\partial\psi(\vec{s}')}{\partial n_v}dS'dS,$$
$$\Rightarrow m_i^{(hom)} = -\frac{\sigma}{4}\int_{\vec{s}\in\partial V}\int_{\vec{s}'\in\partial V} t_i(\vec{s})G(\vec{s},\vec{s}')t_j(\vec{s}')\Omega_j dS'dS. \tag{3.59}$$

Therefore, the homogeneous part of the Magnetic Tensor is symmetric and it has the form,

$$M_{ij}^{(hom)} = -\frac{\sigma}{4}\int_{\vec{s}\in\partial V}\int_{\vec{s}'\in\partial V} t_i(\vec{s})G(\vec{s},\vec{s}')t_j(\vec{s}')dS'dS = M_{ji}^{(hom)}. \tag{3.60}$$

Finally, the Magnetic tensor is symmetric and it can be expressed as,

$$\mathbf{M} = \frac{\sigma}{4}\int_V (r^2\boldsymbol{\mathcal{I}} - \vec{r}\vec{r}^T)dV - \frac{\sigma}{4}\int_{\vec{s}\in\partial V}\int_{\vec{s}'\in\partial V} G(\vec{s},\vec{s}')\vec{t}(\vec{s})\vec{t}^T(\vec{s}')dSdS' = \mathbf{M^T}. \tag{3.61}$$

Proof 2:

The symmetry of $\mathbf{M}$ can be deduced from Onsager's laws for irreversible processes [146, 147]. In thermodynamics, a process is said to be irreversible when the total entropy and therefore the disorder, increases [147]. The thermodynamics of irreversible processes is a macroscopic theory that deals with states and processes out-of equilibrium [147]. Not far from equilibrium, transport irreversible phenomena are governed by linear laws. This is the case of Ohm's law, Fourier's law on thermal conduction or Newton's law on the viscous flow [147].

It has been previously proved that the magnetic moment, $\vec{m}$, and $\vec{\Omega}$ follow the linear relationship $\vec{m} = \mathbf{M}\vec{\Omega}$ where M_{ij} are the proportionality constants. This relationship appears as a consequence of the linearity of Equations (3.30, 3.31) and the boundary condition (3.32) and the subsequent linearity of $\vec{j}(\vec{r})$ with respect to $\vec{\Omega}$.

In our problem, the currents $\vec{j}$ are responsible for the energy dissipation that will be later calculated applying Ohm's and Joule's heating effect, i.e., as a linearised irreversible process. Hence, Onsager's Reciprocal Relations apply and the symmetry of $\mathbf{M}$ is derived in a very straightforward way, as it is shown below.

When irreversible processes take place in the presence of an external magnetic field $\vec{B}$ and/or in a system rotating at an angular velocity $\vec{\omega}$, Onsager's Law foresees two possible relations for $\mathbf{M}$ which are mutually exclusive [147],

$$
\begin{cases}
M_{ik}(\vec{B}, \vec{\omega}) = M_{ki}(-\vec{B}, -\vec{\omega}) \text{ if both (or none) } \vec{m} \text{ and } \vec{\Omega} \\
\qquad\qquad \text{ are proportional to velocities,} \\
M_{ik}(\vec{B}, \vec{\omega}) = -M_{ki}(-\vec{B}, -\vec{\omega}) \text{ if velocities are only included} \\
\qquad\qquad \text{ either in } \vec{m} \text{ or } \vec{\Omega}.
\end{cases}
\tag{3.62}
$$

The previous relationships can be written as $\mathbf{M}(\vec{B}, \vec{\omega}) = \pm\mathbf{M^T}(-\vec{B}, -\vec{\omega})$.

As 'constants', the M_{ik} only depend on the geometry of the body; so they are not dependent on $\vec{B}$ or $\vec{\omega}$. For $\mathbf{M}(\vec{B}) = $ constant, the above relation reduces to two possibilities:

$$
\begin{cases}
\text{A symmetric constant matrix } \mathbf{M} = \mathbf{M^T} \\
\text{Or an antisymmetric constant matrix } \mathbf{M} = -\mathbf{M^T}
\end{cases}
\tag{3.63}
$$

If $\mathbf{M}$ were antisymmetric, the dissipated energy per unit time would be zero, that is, $\dot{W} = 0$, as demonstrated below,

$$
\begin{bmatrix} \Omega_1 & \Omega_2 & \Omega_3 \end{bmatrix}
\begin{bmatrix} 0 & a & b \\ -a & 0 & c \\ -b & -c & 0 \end{bmatrix}
\begin{bmatrix} \Omega_1 \\ \Omega_2 \\ \Omega_3 \end{bmatrix}
= a\Omega_1\Omega_2 + b\Omega_1\Omega_3 + c\Omega_2\Omega_3 - a\Omega_1\Omega_2 - b\Omega_1\Omega_3 - c\Omega_2\Omega_3 = 0.
\tag{3.64}
$$

Therefore, if $\dot{W} = \vec{T} \cdot \vec{\omega} = 0$, then the torque should always be perpendicular to $\vec{\omega}$. This hypothesis contradicts the observed dissipative nature of the eddy current phenomenon and therefore, it must be rejected.

Instead, the other possibility quoted in (3.63) ($\mathbf{M}$ symmetric) allows for non-zero values of the quadratic form given by (3.47). This matches with the observed dissipative nature of the phenomenon if $\mathbf{M}$ has no negative eigenvalues (see next paragraph). Therefore, it can be concluded that $\mathbf{M}$ should be a symmetric tensor.

3.3.3.5   The magnetic tensor has no negative eigenvalues

The eddy current phenomenon is a dissipative effect which generates heat due to Joule's effect [94]. Hence, the derivative of the energy (in our case kinetic energy) must always be $\dot{W} \leq 0$. From Equation (3.47), the previous condition leads to the quadratic form $\vec{\Omega}^T\mathbf{M}\vec{\Omega} \geq 0$. This implies that the magnetic tensor has no negative eigenvalues. If none of the eigenvalues are zero, then the components of $\mathbf{M}$ form a symmetric definite positive 3×3 matrix.

3.3.3.6   Additional properties of the eddy current torque

Additional characteristics of the eddy current phenomenon can be inferred from the torque formula given by (3.45).

1. The eddy current torque (3.45) is invariant under the change $\vec{B} \to -\vec{B}$ for a given $\vec{\omega}$. Therefore, when $\dot{W} < 0$, the component of $\vec{T}$ parallel to $\vec{\omega}$ will always oppose the velocity vector, no matter which sign of $\vec{B}$ is chosen.

2. For a given value of $\vec{\Omega}$, the maximum dissipation occurs when the orientation of $\vec{\Omega}$ coincides with the eigenvector that corresponds to the maximum eigenvalue of $\mathbf{M}$.

3. If $\vec{\omega}$ is parallel to the magnetic field $\vec{B}$, then $\vec{\Omega} = \vec{0}$ and the torque is zero (3.45). Therefore, there is no dissipation of energy (3.47).

4. If $\vec{\omega} = \vec{\omega}_{\shortparallel} + \vec{\omega}_{\perp}$ is composed of a parallel component to the magnetic field $\vec{\omega}_{\shortparallel}$ and a perpendicular component to the magnetic field $\vec{\omega}_{\perp}$, the component perpendicular to the magnetic field $\vec{\omega}_{\perp} \perp \vec{B}$ is damped and the rigid body asymptotically ends rotating in the direction of the magnetic field $\vec{B}$ [114].

This last property of the eddy current phenomenon can be explained as follows. The angular velocity vector is divided into two components, one perpendicular $\vec{\omega}_{\perp}$ and one parallel $\vec{\omega}_{\shortparallel}$ to the magnetic field,

$$\vec{\omega} = \vec{\omega}_{\shortparallel} + \vec{\omega}_{\perp}. \tag{3.65}$$

The parallel component will not be damped if total work is zero $\vec{T} \cdot \vec{\omega}_{\shortparallel} = 0$ and the perpendicular component will be damped if the total work is negative $\vec{T} \cdot \vec{\omega}_{\perp} < 0$. Therefore, these two hypotheses must be proved.

- $\vec{T} \cdot \vec{\omega}_{\shortparallel} = 0$
  The magnetic torque follows the formula (3.24), $\vec{T} = \vec{m} \times \vec{B}$. Therefore, $\vec{T} \perp \vec{B} \Rightarrow \vec{T} \cdot \vec{\omega}_{\shortparallel} = 0$.

- $\vec{T} \cdot \vec{\omega}_{\perp} < 0$
  Taking into account that $\vec{T} \cdot \vec{\omega}_{\shortparallel} = 0$, it holds that $\vec{T} \cdot \vec{\omega}_{\perp} = \vec{T} \cdot \vec{\omega}$. Then, using the expressions (3.24), (3.28) and (3.44), the following relationships hold,

$$\vec{T} \cdot \vec{\omega}_{\perp} = \vec{T} \cdot \vec{\omega} = (\vec{m} \times \vec{B}) \cdot \vec{\omega} = \vec{m}(\vec{B} \times \vec{\omega}) = -\vec{m} \cdot \vec{\Omega} = -(\mathbf{M}\vec{\Omega}) \cdot \vec{\Omega}. \tag{3.66}$$

The vector $\vec{\Omega}$ can be expressed as the sum of three vectors that go along the principal directions of $\mathbf{M}$,

$$\vec{\Omega} = \vec{\Omega}_1 + \vec{\Omega}_2 + \vec{\Omega}_3. \tag{3.67}$$

Therefore, the expression (3.66) may be written as,

$$\vec{T} \cdot \vec{\omega}_{\perp} = -(M_1\Omega_1^2 + M_2\Omega_2^2 + M_3\Omega_3^2) < 0. \tag{3.68}$$

where M_i $(i = 1, 3)$ are the eigenvalues of $\mathbf{M}$. Taking into account that $\mathbf{M}$ has no negative eigenvalues, that is, $M_i \leq 0$ $i = 1, 3$, it can be concluded that $\vec{T} \cdot \vec{\omega}_{\perp} < 0$. The previous statement would not be true if all $M_i = 0$ $i = 1, 3$. This would only take place if the object analysed has no conductive material in which case, no eddy currents would be induced and therefore, the magnetic torque would be zero.

3.3.4 Evaluation of the magnetic tensor by FEM

3.3.4.1 General FEM

The Laplace Equation (3.40) with Neumann conditions (3.41) allows for a Finite Element Method (FEM) solution of the kind,

$$\mathbf{K}\boldsymbol{\Psi} - \boldsymbol{f} = 0, \tag{3.69}$$

where $\boldsymbol{\Psi}$ is a vector that contains all the effective potentials of the N nodes in the FEM ψ_i $(i = 1, ..., N)$, $\mathbf{K}$ is the 'stiffness' matrix, $\boldsymbol{f}$ the 'force' vector given by Zienkiewicz [148]. The stiffness

matrix and force vector of each element of the FEM has the form:

$$K_{ij}^{(el)} = \sigma \int_{V^{(el)}} \left(\sum_{k=1}^{3} \frac{\partial N_i^{(el)}}{\partial x_k} \frac{\partial N_j^{(el)}}{\partial x_k} \right) dV, \tag{3.70}$$

$$f_i^{(el)} = \sigma \int_{V^{(el)} \cup \partial V} (\vec{j}_{part} \cdot \vec{n}_v) N_i^{(el)} dA, \tag{3.71}$$

where the superindex (el) denotes an element of the mesh, $V^{(el)}$ is the volume of each element, $N_i^{(el)}$ are the interpolating functions inside each element and $\vec{j}_{part}$ is given by (3.38).

The FEM will give the solution for the scalar function ψ and the current density vector $\vec{j}$ at the Gaussian points of each element,

$$\vec{j}^{(el)}(\vec{r}) = \vec{j}_{part}(\vec{r}) - \sigma \sum_{i=1}^{n} \psi_i^{(el)} \frac{\partial N_i^{(el)}}{\partial \vec{r}} (\vec{r}) \quad \forall \vec{r} \in V^{(el)}, \tag{3.72}$$

where the sum is for the n nodes of the generic element $V^{(el)}$.

The dissipated energy transforms into heat as a result of Joule's effect [94],

$$-\dot{W} = \int \frac{j^2}{\sigma} dV = \vec{\Omega}^t \mathbf{M} \vec{\Omega}, \tag{3.73}$$

where the linear dependence on $\vec{\Omega}$ of the calculated $\vec{j}$ provides us with the postulated quadratic form for $\dot{W}$. It gives also a practical way for computing $\mathbf{M}$.

First, we must solve the FEM for the three cases $\vec{\Omega}^{(1)} = \begin{bmatrix} 1 \\ 0 \\ 0 \end{bmatrix}$, $\vec{\Omega}^{(2)} = \begin{bmatrix} 0 \\ 1 \\ 0 \end{bmatrix}$, $\vec{\Omega}^{(3)} = \begin{bmatrix} 0 \\ 0 \\ 1 \end{bmatrix}$ and then save the corresponding $\vec{j}^{(k)}(\vec{r})$ ($1 \leq k \leq 3$) for the Gaussian points of all the elements.

Thanks to the linearity of the solution with $\vec{\Omega}$ for a given $\vec{\Omega} = \begin{bmatrix} \Omega_1 \\ \Omega_2 \\ \Omega_3 \end{bmatrix} = \sum_{i=1}^{n} \Omega_i \vec{\Omega}^{(i)}$, the solution for $\vec{j}$ can be expressed as (3.43).

Introducing Equation (3.43) in (3.73), M can be computed by numerical Gaussian integration for all the elements as shown in Equation (3.74),

$$M_{kl} = \sum_{(el)} \int_{V^{(el)}} \frac{\vec{j}^{(k)} \cdot \vec{j}^{(l)}}{\sigma} dV. \tag{3.74}$$

3.3.4.2 The approximate frame model

The frame model can be seen as the simplest FEM model for the previously defined problem. This model allows for a clear comprehension of the eddy current phenomenon and for the derivation of an explicit formula to evaluate the magnetic tensor.

First the rigid body must be divided into m bars and n nodes (see Figure 3.1) where each bar has a length L_k, a conductivity σ_k and a cross section A_k. A constitutive constant is assigned to each bar $D_k = \frac{\sigma_k A_k}{L_k}$. The subindex k denotes the number of the bar ($k = 1, ..., m$).
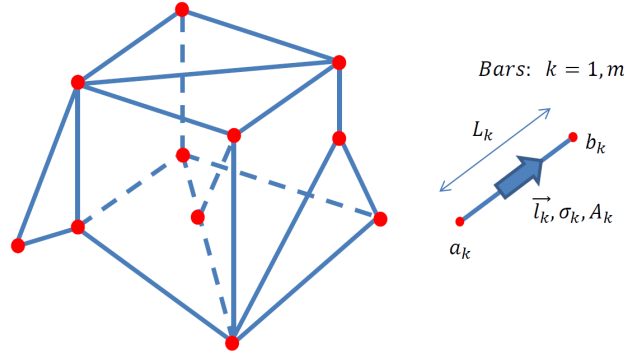
Figure 3.1: FEM based on bars (Frame model).

Each bar has a local coordinate l and a unit vector $\vec{l}_k = \frac{\vec{L}_k}{L_k}$. The position of the centre of gravity of the bar is given by the position vector $\vec{r}_k$. The electric intensity of each bar $J_k = A_k \cdot j_k$ is defined as the product of the electric current density j_k and its cross section A_k. The electric intensities of the m bars can be grouped in one vector as,

$$\mathbf{J} = \begin{bmatrix} J_1 \\ \vdots \\ J_m \end{bmatrix}. \tag{3.75}$$

A scalar function ψ_i (effective potential) is assigned to each node $(i = 1, ..., n)$. ψ_i is a potential function that is defined except for a constant which can be arbitrarily assigned to one of the nodes. The function is set to zero at node n and they can also be grouped in one vector $\mathbf{\Psi}$,

$$\mathbf{\Psi} = \begin{bmatrix} \psi_1 \\ \vdots \\ \psi_{n-1} \\ 0 \end{bmatrix}. \tag{3.76}$$

Using the particular solution (3.38) for the current density vector, the general solution (3.77) for the current density vector is adopted,

$$\vec{j} = \frac{\sigma}{2}(\vec{\Omega} \times \vec{r}) - \sigma \nabla \psi. \tag{3.77}$$

The boundary condition (3.32) allows for the current density vector to be projected in the direction of each bar so that the current stays inside its volume. Therefore, the norm of the current density vector for each bar is equal to

$$j_k = \vec{j}_k \cdot \vec{l}_k = (\frac{\sigma_k}{2}(\vec{\Omega} \times \vec{r}) - \sigma_k \cdot \nabla \psi(\vec{r})) \cdot \vec{l}_k. \tag{3.78}$$

Since $j_k = \frac{J_k}{A_k}$ is constant along the bar, the previous expression can be easily integrated along the length of each bar, giving,

$$J_k = D_k(\frac{1}{2}(\vec{r}_k \times \vec{L}_k) \cdot \vec{\Omega} - \Delta \psi_k). \tag{3.79}$$

The term $\Delta \psi_k = \psi_{bk} - \psi_{ak}$ is the effective potential difference between the nodes a_k and b_k of bar k. A new parameter is defined for each bar $\vec{S}_k = \vec{r}_k \times \vec{L}_k$ and Equation (3.79) can be expressed in matrix form for all the bars,

$$\mathbf{J} = \mathbf{D}(\frac{1}{2}\mathbf{S} \cdot \vec{\Omega} - \mathbf{\Delta\Psi}). \tag{3.80}$$

$\mathbf{J}$ is a vector of dimensions $(m \times 1)$ that contains the intensities of each bar, $\mathbf{D} = diag(D_k)$ is a diagonal matrix of dimensions $(m \times m)$ that contains the constitutive constants for each bar, $\mathbf{S}$ is

a matrix of dimensions $(m \times 3)$ that contains the cross products $\vec{r}_k \times \vec{L}_k$ for each bar and $\boldsymbol{\Delta\Psi}$ is a vector of dimensions $(m \times 1)$ which contains the effective potential difference for each bar. $\mathbf{J}$, $\boldsymbol{\Delta\Psi}$ and $\boldsymbol{\Psi}$ are unknown variables.

Now the continuity equation in all the nodes is imposed, for each node the electric current that goes in, has to go out. This linear system of n equations (one for each node) and m unknown variables (the electric intensity for each bar J_k) can be expressed as shown in (3.81) using a matrix $\mathbf{H}$ that links all the bars. In addition, Equation (3.82) gives the effective potential difference along the bars, $\boldsymbol{\Delta\Psi}$, as a function of the effective potential of each node, $\boldsymbol{\Psi}$.

$$\mathbf{H} \cdot \mathbf{J} = 0, \tag{3.81}$$

$$\boldsymbol{\Delta\Psi} = -\mathbf{H^T}\boldsymbol{\Psi}. \tag{3.82}$$

Combining Equations (3.80, 3.81, 3.82), the solution for the current intensities of the bars is found,

$$\mathbf{J} = \frac{1}{2}(\boldsymbol{\mathcal{I}} - \mathbf{DF})\mathbf{DS}\vec{\Omega}, \tag{3.83}$$

where $\boldsymbol{\mathcal{I}}$ is the identity matrix of dimensions $(m \times m)$ and $\mathbf{F}$ is a symmetric matrix defined as,

$$\mathbf{F} = \mathbf{H^T}(\mathbf{K})^{\mathbf{-1}}\mathbf{H} = \mathbf{H^T}(\mathbf{HDH^T})^{-1}\mathbf{H} = \mathbf{F^T}. \tag{3.84}$$

It must be noted that the system of equations (3.69) does not have a unique solution because the unknown variables Ψ_k are not unequivocally determined and every solution admits the sum of an arbitrary constant. Therefore, the matrix $\mathbf{K}$ is a singular matrix and its inverse, $\mathbf{K^{-1}}$, must be computed as an appropriate pseudoinverse. A *pseudoinverse* of a matrix is a generalisation of the conventional inverse of a matrix when it is singular or even rectangular [149]. The diversity of pseudoinverse matrices is very extensive. In our problem, the pseudoinverse of $\mathbf{K}$ can be easily computed by assigning arbitrarily a zero value to one of the scalar function Ψ_k, for instance, to node n. This way $\mathbf{K}$ can be reduced to $\mathbf{K_{red}}$ by removing the last row and column of the matrix and then compute the inverse of $\mathbf{K_{red}}$. The pseudoinverse of $\mathbf{K}$ will be taken as the inverse of $\mathbf{K_{red}}$ with an additional last row and column of zeros. This numerical process is typical in multitude of FEM problems [148].

Finally, the heat dissipated by all the bars due to Joule's effect is,

$$\vec{\Omega}^t\mathbf{M}\vec{\Omega} = \sum_{k=1}^{m} \frac{J_k^2}{D_k} = \mathbf{J^T}\mathbf{D^{-1}}\mathbf{J} \tag{3.85}$$

and the magnetic tensor is deduced from Equation (3.85) which has the final explicit expression

$$\mathbf{M} = \frac{1}{4}\mathbf{S^T}\mathbf{D}(\boldsymbol{\mathcal{I}} - \mathbf{FD})\mathbf{D^{-1}}(\boldsymbol{\mathcal{I}} - \mathbf{DF})\mathbf{DS}. \tag{3.86}$$

The final formula obtained for the magnetic tensor (3.86) is a compact formula where all the external effects such as the angular velocity vector $\vec{\omega}$ and magnetic field $\vec{B}$, are separated from the geometrical aspects of the body. The magnetic tensor $\mathbf{M}$ contains all the information on the conductive mass distribution of the body. This tensor is a second order tensor which must be computed just once in the integration process of the Euler equations. Once the tensor is known, the evaluation of the torque is a direct formula given by (3.45). All in all, this method gives an alternative to the classical way of analysing the eddy current phenomenon, avoiding the computation of the Poisson equation shown in Equations (3.36, 3.37).

Figure 3.2 summarises in a block diagram the steps to compute the magnetic tensor by means of the frame model theory.
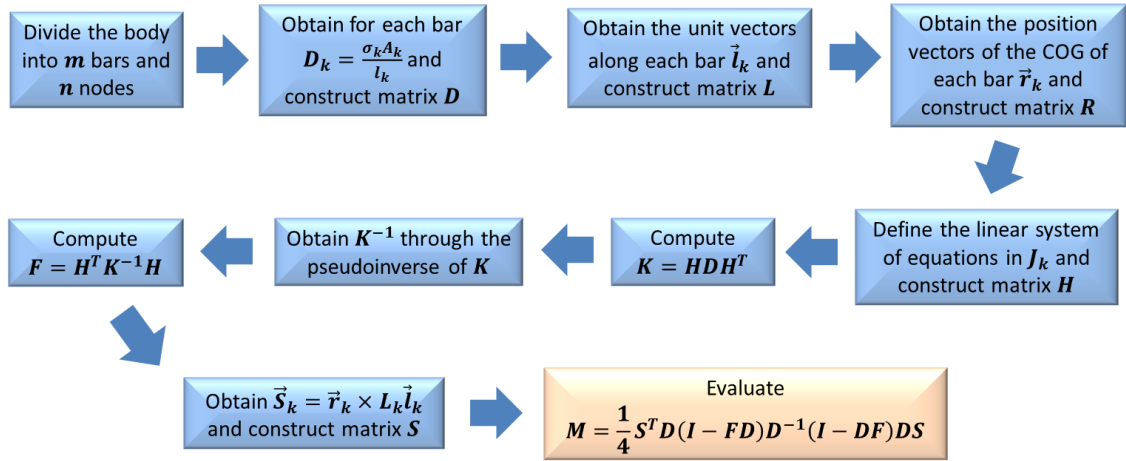
Figure 3.2: Block diagram of the frame model.

3.3.4.3 Frame model implementation example

The example analysed is a rectangular shaped loop which consists of four bars and four nodes (see Figure 3.3). The loop is subjected to a magnetic field $\vec{B} = [B_x, B_y, 0]$ and it is rotating with an angular velocity $\vec{\omega} = [\omega_x, \omega_y, 0]$.
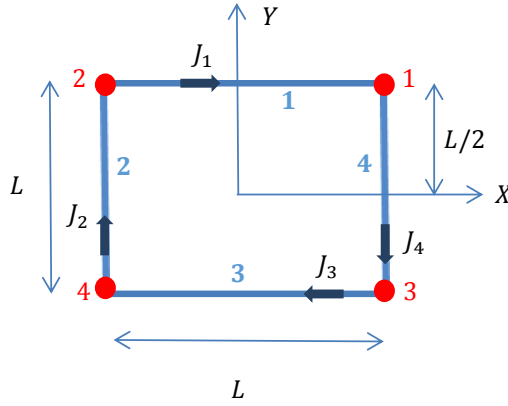
Figure 3.3: Finite element model of the rectangular loop.

The constitutive constant for each bar is $D_k = \frac{\sigma A}{L}$ $(k = 1, 4)$. The constants are put together in matrix $\mathbf{D}$ as follows,

$$\mathbf{D} = \frac{\sigma A}{L} \begin{bmatrix} 1 & 0 & 0 & 0 \\ 0 & 1 & 0 & 0 \\ 0 & 0 & 1 & 0 \\ 0 & 0 & 0 & 1 \end{bmatrix}. \tag{3.87}$$

Then, the unit vectors along each bar $\vec{l}_k$ are grouped in matrix $\mathbf{L}$,

$$\mathbf{L} = \begin{bmatrix} 1 & 0 & 0 \\ 0 & 1 & 0 \\ -1 & 0 & 0 \\ 0 & -1 & 0 \end{bmatrix}. \tag{3.88}$$

Besides, the position vectors of the COG of the bars $\vec{r}_k$ are grouped in matrix $\mathbf{R}$,

$$\mathbf{R} = \frac{L}{2} \begin{bmatrix} 0 & 1 & 0 \\ -1 & 0 & 0 \\ 0 & -1 & 0 \\ 1 & 0 & 0 \end{bmatrix}. \tag{3.89}$$

The linear system of equations in J_k for each node is gathered in the $\mathbf{H}$ matrix,

$$\mathbf{H} = \begin{bmatrix} 1 & 0 & 0 & -1 \\ -1 & 1 & 0 & 0 \\ 0 & -1 & 1 & 0 \\ 0 & 0 & -1 & 1 \end{bmatrix}. \tag{3.90}$$

Now matrix $\mathbf{K}$ is computed as follows,

$$\mathbf{K} = \mathbf{HDH^T} = \frac{\sigma A}{L} \begin{bmatrix} 2 & -1 & 0 & -1 \\ -1 & 2 & -1 & 0 \\ 0 & -1 & 2 & -1 \\ 1 & 0 & -1 & 2 \end{bmatrix}. \tag{3.91}$$

It is observed in Equation (3.91) that matrix $\mathbf{K}$ is singular. Therefore, a pseudoinverse is obtained by first inverting the reduced matrix $\mathbf{K_{red}}$ and then composing $\mathbf{K^{-1}}$.

$$\mathbf{K_{red}} = \frac{\sigma A}{L} \begin{bmatrix} 2 & -1 & 0 \\ -1 & 2 & -1 \\ 0 & -1 & 2 \end{bmatrix}, \tag{3.92}$$

$$\mathbf{K_{red}^{-1}} = \frac{1}{4} \frac{L}{\sigma A} \begin{bmatrix} 3 & 2 & 1 \\ 2 & 4 & 2 \\ 1 & 2 & 1 \end{bmatrix}, \tag{3.93}$$

$$\mathbf{K^{-1}} = \frac{1}{4} \frac{L}{\sigma A} \begin{bmatrix} 3 & 2 & 1 & 0 \\ 2 & 4 & 2 & 0 \\ 1 & 2 & 1 & 0 \\ 0 & 0 & 0 & 0 \end{bmatrix}. \tag{3.94}$$

Once, the inverse of $\mathbf{K}$ is known, the $\mathbf{F}$ matrix is computed,

$$\mathbf{F} = \mathbf{H^T K^{-1} H} = \frac{1}{4} \frac{L}{\sigma A} \begin{bmatrix} 3 & -1 & -1 & -1 \\ -1 & 3 & -1 & -1 \\ -1 & -1 & 3 & -1 \\ -1 & -1 & -1 & 3 \end{bmatrix}. \tag{3.95}$$

Using matrices $\mathbf{R}$ and $\mathbf{L}$, the matrix $\mathbf{S}$ is obtained,

$$\mathbf{S} = -\frac{L^2}{2} \begin{bmatrix} 0 & 0 & 1 \\ 0 & 0 & 1 \\ 0 & 0 & 1 \\ 0 & 0 & 1 \end{bmatrix}. \tag{3.96}$$

And finally the magnetic tensor is,

$$\mathbf{M} = -\frac{AL^3 \sigma}{4} \begin{bmatrix} 0 & 0 & 0 \\ 0 & 0 & 0 \\ 0 & 0 & 1 \end{bmatrix}. \tag{3.97}$$

Moreover, the electric current along each bar is,

$$J_1 = J_2 = J_3 = J_4 = \frac{\sigma A L}{4} [\omega_y B_x - \omega_x B_y]. \tag{3.98}$$

In addition, the total torque that appears on the rectangular frame is,

$$\vec{T} = \sum_{k=1}^{m} -J_k C_k \vec{B} = \frac{\sigma A L^3}{4} \begin{bmatrix} B_y(B_x \omega_y - \omega_x B_y) \\ -B_x(B_x \omega_y - \omega_x B_y) \\ 0 \end{bmatrix}. \tag{3.99}$$

3.3.4.4 N bodies rigidly connected but not electrically connected

Spacecraft contain various metallic components which may not be electrically connected. This may be the case of a satellite which has several metallic propellant tanks which are mutually isolated.

In this section, we will study a rigid body composed of N metallic bodies not electrically connected. It will be demonstrated that the magnetic tensor of the rigid body is equal to the sum of the magnetic tensor of each body.

$$\mathbf{M} = \sum_{i=1}^{N} \mathbf{M_i}. \tag{3.100}$$
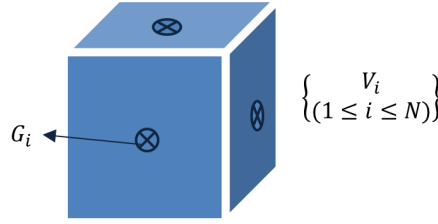
Figure 3.4: Rigid body composed of N bodies.

The overall COG of the rigid body is denoted as G and the COG of each solid is denoted as G_i $(i = 1, N)$. The velocity of a generic point P that belongs to the rigid body is,

$$\vec{V}_P = \vec{V}_G + \vec{\omega} \times \vec{r}_{GP}, \tag{3.101}$$

where $\vec{r}_{GP}$ is the position vector with its origin in G.

Moreover Equation (3.101) can be expressed as,

$$\vec{V}_P = \vec{V}_G + \vec{\omega} \times (\vec{r}_{GG_i} + \vec{r}_{G_iP}) = \vec{V}_{Gi} + \vec{\omega} \times \vec{r}_{G_iP}, \tag{3.102}$$

where $\vec{r}_{G_iP}$ is the position vector with respect to the COG of each solid and $\vec{V}_{Gi}$ is the velocity of each Gi.

For each electrically isolated volume V_i, the continuity equation (3.30) and the boundary condition for $\vec{j}$ (3.32) hold,

$$\nabla \cdot \vec{j} = 0 \ \ \forall P \in V_i, \tag{3.103}$$

$$\vec{j} \cdot \vec{n}_v = 0 \ \ \forall P \in \partial V_i, \tag{3.104}$$

where V_i and ∂V_i are the volume and the contour surface of each body i.

In addition, applying Ohm's law (3.21) to each body,

$$\vec{j} = \sigma(\vec{E} + \vec{V} \times \vec{B}) = \sigma\vec{E} + \sigma(\vec{\omega} \times \vec{r}_{G_iP}) \times \vec{B} + \sigma(\vec{V}_{Gi} \times \vec{B}). \tag{3.105}$$

Assuming that the magnetic field is constant in time and homogeneous $\vec{B}(\vec{r}, t) = \text{constant}$, the curl of Equation (3.105) reduces to,

$$\nabla \times \vec{j} = \sigma \underbrace{\nabla \times \vec{E}}_{=-\frac{\vec{B}}{t}=\vec{0}} + \sigma \underbrace{\nabla \times (\vec{\omega} \times \vec{r}_{G_iP})}_{\vec{\Omega}} \times \vec{B} + \sigma \underbrace{\nabla \times (\vec{V}_{Gi} \times \vec{B})}_{\vec{0}}. \tag{3.106}$$

Therefore, for each solid V_i,

$$\nabla \cdot \vec{j} = 0 \ \ \forall P \in V_i, \tag{3.107}$$

$$\nabla \times \vec{j} = \sigma\vec{\Omega} \ \ \forall P \in V_i, \tag{3.108}$$

$$\vec{j} \cdot \vec{n}_v = 0 \ \ \forall P \in \partial V_i, \tag{3.109}$$

which leads to the solution,

$$\vec{m}_i = \mathbf{M_i}\vec{\Omega}. \tag{3.110}$$

Moreover, the magnetic moment of the overall rigid body follows Equation (3.25)

$$\vec{m} = \frac{1}{2}\int_V \vec{r}_{GP} \times \vec{j}dV = \frac{1}{2}\sum_{i=1}^N \int_{Vi} (\vec{r}_{GG_i} + \vec{r}_{G_iP}) \times \vec{j}dV_i = \frac{1}{2}\sum_{i=1}^N \int_{Vi} \vec{r}_{G_iP} \times \vec{j}dV_i = \sum_{i=1}^N \vec{m}_i, \tag{3.111}$$

because the following integral is zero for each body,

$$\frac{1}{2}\int_{Vi} \vec{r}_{GG_i} \times \vec{j}dV_i = \frac{1}{2}\vec{r}_{GG_i} \times \int_{Vi} \vec{j}dV_i = \vec{0}. \tag{3.112}$$

Taking into account Equation (3.110), then

$$\vec{m} = \mathbf{M}\vec{\Omega} = \sum_{i=1}^N \vec{m}_i = \sum_{i=1}^N \mathbf{M_i}\vec{\Omega} \rightarrow \mathbf{M} = \sum_{i=1}^N \mathbf{M_i}. \tag{3.113}$$

3.3.4.5 Similarities and differences with respect to the inertia tensor

The magnetic tensor bears some similarities to the inertia tensor. The inertia tensor is a symmetric tensor of second order that is derived from the angular momentum as indicated in Section 2.4,

$$\vec{H} = \int_V \rho\vec{r} \times \vec{v}dV = \mathbf{I}\vec{\omega} \rightarrow \mathbf{I} = \int_V \rho(r^2\boldsymbol{\mathcal{I}} - \vec{r}\vec{r}^T)dV. \tag{3.114}$$

A fundamental difference between the inertia and the magnetic tensors is that the inertia tensor depends explicitly on the coordinates $\vec{r}$ while $\mathbf{M}$, given by (3.74), doesn't. As a consequence of this, $\mathbf{I}$ will depend on the selection of the origin of the coordinate system while $\mathbf{M}$ doesn't.

Given a generic coordinate system whose origin is shifted from the COG of the body to a generic point O, the position vectors between both points are related by the following expression,

$$\vec{r}_O = \vec{d} + \vec{r}_G, \tag{3.115}$$

where $\vec{d}$ is the displacement between the COG and the new point O. The inertia tensor expressed in each origin O and G is related by [94],

$$\mathbf{I_O} = \mathbf{I_G} + m(d^2\boldsymbol{\mathcal{I}} - \vec{d}\vec{d}^T). \tag{3.116}$$

However, the magnetic tensor is an invariant under a displacement of the coordinate system's origin. The magnetic moment given by Equation (3.25) is also invariant under a displacement $\vec{r}' = \vec{r} + \vec{d}$,

$$\vec{m}' = \frac{1}{2} \int_V (\vec{r} + \vec{d}) \times \vec{j} dV = \vec{m} + \frac{1}{2} \vec{d} \times \int_V \vec{j} dV = \vec{m}. \tag{3.117}$$

The demonstration of the term $\int_V \vec{j} dV = \vec{0}$ being equal to zero may be found in reference [150].

Moreover, $\vec{\Omega} = \vec{\omega} \times \vec{B}$ is also invariant under a displacement of the coordinate system's origin. Therefore, the magnetic tensor given by Equation (3.44), $\vec{m} = \mathbf{M}\vec{\Omega}$ must also have the same property.

This characteristic of the magnetic tensor together with the property study in Section 3.3.4.4 greatly simplifies its evaluation for a body composed of several metallic components not electrically connected. The magnetic tensor for its component may be evaluated at its COG or a more convenient origin and then sum all the magnetic tensors. Note that the magnetic tensor does not depend on the origin of the coordinate system but it certainly depends on the orientation of the coordinate frame. Therefore, the coordinate frames employed for different components within the same body must all be parallel with respect to each other.

Furthermore, the general expression obtained for $\mathbf{M}$, given by Equation (3.61), used to proof its symmetry is equal to,

$$\mathbf{M} = \mathbf{M^{(part)}} + \mathbf{M^{(hom)}} = \frac{\sigma}{4} \int_V (r^2 \mathcal{I} - \vec{r}\vec{r}^T) dV - \frac{\sigma}{4} \int_{\vec{s} \in \partial V} \int_{\vec{s}' \in \partial V} G(\vec{s}, \vec{s}') \vec{t}(\vec{s}) \vec{t}^T(\vec{s}') dS dS'. \tag{3.118}$$

The solution for $\mathbf{M^{(part)}}$ recalls the general expression to evaluate the inertia tensor. However, note that in this case $\vec{r}$ is the position vector of each incremental volume of the object with respect to its COG. Therefore, assuming that the density and the conductivity is uniform throughout the volume V, the magnetic tensor may be expressed as,

$$\mathbf{M} = \frac{\sigma}{4\rho} \mathbf{I_G} - \frac{\sigma}{4} \int_{\vec{s} \in \partial V} \int_{\vec{s}' \in \partial V} G(\vec{s}, \vec{s}') \vec{t}(\vec{s}) \vec{t}^T(\vec{s}') dS dS'. \tag{3.119}$$

If the boundary condition in Equation (3.51) turns out to be $\frac{\partial \psi}{\partial n_v} = 0$, then the general solution for ψ in Equation (3.50) is $\psi = constant$ [143]. This means that the homogeneous solution vanishes and $\mathbf{M}$ is directly linked to the inertia tensor as,

$$\mathbf{M} = \frac{\sigma}{4\rho} \mathbf{I_G}. \tag{3.120}$$

This situation will only take place for a spherical body, a cylindrical shell when $\vec{\Omega}$ is parallel to its axis of symmetry and a circular flat plate when $\vec{\Omega}$ is perpendicular to its plane.

3.3.5 Analytical solutions of the magnetic tensor and validation of the frame model

The biggest potential of the frame method is that it can be used for any geometrical shape, even when an analytical solution may not be possible due to its complexity. In this subsection, three different geometrical shapes are analysed in order to validate this model; a spherical shell, a cylindrical shell and flat plates.

Moreover, the frame model is used to evaluate the magnetic tensor and the eddy current torque. The numerical and the analytical solutions are compared to assess the accuracy of the frame model for different number of nodes in the mesh. The mesh developed to analyse the three geometrical shapes is based on triangles equally spaced and it has been implemented in MATLAB.

Smith [118] and Ormsby [114] give several analytical solutions of the eddy current torque for certain

canonical shapes and specific orientations of the angular velocity vector $\vec{\omega}$ and the magnetic field $\vec{B}$. These solutions are used to validate the frame model.

The magnetic tensor theory (MTT) allows the torque to be evaluated no matter what the relative orientation of the magnetic field vector is, or the angular velocity vector of the object. Thus, it generalises the solutions given by the previous authors. In addition, in Section 3.3.5.2 an inconsistency found in one of the analytical solutions given by Smith is identified [118].

3.3.5.1 Spherical shell

The well-known analytical solution of the eddy current torque induced on a spherical shell is [114],

$$\vec{T} = \frac{2\pi}{3}\sigma R^4 e(\vec{\omega} \times \vec{B}) \times \vec{B}, \tag{3.121}$$

where R is the radius of the spherical shell, e is its thickness and σ the electrical conductivity.

A frame model is used to design the spherical shell as shown in Figure 3.5.
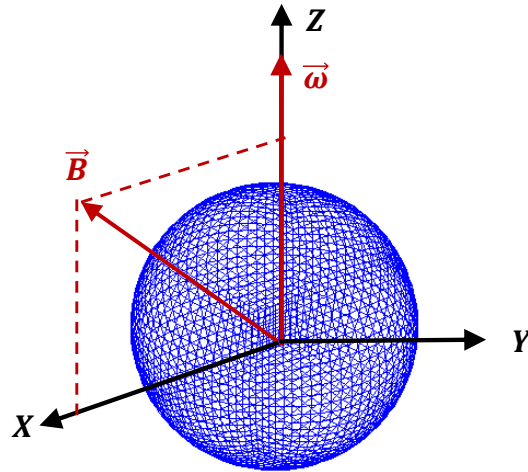
Figure 3.5: Spherical Shell grid.

The torque on the spherical shell is evaluated numerically using the frame model for the following data,

- $\vec{\omega} = [0, 0, 50]$ deg/s

- $\vec{B} = [150, 0, 150]$ µT

- $R = 2$ m

- $e = 0.001$ m

- $\sigma = 35000000$ S/m

Figure 3.6 shows the difference between the torque evaluated using the frame model and the analytical solution given by Ormsby [114]. As the number of nodes is increased, the numerical model becomes more accurate.
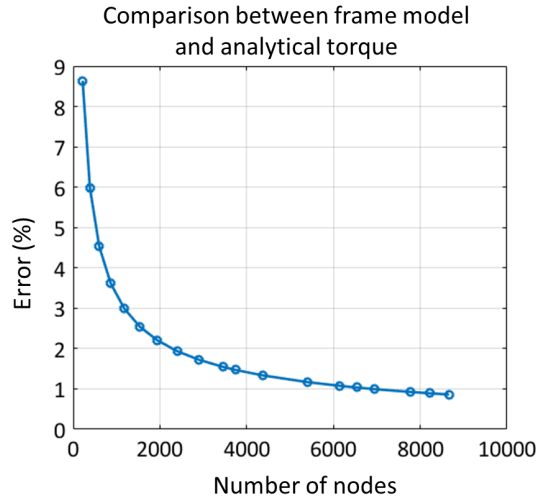
Figure 3.6: Error (%) of the torque obtained with the frame model with respect to the analytical solution for a spherical shell.

The numerical computation was carried out in MATLAB with a computer that has a processor Intel(R) Core(TM) i7-4700MQ CPU of 2.40 GHz and RAM memory of 8 GB. Figure 3.7 indicates the computational time needed to evaluate the magnetic tensor with the frame model and subsequently the torque employing the formula (3.45). For instance, for a grid with 8000 nodes, the error in the evaluation of the torque between the numerical method and the analytical method is approximately a 1% and the computational time needed is approximately 5 minutes.
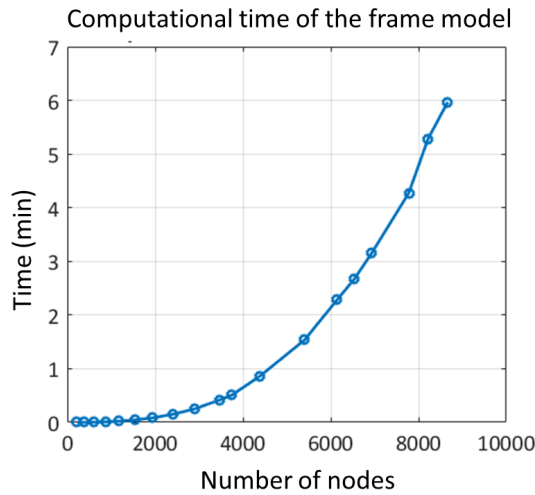
Figure 3.7: Computational time of the frame model to evaluate the torque for a spherical shell.

The analytical solution of the magnetic tensor for a spherical shell has the form,

$$\mathbf{M} = \frac{2\pi}{3} \sigma R^4 e \begin{bmatrix} 1 & 0 & 0 \\ 0 & 1 & 0 \\ 0 & 0 & 1 \end{bmatrix}.$$
(3.122)

Furthermore, the magnetic tensor can also be expressed as a function of the surface area of the

object $S_0 = 4\pi R^2$,

$$\mathbf{M} = \frac{S_0}{6}\sigma R^2 e \begin{bmatrix} 1 & 0 & 0 \\ 0 & 1 & 0 \\ 0 & 0 & 1 \end{bmatrix}. \tag{3.123}$$

Note that a spherical body has a diagonal magnetic tensor with all its diagonal elements equal to each other in all reference frames. This is the only case in which the magnetic torque can be reduced to a formula of the kind,

$$\vec{T}_{sphere} = (\mathbf{M}\vec{\Omega}) \times \vec{B} = k\vec{\Omega} \times \vec{B}, \tag{3.124}$$

where $k = \frac{2\pi}{3}\sigma R^4 e$ is a constant that depends on the physical properties of the body [95, 103]. For asymmetric bodies, a diagonal form of the magnetic tensor can always be found as the magnetic tensor is a real symmetric matrix [144]. However, the components of the diagonal won't, in general, be equal to each other as shown in Subsections 3.3.5.2 and 3.3.5.3.

3.3.5.2   Cylindrical shell with open ends

Smith [118] published the analytical solution in 1962 of the eddy current torque induced on a cylindrical shell with open ends that is rotating about its axis of symmetry. The cylinder is assumed to be rotating about the Z axis with a rotational speed $\vec{\omega} = \omega\vec{k}$ and it is subject to a magnetic field $\vec{B} = B_x\vec{i} + B_z\vec{k}$. The analytical expression of the torque given by Smith is equal to,

$$\vec{T} = \pi\sigma B_x\omega R^3 eL(1 - \frac{2R}{L}tanh(\frac{L}{2R}))(B_x\vec{i} - B_z\vec{k}), \tag{3.125}$$

where R is the radius of the cylinder, L is its length, e is its thickness and σ the electrical conductivity.

A frame model is used to design the cylindrical shell as shown in Figure 3.8, where the Z axis is the axis of symmetry of the cylinder.
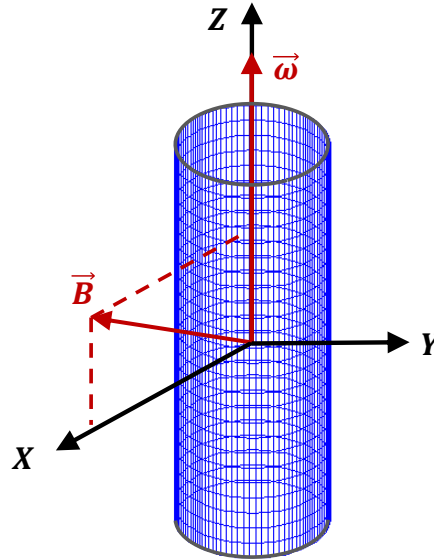
Figure 3.8: Cylindrical Shell grid.

The torque on the cylindrical shell is evaluated numerically using the frame model for the following data,

- $\vec{\omega} = [0, 0, 50]$ deg/s

- $\vec{B} = [150, 0, 50]$ μT

- $R = 1.33$ m

- $L = 7.372$ m

- $e = 0.001$ m

- $\sigma = 35000000$ S/m

Figure 3.9 shows the difference between the torques evaluated using the frame model and the analytical solution given by Smith [118]. As the number of nodes is increased, the numerical model becomes more accurate.
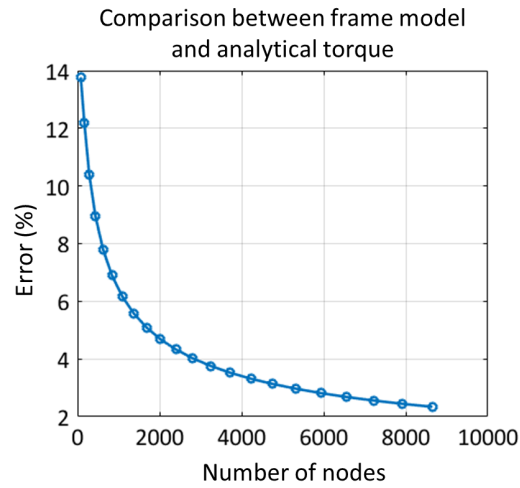
Figure 3.9: Error (%) of the torque obtained with the frame model with respect to the analytical solution for a cylindrical shell.

Figure 3.10 indicates the computational time needed to evaluate the magnetic tensor with the frame model and subsequently the torque employing the formula (3.45).
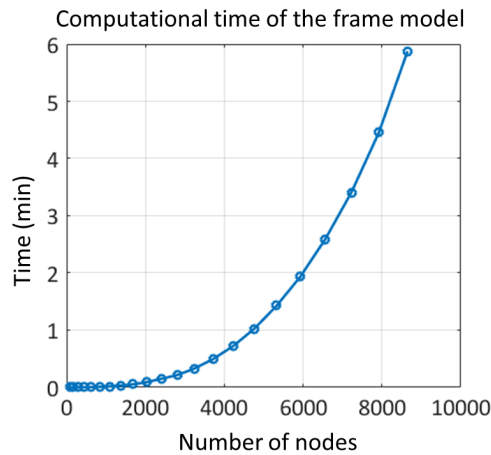
Figure 3.10: Computational time of the frame model to evaluate the torque for a cylindrical shell.

The analytical solution of the magnetic tensor for a open cylindrical shell with its axis of symmetry

parallel to the Z axis has been computed and it has the form,

$$\mathbf{M} = \pi \sigma R^3 eL \begin{bmatrix} \gamma & 0 & 0 \\ 0 & \gamma & 0 \\ 0 & 0 & \frac{1}{2} \end{bmatrix}, \tag{3.126}$$

where $\gamma = 1 - \frac{2R}{L} tanh\frac{L}{2R}$. The components M_{11} and M_{22} are based on the formula (3.125) given by Smith while M_{33} is obtained below analytically. Expression (3.127) generalises the solution given by Smith and it enables the torque to be evaluated for any given direction of the angular velocity vector and the magnetic field.

The magnetic tensor may also be expressed as a function of the surface area of the cylinder $S_0 = 2\pi RL$ as follows,

$$\mathbf{M} = \frac{S_0}{2} \sigma R^2 e \begin{bmatrix} \gamma & 0 & 0 \\ 0 & \gamma & 0 \\ 0 & 0 & \frac{1}{2} \end{bmatrix}. \tag{3.127}$$

In order to evaluate M_{33}, the particular solution (3.38) is used to solve Equations (3.30, 3.31, 3.32) for the configuration shown in Figure (3.11).
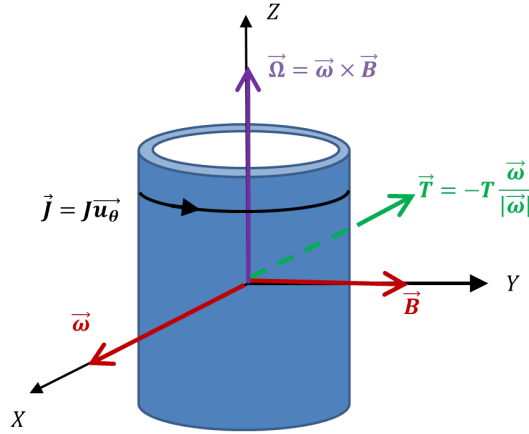
Figure 3.11: Open cylindrical shell rotating along an axis perpendicular to the axis of symmetry.

In this case, the particular solution $\vec{j}_{part}$ is $\vec{j} = j_\theta \vec{u_\theta} = \frac{\sigma}{2}\Omega r \vec{u_\theta}$. This leads to the following Laplace equation in ψ with homogeneous Neumann boundary conditions,

$$\nabla^2 \psi = 0 \ \ \forall P \in V, \tag{3.128}$$

$$\frac{\partial \psi}{\partial n_v} = 0 \ \ \forall P \in \partial V, \tag{3.129}$$

which has the solution $\psi = constant$ [143]. Then, taking into account that the thickness of the cylindrical wall is very small ($e << r$), the current intensity vector can be expressed as $j_\theta = \frac{\sigma}{2}\Omega R$.

Now, in order to evaluate M_{33}, Equation (3.74) is employed with $\vec{\Omega}^{(3)} = \begin{bmatrix} 0 \\ 0 \\ 1 \end{bmatrix}$ and $\vec{j}^{(3)} = \frac{\sigma}{2}R\vec{u_\theta}$,

$$M_{33} = \int_V \frac{\vec{j}^{(3)} \cdot \vec{j}^{(3)}}{\sigma} dV = \left(\frac{\sigma R}{2}\right)^2 \frac{V}{\sigma} = \frac{\pi}{2}\sigma R^3 eL. \tag{3.130}$$

Moreover, an inconsistency found in one of the analytical solutions given by Smith [118] is highlighted. The case depicted in Figure (3.11) corresponds to the case presented by Smith in Section

"Thin-Wall Tumbling Cylinder" for the parameters $\mu = \frac{\pi}{2}$ and $\lambda = \frac{\pi}{2}$. Using Smith's formulation, the current density vector would be zero (Equations (54, 55) in [118]) and also the torque (Equations (56, 57) in [118]). This would lead for a null value for M_{33} which is not possible. This occurs because one the hypothesis made by Smith at the beginning of Section "Thin-Wall Tumbling Cylinder" is not correct. The curl of the current density vector in cylindrical coordinates is,

$$(\nabla \times \vec{j})_r = \frac{1}{r}\frac{\partial j_z}{\partial \theta} - \frac{\partial j_\theta}{\partial z}, \tag{3.131}$$

$$(\nabla \times \vec{j})_\theta = \frac{\partial j_r}{\partial z} - \frac{\partial j_z}{\partial r} \approx -\frac{\partial j_z}{\partial r}, \tag{3.132}$$

$$(\nabla \times \vec{j})_z = \frac{1}{r}\frac{\partial(rj_\theta)}{\partial r} - \frac{1}{r}\frac{\partial j_r}{\partial \theta} \approx \frac{1}{r}\frac{\partial(rj_\theta)}{\partial r}. \tag{3.133}$$

Smith neglects $(\nabla \times \vec{j})_\theta$ and $(\nabla \times \vec{j})_z$ in order to obtain the current density vector. This leads to $\vec{j} = \vec{0}$ for the configuration depicted in (3.11). However, in this case, $(\nabla \times \vec{j})_z = \sigma\Omega_z$ which leads to a constant current j_θ and a torque that opposes the angular velocity. Therefore, $(\nabla \times \vec{j})_z$ can not be neglected.

3.3.5.3 Flat plates

The eddy current torque induced on a circular flat plate can be computed analytically using perturbations theory. Cylindrical coordinates (ρ, θ, z) are used to locate a generic point of the flat plate (see Figure 3.12). This plate is assumed to have a conductivity σ, a thickness e, an external radius a and an internal radius b.
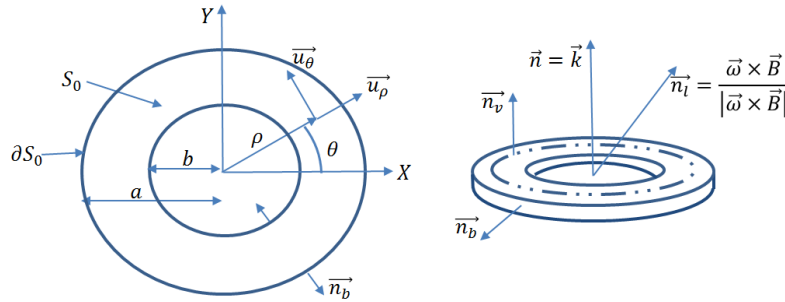
Figure 3.12: Cylindrical coordinates and normal vectors to the circular flat plate.

The particular solution (3.38) is used,

$$\vec{j}_{part} = \frac{\sigma}{2}\vec{\Omega} \times \vec{r} = \frac{\sigma}{2}\Omega\vec{n}_l \times (\rho\vec{u}_\rho + z\vec{k}) =$$
$$\frac{\sigma\Omega}{2}(zn_{l\theta}\vec{u}_\rho + (\rho n_{lz} - zn_{l\rho})\vec{u}_\theta - \rho n_{l\theta}\vec{k}), \tag{3.134}$$

where the vector $\vec{n}_l$ is defined as,

$$\vec{n}_l = \vec{\Omega}/\left|\vec{\Omega}\right| = n_{l\rho}\vec{u}_\rho + n_{l\theta}\vec{u}_\theta + n_{lz}\vec{k}. \tag{3.135}$$

As explained in Section (3.3.2), this particular solution leads to the Laplace Equation (3.40) with Neumann boundary (3.41) conditions for the scalar function ψ. The solution of the Laplace equation can be expressed as (3.136), assuming that the coordinate $z \to 0$.

$$\psi(\rho, \theta, z) = \psi_0(\rho, \theta) + z\psi_1(\rho, \theta) + ... \tag{3.136}$$

Neglecting the terms of order $o(z^2)$, the following Laplace equation is reached,

$$\nabla \psi^2 = \frac{1}{\rho} \frac{\partial}{\partial \rho} \left(\rho \frac{\partial \psi}{\partial \rho} \right) + \frac{1}{\rho^2} \frac{\partial^2 \psi}{\partial \theta^2} + \frac{\partial^2 \psi}{\partial z^2} = \nabla_{\rho\theta} \psi_0 + z \nabla_{\rho\theta} \psi_1 = 0. \tag{3.137}$$

Now, the boundary conditions are imposed. At $z = \pm \frac{e}{2}$, $\vec{j} \cdot \vec{k} = 0$, therefore,

$$\mp \psi_1 \pm \frac{\sigma \Omega}{2} (\vec{n}_l \times \vec{r}) \cdot \vec{k} = 0 \rightarrow$$

$$\rightarrow \mp \psi_1 \mp \frac{\sigma \Omega}{2} \vec{n}_l \cdot \rho \vec{u}_\theta = 0 \rightarrow \psi_1 = -\frac{\Omega \rho}{2} n_{l\theta}. \tag{3.138}$$

Consequently, up to first order infinitesimal terms, ψ is equal to,

$$\psi = \psi(\rho, \theta, z) = \psi_0(\rho, \theta) - z \frac{\Omega \rho}{2} n_{l\theta} \tag{3.139}$$

and $\vec{j}$ is equal to,

$$\vec{j} = -\sigma \frac{\partial \psi_0}{\partial \rho} \vec{u}_\rho + \sigma \left[-\frac{1}{\rho} \frac{\partial \psi_0}{\partial \theta} + \frac{\Omega}{2} (\rho n_{lz} - z n_{l\rho}) \right] \vec{u}_\theta. \tag{3.140}$$

At $\rho = (a, b)$, the condition $\vec{j} \cdot \vec{u}_\rho = 0$ must be met, which leads to the following boundary condition for ψ_0,

$$\frac{\partial \psi_0}{\partial \rho} = 0 \quad at \; \rho = a, b. \tag{3.141}$$

Equation (3.137) results in the following equation for ψ_0,

$$\left(\frac{\partial^2}{\partial \rho^2} + \frac{1}{\rho} \frac{\partial}{\partial \rho} + \frac{1}{\rho^2} \frac{\partial^2}{\partial \theta^2} + \frac{\partial^2}{\partial z^2} \right) \left[\psi_0(\rho, \theta) - \frac{z \rho}{2} \Omega n_{l\theta} \right] = 0. \tag{3.142}$$

Since $n_{l\theta} = -n_{lx} \sin \theta + n_{ly} \cos \theta$ is dependent on θ, Equation (3.142) reduces to the two-dimensional Laplace equation in ψ_0 with homogeneous Neumann boundary conditions,

$$\frac{\partial^2 \psi_0}{\partial \rho^2} + \frac{1}{\rho} \frac{\partial \psi_0}{\partial \rho} + \frac{1}{\rho^2} \frac{\partial^2 \psi_0}{\partial \theta^2} = 0, \tag{3.143}$$

$$\frac{\partial \psi_0}{\partial \rho} = 0 \; for \; \rho = a, b. \tag{3.144}$$

The solution for (3.143, 3.144) is $\psi_0 = constant$ [143]. Therefore, the complete function ψ is,

$$\psi = \psi(\rho, \theta, z) = constant - z \frac{\lambda \rho}{2} n_{l\theta}. \tag{3.145}$$

Using the solution obtained for ψ, the electric current density vector can be easily computed as follows,

$$\vec{j} = \frac{\sigma \Omega}{2} \vec{n}_l \times \vec{r} - \sigma \nabla(\psi) = \frac{\sigma \Omega}{2} [2 z n_{l\theta} \vec{u}_\rho + (\rho n_{lz} - 2 z n_{l\rho}) \vec{u}_\theta]. \tag{3.146}$$

Taking into account that $z \rightarrow 0$, the solution reached for the current density vector, up to first order terms, for a circular flat plate is,

$$\vec{j} = \frac{\sigma}{2} (\vec{\Omega} \cdot \vec{n}) \rho \vec{u}_\theta, \tag{3.147}$$

and the torque for the circular flat plate can be obtained as,

$$\vec{T} = \int \vec{r} \times (\vec{j} \times \vec{B}) dV = \sigma \frac{\pi R^4 e}{8} (\vec{\Omega} \cdot \vec{n}) \cdot (\vec{n} \times \vec{B}). \tag{3.148}$$

The magnetic tensor for a circular flat plate is derived from the torque as follows,

$$\mathbf{M} = \sigma \frac{\pi R^4 e}{8} \vec{n} \cdot \vec{n}^T = \sigma \frac{\pi R^4 e}{8} \begin{bmatrix} 0 & 0 & 0 \\ 0 & 0 & 0 \\ 0 & 0 & 1 \end{bmatrix}. \tag{3.149}$$

It can be easily verified that the preceding mathematical development shows a clear similarity with the Saint Venant torsion theory for beams [151]. As a result of this, the magnetic tensor can be easily generalised for other geometries by introducing a constant inherent to the specific geometry of the plate C_T. This constant corresponds to the torsional rigidity of St Venant. The Saint Venant torsion theory of beams is governed by a Laplace equation with Neumann boundary conditions, where the boundary conditions only differ in a constant factor from our Equations (3.40,3.41) [151]. By comparing the exact solution of Saint Venant theory for a beam of circular section and our circular flat plate, a factor $e/4$ needs to be introduced in our solution for the magnetic tensor. Finally, the general solution of the magnetic tensor for a flat plate can be expressed as,

$$\mathbf{M} = \frac{1}{4} \sigma e C_T \vec{n} \cdot \vec{n}^T. \tag{3.150}$$

Figure 3.13 gives the C_T constants computed for different flat plate shapes [151].

$$S_0 = \pi a^2, \quad \frac{C_T}{4S_0} = \frac{a^2}{8}$$

$$S_0 = \pi a b, \quad \frac{C_T}{4S_0} = \frac{b^2}{4(1 + b^2/a^2)}$$

$$2b < 2a \quad S_0 = 4ab, \quad \frac{C_T}{4S_0} \approx \frac{b^2}{3\left(1 + 1.38\left(\frac{b^2}{a^2}\right)^{1.6}\right)}$$

$$S_0 = 4a^2, \quad \frac{C_T}{4S_0} = \frac{a^2}{7.11}$$
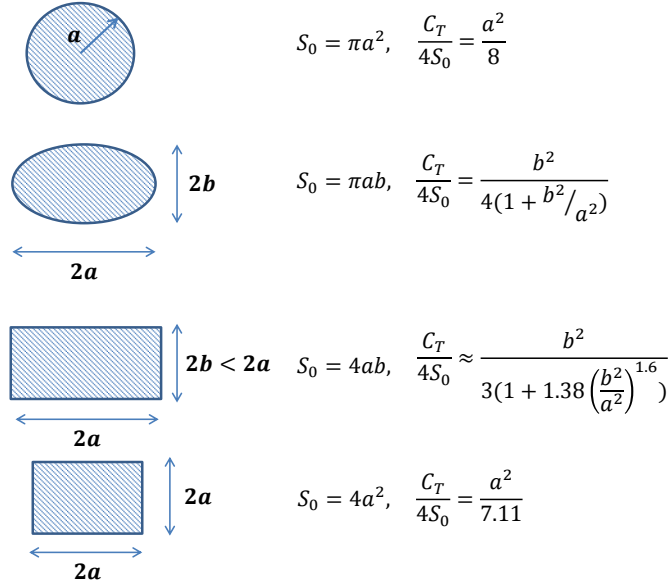
Figure 3.13: Flat Plates constants to evaluate the magnetic tensor.

In the following example, the eddy currents induced on a square flat plate are analysed using the frame model and the analytical solution obtained in this section. The flat plate considered has dimensions of $L \times L = 1 \times 1$ m, a thickness of $e = 0.001$ m and a conductivity of 35000000 S/m.

The analytical solution for the magnetic tensor is,

$$\mathbf{M_{analytic}} = \frac{1}{4} \sigma e \frac{L^4}{7.11} \begin{bmatrix} 0 & 0 & 0 \\ 0 & 0 & 0 \\ 0 & 0 & 1 \end{bmatrix} = \begin{bmatrix} 0 & 0 & 0 \\ 0 & 0 & 0 \\ 0 & 0 & 1.23 \cdot 10^3 \end{bmatrix} \text{S} \cdot \text{m}^4. \tag{3.151}$$

The instant of time chosen corresponds to the plate located in the XY plane, rotating with an angular velocity $\vec{\omega} = 0.87\vec{i}$ rad/s and subject to a magnetic field $\vec{B} = 150\vec{j}$ μT. The analytical solution for the torque is,

$$\vec{T}_{analytic} = (\mathbf{M_{analytic}} \, \vec{\Omega}) \times \vec{B} = -2.416 \cdot 10^{-5} \, \vec{i} \text{ N} \cdot \text{m}. \tag{3.152}$$

Just as an example, a finite element model with 12321 nodes is developed. The mesh selected corresponds to the maximum amount of virtual memory that can be allocated by MATLAB to compute the tensor. The magnetic tensor that is obtained using the frame model is equal to,

$$\mathbf{M_{frames}} = \begin{bmatrix} 0 & 0 & 0 \\ 0 & 0 & 0 \\ 0 & 0 & 1.275 \cdot 10^3 \end{bmatrix} \mathrm{S} \cdot \mathrm{m}^4. \tag{3.153}$$

and the magnetic torque is equal to,

$$\vec{T}_{frames} = (\mathbf{M_{frames}} \, \vec{\Omega}) \times \vec{B} = -2.503 \cdot 10^{-5} \, \vec{i} \, \mathrm{N} \cdot \mathrm{m}. \tag{3.154}$$

The torque obtained with the frame model theory is slightly higher. This makes sense because the current moves along a longer circuit as shown in Figure 3.14.
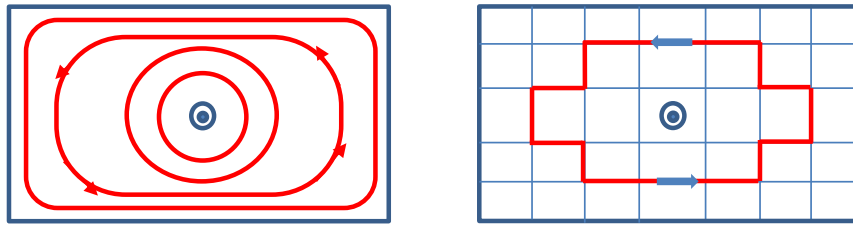
Figure 3.14: The left figure is the exact solution of the currents profile. The right figure is the approximate solution obtained with the frame model.

In addition, the magnetic tensor and the torque were evaluated for different number of nodes of the mesh. Figure 3.15 shows how the error of the solution increases as the size of the grid decreases.
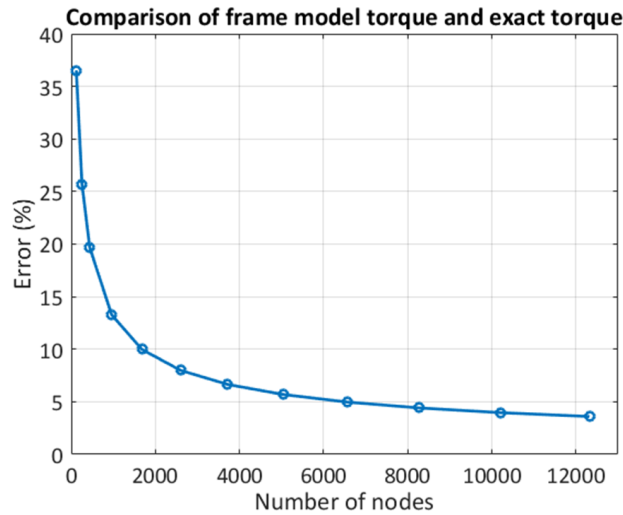
Figure 3.15: Comparison of the solution obtained with the analytical model and the frame model for a flat plate.

Finally, Figure 3.16 indicates the computational time needed to evaluate the magnetic tensor with the frame model and subsequently the torque employing the formula (3.45).
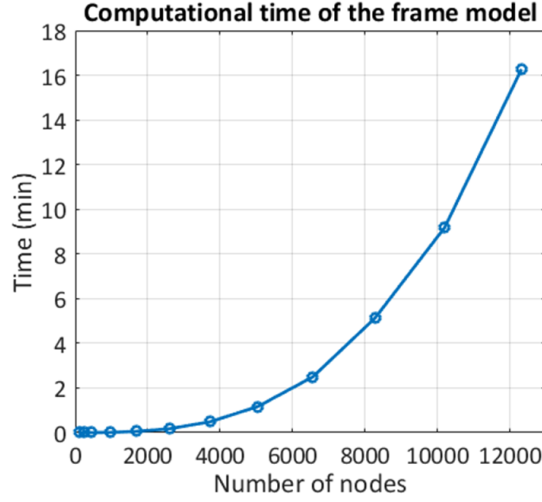
Figure 3.16: Computational time of the frame model to evaluate the torque for a flat plate.

3.3.6 Numerical errors due to uncertainties in the rotational velocity vector and the magnetic field

The analytical and numerical solutions studied in Section 3.3.5, analysed the error that appears due to inaccuracies in the computation of the magnetic tensor. In this Section, what happens to the eddy current torque is analysed if inaccuracies exist in the angular velocity or the magnetic field vectors.

It was shown in Section (3.3.3) that the derivative of the kinetic energy is always negative or zero due to the dissipative effect of the eddy currents. Now it is assumed that there exists a perturbation in Ω which has a null mean value $\overline{\delta\Omega} = 0$:

$$\Omega(t) = \overline{\Omega}(t) + \delta\Omega, \tag{3.155}$$

where $\overline{\Omega}(t)$ is the exact value of Ω and $\delta\Omega$ is the perturbation. If $\overline{\delta\Omega} = 0$ then the next relationship applies,

$$\overline{\Omega(t)^2} = (\overline{\Omega}(t))^2 + \overline{\delta\Omega^2}. \tag{3.156}$$

Equation (3.156) is demonstrated below,

$$\Omega(t)^2 = (\overline{\Omega}(t))^2 + \delta\Omega^2 + 2\overline{\Omega}(t)\delta\Omega, \tag{3.157}$$

$$\overline{\Omega(t)^2} = (\overline{\Omega}(t))^2 + \overline{\delta\Omega^2} + 2\overline{\Omega}(t)\overline{\delta\Omega} = (\overline{\Omega}(t))^2 + \overline{\delta\Omega^2}. \tag{3.158}$$

In the principal directions of M, the kinetic energy can be expressed as,

$$\dot{K} = -\sum_{i=1}^{3} M_i {\Omega_i}^2. \tag{3.159}$$

Taking into account that the magnetic matrix is constant, the mean value of $\dot{K}$ acquires the form,

$$\overline{\dot{K}} = -\sum_{i=1}^{3} M_i \overline{{\Omega_i}^2} = -\sum_{i=1}^{3} M_i \overline{\Omega}_i^2 - \sum_{i=1}^{3} M_i \overline{{\delta\Omega_i}^2}. \tag{3.160}$$

As the eigenvalues of $\mathbf{M}$ are positive or zero, any perturbing effect on $\overline{K}$ due to $\vec{\omega}$ or $\vec{B}$ will always add a negative component and therefore, it will increase the absolute value of kinetic energy. This means that any error in the angular velocity or the magnetic field will translate to an increase of

the dissipative effect, overestimating the eddy current torque.

A simplification that is usually done when analysing the effect of the Earth's magnetic field on spacecraft is to obtain an average value of the magnetic field per orbit. For instance, this simplification is done by Smith [119] when analysing the time of decay of the rotational speed due to this effect. It must be taken into account that this will increase the dissipative effect resulting in a smaller time of decay, while the real time will be longer. Other sources of error may be numerical errors in the integration process of the evolution of the angular velocity vector which will also lead to this effect.

3.3.7 Non-uniformity of the magnetic field

Up to now in Section 3.3, the magnetic field has been assumed to be homogeneous and constant in time $\vec{B}(\vec{r}, t) = constant$. This approximation can be used, for instance, in order to analyse the eddy currents induced on spacecraft due to the Earth's magnetic field. The size of the spacecraft is negligible compared to the size of the Earth and the magnetic field created by the Earth can be assumed to be homogeneous inside the satellite.

Under these assumptions, the net force generated on the object is zero,

$$\vec{F} = \int \vec{j} \times \vec{B} \, dV = (\int \vec{j} dV) \times \vec{B} = \vec{0}. \tag{3.161}$$

The term $\int \vec{j} dV = \vec{0}$ can be proved to be zero by using the continuity equation $\nabla \cdot \vec{j} = 0$ as demonstrated by Boyer in [150].

However, there are cases in which the non-uniformity of the magnetic field can not be neglected. This is the case of the 'eddy brake' method presented in Chapter 5. This is an active contactless de-tumbling method carried out by a chaser spacecraft which has a magnetic coil pointing towards the rotating target object that needs to be de-tumbled. Eddy currents are generated on the metallic components of the target which create dissipative torques that reduce its angular velocity. In this case, the magnetic field can no longer be assumed to be uniform inside the target and therefore, the theory developed in Section 3.3 needs some additional considerations.

First of all, a reduction in the efficiency of the de-tumbling process will take place and this is quantified, in an approximate way, by introducing an efficiency factor on the magnetic tensor (see Section 3.3.7.1).

Secondly, net forces between the chaser and the target will appear. A direct formula based on the magnetic tensor to evaluate this force is developed in Section 3.3.7.2.

3.3.7.1 Effective magnetic tensor

In order to analyse the non-uniformity of the magnetic field, an effective magnetic tensor $\mathbf{M_{eff}}$ is defined under several simplifying hypotheses explained below. $\mathbf{M_{eff}}$ is related to the magnetic tensor M expressed in its principal axes through some coefficients μ_{effi}:

$$\mathbf{M_{eff}} = \begin{bmatrix} \mu_{eff1} M_1 & 0 & 0 \\ 0 & \mu_{eff2} M_2 & 0 \\ 0 & 0 & \mu_{eff3} M_3 \end{bmatrix}. \tag{3.162}$$

The following simplifications are taken into account:

1. The gradient of the magnetic field is assumed to be small enough to linearise the magnetic field $\vec{B}$ around the COG of the body,

$$\vec{B} = \vec{B}_G + \left. \frac{\partial \vec{B}}{\partial \vec{r}} \right|_G (\vec{r} - \vec{r}_G). \tag{3.163}$$

Using Equation (3.163), up to a first order approximation, the magnetic moment is expressed as:

$$\vec{m} = \mathbf{M_{eff}}(\vec{\omega} \times \vec{B}_G) = \mathbf{M_{eff}}\vec{\Omega}_G, \tag{3.164}$$

where B_G is the magnetic field at the COG of the body.

2. It will be assumed that $\vec{\Omega} = \vec{\omega} \times \vec{B} = \Omega\vec{n}$ is oriented along one of the principal directions of the magnetic tensor so that,

$$\vec{m} = M_{\text{effi}}\vec{\Omega}_G = \mu_{\text{effi}}M_i\vec{\Omega}_G, \tag{3.165}$$

being M_{effi} one of the eigenvalues of the effective magnetic tensor.

3. It is assumed that the geometry of the target body is such that the distribution of the eddy current loops lie on flat planes ($\vec{n} =$uniform).

The second and third hypotheses are true for a spherical shell for any orientation of $\vec{\Omega}$. Therefore, the proposed analysis may be adequate for quasi-spherical shells. More specifically, it will be considered in the following mathematical development that the target body is an ellipsoidal shell with its three semi-axes similar in size, subject to a magnetic field $\vec{B}(\vec{r})$ symmetric with respect to one of the planes of symmetry of the ellipsoid (see Figure 3.17).

The magnetic flux φ given by Faraday's law is [112],

$$\varphi = \iint_{S_0} \vec{n} \cdot \vec{B} dS_0 = \vec{n} \cdot \iint_{S_0} \vec{B} dS_0 = S_0\vec{n} \cdot \vec{B}_{\text{eff}}, \tag{3.166}$$

where $\vec{B}_{\text{eff}} = \frac{1}{S_0} \iint_{S_0} \vec{B} dS_0$.
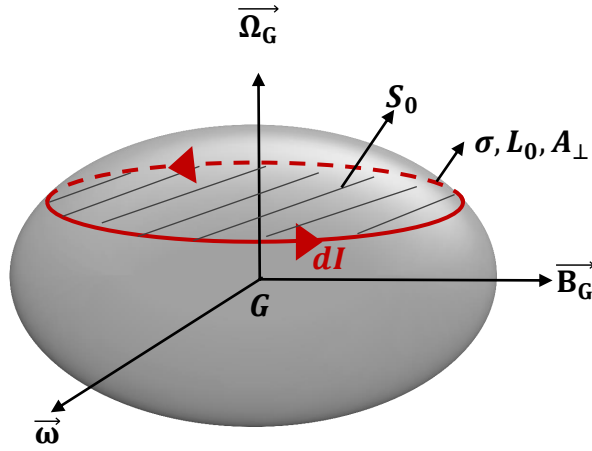
Figure 3.17: Ellipsoid quasi-spherical shell.

Assuming a non-uniform magnetic field but constant in time, $\dot{\varphi}$ is obtained as:

$$\dot{\varphi} = \iint_{S_0} (\vec{\omega} \times \vec{n}) \cdot \vec{B} dS_0 =$$
$$= -(\vec{n} \times \vec{\omega}) \cdot \iint_{S_0} \vec{B} dS_0 = -S_0\vec{n}(\vec{\omega} \times \vec{B}_{\text{eff}}) = -S_0\Omega_{n,\text{eff}}. \tag{3.167}$$

The vector $\vec{n}$ has the direction $\vec{n}_G = \frac{\vec{\Omega}_G}{\Omega_G}$ where $\vec{\Omega}_G = \vec{\omega} \times \vec{B}_G$ and G is the COG of the body. Two new variables are defined $\Omega_{n,\text{eff}}$ and ρ_{eff} as,

$$\Omega_{n,\text{eff}} = \vec{n}_G \cdot (\vec{\omega} \times \vec{B}_{\text{eff}}), \tag{3.168}$$

$$\rho_{\text{eff}} = \frac{\Omega_{n,\text{eff}}}{\Omega_G}. \tag{3.169}$$

Lenz's Law establishes the relationship between the electromotive force (e.m.f) and the magnetic flux (3.170). Considering this relationship and using Equation (3.167), the e.m.f. can be written as,

$$\mathcal{E} = -\frac{d\varphi}{dt} = S_0\Omega_{n,\text{eff}}. \tag{3.170}$$

In addition, Ohm's Law gives the relationship between the e.m.f. and the current intensity I for one conductive circuit, as voltage divided by the resistance of the circuit,

$$I = \frac{\mathcal{E}}{L_0/\sigma A_\perp} = \mathcal{E}\sigma\frac{V_0}{L_0^2} = \sigma\frac{S_0 V_0}{L_0^2}\Omega_{n,\text{eff}}, \tag{3.171}$$

where $A_\perp$ is the cross section of the electrical circuit, L_0 is its longitude and $V_0 = A_\perp L_0$ is its volume.

Now, considering $A_\perp$ and therefore, V_0 as infinitesimal magnitudes, the intensity of each eddy current loop, can be expressed as,

$$dI = \sigma\frac{S_0}{L_0^2}\Omega_{n,\text{eff}}dV_0 \tag{3.172}$$

and the induced magnetic moment in each eddy current loop is,

$$d\vec{m} = S_0\vec{n}_G dI = \sigma\frac{S_0^2}{L_0^2}dV_0\rho_{\text{eff}}\vec{\Omega}_G = \frac{\sigma}{4}R_0^2\rho_{\text{eff}}dV_0\vec{\Omega}_G, \tag{3.173}$$

where $R_0 = \frac{2S_0}{L_0}$ is the mean radius of the differential eddy current loop. Integrating the magnetic moment over the whole volume and taking into account Equation (3.164), each eigenvalue of the effective magnetic tensor acquires the form,

$$M_{\text{effi}} = \frac{\sigma}{4}\int_{V0}\rho_{\text{eff}}R_0^2dV_0 = \mu_{\text{effi}}M_i. \tag{3.174}$$

Since M_i must be obtained when $\rho_{\text{eff}} = 1$, the correction factor μ_{eff} for each eigenvalue of the magnetic tensor M can be written as,

$$\mu_{\text{eff}} = \frac{M_{\text{effi}}}{M_i} = \frac{\int_{V_0}\rho_{\text{eff}}R_0^2dV_0}{\int_{V_0}R_0^2dV_0}. \tag{3.175}$$

The factor ρ_{eff} defined in (3.169) is developed further in (3.176). It must be noted that when computing $\vec{B}_{\text{eff}} \times \vec{n}_G$ in each S_0, only the components of $\vec{B}_{\text{eff}}$ parallel to S_0 are necessary, since the normal to the surface S_0 is precisely $\vec{n}_G$. In addition, the average of $\vec{B}_{\text{eff}} \times \vec{n}_G$ perpendicular to $\vec{B}_G$ can be considered null due to the hypotheses considered. This condition occurs because the magnetic field and the object are symmetric with respect to the plane $O_c - G - O$, where O_c is the centre of the magnetic coil and O is the COG of the surface S_0 (see Figure 3.18).

$$\rho_{\text{eff}} = \frac{\Omega_{n,\text{eff}}}{\Omega_G} = \frac{\vec{n}_G \cdot (\vec{\omega} \times \vec{B}_{\text{eff}})}{\vec{n}_G \cdot (\vec{\omega} \times \vec{B}_G)} = \frac{\vec{n}_G \times \vec{B}_{\text{eff}}}{\vec{n}_G \times \vec{B}_G} =$$
$$= \frac{\iint_{S_0}\vec{B} \cdot \vec{B}_G dS_0}{B_G^2 S_0}. \tag{3.176}$$

Further simplification may be obtained if the gradient of the $\vec{B}(\vec{r})$ is small enough to linearise the field around point O. Then $\vec{B} = \vec{B}_0 + \frac{\partial \vec{B}}{\partial \vec{r}}\Big|_0 (\vec{r} - \vec{r}_0)$ and the parameters ρ_{eff} and μ_{eff} become

$$\rho_{\text{eff}} \approx \frac{\vec{B}_0 \cdot \vec{B}_G}{B_G^2}, \tag{3.177}$$

$$\mu_{\text{eff}} \approx \frac{\int_{V_0} \frac{\vec{B}_0 \cdot \vec{B}_G}{B_G^2} R_0^2 dV_0}{\int_{V_0} R_0^2 dV_0}. \tag{3.178}$$

In the case of a spherical shell, this efficiency factor μ_{eff} becomes,

$$\mu_{\text{eff}} = \frac{3}{2} \int_0^{\pi/2} \frac{\vec{B}_0 \cdot \vec{B}_G}{B_G^2} \sin^3 \alpha \, d\alpha. \tag{3.179}$$

where α is the azimuthal spherical coordinate.

Figures in 3.19 show how the efficiency factor varies for different coil sizes and relative distances between the magnetic coil and the target surface. The two cases analysed correspond to a spherical shell of 2 metres and 5 metres respectively. The reason why the efficiency factor increases with the relative distance is that the magnetic field becomes more homogeneous inside the target domain. The torque induced on the space debris object is linear with respect to the effective magnetic tensor, which increases with the distance, and it is also proportional to the square of the magnetic field, which diminishes with the distance. This decrease of the strength of the magnetic field is more significant than the effect of the efficiency factor as shown as shown in Figure 3.20 and therefore, it is still more convenient to place a coil as close as possible to a target object to enhance the dissipative effect.
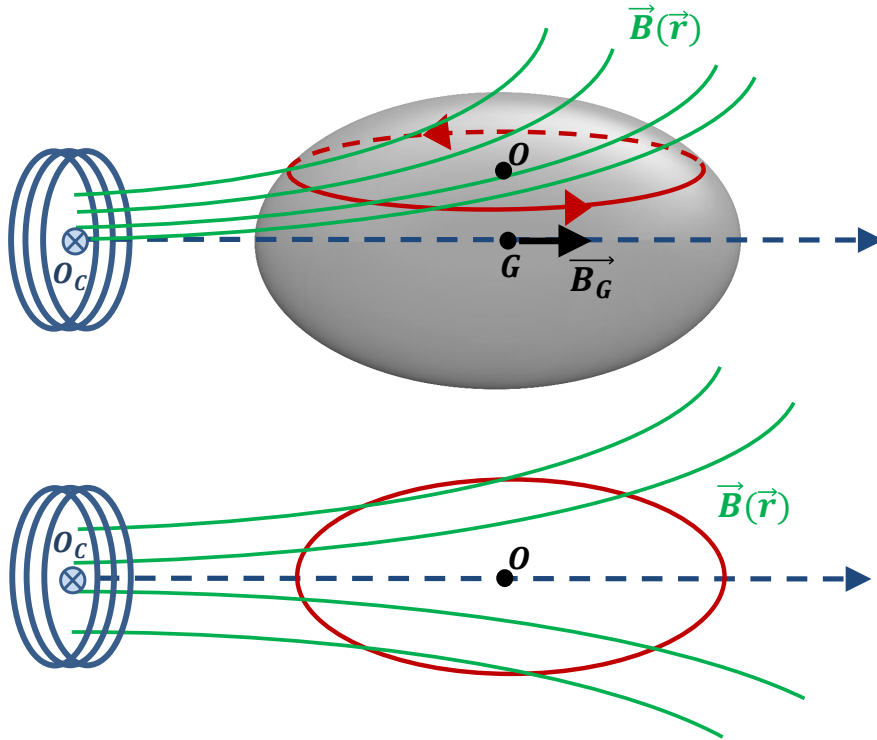
Figure 3.18: Non homogeneous magnetic field on a quasi-spherical body.

For a relative distance between the magnetic coil and the target surface of 5 metres, the efficiency is above 95% in the first case and 85% in the second case. This first analysis shows that the loss of efficiency due to the spatial gradient of the magnetic field may not be drastic and that the design presented for the de-tumbling process in Chapter 5 could be a viable option. Nonetheless, due to the simplifying hypotheses carried out, the results here provided, should not be regarded as definitive. It does, however, show that the first design can not be discarded a priori. Consequently, this first analysis may serve as the basis for further investigation on the geometries of real space debris objects.
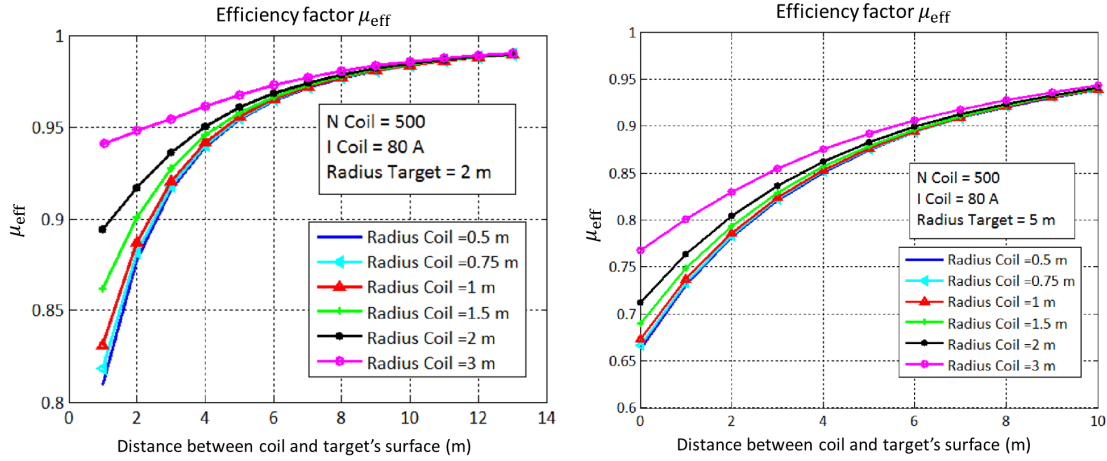
Figure 3.19: μ_{eff} for a spherical shell of 2 metres (right Figure) and 5 metres (left Figure) of radius subject to a magnetic field induced by an electromagnetic coil with an intensity of 80 A and 500 turns of wire for different radius of the coil and different relative distances between the coil and the target surface.
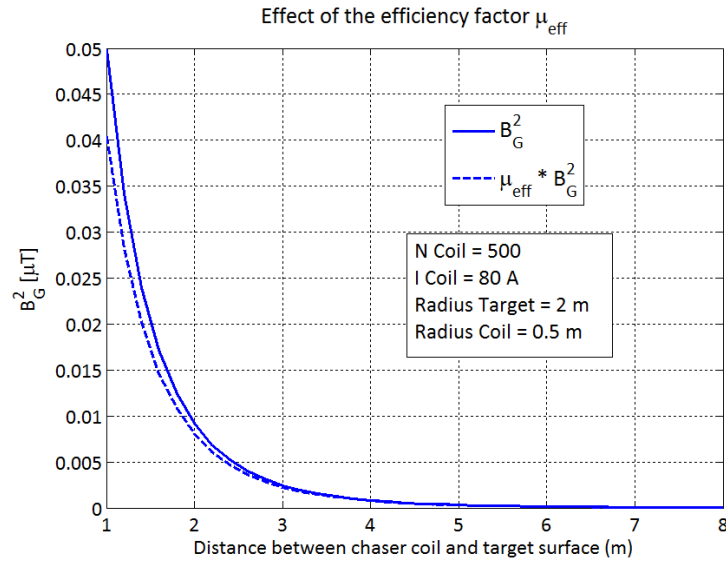
Figure 3.20: Magnetic field at the COG of the target for different relative distances with and without efficiency factor.

3.3.7.2 Magnetic force

Another consequence of the non-uniformity of the magnetic field is the appearance of net forces between the coil and the target object. This effect is analysed using perturbations theory by expanding in Taylor series the magnetic field about the centre of gravity of the target object [112, 150],

$$\vec{B} = \vec{B}_G + \mathbf{\Lambda_G}(\vec{r} - \vec{r}_G). \tag{3.180}$$

$\vec{B}_G$ is the value of the magnetic field at the centre of gravity G of the target, $\vec{r}_G$ is the position vector of the COG and $\mathbf{\Lambda_G}$ is the Jacobian matrix which contains the partial spatial derivatives of the magnetic field particularised at the COG of the target $\Lambda_{ij} = \frac{\partial B_i}{\partial r_j}\Big|_G$. Introducing this term

in the general Lorentz force formula, the following expression for the force is reached [150]:

$$\vec{F} = \int_V \vec{j} \times \vec{B} dV = \overbrace{\int_V \vec{j} \times \vec{B}_G dV}^{I_1 = 0} + \int_V \vec{j} \times \boldsymbol{\Lambda_G}(\vec{r} - \vec{r}_G) dV \Rightarrow \tag{3.181}$$

$$\Rightarrow \vec{F} = \boldsymbol{\Lambda_G^T} \vec{m},$$

where the first term I_1 is zero due to the fact that the integral $\int_V \vec{j} dV = \vec{0}$ as demonstrated in [150]. Note that when the magnetic field is homogeneous ($\vec{B}(\vec{r}, t) = \vec{B}(\vec{r})$), no magnetic forces are induced.

The magnetic force results in a simple formula which contains the product of the Jacobian tensor and the magnetic moment. In addition, the Jacobian matrix is a symmetric matrix. This is proved as follows. The electrical currents on the electromagnetic coil of the chaser $\vec{j}_c$, generate a magnetic field $\vec{B}$ that follows Maxwell's equations:

$$\nabla \times \frac{\vec{B}}{\mu} = \vec{j}_c + \frac{\partial}{\partial t}(\epsilon \vec{E}), \tag{3.182}$$

$$\nabla \cdot \vec{B} = 0, \tag{3.183}$$

where ϵ and μ are the electric permittivity and the magnetic permeability of the conductor.

In free space, outside the source, Equation (3.182), turns out to be $\nabla \times \vec{B} = \vec{0}$ and therefore, $\vec{B}$ can be expressed as the gradient of a scalar potential,

$$\vec{B} = -\mu_0 \nabla \xi = -\mu_0 \frac{\partial \xi}{\partial \vec{r}} \tag{3.184}$$

where ξ is the magnetic scalar potential [112] and the Jacobian matrix acquires the form,

$$\Lambda_{ki} = \frac{\partial B_k}{\partial r_i} = -\mu_0 \frac{\partial^2 \xi}{\partial r_i \partial r_k} = \Lambda_{ik}. \tag{3.185}$$

Therefore, $\boldsymbol{\Lambda} = \boldsymbol{\Lambda^T}$ is a symmetric matrix and the force is equal to,

$$\vec{F} = \boldsymbol{\Lambda_G} \vec{m}. \tag{3.186}$$

Considering the relationship between the magnetic moment $\vec{m}$ and the effective magnetic tensor $\mathbf{M_{eff}}$, given by (3.164), the final formula of the force is expressed as,

$$\vec{F} = \boldsymbol{\Lambda_G}(\mathbf{M_{eff}}(\vec{\omega} \times \vec{B}_G)) = \boldsymbol{\Lambda_G} \mathbf{M_{eff}} \vec{\Omega}. \tag{3.187}$$

This implies that the force given by (3.187) can be expressed by means of one single matrix $(\boldsymbol{\Lambda_G} \mathbf{M_{eff}})$.

Moreover, the magnetic tensor theory is now compared with respect to the magnetic dipole approximation in order to validate the formula (3.187) and to highlight their differences. The magnetic dipole approximation is only valid when the relative distance between the two objects is very big compared with the size of the objects. For the eddy brake, the size of the coil, the target object and their relative distance may be of the same order of magnitude and therefore, this approximation will be less accurate than the MTT. However, the magnetic dipole approximation avoids the need to compute the Jacobian tensor of the magnetic field and it is a fast way to obtain a first approximation of the magnetic force. The direction of the force coincides between both models but its magnitude will only be approximate when the relative distance between the chaser and the target increases.

The magnetic field produced by a magnetic dipole $\vec{m}$ is [112],

$$\vec{B} = \frac{\mu_0}{4\pi}\left[\frac{3(\vec{m}\cdot\vec{r})\cdot\vec{r}}{r^5} - \frac{\vec{m}}{r^3}\right], \tag{3.188}$$

where $\mu_0 = 4\pi \cdot 10^{-7}$ NA^{-2} is the vacuum permeability and $\vec{r}$ the position vector with respect to the magnetic dipole.

Furthermore, the force between two magnetic dipoles $\vec{m}_t$ and $\vec{m}_c$ is [112],

$$\vec{F} = \frac{3\mu_0}{4\pi r^5}\left((\vec{m}_t\cdot\vec{r})\vec{m}_c + (\vec{m}_c\cdot\vec{r})\vec{m}_t + (\vec{m}_c\cdot\vec{m}_t)\vec{r} - \frac{5(\vec{m}_t\cdot\vec{r})(\vec{m}_c\cdot\vec{r})}{r^2}\vec{r}\right). \tag{3.189}$$

The force will be evaluated for a coil that is pointing towards the COG of the target object. In addition, the target object is considered to be an aluminium spherical shell of the following characteristics;

- radius of the target: $R_t = 2$ m,

- thickness: $e_t = 0.001$ m,

- electrical conductivity: $\sigma_t = 3.5e7$ S/m,

- angular velocity: $\dot{\epsilon}_a = 50$ deg/s.

The coil on-board the chaser spacecraft has the properties defined in Section 5.7.

Figure 3.21 shows the force computed using both models. The magnetic dipole force better approximates the force given by the Equation (3.187) when the distance between the two objects increases. In addition, the force given by the magnetic dipole approximation overvalues the generated force.
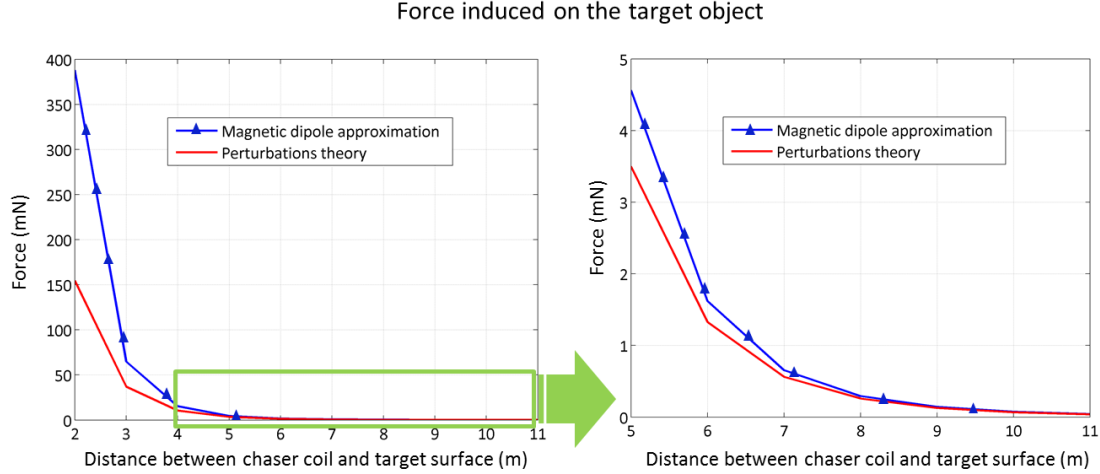
Figure 3.21: Force model comparison between perturbations theory and the magnetic dipole model for different relative distances.

Furthermore, the magnetic dipole approximation does not take into account variations in the non-uniformity of the magnetic field. In order to visualise this difference between the two models, the following properties have been considered, a magnetic field at the COG of the target equal to $B_{Gt} = 150$ µT and a relative distance between the coil and the COG of the target of 10 metres. Figure 3.22 shows the magnetic field foreseen by both models when the radius of the coil varies. The magnetic field at the COG of the target is assumed to be constant and the intensity of the coil is adjusted accordingly to have the same field in all the cases. When the radius of the coil increases, the magnetic field becomes more uniform inside the target object and therefore, the

force must decrease as foreseen by the MTT. This phenomenon is not well characterised by the magnetic dipole approximation as the force increases when it should decrease.
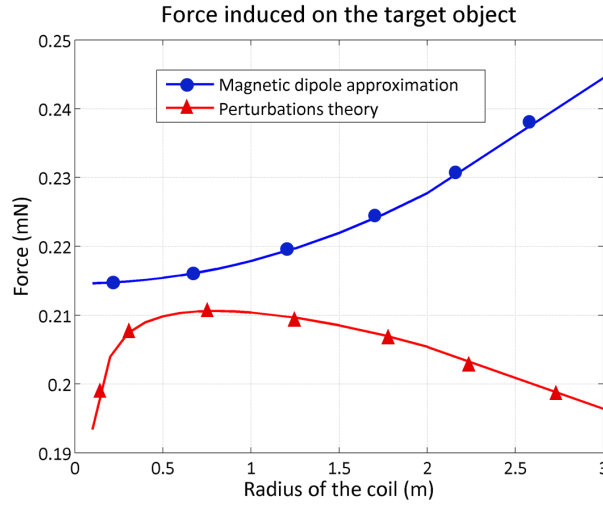
Figure 3.22: Force model comparison between perturbations theory and the magnetic dipole model for different radii of the coil.

3.4 Generalised magnetic tensor theory

The magnetic tensor theory developed in Section 3.3 focuses on the eddy currents induced on a rotating object subject to a constant magnetic field. In this section, the theory is extended to a conductor that may have relative linear or angular velocity with respect to the magnetic source, may be subject to time-varying magnetic fields or a conductor which may have ferromagnetic material.

Considering a target that is moving with a linear velocity $\vec{v}(t)$ and an angular velocity $\vec{\omega}(t)$ which is subject to a time-varying and homogeneous magnetic field $\vec{B}(t)$. The target object is assumed to be a rigid body that contains metallic materials with a relative permeability μ_r close to 1 (e.g. aluminium, titanium).

The electric current that appears on the target object is derived from the generalised Ohm's Law:

$$\vec{j} = \sigma \left[\vec{E} + \vec{v} \times \vec{B} + (\vec{\omega} \times \vec{r}) \times \vec{B} \right],$$ (3.190)

where σ is the conductivity of the target object.

In addition, according to Maxwell's equation derived from Faraday's Law:

$$\nabla \times \vec{E} = -\frac{\partial \vec{B}}{\partial t}.$$ (3.191)

Combining Equations (3.190) and (3.191), the following equation is reached for $\vec{j}$:

$$\nabla \times \vec{j} = \sigma \Big(-\frac{\partial \vec{B}}{\partial t} + \overbrace{\nabla \times (\vec{v} \times \vec{B})}^{(a)} + \overbrace{\nabla \times ((\vec{\omega} \times \vec{r}) \times \vec{B})}^{(b)} \Big).$$ (3.192)

Taking into account Maxwell's equation $\nabla \cdot \vec{B} = 0$, the term (a) can be written as:

$$\nabla \times (\vec{v} \times \vec{B}) = ((\nabla \cdot \vec{B})\boldsymbol{\mathcal{I}} - \boldsymbol{\Lambda})\vec{v} = -\boldsymbol{\Lambda}\vec{v},$$ (3.193)

where $\mathcal{I}$ is the identity matrix and $\mathbf{\Lambda} = \frac{\partial \vec{B}}{\partial \vec{r}}$ is the Jacobian matrix of the magnetic field.

Assuming that the magnetic field is homogeneous, $\vec{B}(\vec{r}, t) = \vec{B}(t)$, Equation (3.193) is identically zero,

$$\nabla \times (\vec{v} \times \vec{B}) = \vec{0}. \tag{3.194}$$

The second term (b) can be written as,

$$\nabla \times ((\vec{\omega} \times \vec{r}) \times \vec{B}) = \vec{\omega} \times \vec{B} - (\vec{\omega} \times \vec{r})\mathbf{\Lambda}. \tag{3.195}$$

Assuming that the magnetic field is homogeneous, Equation (3.195) simplifies to the following

$$\nabla \times ((\vec{\omega} \times \vec{r}) \times \vec{B}) = \vec{\omega} \times \vec{B}. \tag{3.196}$$

Taking into account Equations (3.194) and (3.196), Equation (3.192) results in,

$$\nabla \times \vec{j} = \sigma \vec{\Omega}_{tot}, \tag{3.197}$$

where $\vec{\Omega}_{tot}$ is defined as,

$$\vec{\Omega}_{tot} = (-\frac{\partial \vec{B}}{\partial t} + \vec{\omega} \times \vec{B}). \tag{3.198}$$

Equations (3.197, 3.198) contain two different effects which can generate eddy currents in the target object; time-varying magnetic fields and rotational motion of target with respect to the external magnetic field.

The continuity Equation (3.30) and boundary conditions (3.32) are still valid in this context and therefore, the differential system of equations that determine $\vec{j}$ are,

$$\nabla \cdot \vec{j} = \vec{0} \ \forall P \ \in \ V, \tag{3.199}$$

$$\nabla \times \vec{j} = \sigma \vec{\Omega}_{tot} \ \forall P \ \in \ V, \tag{3.200}$$

$$\vec{j} \cdot \vec{n}_v = 0 \ \forall P \ \in \ \partial V. \tag{3.201}$$

Equations (3.199, 3.200, 3.201) are linear in the parameter $\vec{\Omega}_{tot} = \vec{\Omega}_{tot}(t)$ and they have the same structure as Equations (3.30, 3.31, 3.32). Therefore, the solutions obtained in Sections (3.3.2, 3.3.3) are applicable here. Using the second particular solution obtained in Section 3.3.2.2, the general solution for $\vec{j}$ is,

$$\vec{j} = \frac{\sigma}{2}(\vec{\Omega}_{tot} \times \vec{r}) - \sigma \nabla \psi. \tag{3.202}$$

The magnetic moment induced on the target object $\vec{m}$ is also linear in $\vec{\Omega}_{tot}$ as proved in (3.3.3) and the constant of proportionality is the magnetic tensor $\mathbf{M}$,

$$\vec{m} = \mathbf{M}\vec{\Omega}_{tot}. \tag{3.203}$$

3.4.1 Ferromagnetism

So far, it has been assumed that the magnetic permeability of the materials studied is close to $\mu = 1$. In general, the relationship between the *magnetic induction*, $\vec{B}$, and the *magnetic field intensity*, $\vec{\mathcal{H}}$, is equal to [112],

$$\vec{B} = \mu\vec{\mathcal{H}} = \mu_0(1 + \chi_m)\vec{\mathcal{H}}, \tag{3.204}$$

where χ_m is the magnetic susceptibility and μ_0 is the vacuum magnetic permeability.

Moreover, the magnetisation $\vec{\mathcal{M}}$ is the dipole moment per unit volume and it is defined as [112],

$$\vec{\mathcal{M}} = \chi_m \vec{\mathcal{H}}. \tag{3.205}$$

For ferromagnetic materials, $\chi_m >> 1$ and the relationship between the magnetic induction and the magnetic field is,

$$\vec{B} = \mu_0(\vec{\mathcal{H}} + \vec{\mathcal{M}}) = \mu_0 \frac{1 + \chi_m}{\chi_m}\vec{\mathcal{M}} \approx \mu_0\vec{\mathcal{M}}. \qquad (3.206)$$

In addition, the magnetic moment of the ferromagnetic component can be expressed as,

$$\vec{m}_{fer} = V_{fer}\vec{\mathcal{M}} = V_{fer}\frac{\vec{B}_{Gfer}}{\mu_0}, \qquad (3.207)$$

where V_{fer} is the volume of ferromagnetic material and $\vec{B}_{Gfer}$ is the magnetic field at the COG of the ferromagnetic component.

It is assumed here that the volume of ferromagnetic material is small compared to the total volume of the target object $V_{fer} << V$ which is generally the case for satellites. Combining Equations 3.203 and 3.207, the total magnetic moment induced on the target object is,

$$\vec{m} = \vec{m}_{fer} + \mathbf{M}\vec{\Omega}_{tot}$$

$$= \frac{V_{fer}}{\mu_0}\vec{B}_{Gfer} - \mathbf{M}\frac{\partial \vec{B}}{\partial t} + \mathbf{M}(\vec{\omega} \times \vec{B}). \qquad (3.208)$$

Furthermore, ferromagnetic materials do not generally exhibit a linear dependence between $\vec{B}$ and $\vec{\mathcal{H}}$, that is, the magnetic permeability and susceptibility vary with time. This phenomenon is known as *hysteresis* and it leads to a curve like the one shown in Figure 3.23. If a hysteresis loop takes place, additional heat losses to the ones generated by the eddy currents appear which leads to a faster decrease in the angular velocity [152].
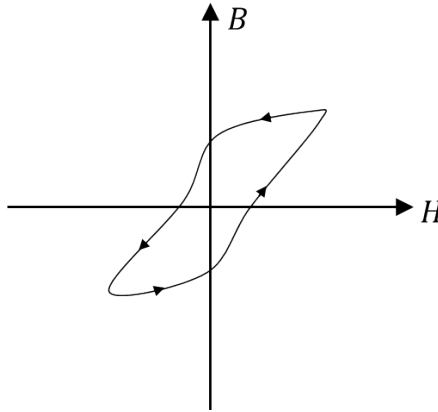
Figure 3.23: Typical hysteresis loop of a ferromagnet.

Nonetheless, the use of ferromagnetic materials is typically avoided in spacecraft. First of all, owing to their high density, they are seldom used for large structural components [31]. Secondly, remnant magnetic fields can create disturbance torques which affect attitude control systems and thirdly residual magnetic dipoles may limit the efficiency of some detectors such as magnetometers [31]. For these reasons, a maximum allowable dipole moment is usually required in spacecraft design which lies between 0.1 and 10 A·m^2 [113].

The factors affecting magnetic properties of metals include their crystal structure and *Curie temperature*. Above this temperature, certain materials change their magnetic behaviour and may change, for instance, from being ferromagnetic to paramagnetic. Materials such as iron, cobalt or nickel have very high Curie temperatures ($T > 300$ºC) and this is why they are considered ferromagnetic. However, there are various alloys which contain a combination of the aforementioned ferromagnetic materials which have very low Curie temperatures and they may be considered paramagnetic for practical purposes. This is the case of some Inconel alloys or austenitic steels

[31]. For instance, the alloy Inconel 600 used in the HM7B engine of the Ariane upper stage has a Curie temperature of -124°C [31]. Moreover, Table 3.2 shows typical equilibrium temperatures for spacecraft in LEO for three different surface finishes defined by their absorptivity, α, and emissivity, ε [25]. Additional details on typical metallic alloys used in spacecraft may be found in Section A.4 of the Annex.

Surface finish	White paint ($\alpha = 0.15, \varepsilon = 0.9$)	Black paint ($\alpha = 0.9, \varepsilon = 0.9$)	Electroplated gold ($\alpha = 0.25, \varepsilon = 0.04$)
No eclipse	-61°C	+20°C	+176°C
Eclipse	-70°C	-2°C	+138°C

Table 3.2: Equilibrium temperatures for a simple spacecraft in LEO [25].

Hereinafter, the effects produced by ferromagnetic materials have been neglected as their use in satellite design is minimal. Nevertheless, the MTT has been generalised in this section in case their effects need to be considered.

3.5   Case study: Envisat spacecraft

In April 2012, the control of the Envisat satellite was lost. The European Space Agency (ESA) announced that the communication link between Envisat and ground ceased abruptly [153]. The defunct Envisat satellite now belongs to the category of critical objects in orbit due its huge mass (≈ 8 tons) and its location in one of the most densely populated areas in the near-Earth region [154].

The first optical and radar measurements carried out in 2012 for the Envisat spacecraft showed intrinsic rotations of 0.2 deg/s about the axis normal to the orbital plane which coincided approximately with the minimum axis of inertia of the spacecraft [155]. However, later radar measurements showed a fast increase of the rotational speed at the beginning of 2013, up to 2.8 deg/sec [2, 93]. In April 2013, the rotational speed began to decrease again at a slower pace (see Figure 3.24) until the last measurements made in June 2015 which revealed an average rotation rate of 2.5 deg/s [2, 153]. While the causes of the acceleration period still remain unexplained, the deceleration period is attributed mainly to the effect of the eddy currents. As it has already been highlighted, its understanding is of utmost importance for the Envisat's active debris removal mission, *e.Deorbit*, planned for 2021 by ESA [36, 156].

This case study carries out a simulation of the evolution of Envisat's inertial position and attitude when subject to the most important environmental perturbations. This analysis is used to check the veracity of the hypothesis made which states that the most probable cause of the decrease in the spin rate is the eddy current phenomenon.

In 2013 the Satellite Laser Ranging (SRL) station Graz in Austria obtained very accurate data of the evolution of the Envisat's attitude [93]. The results showed that the inertial spin axis direction was perpendicular to the along-track direction Y_0 and it formed an angle of 62 degrees with the nadir direction X_0 (see Figure 3.24). Moreover, a decrease in the spin rate of 0.00156 deg/s per day (or an increase of the spin period equal to 0.0367 s/day) was measured after the 100th day of 2013. This data will be compared with the results obtained from the numerical simulations.
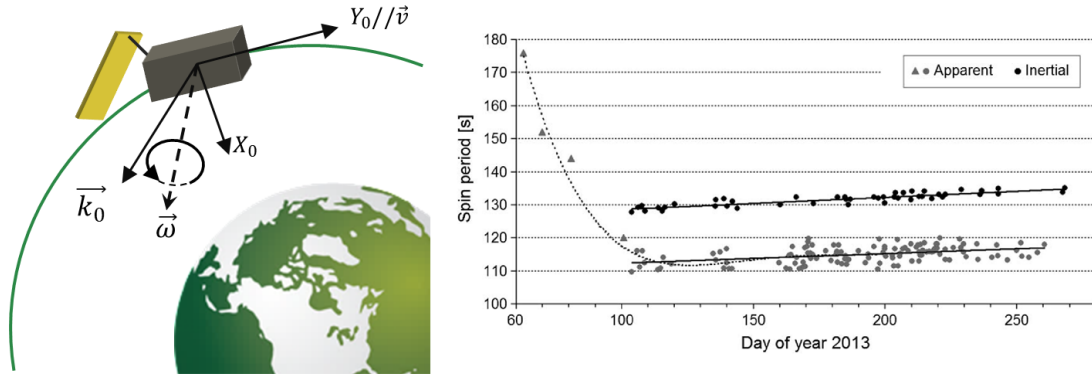
Figure 3.24: Envisat's attitude observations made throughout the year 2013.

3.5.1 Numerical simulator

This section describes the numerical simulator that has been developed in MATLAB including 3D translational and rotational dynamics of an Earth-orbiting object. The numerical integration process is a complex problem as it includes 12 non-linear first order differential equations.

Here, it is assumed that the object is a rigid body. The subindex in indicates that the variable is expressed in an inertial reference frame and subindex b denotes that the variable is expressed in the body reference frame. The state vector that represents the translational and rotational kinematics of a body are represented by the vector $\vec{y}$ shown in Equation (3.209),

$$\vec{y} = \begin{bmatrix} \vec{r}_{in} \\ \vec{v}_{in} \\ \vec{\alpha}_{in} \\ \vec{\omega}_b \end{bmatrix}.$$

(3.209)

Vectors $\vec{r}_{in}$ and $\vec{v}_{in}$ are the object's inertial position and velocity and they describe the translational kinematics. Moreover, the components of vector $\vec{\alpha}_{in} = \alpha\vec{h}$ are the Euler parameters used to describe the attitude of the object. If a rigid body is rotating with a certain angular velocity, this rotation can always be represented by a rotation angle α around a certain axis $\vec{h}$. These four parameters $(\alpha, \vec{h})$ are called Euler parameters [95]. Finally, $\vec{\omega}_b$ is the rotational velocity vector of the body frame with respect to the inertial reference frame expressed in the body frame, defined in Section A.1 of the Annex.

The translational dynamical equations are governed by Newton's second law [95]. In addition, the rotational dynamics are determined using Euler's equations and the differential equation for $\vec{\alpha}_{in}$ is given by Equation (3.210) [95],

$$\dot{\vec{\alpha}}_{in} = \vec{\omega}_{in} + \frac{\alpha}{2}(\vec{\omega}_{in} \times \vec{h}_{in} + \frac{\alpha^2}{12}(\vec{h}_{in} \times (\vec{h}_{in} \times \vec{\omega}_{in})) + o(\alpha^3) = f(\alpha, \vec{h}_{in}, \vec{\omega}_{in}).$$

(3.210)

Hence, the system of 12 non-linear differential equations that needs to be solved is equal to,

$$\begin{bmatrix} \dot{\vec{r}}_{in} \\ \dot{\vec{v}}_{in} \\ \dot{\vec{\alpha}}_{in} \\ \dot{\vec{\omega}}_b \end{bmatrix} = \begin{bmatrix} \vec{v}_{in} \\ \sum \vec{F}_{ext}/m \\ f(\alpha, \vec{h}_{in}, \vec{\omega}_{in}) \\ \mathbf{I^{-1}}(\sum \vec{T}_{ext} - (\vec{\omega}_b \times \mathbf{I}\vec{\omega}_b)) \end{bmatrix},$$

(3.211)

where $\sum \vec{F}_{ext}$ and $\sum \vec{T}_{ext}$ are the sum of all the external forces and torques acting upon the object, m is the mass and $\mathbf{I}$ is the inertia of the object.

Furthermore, in each time step of the integration process $\Delta t = t - t_0$, the rotation matrix between

the body frame and the inertial reference frame, $R(t)$, is computed as the composition of two rotation matrices; the rotation matrix $R(t_0)$ between the beginning of the simulation $t = 0$ and the initial time in the propagation step t_0 and the rotation matrix $A(\alpha_{in}(t))$ which gives the rotation during that time step $t' \in [t_0, t]$ [95],

$$R(t) = A(\alpha_{in}(t)) \cdot R(t_0), \tag{3.212}$$

where the matrix $A(\alpha_{in}(t))$ has the form [95],

$$A = \begin{bmatrix} (1 - \cos(\alpha_{in}))h_x^2 + \cos(\alpha_{in}) & (1 - \cos(\alpha_{in}))h_x h_y - h_z \sin(\alpha_{in}) & (1 - \cos(\alpha_{in}))h_x h_z + h_y \sin(\alpha_{in}) \\ (1 - \cos(\alpha_{in}))h_x h_y + h_z \sin(\alpha_{in}) & (1 - \cos(\alpha_{in}))h_y^2 + \cos(\alpha_{in}) & (1 - \cos(\alpha_{in}))h_y h_z - h_x \sin(\alpha_{in}) \\ (1 - \cos(\alpha_{in}))h_x h_z - h_y \sin(\alpha_{in}) & (1 - \cos(\alpha_{in}))h_y h_z + h_x \sin(\alpha_{in}) & (1 - \cos(\alpha_{in}))h_z^2 + \cos(\alpha_{in}) \end{bmatrix}. \tag{3.213}$$

Furthermore, the following perturbations have been included in the propagator;

- Earth's gravity field: The force due to the Earth's gravity field has been modelled including 4 zonal harmonic coefficients J_i ($i = 2, 3, 4$) from the JGM-3 gravitational model [157]. The Earth's gravity gradient has been modelled employing Equation (2.13).

- Atmospheric drag: The atmospheric force and torque have been included in the propagator [103]. The atmospheric density has been computed using the Jacchia 1970 model for medium solar activity (F10=140, Ap=15) [124].

- Solar radiation pressure: The SRP force and torque have been included in the propagator [103]. This perturbation is only taken into account when the spacecraft comes out of eclipse. The mean radiation flux considered is $P = 4.7 \cdot 10^{-6}$ N·m^{-2} which is the typical value considered for LEO [95].

- Earth's magnetic field: The Earth's magnetic field has been modelled based on the International Geomagnetic Reference Field IGRF-11. The eddy current torques have been modelled employing the magnetic tensor theory. In addition, the torque due to a residual magnetic dipole has been included.

Figure 3.25 summarises the key aspects of the propagator developed and the numerical integration process. The integration method employed is the explicit method Runge Kutta of 4th order [158] and the time step is equal to 1 second.

The process starts with the initialisation of the state vector $\vec{y}$ and the computation of the environmental forces and torques $\sum \vec{F}_{ext}, \sum \vec{T}_{ext}$. Then, the derivatives of the state vector components can be obtained $F(t, \vec{y})$ based on the dynamical equations given by Equation (3.211) and the Runge Kutta integration method is applied to obtain the state vector at the next time step, $\vec{y}(t + \Delta t)$. The new state vector is computed by means of the weighted average of four increments, $\vec{k}_1, \vec{k}_2, \vec{k}_3, \vec{k}_4$, where each increment is the product of the size of the interval, Δt, and an estimated slope specified by function $F(t, \vec{y})$. Finally, the process is repeated for each time step of the numerical integration.
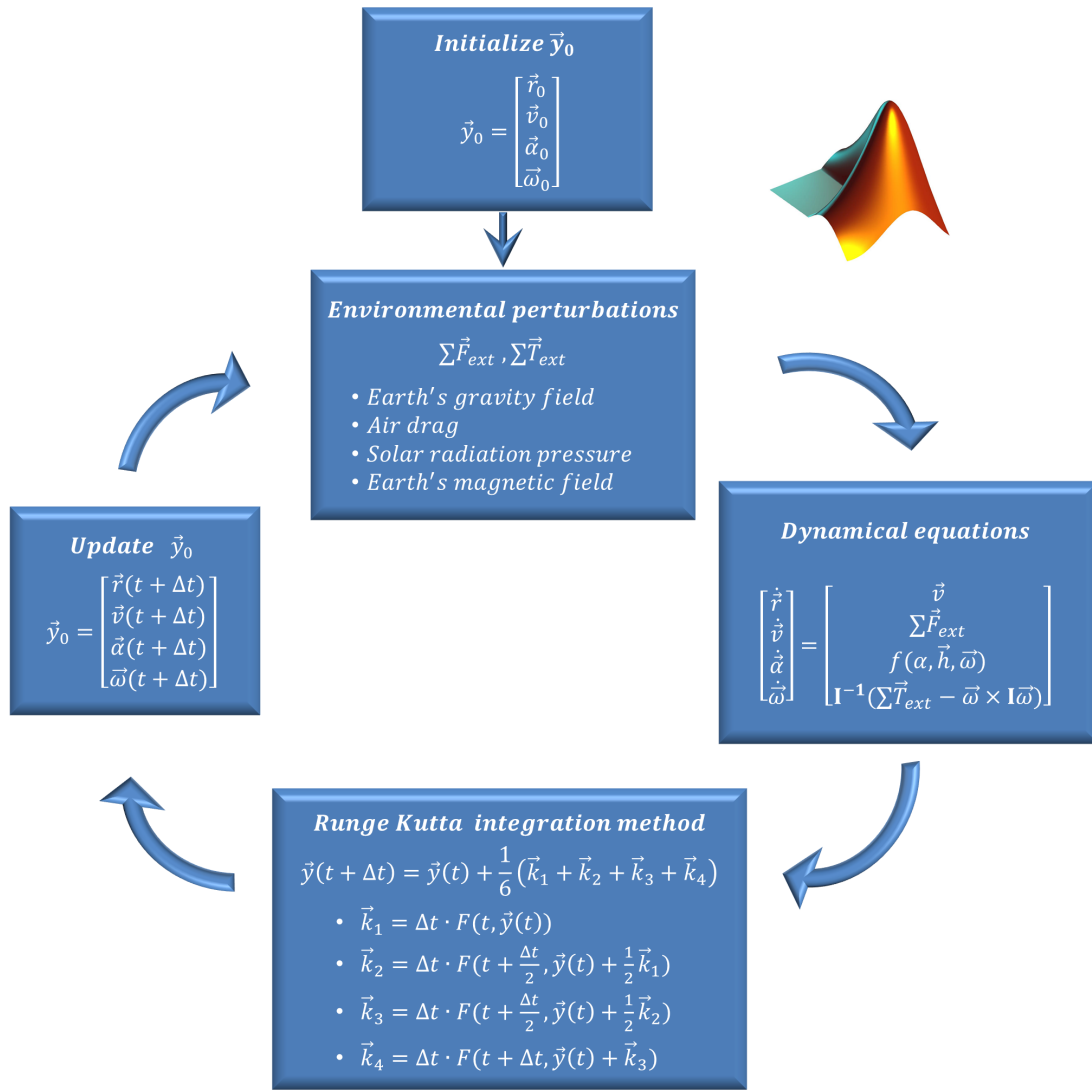
Figure 3.25: Propagator diagram.

3.5.2 Envisat model

Envisat is currently in a low Earth orbit at an altitude of 770 km and an inclination of 98 degrees [154]. The dry mass of Envisat is 7827.9 kg and the inertia tensor of the spacecraft in its principal axes is [5, 123]:

$$\mathbf{I} = \begin{bmatrix} 129180.25 & 0 & 0 \\ 0 & 124801.21 & 0 \\ 0 & 0 & 16979.74 \end{bmatrix} \text{kg} \cdot \text{m}^2. \tag{3.214}$$

In addition, the following hypotheses have been made for the air drag model.

- Drag coefficient: a mean value of the drag coefficient equal to $C_D = 2.3$ has been adopted.

- Lever arm: a mean value of the lever arm has been considered as a compromise between the best and the worst case. The lever arm has been computed for the best and the worst case as the distance between the COG and the geometrical centre of the satellite when the maximum and the minimum areas are exposed to the incident air flow. The lever arm used in the simulations is equal to 3.5 metres.

- Air drag area: a mean value between the maximum and the minimum air drag area has been used and it is equal to $S = 52\text{m}^2$.

Furthermore, the following hypotheses have been made for the SRP model.

- Solar coefficients: A diffuse reflection has been assumed with a coefficient of diffuse reflection equal to $f_d = 1.3$ and a coefficient of specular reflection equal to zero, $f_s = 0$.

- Lever arm: a mean value of the lever arm has been considered as a compromise between the best and the worst case. The worst case is considered to be the torque created by the solar panel when it is perpendicular to the solar radiation and the best case is assumed to take place when the solar panel is perpendicular to the solar radiation. A lever arm of 5.5 metres has been considered.

- SRP area: a mean value between the maximum and the minimum SRP area has been used and it is equal to $S = 20\text{m}^2$.

Furthermore, the following hypotheses have been made for the Earth's magnetic field torques.

- Residual magnetic dipole: An average value of 10^{-3} A·m^2/kg has been considered.

- Eddy currents: A magnetic tensor equal to Equation (3.218) has been considered.

The torque generated by the Earth has been computed employing the MTT. In order to obtain the Envisat's magnetic tensor, the model depicted in Figure 3.26 has been used.

Envisat's platform is based on the polar platform manufactured by Airbus Defence & Space. Most of the metallic structural material is concentrated on the service module while the structural materials of the payload module are mainly composed of composite materials [159]. The structural model employed accounts for the effective metallic material which will generate eddy currents (e.g. shielded components will not be affected by the magnetic field and the contribution from unconnected plates is disregarded) including the service module structure, the solar panel structure and the propellant tanks.

The service module structure was modelled as an aluminium 6061-T6 cubical shell of $4 \times 4 \times 4$ m^3 with a thickness of 0.0003 m [159]. This aluminium alloy has a conductivity of $\sigma = 2.7 \cdot 10^7$ S/m. The magnetic tensor of the service module has been obtained by means of the frame model with a mesh of 6980 bars and 3491 nodes. The mesh selected corresponds to the maximum amount of virtual memory that can be allocated by MATLAB to compute the tensor. The result obtained is equal to:

$$\mathbf{M_{SM}} = \begin{bmatrix} 6.262 & 0 & 0 \\ 0 & 6.262 & 0 \\ 0 & 0 & 6.262 \end{bmatrix} \cdot 10^5 \ \text{S} \cdot \text{m}^4. \tag{3.215}$$

Moreover, Envisat has four 112 litre propellant tanks containing 300 kg of hydrazine [160]. In the absence of data for the tank's materials and dimensions, the tank, Surface Tension Tank OST 31/0, manufactured by Airbus Defence & Space was considered. The tank net volume ranges between 104 and 117 litres and it is made of the alloy Ti6AI4V. The four tanks were modelled as four metallic spherical shells of $R = 0.3$ m of radius, $e = 0.0014$ m of thickness and $\sigma = 5.62 \cdot 10^5$ S/m of conductivity. Further details on the dimensions and materials of this tank can be found in Section A.5 of the annex.

$$\mathbf{M_{tanks}} = 4 \cdot (\frac{2}{3}\sigma\pi R^4 e) \begin{bmatrix} 1 & 0 & 0 \\ 0 & 1 & 0 \\ 0 & 0 & 1 \end{bmatrix} = 49.532 \begin{bmatrix} 1 & 0 & 0 \\ 0 & 1 & 0 \\ 0 & 0 & 1 \end{bmatrix} \ \text{S} \cdot \text{m}^4. \tag{3.216}$$

The electrical conductivity of solar cells is typically very low, in the order of $\sigma = 100 - 1000$ S/m [161]. However, solar panels typically have aluminium honeycomb structures that support the solar cells. Here it will be assumed that Envisat's solar panel has an aluminium honeycomb structure of the same material as the one used for the service module. The panel has been model as a rectangular flat plate with an area and thickness of 5×14 m and 0.0003 m respectively. The
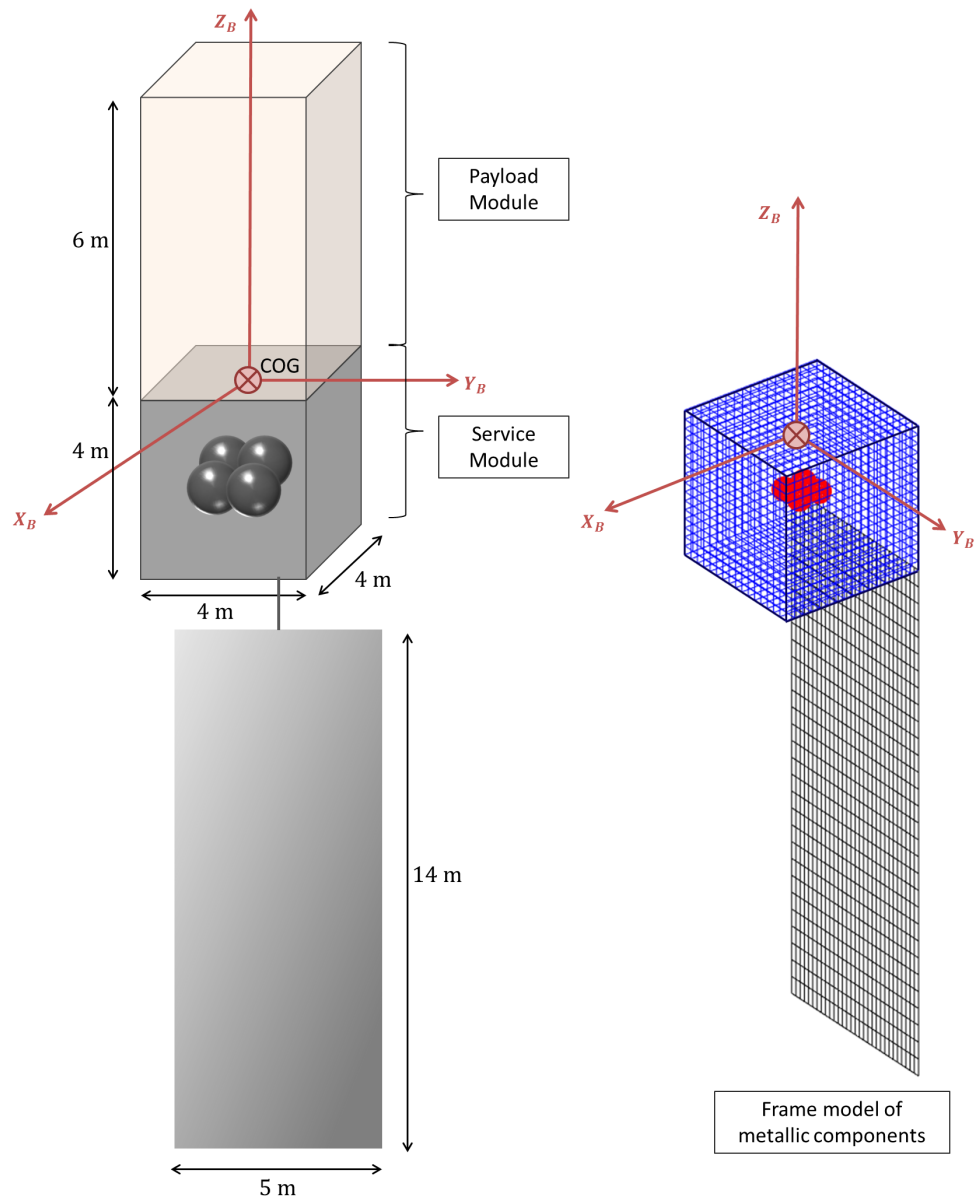
Figure 3.26: Envisat metallic structure model.

magnetic tensor of the solar panel in expressed in Envisat's reference frame is equal to:

$$\mathbf{M_{SP}} = \frac{1}{4}\sigma e C_T \begin{bmatrix} 1 & 0 & 0 \\ 0 & 0 & 0 \\ 0 & 0 & 0 \end{bmatrix} = \begin{bmatrix} 1.124 & 0 & 0 \\ 0 & 0 & 0 \\ 0 & 0 & 0 \end{bmatrix} \cdot 10^6 \ \mathrm{S \cdot m^4}, \qquad (3.217)$$

where C_T is defined in 3.13 for rectangular flat plates.

The total amount of effective conductive material is 3.8% of the total mass of the spacecraft. Note that the contribution of the propellant tanks to the overall magnetic tensor is negligible with respect to the other two components.

The magnetic tensor obtained for Envisat is shown in (3.218)

$$\mathbf{M} = \mathbf{M_{SM}} + \mathbf{M_{tanks}} + \mathbf{M_{SP}} = \begin{bmatrix} 1.75 & 0 & 0 \\ 0 & 0.63 & 0 \\ 0 & 0 & 0.63 \end{bmatrix} \cdot 10^6 \ \mathrm{S \cdot m^4}. \qquad (3.218)$$

3.5.3   Simulation results

The numerical simulation employs as initial data, the measurements from 25$^{\text{th}}$ September 2013 made by the SRL Graz station [93]. The measured spin rate of Envisat on the aforementioned date is 2.67 deg/s. The spin axis is located in the positive quadrant of the orbital reference frame plane defined by (X_0, Z_0) and it makes an angle of 62 degrees with the nadir axis X_0. Regarding the initial attitude, the minimum axis of inertia is assumed to be pointing in the along-track direction (parallel to the velocity vector) and that the maximum axis of inertia is parallel to the nadir direction [93].

The following initial conditions were considered for the simulation:

- Initial date: 25-September-2013

- Initial orbit: Circular orbit, 770 km of altitude and 98 deg of inclination

- Initial attitude: minimum axis of inertia parallel to Y_0 and maximum axis of inertia parallel to X_0

- Initial angular velocity vector in the inertial reference frame $\vec{\omega}_0 = [1.25, -2.33, -0.35]$ deg/s

Figure 3.27 depicts the evolution of the angular velocity vector of Envisat's body reference frame with respect to the ECI reference frame expressed in the ECI reference frame. The components of the angular velocity vector exhibit oscillatory variations and no monotonous increase or decrease can be observed from these results. However, the magnitude of the angular velocity in Figure 3.28 clearly shows a decrease of the spin rate with time. The secular decrease is obtained from a least square fitting curve from the numerical values.

The decrease in the spin period obtained from the simulation is equal to 0.00149 deg/s per day. This value is of the same order of magnitude as the one given by the SRL Graz station in 2013 which corresponds to a decrease in the spin rate of 0.00156 deg/s per day. The difference between the two values may occur due to inaccuracies in the structure employed to evaluate the magnetic tensor and more detailed information on Envisat's structure and materials would be necessary in order to improve this error.
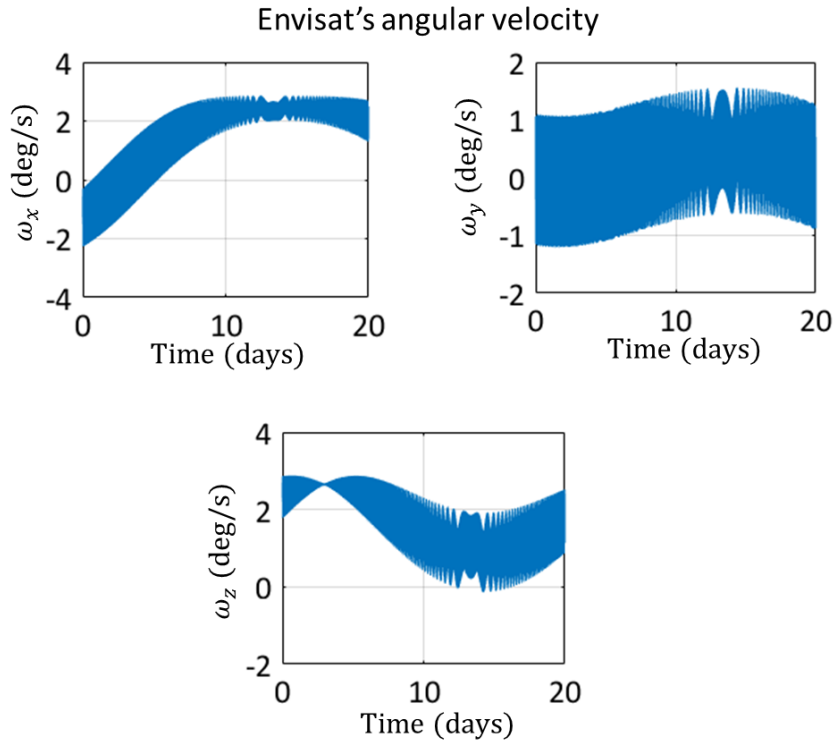
Figure 3.27: Envisat's angular velocity vector.
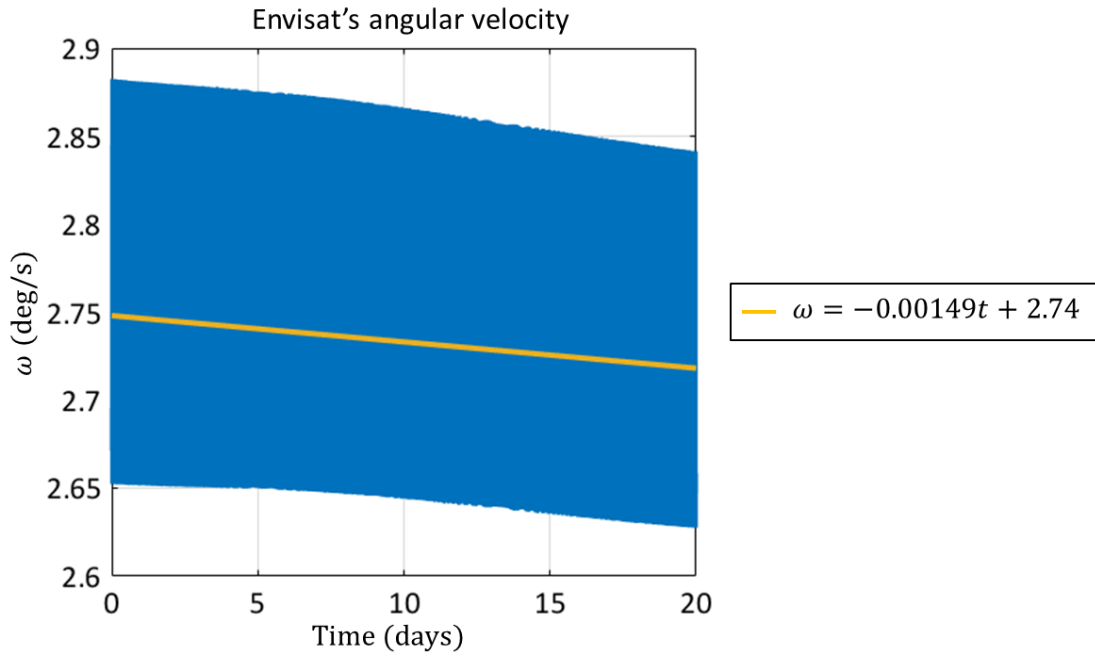
Figure 3.28: Envisat's angular velocity magnitude.

Moreover, Figure 3.29 depicts the evolution of the environmental torques. It should be pointed out that this evolution is based on and limited by the assumptions listed previously. In this simulation, the two most important effects are the gravity gradient torque and the Earth's magnetic field. The

gravity gradient torque is conservative while the eddy current phenomenon is dissipative. The sum of both effects together leads to a decrease of the angular velocity. This goes in line with the conclusions derived from the observations made in 2013.
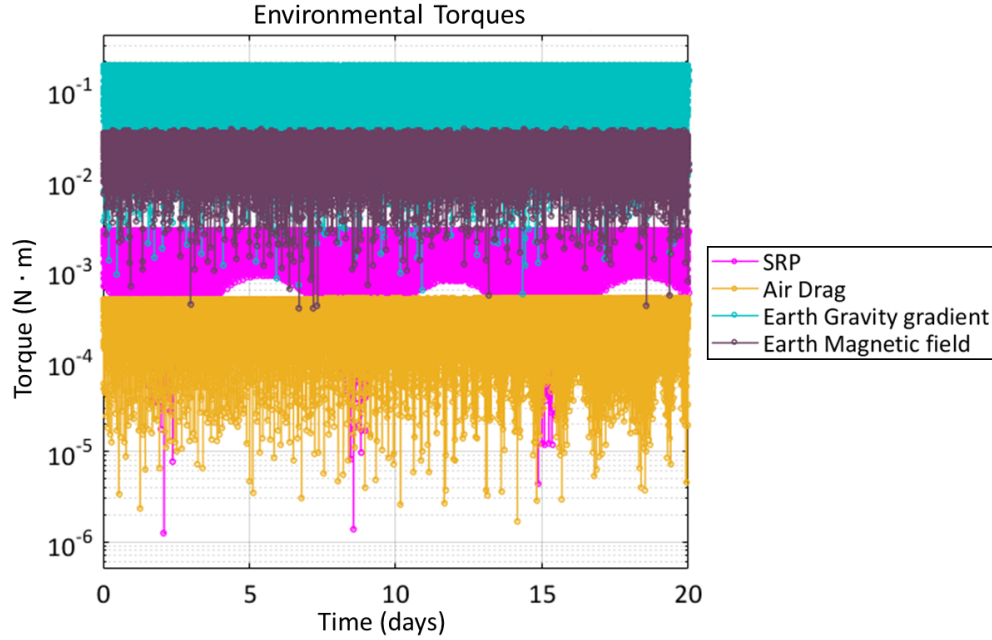
Figure 3.29: Envisat's environmental perturbations.

3.6 Chapter summary

The major contribution of this chapter is the development of the *'magnetic tensor theory'*. This theory generalises the existing analytical models to evaluate the magnetic moment for any object subject to any orientation of the angular velocity vector and the magnetic field. Typical numerical methods employed to solve the eddy current problem need to deal with the classical Poisson equation with Neumann conditions in each time step of the integration process, resulting in complex and computationally expensive processes. However, the magnetic tensor theory provides a direct formula to evaluate the magnetic forces and torques.

The theory is based on the computation of a new tensor called the *'magnetic tensor'*, which gives an insight of how the conductive material is distributed throughout a body. The existence of this tensor as well as its properties were proved in Section 3.3.3. The magnetic tensor is a symmetric Cartesian tensor of second order which has no negative eigenvalues. These properties allow this tensor to be derived from the computation of the dissipated energy of the eddy current phenomenon. A method to evaluate this tensor based on a generic finite element method was provided in Section 3.3.4.1 as well as a particularization for a specific FEM, called the *'frame model'*, which leads to a direct formula to evaluate this tensor (see Section 3.3.4.2). In addition, analytical solutions of this tensor were presented in Section 3.3.5 for a spherical shell, a cylindrical shell with closed ends and flat plates which are typical geometrical shapes found in metallic components of a satellite (e.g. propellant tanks, structures). These results were then compared with existing solutions in the literature for the eddy current torque in Section 3.3.5 seeking to numerically validate the magnetic tensor theory.

Subsequently, in Section 3.3.7 the effects produced by the non-uniformity of the magnetic field were analysed. The magnetic field may be assumed to be uniform for satellites subject to the Earth's magnetic field. However, this assumption is not valid for magnetic fields generated by coils of a

similar size to that of a spacecraft. The non-uniformity of the field results in a loss of efficiency which depends on the dimensions of the target object, the dimensions of the magnetic coil and the relative distance between both objects. The analyses conducted for a quasi-spherical object result in an efficiency penalty of approximately 5% for a relative distance of 5 metres between the coil and the target surface. In addition, an explicit formula to evaluate the net force that appears due to the non-uniformity of the field was obtained in Section 3.3.7.2 which is proportional to the magnetic tensor.

Furthermore, the eddy current solution based on the magnetic tensor is generalised in Section 3.4 for time-varying magnetic fields, relative linear velocity and angular velocity and the existence of ferromagnetic materials. The linearity in Ω of the differential equations for the electric current density vector is kept which enables the use of the magnetic tensor theory.

The theoretical analysis is concluded with a case study for the Envisat spacecraft in Section 3.5. Active debris removal is bound to become a reality in the next decade, with the Envisat spacecraft being one of the most hazardous objects in orbit in this regard. In April 2012, the control of the Envisat satellite was lost and regular observation campaigns have been carried out since then to monitor its position and attitude. The measurements carried out from 2013 until 2015 show a gradual decrease in the angular velocity whose cause is attributed to the Earth's magnetic field. The goal of this case study was to validate this hypothesis and to compare the numerical spin rate change with the observed values. For this purpose, a simulator was developed in MATLAB, which took into account the most important environmental perturbations. These include the Earth's gravity potential up to fourth order, the gravity gradient torques, the air drag force and torque, the solar radiation force and torque and the Earth's magnetic field torque. The eddy currents induced by the Earth's magnetic field are analysed employing the magnetic tensor theory. The numerical results show a secular decrease in the spin rate of Envisat equal to 0.00149 deg/s per day which is of the same order of magnitude to the observations made. This result highlights the effectiveness of the theory developed in providing reliable results.

MAGNETIC TENSOR THEORY: EXPERIMENTAL VALIDATION

4.1 Introduction

This chapter provides a detailed description of a set of experimental tests conducted at Airbus Defence & Space (Stevenage, UK). These tests were carried out during a three-month secondment conducted at this location (from October 2014 until December 2014). This site of Airbus Defence & Space focuses on the design and manufacture of advanced satellites and systems for telecommunications, Earth observation, navigation and science programmes. The experimental tests were carried out in a specially prepared clean room.

The goal of these experimental tests was to empirically validate the magnetic tensor theory (MTT). Note that the theory has already been numerically validated through the comparison of the magnetic torque provided by the MTT and available results from previous authors as described in the previous chapter (see Section 3.3.5). Experimental tests were conducted to provide empirical validation in order to further consolidate this theory.

The main goals of these tests were,

- to empirically validate the magnetic tensor theory,

- to analyse the characteristic time of decay for different magnetic field intensities and

- to analyse the eddy current effects on different shapes and orientations.

The chapter starts with a comprehensive description of the experimental set-up (Section 4.2) detailing all the equipment employed. Then, Section 4.3 provides a theoretical analysis of the expected dynamical behaviour of the tested metallic objects. Subsequently, Section 4.4 includes a detailed description of the test plan campaign and the experimental procedures. Although the arrangement and procedure varied slightly from test to test, the procedures described are considered representative, discussing any deviations on a case-by-case basis within the relevant subsection. Finally Section 4.5 gathers all the test results.

4.2 Experimental setup

The experimental tests consisted of an object suspended from a strut through a torsion wire with an oscillatory uniaxial rotation about the axis of the wire. The object was subjected to a homogeneous

and constant magnetic field, perpendicular to its angular velocity, created by a Helmholtz coil (see Figure 4.1). This process allows eddy currents to be induced in the object in order to damp its angular velocity.

Three different metallic objects were tested: a spherical shell, a cylindrical shell and aluminium honeycomb structure. The spherical and cylindrical shells represent possible propulsion components (e.g. propellant tanks), whereas the aluminium honeycomb panels represent typical structural components employed in satellites.
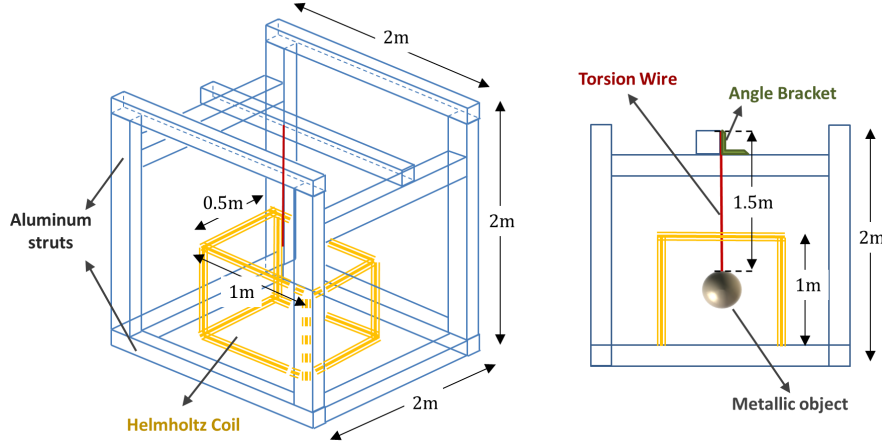
Figure 4.1: Sketch of the experimental test set-up.

The Helmholtz electromagnetic coil, the power supply and the aluminium honeycomb structure were provided by Airbus Defence and Space. Section A.2 includes a list of the equipment that was purchased including the supplier and overall budget.

4.3 Theoretical analysis

4.3.1 Static torsion of a rod with a circular section

The torsion given by the wire, T_{wi}, is [151],

$$T_{wi} = -\kappa_{wi}\,\theta,$$
$$\kappa_{wi} = \frac{G_{wi}}{L_{wi}}\frac{\pi d_{wi}^4}{32}, \tag{4.1}$$

where θ is the rotational displacement angle wound by the wire, κ_{wi} is the wire torsion coefficient, d_{wi} is the diameter of the wire, L_{wi} is the length of the wire and G_{wi} is the shear modulus of the wire.

The maximum shear stress, τ_{wi}^{stress}, that appears on the wire is [151, 162],

$$\tau_{wi}^{stress} = |T_{wi}|\frac{16}{\pi d_{wi}^3} \tag{4.2}$$

and the tensile stress, σ_{wi}^{stress}, is,

$$\sigma_{wi}^{stress} = \frac{m_{obj}\,g}{A_{wi}}, \tag{4.3}$$

where m_{obj} is the mass of the object, $g = 9.81 \ m/s^2$ is the gravitational acceleration and $A_{wi} = \frac{\pi d_{wi}^2}{4}$ is the cross section of the wire.

Figure 4.2 depicts the shear and tensile stresses that appear on the wire due to the torsion torque and the gravitational force.
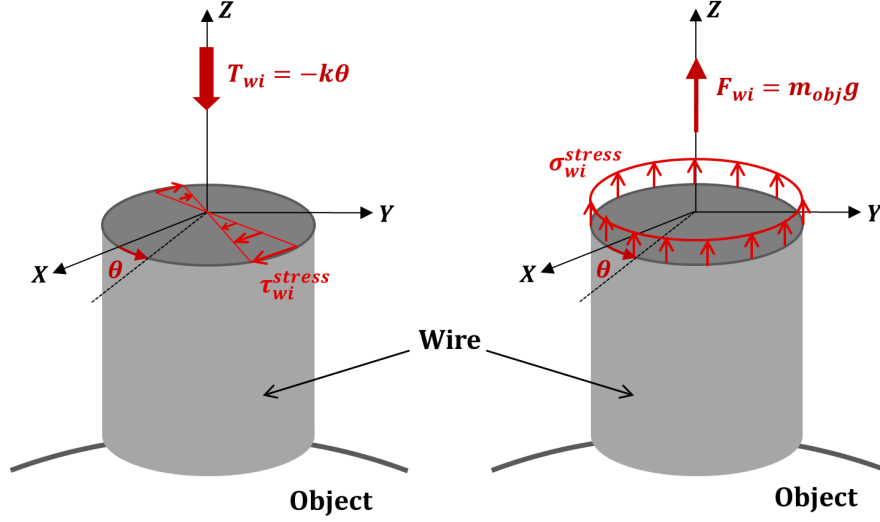
Figure 4.2: Sketch of the shear stress and tensile stresses on the wire.

In order to avoid entering into the plastic region of the wire, the Von Mises' yield criterion is considered [162]. The Von Mises stress or effective tensile stress, σ_{eff}^{stress}, is equal to

$$\sigma_{eff}^{stress} = \sqrt{(\sigma_{wi}^{stress})^2 + 3(\tau_{wi}^{stress})^2} \tag{4.4}$$

and this stress must be lower than the allowable stress, σ_{all}^{stress}, which is typically defined as the elastic limit or yield strength, $\sigma_{0.1\%}^{stress}$, divided by a safety factor.

$$\sigma_{eff}^{stress} \leq \sigma_{all}^{stress} = \frac{\sigma_{0.1\%}^{stress}}{Safety \ Factor}. \tag{4.5}$$

The torsion wire used for the experimental tests has the following properties given by the manufacturer [163],

- Material: Tungsten

- Shear Modulus: $G_{wi} = 161 \cdot 10^9$ Pa

- Yield stress: $\sigma_{0.1\%}^{stress} = 550 \cdot 10^6$ Pa

- Density: $\rho_{wi} = 19250$ kg/m^3

- Electrical conductivity: $\sigma_{wi} = 1.89 \cdot 10^7$ S/m (at 20^oC)

- Length: $L_{wi} = 1$ m

Figures 4.3 depicts the ratio $\frac{\sigma_{eff}^{stress}}{\sigma_{all}^{stress}}$ for different diameters and lengths of the wire for the spherical and cylindrical shells. The angular displacement considered is $\theta = 360$ degrees (i.e. 1 turn) and the safety factor considered is 1.5. It can be observed that the longer the wire, the lower the risk of entering into the plastic region. Due to height constraints of the clean room where the tests were carried out, a wire of a length of 1.5 metres was used. In addition, in order to operate well below the allowable stress, a diameter of 0.0004 m was selected. This diameter was chosen instead

of lower values due to the available inventory by the selected manufacturer [163]. Additional data on the supplier and model of the wire employed may be found in the Section A.2 of the Appendix.
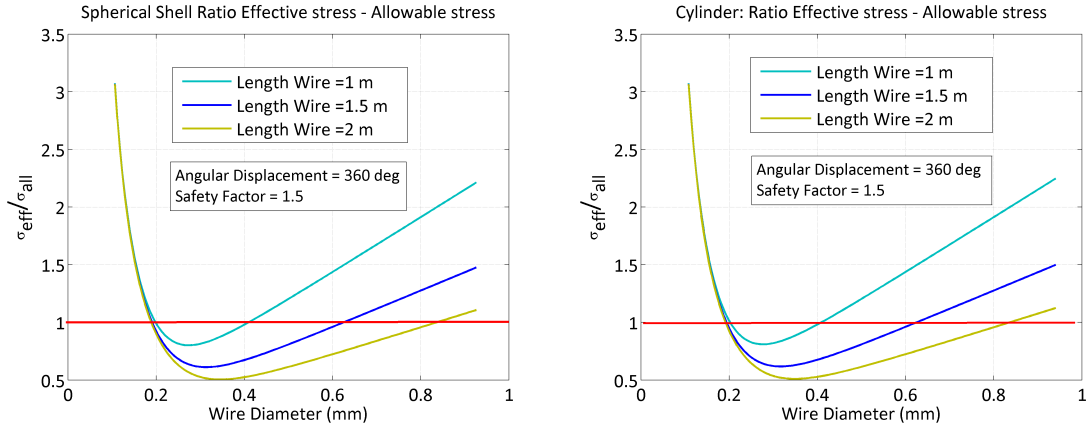
Figure 4.3: Allowable stress for the spherical shell (left Figure) and the cylindrical shell (right Figure) for $\theta = 360$ deg.

4.3.2 Dynamical torsion of the system: wire and metallic object

The present dynamical problem has only one unknown variable, the angular displacement, θ. The object is rotating with a time varying angular velocity but with a known direction, $\vec{\omega}(t) = \omega(t)\vec{k}$. Figure 4.4 depicts the angular displacement with respect to the equilibrium position and the angular velocity vector.
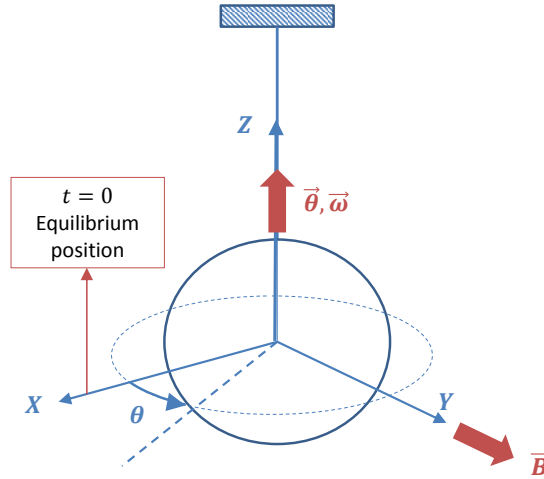
Figure 4.4: Angular displacement with respect to the equilibrium position.

The differential equation in θ is obtained projecting Euler's Equations in the direction of the angular displacement vector, $\vec{k}$,

$$(\mathbf{I}\dot{\vec{\omega}} + \vec{\omega} \times \mathbf{I}\vec{\omega} = \sum \vec{T}) \cdot \vec{k},$$
$$\dot{\theta}\vec{k} = \vec{\omega}\vec{k}, \tag{4.6}$$

where $\mathbf{I}$ is the inertia tensor of the metallic object and the wire.

The external torques that need to be considered are the torque induced by the wire, $\vec{T}_{wi}$, and the torque induced by the eddy currents, $\vec{T}_{eddy}$,

$$\vec{T}_{wi} = -\kappa_{wi}\theta, \tag{4.7}$$

$$\vec{T}_{eddy} = (\mathbf{M}(\vec{\omega} \times \vec{B})) \times \vec{B}. \tag{4.8}$$

This leads to a differential equation of the type,

$$\begin{aligned}
\ddot{\theta} + C\dot{\theta} + \omega_0^2 \theta &= 0, \\
\theta(t=0) &= \theta_0 > 0, \\
\dot{\theta}(t=0) &= 0.
\end{aligned} \tag{4.9}$$

where C is the damping coefficient and ω_0 the natural frequency of the system. The damping coefficient is equal to the inverse of half of the characteristic time of decay, τ, of the de-spinning process. The characteristic time of decay is split into two components, one due to the eddy current phenomenon, τ_B, and the other due to external factors, τ_0 (e.g. wire damping, air drag). C_0 is referred to as the *noise damping coefficient* and C_B *eddy current damping coefficient*.

$$C = \frac{2}{\tau} = C_B + C_0 = \frac{2}{\tau_B} + \frac{2}{\tau_0}. \tag{4.10}$$

The natural frequency, ω_0, and the period, P_0, of the phenomenon are related to the wire torsion coefficient and the inertia in the direction of the wire, denoted as I_k,

$$\omega_0 = \frac{2\pi}{P_0} = \sqrt{\frac{\kappa_{wi}}{I_k}}. \tag{4.11}$$

The damping ratio ζ is defined as,

$$\zeta = \frac{C}{2\omega_0}. \tag{4.12}$$

This parameter indicates if the system is *overdamped* ($\zeta > 1$) or *underdamped* ($\zeta < 1$).

- The solution of an underdamped system decreases exponentially in combination with an oscillatory motion as shown in Equation (4.9),

$$\theta(t) = \theta_0 e^{-\omega_0 \zeta t} \cos(\omega_d t), \tag{4.13}$$

where ω_d is equal to,

$$\omega_d = \omega_0 \sqrt{1 - \zeta^2} = \sqrt{\omega_0^2 - \frac{C^2}{4}}. \tag{4.14}$$

- The solution of an overdamped system simply decays exponentially with no oscillation and has the general form,

$$\theta(t) = \frac{\theta_0}{2\sqrt{\zeta^2 - 1}}((\zeta + \sqrt{\zeta^2 - 1})e^{\omega_0(-\zeta + \sqrt{(\zeta^2 - 1)})t} + (-\zeta + \sqrt{\zeta^2 - 1})e^{\omega_0(-\zeta - \sqrt{(\zeta^2 - 1)})t}). \tag{4.15}$$

Both responses are depicted in Figure 4.5.

In order to have a first order of magnitude of the regime in which the tests will take place, the damping ratio due to eddy currents is analysed for one of the objects, in particular, the spherical shell. The natural frequency for the spherical shell is,

$$\omega_0 = \sqrt{\frac{\kappa_{wi}}{I_k}} = \sqrt{\frac{\frac{G_{wi}}{L_{wi}}\frac{\pi d_{wi}^4}{32}}{\frac{8\pi}{3}R_{sph}^4 e_{sph}\rho_{sph}}} = \frac{\sqrt{3}}{16}\frac{d_{wi}^2\sqrt{G_{wi}}}{\sqrt{L_{wi}}}\frac{1}{R_{sph}^2\sqrt{e_{sph}\rho_{sph}}}. \tag{4.16}$$
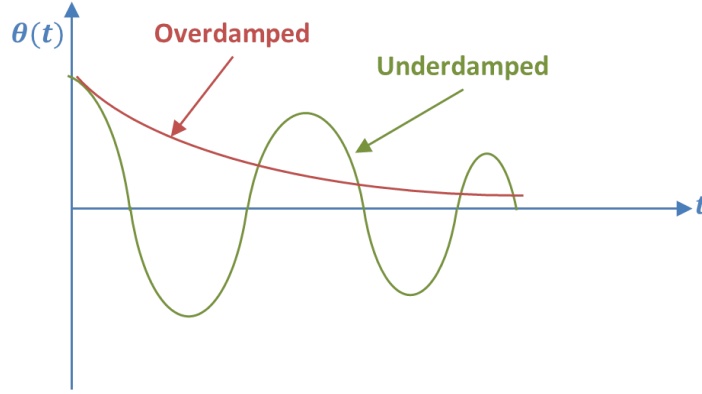
Figure 4.5: Underdamped and overdamped responses.

Using the analytical formula of the magnetic tensor for a spherical shell (3.122), the eddy current damping coefficient can be obtained as,

$$C_B = \frac{\sigma_{sph} B^2}{2\rho_{sph}}$$

(4.17)

and therefore, the eddy current damping coefficient, ζ_B, for a spherical shell is equal to,

$$\zeta_B = \frac{C_B}{2\omega_0} = \frac{1}{\sqrt{3}} B_d^2 \frac{\sigma_{sph} R_{sph}^2 \sqrt{e_{sph}}}{\sqrt{\rho_{sph}}} \frac{\sqrt{L_{wi}}}{d_{wi}^2 \sqrt{G_{wi}}}.$$

(4.18)

The maximum magnetic field that can be provided by the Helmholtz coil is $B = 3000$ µT. Figure 4.6 shows the damping ratio for this magnetic field and different wire lengths. In all cases, the sphere remains in the underdamped regime, which is the behaviour that ought to be expected in the experimental tests.
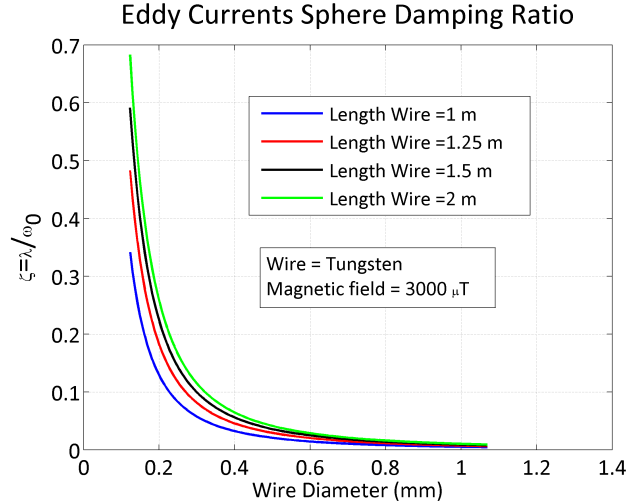
Figure 4.6: Damping ratio due to the eddy currents for a spherical shell.

4.4 Test plan

A total of 23 tests were conducted overall, following an identical test procedure for each object, described as follows: the metallic object was suspended from the torsion wire; a video camera was

placed pointing towards the object in order to record the process; markings were placed on the objects around their surface in order to indicate the rotated angle from the equilibrium position, θ_{max},; an initial angular displacement of 360 degrees (i.e. 1 turn) was manually imposed to the object and subsequently the object was released to rotate freely; the process was recorded until the angular velocity of the object was negligible to the naked eye. The optical measurements are provided until the accuracy of the measurements is too low, preventing further measurements from being taken.

The post-processing of the videos consisted in identifying the rotated angle and the time when it occurs in order to construct the function $f(\theta_{max}, t)$. These optical measurements were obtained based on the markers placed on the object as well as a grid structure of the post-processing video toolbox, 'VLC Media Player' and 'Microsoft Movie Maker'.
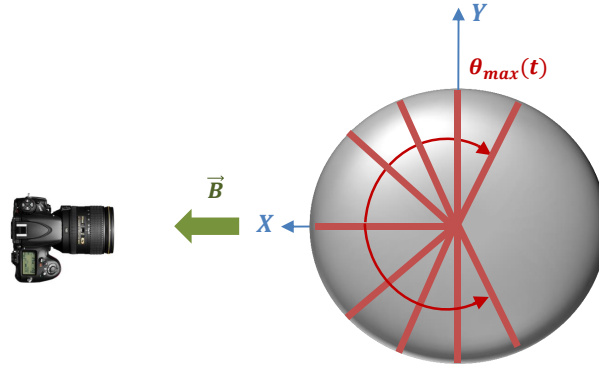
Figure 4.7: Sketch of the rotating object and the camera.

Note that for all tests, the Earth's magnetic field was compensated by placing the coil in a specific orientation so that this field was cancelled out.

The first test was conducted without an applied magnetic field. In this case, the coil was only used to compensate for the Earth's magnetic field. This test was used to measure the natural frequency, ω_0, and the noise damping, C_0. The subsequent tests were carried out for different magnetic fields in order to obtain the characteristic time of decay as a function of the magnetic field.

For each test, the evolution of the maximum angular displacement with time, $\theta_{max}(t, B)$, was obtained from the video recording as shown in Figure 4.8. The characteristic time of decay was then obtained from the measurements and compared with the predicted values by the magnetic tensor theory.
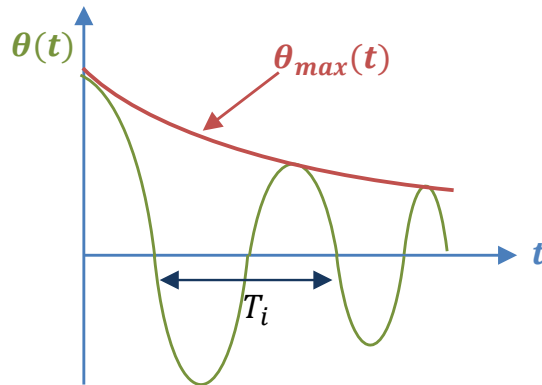
Figure 4.8: Angular displacement and maximum angular displacement evolution with time.

4.5 Experimental test results

4.5.1 Spherical shell

The spherical shell used for the experimental tests has the following properties given by the manufacturer:

- Material: Aluminium alloy 6082

- Electrical conductivity: $\sigma_{sph} = 2.63 \cdot 10^7$ S/m (at 20°C)

- Density: $\rho_{sph} = 2700$ kg/m^3

- Radius: $R_{sph} = 0.1$ m

- Thickness: $e_{sph} = 0.003$ m

Figure 4.9 shows a photograph of the testbed of the spherical shell. The sphere was suspended from a strut through the torsion wire and was located at the centre of the Helmholtz coil to generate a homogeneous magnetic field.
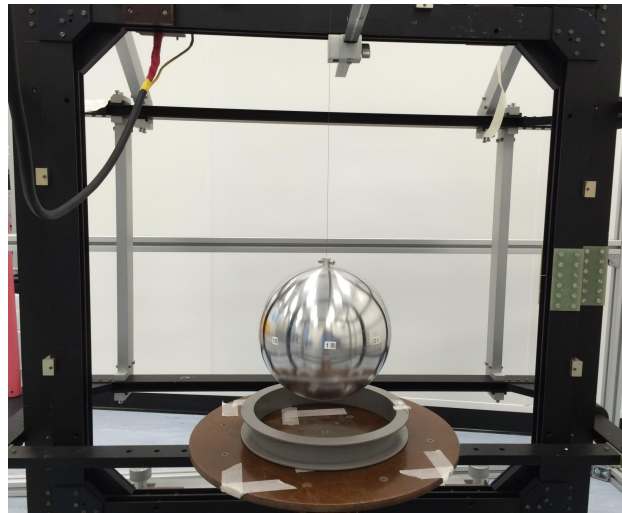
Figure 4.9: Testbed for the spherical shell.

In this case, an analytical solution for the evolution of the angular velocity vector can be obtained because the characteristic time of decay due to the eddy current phenomenon, $\tau_{B,MTT}$, is constant. The inertia tensor for the spherical shell in its body axes is:

$$\mathbf{I} = I_{sph} \begin{bmatrix} 1 & 0 & 0 \\ 0 & 1 & 0 \\ 0 & 0 & 1 \end{bmatrix} \text{ kg} \cdot \text{m}^2, \tag{4.19}$$

where $I_{sph} = \frac{8}{3}\pi R_{sph}^4 e_{sph}\rho_{sph}$ and the magnetic tensor of the spherical shell in its body axes is:

$$\mathbf{M} = M_{sph} \begin{bmatrix} 1 & 0 & 0 \\ 0 & 1 & 0 \\ 0 & 0 & 1 \end{bmatrix} \text{ S} \cdot \text{m}^4. \tag{4.20}$$

where $M_{sph} = \frac{2}{3}\pi R_{sph}^4 e_{sph}\sigma_{sph}$.
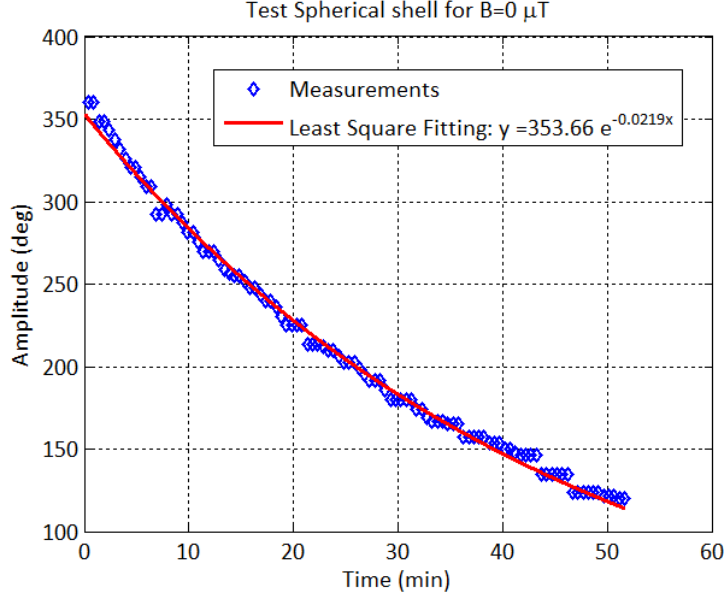
Figure 4.10: Experimental amplitude evolution of the spherical shell for $B = 0$ µT.

The differential equation in θ is obtained from Equation (4.6) and it has the form,

$$(\mathbf{I}\dot{\vec{\omega}} + \vec{\omega} \times \mathbf{I}\vec{\omega} = \vec{T}_{wi} + \vec{T}_{eddy}) \cdot \vec{k} \Rightarrow \ddot{\theta} = -\omega_0^2\theta - C_0\dot{\theta} - \frac{M_{sph}}{I_{sph}}\dot{\theta}B^2. \tag{4.21}$$

Therefore, the characteristic time of decay due to the eddy currents, predicted by the MTT, is,

$$\tau_{B,MTT} = \frac{2}{C_B} = \frac{I_{sph}}{M_{sph}B^2} = \frac{8\rho_{sph}}{\sigma_{sph}B^2}. \tag{4.22}$$

In addition, the total damping coefficient predicted by the MTT is,

$$C = \frac{2}{\tau_0} + \frac{2}{\tau_{B,MTT}} = \frac{2}{\tau_0} + \frac{\sigma_{sph}B^2}{4\rho_{sph}}. \tag{4.23}$$

The first test with zero magnetic field allows the characteristic time of decay due to external factors other than the eddy currents, τ_0, to be determined. The sphere was initially given one turn and was subsequently released to rotate freely. Figure 4.10 shows the optical measurements made of the amplitude of the oscillations, $\theta_{max}(t)$, and the least square fitting curve for the measurements. As previously stated, the optical measurements are provided until the accuracy of the measurements is too low, preventing further measurements from being taken.

The characteristic time of decay for this first test is obtained from the least square fitting curve as follows,

$$y = 353.66e^{-0.0219x} = y_0e^{-\frac{x}{\tau_0}} \rightarrow \tau_0 = 45.75\text{min}. \tag{4.24}$$

This test was repeated to check the consistency of the decay. The characteristic time of decay obtained for the second test was $\tau_0 = 46.5$min which confirms the consistency of the decay value.

Then, the test was repeated for five different magnetic fields: 900 µT, 1200 µT, 1800 µT, 2400 µT and 3000 µT.

Figure 4.11 shows the optical measurements obtained for each test (depicted as blue diamond markers) and the least square fitting curve of the measurements (depicted as red lines). In addition, the results predicted by the magnetic tensor theory are also provided (depicted as green dashed lines) to allow for a visual comparison with respect to the experimental tests.
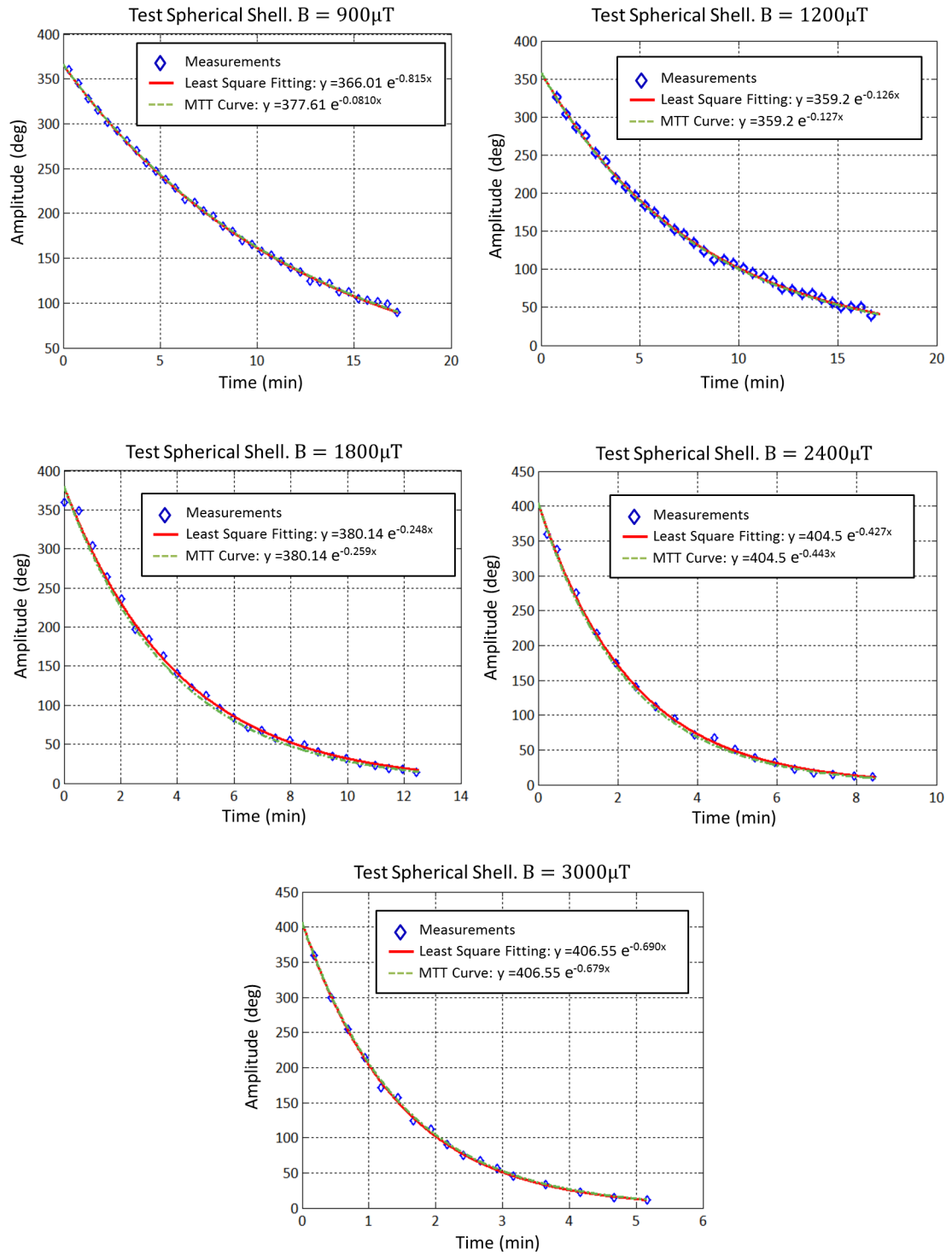
Figure 4.11: Experimental measurements and MTT prediction of the amplitude of the oscillations of the spherical shell.

4.5.1.1 Analysis of the results for the spherical shell

First of all, the characteristic times, τ_{test} and $\tau_{B,test}$, are inferred from the empirical data.

- τ_{test} is the characteristic time of decay of each test which takes into account the effect of the magnetic field as well as the noise damping. This value is obtained from the least square fitting curve of the measurements.

- $\tau_{B,test}$ is the characteristic time of decay due to the magnetic field for each test and it is computed by subtracting τ_0 as follows,

$$\frac{1}{\tau_{B,test}} = \frac{1}{\tau_{test}} - \frac{1}{\tau_0}. \tag{4.25}$$

Then, the characteristic time of decay due to the magnetic field predicted by the MTT, $\tau_{B,MTT}$, is computed with the Equation (4.22).

Table 4.1 contains a summary of the tests carried out for the spherical shell. In this table $\tau_{B,test}$ and $\tau_{B,MTT}$ are compared and it can be observed that the mean value is almost 1 and the standard deviation is 2.4%.

B [μT]	τ_{test} [min]	$\tau_{B,test}$ [min]	$\tau_{B,MTT}$ [min]	$\frac{\tau_{B,test}}{\tau_{B,MTT}}$	Error %
900	12.265	16.757	16.899	0.9916	0.84
1200	7.937	9.603	9.542	1.0064	0.64
1800	4.039	4.431	4.225	1.0488	4.87
2400	2.342	2.376	2.468	0.9627	3.72
3000	1.448	1.521	1.496	1.0167	1.67
Mean value				1.0052	
Standard dev.					2.4%

Table 4.1: Summary of spherical shell tests.

Figure 4.12 contains the evolution of the amplitude for all the tests, by portraying all the square fitting curves obtained for each set of measurements.
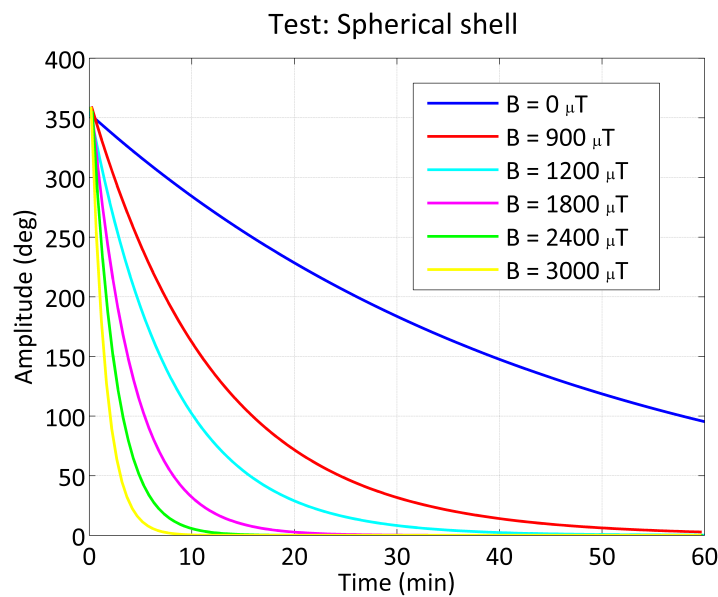
Figure 4.12: Experimental amplitude evolution of the spherical shell for different magnetic fields.

Note that both the empirical data and the curve obtained with the MTT model may have inaccuracies.

The MTT model employed for the spherical shell is based on Equation (4.22) where an isotropic density and conductivity is assumed throughout the volume. If there were any flaws associated with the manufacturing process or impurities in the alloy used, small deviations could appear in the density and conductivity which could lead to the observed discrepancies between both results. In addition, a constant and homogeneous field is considered in the MTT predictions. However, the magnetic field generated by the Helmholtz coil is not perfectly uniform throughout the overall volume between the two coils. Furthermore, the power source used generated small fluctuations of the intensity which led to small fluctuations of the magnetic field which may have introduced some additional imprecisions in the model.

With respect to the empirical data, imprecisions may have been introduced due to inaccuracies associated with the optical measurements. In order to minimise these errors, further repetitions of the experimental tests should be done. However, due to time constraints, each test could only be performed once. All the possible causes of the observed deviations between the empirical data and the MTT predictions are further analysed in Subsection 4.6.

Nonetheless, the results obtained for the spherical shell display a remarkable similarity and a noticeably good agreement between the optical measurements and the MTT predicted behaviour, with a standard deviation of just 2.4%.

4.5.2 Cylindrical shell

The cylindrical shell with closed ends employed for the tests is sketched in Figure 4.13 and it has the following physical properties:

- Material: Aluminium alloy 6082

- Electrical conductivity: $\sigma_{cyl} = 2.63 \cdot 10^7$ S/m (at 20°C)

- Density: $\rho_{cyl} = 2700$ kg/m^3

- Radius: $R_{cyl} = 0.075$ m

- Length: $L_{cyl} = 0.2$ m

- Thickness: $e_{cyl} = 0.003$ m

The body axes used for the cylinder are represented in Figure 4.13. The Z_B axis goes along the minimum axis of inertia of the cylinder and X_B and Y_B axes are both maximum axes of inertia. The inertia tensor $\mathbf{I}$ and magnetic tensor $\mathbf{M}$ are computed in these three axes. The inertia tensor of the cylinder is the following:

$$I_{X_B} = I_\perp = I_{Xcyl} + 2 \cdot I_{Xcover} = \frac{1}{12}m_{cyl}\left(6R^2 + H^2\right) + 2 \cdot \left(\frac{1}{4}m_{cover}R^2 + m_{cover}\left(\frac{H}{2}\right)^2\right), \quad (4.26)$$

$$I_{Y_B} = I_\perp, \quad (4.27)$$

$$I_{Z_B} = I_\parallel = I_{Zcyl} + 2 \cdot I_{Zcover} = m_{cyl}R^2 + 2 \cdot \left(\frac{1}{2}m_{cover}R^2\right), \quad (4.28)$$

where m_{cyl} is the mass of the cylindrical part of the body and m_{cover} is the mass of each cover. The inertia tensor for the studied cylinder is:

$$\mathbf{I} = \begin{bmatrix} I_\perp & 0 & 0 \\ 0 & I_\perp & 0 \\ 0 & 0 & I_\parallel \end{bmatrix} = \begin{bmatrix} 0.008 & 0 & 0 \\ 0 & 0.008 & 0 \\ 0 & 0 & 0.0051 \end{bmatrix} \text{kg} \cdot \text{m}^2. \quad (4.29)$$
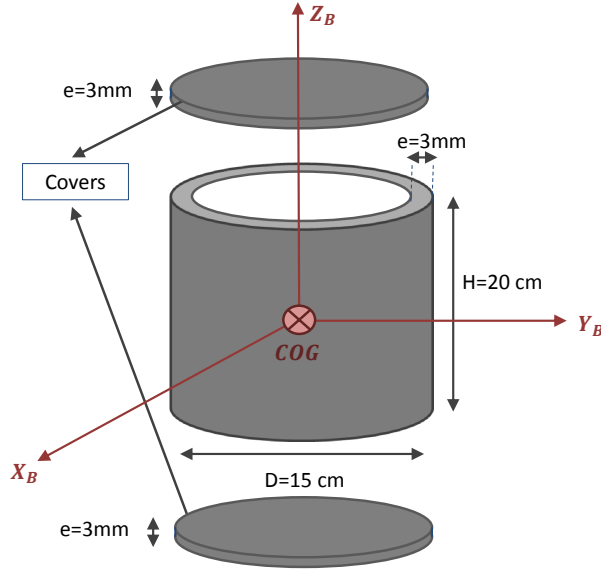
Figure 4.13: Cylindrical Shell Model.

In order to compute the magnetic tensor, the frame model has been used with 19200 bars and 9602 nodes. The mesh selected corresponds to the maximum amount of virtual memory that can be allocated by MATLAB to compute the tensor. The magnetic tensor obtained is:

$$\mathbf{M} = \begin{bmatrix} M_\perp & 0 & 0 \\ 0 & M_\perp & 0 \\ 0 & 0 & M_\parallel \end{bmatrix} = \begin{bmatrix} 12.1554 & 0 & 0 \\ 0 & 12.1554 & 0 \\ 0 & 0 & 9.5250 \end{bmatrix} \mathrm{S \cdot m^4}. \tag{4.30}$$

The cylinder was tested in three different positions:

- Rotation about the minimum axis of inertia

- Rotation about the maximum axis of inertia

- Rotation about an inclined axis

The photographs in Figure 4.14 show the three tested positions and the complete testbed. Note that add additional angle markers were used on the horizontal and inclined cylinders in order to facilitate the post-processing of the videos.

4.5.2.1 Rotation about the minimum axis of inertia

The first set of tests for this object consisted of the cylinder rotating about the minimum axis of inertia (Z_B axis).

In this case, an analytical solution for the evolution of the angular velocity vector can be obtained because the characteristic time of decay due to the eddy current phenomenon, $\tau_{B,MTT}$, is constant. This constant can be obtained from Equation (4.6) and it has the form:

$$\tau_{B,MTT} = \frac{2I_\parallel}{M_\perp B^2}. \tag{4.31}$$

In addition, the total damping coefficient predicted by the MTT is:

$$C = \frac{2}{\tau_0} + \frac{2}{\tau_{B,MTT}} = \frac{2}{\tau_0} + \frac{M_\perp B^2}{I_\parallel}. \tag{4.32}$$
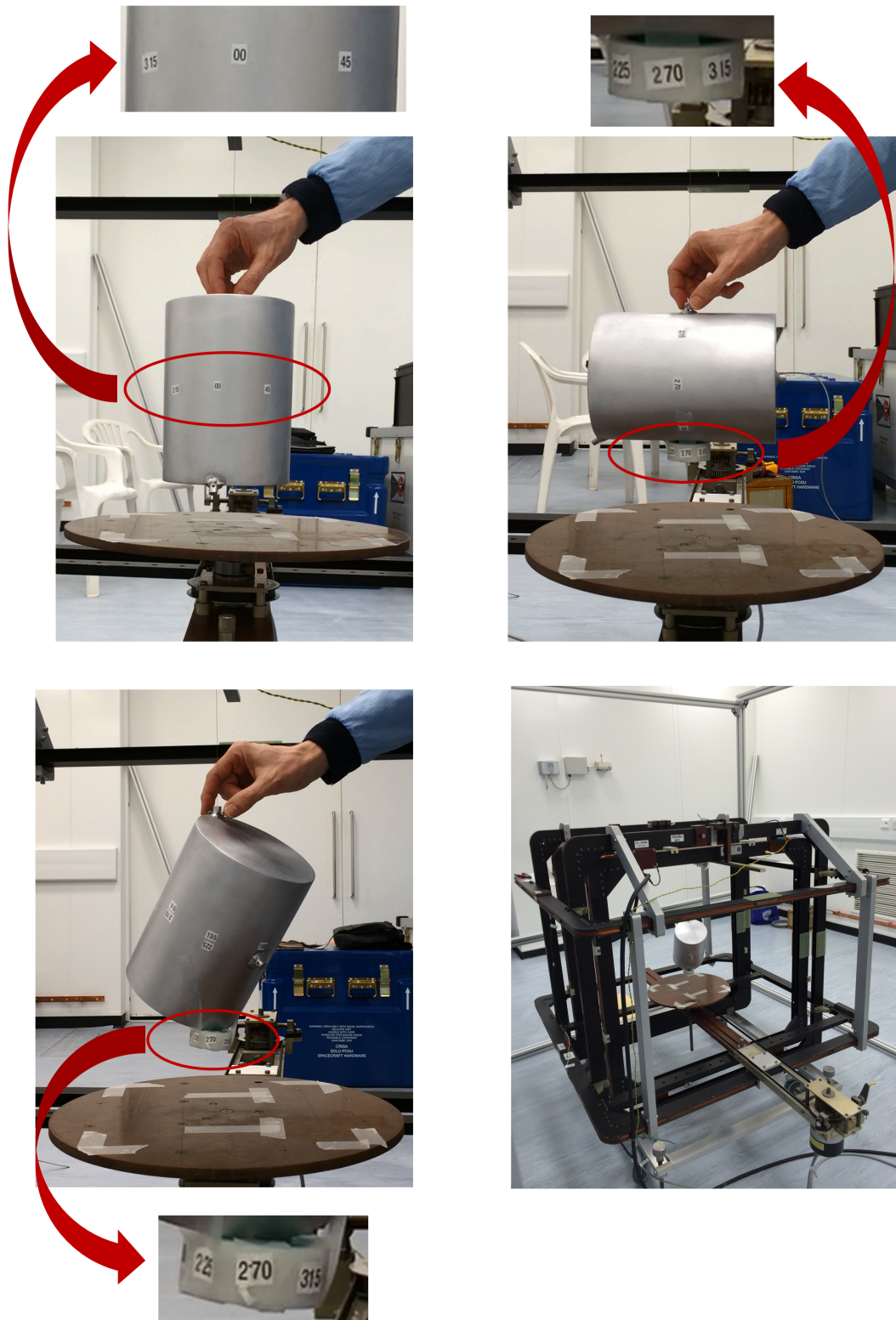
Figure 4.14: Photographs of the three positions tested for the cylinder and the complete test bed.

The first test with zero magnetic field allows the characteristic time of decay due to external factors other than the eddy currents, τ_0, to be determined. The cylinder was initially given one turn and was subsequently released to rotate freely about the Z_B axis. Figure 4.15 shows the optical measurements carried out of the amplitude of the oscillations $\theta_{max}(t)$ and the least square fitting curve for the measurements. As previously stated, the optical measurements are provided until the accuracy of the measurements is too low and it prevents from taking further measurements of the rotation of the object.
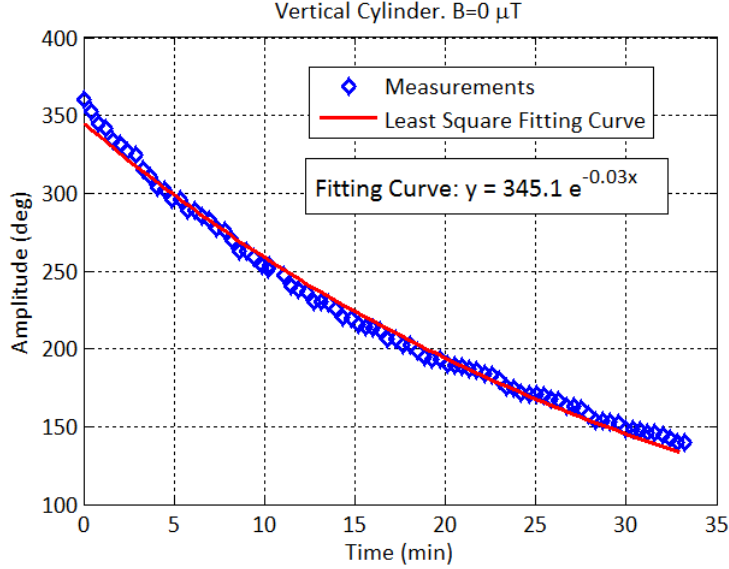
Figure 4.15: Experimental amplitude evolution of the vertical cylinder for zero magnetic field.

The characteristic time of decay of this first test is obtained from the least square fitting curve as follows,

$$y = 345.1e^{-0.03x} = y_0e^{-\frac{x}{\tau_0}} \rightarrow \tau_0 = 34.69 \text{ min.} \tag{4.33}$$

Then, the test was repeated for four different magnetic fields: 1200 µT, 1800 µT, 2400 µT and 3000 µT. Due to time constraints, these tests could only be performed once.

Figure 4.16 shows the optical measurements obtained for each test (depicted as blue diamond markers) and the least square fitting curve of the measurements (depicted as red lines). In addition, the predicted data by the MTT is also provided (depicted as green dashed lines) to allow for a visual comparison with respect to the experimental tests.

4.5.2.2 Analysis of the results for the cylindrical shell rotating about the minimum axis of inertial

First of all, the characteristic times, τ_{test} and $\tau_{B,test}$, are inferred from the results as explained in the previous section. Then, $\tau_{B,MTT}$ is evaluated based on Equation (4.31).

Table 4.2 contains a summary of the tests carried out for the cylindrical shell. In this table $\tau_{B,test}$ and τ_B are compared and it can be observed that the standard deviation is 11.6%. Section 4.6 analyses the possible causes of these deviations.

Figure 4.16: Experimental measurements and MTT predictions of the amplitude of the oscillations of the cylinder rotating about the minimum axis of inertia for different magnetic fields.

	B $[\mu \mathbf{T}]$	τ_{test} [min]	$\tau_{B,test}$ [min]	$\tau_{B,MTT}$ [min]	$\frac{\tau_{B,test}}{\tau_{B,MTT}}$	Error %
	1200	6.899	8.613	9.711	0.887	11.3
	1800	3.423	3.798	4.316	0.879	12.1
	2400	2.008	2.130	2.428	0.877	12.3
	3000	1.336	1.389	1.554	0.894	10.6
Mean value					0.884	
Standard dev.						11.6%

Table 4.2: Tests summary of the cylinder rotating about the minimum axis of inertia.

Figure 4.17 contains the evolution of the amplitude for all the tests, by portraying all the square fitting curves obtained for each set of measurements.
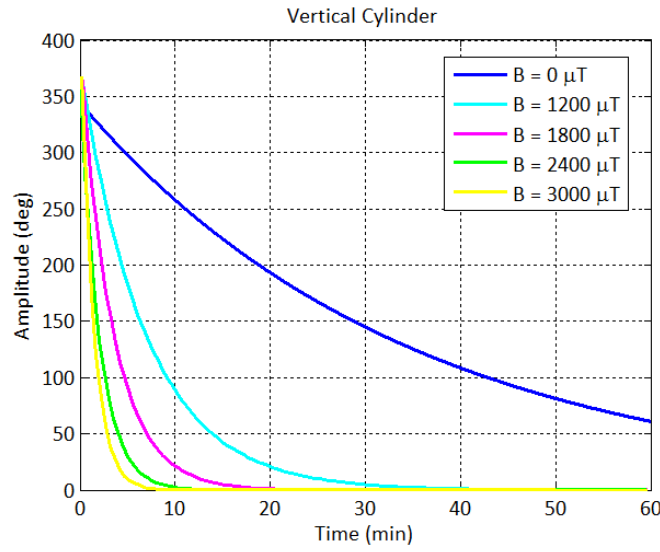
Figure 4.17: Experimental amplitude evolution of the vertical cylinder for all tests.

The standard deviation between the MTT model and measured values is 11.6%. A tendency towards an underestimation of the decay due to the eddy current phenomenon is observed. An additional possible cause of error appears in these tests compared to the spherical shell tests due to the use of the frame model. The accuracy of the frame model is limited by the number of finite elements used to obtain the magnetic tensor. This limitation can be overcome by employing a programming language that provides more optimised memory allocation performance (e.g. C++) or a more powerful computer.

4.5.2.3   Rotation about the maximum axis of inertia

The second set of tests consisted of the cylinder rotating about the maximum axis of inertia (Y_B axis). In this case, there is no analytical solution for the evolution of the angular velocity vector because the characteristic time of decay due to the eddy current phenomenon is not constant. τ_B is obtained from Equation (4.6) and it depends on the angular displacement θ of the cylinder with respect to the equilibrium position (see Figure 4.18),

$$\tau_B = \frac{2I_\parallel}{(M_\perp \sin^2 \theta + M_\parallel \cos^2 \theta)B^2}. \tag{4.34}$$
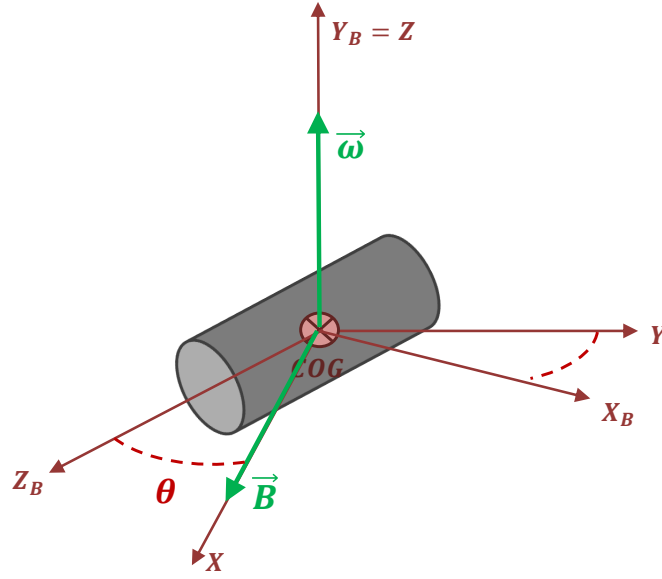
Figure 4.18: Oscillatory angular displacement of the cylindrical shell about the maximum axis of inertia.

In addition, the total damping coefficient is equal to,

$$C = \frac{2}{\tau_0} + \frac{2}{\tau_B} = \frac{2}{\tau_0} + \frac{(M_\perp \sin^2 \theta + M_\parallel \cos^2 \theta)B^2}{I_\parallel}. \tag{4.35}$$

In this case, the differential equation (Eq. 4.36) in θ needs to be integrated numerically for each test,

$$\ddot{\theta} + 2\left(\frac{1}{\tau_0} + \frac{(M_\perp \sin^2 \theta + M_\parallel \cos^2 \theta)B^2}{2I_\parallel}\right)\dot{\theta} + \omega_0^2\theta = 0. \tag{4.36}$$

The first step is to obtain the natural frequency of the system and the noise damping. The first experimental test was carried out without magnetic field in order to find those two parameters. The cylinder was initially given one turn and was subsequently released to rotate freely about the Y_B axis. Figure 4.19 shows the optical measurements carried out of the amplitude of the oscillations, $\theta_{max}(t)$, and the least square fitting curve for the measurements. As previously stated, the optical measurements are provided until the accuracy of the measurements is too low.

The noise damping is obtained from the least square fitting curve as follows,

$$y = 347.1e^{-0.0012x} = y_0 e^{-\frac{x}{\tau_0}} \rightarrow C_0 = \frac{2}{\tau_0} = 0.0024 \text{ s}^{-1}. \tag{4.37}$$

Furthermore, the natural frequency of the system must be obtained from the oscillatory evolution of the rotated angle. As already explained in Section 4.3.2, an overdamped system follows Equation (4.13). First, ω_d is inferred from the periodical oscillations of the system, depicted in Figure 4.8, as follows,

$$\omega_d = \frac{1}{N} \sum_{i=1}^{N} \frac{2\pi}{T_i}, \tag{4.38}$$

where T_i is the period of each oscillation made by the cylinder and ω_d is obtained by averaging all the periodical oscillations measured in the test.
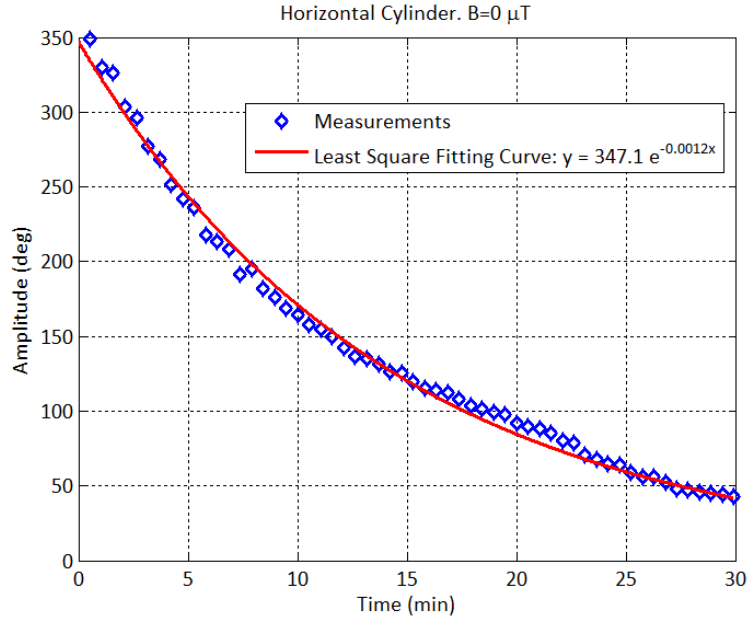
Figure 4.19: Experimental amplitude evolution of the horizontal cylinder for zero magnetic field.

Once ω_d is known, ω_0 can be computed using Equation (4.14) as follows,

$$\omega_d = \to \omega_0 = \sqrt{\omega_d^2 + \frac{C^2}{4}} = 0.1996 \text{ s}^{-1}. \tag{4.39}$$

Then, four additional experimental tests were carried out for the following magnetic fields: 1200 μT, 1800 μT, 2400 μT and 3000 μT. Due to time constraints, these tests could only be performed once. Figure 4.20 shows the optical measurements obtained for each test (depicted as blue triangle markers) and the predicted data by the MTT (depicted as green dashed lines) which has been obtained by numerical integration.

4.5.2.4 Analysis of the results for the cylindrical shell rotating about the maximum axis of inertial

In order to analyse the deviations between the empirical measurements and the MTT model, the following mean square error is used:

$$\varepsilon = \sqrt{\frac{\sum (y_{MTT} - y_{test})^2}{N}} \tag{4.40}$$

where y_{MTT} are the MTT predictions and y_{test} are the measurements.

In addition, the percentage error between the predicted data by the MTT and the empirical measurements is computed as:

$$\varepsilon_{\%} = 100 \cdot \frac{\sqrt{\frac{\sum (y_{MTT} - y_{test})^2}{N}}}{\sqrt{\frac{\sum y_{MTT}^2}{N}}}. \tag{4.41}$$

Table 4.3 shows the error between the optical measurements and the MTT numerical prediction.
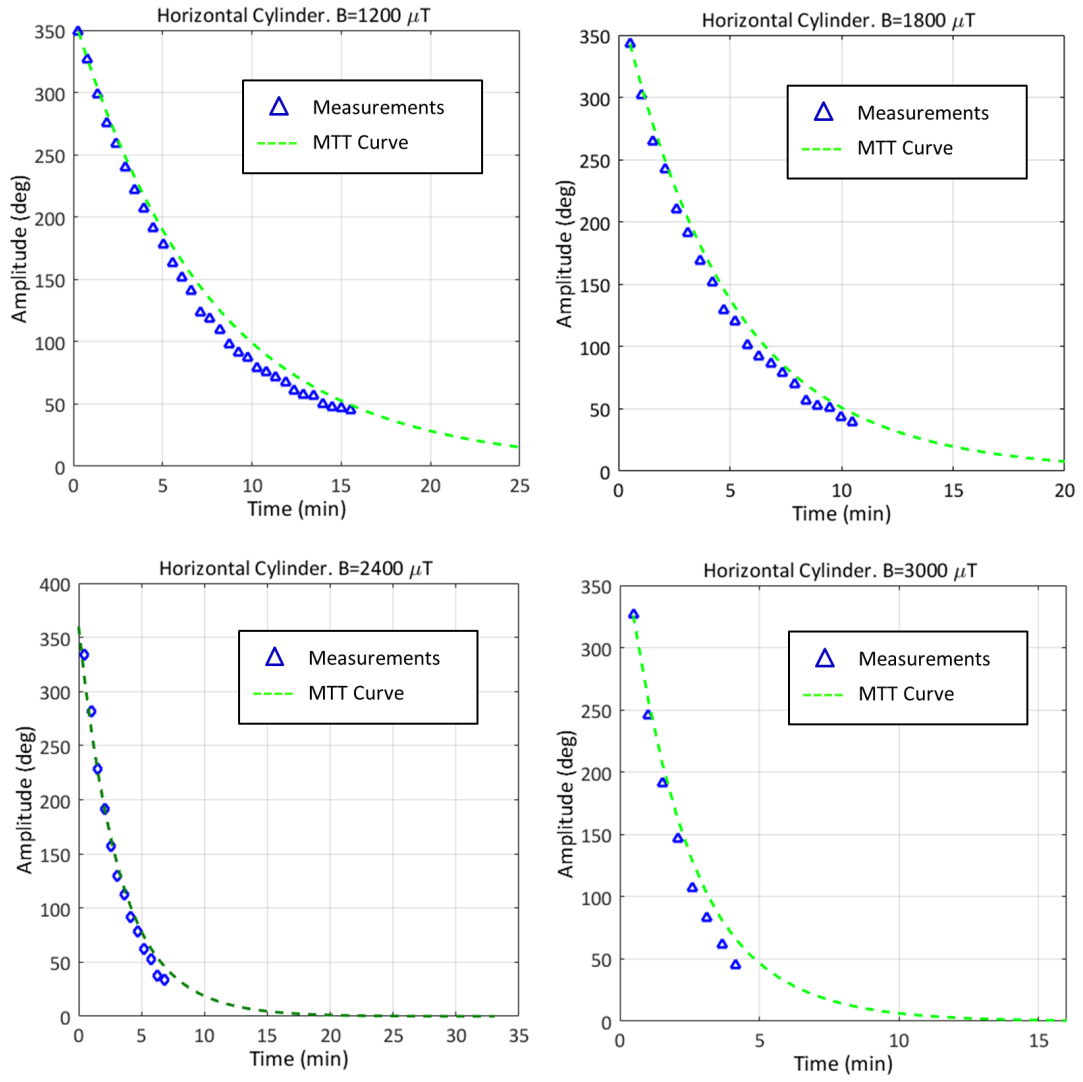
Figure 4.20: Experimental measurements and MTT predictions of the amplitude of the oscillations of the cylinder rotating about the maximum axis of inertia for different magnetic fields.

	B [μT]	Error %
	1200	7.00
	1800	6.30
	2400	8.65
	3000	9.32
Standard Deviation		7.8%

Table 4.3: Tests summary of cylinder rotating about the maximum axis of inertia.

In addition, Figure 4.21 contains the evolution of the amplitude of the oscillations for all the tests that were carried out.
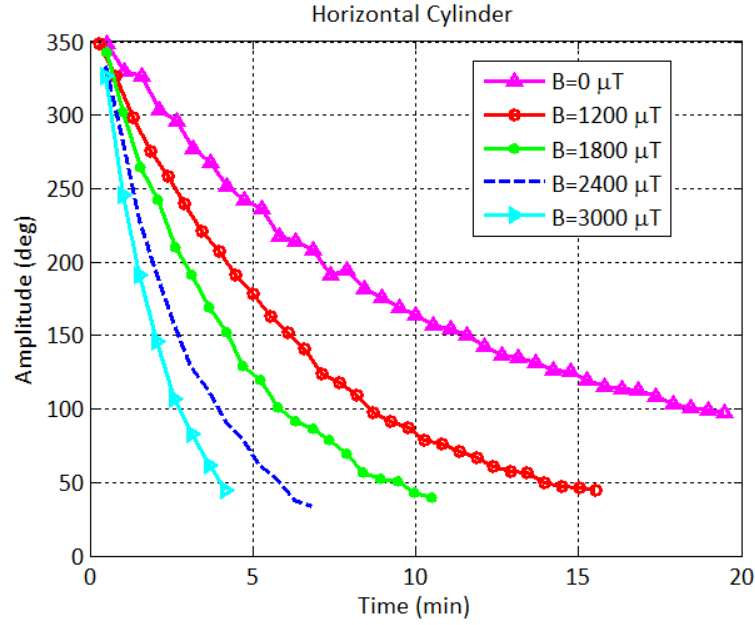
Figure 4.21: Experimental measurements of the amplitude evolution of the horizontal cylinder for all the tests.

The mean deviation between the MTT model and measured values is 7.8% improving the results of the previous test campaign (4.5.2.1). Again, a tendency towards an underestimation of the decay due to the eddy current phenomenon is observed. Section 4.6 analyses at greater length the possible causes of these deviations.

4.5.2.5   Rotation about an inclined axis

The third set of tests for this object consisted in the cylinder rotating about an inclined axis. Figure 4.22 shows the body axes and inertia axes employed. The vertical axis of the cylinder, Z_B, is inclined $\alpha = 37$ degrees with respect to the inertia axis, Z.

In this case, there is no analytical solution for the evolution of the angular velocity vector because the characteristic time of decay due to the eddy current phenomenon is not constant. The characteristic time of decay due to the eddy currents, τ_B, is obtained from Equation (4.6) and is a function of θ:

$$\tau_B = \frac{2(I_\parallel \cos^2(\alpha) + I_\perp \sin^2(\alpha))}{(M_\perp (\sin^2(\theta) \cos^2(\alpha) + \cos^2(\theta)) + M_\parallel \sin^2(\theta) \sin^2(\alpha))B^2}, \tag{4.42}$$
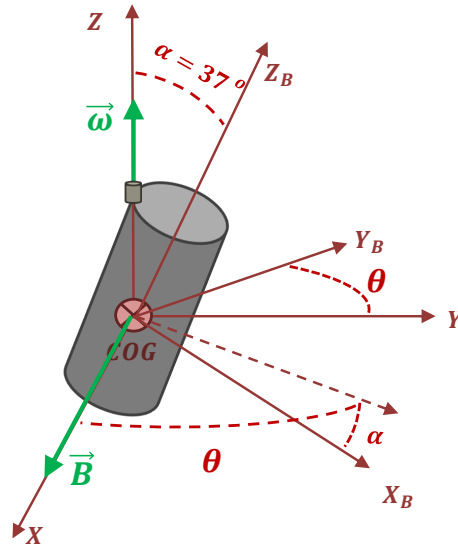
Figure 4.22: Oscillatory rotation about an inclined axis.

The results from the test with zero magnetic field are used to obtain the noise damping and the natural frequency of the system. Figure 4.23 show the results of this first test, which include the curve of the measured values and the least square fitting curve. As previously stated, the optical measurements are provided until the accuracy of the measurements is too low. The values obtained for the parameters ω_0 and C_0 are:

$$\omega_0 = 0.2402 \text{ s}^{-1}, \tag{4.43}$$

$$C_0 = \frac{2}{\tau_0} = 0.00168 \text{ s}^{-1}. \tag{4.44}$$
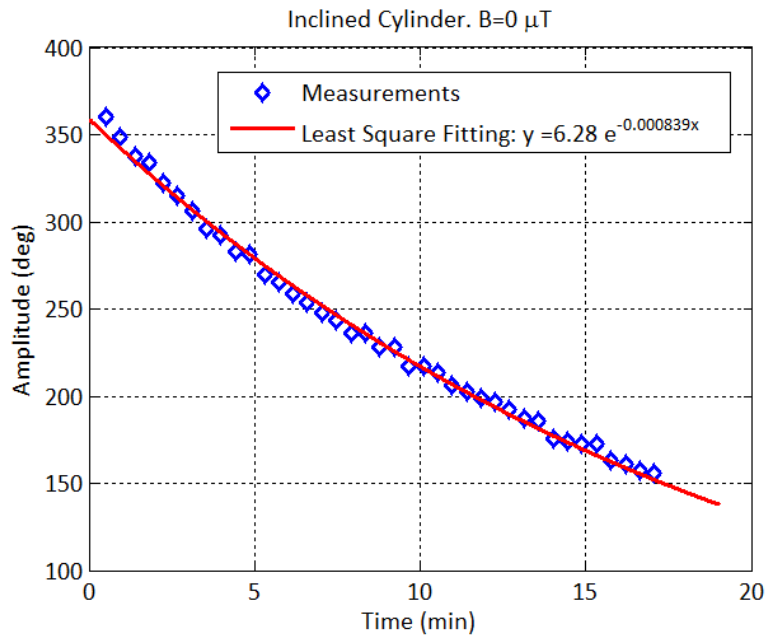
Figure 4.23: Experimental amplitude evolution of the inclined cylinder for zero magnetic field.

Then, four additional experimental tests were carried out for the following magnetic fields: 1200 µT, 1800 µT, 2400 µT and 3000 µT. Due to time constraints, these tests could only be performed once. Figure 4.24 shows the optical measurements obtained for each test (depicted as blue triangle markers) and the predicted data by the MTT (depicted as green dashed lines) which has been obtained by numerical integration.
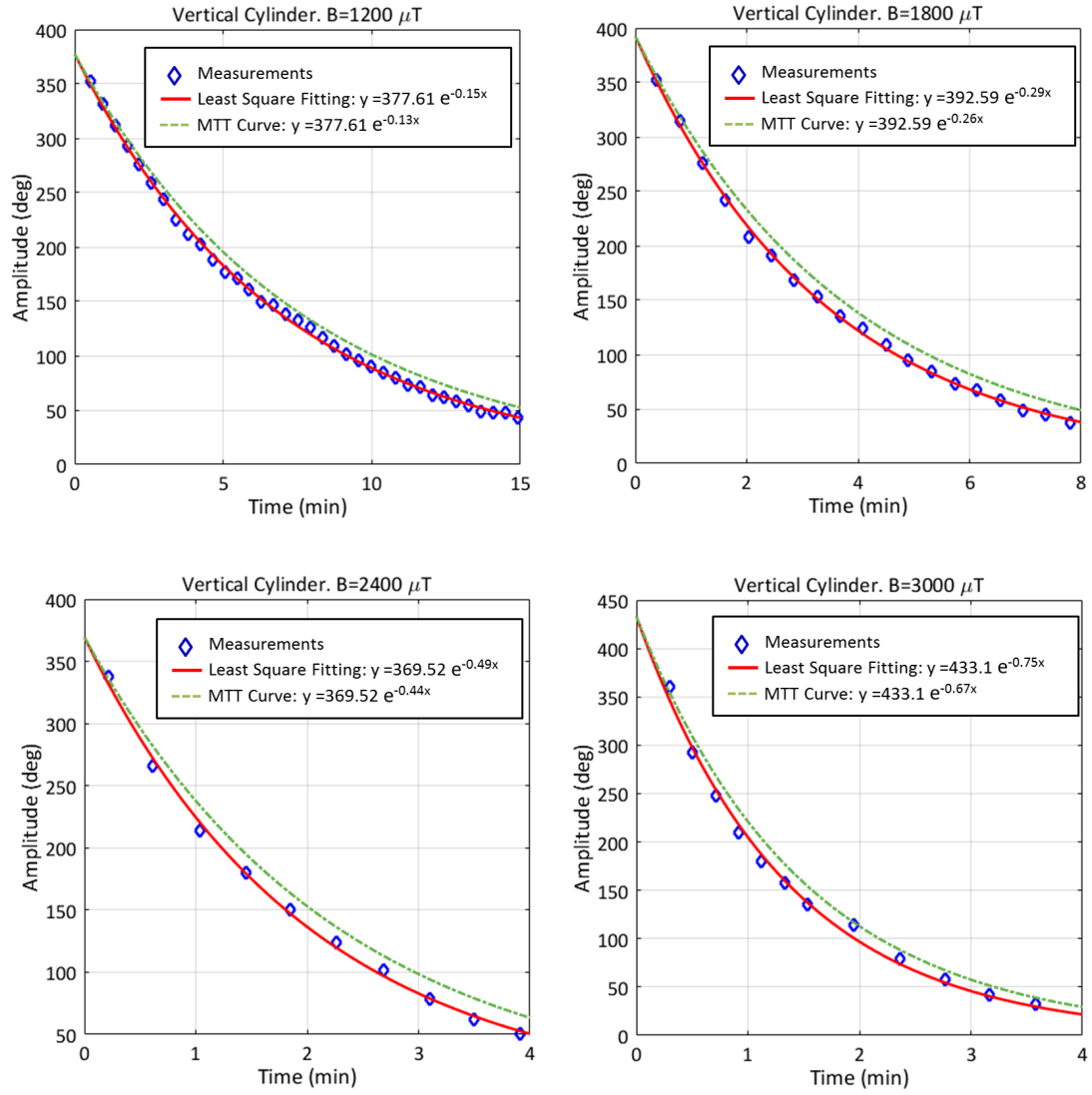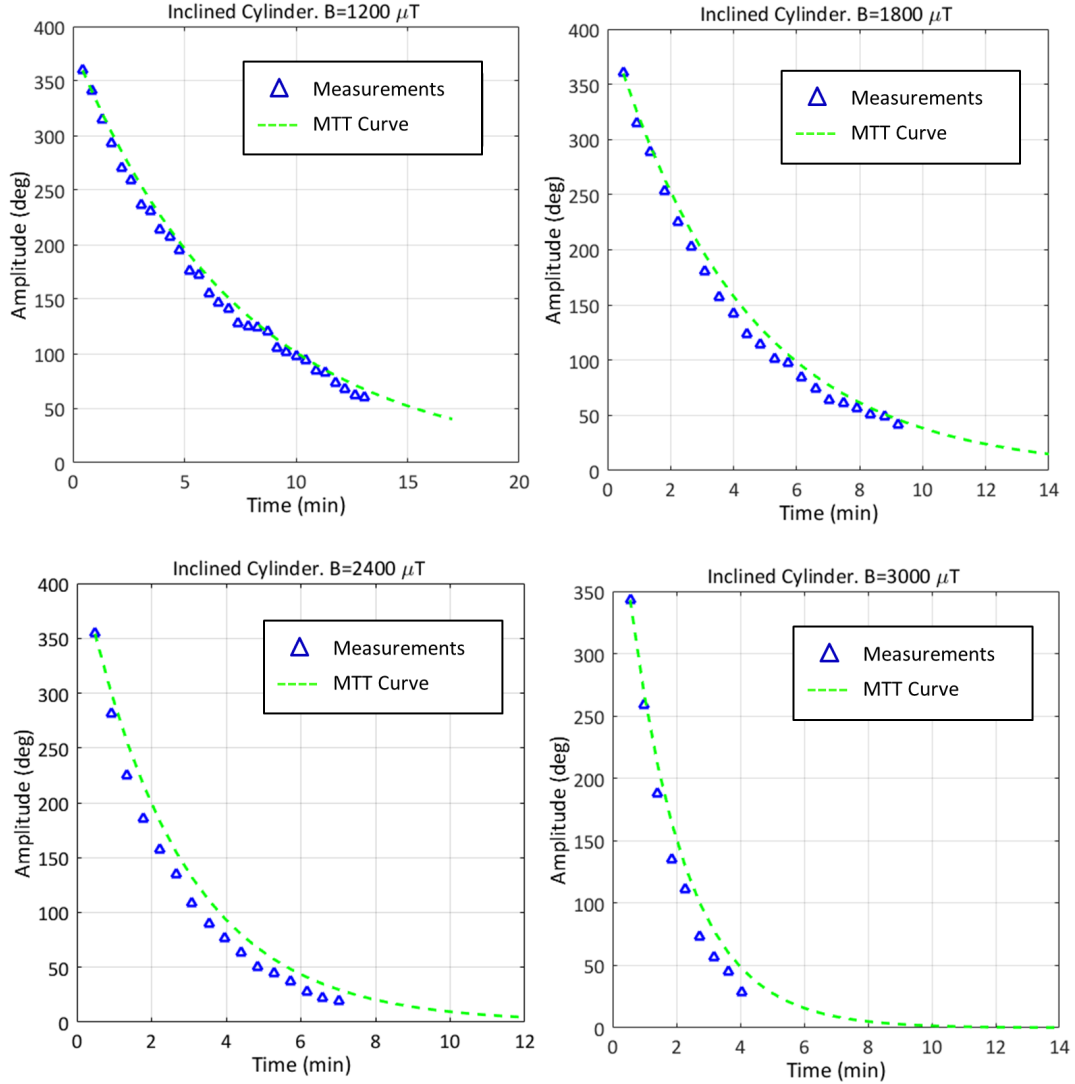

Figure 4.24: Experimental measurements and MTT predictions of the amplitude of the oscillations of the cylinder rotating an inclined axis for different magnetic fields.

4.5.2.6   Analysis of the results for the cylindrical shell rotating about an inclined axis

Table 4.4 shows the deviation between the optical measurements and the MTT model based on Equation (4.41).

	B [μT]	Error %
	1200	4.82
	1800	6.39
	2400	11.30
	3000	10.91
Standard Deviation		8.3%

Table 4.4: Tests summary of the inclined cylinder.

Finally, Figure 4.25 contains the evolution of the amplitude for all the tests that were carried out.
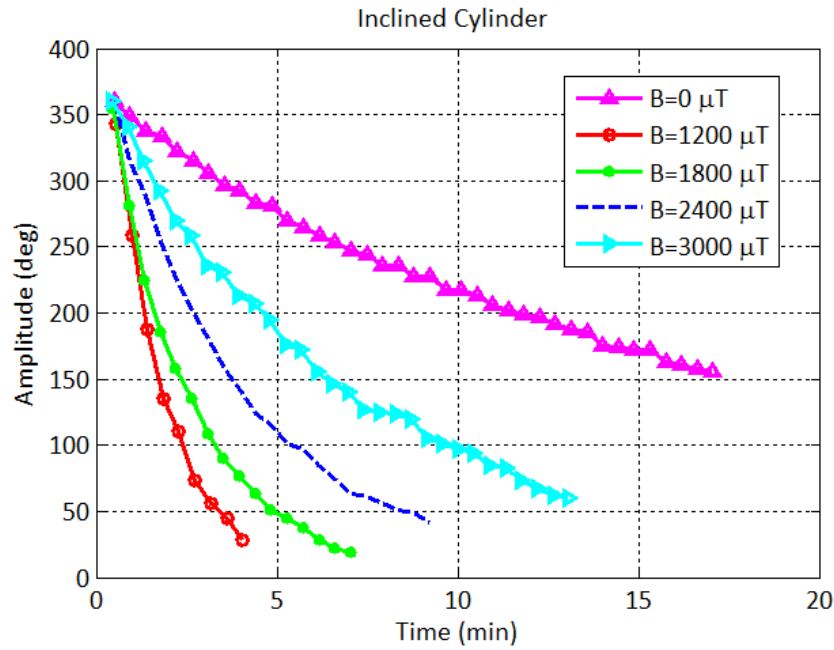
Figure 4.25: Experimental measurements of the amplitude evolution of the inclined cylinder for all the tests.

Here, the mean deviation between the MTT model and empirical values is 8.3%.

4.5.3 Aluminium honeycomb cube

The structure that was tested contains 4 aluminium honeycomb panels. Each panel is 0.5×0.5 m in size and 0.02 m thick. The central aluminium honeycomb core was covered by an aluminium skin of 0.0002 m of thickness. Figure 4.26 shows a sketch of the structure and dimensions, as well as a photograph of the testbed employed for the tests.

In addition, the panel structure contains inserts, screws and metallic connections between the panels (see Figure 4.27) as well as a loop heat pipe (LHP) in one of the panels.

Figure 4.27: Metallic connectors between the panels, inserts and LHP.
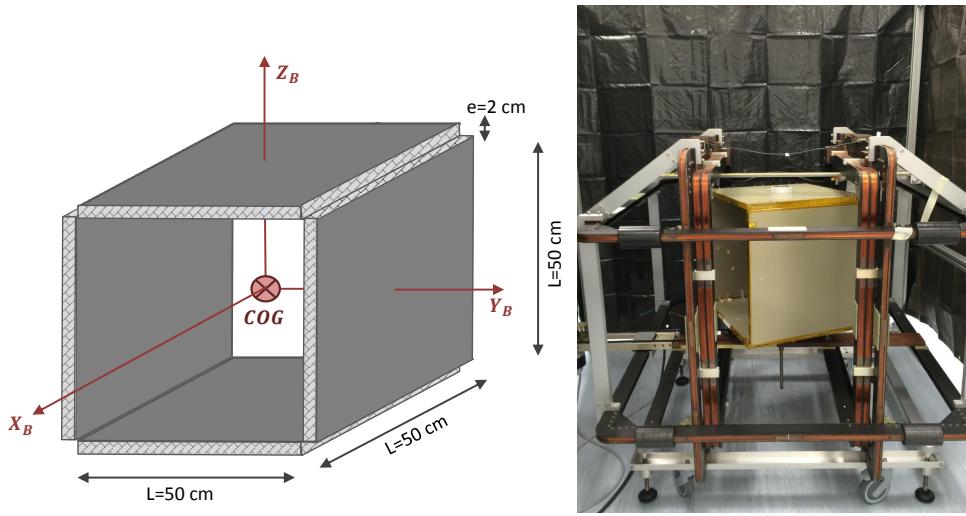
Figure 4.26: Sketch of the aluminium honeycomb cube and testbed.

The body axes used for the cube are represented in the Figure 4.26. The Z_B axis is parallel to the angular velocity vector of the structure and the X_B axis points towards the open side of the cube. The inertia tensor I and magnetic tensor M are computed in these three axes. The inertia tensor of the cube is the following:

$$I_{X_B} = 4 \cdot \left(\frac{1}{12} m_{panel}(L^2 + e^2) + m_{panel}(\frac{L}{2})^2 \right), \tag{4.45}$$

$$I_{Y_B} = 2 \cdot \left(\frac{1}{6} m_{panel}(L^2) + \frac{1}{12} m_{panel}(L^2 + e^2) + m_{panel}(\frac{L}{2})^2 \right), \tag{4.46}$$

$$I_{Z_B} = I_{Y_B}, \tag{4.47}$$

where m_{panel} is the mass of each aluminium honeycomb panel, L is the length of the panel and e is the thickness.

The total mass of the structure is 4.178 kg, therefore, as a first approximation, the mass of each panel has been computed as:

$$m_{panel} = \frac{m_{total}}{4} = 1.0445 \text{ kg.} \tag{4.48}$$

and the inertia tensor of the structure in the body axes is,

$$\mathbf{I} = \begin{bmatrix} 0.3483 & 0 & 0 \\ 0 & 0.2612 & 0 \\ 0 & 0 & 0.2612 \end{bmatrix} \text{kg} \cdot \text{m}^2. \tag{4.49}$$

In order to compute the magnetic tensor, only the aluminium skins of the honeycomb structure have been considered and it is assumed that the eddy current loops are localised in each aluminium skin. The core and the skin are joined together with an adhesive skin which means that they are electrically independent. The eddy current loops that may appear in the metallic connectors, screws and LHP are neglected due to their small relative size. The magnetic tensor for each square flat plate (aluminium skin) is given by Equation (3.150) and it has the form,

$$M_{skin} = \frac{1}{4}\sigma t \frac{L^4}{7.11}\vec{n} \cdot \vec{n}^T, \tag{4.50}$$

where σ is the electrical conductivity of the skin, t is the thickness of the skin, L is the length and $\vec{n}$ is the unitary vector normal to the skin. As each panel is treated as electrically independent, the total magnetic tensor is equal to the sum of each tensor (as demonstrated in Section 3.3.4.4).

Taking into account that each honeycomb panel has two skins, the magnetic tensor of the structure in its body axes is equal to,

$$\mathbf{M} = M_1 + M_2 + M_3 + M_4 = \begin{bmatrix} 0 & 0 & 0 \\ 0 & \sigma t \frac{L^4}{7.11} & 0 \\ 0 & 0 & \sigma t \frac{L^4}{7.11} \end{bmatrix} = \begin{bmatrix} 0 & 0 & 0 \\ 0 & 46.24 & 0 \\ 0 & 0 & 46.24 \end{bmatrix} \text{S} \cdot \text{m}^4. \tag{4.51}$$

This final set of tests consisted of an aluminium honeycomb structure rotating about one axis (Z_B axis). In this case, there is no analytical solution for the evolution of the angular velocity vector as the characteristic time of decay due to the eddy current phenomenon is not constant. The characteristic time of decay will depend on the angular rotation of the cube with respect to the magnetic field vector as shown in Equation (4.52),

$$\tau_B = \frac{2I_{ZB}}{(M_{YB}\sin^2\theta)B^2}, \tag{4.52}$$

where θ is the rotated angle of the cube with respect to the equilibrium position. The differential equation that needs to be integrated numerically is,

$$\ddot{\theta} + 2\left(\frac{1}{\tau_0} + \frac{(M_{YB}\sin^2\theta)B^2}{2I_{ZB}}\right)\dot{\theta} + \omega_0^2\theta = 0. \tag{4.53}$$

The first test carried out used no magnetic field and the results obtained are shown in Figure 4.28, which includes the measurements carried out as well as the least square fitting curve for the measurements.

The results from this test are used to obtain the noise damping and the natural frequency of the system. The values obtained are,

$$\omega_0 = 0.0392 \text{ s}^{-1}, \tag{4.54}$$

$$C_0 = \frac{2}{\tau_0} = 0.00376 \text{ s}^{-1}. \tag{4.55}$$

The second test was conducted for a magnetic field of $B = 3000$ μT. In this case, only the maximum level of magnetic field was tested due to the long characteristic time of decay obtained for the zero-magnetic field case.

Figure 4.29 shows the results obtained for this field and it includes the obtained measurements (depicted as blue triangle markers) and the predicted data by the MTT obtained by the numerical integration of Equation (4.53) (depicted as a green dashed line).
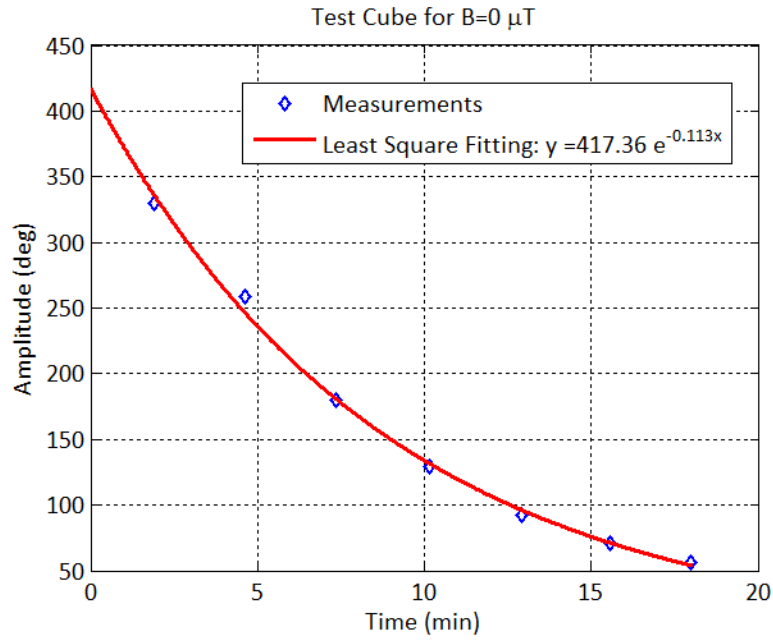
Figure 4.28: Experimental amplitude evolution of the cube for zero magnetic field.
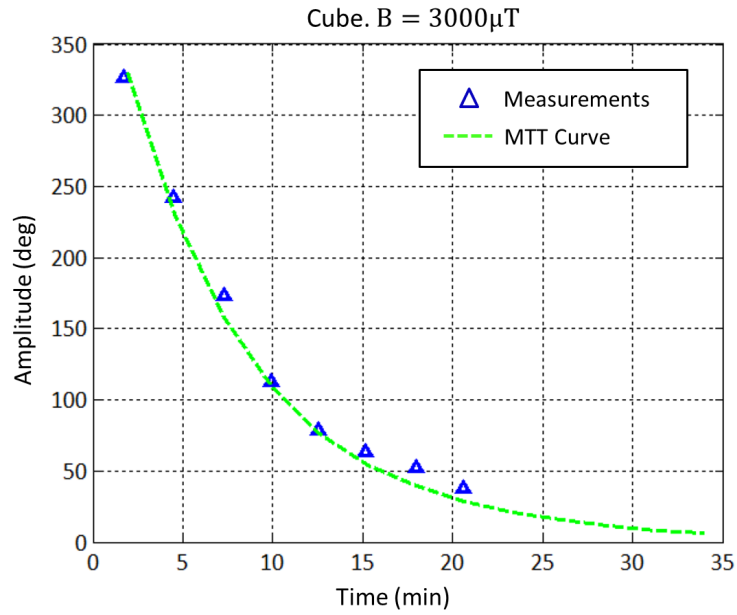
Figure 4.29: Experimental amplitude evolution of the cube for $B = 3000$ µT.

4.5.3.1   Analysis of the results for the honeycomb aluminium cube

In this test, no decay in the angular rotation could be appreciated. This is due to the fact that the characteristic time of decay for the case of zero magnetic field ($B = 0$ T) is much longer than the characteristic time of decay of the eddy currents.

The characteristic time of decay for $B = 0$ T is,

$$\tau_0 = \frac{2}{C_0} = 8.87 \text{ min.} \tag{4.56}$$

The characteristic time of decay due to the eddy currents varies with θ. It will be infinite for $\theta = 0$ degrees and it has a minimum value of:

$$\tau_{Bmin} = 20.92 \text{ min,} \tag{4.57}$$

which is almost three times τ_0. This explains why the decay due to the eddy currents is negligible in this experimental test.

The MTT analysis predicts that the characteristic time of decay due to the eddy currents is very small compared to the characteristic time of decay for no magnetic field $B = 0$ T, which corroborates the results obtained experimentally. It should also be noted that due to the large size of the cube, most of the available space between the two coils is occupied. Thus, the magnetic field is no longer homogeneous for the cube. The magnetic field generated by a Helmholtz coil is maximum at its centre, where the magnetic field was approximately $B = 3000$ µT. The panels were located further away from the central region and, hence, they were subject to a less intense magnetic field.

In order to evaluate the eddy current phenomenon on aluminium honeycomb panels with the present methodology, higher values of the magnetic field should be employed. Unfortunately, this was not possible with the available equipment as the Helmholtz coil could only provide up to 3000 µT. Another solution would be to carry out these tests in a vacuum chamber in order to eliminate the effect of the air drag.

4.6 Error analysis

A deviation between the numerical and experimental results ranging between 0.7% and 12.3% has been observed during the test campaign.

As explained previously in Subsection (4.5.1.1), errors will appear both in the experimental data and the MTT predictions.

The empirical data may lead to inaccuracies primarily due to imprecisions of the optical measurements:

- Inaccuracies in the measurement of the object's attitude. To this end, various markers were attached to each object in order to optically measure the attitude from the video recordings. The accuracy of this method is subject to the imprecisions associated with the naked eye. The achievable accuracy in the attitude measurement is approximately $\epsilon = \pm 10$ deg.

The MTT model depends on the physical properties of the target object (e.g. conductivity, density) and the external magnetic field applied. Therefore, any imprecisions of these input parameters will generate deviations from the real behaviour. The possible causes of errors in the MTT predictions are:

- Flaws in the manufacturing of the metallic object. These flaws can be associated with imperfections in the welding process or impurities in the alloy which may lead to small deviations in the conductivity and/or density of the object.

- Fluctuations of the magnetic field. Small fluctuations of the intensity provided by the power source entailed magnetic field variations in the order of few µT. This may have introduced small imprecisions in the field.

- Inaccuracies in the measurement of the magnetic field. The magnetometer employed throughout the experimental tests could only measure fields up to 100 µT. For higher fields the instrument would be saturated. Therefore, higher magnetic fields were inferred from the

intensity circulating through the coil and the measurements made for lower fields with the magnetometer.

- **Magnetic field not perfectly homogeneous.** The Helmholtz coil does not provide a perfectly homogeneous field throughout the overall space between the two coils. The further away from the geometrical centre between the two coils, the less homogeneous the field is. The tested pieces occupied a fraction of the space between the two coils which may lead to small inaccuracies in the results.

- **Influence of the Earth's magnetic field.** Last but not least, the Earth's magnetic field needed to be compensated in every test by the right positioning of the Helmholtz coil within the room. Any misalignments in the coil could have introduced slight perturbations in the magnetic field.

- **Inaccuracies of the frame model used.** If the magnetic tensor is obtained by means of the frame model, additional deviations will appear due to the fact that the frame model accuracy is limited by the amount of finite elements employed as described in Section 3.3.4.

Now the deviations of the eddy current characteristic time, τ_B, caused by inaccuracies in the density, conductivity, magnetic field and computation of the magnetic tensor based on the frame model are quantified. The characteristic time of decay of the studied canonical shapes has the form,

$$\tau_B \propto \frac{I_i}{M_j B^2}, \tag{4.58}$$

where I_i is the corresponding component of the inertia tensor and M_j is the corresponding component of the magnetic tensor.

Taking into account that the inertia tensor is proportional to the density, ρ, the error caused by deviations in the density, ϵ_ρ, can be computed as follows:

$$\epsilon_\rho = \left| \frac{\frac{\rho}{M_j B^2} - \frac{\rho + \Delta\rho}{M_j B^2}}{\frac{\rho}{M_j B^2}} \right| = \left| \frac{\Delta\rho}{\rho} \right|, \tag{4.59}$$

Moreover, taking into account that the magnetic tensor is proportional to the conductivity, σ, the error caused by deviations in the conductivity, ϵ_σ, can be computed as follows:

$$\epsilon_\sigma = \left| \frac{\frac{I_i}{\sigma B^2} - \frac{I_i}{(\sigma + \Delta\sigma) B^2}}{\frac{I_i}{\sigma B^2}} \right| \approx \left| \frac{\Delta\sigma}{\sigma} \right|, \tag{4.60}$$

Furthermore, inaccuracies in the numerical computation of the magnetic tensor, ϵ_M, may be computed as follows:

$$\epsilon_\sigma = \left| \frac{\frac{I_i}{M_j B^2} - \frac{I_i}{(M_j + \Delta M_j) B^2}}{\frac{I_i}{M_j B^2}} \right| \approx \left| \frac{\Delta M_j}{M_j} \right|, \tag{4.61}$$

Finally, the error caused by fluctuations of the magnetic field, ϵ_B, may be computed as follows:

$$\epsilon_B = \left| \frac{\frac{I_i}{M_j B^2} - \frac{I_i}{M_j (B + \Delta B)^2}}{\frac{I_i}{M_j B^2}} \right| \approx \left| \frac{2\Delta B}{B} \right|, \tag{4.62}$$

A deviation of 5% in the conductivity or density will result in a deviation of 5% between the MTT and the experimental measurements. In contrast, the same deviation in the magnetic field will result in twice the deviation (i.e. 10%). This last deviation in the magnetic field together with inaccuracies associated with the optical measurements are the most probable causes of the observed differences between the MTT and empirical results.

Figures 4.30 and 4.31 depict the experimental errors obtained for all the tested cases. The deviation

registered in the experimental tests ranged from 0.7% in the best case to 12.3% in the worst case and the mean value was 7.2%.

Summary of the experimental errors
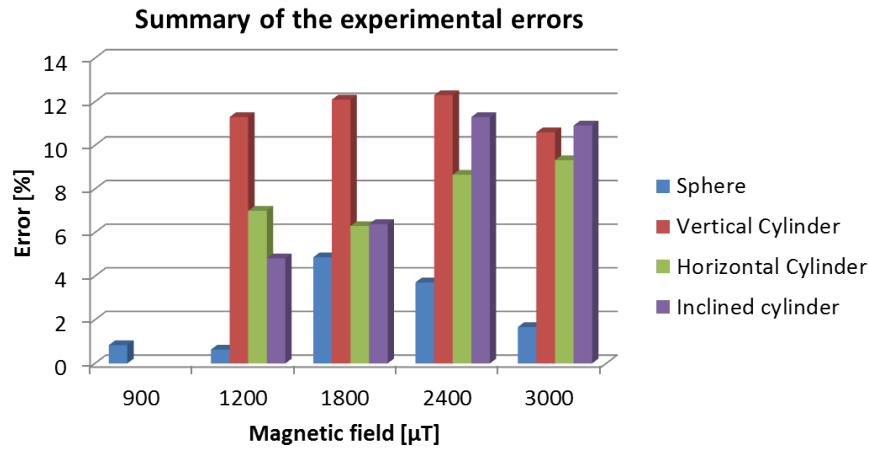
Figure 4.30: Summary of the experimental errors for each tested object and magnetic field.

Summary of the experimental errors
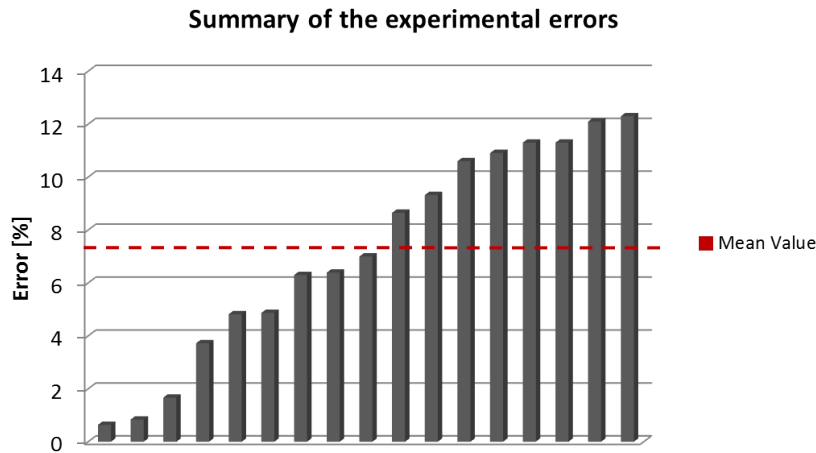
Figure 4.31: Summary of the experimental errors sorted by size.

Deviations of this order of magnitude may be accounted for by fluctuations of the magnetic field in the order of few tens of μT (for a field of 1000 μT, a fluctuation of 50 μT will result in a deviation of 10%).

4.7 Chapter summary

Experimental tests were carried out at Airbus Defence & Space in Stevenage (UK) in order to empirically validate the magnetic tensor theory.

The tests consisted in measuring the evolution of the rotation rate of several metallic objects subject to a constant and homogeneous magnetic field. Three different metallic objects were tested: a spherical shell, a cylindrical shell and an aluminium honeycomb structure.

The pieces were suspended from a strut with a torsion wire in order to generate a uniaxial angular velocity and they were placed at the centre of a Helmholtz coil. Different values of the magnetic

fields were analysed in order to obtain the characteristic time of decay of the spin rate of the objects. The experiments allowed for the visualization of the decay rates for different magnetic fields as well as different spin axes. The measurements obtained closely matched the expected numerical results. The deviation between the empirical results and the analytical values ranged from 0.7% to 12.3%.

Finally, Section 4.6 analysed the possible causes of the observed deviations indicating that the most probable sources of error are the registered fluctuations in the magnetic field together with inaccuracies associated with the optical measurements. The results show that the eddy current phenomenon was noticeable for the spherical and cylindrical shells while it was imperceptible for the aluminium honeycomb panels. This last result was due to the small amount of metallic material present in the panels and the electrical isolation of the four panels. Thus, the most noticeable eddy current effects on spacecraft will appear on fully metallic components, such as propellant tanks. Nevertheless, it should be noted that the effect on the aluminium honeycomb panels should be noticeable for higher values of the magnetic field than those used in these experimental tests. Therefore, further tests would be needed to investigate this.

Overall, from the tests performed it has been found that the analytical model closely correlates to the experimental data, within the error ranges of the tests performed. This enables the model to be used with greater confidence in practical space applications.

EDDY BRAKE: SYSTEMS ENGINEERING DESIGN

5.1 Introduction

Past space debris attitude observations, described in Section 2.3, have shown that some of these defunct objects possess a high spin rate (> 30 deg/s) and these fast rotators are located in densely populated regions such as low-Earth orbit (LEO) [92], geostationary transfer orbit (GTO) [82] and geostationary orbit (GEO) [84]. This situation drives the need to include a de-tumbling phase for active debris removal methods.

The most frequent de-tumbling process proposed for ADR missions is based on a synchronisation phase between the target and the chaser that seeks to match the rotational motion of the target. If the synchronisation is achieved, the chaser would then proceed with the capturing phase and then de-tumble the compound chaser-target system. However, this process encounters a large number of difficulties. First of all, the target may have a complex rotational motion such as a rotation around its three principal axes of inertia. This situation would greatly hinder the synchronisation process which needs to locate the chaser close enough to the desired grabbing feature and avoid a collision with any existing appendages on the target's surface. Secondly, the synchronisation will not be feasible if the spin rate of the target is above a certain threshold. This threshold will depend on the chaser's slewing manoeuvring rate capacity and its guidance, navigation and control precision and robustness. Finally, the de-tumbling and stabilisation process of the compound system requires specific structural requirements which in the case of a robotic arm can only capture and stabilise objects rotating slower than 3 to 10 deg/s [8, 45, 58].

Additional de-tumbling strategies have been proposed based on contactless methods as described in Section 2.5. Every method has its restrictions and limitations and therefore, there isn't a unique solution that can tackle all the existing targets within the space debris population. Moreover, the maturity (technology readiness level, TRL) of these methods is still very low and their feasibility in a real ADR mission is still not guaranteed.

This chapter focuses on the design of a contactless de-tumbling method based on the generation of eddy currents. Natural rotation damping due to the Earth's magnetic field has been observed in LEO orbits [88, 89, 115]. The idea presented here is to subject a space debris object to an enhanced magnetic field in order to damp its rotation and allow for its capture and subsequent de-orbiting phase. This idea was first introduced by Kadaba and Naishadham in 1995 [11, 138] but little work has been carried out since then. The goal of this part of the dissertation is to recover this idea and gain a deeper insight into the possible configurations and subsystems' requirements in order to present a viable design. Great progress has been made since 1995 in space sensors and actuators

as well as materials employed for electromagnetic coils which facilitate the accomplishment of this endeavour.

A new de-tumbling design based on the generation of the eddy currents, called the *'eddy brake'* is investigated here. The design consists of an electromagnetic coil made of High Temperature Superconducting (HTS) wires that is carried on-board the chaser spacecraft which is placed several metres away from the target object (see Figure 5.1).
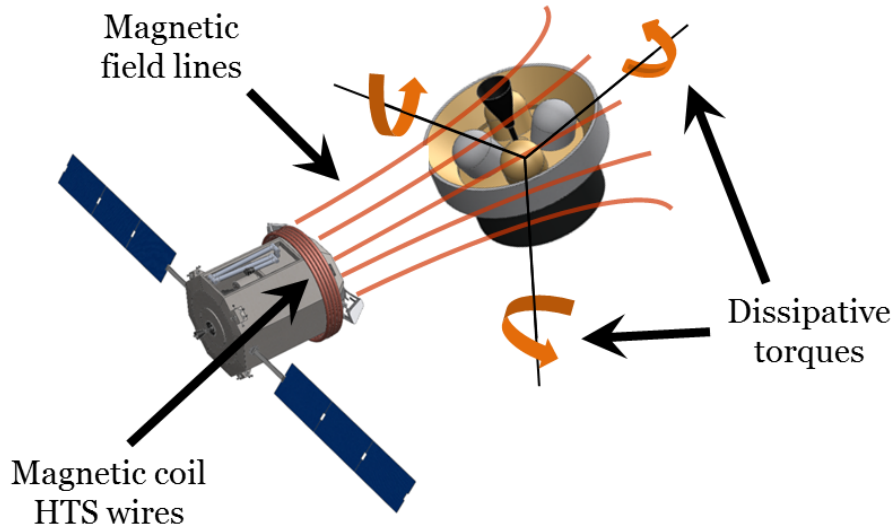
Figure 5.1: Eddy brake method.

This method has several advantages with respect to other proposed de-tumbling processes.

- Contactless method: this eliminates the hazards associated with complicated proximity operations and docking/grabbing of a non-cooperative rotating object.

- Non-invasive technique: the risk of damaging the defunct object and generating more debris is very low. The decrease of the angular velocity occurs gradually thanks to Joule's effect that dissipates the kinetic energy of the object into heat. Therefore, this method is less aggressive for the target object than other de-tumbling methods which generate impulsive forces that can damage the object or that are based on the sublimation of the surface material.

- Target's angular velocity control: the control of the target's angular velocity is easier than those methods based on the generation of off-axis forces which need to know precisely the angular velocity vector, the target's COG and inertias. The eddy current torques will always oppose the angular velocity of the object, thus, there is no risk of increasing the spin rate of the object.

However, there are some constraints which have been taken into account in the design process:

- Metallic material: The basic requirement to generate eddy currents is the existence of metallic material on the target. Luckily, metallic materials such as aluminium and titanium alloys are commonly employed in space structures and components (e.g. propellant tanks). The effectiveness of the eddy brake will be directly linked to the amount of conductive material on the target. For instance, upper stages are good candidates for this method as they typically contain large metallic propellant tanks.

- Relative distance: The eddy current torque is inversely proportional to the square of the distance. Therefore, the efficiency of this method decreases with the distance-chaser target.

A compelling system based on HTS materials has been designed which allows for relative distances in the order of metres between the chaser and the target.

- Duration: The estimated duration of the de-tumbling can be in the order of weeks. The time needed will depend primarily on the amount of the metallic material present and the relative distance between the coil and the target.

This chapter focuses on the systems engineering design of the eddy brake including the following aspects,

- Coil design: This design is based on high temperature superconducting wires (HTS wires). The reasons for selecting this material as well as the final baseline design of the coil are presented in Section 5.3.

- Thermal subsystem design: HTS wires need a suitable thermal subsystem which can guarantee that the coil will always work below its critical temperature. Several possible solutions for the thermal subsystem are investigated and compared in Section 5.4.

- GNC subsystem design: key aspects of the guidance, navigation and control (GNC) subsystem are addressed in Section 5.5. This subsystem needs to guarantee a safe relative distance between the chaser and the target and an appropriate relative pointing of the coil throughout the whole de-tumbling process. The major requirements for the GNC are described as well as the most suitable sensors and actuators.

- Electromagnetic interferences: The possible electromagnetic interferences are discussed in Section 5.6 and several recommendations are provided for the eddy brake design.

- Baseline design and system budgets: The final baseline design is presented in Section 5.7 together with the corresponding mass and power budgets.

The chapter concludes with the phase 0 study for the Agora mission (Active Grabbing & Orbital Removal of Ariane) conducted in collaboration with the University of Strathclyde (Glasgow, UK), the DFKI Robotics Innovation Centre (Bremen, Germany) and the companies Dinamica Srl and D-Orbit Srl (Italy). Agora is an in-orbit demonstration mission whose main goal is to demonstrate technologies to autonomously remove an Ariane R/B in a controlled manner. Its payload consists of three primary elements: the eddy brake de-tumbling system, a robotic manipulation system (consisting in a clamp mechanism and a robotic arm) and the de-orbit kit.

5.2 Preliminary analysis

The first step in the design of the eddy brake method is to estimate the braking time of the de-tumbling process for different values of the magnetic field and percentage of conductive material inside the target. For this purpose, a spherical shell is analysed due to the fact that an analytical solution to Euler's equations can be achieved for this object. Moreover, potential targets such as defunct satellites and upper stages contain propellant tanks with spherical or cylindrical shapes which also justifies the analysis of the spherical shell as a starting point.

5.2.1 Characteristic time of decay

The magnetic interaction between the chaser and the target is analysed using the Magnetic Tensor Theory (MTT).

A rotating metallic object (i.e. target) is subject to an external magnetic field created by a chaser which leads to the appearance of eddy current loops inside the target. These electric current loops generate a dissipative torque that decreases the angular velocity of the target. Moreover, the magnetic field created by the coil on-board the chaser spacecraft is a non-uniform field. This results in a reduction of the magnetic tensor. This loss in efficiency is approximately quantified

by the efficiency factor μ_{eff} defined in Section 3.3.7.1. This factor multiplies the magnetic tensor resulting in an effective magnetic tensor given by Equation (5.1),

$$\mathbf{M_{eff}} = \mu_{\text{eff}}\mathbf{M}. \tag{5.1}$$

Furthermore, the induced magnetic moment on the target is equal to,

$$\vec{m} = \mathbf{M_{eff}}(\vec{\omega}_t \times \vec{B}_{Gt}), \tag{5.2}$$

where the subindex t denotes the target, $\vec{\omega}_t$ is the target's angular velocity and $\vec{B}_{Gt}$ is the magnetic field at the COG of the target (denoted by the subscript Gt).

Moreover, the induced torque $\vec{T}_{ct}$ on the target by the chaser is given by Equation (5.3),

$$\vec{T}_{ct} = (\mathbf{M_{eff}}(\vec{\omega}_t \times \vec{B}_{Gt})) \times \vec{B}_{Gt}. \tag{5.3}$$

Introducing the eddy current torque (5.3) into Euler equations (2.12), the following equation is obtained,

$$\mathbf{I_t}\dot{\vec{\omega}}_t + \vec{\omega}_t \times \mathbf{I_t}\vec{\omega}_t = \left(\mathbf{M_{eff}}\left(\vec{\omega}_t \times \vec{B}_{Gt}\right)\right) \times \vec{B}_{Gt}. \tag{5.4}$$

In the case of a spherical shell, both $\mathbf{I_t}$ and $\mathbf{M_{eff}}$ are diagonal tensors and the term $\vec{\omega}_t \times \mathbf{I_t}\vec{\omega}_t$ is zero. Therefore, Equation (5.4) is simplified to the following,

$$\dot{\omega}_{\perp,t} + \frac{\omega_{\perp,t}}{\tau} = 0, \tag{5.5}$$

where $\omega_{\perp,t}$ is the perpendicular component of the angular velocity of the target with respect to the magnetic field and τ is the characteristic time of decay. This parameter corresponds to the time at which the spin rate has decreased by almost a third of its initial value $1/e = 1/2.71828$.

Consequently, only the perpendicular component of the rotational speed is damped and this component has an exponential decay equal to,

$$\omega_{\perp,t} = \omega_{\perp 0} \cdot e^{-\frac{t}{\tau}}, \tag{5.6}$$

For a spherical shell, the characteristic time of decay acquires the form shown in (5.7),

$$\tau_i = \frac{I_i}{\mu_{\text{eff}}M_i B^2} \quad I_1 = I_2 = I_3, \ M_1 = M_2 = M_3, \tag{5.7}$$

where the subscripts $i = 1, 3$ correspond to the principal axes of inertia and the magnetic tensor which lead to a diagonal form of both tensors. Due to the symmetries of the spherical shell, all axes of the spherical shell are principal axes and therefore, both the inertia and the magnetic tensors are isotropic matrices.

In general, the principal directions of the inertia tensor and the magnetic tensor will not coincide for a non-spherical body. Hence, Equation (5.4) can not always be simplified, making it necessary to integrate Euler equations numerically. Nonetheless, expression (5.7) gives some qualitative information of this process.

The characteristic time of decay is inversely proportional to the square of the magnetic field. Consequently, the magnitude of the magnetic field plays an important role on the braking time. In addition, the ratio of non-conductive material versus conductive material is related to the ratio I_i/M_i due to the fact that the inertia tensor depends on the overall mass distribution (both conductive and non-conductive materials) while the magnetic tensor depends on the mass distribution of the conductive material. Therefore, the higher the amount of conductive material in the body, the lower the characteristic time of decay as it is expected in the eddy current phenomenon. This fact can be seen in the following target object analysed.

Now, a sphere with a conductive crust and a non-conductive core is considered (see Figure 5.2).
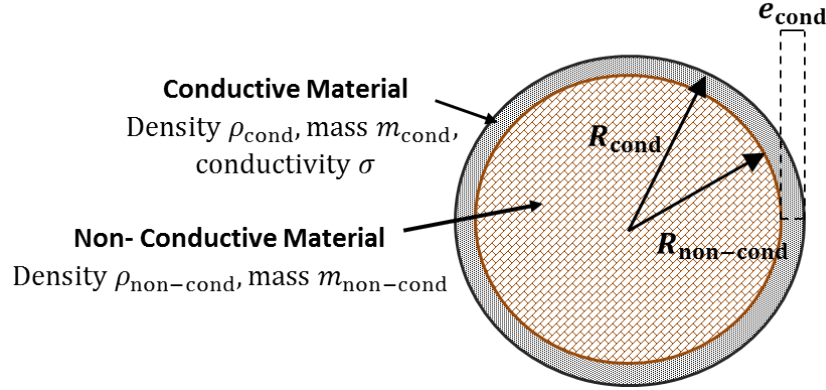
Figure 5.2: Sphere made of conductive and non-conductive material.

Using Equation (5.7), the characteristic time of decay, τ_{sph}, is obtained in Equation (5.8).

$$
\begin{aligned}
\tau_{sph} &= \frac{(\rho_{\text{cond}}4\pi R_{\text{cond}}^2 e_{\text{cond}})R_{\text{cond}}^2 + \frac{3}{5}(\rho_{\text{non-cond}}\frac{4}{3}\pi R_{\text{non-cond}}^3)R_{\text{non-cond}}^2}{\pi\mu_{\text{eff}}\sigma B^2 R_{\text{cond}}^4 e_{\text{cond}}} \\
&\approx \frac{4}{\mu_{\text{eff}}B^2}\frac{1 + \frac{1}{5}\frac{R_{\text{non-cond}}\rho_{\text{non-cond}}}{e_{\text{cond}}\rho_{\text{cond}}}}{\frac{\sigma}{\rho_{\text{cond}}}}
\end{aligned}
\tag{5.8}
$$

where the subindex 'cond' stands for the conductive material while the subindex 'non-cond' stands for the non-conductive material. Here, it was assumed that the thickness of the metallic spherical shell is very small $e_{\text{cond}} << 1$ and, therefore, it can be assumed that the radius of the crust, R_{cond}, and the radius of the non-conductive core, $R_{\text{non-cond}}$, are equal $R_{\text{cond}} \approx R_{\text{non-cond}}$.

In addition, the ratio between the mass of the non-conductive material and conductive material is computed as follows taking into account that $R_{\text{cond}} \approx R_{\text{non-cond}}$,

$$
\frac{m_{\text{non-cond}}}{m_{\text{cond}}} = \frac{\frac{4}{3}\pi R_{\text{non-cond}}^3 \rho_{\text{non-cond}}}{4\pi R_{\text{cond}}^2 e_{\text{cond}}\rho_c} \approx \frac{R_{\text{non-cond}}\rho_{\text{non-cond}}}{3e_{\text{cond}}\rho_{\text{cond}}}
\tag{5.9}
$$

Now, introducing Equation (5.9) in Equation (5.8), the following formula for the characteristic time of decay is obtained,

$$
\tau_{sph} = \frac{4}{\mu_{\text{eff}}B^2}\frac{1 + \frac{3}{5}\frac{m_{\text{non-cond}}}{m_{\text{cond}}}}{\frac{\sigma}{\rho_{\text{cond}}}},
\tag{5.10}
$$

It is observed that the characteristic time of decay only depends on the magnitude of the magnetic field, the physical properties of the conductive material, the percentage of conductive material and the efficiency factor μ_{eff}.

Figure 5.3 displays the characteristic time versus the percentage of conductive material for different distances between the coil and the COG of the target, indicated in the legend as the parameter d. The selected target is a sphere of 2 metres of radius which has a metallic spherical shell made of a typical aluminium alloy used in space structures, 6061-T6 [164]. Note that the characteristic time represents the time needed to decrease the angular velocity by a factor $1/e$. The efficiency factor has been computed with Equation (3.179) which also varies with the relative distance as shown in the right image of Figure 5.3. As it was explained in Subsection 3.3.7.1, the efficiency factor must increase with the relative distance due to the fact that the magnetic field becomes more uniform inside the target domain. However, the characteristic time is proportional to the

inverse of the square of the magnetic field, which diminishes with the distance. The decrease of the strength of the magnetic field is more significant than the effect of the efficiency factor, as explained in Subsection 3.3.7.1. This is the reason why the characteristic time of decay increases with the relative distance d.

The results show that the time can vary from a few hours up to several months depending on the amount of conductive material and the relative distance. Typically, the satellite's structure subsystem represents 20% of the total dry mass [3]. Assuming a metallic structure, which represents 20% of the overall mass, and a relative distance of 10 metres, the characteristic time of decay would be of 2 days. Hence, if the object is initially rotating at 10 deg/s, it would take 2 days to decrease its spin rate to 3.7 deg/s.
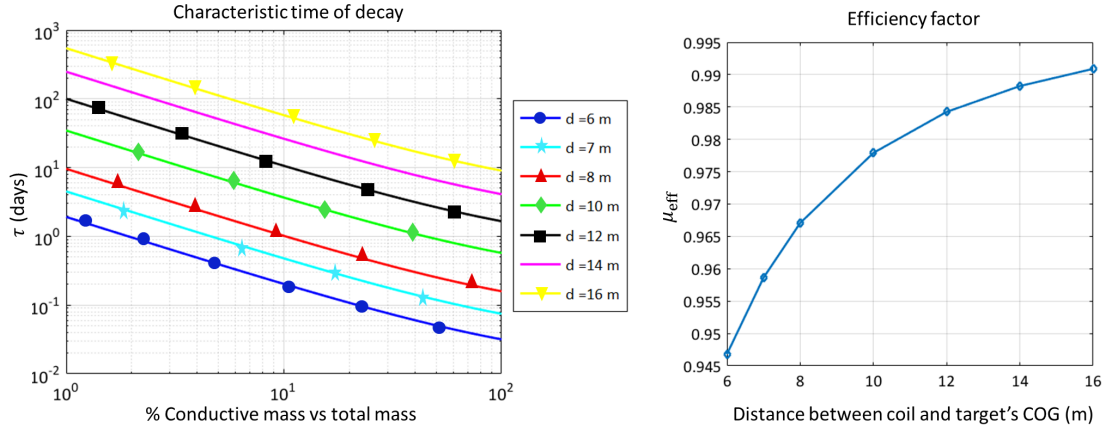
Figure 5.3: Characteristic time of decay spherical shell versus percentage of non-conductive material.

It must be highlighted that in this example it is assumed that the conductive material is homogeneously distributed throughout the body. This could be the case for upper stages which are big metallic capsules. However, each spacecraft needs a customised analysis as the distribution of conductive material will vary. In general, assuming the magnetic field at the COG of the target is perpendicular to its angular velocity vector, the characteristic time of decay for a non-homogeneous body will be between a minimum and a maximum value depending on its inertia and magnetic tensor,

$$\tau \in (\tau_{min}, \tau_{max}) = (\frac{I_{min}}{\mu_{\text{eff}} M_{max} B_{Gt}^2}, \frac{I_{max}}{\mu_{\text{eff}} M_{min} B_{Gt}^2}), \qquad (5.11)$$

where I_{max} and I_{min} are the maximum and minimum eigenvalues of the inertia tensor and M_{max} and M_{min} are the maximum and minimum eigenvalues of the magnetic tensor.

5.2.2 Orientation change in the axis of rotation

The orientation change in the axis of rotation appears when there is a component of the angular velocity vector parallel to the magnetic field. This component is not damped and it will cause the axis of rotation of the object to change its orientation. As explained in Section 3.3.3, the perpendicular component of the angular velocity is damped asymptotically and the body ends up rotating with an angular velocity parallel to the magnetic field vector.

In order to visualise this effect a fully conductive aluminium spherical shell is considered with the following characteristics:

- $\vec{\omega}(t = 0) = [0, 0, 50]$ deg/s
- $\vec{B} = [150, 0, 150]$ µT

- Radius $R = 2$ m

- Thickness $e = 0.001$ m

- Electric conductivity $\sigma = 35000000$ S/m (at 20^oC)

Figure 5.4 displays the evolution of the angular velocity vector in the body reference frame (right image) and in an inertial reference frames (left image). In this example, the magnetic field and the angular velocity vectors initially form an angle of 45 degrees. Therefore, the angular velocity asymptotically decreases in a factor of $\frac{\sqrt{2}}{2}$.

This results in a decay of the rotational speed from $\omega_0 = 50$ deg/s to $\omega_f = \frac{\sqrt{2}}{2}50 = 35.4$ deg/s as illustrated in the right image of Figure 5.4. The left image in Figure 5.4 shows that the final angular velocity vector is parallel to the magnetic field. In addition, Figure 5.5 depicts the initial and final configurations of the rotating sphere.
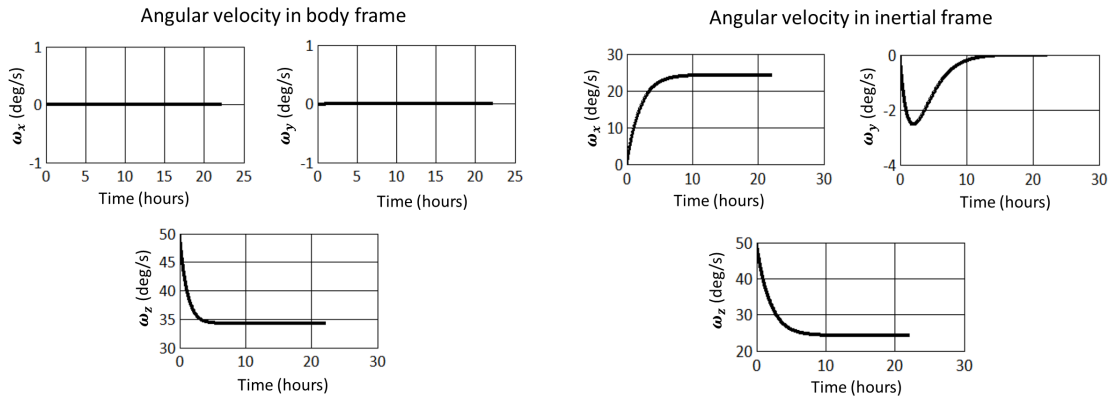
Figure 5.4: Evolution of the rotational velocity in the body reference frame (left image) and in the inertial reference frame (right image).
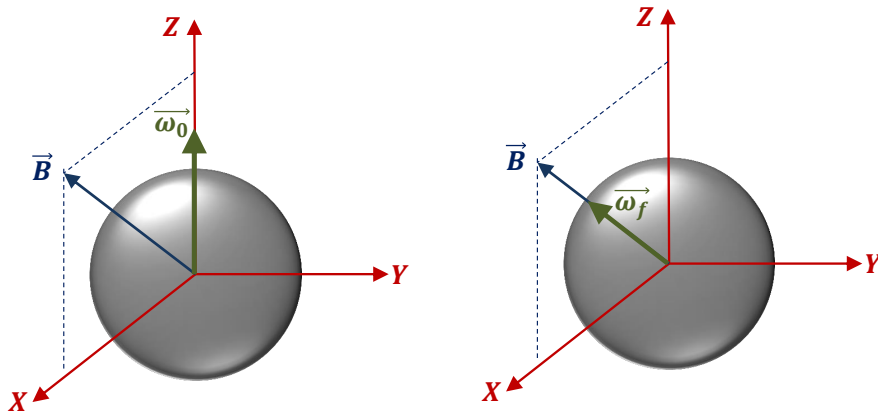
Figure 5.5: Orientation change of the rotation axis and motion of the spherical shell.

In order to damp all the components of a space debris object during the de-tumbling process, the chaser may need to change the relative position of the electromagnetic coil with respect to the target.

5.3 Materials and coil design

The next point that needs to be addressed is the design of the electromagnetic coil with respect to the materials, mass, power and dimensions needed as a function of the characteristic time of decay.

5.3.1 Conventional materials

For the manufacturing of the coil, conventional materials (e.g. copper, aluminium) are discarded due to the high mass ($\sim$hundreds of kg) and high power ($\sim$kW) needed.

The coil design shown in Figure 5.6 consists of N turns of wires, each one with a cross section, A_w and a coil mean radius of the coil, R_c.
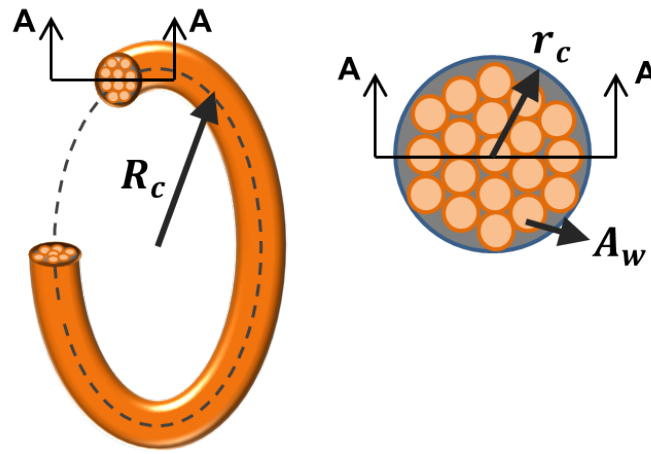
Figure 5.6: Coil Parameters.

The mass of the coil may be approximated by the formula 5.12) which is proportional to its radius, R_c, number of turns, N, cross section, A_w, and density, ρ_c. Moreover, the power dissipated, P_c, by a conventional coil is given by the formula (5.13), where $\mathcal{R}$ is the resistance of the coil defined in Equation (5.14) and I is the electric current flowing through the coil.

$$m_c = 2\pi R_c N \rho_c A_w, \tag{5.12}$$

$$P_c = \mathcal{R} I^2, \tag{5.13}$$

$$\mathcal{R} = \frac{2\pi R_c N}{\sigma A_w}. \tag{5.14}$$

The ampacity is defined as the amount of current a conductor can carry before sustaining some kind of deterioration and it is directly linked to the wire diameter [165]. The cross section of the wires can not be below a certain threshold due to manufacturing constraints and heat dissipation constraints. A typical value for conventional coils is $\frac{I}{A_w} = 8$ A/mm^2 [165].

Figures 5.7 and 5.8 display the mass and dissipated power of an aluminium and copper coils for different radius and number of loops. These figures have been included in order to compare their performance with respect to HTS materials (described in Section 5.3.2) and to justify why these conventional materials have been discarded in the coil design. The maximum coil diameter considered coincides with the diameter of the fairing of the biggest European launcher, Ariane-5

[121]. It is observed that the mass can easily surpass 100 kg and the dissipated power is of the order of tens of kW. While the mass is high but still in the range of typical on-board spacecraft payloads, the power greatly exceeds the typical power consumptions of spacecraft payloads [25].
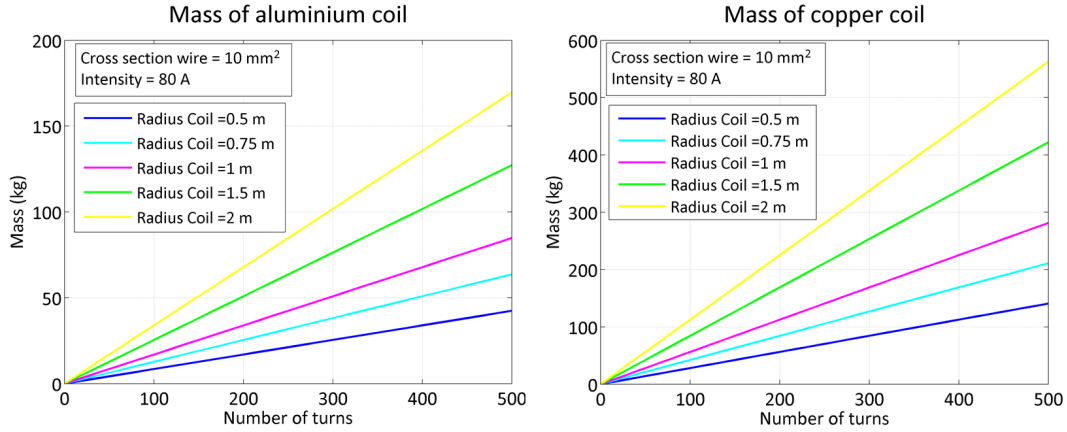
Figure 5.7: Mass of an aluminium coil (left) and copper coil (right) for different radius and number of loops.
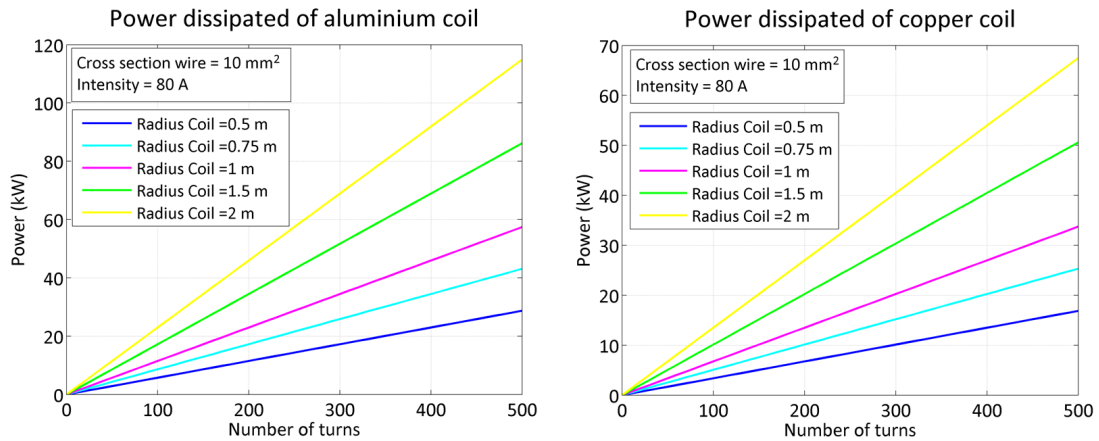
Figure 5.8: Power dissipated by an aluminium coil (left) and copper coil (right) for different radius and number of loops.

5.3.2 High temperature superconducting wires

Superconductors have evolved enormously since their discovery in 1911 by the Dutch physicist Heike Kamerlingh Onnes [166].

The first superconductors that were discovered (called type I) were pure metals such as aluminium, lead or mercury. Type I superconductors have a critical temperature and a critical magnetic field above which superconductivity disappears. This type of superconducting materials would not allow for industrial manufacturing of magnetic coils because their superconducting behaviour is abruptly destroyed when they carry a small electric current or when they are exposed to a small magnetic field.

In 1986 a new era started for superconductivity. It was found that complex cuprate oxides exhibit a superconducting behaviour at unusually high temperatures. This new type of superconducting

materials were called *'high temperature superconducting'* or HTS materials. Among the HTS superconductors that are already industrially manufactured, one can find the Rare Earth-Barium-Copper-Oxide (ReBCO) and the Bismuth-strontium-calcium-copper-oxide (BSCCO). The BSCCO is the first HTS generation (1G HTS) and the ReBCO is the second HTS generation (2G HTS). The HTS Yttrium-barium-copper-oxide (YBCO) is one of the most common HTS manufactured nowadays [166]. Additional information on the manufacturers and characteristics of these wires can be found in Section A.3 of the Annex.

HTS materials were first successfully used in space on-board the Israeli microsatellite, TECHSAT II, launched in 1998. The system consisted of a thin $YBa_2Cu_3O_7$ film integrated with a cryocooler [167]. An additional in-orbit experiment was conducted in 1999 for the High Temperature Superconducting Space Experiment II (HTSSE-II) sponsored by an international consortium. The goal of these experiments were to demonstrate the performance of eight HTS materials in a microwave system setting (semiconductors and RF devices) at temperatures of 77 K maintained by cryocoolers [168].

The use of HTS coils in space was proposed for the Electromagnetic Formation Flight (EMFF) mission almost a decade ago [169, 170]. The goal of this mission was to replace thrusters with high temperature superconducting electromagnetic coils for formation flying purposes. The envisioned satellites contain three orthogonal electromagnetic coils with diameters of 2 metres (see Figure 5.9). Various experimental tests were carried out at MIT Space Systems Laboratory which proved the efficiency of HTS coils with respect to conventional materials (i.e. aluminium, copper). The eddy brake coil design has been inspired by the EMFF mission to a large extent due to the similarities with the magnetic requirements of the de-tumbling subsystem.
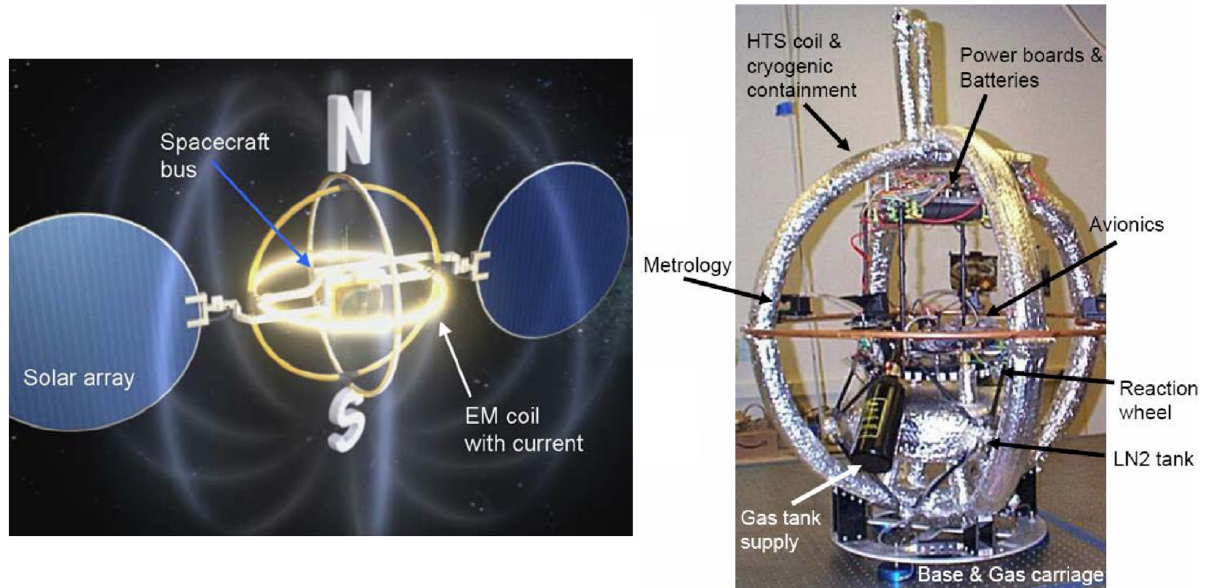
Figure 5.9: EMFF artistic impression of the satellite (left image) and testbed by the MIT Space Systems Laboratory (right image) [13].

5.3.2.1 Relationship between the electric current, the magnetic field and the temperature

The critical current density of this type of wires varies with the magnetic field they are subjected to, the temperature and the orientation of the magnetic field θ. Figures 5.10, courtesy of American Superconductor Corporation (AMSC), outline the typical anisotropic behaviour of 2G HTS wires. The critical current intensity decreases with the temperature and the applied magnetic field.
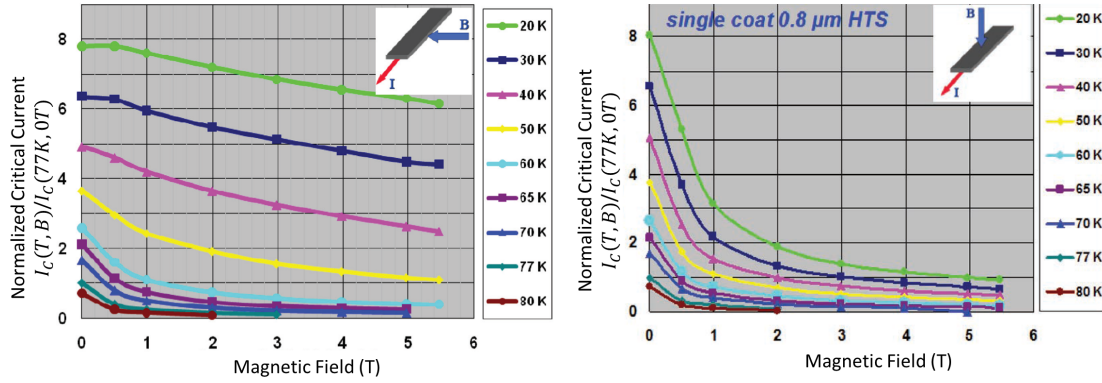
Figure 5.10: Critical current intensity for a magnetic field parallel to the tape and perpendicular to the tape (courtesy of AMSC).

As a first approximation, the magnetic field seen from the other wires in the stack may be assumed to be approximately parallel to the surface [169]. The information in Figure 5.10 is used to obtain the least square fitting curves of the critical intensity for different working temperatures. The critical intensity depicted in Figure 5.11 is normalised with the critical intensity for a temperature of $T_c = 77$ K and magnetic field equal to $B_N = 0$T. The company SuperPower gives this reference current density $J_c(77K, 0T) = 250$ A/m^2.
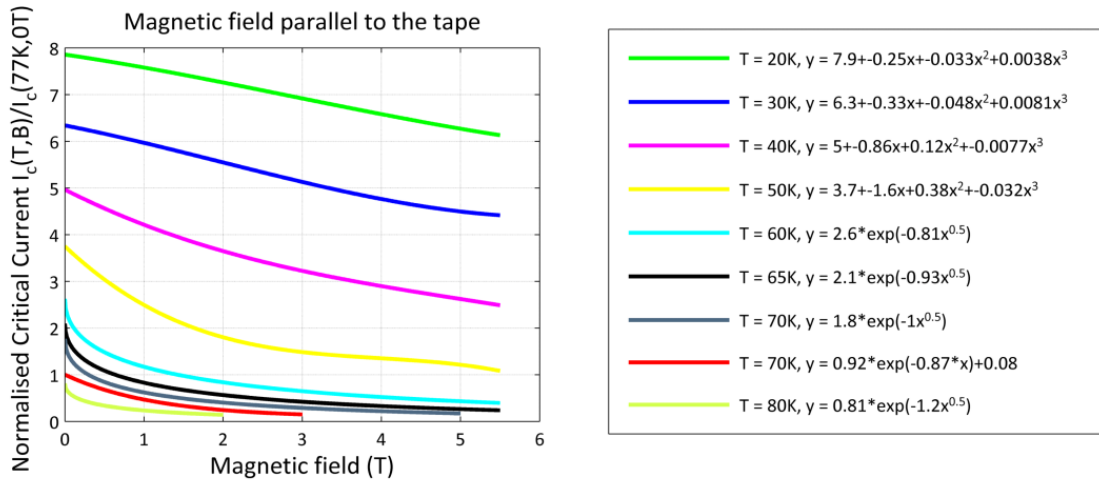
Figure 5.11: Least square fitting curves for the critical intensity with parallel magnetic field.

Each loop of wire will see the magnetic field generated by the rest of the coils and the coil that will see the maximum magnetic field will be the coil at the end of the stack. This maximum magnetic field for a coil with N loops follows the formula [169]:

$$B_N = \frac{\mu_0\, I}{2\pi r} \sum_{k=2}^{N} \frac{1}{k-1}, \qquad (5.15)$$

where r is the distance between two coil loops and I is the electric current of the wire. Hereinafter, the distance between the coils will be assumed to be $r = 400$ μm [169]. The term $\sum_{k=2}^{N} \frac{1}{k-1}$ is a

harmonic series and the nth partial sum can be written as:

$$\sum_{k=2}^{N} \frac{1}{k-1} = \sum_{k=1}^{N-1} \frac{1}{k} = \log(N-1) + \gamma \tag{5.16}$$

and γ is the Euler-Mascheroni constant $\gamma = 0.5772156649....$ Combining Equations (5.15) and (5.16), the relationship between the magnetic field B_N, the critical intensity, I_c and the number of coils is shown in Equation (5.17),

$$B_N = \frac{\mu_0 \, I_c(B_N, T)}{2\pi r}(\log(N-1) + \gamma). \tag{5.17}$$

5.3.2.2 Parametric analysis

First of all, a parametric analysis of the mass is done for different number of turns and radii of the coil. The mass of the coil m_c follows the formula (5.18). For the design of the coil, a standard 2G HTS wire (SCS4050 wire) is selected, manufactured by AMSC and SuperPower (see Section A.3 for specifications). The cross section of the wire is $A_w = 0.0004$ m^2, its critical intensity is $I_c(77K, 0T) = 100$A and its volumetric mass density is $\rho_c = 8910$ kg/m^3.

$$m_c = 2\pi R_c N \rho_c A_w. \tag{5.18}$$

Figure 5.12 displays the mass versus the number of coils for the selected wire and different radius of the coil.
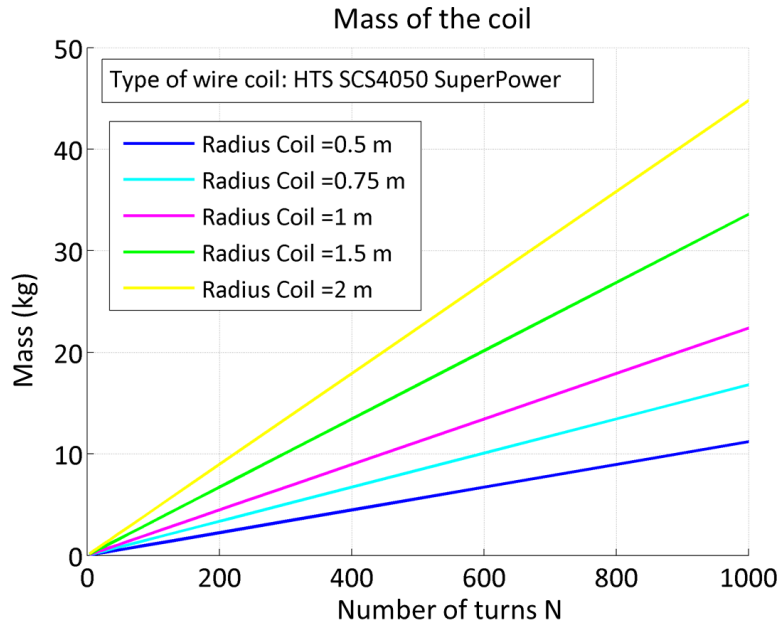
Figure 5.12: Mass of the coil for different number of loops and radius.

When comparing Figures (5.12) and (5.7), a noticeable mass reduction is perceived between HTS and conventional wires. The mass decreases by a factor of 7 with respect to aluminium coils and the mass reduces by a factor of 20 with respect to copper coils. Therefore, these results highlight the great advantage of employing HTS materials.

Now the magnetic field generated by coil at a distance d is evaluated. While the mass of the coil should be minimised, the magnetic field should be maximised in order to accelerate the de-tumbling

process. The magnetic field generated by the coil along its axis follows the formula (5.19),

$$B_c = \frac{\mu_0 \ N I_c}{2} \frac{R_c^2}{(R_c^2 + d^2)^{\frac{3}{2}}}.$$

(5.19)

The magnetic field at the centre of the coil B_c is proportional to the total current $I_t = N I_c$. As the number of turns N grows, the total current I_t increases. However, with the number of turns, the critical current I_c decreases because the magnetic field at the end of the stack B_N increases (see Figure 5.11). Therefore, it is necessary to evaluate if adding additional turns will increase or decrease the total loop current.

Figure 5.13 shows the total loop current versus the number of turns in the coil at 77K. The red line represents the total loop current I_{t0} which is not affected by the applied magnetic field while the blue line represents the real total loop current I_t which is affected by the applied magnetic field. It can be seen that the total loop current I_t is smaller than I_{t0} but they both increase with the number of turns.

It can be concluded that when the number of loops is increased the magnetic field generated by the coil increases. Therefore, from the point of view of the time consumption, it is more convenient to increase the number of loops. However, from the mass point of view, increasing the number of loops is undesirable because then the total mass of the coil would increase. Hence, a compromise must be met.
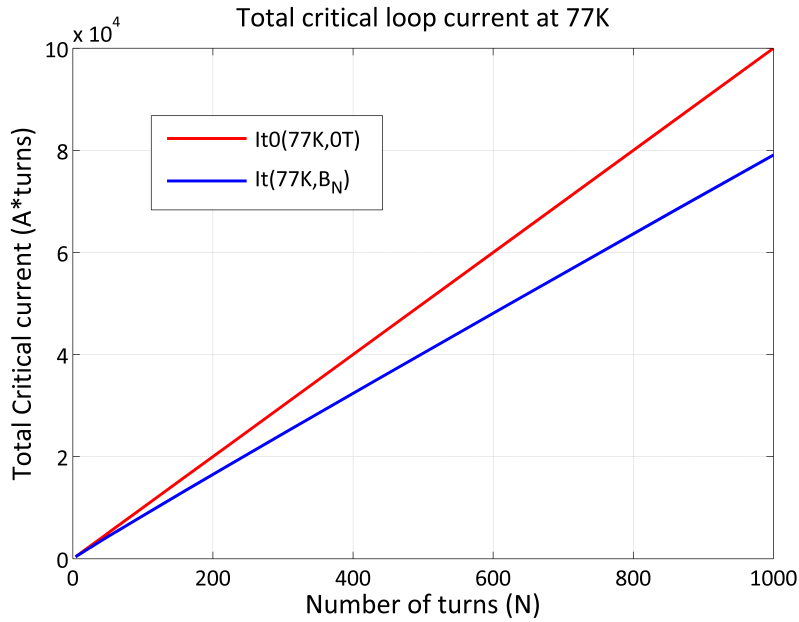
Figure 5.13: Total Loop Current at 50K and 77K.

In order to assess the characteristic time of decay, the same object as the one analysed in Section 5.2 will now be considered. Figures 5.14 show the mass of the coil and characteristic time of decay of the de-tumbling process for different radii of the coil. The two cases analysed consist of a spherical shell which has 20% (left Figure) and 100% (right Figure) of conductive material (6061-T6 aluminium alloy) respectively and the distance between the coil and the COG of the target is assumed to be 10 metres.
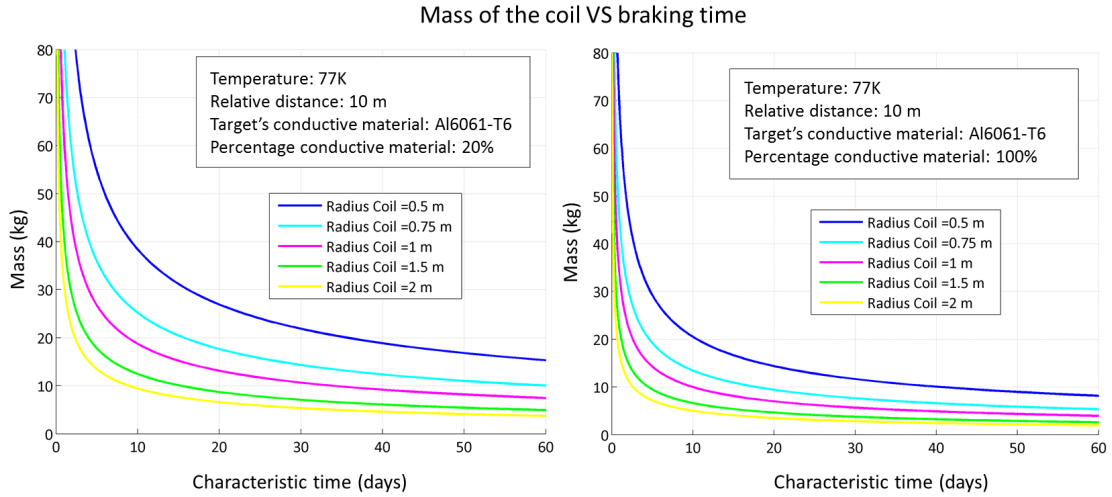
Figure 5.14: Mass of the coil versus characteristic time of decay for an aluminium spherical target with 20% (left Figure) and 100% (right Figure) of conductive material at 77 K.

Figure 5.15 illustrates the magnetic field that is generated by a 2 metre radius coil at its critical intensity and 77 K for 100 loops and 500 loops. This gives a first insight into the values of the magnetic field that can be achieved for different distances and sizes of the coil.
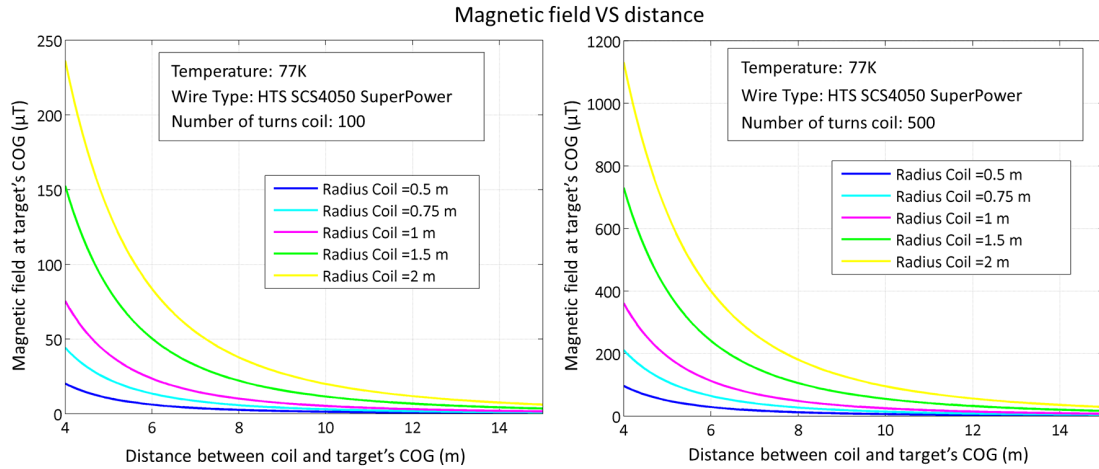
Figure 5.15: Magnetic field generated by a 2 m coil working at 77 K and at its critical intensity with 100 turns and 500 turns respectively.

The required strength of the magnetic field at the axis of the coil (see Eq. 5.19) decreases rapidly as a function of distance from the coil to the target. Therefore this de-tumbling method will be much more effective when the coil is close to the target (as previously identified in Section 5.1).

In addition, Figure 5.16 depicts the mass of the coil versus the characteristic time of decay and different relative distances. Now the radius of the coil has been fixed to 2 metres and the operating temperature is 77 K.
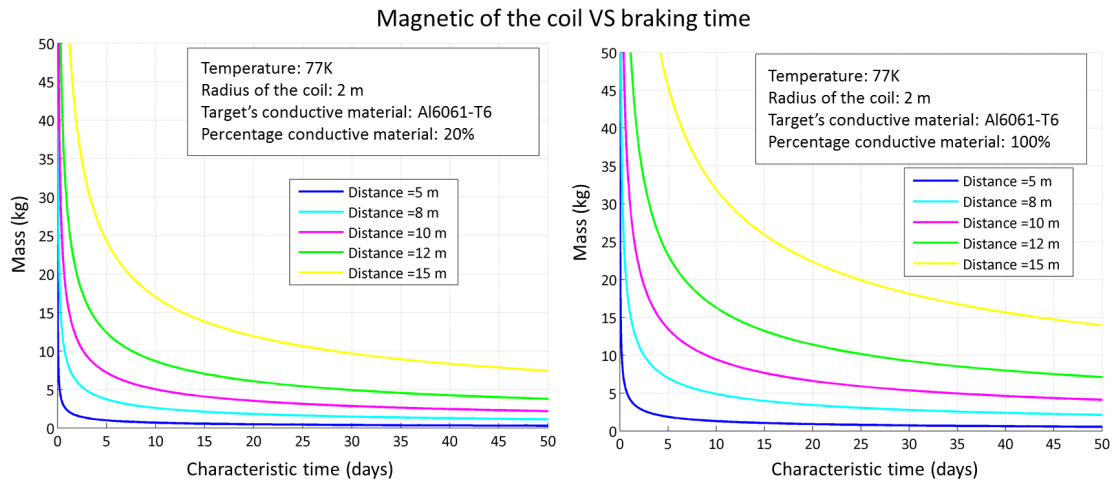
Figure 5.16: Mass of the coil versus characteristic time of decay and varying relative distances for a aluminium spherical target with 20% (right Figure) and 100% (left Figure) of conductive material at 77 K.

Figures (5.12-5.16) provide a greater insight into the requirements of the design of the coil for the eddy brake. The eddy brake subsystem should be treated as an additional instrument of an ADR mission in which specific requirements must be met. Some of the possible requirements are:

- <u>Maximum allowable volume</u>: This requirement may appear due to the selection of a specific launcher for the mission which translates in a maximum coil radius.

- <u>Maximum allowable mass</u>: This requirement may appear again due to specific launcher's restrictions.

- <u>Minimum relative distance</u>: This condition will strictly depend on the target's size and shape. Moreover, the chaser spacecraft will be able to keep a minimum relative distance with respect to the target which will depend on the robustness of the chaser's GNC subsystem and a risk analysis that must be done to minimise the collision risk between both objects.

- <u>Maximum characteristic time of the de-tumbling process</u>: This requirement may appear due to restrictions in the cost which are directly linked to the operational time of the ground stations and the mission control centre or the maximum amount of propellant on the chaser which will depend on the time needed for the formation flying operations during the de-tumbling phase.

So far the characteristics of the coil in terms of mass and volume (i.e. wire cross section) have been analysed and the performance compared to conventional materials is clearly enhanced. In terms of power, HTS wires have zero resistance when operating in the superconducting regime which undoubtedly makes these materials much more attractive than conventional materials that showed power consumptions in the order of kW (see Figure 5.8). However, the superconductive behaviour is only achieved by keeping the working temperature of the coil below a certain threshold. Therefore, the thermal subsystem is of paramount importance for the eddy brake which is analysed subsequently in Section 5.4.

For the eddy brake method the following characteristics are chosen for the coil. The selected HTS wire corresponds to a standard 2G HTS wire (SCS4050 wire) and the selected working temperature is 77 K. Similarly to the EMFF design, the coil for the eddy brake subsystem will be modelled as a torus with a major radius R_c and a minor radius r_c (see Figure 5.6). The minor radius is computed approximately based on the EMFF design which has an minor radius, $r_{c,EMFF}$, of 0.02

m for 100 turns of wire, N_{EMFF},

$$r_c = \sqrt{N}\frac{r_{c,EMFF}}{\sqrt{N_{EMFF}}} = 0.002\sqrt{N}. \tag{5.20}$$

The selected radius of the coil is equal to $R_c = 2$ m which corresponds to the maximum fairing diameter of the existing European launchers. The chosen number of turns is equal to $N = 500$ which leads to a total mass equal to 22.4 kg. This value is considered to be a compromise between the coil mass and the magnetic field generated at a certain distance. The relative distance needs to be customised depending on the target's size and shape. For instance, for a relative distance equal to 10 metres, $B = 95.5$ µT. For the selected coil and a spherical target with 20% of conductive aluminium material, the characteristic time of decay would be in the order of 5.4 days (see Figure 5.16.

Finally, Table 5.1 contains the baseline properties of the magnetic coil.

Coil specifications	
Wire type	2G HTS SCS4050 wire
Working temperature	$T_c = 77$ K
Critical intensity	$I_c = 80$ A
Major coil radius	$R_c = 2$ m
Minor coil radius	$r_c = 0.045$ m
Number of turns	$N = 500$
Coil mass	$m_c = 22.4$ kg

Table 5.1: Coil specifications.

5.4   Thermal subsystem

The superconducting material has zero power dissipation when operating in the superconducting regime. This behaviour is achieved assuming the HTS wires are always working below their critical temperature. The appearance of any heat losses would lead to a warming up of the coil which could be very detrimental for their correct operation. The major sources of heat dissipation which need to be taken into account in the coil design are [171]:

- AC losses: It is assumed that the coil will work in the direct current (DC) regime and therefore, these losses are not taken into account. However, the use of alternating current (AC) of low frequency will give rise to some benefits in the de-tumbling operations which are later discussed in Section 5.5.4.

- Splice or joint resistance: Splices between HTS wires may be necessary in the coil design. Two HTS wires are electrically joined by a solder layer which will have a certain resistance. The typical joint resistance is $20 \cdot 10^{-9}$ Ohms over a 0.1 m lap [172]. This source of power dissipation is negligible compared to other heat sources such as the heat received from the Sun and the Earth.

- External environmental heating sources: The chaser spacecraft is exposed to external environmental heat sources (e.g. Sun, Earth) that will increase the temperature of the coil and a proper cooling system is necessary to overcome an undesired warming up of the coil.

- Spacecraft body: The spacecraft body will also transmit heat via conduction and radiation to the coil. The thermal coupling between the coil and the spacecraft body can be strong unless the coil has a perfect isolation. This term will be neglected in this analysis assuming a perfect isolation of the coil from the spacecraft main body.

The operation of the coil will be driven by the point of maximum temperature throughout its perimeter. Therefore, it is of paramount importance to cool down the coil homogeneously.

One of the main responsibilities of the thermal subsystem is to guarantee that the HTS coil does not quench. A quench is an abnormal termination of magnet operation that occurs when part of the superconducting coil enters the resistive state due to a localised temperature growth and it can cause permanent degradation of the conductor [171]. HTS wires have shown to be more stable than low temperature superconducting (LTS) wires with respect to a premature quenching. The 'stability margin', which is defined as the maximum energy density that a composite superconductor can absorb and still remain fully superconducting, is much higher in the case of HTS wires. Therefore, HTS magnets are less susceptible to quenching induced by a disturbance.

HTS wires have proved to be superconducting up to temperatures of 100 K or even higher. However, the system will be more stable when working at lower temperatures and a working temperature in the range of 65K-77K is typically recommended [171].

5.4.1 Thermal balance

Assuming the resistance of the coil splices is negligible and that there are no AC losses, the major heating source is due to the Sun and the Earth. A spacecraft in space can interact with the environment only by radiation and an exchange of energy takes place due to the following causes (see also Figure 5.17) [25]:

- Direct solar radiation

- Solar radiation reflected from near planets (albedo radiation)

- Thermal energy radiated from nearby planets (planetary radiation)

- Radiation from the spacecraft to deep space
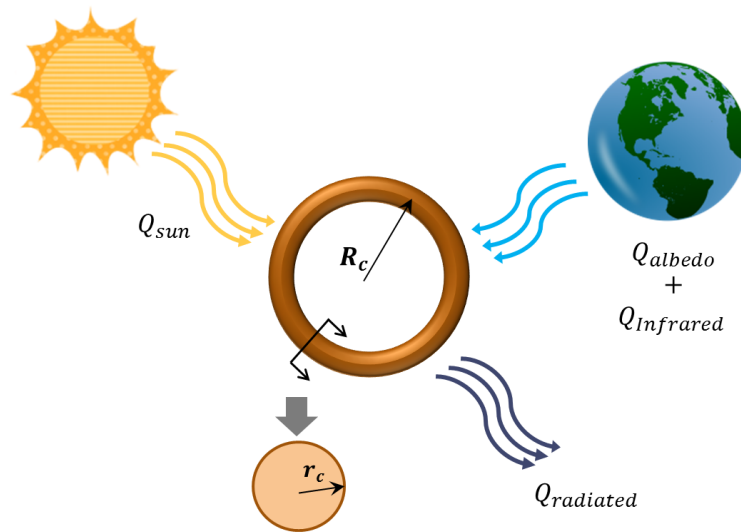
Figure 5.17: Heat exchange between the coil and the environment.

Hereinafter, we will refer to 'worst case scenario' to the scenario in which the coil reaches the maximum temperature and 'best case scenario' to the scenario in which the coil reaches the minimum temperature.

First of all, it is necessary to explore the thermal constraints of the superconducting coil to determine what type of thermal system is capable of achieving the thermal requirements. In order to do so, a thermal balance of the coil must be carried out to find out which is the equilibrium temperature that is reached. The thermal balance shown in Equation (5.21) takes into account the heat received from external sources and the heat radiated to space [25]. In addition, it will be

assumed that the coil is covered with a containment material which has a specific absorptivity α and emissivity ε. The absorptivity refers to the fraction of irradiation absorbed by the surface and emissivity measures the ability to emit energy in the infrared region. In our problem, low values of α/ε are desired so that the equilibrium temperature reached is low enough. Silvered Teflon is selected which has an absorptivity of $\alpha = 0.08$ and an emissivity of $\varepsilon = 0.66$ and it is a common coating material employed in space.

$$Q_{sun} + Q_{albedo} + Q_{planetary} = Q_{radiated}. \tag{5.21}$$

The first term Q_{sun} in Equation (5.21) is the heat received from the Sun. Its general formula is (5.22) and it depends on the absorptivity of the surface material on the coil α, the projected area, A_{sun}, with respect to the incident sunlight and the solar constant in the vicinity of the Earth $G_s = 1371$ W/m^2.

$$Q_{sun} = \alpha G_s A_{sun}. \tag{5.22}$$

The second and the third term are only important for low Earth orbits. Q_{albedo} is the albedo contribution of the Earth and $Q_{planetary}$ is the planetary radiation contribution [25].

The Earth's albedo corresponds to the fraction of the solar radiation that is reflected from the surface and/or the atmosphere of the Earth and the heat due to the albedo of the Earth is governed by Equation (5.23). It depends on the Earth albedo a and a mean value of 0.33 will be considered, F is albedo irradiation and A_{albedo} is the projected area of the magnetic coil with respect to the albedo. The worst case is considered for the albedo irradiation. This occurs when the spacecraft is over the midday meridian on the Earth Sun vector (i.e. the angle between the local vertical and the Sun's arrays is zero degrees). The F factor for this case follows Equation (5.24) ([169]) where $R_{Earth} = 6371$ km is the mean equatorial radius of the Earth and H is the altitude of the orbit.

$$Q_{albedo} = aF\alpha G_s A_{albedo}, \tag{5.23}$$

$$F = (0.664 + 0.521\rho - 0.203\rho^2)\sin(\rho),$$
$$\sin(\rho) = \frac{R_{Earth}}{H + R_{Earth}}. \tag{5.24}$$

Moreover, the term $Q_{planetary}$ in Equation (5.21) can be approximated as shown in Equation (5.25). $A_{planetary}$ is the projected area exposed to the incident Earth radiation, ε is the emissivity of the containment material of the magnetic coil and the IR energy flux has a mean value $q_{IR} = 237$ W/m^2 [25].

$$Q_{planetary} = A_{planetary}\varepsilon q_{IR}\left(\frac{R_{Earth}}{H + R_{Earth}}\right)^2. \tag{5.25}$$

The last term in the thermal balance is $Q_{radiated}$ which can be expressed as,

$$Q_{radiated} = \sigma_{sb}\varepsilon A_{surface}(T_{eq}^4 - T_{space}^4), \tag{5.26}$$

where σ_{sb} is the Stefan-Boltzmann constant equal to 5.67×10^{-8} W·m^{-2}·K^{-4}, $A_{surface}$ is the emitting area, T_{space} is the temperature of the space environment which is approximately 4 Kelvin and T_{eq} is the temperature of equilibrium [25].

The coil is modelled as a torus which contains a bundle of HTS wires which has the geometrical properties listed in Table 5.1. The coil is assumed to show the maximum projected area to both the Sun and the Earth so that the worst case is analysed. Under this hypothesis, the projected areas exposed to both the Sun and the Earth are equal to $A = 4\pi R_c \cdot r_c = 1.1$m^2 and the emitting area of the coil is $A_{surface} = 4\pi^2 R_c \cdot r_c = 3.5$m^2.

Solving the polynomial Equation (5.21), the equilibrium temperature is obtained for different orbit altitudes both during eclipse and out of eclipse periods. Figure 5.18 shows that in all the cases,

the equilibrium temperature is well above the desired temperature for the coil. This indicates that a proper thermal cooling system must be included in the design.
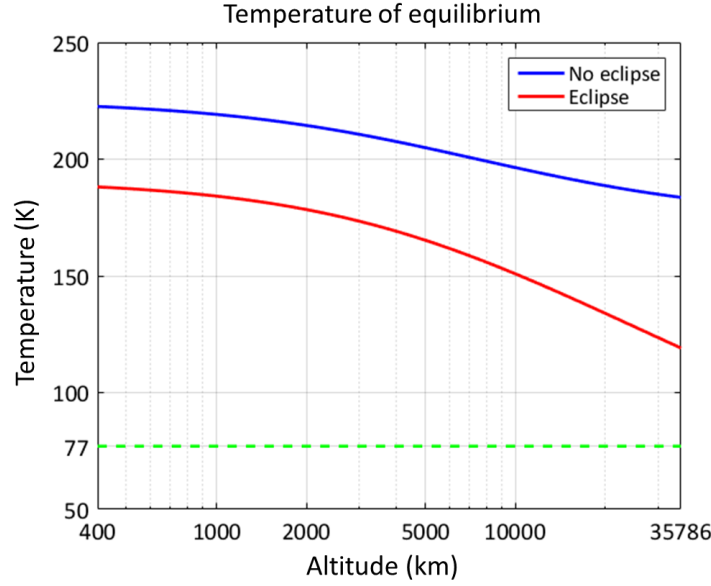
Figure 5.18: Temperature of equilibrium of the HTS coil.

5.4.2 Thermal control techniques

5.4.2.1 Thermal insulator

A thermal insulator is one of the most common passive thermal control techniques used in space. A thermal insulator is added to the coil in order to minimise radiative exchanges in the vacuum of space and to check if it is possible to keep the HTS wires below the critical temperature T_c.

The magnetic coil is insulated with MLI (Multi-Layer Insulation) which among the most common thermal-control elements on spacecraft [16]. The MLI is modelled as a solid insulator with a thermal conductivity of $k = 0.0004$ W·m^{-1}·K^{-1} at a pressure of 10^{-5} Torr [16].

Now the insulator is included in the thermal balance shown in Equation (5.27),

$$Q_{sun} + Q_{albedo} + Q_{planetary} = Q_{radiated} + Q_{insulation}. \tag{5.27}$$

The insulator will reach a temperature of equilibrium $T_{eq,ins}$ based on the heat received from the Sun, Q_{sun} and the Earth, $Q_{albedo} + Q_{planetary}$, the heat radiated to space $Q_{radiated}$ and the heat exchanged by conduction between the insulator and the HTS wires $Q_{insulation}$.

The heat transfer through a toroidal insulator follows the Equation (5.28),

$$Q_{insulation} = \frac{4\pi R_c k(T_{eq,ins} - T_c)}{ln\frac{r_{in}}{r_c}}, \tag{5.28}$$

where k is the thermal conductivity of the insulator, $T_{eq,ins}$ is the equilibrium temperature of the insulator, $T_c = 77$K is the desired working temperature for the HTS wires, r_c is the radius of the bundle of HTS wires and r_{in} is the radius the insulator that covers the HTS wires [169].

Figure 5.19 illustrates the conductive heat flow between the insulator and the HTS wires. The fact that $Q_{insulation} > 0$ indicates that the temperature of the insulator is higher than the temperature of the HTS wires, $T_c = 77$K, and the heat flows from the insulator into the wires. This result

indicates that the heat $Q_{insulation}$ needs to be extracted from the system by an additional cooling system. An insulator's thickness of 0.01 m will be included in the coil's design and the heat flow for this thickness ranges between 5 watts and 7 watts.
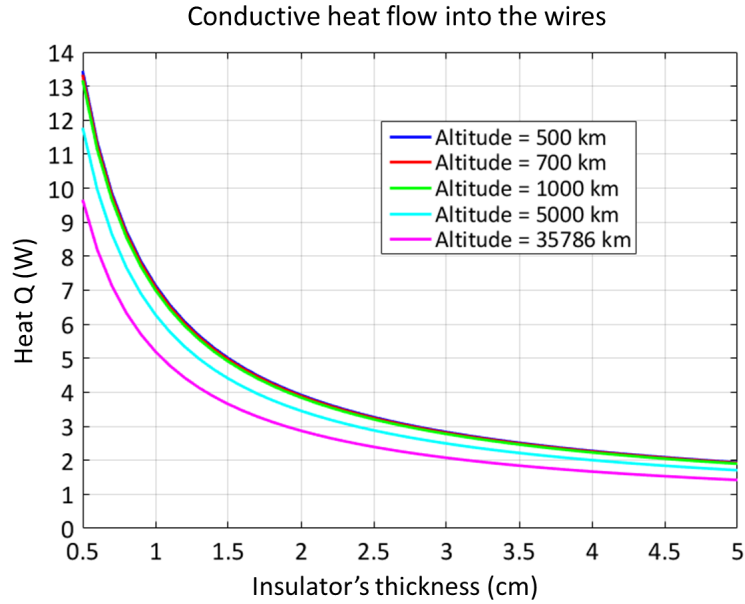
Figure 5.19: Heat flow to HTS wires at different altitudes.

5.4.2.2 Thermal shield

The thermal shield is a passive thermal control technique used to block the radiation. Thermal shields are typically used for telescopes which must be cooled down to low temperatures such as the Gaia mission operational since 2013 or the James Webb Space Telescope (JWST) which is due for launch in October 2018 [14, 173]. In both cases, the selected orbit is located near the second Lagrange point (L2) of the Earth-Sun system where the thermal shield can effectively prevent the science instrument from receiving any radiation from the Earth or the Sun.

Figure 5.20: Thermal shield used for the James Webb Space Telescope (left image) [14] and for Gaia (right image) (courtesy of ESA).

However, in LEO it is complicated to use thermal shields that can shadow the spacecraft from both the Sun and the Earth. A deployable sunshield has been proposed as a possible solution to provide long term storage for cryogenic fluids, called *'cryogenic propellant depots'*, in LEO in order to refuel space vehicles in orbit [15]. The thermal shield has a conical shape with an open end that

allows the residual heat to radiate to the cold of deep space, while the closed cone layers attenuates the radiative heat from the Sun and Earth. This way, the boil-off of the liquid inside the tank is slowed down.
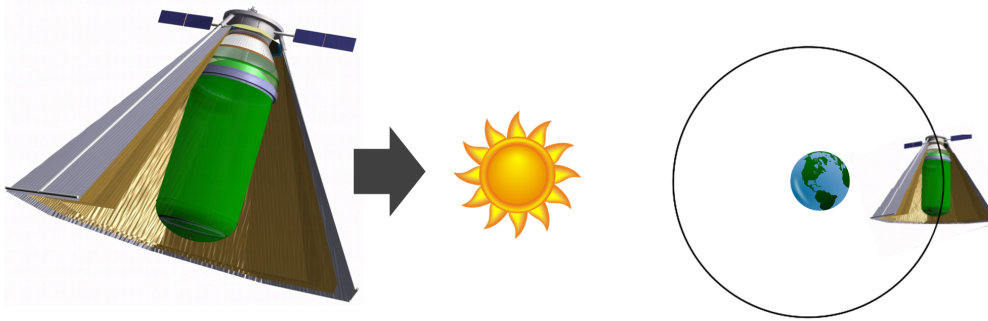
Figure 5.21: Cryogenic Propellant Depot [15].

However, employing such a thermal shield for the eddy brake would greatly restrain its relative attitude with respect to the target that needs to point the coil towards the most suitable direction in order to damp the target's angular velocity vector. This thermal control technique is a risky option as it can not guarantee that the radiation from both the Earth and the Sun will be blocked no matter what the relative attitude is with respect to the target. Therefore, this option is discarded.

5.4.2.3 Radiator

Radiators are passive cooling systems which emit infrared radiation. The radiation emitted is proportional to the area A, the emissivity ε and to the fourth power of its temperature as shown in Equation (5.29),

$$Q_{rad} = \sigma_{sb} A \varepsilon (T^4 - T_{space}^4), \tag{5.29}$$

where σ_{sb} is the Stefan-Boltzmann constant and T_{space} is the temperature of the space environment.

This thermal mechanism is only efficient for large areas and temperatures above 100 K [173]. Another limitation is their orientation because they need to be shaded both from the solar and the Earth radiation. They must look at the dark space in order to efficiently radiate.

For all these reasons, radiators are not a suitable thermal control subsystem for the HTS coil, which needs to work below 77 K in a near-Earth orbit.

5.4.2.4 Loop heat pipe + cryocooler

Another method that can guarantee a uniform cooling down of the coil consists in embedding the HTS wires in a loop heat pipe (LHP) that works with a cryogenic fluid. In addition, a cryocooler is employed for heat extraction. This thermal control system was designed and tested on the ground for the Electromagnetic Formation Flight (EMFF) mission. Figure 5.9 shows the model designed at MIT Space Systems Laboratory [13, 174].

The loop heat pipe is a good solution as the distribution of the working fluid occurs inside the LHP passively and it is able to maintain isothermalization of the coil. The LHP is a closed cycle refrigeration system. It has three main regions: a condenser, an evaporator and an adiabatic region. The working fluid receives heat and evaporates at the evaporator. Then, the vapour travels to the condenser due to the pressure difference where it is cooled down and condensed again. Finally, the liquid travels to the evaporator thanks to the capillary pressure drop and the cycle starts again.
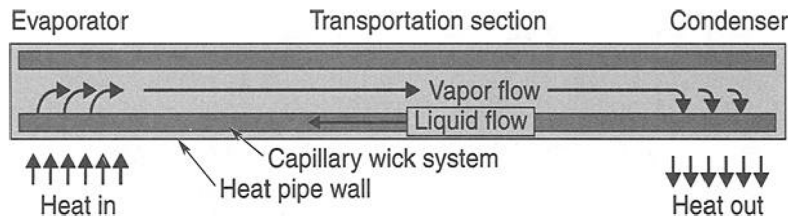
Figure 5.22: Heat Pipe Diagram [16].

The design of heat pipes is a complex process as there are numerous design parameters which must be taken into account. First of all, the heat pipe working fluid is selected based on the operating temperature range of the application which in our case is 77 K and an appropriate working fluid is liquid nitrogen. Figure 5.23 indicates the operating ranges of heat pipes based on the working fluid. In the case of nitrogen, the useful range is between 65 K and 100 K approximately which allows for some flexibility in the design.
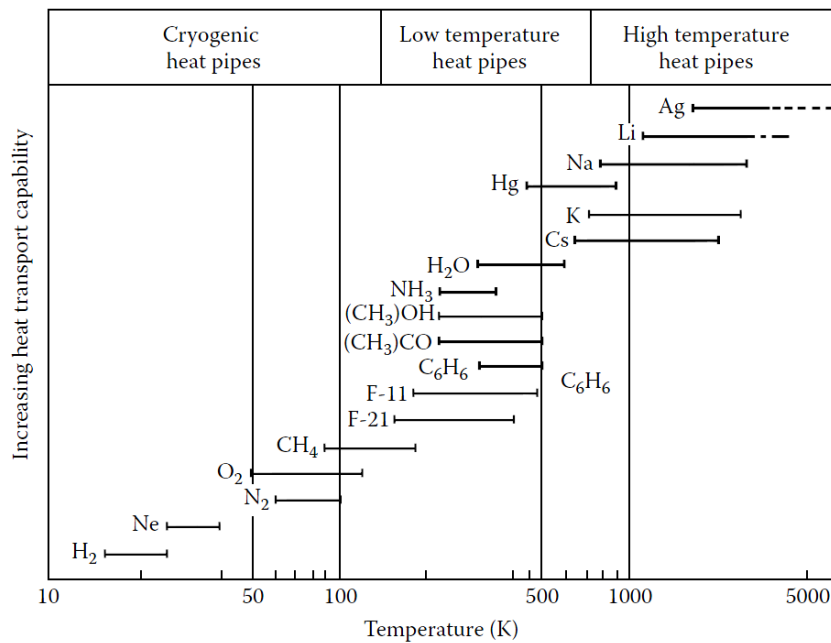
Figure 5.23: Operating ranges of heat pipe [17].

Once the working fluid is selected, the wick structure and the containment must be designed. The main function of the wick is to generate capillary pressure to transport the working fluid from the condenser to the evaporator. Typically, the wick design is based on an optimisation process to find the desired heat transfer capacity, pumping capability and temperature drop [17]. The outer container usually consists of a metal tube and it provides mechanical support and pressure containment. The thickness of the envelope will depend upon the internal pressure of the heat pipe [17].

Moreover, the material selection of the envelope and wick are of paramount importance. Their choice depends on several factors such as their chemical compatibility with the working fluid to prevent corrosion and/or gas formation, their thermal conductivity or their ease of fabrication (e.g. weldability, machinability). For instance, nitrogen is compatible with aluminium, copper, stainless steel and nickel [17].

The selected materials for the EMFF testbed were stainless steel for the wicking structure and

copper for the containment material [13]. The copper material was selected in the EMFF due to its high conductivity and the stainless steel mesh was selected due to the existence of commercial off-the-shelf (COTS) meshes with the desired pore radius. Moreover, it was identified that a combination of two outer layers of a course #100 mesh screen and two inner layers of a fine #250 mesh screen met the power requirements and provided a suitable capillary pumping pressure. The mesh number #N indicates the porosity of the mesh and it increases as the pore radius decreases [13].

The amount of cryogen accounts for the working fluid in gaseous state in the vapour space and in the liquid state in the wick. The working fluid inventory is an important design parameter because both an excess or a deficiency of working fluid can lead to a heat pipe failure. In general, the amount of working fluid can be computed as [13]:

$$m_{cryogen} = \rho_v \pi (\frac{d_v}{2})^2 L + \rho_l A_w \epsilon_p L, \tag{5.30}$$

where ρ_v and ρ_l are the densities of the cryogen in the gaseous and liquid states, d_v is the diameter of the vapour space, L is the overall length of the pipe, A_w is the wick area and ϵ_p is the porosity of the mesh.

Once the working fluid as well as the case, wick materials and sizes have been selected, the operating limits must be analysed. These are the wicking limit, the entrainment limit, the boiling limit, the sonic limit and the viscous limit [17].

- Wicking limit: The capillary structure is able to provide circulation of a fluid up to a certain limit which depends on the wick structure and properties of the working fluid.

- Entrainment limit: The vapour flow exerts a shear force on the liquid in the wick, which flows in opposite direction to the vapour. If the shear force exceeds the resistive surface tension of the liquid, the vapour flow entrains small liquid droplets impeding the correct liquid flow to the evaporator.

- Boiling limit: If high local heat fluxes appear, nucleate boiling may take place which produces vapour bubbles in the liquid layer.

- Sonic limit: This effect occurs when the vapour pressure is too low and the velocity of the vapour at the exit of the evaporator reaches the speed of sound. The vapour flow is then said to be 'chocked' which limits the vapour flow rate. This is typically only a problem during the start-up of the heat pipe.

- Viscous limit: In long pipes at low temperatures, the vapour pressure is low and the effect of the viscous friction on the vapour flow may dominate over inertial forces. This effect prevents the working fluid from flowing adequately and consequently, the heat transfer through the pipe is reduced. This limit is a major design restriction for cryogenic heat pipes.

If the selected LHP design complies with all the aforementioned limits, then the final step in the design process ends by checking if the heat transfer capacity of the heat pipe is above the desired value as well as other design parameters such as the thermal resistance of the pipe [17]. The maximum power capacity of the heat pipe, given by Equation (5.31), depends on various parameters of the working fluid and wick,

$$Q_{max} = 2 \frac{\rho_l \gamma C_v}{\mu_l} \frac{A_w}{L_{eff}} \frac{\kappa}{r_p}, \tag{5.31}$$

where ρ_l is the liquid density, γ is the surface tension, C_v is the heat of vaporisation, μ_l is the liquid viscosity, L_{eff} is the effective length of the heat pipe defined as the distance from the centre of the condenser to the centre of the evaporator, κ is the permeability of the wick and r_p is the pore radius of the mesh [17].

In order to obtain a rough estimate of the structural mass of the heat pipe for the eddy brake several assumptions are made. It must be pointed out that the present computations are just done for qualitative purposes and that a more in-depth analysis should be done if this thermal control

option were selected. The LHP is modelled as a toroidal tube with a minor radius of $r_c = 0.045$ m and a major radius of $R_c = 2$ m which contains the coil specified in Table (5.1). Two effects are analysed in order to dimension the thickness of the outer container (see Figure 5.24). On the one hand, the working fluid will exert the maximum internal pressure on ground when all the working fluid is gaseous [17]. On the other hand, the coil will be subject to opening radial forces that tend to expand the coil when electrical current flows through the HTS wires [171]. This second effect will take place in orbit when the electromagnetic coil is employed.
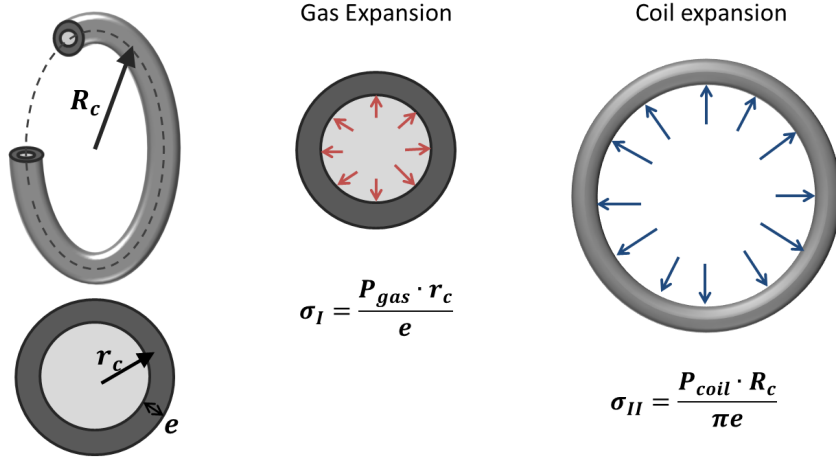
Figure 5.24: LHP internal pressure due to the gas expansion and the coil expansion.

First of all, the thickness of the outer container must be computed based on the internal pressure of the working fluid. The thickness is typically assessed at room temperature (300 K) when all the working fluid is gaseous and the internal pressure is maximum [17]. The pressure exerted by the gas nitrogen is given by its equation of state, that is, a function of the kind $P = P(\rho, T)$ which only depends on its density and temperature. Assuming the density of the working fluid is equal to the one obtained for the EMFF design, the pressure exerted by the gas will also be the same and it is equal to $P_{gas} = 2.02$MPa at 300K [13].

Moreover, in order to obtain the necessary thickness of the envelope, Equation (5.32) is employed [148],

$$\sigma_{0.2\%} = \frac{P_{gas} \cdot r_c \cdot SF}{e}, \tag{5.32}$$

where $\sigma_{0.2\%}$ is the tensile yield strength, P is the pressure exerted by the gas, r_c is the minor radius of the tube, e is the thickness and $SF = 1.5$ is the safety factor considered. Table 5.2 indicates the masses necessary for the envelope for three different materials which are compatible with liquid nitrogen [17]. Among the three options presented, an aluminium container is the most beneficial solution in terms of mass.

Material	$\sigma_{0.2\%}$ (MPa)	e (mm)	Density (kg/m³)	Mass (kg)
Aluminium 6061-T6	276	0.5	2700	4.8
Copper	100	1.35	8950	42.9
Stainless Steel 304	215	0.6	7999.5	17.1

Table 5.2: Mass of the envelope.

The second effect occurs due to the interaction between the windings of the electromagnetic coil. The electric current density vector of each winding, $\vec{j}$, will interact with the magnetic field generated by the rest of the windings resulting in a radial force (see Equation (3.23)). This expansion may be

studied as if there were in internal gas which exerts a radial force on the coil. The radial pressure, also referred to as *magnetic pressure*, may be computed as [171],

$$P_{mag} = \frac{B_0^2}{2\mu_0} = 62\text{Pa}, \tag{5.33}$$

where B_0 is the magnetic field at the centre of the coil. The tube thickness is now obtained from Equation (5.34), which relates the hoop stress with the magnetic pressure,

$$\sigma_{0.2\%} = \frac{P_{mag} \cdot R_c \cdot SF}{\pi e'}. \tag{5.34}$$

For an aluminium tube and a safety factor equal to $SF = 1.5$, the necessary thickness is $e' = 0.0002$ mm which is various orders of magnitude lower than the previous case. Therefore, the dominant pressure is the one generated by the working fluid and the thickness of the outer container must be designed based on that effect.

With respect to the wick structure, it will be assumed that the same number and type of mesh layers of the EMFF design are valid for the eddy brake. The screen meshes must cover a surface equal to $A_{mesh} = 4\pi^2 R_c r_c$. Using COTS screen meshes manufactured by TWP [175], Table 5.3 shows the total mass needed of the wick.

Mesh screen	Density (kg/m^2)	Number	Mass per unit (kg)	Total mass (kg)
Stainless steel #100	0.69	2	2.45	4.9
Stainless steel #250	0.2	2	0.71	1.4
Total mass				6.3

Table 5.3: Mass of the wick.

In addition, with respect to the amount of working fluid, its contribution to the overall mass is expected to be small. The amount of working fluid computed for the EMFF design was 420 g for a coil of 1 metre radius [13]. Taking into account that Equation (5.30) is proportional to the length of the heat pipe and in the absence of a more detailed analysis, the amount of cryogen needed for a 2 metre radius coil should be in the order of 1 kg. All in all, the expected mass of the LHP is equal to,

$$m_{LHP} = m_{envelope} + m_{wick} + m_{N2} = 4.8 + 6.3 + 1 = 12.1\text{kg}. \tag{5.35}$$

Moreover, this thermal control system carries a cryocooler which works in conjunction with the LHP. Cryocoolers transform mechanical work produced by moving parts into refrigerating power. They are usually classified into two groups; regenerative coolers (e.g. Stirling, pulse tube, Gifford coolers) and recuperative cycles (Joule-Thomson, Brayton coolers) [173]. The regenerative coolers have a compressor which cyclically expands and compresses a gas. The heat is extracted at the cold end when the gas expands and rejected at the warm end when the gas is compressed. The recuperative coolers contain a working fluid which flows steadily in one direction through low and high pressure lines and there is a counterflow heat exchange between the flows at different pressure and temperature.

The main disadvantage of this device is that it is an active cooling system which requires input power. Moreover, the moving pistons may induce vibrations which are undesirable for the satellite's stability.

With respect to the cryocooler selection, there is a major difference between the eddy brake and other space missions which required a cryocooler system. Space-qualified coolers are usually built to operate for multiple years in space. In order to ensure such a high reliability, their design requirements are very strict, increasing their cost to a great extent (order of million Euros [173]). However, the de-tumbling phase should only last for several weeks/months and a non-space cryocooler could be suitable which then would lead to a significant reduction in cost. The major

reason why this type of cooler is not used in space is the fact that they have seals (e.g. o-rings) and bearings that can not be relied upon for a typical 10 year mission. Nonetheless, this type of cryocooler should still need to go through an exhaustive test campaign in order to guarantee that the cryocooler can survive the launch vibrations, space environment, etc.

This process has already been performed for the VIRTIS instrument on the Rosetta mission. The cryocooler K508 manufactured by RICOR company was space-qualified [26, 176]. In our design, the cryocooler K535 is selected as it meets the eddy brake requirements in terms of cooling power. This cryocooler would still need to go through a similar test and verification campaign as it was done for Rosetta but the overall cost could be reduced. Table 5.4 contains the specifications of a cryocooler that could potentially be included in the design of the thermal subsystem for the de-tumbling process. Further details of this cryocooler can be found in Section A.7.

Model	Cooling power	Weight	Input voltage	Max input power	Steady state power
K535	7W, 65K	9.5 kg	220V/110V	300 Wdc	200Wdc (5W, 65K)

Table 5.4: Cryocooler K535 manufactured by RICOR [26].

Due to the fact that the cryocooler is a single point failure item, the thermal subsystem should count on two cryocoolers placed on opposite sides of the coil. The two instruments would then operate at half power unless one of them fails, at which time the still operative cryocooler would operate at full power. This way, the thermal subsystem becomes more robust and the temperature achieved throughout the coil will be more homogeneous.

On top of the mass of the cryocooler, the structure and electronics for this device must be taken into account. Airbus Defence & Space gave a first assessment of this additional mass to be around 30 kg for the two cryocoolers.

Table 5.5 summarises the mass budget of this thermal subsystem including 20% margin as it is conventionally done in a preliminary process design [3].

Component	Mass per unit	Number	Total Mass	Comment
LHP structure	11.1 kg	1	11.1 kg	Al. envelope+wick
LHP working fluid	1 kg	1	1 kg	
Cryocooler	9.5 kg	2	19 kg	
Misc. cryocoolers	30 kg	1	30 kg	Structure+electronics
Margin (%)			20%	
Total mass incl. margin			73.3 kg	

Table 5.5: Mass budget of the thermal subsystem.

5.4.2.5   Cryogenic dewar

The dewar system stores the liquid cryogen that would be gradually boiled away. The excess heat is extracted through evaporation of the liquid which must then be vented to space without applying momentum to the spacecraft (e.g. two thrusters symmetrically opposed around the COG) [177].

This thermal control technique has been used in past space missions primarily to cool down telescope detectors. For instance, it was employed for the Hershel Space Observatory. Herschel was the largest infrared telescope ever launched and it was operational from 2009 until 2013. A helium dewar system was employed in order to keep the detectors below 2K and the system contained 2300 litres of cryogenic liquid which gradually boiled away [173].

In addition, the dewar needs liquid and vapour transport lines that connect the dewar with the coil [177]. The cryogen can be passively pumped into a vessel that surrounds the coil by means of a heat pipe as described in the previous thermal control subsystem.

The main advantage with respect to the previous option (Cryocooler+LHP) is that here there is no power consumption. However, the lifetime of the superconducting device is driven by the amount of liquid that can be carried on-board. Therefore, the additional value for using a dewar is subject to the required volume and mass to carry the liquid cryogen.

Two different cryogenic fluids are analysed; helium and nitrogen and their thermal properties are listed in Table 5.6.

Cryogenic fluid	Heat of vaporisation (KJ/kg)	Normal boiling point (K)
Helium	21	4.2
Nitrogen	200	77

Table 5.6: Cryogenic working fluids.

The mass flow rate needed to absorb a certain heat Q can be computed as follows [177],

$$m_f = \frac{Q \cdot t}{C_v},$$

(5.36)

where m_f is the mass of cryogen, C_v its heat of vaporisation and t is the time. Figure 5.25 outlines the necessary mass of helium and nitrogen for different heat loads and times of operation.

A liquid nitrogen dewar-based system could be a viable option to keep the temperature of the coil below the critical temperature, $T_c = 77$K. For a de-tumbling process of 30 days and heat load of 7 Watts, the total mass of nitrogen is 90 kg which is equal to 111 litres at the normal boiling point. The company Janis [27] manufactures dewars which have been used in space applications and the properties of some liquid nitrogen dewars manufactured by them are listed in Table 5.7.

Model	Capacity	Outside diameter	Height	Filled weight	Empty weight
LN-35	35 litres	0.47 m	0.635 m	42.6 kg	14.1 kg
LN-50	50 litres	0.47 m	0.776 m	57.6 kg	17.2 kg
LN-100	100 litres	0.47 m	0.127 m	81.2 kg	31.3 kg

Table 5.7: Nitrogen dewars manufactured by Janis [27].
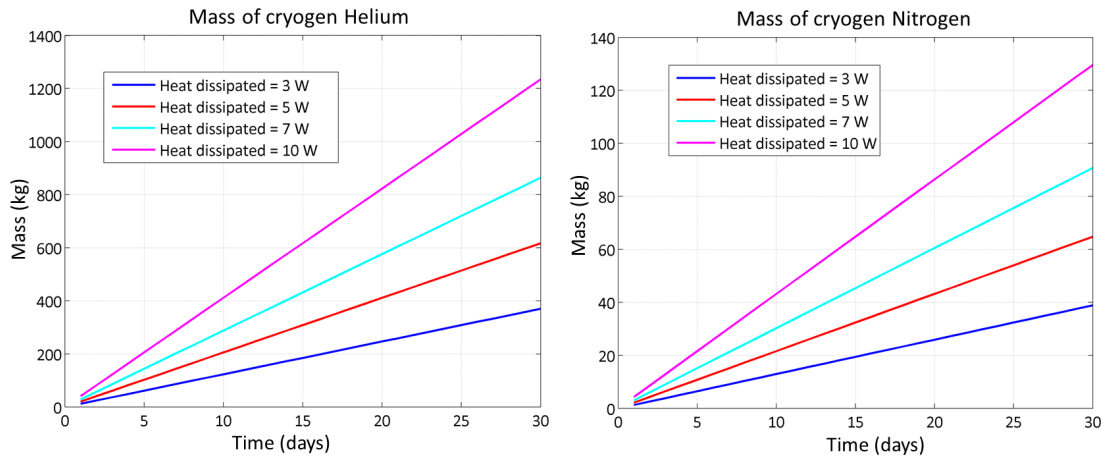
Figure 5.25: Mass of helium and nitrogen needed for a dewar-based system for different heat loads and times of operation.

Taking into account the same heat pipe structural mass as the one computed for the previous thermal control subsystem (see Table 5.5), the total mass for the dewar-based system is now computed. The mass budget accounts for the amount of cryogen, the weight of the tank, computed with the data from Table 5.7, and the heat pipe structure.

Using the data from Table 5.7, Figure 5.26 shows the total mass needed including both the tank and the cryogenic liquid for different operational times.
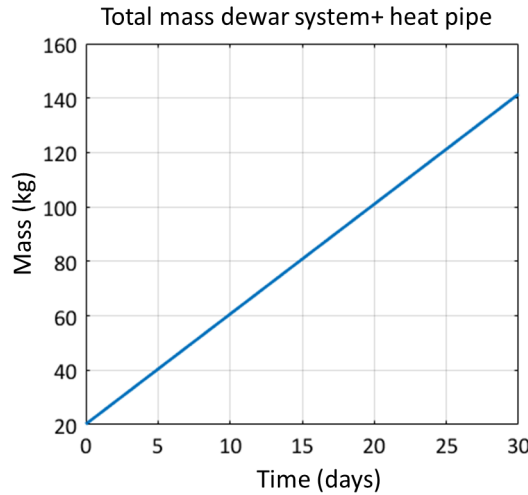
Figure 5.26: Total mass of the dewar system including the tank and the liquid cryogen.

5.4.2.6   Trade-off between the cryogenic dewar and the LHP+cryocooler

Here the two viable options are compared; the loop heat pipe with a cryocooler or a dewar based-system. Table 5.27 indicates the pros and cons of each option. On the one hand, the dewar-based system needs no power consumption, it generates no vibrations and it is less expensive. On the other hand, the dewar-based system is more massive and more voluminous, it limits the operational time based upon the amount of cryogen on-board and it may generate some disturbances when venting excess gas.

	LHP + Dewar-based system	LHP + cryocooler
Power consumption	None	Input power needed by the cryocooler
Volume	Volumetric cryogenic tank is needed	Less volume is needed
Mass	Higher mass	Lower mass
Lifetime	Limited to the amount of cryogen	Unlimited
Vibrations	Stable, low vibration	Vibrations
Outgassing	Excess gas is vented to space. Torques must be compensated.	The cryogen is reutilised
Cost	Less expensive	Cryocoolers are very expensive

Figure 5.27: Thermal control subsystems trade-off.

For short de-tumbling operations (i.e. in the order of days), the dewar-based system is the preferred option as it reduces the power needs, the cost and the complexity of the de-tumbling subsystem. However, the LHP+cryocooler option is more favourable for longer de-tumbling operations due to the mass and volume requirements of the dewar-based system. The cryocooler does not limit the operational time of the de-tumbling process and reduces drastically the mass and the volume. Therefore, this thermal control technique is more versatile as it is valid for all ADR objects and it could also be employed in an ADR multi-target mission. For these reasons, this option is chosen as the baseline option for the thermal design.

5.5 GNC subsystem

5.5.1 Main requirements

The main function of the GNC subsystem is to ensure a suitable chaser-target configuration for the de-tumbling process to be effective. The two main requirements for this subsystem are:

- Adequate relative pointing of the coil: There are two relevant practical configurations, referred to as ($\parallel$) and ($\perp$) and these are further analysed in the following chapter in Section 6.2.2. The first one, ($\parallel$), consists in pointing the coil towards the target object, that is, the magnetic moment of the coil should be parallel to the relative position vector between the coil and the COG of the target. In this case the magnetic field created inside the target is maximum and therefore, the de-tumbling time is minimum. The second interesting configuration, ($\perp$), consists in pointing the coil perpendicularly towards the target object, that is, the magnetic moment of the coil should be perpendicular to the relative position vector between the coil and COG of the target. This configuration can cancel out the magnetic forces between the two objects if some constraints with respect to the angular velocity and induced magnetic moment of the target are met.

- Adequate relative distance between the chaser and the target: The relative distance between the two objects is selected based on the desired value of the magnetic field that wants to be induced inside the target and the maximum allowable risk of collision between the two objects. The GNC subsystem has to maintain the selected distance throughout the de-tumbling phase. Furthermore, in case of an unexpected event which may endanger the safety of the vehicles, the GNC subsystem must be able to carry out a collision avoidance manoeuvre (CAM) that will move the chaser to a safe relative position.

5.5.2 Pose estimation sensors

The de-tumbling process requires the measurement of the relative position and attitude of the target object. There are two possibilities to infer the pose of the target. It can be measured directly by sensors on-board the chaser or it can be obtained indirectly from the magnetic interactions induced on the chaser as a result of the eddy currents generated on the target. This latter option may be very challenging due to the fact that the magnetic forces and torques on the chaser are expected to be of the order of milliNewtons and milliNewtons metres (see the examples presented in Section 6.3). These small effects will be covered up by other perturbations that appear on the chaser and therefore, it would be difficult to discriminate each effect. For these reasons, the chaser should carry pose estimation sensors to derive the state of the target.

As explained earlier in Section 2.2.1, pose estimation for active debris removal missions entails various difficulties due to the fact that the target is non-cooperative (e.g. no supportive markers on the surface) and that the physical state of the object may be unknown or uncertain (e.g. fuel left on-board, possible deterioration of the target, etc.).

Current pose estimation sensors for proximity operations can be divided into two major groups; passive camera-based sensors or active light detection and ranging (LIDARs) [46, 60]. Passive sensors may work in the visible range or infrared range and they have lower hardware complexity than active sensors, they are cheaper and their mass and power consumption is lower [64, 65]. However, their resolution is usually poorer than the one of active sensors. Furthermore, visible passive cameras are very sensitive to illumination conditions and they can not be used during eclipse.

Active sensors such as the LIDARs actively illuminate the target with a laser and measure the reflected signal. They are robust sensors with respect to the illumination conditions and they usually have a better resolution than the one provided by passive sensors [64]. However, it should be noted that both active and passive sensors experience problems in the detection of very reflective materials (e.g. MLI) in the short range and low-reflective materials in the long range [61].

Moreover, LIDARs can be scanning LIDARs which sweep the scene with a narrow laser beam, array LIDAR systems (e.g. flash LIDAR) that illuminate the entire scene at once or a combination of both [178, 179]. One of the advantages of the flash LIDAR is that it has no moving components which reduces the risk of failure of the sensor. The scanning LIDAR is usually more effective in the longer range as smaller field of views (FOVs) are needed and therefore, less energy to illuminate the target. As the chaser approaches the target, the scanning LIDAR becomes less efficient because it needs to scan larger FOVs at a faster frame rate. The main disadvantage of the flash LIDAR is that it consumes more power than the scanning LIDAR for the same performance [179].

The pose estimation sensors used for the Eddy Brake should cope with the following requirements:

- Sensor range: The pose estimation sensor should be able to cope with a relative distance in the order of meters for the de-tumbling phase (baseline distance is 10 meters) and the range accuracy should be of the order of centimetres or less.

- FOV: Typical objects targeted for ADR are big size objects (e.g. upper stages) that may be several meters in diameter. The algorithms used for tracking the pose of the target are more accurate if the full target is detected within the FOV of the sensor. Therefore, the selected sensor should have a big FOV in the order of tens of degrees.

- Robustness with respect to any illumination conditions: The magnetic field generated by the chaser should be perpendicular to the angular velocity of the target in order to maximise the induced eddy currents. In addition, the chaser spacecraft may need to acquire different relative configurations in order to damp all the components of the angular velocity of the target object. The necessary relative position of the chaser and target object may not be optimum in terms of illumination conditions (geometry Sun-target-chaser) and operations during eclipse may be necessary.

- Low exposure time and suitability for rapid ranging scenes: The target's angular velocity may be quite high (> 10 deg/s) and therefore, the exposure time of the sensor should be low.

- Minimal computational time: The time needed to process the data should be minimal to avoid any delays in the control algorithm as they may affect the stability of the GNC control loop system.

For a relative distance of several meters, the most accurate sensors to measure the pose are the scanning and flash LIDARs. Furthermore, these sensors are less affected by the illumination conditions with respect to optical instruments. The flash LIDAR has some advantages with respect to the scanning LIDAR which makes it a more adequate instrument for the eddy brake. The flash LIDAR illuminates and gets the data of the scene at once, achieving a high rate of frames per second, while the scanning LIDAR needs to scan the scene. Therefore, this makes scanning LIDARs less suitable for rapid ranging scenes such as an object with a high spin rate. Moreover, the flash LIDAR has no moving parts which makes the sensor more reliable. All in all, a flash LIDAR is recommended here as the most suitable pose estimation sensor for the eddy brake.

One possibility is the DragonEye 3D flash LIDAR manufactured by ASC which already has some flight heritage (missions STS-127, STS-133) [60].

Model	Mass	Power	FOV	Capture rate	Range
DragonEye 3D	3 kg	35 W	45×45 deg	5 Hz nominal (up to 30 Hz)	< 1.5 km

Table 5.8: DragonEye 3D flash LIDAR by ASC [28].

Note that additional sensors will be needed for an ADR mission during the far and close rendezvous, capture and de-orbiting phases. A typical GNC suite should contain star trackers, Sun sensors, inertial measurement units (IMUs), a far field camera and a Global Positioning System (GPS) [3]. The goal of Sections 5.5.2 and 5.5.3 is to focus on the specific sensors and actuators that are required during the de-tumbling process.

5.5.3 Actuators

The chaser spacecraft needs to have a complete suite of reaction control system (RCS) thrusters for translation and attitude control. For instance, the European e.deorbit mission for ADR has twenty-four 22N RCS thrusters of 0.65 kg each [156].

Moreover, in order to reduce the propellant consumption, momentum and reaction wheels are typically included in the design. These actuators can store angular momentum and provide internal torques. Therefore, they can redistribute the angular momentum of the chaser providing attitude control but they can not modify the total angular momentum of the body. Moreover, when they reach their maximum momentum storage capacity (saturation limit), they need to be desaturated by means of an actuator that can provide external torques (e.g. thrusters) [103].

The major external disturbance on the chaser will be caused by the Earth's magnetic field which will cause a torque given by Equation (5.37),

$$\vec{T}_\oplus = \vec{m}_c \times \vec{B}_\oplus, \tag{5.37}$$

where $\vec{m}_c$ is the magnetic moment of the coil and $\vec{B}_\oplus$ is the Earth's magnetic field vector. Figure 5.28 displays the maximum torque which occurs when the magnetic moment is perpendicular to the field for different altitudes. For this analysis, the reference coil defined previously in Table 5.1 has been used which has a magnetic moment equal to 502654.8 A·m². The results show that the torque may be in the order of 10 N·m in LEO while it may be in the order of 0.1 N·m in GEO. Therefore, the type of actuators needed will depend on the type of orbit.
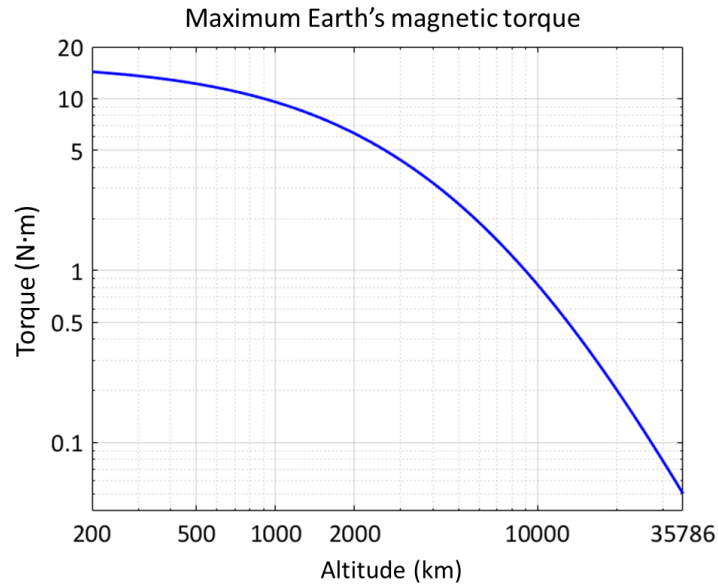
Figure 5.28: Maximum Earth's magnetic torque.

Figure 5.29 shows a sample of the torques provided by commercial reaction wheels and control moment gyros (CMGs) [18]. Reaction wheels can typically provide control torques below 1 N·m while CMGs can provide up to 100 N·m. Therefore, RWs should suffice the attitude control needs in GEO and CMGs in LEO. Table 5.9 contains the details of two commercial RW and CMG that meet the eddy brake requirements in GEO and LEO respectively.
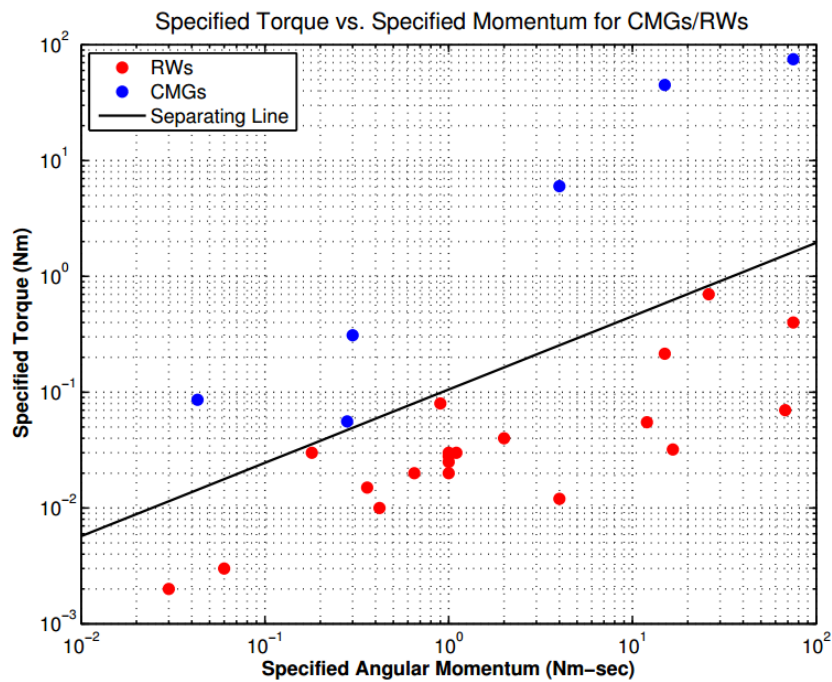
Figure 5.29: Commercial reaction wheels and control moment gyros [18].

Model	RW 250	CMG 15-45S
Manufacturer	Astro und Feinwerktechnik Adlershof GmbH	Airbus Defence & Space
Nominal ang. momentum	4 N·m·s	15 N·m·s
Nominal torque	0.1 N·m	45 N·m
Mass	2.7 kg	18 kg
Power	18 W	25 W

Table 5.9: Commercial RW [29] and CMG [30].

5.5.3.1 Inaccuracies and delays

The sensors and actuators employed in the GNC loop will introduce inaccuracies and delays in the control which may affect the stability of the system [180]. These effects can derive from,

- Sensors on-board the chaser including those sensors that measure its inertial position (e.g. Inertial measurement units (IMUs), star trackers) and pose estimation sensors that measure the relative pose of the target with respect to the chaser.

- Actuators on-board the chaser

- Communications with ground. In this article, it will be assumed that the GNC subsystem is fully autonomous and therefore, this last source of possible error is disregarded.

Typical accuracies achieved during in-orbit tests with passive camera sensors lie in the range of a few centimetres for the relative distance and a few degrees for the relative attitude [60, 65]. Additional sensors such as the TRIDAR have been tested on-board the Space Shuttle for automatic acquisition of the ISS and real-time tracking [61]. The TRIDAR sensor combines a laser based three-dimensional sensor with a thermal imager. The pose accuracies achieved are on the order of 1 cm/1 degree in real time (5 Hz) for final capture operations (< 10 m). Additional passive and active sensors tested in space for pose estimation are listed in Table 5.10 including their performance parameters provided by the corresponding manufacturer.

Sensor	Manufacturer	FOV	Range	Accuracy at 10m	Nominal rate
AVGS	NASA	8 deg	$1-300$m	0.15m/0.5deg	5 Hz
DragonEye 3D	ASC	45 deg	< 1.5km	15cm (3σ)	5 Hz
TRIDAR	Neptec	30 deg	0.5m-2km	1cm/1deg	$5-10$ Hz
RVS 3000 3D	Jena Optronik	40 deg	1m-3km	1 deg	2 Hz
VNS Flash LIDAR	Ball Aerospace	20 deg	< 5km	10-20cm (3σ)	< 30 Hz

Table 5.10: Performance of pose estimation sensors tested in space.

Additional inaccuracies may arise from the actuators employed to execute the manoeuvres. For instance, the accuracies achieved by thrusters depend on its minimum impulse bit. This parameter quantifies the minimum thrust that can be commanded by the satellite and the lower the specific impulse of the propellant subsystem, the lower the impulse bit [181]. Hence, a possible way to increase the accuracy of thrusters is to decrease the magnitude of the force. Additional thrust direction errors can be caused by errors in the measurements of inertial attitude sensors or geometric misalignments of the thrusters.

With respect to the possible sources of delays, there is the computational time needed to process the data from pose estimation sensors, the computation of the control manoeuvres and their execution. The computational time for the data processing and the control law is usually very low, in the order of milliseconds [65]. Time delays in thrust actuators are due to electrical and mechanical delays in the valve circuits and due to the time needed for the propellant to flow from the valves to the thrusters [103]. Typical values for these delays are in the range of few milliseconds to a

few hundreds of milliseconds. For example, a total delay of $\tau = 0.025$ s has been estimated for a bi-propellant 10 N thruster [181].

Typical global delays, including the sensors, actuators and communication delays, considered in the analysis of GNC close-loops for spacecraft lie in the order of 1-10 seconds [180, 182].

5.5.4 Alternating current

So far, it has been assumed that the coil will work with DC current. However, the use of alternating current (AC), $I_c(t) = I_{max} \sin(\omega_{ac} t)$, of low frequency offers some attractive advantages as the Earth's magnetic torque on the coil can be cancelled out.

5.5.4.1 Magnetic interactions with AC current

The magnetic moment of a solenoid is proportional to the number of turns, N, its radius, R_c, and the electric current, I_c,

$$\vec{m}_c = \pi R_c^2 N I_c(t) \vec{u}_m, \tag{5.38}$$

where $\vec{u}_m$ is the unitary vector in the direction of the magnetic moment.

The Earth's magnetic field generates a torque on the chaser's coil given by Equation (5.37). However, the magnetic torque over a complete cycle of the AC current is zero as demonstrated in (5.39). Here it is assumed that the cross product $\vec{u}_m \times \vec{B}_\oplus$ is approximately constant during the cycle period T. This assumption is reasonable for short cycle periods in the order of 1s or less.

$$\left\langle \vec{T}_\oplus \right\rangle = \frac{1}{T} \int_0^T \vec{m}_c \times \vec{B}_\oplus dt \approx \frac{\pi R_c^2 N I_{max}}{T} \left(\int_0^T \sin(\omega_{ac} t) dt \right) \vec{u}_m \times \vec{B}_\oplus = \vec{0}. \tag{5.39}$$

However, alternating currents cause dissipation of energy which is an undesirable phenomenon and it is typically referred to as *'AC losses'*. The physical mechanism of the AC losses is briefly explained in this section. The alternating magnetic field induces an electric field given by Faraday's law $\nabla \times \vec{E} = -\partial \vec{B} / \partial t$. This electric field generates in turn some screening currents which lead to resistive losses. There are three types of AC losses depending on the frequency of the AC current [171, 183]:

- Hysteresis loss: The screening currents give the superconductor a magnetic moment, $\vec{m}$, that changes with the magnetic field. The changes in magnetic moment are irreversible, that is, they depend on the previous history of the magnetic field. The magnetisation loss in Joules per field cycle, p_{hyst}, is found as the area of the magnetisation curve,

$$p_{hyst} = \oint \vec{m} \cdot d\vec{B}. \tag{5.40}$$

  The AC loss per magnetic field cycle depends only on the field amplitude and the superconductor properties. This loss is dominant at low frequencies (< 200 Hz) and it is proportional to the AC frequency to the first power

- Eddy current loss: Eddy currents are induced due to Faraday's law in the metallic parts of the superconducting tape. These losses are quadratically proportional to frequency and their contribution is typically noticeable for frequencies above 200 Hz.

- Coupling loss: These losses have a similar nature to that of eddy currents and they are sometimes classified in the same group of AC losses. They are caused by the current coupling two or more superconducting filaments through the metallic regions separating them. These losses are quadratically proportional to frequency and their contribution is typically noticeable for frequencies above 200 Hz.

Therefore, the most important effect at low frequencies are the hysteresis losses. For a cycle period of 1 second, the hysteresis losses are almost negligible and it would serve to cancel out the Earth's

magnetic torque. Every half cycle, the torque will change direction. Hence, we need to compute the satellite's rotated angle after half cycle. Considering the worst case scenario in which the magnetic moment is always perpendicular to the external field, the average torque after half cycle, T_{half}, is equal to,

$$T_{half} = \sqrt{\frac{2}{T} \int_0^{\frac{T}{2}} \vec{T}_\oplus^2 dt} = \frac{\pi R_c^2 N I_{max} B_\oplus}{\sqrt{2}}. \tag{5.41}$$

Moreover, the angle rotated by the spacecraft, θ, due to the external torque $T_{T/2}$ may be computed in an approximate way by Equation (5.42),

$$\theta = \frac{1}{2} \frac{T_{half}}{I_{mean}} t^2, \tag{5.42}$$

where I_{mean} is the mean inertia of the spacecraft and t is the time passed.

Considering an AC current with a cycle period of 1 second, which is high enough to neglect any AC losses, flowing through our baseline coil defined in Table 5.1 and the chaser spacecraft defined for the Agora mission (see Section 5.8) with a mean inertia of $I_{mean} = 1962$ kg·m^2, the maximum rotated angle has been computed for different altitudes. It is observed in the results shown in Figure 5.30 that small deviations are generated for the worst case scenario ($\theta < 0.035$ deg) which means that the presented method is an interesting solution to cancel out the perturbations generated by the Earth's magnetic field.
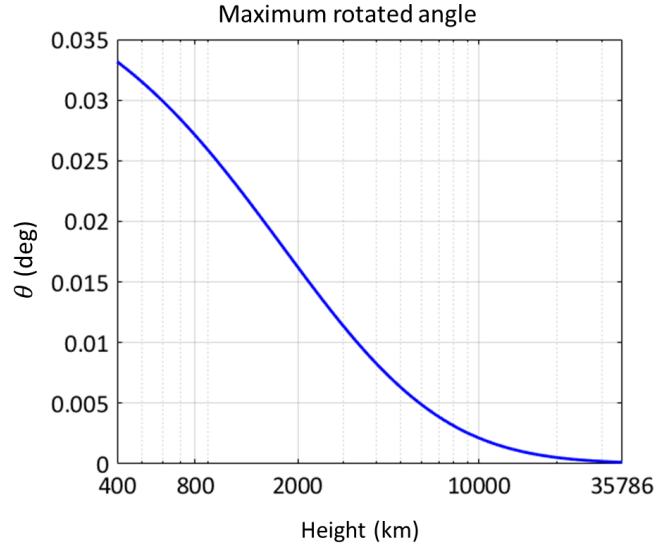
Figure 5.30: Spacecraft rotated angle in the worst case scenario for an AC current of a cycle period of 1 second.

Furthermore, the effect of an alternating magnetic field on the target object must be assessed. Section 3.4 provides a generalisation of the MTT which includes the effect of alternating currents. For a rotating target subject to a time-varying magnetic field, the induced magnetic moment has the form,

$$\vec{m} = \mathbf{M}\vec{\Omega}_{tot} = \mathbf{M}(-\frac{\partial \vec{B}}{\partial t} + \vec{\omega} \times \vec{B}) = \vec{m}_1 + \vec{m}_2. \tag{5.43}$$

Moreover, as the field generated by the coil is non-homogeneous, the effective magnetic tensor defined in Subsection 3.3.7.1 should be used to account for the efficiency loss derived from the non-uniformity of the field.

The first term in Equation (5.43), proportional to $-\frac{\partial \vec{B}}{\partial t}$ will neither contribute to the magnetic torque nor on the magnetic force of the target. The magnetic field created at a certain point in

space, $\vec{r} = (x, y, z)$, by the coil on-board the chaser spacecraft is a function of the position vector and the intensity of the coil,

$$\vec{B}(\vec{r}, t) = I_c(t) \cdot \vec{b}(\vec{r}), \tag{5.44}$$

where $\vec{b}(\vec{r})$ is the magnetic field created by a unitary electric current.

In addition, the Jacobian tensor of the magnetic field is,

$$\mathbf{\Lambda}(\vec{r}, t) = I_c(t) \cdot \boldsymbol{\lambda}(\vec{r}), \tag{5.45}$$

where $\boldsymbol{\lambda}(\vec{r})$ is the Jacobian tensor generated by a unitary electric current.

The magnetic torque generated by $\vec{m}_1$ over one AC cycle is zero as demonstrated below,

$$\left\langle \vec{T}_1 \right\rangle = \frac{1}{T} \int_0^T \vec{m}_1 \times \vec{B} dt = \frac{1}{T} \int_0^T (-\mathbf{M} \frac{\partial \vec{B}}{\partial t}) \times \vec{B} dt = -\frac{1}{T} \overbrace{(\int_0^T \dot{I}_c(t) I_c(t) dt)}^{=0} (\mathbf{M}\vec{b}) \times \vec{b} = \vec{0}, \tag{5.46}$$

$$\int_0^T \dot{I}_c(t) I_c(t) dt = I_{max}^2 \omega_{ac} \int_0^T \sin(\omega_{ac} t) \cos(\omega_{ac} t) dt = 0. \tag{5.47}$$

Note that in (5.46) it has been assumed that the angle between $(\mathbf{M}\vec{b})$ and $\vec{b}$ does not change with time during one AC cycle.

Furthermore, the magnetic force that appears due to the non-homogeneity of the field is also zero as proven subsequently,

$$\left\langle \vec{F}_1 \right\rangle = \frac{1}{T} \int_0^T \mathbf{\Lambda} \vec{m}_1 dt = -\frac{1}{T} \int_0^T \mathbf{\Lambda} \mathbf{M} \frac{\partial \vec{B}}{\partial t} dt = -(\frac{1}{T} \int_0^T \dot{I}_c(t) I_c(t) dt) \boldsymbol{\lambda} \mathbf{M} \vec{b} = \vec{0}. \tag{5.48}$$

The second term in Equation (5.43), proportional to the angular velocity of the target, will generate a dissipative torque as studied in Chapter 3. Note that the current intensity of the chaser's coil will change direction periodically and thus, the magnetic field. However, due to the eddy currents dissipative nature, the generated torque on the target will always oppose its angular velocity, no matter the direction of the field (unless the magnetic field is parallel to the angular velocity vector which generates no torque).

However, the efficiency of the de-tumbling process will decrease by a factor of 2 with respect to the DC current as the average value of the magnetic torque over 1 cycle is equal to,

$$\left\langle \vec{T}_2 \right\rangle = \frac{1}{T} \int_0^T \vec{m}_2 \times \vec{B} dt = \frac{1}{T} \int_0^T (\boldsymbol{M}(\vec{\omega} \times \vec{B})) \times \vec{B} dt = \frac{1}{T} [\int_0^T (I_c(t))^2 dt] (\boldsymbol{M}(\vec{\omega} \times \vec{b}_r)) \times \vec{b}_r =$$

$$= \frac{I_{max}^2}{2} (\boldsymbol{M}(\vec{\omega} \times \vec{b}_r)) \times \vec{b}_r = \frac{1}{2} \vec{T}_{DC}, \tag{5.49}$$

where $\vec{T}_{DC}$ is the torque generated by a DC current of intensity I_{max}. Note that in (5.49) it has been assumed that the variation of angular velocity of the target, $\vec{\omega}$, over one cycle is negligible, as well as the angle made by $\vec{\omega}$ and $\vec{b}_r$.

Therefore, the AC magnetic field received by the target may be averaged as,

$$B_{AC} = \frac{B_{DC}}{\sqrt{2}}. \tag{5.50}$$

Similarly, the magnetic force generated on the target is equal to,

$$\left\langle \vec{F_2} \right\rangle = \frac{1}{T} \int_0^T \boldsymbol{\Lambda} \vec{m}_2 dt = \frac{1}{T} \int_0^T \boldsymbol{\Lambda M}(\vec{\omega} \times \vec{B}) dt = \frac{1}{T} [\int_0^T (I_c(t))^2 dt] \boldsymbol{\lambda M}(\vec{\omega} \times \vec{b}_r) =$$
$$= \frac{I_{max}^2}{2} \boldsymbol{\lambda M}(\vec{\omega} \times \vec{b}_r) = \frac{1}{2} \vec{F}_{DC}. \tag{5.51}$$

All in all, the use of an AC current throughout the de-tumbling process seems a promising solution to avoid the Earth's magnetic perturbations on the chaser at the expense of increasing the characteristic time of the de-tumbling process by a factor of 2. A trade-off will need to be carried out for each specific mission depending on the orbit altitude and the coil employed. For instance, for altitudes in the geostationary region, the Earth's magnetic interactions are very small and it should be more advantageous to work in the DC regime.

5.5.4.2 Skin effect

As the frequency increases, the electric current tends to be concentrated near the surface of a conductor. This phenomenon is known as the *skin effect* [111]. This effect is due to opposing eddy currents induced by the changing magnetic field resulting from the alternating current.

As a first approximation, the skin depth, δ, may be obtained using the following formula [140],

$$\delta = \sqrt{1} \mu_r \mu_0 \sigma f, \tag{5.52}$$

where μ_r is the relative permeability of the conductor, μ_0 is the permeability of free space, σ is the conductivity of the conductor and f is the frequency of the AC currents.

Figure 5.31 plots the skin depth against various frequencies for an aluminium conductor. It is outlined that the computed skin depth is much bigger than typical metallic thicknesses of satellite components and structures, which are in the order of few millimetres or less. Therefore, this effect may be neglected for the low AC frequencies analysed in the previous section.
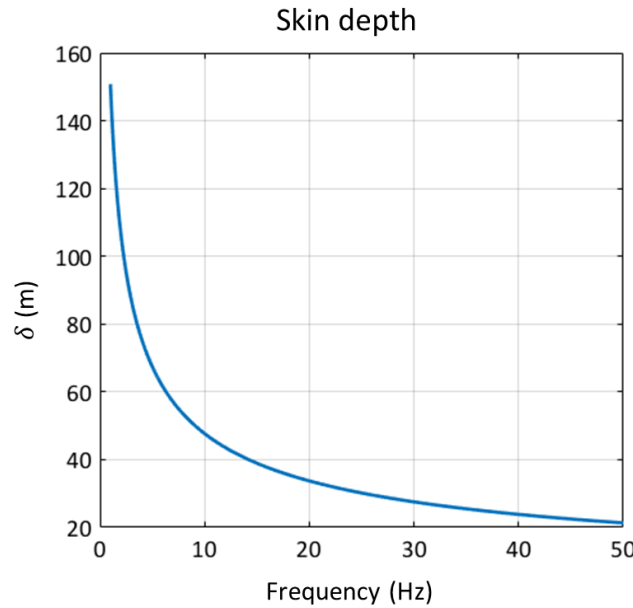
Figure 5.31: Skin Depth.

5.6   Electromagnetic interferences and coil configuration

With respect to the electromagnetic interferences, some instruments may suffer performance degradation in the presence of a magnetic field.

For instance, information that is magnetically recorded can be altered or erased. In addition, the magnetic fields will also deviate moving charged particles which can alter the functioning of the concerned device. Furthermore, if there are instruments on-board which have ferromagnetic materials, this may saturate and deteriorate the device performance. Forces will also be generated between the coil and the ferromagnetic material. Therefore, the use of ferromagnetic components in the chaser's design should be avoided or adequately shielded.

Some of the sensitive equipment that has been identified is listed below [113]:

- Magnetometers

- Magnetic latching relays

- Photomultipliers

- Travelling wave tubes

- Coaxial switches

- Tape recorders

From an instrumentation perspective, the use of coils in space missions that generate high magnetic fields is achievable with careful design as demonstrated in the missions alpha magnetic spectrometer AMS-01 and AMS-02 [184, 185]. The AMS-01 was a simplified version of AMS-02, launched the Space Shuttle Discovery on STS-91 in June 1998. After the flight of the prototype, AMS-02 was launched and installed as an external module on the International Space Station in 2011. The AMS-02 mission goal is to carry out precise measurements of cosmic rays fluxes in LEO. The AMS-02 magnet was built with permanent magnets made of Nd-Fe-B, it weighs 6717 kg and it consumes between 2 kW and 2.5 kW. The instrument produces a maximum magnetic field of 0.15 Teslas in the inner part and a weaker field with a value of 0.02 T in the external part, in order to avoid electromagnetic interferences and mechanical stresses to the ISS and to the other nearby ISS payloads [184, 185].

The maximum value of the magnetic field will appear at the centre of coil. For a coil based on the specifications listed in 5.1, the magnetic field generated at the centre of the coil is equal to 0.013 T which is lower than the field produced by the AMS-02 magnet. Although the results obtained for the eddy brake are promising, a thorough analysis still needs to be done to assess if the chaser's equipment can cope with the maximum value of the field. In general, it is advisable to avoid the use of the sensitive equipment listed above as well as the use of ferromagnetic materials.

In addition, the electromagnetic coil can be fixed to the main body of the chaser or moved away from the main body using a deployable structure. The first option reduces the complexity of the design as no mechanisms and additional structures are used. The second option is based on a deployable structure that moves away the coil from the main body of the chaser minimizing the electromagnetic interferences. Furthermore, additional mechanisms could be added in order to give the coil independent pointing control instead of rotating the whole spacecraft (see Figure 5.32).
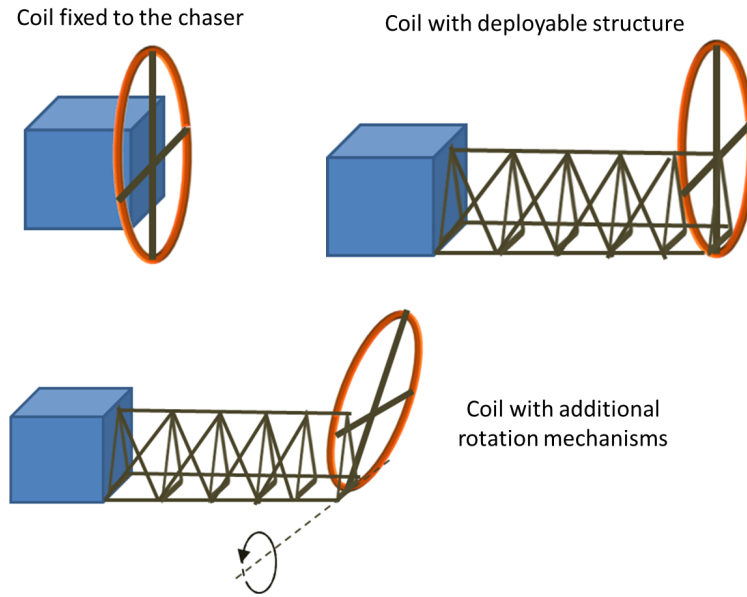
Figure 5.32: Possible configurations of the coil on-board the chaser spacecraft.

Nevertheless, the use of a deployable structure would greatly increase the complexity and the risk of the mission as indicated in Table 5.34. Moreover, the thermal subsystem based on a cryocooler and a LHP would need to be also deployed together with the coil. This means that the chaser's inertia would greatly change between the stowed and the deployed configuration, creating a highly asymmetric spacecraft. This situation together with the fact that the structure will introduce some flexible modes in the system, would lead to an increase in the complexity of the operations and the attitude control. Therefore, the introduction of deployable structures in the design is not desirable.

Moreover, there is an additional design option based on the use of a deployable coil (see Figure 5.33). Some studies on deployable HTS magnetic coils have been carried out for human space applications [186, 187] but the TRL is still very low. When an electric current flows through a coil, radial forces appear on the coil which would passively expand it. This option would allow the size of the coil to be increased which is fixed otherwise by the maximum fairing diameter of the launcher. In spite of the fact that this idea seems appealing in terms of volume and efficiency, it still involves numerous challenges which highly increase the risk of the mission. The most important one is related to the thermal control subsystem because at present, deployable heat pipes do not exist and they are critical in solving the thermal constraints as highlighted in Subsection 5.4.2.
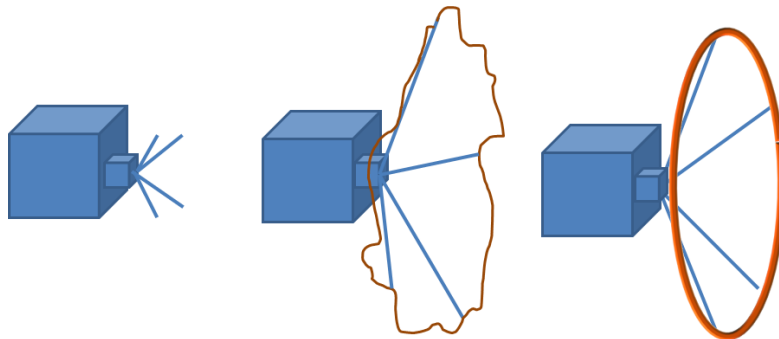
Figure 5.33: Deployable coil.

Finally, Table 5.34 compares all the possible options. The fixed coil is the preferred option because

it minimises the complexity and the risk of the mission.
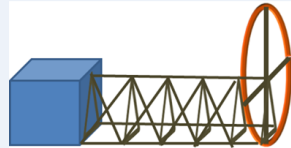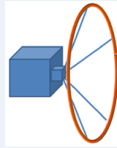
	Fixed coil to the chaser	Deployable structure	Deployable coil
Mass	Mass given by the coil	A deployable structure is needed	A deployable structure is needed
Volume	Volume given by the coil	Additional volume needed (coil +stowed structure)	Less volume required (coil and the structure are stowed)
Risk	No mechanical or moving parts	If the structure is not deployed, the coil could still work	If the coil is not deployed → complete failure
TRL	Similar coil designs have been tested on ground (e.g. EMFF)	A customized deployable structure must be designed	Only conceptual studies exist
Operations complexity	Fixed-size system should be inherently more rigid.	Inertia is modified between the stowed and deployed config. Flexible modes.	Inertia is modified between the stowed and deployed config. Flexible modes.
Electromagnetic interference	Higher interferences	Less interference.	Less interference.
Thermal control	Less complex	More complex	More complex
Sketch			

Figure 5.34: Configuration trade-off.

5.7   Baseline design and system budgets

The baseline design specifications for the electromagnetic coil are listed in Table 5.11.

Design specifications	
Wire type	2G HTS SCS4050 wire
Working temperature	$T_c = 77$ K
Coil intensity	$I_c = 80$ A
Major coil radius	$R_c = 2$ m
Minor coil radius	$r_c = 0.045$ m
Number of turns	$N = 500$
Insulation	MLI layer of 0.01 m thick
Thermal control	LHP+cryocooler
Configuration	Fixed coil

Table 5.11: Design specifications.

Moreover, the mass and power budgets are outlined in Tables 5.12, 5.13, 5.14 and 5.15. Note that these budgets just show the most important equipment required by the eddy brake.

Two different scenarios are analysed. The first one assumes that CMGs are needed within the AOCS/GNC subsystem (see Tables 5.12 and 5.14) and the second one assumes that RWs can be employed instead of CMGs (see Tables 5.13 and 5.15).

In case CMGs are needed in the systems engineering design, the total mass of the eddy brake including 20% margin is equal to 214.7 kg and in the case of RWs, the total mass is 141.2 kg. This difference in mass is an important consideration to be kept in mind in the design. For instance,

CMGs may be avoided in LEO if an AC current is employed instead of a DC current as explained in Section 5.5.4.

Component	Mass per unit	Number	Total Mass	Comment
Electromagnetic coil				
Coil	22.4	1	22.4 kg	
Thermal Subsystem				
LHP structure	15.9 kg	1	15.9 kg	Al. envelope+wick
LHP working fluid	1 kg	1	1 kg	
Cryocooler K535	9.5 kg	2	19 kg	
Misc. cryocooler	15 kg	2	30 kg	Structure+electronics
GNC Subsystem				
DragonEye 3D	3 kg	1	3 kg	
22N RCS Thrusters	0.65 kg	24	15.6 kg	
CMG 15-45S	18 kg	4	72 kg	
Margin (%)			20%	
Total mass incl. margin			214.7 kg	

Table 5.12: Total mass budget with CMGs.

Component	Mass per unit	Number	Total Mass	Comment
Electromagnetic coil				
Coil	22.4	1	22.4 kg	
Thermal Subsystem				
LHP structure	15.9 kg	1	15.9 kg	Al. envelope+wick
LHP working fluid	1 kg	1	1 kg	
Cryocooler K535	9.5 kg	2	19 kg	
Misc. cryocooler	15 kg	2	30 kg	Structure+electronics
GNC Subsystem				
DragonEye 3D	3 kg	1	3 kg	
22N RCS Thrusters	0.65 kg	24	15.6 kg	
RW 250	2.7 kg	4	10.8 kg	
Margin (%)			20%	
Total mass incl. margin			141.2 kg	

Table 5.13: Total mass budget with RWs.

Moreover, the average power consumption is 402 W if CMGs are employed and 368.4 W if RWs are employed. All in all, the use of RWs lead to a significant decrease both in terms of mass and power which favours the use of RWs instead of CMGs if the mission requirements allow for it.

Component	Number	Average power	Peak power	Total av. power	Total peak power
Cryocooler K535	2	100 W	150 W	200 W	300 W
DragonEye 3D	1	35 W	-	35 W	-
CMG 15-45S	4	25W	-	100W	-
Margin (%)				20%	
Total av. power incl. margin				402 W	

Table 5.14: Power budget with CMGs.

Component	Number	Average power	Peak power	Total av. power	Total peak power
Cryocooler K535	2	100 W	150 W	200 W	300 W
DragonEye 3D	1	35 W	-	35 W	-
RW 250	4	18W	-	72W	-
Margin (%)				20%	
Total av. power incl. margin				368.4 W	

Table 5.15: Power budget with RWs.

5.8 The Agora mission

Agora (Active Grabbing & Orbital Removal of Ariane) is a proposed technology demonstration mission geared towards raising the TRL of key ADR technologies [19, 188].

The phase 0 study for this mission was conducted between November 2014 until January 2016 in collaboration with the University of Strathclyde (Glasgow, UK), the DFKI Robotics Innovation Centre (Bremen, Germany) and the companies Dinamica Srl and D-Orbit Srl (Italy) as part of the Stardust Programme [189].

This study enabled the opportunity to analyse the eddy brake as part of an overall ADR mission system design. The present section aims at providing a brief overview of the mission and overall system characteristics in Subsections 5.8.1 and 5.8.3. Subsequently, special emphasis is laid on the de-tumbling subsystem design and operation in 5.8.4.

5.8.1 Mission overview

Agora is an in-orbit demonstration mission with the main goal of demonstrating technologies to autonomously remove an Ariane R/B in a controlled manner. The chaser is launched as a secondary payload of the Ariane-5 launcher in the SYLDA dispenser [121] into a GTO orbit along with the proposed target which is the Ariane-5 Etage Propergols Stockables (EPS) upper stage.

The Ariane-5 upper stage depicted previously in Figure 2.9 is composed of three main parts; the Storable Propellant Stage (EPS), the Vehicle Equipment Bay (VEB) and the Separation and Distancing Module (SDM). Additional data on the mass, inertia and dimensions is provided in Table 5.16. This upper stage has the capability of re-ignition and therefore, controlled re-entry in case of failure of the mission. Moreover, the VEB of the upper stage contains two on-board computers (OBCs), two inertial guidance units, electrical power supplies and telemetry equipment which allow the target to be monitored from ground. Furthermore, the VEB comprises a hydrazine attitude control system which provides the R/B with full attitude control capability.

The payload consists of three primary elements:

1. the eddy brake de-tumbling system,

2. a robotic manipulation system, consisting in a clamp mechanism and a robotic arm,

3. and the de-orbit kit.

These elements are illustrated in Figure 5.35.
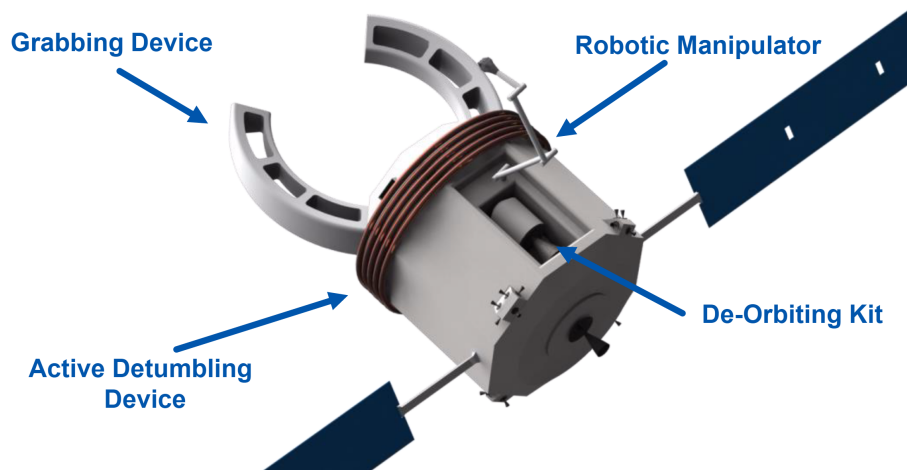
Figure 5.35: Agora spacecraft concept.

The mission phases are described subsequently:

- Far-range rendezvous phase: Given the fact that the target is the upper stage of the launcher, both objects should be placed at the same orbital plane, separated by tens of km. Thus, this eliminates the need for phasing. The chaser will then need to reduce the relative distance down to a few hundreds of metres.

- Fly-around phase: This phase consists in a visual inspection of the target in order to estimate its pose. The data obtained by the chaser is compared with the data provided by the target's AOCS sensors to fully validate the pose estimation techniques employed by the chaser.

- De-tumbling phase: A set of in-orbit demonstration experiments defined in Subsection 5.8.4 will be carried out to raise the TRL of this technology. The target will then stabilise itself to reach a tumbling rate below 1 deg/s.

- Attitude estimation phase: The attitude of the target will be determined once again by the chaser.

- Approach phase: The chaser will reduce its relative distance down to few meters with full contingency measures in place.

- Capture and stabilisation phase: The clamping mechanism will capture the target while damping any residual relative motion. The self-locking mechanism will be activated and the compound chaser-target stabilised.

- De-orbit kit insertion phase: The robotic arm will be deployed and used to insert the de-orbit kit inside the nozzle of the target's main engine.

- Disengagement phase: The chaser will re-orient the composite system to the required position and attitude and then it will disengage from the target and separate by 50 metres.

- De-orbiting phase: The de-orbit kit will be ignited and carry out a controlled re-entry of the target by a single burn.

The de-tumbling phase, capturing phase and de-orbit kit insertion phase are illustrated in Figure 5.36.
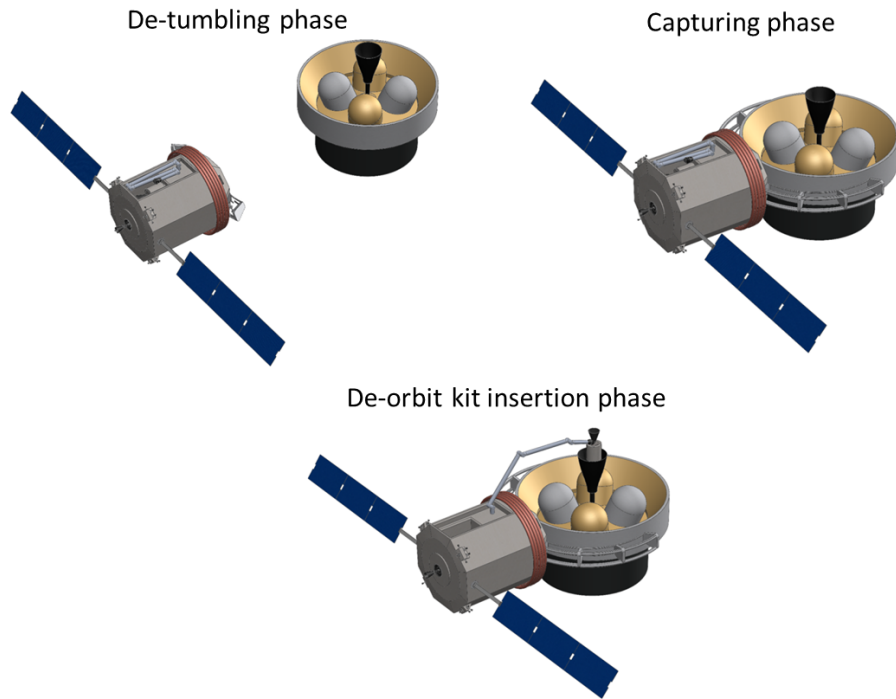
Figure 5.36: Agora de-tumbling, capturing and de-orbit kit insertion phases.

Tables 5.16, 5.17 and 5.18 list the main mission parameters and provide a global system overview.

Mission description	
Launcher	Ariane-5 as secondary payload
Launch Date	2025
Lifetime	4 months
Orbit	GTO
Cost budget	200 MEuro
Overall chaser's characteristics	
Mass	Dry Mass: 1466 kg (incl. margins)
	Wet Mass: 1833 kg
	Launch Mass: 1983 kg (incl. adapter)
Dimensions	Stowed: 5.32 m (L) × 4.00 m (W) × 3.37 m (H).
	Deployed: 6.89 m (L) × 17.38 m (W) × 3.37 m (H).
Principal inertias	$I_{xx} = 2128$ kg·m^2, $I_{yy} = 2128$ kg·m^2, $I_{zz} = 1631$ kg·m^2
Overall target's characteristics	
Target type	Ariane-5 EPS upper stage
Mass	Dry Mass: 2550 kg. Wet Mass: 3550 kg
Dimensions	Length: 4.6 m. Diameter: 5.6 m
Principal inertias	$I_{xx} = 11148$ kg·m^2, $I_{yy} = 8058$ kg·m^2, $I_{zz} = 6479$ kg·m^2

Table 5.16: Agora system overview [19].

Payload	
Eddy brake	HTS coil, 500 turns of wire SCS 4050 model manufactured by SuperPower. Major radius 1.65 m. Total mass 22.2 kg.
Clamp	Custom design based on a semi-rigid structure consisting of two fingers made of rubber and metal, thermoset plastic insets and reinforced strings. Total mass 130 kg. Finger's length 4.73 m and width 0.62 m.
Robotic arm	Design based on the DEOS mission. Seven connected joints connected with an aluminium alloy structure. Total mass 55 kg. Length 5.25 m and diameter 0.14 m.
De-orbit kit	D3 de-orbit kit under development at D-Orbit. Solid propulsion kit, equipped with avionics system. Total mass: 144 kg

Table 5.17: Agora payload [19].

Subsystems	
Structure	Octagonal bus structure based on ESA's Automated Transfer Vehicle (ATV)
Power	Power consumption: 718 W Solar array: Two rotating deployable solar array wings of 6.3 m^2 each, three panels per wing and total EoL Power: 1703 W Batteries: 2 modules Li-Ion rechargeable 30 A·h
Mechanisms	SA deployment mechanism
AOCS/GNC	Four CMGs, two near-field cameras, two 3D flash LIDARs, two far field infrared cameras, two Sun sensors, three star trackers, three IMUs and two GPS receivers
Comms.	Three omni-directional X-band antennas. Three TDRS S-band antennas.
Propulsion	Bipropellant thruster of 400 N 24 bipropellant attitude control thrusters (22 N each)
Thermal	Active thermal for the eddy brake based on a LHP and two cryocoolers Service module thermal control based on MLI blankets, HPs and radiators

Table 5.18: Agora subsystems [19].

Figure 5.37 illustrates the overall dimensions of the Agora spacecraft.
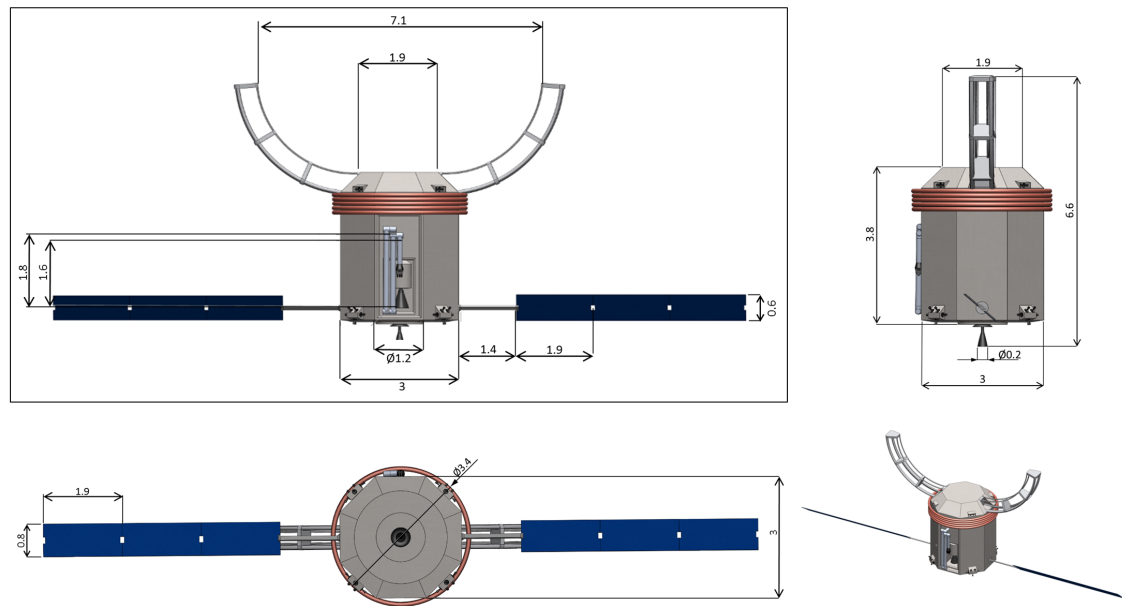
Figure 5.37: Agora chaser's dimensions (in metres) [19].

5.8.2 Systems budgets

The mass and power budgets are summarised in Tables 5.19 and 5.20. It may be observed that the highest power consumption mode is the de-tumbling mode.

Subsystem	Mass [kg]
Comms	16
GNC	137
Harness	8
Mechanism	20
OBDH	18
Payload	380
Power	97
Propulsion	93
Structure	276
Thermal	88
Dry Mass	**1222**
Dry Mass incl. margin	1466
Propellant	367
Wet mass	1833
Launch adapter	150
Launch mass	**1983**

Table 5.19: Agora mass budget [19].

Mission Modes	Average power [W]	Peak power [W]
Launch Mode	18	18
Init Mode	104	105
Rendezvous/Homing Mode	198	248
Prox. Operations	158	208
De-tumbling Mode	718	759
Manipulation/Grabbing Mode	263	364.5
Safe Mode	119	120
CAM Mode	88	88

Table 5.20: Agora power budget [19].

5.8.3 Main trade-offs

Figure 5.38 illustrates the key mission trade-offs that were performed during the phase 0 study which helped to elucidate the decisions taken to arrive at the mission concept.
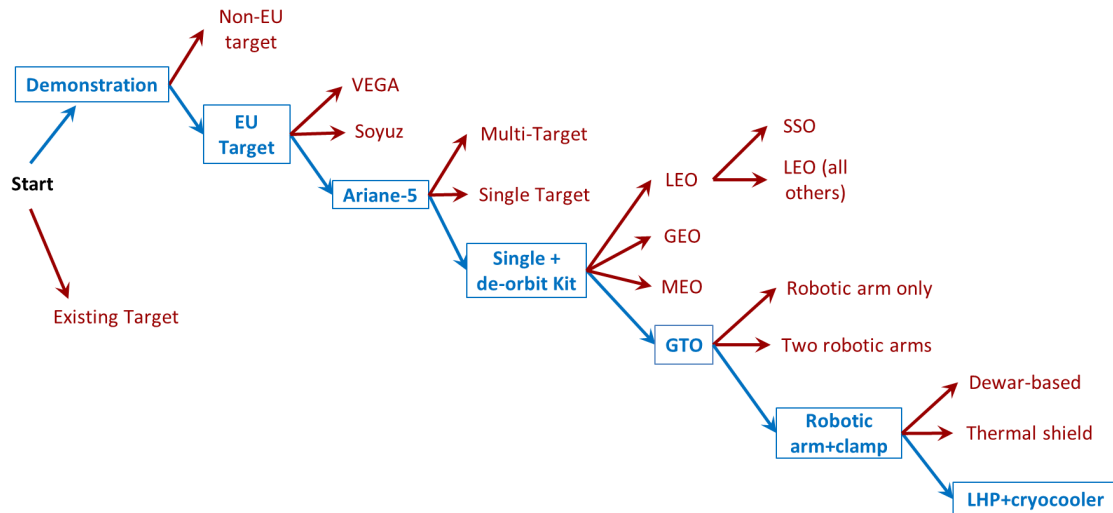
Figure 5.38: Agora decision tree.

- Mission type: The two options considered were a demonstration mission which captures and de-orbits the mission R/B or a real mission which captures an existing R/B in orbit. Due to the current immaturity of ADR processes and technologies, the next logical step is to perform an in-orbit demonstration mission in order to raise the TRL of these technologies. In this context, Agora could serve as a stepping stone for future ADR missions.

- Target type: First of all, a European target was selected as it is more likely to pose less schedule risk and less political opposition. Among the current European R/Bs, three options were traded-off, the Ariane-5 EPS, the Ariane-5 ESC-A and Vega AVUM upper stages. The first option was selected due to the re-ignition capability of the EPS which guarantees a controlled and safe de-orbiting in case of mission failure.

- Single/multi target: ADR technology roadmaps tend to consider multi-target missions in the long term in order to reduce the overall cost per target removed. The decommissioning devices manufactured by the company D-Orbit Srl [190] or the project SPADES studied by ESA [191] are some of the proposed solutions for undertaking multi-target missions with de-orbit kits. Under this rationale, it was decided to design a single target mission with one de-orbit kit from D-Orbit Srl in order to raise the TRL of this technology.

- Orbit type: The orbit selection was driven by cost requirements and the likelihood for future launch opportunities. In order to reduce costs, it was decided that Agora should be launched as a secondary payload of the Ariane-5. Consequently, the final orbit reached will be selected by the primary payload and the vast majority of Ariane-5 launches go to GTO. Hence, from a programmatic point of view, the baseline of GTO results in much lower overall risk to the mission goals. Nonetheless, proximity operations in a highly elliptical orbit pose a great challenge for mission analysis and the GNC subsystem. This led to the decision to restrain the de-tumbling in-orbit experiments and the capturing phase during the passes in the vicinity of the apogee. For GTO, there is not a clear consensus on the mitigation practices recommended. Some guidelines recommend a re-orbit by increasing the perigee above the LEO protected region, $h_p > 2000$ km, [40] while others recommend an apogee burn to lower the orbit perigee altitude and achieve a direct de-orbit [38, 192]. A controlled re-entry was adopted to comply with the European mitigation guidelines of ESA and CNES [38, 192].

- Grabbing mechanism: Given the versatility of a robotic manipulator, different approaches for the capturing and placing of the de-orbit kit were envisioned. For instance, the alternative of the robotic manipulator only (no clamp) was analysed. However, due to unconstrained passive gimbal movement of the main engine's nozzle and substantial dynamic coupling between the base spacecraft and the robotic arm, this option was disregarded. Moreover, the option of two robotic arms was traded-off against the clamp + robotic arm option. The capturing process with a clamp offers several advantages in terms of control capability for the selected target and it was decided to select this solution.

- Eddy brake thermal control and coil configuration: Various trade-offs were carried out for the eddy brake subsystem which have already been thoroughly discussed in Sections 5.4 and 5.6. It was resolved to design a fixed-size coil attached to the main bus and an active thermal subsystem based on a LHP and two cryocoolers.

5.8.4 De-tumbling phase

5.8.4.1 Coil design

Based on the trade-offs discussed in Section 5.6, it was decided to fix the coil to the main body of the chaser. The selected radius was chosen based on the maximum radius allowed by the fairing of the Ariane-5 SYLDA launcher. The nominal design for the coil has a radius of $R_c = 1.65$ m and $N = 500$ turns. Moreover, a standard 2G HTS wire was selected, SCS4050 manufactured by SuperPower (see Section A.3 for more detailed specifications). The total mass of wiring needed is 18.5 kg. In addition, it was decided to operate the coil at 65 K which allows for a maximum current intensity of $I_c = 115$ A. In order to keep an isothermal temperature along the coil, the wire is insulated and embedded in a LHP and two cryocoolers are employed for heat extraction as assessed in Section 5.4.

An important aspect to be considered in the chaser design is the possible electromagnetic interference caused by the coil. The maximum field will appear at the centre of the coil and for the baseline design it corresponds to 0.022 T. The recommendations indicated in Section 5.6 were followed in the design such as the avoidance of sensitive equipment (e.g. magnetorquers) or the suppression of ferromagnetic materials where possible.

5.8.4.2 Ariane-5 EPS characterisation

The magnetic tensor of the target was determined based on the available information on the materials present in the Ariane-5 EPS upper stage. This target contains four aluminium propellant tanks for the storage of N_2O_4 and monomethyl hydrazine of 1.410 m in diameter [193] and they are constructed from AA2219 (Al Cu6Mn alloy) which has an electrical conductivity of $\sigma = 17.5 \cdot 10^6$ S/m [31]. They will be assumed to have a thickness of 0.003 m [31]. In addition, the upper stage contains two 30 kg Helium pressurant tanks whose material composition is unknown and therefore,

they won't be included in this study. In addition, the hydrazine attitude control system located at the VEB contains between two and six titanium (Ti6Al4V) spherical hydrazine tanks (whose total number depends on the mission) and 0.0009 m thickness [194]. Additional specifications of the hydrazine tanks adopted for the EPS may be founds in Section A.5 of the Annex. Figure 5.39, illustrates the VEB for flight VA205 launched in 2012 from Kourou where these hydrazine tanks are visualised [20].
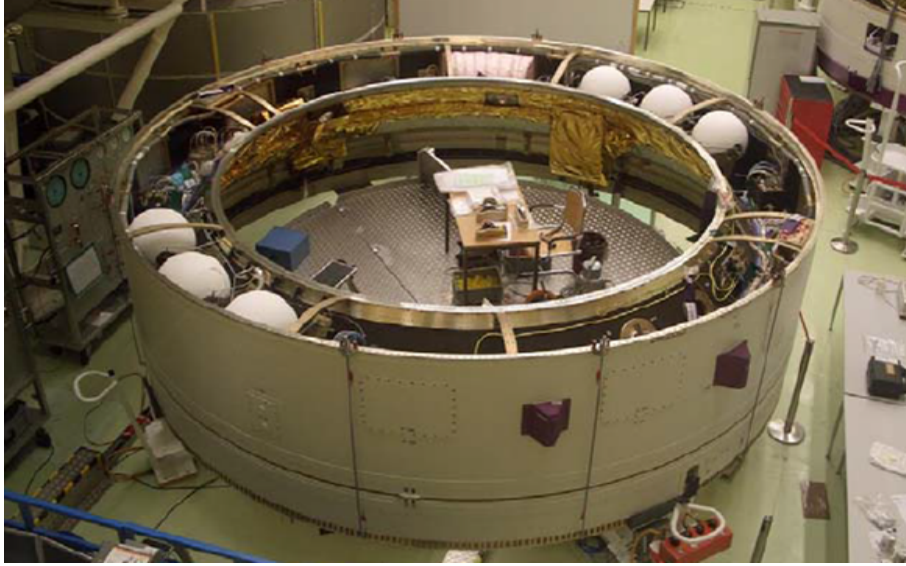
Figure 5.39: Ariane-5 EPS VEB launched in 2012 [20].

Moreover, Ariane-5 nozzles are now typically manufactured with advanced ceramic composite materials (C/SiC) which aims at reducing the mass of older nozzle designs which employed heavy metals [195]. Hence, it will be assumed that this part does not contribute to the eddy current phenomenon.

The VEB structure is typically composed of CFRP (Carbon Fibre Reinforced Plastics) [20, 196]. This part of the upper stage also contains various equipment such as OBCs, electrical power supplies, telemetry equipment, ACS equipment, etc., which should further contribute to the eddy current loop generation. However, in the absence of more detailed information, these components could not be taken into consideration.

The SDM provides the mechanical interface with the spacecraft and it is typically made of CFRP and aluminium structures [197]. The SDM has a length of 1.9 m and a diameter of 3.9 m [7]. In the absence of more detailed information, the SDM was modelled as a cylindrical structure with open ends which has an aluminium skin of 0.0002 m of thickness which is a typical thickness in honeycomb structures and made of the aluminium alloy Al-7075-T6 which is a common alloy used in spacecraft structures [3].

Overall, the magnetic tensor for the upper stage is computed as the sum of three magnetic tensors; the tensor corresponding to the titanium helium tanks $M_{Ti,tanks}$, the aluminium propellant tanks $M_{Al,tanks}$ and the SDM M_{SDM},

$$\boldsymbol{M_{Ti,tanks}} = 2 \cdot (\frac{2}{3}\sigma\pi R_{ti}^4 e_{ti}) \begin{bmatrix} 1 & 0 & 0 \\ 0 & 1 & 0 \\ 0 & 0 & 1 \end{bmatrix} = \begin{bmatrix} 2.11 & 0 & 0 \\ 0 & 2.11 & 0 \\ 0 & 0 & 2.11 \end{bmatrix} \cdot 10^1 \ \text{S} \cdot \text{m}^4, \tag{5.53}$$

where the tanks radii is equal to $R_{ti} = 0.240$ metres, the thickness is $e_{ti} = 0.0009$ m and the

conductivity $\sigma_{ti} = 5.62 \cdot 10^5$ S/m,

$$M_{Al,tanks} = 6 \cdot (\frac{2}{3}\sigma_{al}\pi R_{al}^4 e_{al}) \begin{bmatrix} 1 & 0 & 0 \\ 0 & 1 & 0 \\ 0 & 0 & 1 \end{bmatrix} = \begin{bmatrix} 1.08 & 0 & 0 \\ 0 & 1.08 & 0 \\ 0 & 0 & 1.08 \end{bmatrix} \cdot 10^5 \text{ S} \cdot \text{m}^4, \quad (5.54)$$

where the tanks radii is equal to $R_{al} = 0.705$ metres, the thickness is $e_{al} = 0.003$ m and the conductivity $\sigma_{al} = 17.4 \cdot 10^6$ S/m,

$$M_{SDM} = \pi\sigma_{sdm}R_{sdm}^3 e_{sdm}L_{sdm} \begin{bmatrix} \gamma & 0 & 0 \\ 0 & \gamma & 0 \\ 0 & 0 & \frac{1}{2} \end{bmatrix} = \begin{bmatrix} 1.13 & 0 & 0 \\ 0 & 1.13 & 0 \\ 0 & 0 & 7.70 \end{bmatrix} \cdot 10^4 \text{ S} \cdot \text{m}^4, \quad (5.55)$$

where the SDM radius is equal to $R_{sdm} = 1.95$ metres, the SDM length is equal to $L_{sdm} = 1.9$ m, the thickness is $e_{sdm} = 0.0002$ m and the conductivity $\sigma_{sdm} = 19.42 \cdot 10^6$ S/m.
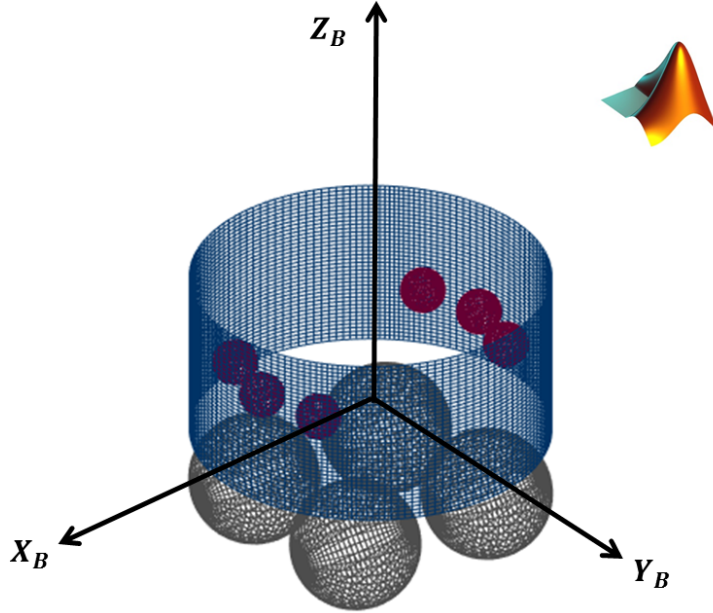
Figure 5.40: Ariane-5 EPS metallic components.

Furthermore, an efficiency factor, μ_{eff}, needs to be added in order to account for losses derived from the non-uniformity of the field. Note that the theory developed in Section 3.3.7 is only valid for quasi-spherical objects. However, the Ariane upper stage is quite a homogeneous body and this theory will be used as an approximation to estimate μ_{eff}. The upper stage sizing envelope is equal to $4.55 \times 5.4 \times 5.4$ metres (see Figure 2.9). In order to compute the efficiency factor, the EPS is modelled as a sphere of $R_{mean} = 2.6$ metres. Figure 5.41 displays the efficiency factor obtained using Equation (3.179) for different relative distances between the coil and the target's COG. For the baseline distance of 10 metres, the efficiency factor is equal to $\mu_{\text{eff}} = 0.963$.

Now, taking into account the additivity property for N bodies rigidly connected but not electrically connected (see Section 3.3.4.4), the overall magnetic tensor is equal to,

$$M_{EPS} = \mu_{\text{eff}}(M_{Al,tanks} + M_{Al,tanks} + M_{SDM}) = \begin{bmatrix} 1.15 & 0 & 0 \\ 0 & 1.15 & 0 \\ 0 & 0 & 1.78 \end{bmatrix} \cdot 10^5 \text{ S} \cdot \text{m}^4. \quad (5.56)$$
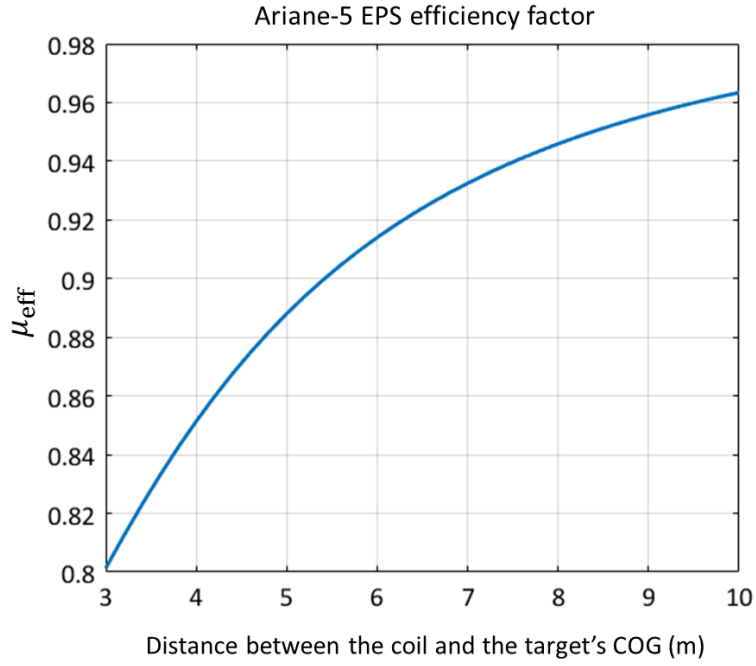
Figure 5.41: Ariane-5 EPS efficiency factor.

The percentage of conductive material considered represents 9.1% of the total target's mass which is a low percentage for the eddy brake to be effective. The characteristic time of decay is now computed for the best and the worst case depending on the relative attitude of the spacecraft. For the baseline Agora coil defined in the previous section (5.8.4.1), the magnetic field generated at a distance of 10 metres is equal to,

$$B_{G,t} = \frac{\mu_0 N I_c}{2} \frac{R_c^2}{(R_c + d)^{\frac{3}{2}}} = 94.5, \mu T \tag{5.57}$$

where Equation (5.57) computes the magnetic field generated along the coil axis at a certain distance d [112], that is, the magnetic moment of the coil is parallel to the relative position vector between the coil and the COG of the target. The various possible configurations for the relative pointing of the coil are further analysed in the next chapter in Section 6.2.2.

Moreover, based on the analysis carried out in Section 5.2, the range in the characteristic time of decay is computed as follows;

$$\tau(d) \in [\tau_{min}(d), \tau_{max}(d)] = \left[\frac{I_{min}}{\mu_{\text{eff}}(d) \cdot M_{max} \cdot B^2(d)}, \frac{I_{max}}{\mu_{\text{eff}}(d) \cdot M_{min} \cdot B^2(d)} \right]. \tag{5.58}$$

The characteristic time of decay is plotted against different relative distances in Figure 5.42. It may also be observed that even if the efficiency factor increases with the relative distance, it is still more beneficial to decrease the relative distance between the two objects to achieve lower values of τ. For the Agora baseline distance of 10 metres, the characteristic time of decay ranges between 49 days and 131 days.
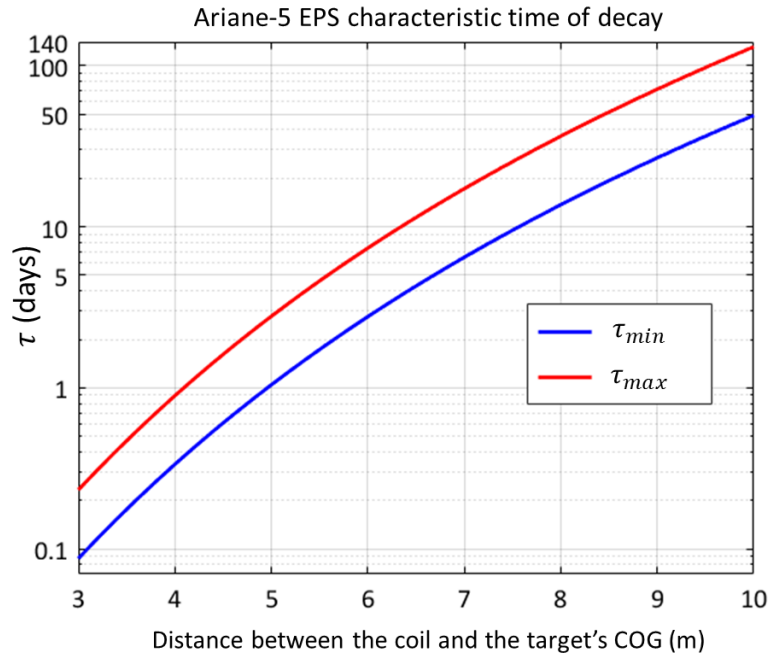
Figure 5.42: Ariane-5 EPS characteristic time of decay.

5.8.4.3 In-orbit experiments

As previously outlined, the goal of the in-orbit demonstration mission for the eddy brake is to raise the TRL of the de-tumbling subsystem. In order to do so, a set of experimental tests have been defined in which a range of parameters will be varied and any changes in the rotational state of the target will be recorded by the sensors on-board the chaser and the target itself. These changes will then be compared against the expected theoretical results obtained with the MTT. The parameters of the system that will be varied include the initial angular velocity of the target, ω_0, the current intensity in the coil, I_c and the relative orientation of the coil with respect to the target.

Figure 5.43 provides an overview of the configuration of the chaser-target setup for the de-tumbling phase. The relative orientation of the coil is given by the angle, θ_C, which corresponds to the angle between the magnetic moment of the coil, $\vec{m}_c$, and the relative position vector, $\vec{r}$. In addition, the angle between the target's angular velocity vector, $\vec{\omega}_t$, and the relative position vector is denoted by α.
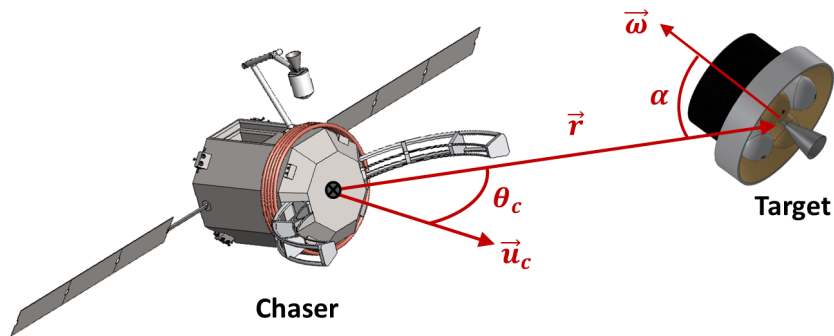
Figure 5.43: Definition of the relative configuration for the de-tumbling phase.

Moreover, the experiments will be carried out throughout a fraction of the GTO orbit in order to minimise the magnetic torques generated by the Earth's magnetic field. The left image in Figure 5.44 plots the orbit altitude against time for two GTO orbits with an apogee altitude of 35786 km and a perigee altitude of 200 km and 600 km. Typically, the perigee of GTO orbits are located within that range of altitudes. For instance, if the duration of the experiment is 10 hours, the de-tumbling process will be conducted within the altitude range [3000-35786] km approximately which is still well above the LEO region and the perturbations introduced by the Earth's magnetic field will be small.
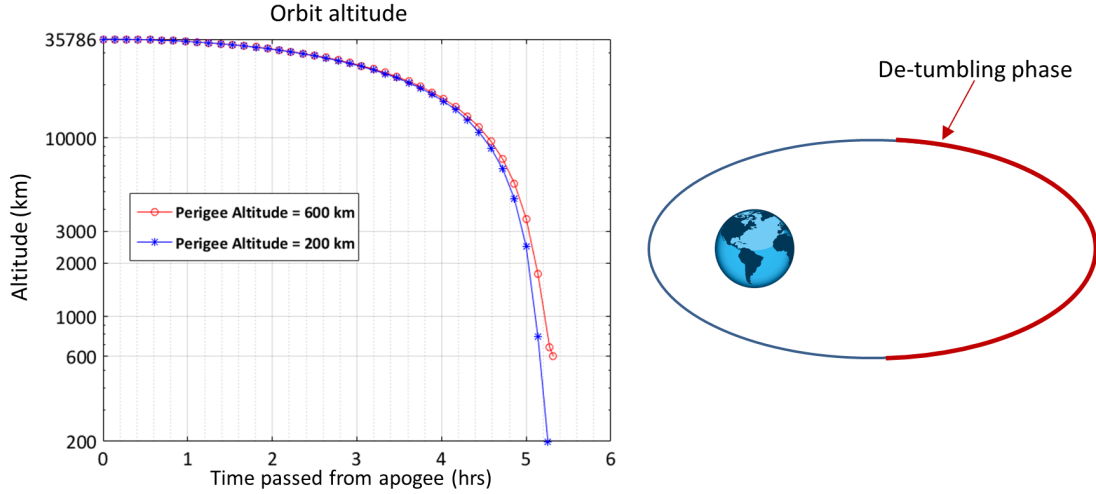
Figure 5.44: Orbit altitude plotted against time (left image) and example of the de-tumbling phase throughout one orbit (right image).

In order to make a rough estimate of the achievable change of the target's spin rate within the aforementioned time frame, a mean characteristic time of decay is first obtained by means of an average value of the inertia and the magnetic tensors of the upper stage,

$$\tau_{av} = \frac{I_{mean}}{\mu_{\text{eff}} \cdot M_{mean} \cdot B^2}. \tag{5.59}$$

Furthermore, as the target object is quite homogeneous in terms of the inertia and magnetic tensors, the spin rate decay, $\Delta\omega(t)$, will be assumed to be equal to that of a spherical shell (see Section 5.2). In Equation (5.60), it has been assumed that the magnetic field vector is perpendicular to the angular velocity vector.

$$\omega(t) = \omega_0 e^{-\frac{t}{\tau}} \rightarrow \Delta\omega(t) = \omega_0(1 - e^{-\frac{t}{\tau}}). \tag{5.60}$$

Moreover, Figure 5.45 plots the average spin rate decrease, $\Delta\omega(t)$ as a function of the time passed and the initial angular velocity of the target. For a test duration of 10 hours, the achievable spin rate decrease ranges between [0.025-0.25] deg/s depending on the initial angular velocity (the higher the initial angular velocity the larger the rate of decrease). The accuracy of the sensors on-board the chaser and the target will be crucial in determining the initial spin rate of the target and the duration of the tests.
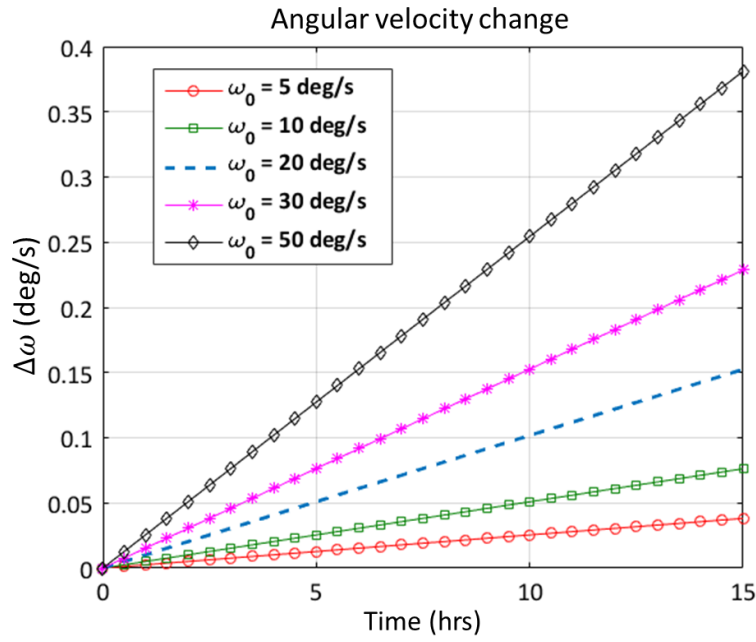
Figure 5.45: Average variation of the target's spin rate plotted against time for different initial angular velocities.

A total number of six different tests are defined and each test should be repeated three times. Taking into account that only one test will be done per orbit, a total amount of 18 days should be dedicated to the experimental tests for the de-tumbling phase. The model philosophy of the in-orbit experimental tests is similar to the process conducted for the laboratory experiments conducted at Airbus Defence & Space described in Chapter 4. First a calibration test is carried out (test #1) with no magnetic field with the goal of determining any spin rate changes caused by the near-Earth environment. The results of this test will determine the noise damping characteristic time of decay, τ_0, which needs to be subtracted from the total characteristic time when adding the effect of the coil. The following tests (#2-#6) include the magnetic field generated by the chaser, varying the electrical intensity of the coil and the relative orientation with respect to the target in each test. Test #2 maximises the eddy current effect as the intensity of the coil is maximum, $I_c = 115$ A, and the magnetic field vector is perpendicular to the angular velocity vector. Test #3 maintains the same intensity but decreases the angle between the magnetic field and the angular velocity vector to 45 deg which will result in a decrease of the spin change. Subsequently, throughout test #4, no change will be caused by the coil as the magnetic field and the angular velocity vectors are parallel. Then, in test #5 the intensity of the coil is reduced in order to visualise a decrease on the spin rate change with respect to test #2. Finally, in test #6, an alternating current is employed in order to assess the loss of efficiency with respect to the DC current. It would also be interesting to test this type of current at lower altitudes in order to verify that the Earth's magnetic field has a negligible effect on the chaser's coil.

#	I_c (A)	θ_c (deg)	α (deg)	d (m)	Duration (hrs)	Iterations
1	0	-	-	10	6	3
2	115	0	90	10	6	3
3	115	0	45	10	6	3
4	115	0	0	10	6	3
5	80	0	90	10	6	3
6	$115 \cdot \sin(\omega_{AC} t)$	0	90	10	6	3

Table 5.21: Agora in-orbit demonstration test plan for the eddy brake.

5.9 Chapter summary

Contact methods for ADR have to deal with challenging procedures such as the capture and stabilisation of tumbling objects. This chapter focuses on the systems engineering design of a novel de-tumbling method called the *eddy brake*.

The eddy brake is an active, contactless, de-tumbling method based on the generation of eddy currents on a rotating metallic object subject to an enhanced magnetic field. Most man-made objects in orbit contain a high ratio of conductive materials (e.g. aluminium, titanium) that make it possible to induce eddy currents. The de-tumbling process is carried out actively by the chaser which has an electromagnetic coil on-board based on high temperature superconducting wires. This technology allows the chaser to be placed several metres away from the target and still generate noticeable magnetic fields inside the space debris object. This way the de-tumbling process may be contactless and thus, eliminate the hazards associated with complicated proximity operations and docking/grabbing of a non-cooperative rotating object.

The electromagnetic coil size will be driven by the fairing diameter of the mission launcher. The selected baseline coil design has a radius of 2 metres and 500 turns. Moreover, the results obtained from the thermal analysis unveiled that the radiation received from the Sun and the Earth are the principal sources that provoke an undesirable warming up of the coil. The baseline thermal design also contains a MLI insulator that protects the HTS wires and slows down the heating process of the coil.

The two most relevant chaser subsystems to support the operation of the eddy brake are the thermal subsystem and the guidance, navigation and control (GNC) subsystem. The thermal subsystem has to guarantee that the coil will always work below its critical temperature and, for this purpose, a loop heat pipe (LHP) plus a cryocooler or a dewar based system could be employed. The cryocooler option is more advantageous in terms of mass and volume and it does not limit the operational lifetime of the coil. However, these benefits are achieved at the expense of high power consumption by the cryocooler which would be avoided otherwise by the dewar-based system. Hence, the dewar-based system is the preferred option for short de-tumbling operations (i.e. in the order of days) while the cryocooler option is more favourable for longer de-tumbling operations.

Moreover the GNC subsystem, which is developed further in Chapter 6, has to ensure a suitable constant relative pointing of the coil and relative distance between the chaser and the target. Within the present chapter, the main requirements as well as the most suitable sensors and actuators for the eddy brake were selected. Moreover, the major environmental perturbation that affects the chaser during the de-tumbling operations was assessed. This perturbation corresponds to the Earth's magnetic field which interacts with the magnetic moment of the chaser's coil yielding an external torque that modifies the satellite's attitude. A way to cancel out the Earth's magnetic torque was identified by employing an alternating electric current of low frequency instead of a direct current. This solution greatly simplified the chaser's attitude control but it increases the characteristic time of the de-tumbling process by a factor of 2.

The chapter concludes with a brief description of the phase 0 study conducted for Agora which stands for Active Grabbing & Orbital Removal of Ariane. This study was performed in the frame of the Stardust programme in collaboration with additional universities and private companies. Agora is a proposed technology demonstration mission geared towards raising the TRL of key ADR technologies. The chaser has three key technologies: a de-orbit kit, a robotic manipulation system, consisting in a clamp mechanism to capture the target and a robotic arm to place the de-orbit kit inside the target's nozzle and the eddy brake de-tumbling system. This study enabled the eddy brake concept to be studied as part of a complete ADR mission system.

CHAPTER

SIX

EDDY BRAKE: DYNAMICS CHASER-TARGET AND EXPERIMENTAL TESTS

6.1 Introduction

The goal of this chapter is to carry out a comprehensive analysis on the dynamics of the chaser-target system based on the magnetic tensor theory and the necessary control throughout the de-tumbling process. The 3D numerical integration process of the eddy brake is a complex problem as it includes a set of non-linear differential equations where the translational and rotational dynamics of the two objects are coupled. The complexity of the problem increases when adding inaccuracies and delays in the control derived from the sensors and actuators which can easily lead to instabilities unless proper control manoeuvres are included.

Within this context, the magnetic interactions based on the MTT are first formulated in Subsection 6.2.1. Then, two relevant relative configurations of the chaser-target system are outlined in Subsection 6.2.2. The first configuration maximises the magnetic field inside the target and thus, minimises the time needed for the de-tumbling process. The second configuration cancels out the relative forces between the chaser and the target.

Subsequently, the set of generalised 3D differential equations is derived in 6.2.3 and Subsection 6.2.4 presents the selected control parameters and control strategy. The control is based on a proportional-derivative (PD) controller in which some calibration parameters, referred to as characteristic times for the manoeuvres, are included and an optimisation criterion to select these parameters is described. In addition, Subsection 6.2.4.1 derives again the 3D dynamical equations for the problem including the proposed control strategy as well as possible inaccuracies and delays derived from sensors and actuators on-board the chaser.

Various case studies of the eddy brake process are included in Section 6.3. Firstly, the numerical simulator developed for this purpose is described in Subsection 6.3.2 which includes the most important environmental perturbations, the magnetic interactions and the control manoeuvres with inaccuracies and delays.

The chapter concludes with some experimental tests that were carried out at the Robotics Innovation Centre, DFKI GmbH, in Bremen (Germany) during a three-month secondment in 2015. These experiments consisted of testing open loop controlled trajectories that simulate the de-tumbling process and the acquisition of real data of the pose of the target using a Bumbleebee2 stereo camera [21].

6.2 Dynamics chaser-target

6.2.1 Magnetic interactions

The first step in the analysis of the dynamics of the chaser-target system is to analyse the magnetic interactions. For this purpose, the MTT developed in Chapter 3 is employed. As explained in Section 5.2, the induced magnetic torque on a rotating metallic target subject to a non-homogeneous magnetic field is equal to,

$$\vec{T}_{ct} = (\mathbf{M_{eff}}(\vec{\omega}_t \times \vec{B}_{Gt})) \times \vec{B}_{Gt}, \tag{6.1}$$

where $\mathbf{M_{eff}}$ is the effective magnetic tensor, $\vec{\omega}_t$ is the angular velocity of the target and $\vec{B}_{Gt}$ is the magnetic field at the target's COG.

Moreover, a force $\vec{F}_{ct}$ is also generated on the target by the chaser due to the non-homogeneity of the field which is given by Equation (6.2),

$$\vec{F}_{ct} = \mathbf{\Lambda_{Gt}}\mathbf{M_{eff}}(\vec{\omega}_t \times \vec{B}_{Gt}), \tag{6.2}$$

where $\mathbf{\Lambda_{Gt}}$ is the Jacobian tensor of the magnetic field at the COG of the target.

Taking into account the conservation of momentum of the chaser-target system, a force of equal magnitude and opposite direction will be generated on the chaser $\vec{F}_{tc}$,

$$\vec{F}_{tc} = -\vec{F}_{ct}. \tag{6.3}$$

The previous relation (6.3) can be also derived from the magnetic dipole approximation. The validity of the dipole formalism is restricted for high relative distances between the two objects. The chaser has a magnetic moment $\vec{m}_c$ and the target a magnetic moment $\vec{m}_t$. The magnetic field created by the chaser dipole is [112],

$$\vec{B}_c = \frac{\mu_0}{4\pi}\left(\frac{3(\vec{m}_c \cdot \vec{r})\vec{r}}{r^5} - \frac{\vec{m}_c}{r^3}\right), \tag{6.4}$$

where $\vec{r}$ is the position vector from the magnetic dipole c. In addition, the Jacobian tensor is equal to,

$$\mathbf{\Lambda_c} = \frac{3\mu_0}{4\pi r^5}\left[(\vec{m}_c \cdot \vec{r})(\mathcal{I} - \frac{5}{r^2}\vec{r}\vec{r}^T) + \vec{m}_c\vec{r}_T + \vec{r} \cdot \vec{m}_c^T\right]. \tag{6.5}$$

Using Equation (3.186) to evaluate the force exerted on the target by the chaser, it results in,

$$\vec{F}_{ct} = \mathbf{\Lambda_c}\vec{m}_t. \tag{6.6}$$

Now, introducing Equation (6.5) in (6.6), the following result is obtained,

$$\vec{F}_{ct} = \frac{3\mu_0}{4\pi r^5}\left[\vec{r}(\vec{m}_c \cdot \vec{m}_t) + \vec{m}_c(\vec{r} \cdot \vec{m}_t) + \vec{m}_t(\vec{r} \cdot \vec{m}_c) - 5\vec{r}(\frac{(\vec{r} \cdot \vec{m}_t)(\vec{r} \cdot \vec{m}_c)}{r^2})\right] = -\vec{F}_{tc}. \tag{6.7}$$

This simply corresponds to Newton's third law that states that when one body exerts a force on a second body, the second body simultaneously exerts a force equal in magnitude and opposite in direction on the first body. Therefore, the force exerted on the target by the chaser is equal to the force exerted on the chaser by the target with opposite direction.

Furthermore, by computing the resultant torques acting on the chaser-target system, the torque that acts on the chaser $\vec{T}_{tc}$ can be derived,

$$\vec{T}_{tc} + \vec{T}_{ct} + (\vec{r} \times \vec{F}_{ct}) = \vec{0} \rightarrow \vec{T}_{tc} = -\vec{T}_{ct} - (\vec{r} \times \vec{F}_{ct}), \tag{6.8}$$

where $\vec{r}$ is the position vector of the COG of the target with respect to the COG of the chaser.

Figure 6.1 depicts an example of the chaser-target interactions for a spherical target, assuming the

magnetic field is perpendicular to the target's angular velocity.
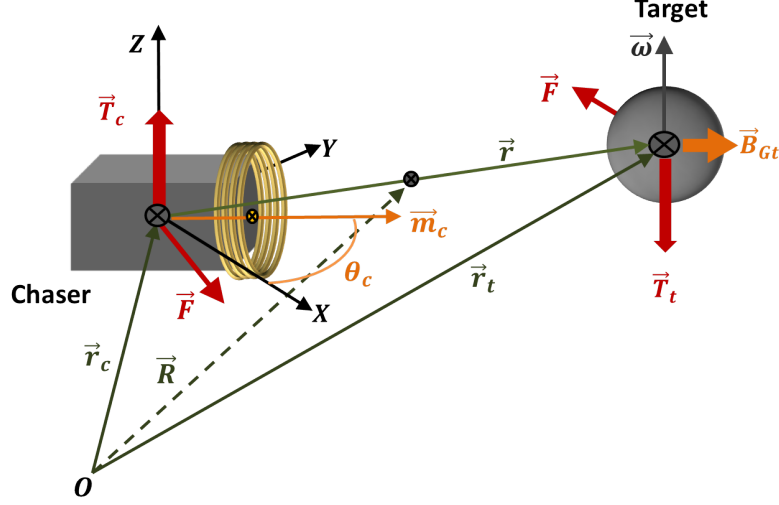
Figure 6.1: Chaser-target interactions.

6.2.2 Relevant relative configurations

Two limiting extreme configurations of the coil with respect to the target for the de-tumbling process are presented in this section (i.e. all other pointing configurations can be expressed as a combination of the two cases described here). The first one, named as ($\parallel$), consists in pointing the coil towards the COG of the target object, that is, the magnetic moment of the coil should be parallel to the relative position vector between the coil and the COG of the target. In this case the magnetic field created inside the target is maximum and therefore, the de-tumbling time is minimum.

The second interesting configuration, named as ($\perp$), consists in pointing the coil perpendicularly towards the target object, that is, the magnetic moment of the coil should be perpendicular to the relative position vector between the coil and the COG of the target. This configuration can minimise or cancel out the magnetic forces between the two objects if some constraints are met. However, the magnetic field decreases to half of the value with respect to configuration ($\parallel$) and the characteristic time of the de-tumbling process is divided by four, which makes the de-tumbling process more time-consuming.

In this section, an analytical development based on magnetic dipoles is used to identify the geometries which result in no magnetic forces appearing during the de-tumbling process. The force between two magnetic dipoles is given by Equation (6.7).

Consequently, in order to have no forces between the two objects, the following conditions must be met,

- The magnetic moment of the coil must be perpendicular to $\vec{r}$ ($\vec{m}_c \perp \vec{r}$).

- The magnetic moment of the target must be perpendicular to $\vec{r}$ ($\vec{m}_t \perp \vec{r}$).

- The magnetic moment of the target and the chaser must be perpendicular to each other ($\vec{m}_t \perp \vec{m}_c$).

The previous conditions apply to any type of object. In the case of a spherical shell, the relative configuration that cancels out the magnetic forces can be easily identified as follows. The magnetic moment of a spherical target of radius R_t, thickness e_t and conductivity σ_t is given by

$$\vec{m}_t = \mathbf{M_{eff}}\vec{\Omega}_{Gt} = \frac{2\pi}{3}\mu_{eff}\sigma_t R_t^4 e_t(\vec{\omega}_t \times \vec{B}_{Gt}) \qquad (6.9)$$

and the force will be zero when the configuration depicted in Figure 6.2 takes place.
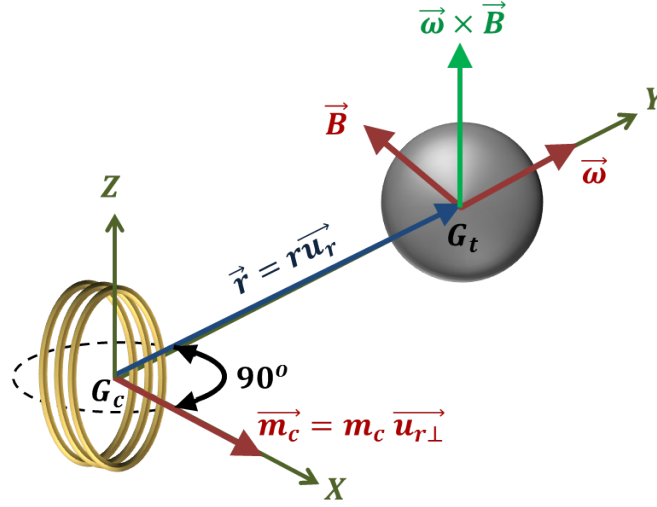
Figure 6.2: Configuration of null force on a spherical shell.

A priori, configuration ($\perp$) may seem interesting to pursue to reduce fuel consumption (as there are no magnetic forces that would separate both bodies). However, this configuration depends on the directions of the angular velocity and magnetic moment of the target, which may also be time-varying with respect to an Earth Centred Inertial (ECI) reference frame. Hence, configuration ($\perp$) may require complex operations for a longer period of time that would increase the total ΔV instead of reducing it. The configuration ($\perp$) would only be of interest if the angular velocity of the target and its physical properties would be such that the chaser could be positioned in the same orbit as the target in order to avoid costly manoeuvres due to differences in the orbital velocities of the two objects.

Therefore, configuration ($\parallel$) seems more realistic from the operational point of view as it will reduce the operational times of the de-tumbling process and it gives more freedom in the choice of the formation flying configurations.

6.2.3 3D Dynamical equations

The full 3D dynamical problem is described by a set of non-linear differential equations listed in (6.10, 6.11, 6.12, 6.13) which involve the position and attitude of the chaser and the target. Equations (6.10, 6.11) indicate the motion of the COG of each object and they are expressed in the ECI reference frame. Equations (6.12, 6.13) are Euler's equations which indicate the angular evolution for each object and it should be noted that these equations are expressed in the body reference frames of each object [95]. The body reference frame is a fixed reference frame to a certain body with its origin at the COG of the object.

$$m_t \ddot{\vec{r}}_t = \vec{F}_{ct} + \sum_i \vec{F}_{ext_i,t}, \tag{6.10}$$

$$m_c \ddot{\vec{r}}_c = \vec{F}_{tc} + \sum_i \vec{F}_{ext_i,c} + \sum_i \vec{F}_{mi,c}, \tag{6.11}$$

$$\mathbf{I_t} \dot{\vec{\omega}}_t + \vec{\omega}_t \times \mathbf{I_t} \vec{\omega}_t = \vec{T}_{ct} + \sum_i \vec{T}_{ext_i,t}, \tag{6.12}$$

$$\mathbf{I_c} \dot{\vec{\omega}}_c + \vec{\omega}_c \times \mathbf{I_c} \vec{\omega}_c = \vec{T}_{tc} + \sum_i \vec{T}_{ext_i,c} + \sum_i \vec{T}_{mi,c}, \tag{6.13}$$

where m_i is the mass of the studied body ($i = t, c$), $\mathbf{I_i}$ is the inertia tensor, $\vec{r}_i$ is the inertial position in the ECI reference frame, $\vec{\omega}_i$ is the angular velocity vector of the body reference frame with respect to the ECI reference frame, expressed in the body reference frame. Moreover, the sum of forces $\sum_i \vec{F}_{ext_i}$ and torques $\sum_i \vec{T}_{ext_i}$ are the external environmental perturbations that may affect each body and the forces and torques named as $\sum_i \vec{F}_{mi,c}$ and $\sum_i \vec{T}_{mi,c}$ are the manoeuvres executed by the chaser.

In Subsection 6.3.2, Equations (6.10, 6.11, 6.12, 6.13) are transformed in the usual way for their numerical integration by adding function derivatives which results in a system of first order differential equations. This numerical integration process is used to solve the numerical simulations in Sections 6.3.

6.2.4 Control manoeuvres

The selected control strategy is based on a proportional-derivative (PD) controller. This classical and simple approach is frequently used for the GNC design [46],[65]. This 3D control strategy is applied in the final case studies (see Section 6.3) in order to test numerically the validity of the proposed manoeuvres.

The control variables identified to achieve a stable configuration throughout the de-tumbling process are:

- Error in the relative distance, ϵ_r, with respect to the desired relative distance d

$$\epsilon_r = \frac{|\vec{r}| - d}{d}, \tag{6.14}$$

$$\vec{r} = r\vec{u}_r = \vec{r}_t - \vec{r}_c, \quad \vec{u}_r = \frac{\vec{r}}{|\vec{r}|}. \tag{6.15}$$

- Error in the relative pointing of the coil, ϵ_θ. If the desired angle between the magnetic moment of the coil $\vec{m}_c$ and the relative vector $\vec{r}$ is θ_d, a possible way to define ϵ_θ is,

$$\epsilon_\theta = \cos(\theta_d) - \vec{u}_r \cdot \frac{\vec{m}_c}{|\vec{m}_c|}, \tag{6.16}$$

although other equivalent functions to control the relative pointing may be more convenient depending on each specific problem.

- Relative angular velocity of the target with respect to the chaser, $\dot{\vec{\epsilon}}_a$, shown in Equation (6.17). It must be noted that the final goal of the de-tumbling process is to nullify $\dot{\epsilon}_a$, so that the target no longer rotates with respect to the chaser.

$$\dot{\vec{\epsilon}}_a = \vec{\omega}_t - \vec{\omega}_c. \tag{6.17}$$

- Modulus of inertial angular velocity of the chaser $\omega_c = |\vec{\omega}_c|$. The inclusion of this last control variable, which may not be as intuitive as the previous ones, is explained subsequently.

All the control variables are gathered in vector $\vec{Z}$ defined in the expression (6.18),

$$\vec{Z} = \begin{bmatrix} \epsilon_r \\ \epsilon_\theta \\ \epsilon_a \\ \omega_c \end{bmatrix}. \tag{6.18}$$

The first three control variables are related to the relative motion between the chaser and the target object. However, it has been identified that at least one inertial control variable (forth control variable) is necessary in the control. Section A.9 in the Appendix provides an analysis of

a simplified 2D configuration where an analytical approach is viable. The approximate theoretical approach developed in Section A.9 is a useful tool to further understand the local behaviour of the system, before dealing with costly and time consuming 3D numerical simulations presented in the following section.

The derivatives $\dot{\epsilon}_r$ and $\dot{\epsilon}_\theta$, which will also be used for the control, may be computed as shown in Equations (6.19, 6.20).

$$\dot{\epsilon}_r = \frac{\left|\dot{\vec{r}}\right|}{d}, \tag{6.19}$$

$$\dot{\epsilon}_\theta = -\left(\vec{\omega}_c \times \frac{\vec{m}_c}{|\vec{m}_c|}\right) \cdot \vec{u}_r - \left(\frac{\dot{\vec{r}}}{|\vec{r}|} - \frac{(\vec{r} \cdot \dot{\vec{r}})}{|\vec{r}|^3}\vec{r}\right) \cdot \frac{\vec{m}_c}{|\vec{m}_c|}. \tag{6.20}$$

Equations (6.21, 6.22, 6.23) indicate the manoeuvres executed by the chaser which are proportional to the control variables and their derivatives as formulated by the PD control. The parameters τ_{mi} $(i = 1, 5)$ that appear in the formulas below are some *'characteristic times of the manoeuvres'* which need to be calibrated in order to achieve a stable and optimal control.

$$\vec{F}_{mc1} = m_c d\left(\frac{\epsilon_r}{\tau_{m1}^2} + \frac{\dot{\epsilon}_r}{\tau_{m2}}\right)\vec{u}_r, \tag{6.21}$$

$$\vec{F}_{mc2} = \left(\frac{m_c d}{\tau_{m3}}\right)(\vec{\omega}_c \times \vec{u}_r), \tag{6.22}$$

$$\vec{T}_{mc1} = \left(\frac{\epsilon_\theta}{\tau_{m4}^2} + \frac{\dot{\epsilon}_\theta}{\tau_{m5}}\right)\mathbf{I_c}\left(\frac{\vec{m}_c}{|\vec{m}_c|} \times \vec{u}_r\right). \tag{6.23}$$

It will be shown in subsequent case studies that an efficient criterion to deduce these characteristic times τ_{mi} is based on the minimization of the total energy consumption, that is, the minimization of the total ΔV of the de-tumbling process. The objective function of the optimisation problem is expressed by Equation (6.24) together with additional possible constraints on the control variables represented by Equations (6.25),

$$\min(\Delta V) = \min\left(\sum_i \int_0^{t_f} \frac{1}{m_c(t)}\left|\vec{F}_{mc_i}(t)\right| dt + \sum_i \int_0^{t_f} \frac{1}{d_{th}m_c(t)}\left|\vec{T}_{mc_i}(t)\right| dt\right), \tag{6.24}$$

$$|\epsilon_r| \leq c_1, \ \ |\epsilon_\theta| \leq c_2, \ \ |\dot{\epsilon}_a| \leq c_3, \ \ |\omega_c| \leq c_4, \tag{6.25}$$

where t_f is the final time of the de-tumbling process, d_{th} is the sum of the lever-arm distances of the thrusters on-board the chaser and c_i $(i = 1, 4)$ are the constraints given to each control variable.

6.2.4.1 Inaccuracies and delays formulation

As explained in Subsection 5.5.3.1, inaccuracies in the control process may come from measurement inaccuracies of the sensors or errors in the execution of the manoeuvres by the actuators. In order to include the possible inaccuracies in the control, the characteristic times of the control manoeuvres and the related parameters R_{mi}, $(R_{m1} = \frac{1}{\tau_{m1}^2}, R_{m2} = \frac{1}{\tau_{m2}}, R_{m3} = \frac{1}{\tau_{m3}}, R_{m4} = \frac{1}{\tau_{m4}^2}, R_{m5} = \frac{1}{\tau_{m5}})$, are treated as functions of time in the numerical integration process. The following change in the R_{mi} parameters is performed using,

$$R_m = constant \rightarrow R_m + \delta R_m(t) = (1 + \chi(t))R_m, \tag{6.26}$$

where a new function $\chi(t)$ is introduced in order to take into account the inaccuracies derived from sensors and actuators. This is modelled as a stochastic variable with mean null value and root

mean square error χ_{cm},

$$\overline{\chi} = 0, \quad \sqrt{\overline{\chi^2}} = \chi_{cm}. \tag{6.27}$$

The function $\chi(t)$ is generated with a random function RND of uniform probability as,

$$\chi(t) = \sqrt{3}(2 \cdot RND - 1)\chi_{cm}, \tag{6.28}$$

which complies with the conditions shown in Equation (6.27). Based on the literature review done in Subsection 5.5.3.1, current pose estimation sensors achieve range accuracies in the order of few centimetres or less at a relative distance of 10 metres, which is approximately 0.1% error ($\chi_{cm} = 0.001$). Attitude accuracies for pose estimation sensors are in the order of 1 degree or less, which is approximately 0.3% error ($\chi_{cm} = 0.003$). Additional errors may come from other sensors and the on-board actuators.

The time delays derived from the software and hardware on-board the chaser also need to be included in the control. For this purpose, a certain delay τ is introduced in the manoeuvres executed by the chaser spacecraft.

All in all, the generic 3D dynamical equations including all these effects are listed in (6.29),

$$m_t \ddot{\vec{r}}_t(t) = \vec{F}_{ct}(t) + \sum_i \vec{F}_{ext_i,t}(t),$$

$$m_c \ddot{\vec{r}}_c(t) = \vec{F}_{tc}(t) + \sum_i \vec{F}_{ext_i,c}(t) + \sum_i (1 + \chi_i(t-\tau))\vec{F}_{mi,c}(t-\tau),$$

$$\mathbf{I_t}\dot{\vec{\omega}}_t(t) + \vec{\omega}_t(t) \times \mathbf{I_t}\vec{\omega}_t(t) = \vec{T}_{ct}(t) + \sum_i \vec{T}_{ext_i,t}(t),$$

$$\mathbf{I_c}\dot{\vec{\omega}}_c(t) + \vec{\omega}_c(t) \times \mathbf{I_c}\vec{\omega}_c(t) = \vec{T}_{tc}(t) + \sum_i \vec{T}_{ext_i,c} + \sum_i (1 + \chi_i(t-\tau))\vec{T}_{mi,c}(t-\tau). \tag{6.29}$$

6.3 Case studies

The goal of the case studies is to numerically test the eddy brake's control method on real targets under realistic environmental conditions.

The chaser considered has an electromagnetic coil with the characteristics defined in Section 5.3.2.2. Moreover, the chaser's mass and inertias are equal to those obtained for the Agora study (see Section 5.8).

6.3.1 Optimisation problem definition

First of all, an optimisation process is carried out to find the characteristic times of the control manoeuvres τ_{mi} that minimise the overall ΔV. The search space considered has been restricted to $\tau_{mi} = [10^{-8}, 10^5]$ s and the optimisation process has the following goal and constraints:

- Goal: Decrease the angular velocity of the target from 10 deg/s until 3 deg/s with the minimum propellant consumption.

- Constraints:

    - Relative distance $d = 10 \pm 0.2$ m.

    - Relative pointing $\epsilon_\theta = \pm 10$ deg.

    - Angular velocity $\omega_c < 3$ deg/s.

6.3.2 Numerical simulator

The numerical simulator described in Section 3.5.1 has been upgraded in order to numerically simulate the eddy brake de-tumbling method. To this end, the translational and rotational dynamics of the chaser and the target object must be incorporated including the environmental perturbations that affect each object separately as well as the magnetic interactions between the two objects. In addition, the chaser must execute control manoeuvres in order to keep the selected formation flying configuration throughout the de-tumbling process. Furthermore, delays and inaccuracies have been introduced in the execution of the manoeuvres in order to reproduce a realistic environment for the eddy brake method.

The numerical integration process is a complex problem as it includes 24 non-linear first order differential equations (12 equations for the chaser and 12 equations for the target). The state vector that represents the translational and rotational kinematics for each body is represented by the vector $\vec{y}$ as described in Section 3.5.1,

$$\vec{y} = \begin{bmatrix} \vec{r}_{in} \\ \vec{v}_{in} \\ \vec{\alpha}_{in} \\ \vec{\omega}_b \end{bmatrix}. \tag{6.30}$$

The system of 12 non-linear differential equations that needs to be solved for each body is equal to,

$$\begin{bmatrix} \dot{\vec{r}}_{in} \\ \dot{\vec{v}}_{in} \\ \dot{\vec{\alpha}}_{in} \\ \dot{\vec{\omega}}_b \end{bmatrix} = \begin{bmatrix} \vec{v}_{in} \\ \sum \vec{F}_{ext} \\ f(\alpha, \vec{h}_{in}, \vec{\omega}_{in}) \\ \mathbf{I}^{-1}(\sum \vec{T}_{ext} - (\vec{\omega}_b \times \mathbf{I}\vec{\omega}_b)) \end{bmatrix}, \tag{6.31}$$

where $\sum \vec{F}_{ext}$ and $\sum \vec{T}_{ext}$ are the sum of all the external forces and torques acting upon the object, including the environmental perturbations and the manoeuvres for the control.

The integration method employed is the explicit method Runge Kutta of 4th order [158] and the timestep is equal to 1 second. Furthermore, the following external forces and torques have been included in the propagator;

- Earth's gravity field: The force due to the Earth's gravity field has been modelled including 4 zonal harmonic coefficients J_i ($i = 2, 3, 4$) from JGM-3 gravitational model [157]. The Earth's gravity gradient has been modelled employing Equation (2.13).

- Atmospheric drag: The atmospheric force and torque have been included in the propagator [103]. The atmospheric density has been computed using the Jacchia 1970 model for medium solar activity (F10=140, Ap=15) [124]. In addition, a mean value of the drag coefficient equal to $C_D = 2.3$ has been adopted for every object in orbit.

- Solar radiation pressure: The SRP force and torque have been included in the propagator [103]. This perturbation is only considered when the spacecraft comes out of eclipse. A diffuse reflection has been assumed for every object with solar coefficients ($f_s = 0$, $f_d = 1.3$)

- Earth's magnetic field: The Earth's magnetic field has been modelled based on the International Geomagnetic Reference Field IGRF-11.

    - The eddy current torques on the target have been modelled with the MTT.

    - A residual magnetic moment of 10^{-3} A·m^2/kg has been included on the target and the chaser.

    - The magnetic torque due to the magnetic moment of the coil has been included for the chaser.

- Eddy brake: The eddy current force and torque on the target object generated by the coil onboard the chaser have been included employing the Magnetic Tensor Theory (MTT) as well

as the corresponding reaction force and torque on the chaser. The baseline coil parameters are defined in 5.7. An efficiency factor of $\mu_{\text{eff}} = 95\%$ has been employed.

- Chaser's manoeuvres: The control forces and torques described in Section 6.2.4 have also been incorporated in the simulator including inaccuracies and delays as formulated in Section 6.2.4.1. All the case studies take into account a delay of $\tau = 1$s and an inaccuracy of 1% in the manoeuvres executed by the chaser

Figure 6.3 includes a diagram of the propagator developed for the eddy brake.
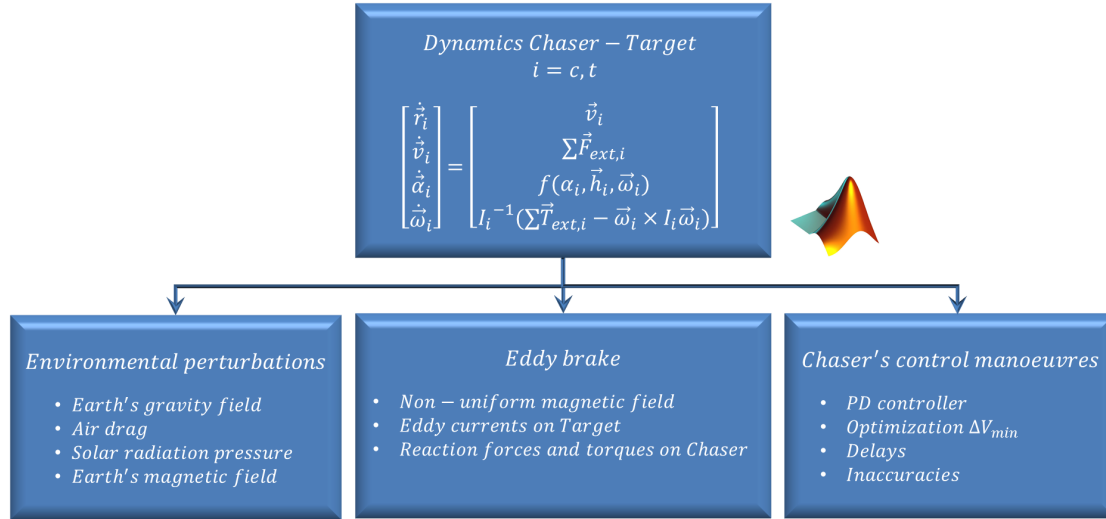
Figure 6.3: Propagator diagram.

6.3.3 Ariane-4 H10 model

Within the current space debris population, rocket bodies (R/Bs), i.e. spent upper stages, represent a significant mass fraction of the current space debris population and pose a major risk to operational satellites [42]. Upper stages typically contain a large amount of metallic material [31] making them suitable targets for the eddy brake method. Figure 6.4 shows the data obtained from the European DISCOS database [198] and the Space-Track.Org database [199]. The Russian SL-type R/Bs outnumber the rest of the population by several hundreds of objects in all the near-Earth regions. Ariane R/Bs have been selected as targets for the present case studies due to the fact that they are European targets, which pose less political opposition within ADR processes in the European Union.
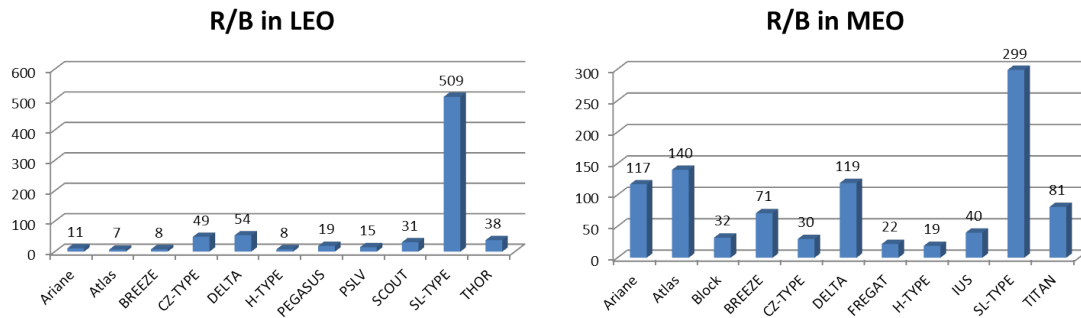
Figure 6.4: Distribution of R/Bs in LEO (left image) and MEO (including GTO and GEO) (right image).

Within the Ariane R/Bs population, the Ariane-4 and the Ariane-5 upper stages are the most numerous. The subsequent case studies will focus on the Ariane-5 EPS upper stage, already modelled in subsection 5.8.4.2 and the Ariane-4 H10 upper stage.

The magnetic tensor of the Ariane-4 H10 upper stage is determined based on the available information on its dimensions and materials. The dimensions of this object (see Figure 2.8), total mass, centre of gravity and inertia tensor were provided by Centre National dEtudes Spatiales (CNES). The total mass of the object including the Vehicle Equipment Bay (VEB) is 2154 kg.

The rocket body consists of three main parts;

- the engine HM-7B,

- the H10 stage and

- the vehicle equipment bay (VEB).

First of all, the H10 stage has two concentric propellant tanks (oxygen and hydrogen tanks). The tanks were modelled as a single cylindrical capsule with two hemispherical bulkheads with a diameter of 2.6 m and length 8.3 m [120, 200]. Its total dry mass is 700 kg and they are entirely made of aluminium alloy 7020 [122, 200]. Given the mass and the overall size, a thickness of 0.0038 m has been assumed which matches the average thickness value of Ariane aluminium tanks [201]. Moreover, the electrical conductivity of the 7020 aluminium alloy is equal to $\sigma = 2.2 \cdot 10^7$ S/m at 20°C. Note that the conductivity increases as the temperature decreases so it is likely that the electrical conductivity will be higher in-orbit. Nonetheless, a conservative approach is considered here and the aforementioned conductivity will be considered.

$$\mathbf{M_{H10}} = \begin{bmatrix} 3.76 & 0 & 0 \\ 0 & 3.76 & 0 \\ 0 & 0 & 1.12 \end{bmatrix} \cdot 10^6 \ \text{S} \cdot \text{m}^4. \tag{6.32}$$

The second part is the VEB. Its structure is made of CFRP and aluminium sandwich panels [122, 202]. In order to account for the metallic parts of the VEB, it is modelled as a conical frustum made of the aluminium alloy Al-7075-T6 which is a common alloy used in spacecraft structures and 0.0002 m of thickness which is a typical thickness in honeycomb structures [3]. The major radius is equal to 1.968 m, the minor radius is equal to 1.312 m and it has a height of 1.031 m [202].

$$\mathbf{M_{VEB}} = \begin{bmatrix} 0.17 & 0 & 0 \\ 0 & 0.17 & 0 \\ 0 & 0 & 3.00 \end{bmatrix} \cdot 10^4 \ \text{S} \cdot \text{m}^4. \tag{6.33}$$

Finally the nozzle of the HM7B engine is made of the alloy Inconel 600. It was explained in Section 3.4.1 that although this alloy is primarily made of nickel and chromium, it is a paramagnetic alloy which has a low Curie temperature [31]. The nozzle has been modelled as a conical frustum of 1.5 m in height, major radius of 0.99 m, minor radius of 0.5 m and 0.0005 metres thick [31]. The combined simulated geometry can be seen in Figure 6.5. Moreover, the magnetic tensor has been computed by means of the frame model.

$$\mathbf{M_{HM7B}} = \begin{bmatrix} 2.27 & 0 & 0 \\ 0 & 2.27 & 0 \\ 0 & 0 & 5.47 \end{bmatrix} \cdot 10^2 \ \text{S} \cdot \text{m}^4. \tag{6.34}$$

Now, taking into account the additivity property for N bodies rigidly connected but not electrically connected (see Section 3.3.4.4), the overall magnetic tensor is equal to,

$$\mathbf{M_{Ariane4}} = \mu_{\text{eff}}(\mathbf{M_{H10}} + \mathbf{M_{VEB}} + \mathbf{M_{HM7B}}) = \begin{bmatrix} 3.76 & 0 & 0 \\ 0 & 3.76 & 0 \\ 0 & 0 & 1.15 \end{bmatrix} \cdot 10^6 \ \text{S} \cdot \text{m}^4. \tag{6.35}$$
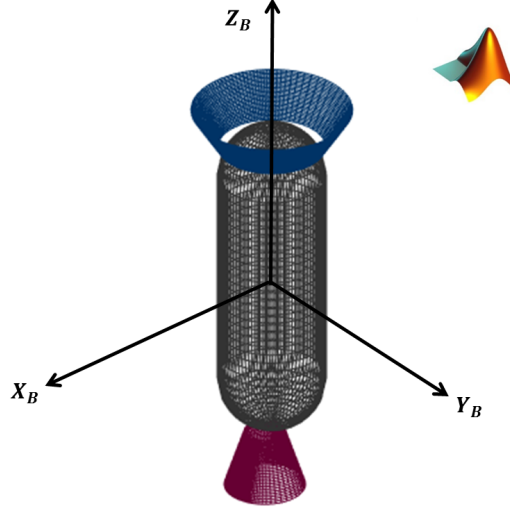
Figure 6.5: Ariane-4 model.

6.3.4   Case 1: Ariane-4 in LEO

This first case study analyses the de-tumbling process of an Ariane-4 H10 upper stage in LEO. The target's NORAD ID considered is 27422 which has the following initial osculating orbital parameters for the propagation:

- Perigee $h_p = 792.1$ km

- Apogee $h_a = 810.7$ km

- Inclination $i = 98.2$ deg

- Argument of perigee $\omega = 0$ deg

- Right ascension of the ascending node $RAAN = 0$ deg

- True anomaly $\nu = 0.0000799$ deg

- Initial date 01/06/2016

The target's initial angular velocity between its body reference frame and the ECI frame is equal to $\vec{\omega}_0 = [5.8, 5.8, 5.8]$ deg/s ($|\vec{\omega}_0| = 10$ deg/s). This is an average value of the possible spin rates that may be found for upper stages in LEO as previously explained in Section 2.3. However, this spin rate is too high to be controlled by the existing contact ADR methods and it has been decided to be decreased to 3 deg/s which is an acceptable threshold for some robotic manipulators [8, 45, 58].

In order to cancel out the effect of the Earth's magnetic field on the chaser, an AC current of low frequency (i.e. $f < 10$ Hz) will be employed equal to $I_c = I_{c,DC} \sin(\omega_{ac}t)$ and $I_{c,DC} = 80$ A.

The characteristic times of the control manoeuvres derived from the optimisation process are $\tau_{m1} = 50$ s, $\tau_{m2} = 0.5$ s, $\tau_{m3} = 1e-6$ s, $\tau_{m4} = 800$ s, $\tau_{m5} = 2500$ s and the total ΔV needed to decrease the angular velocity from $\omega_0 = 10$ deg/s to $\omega_f = 3$ deg/s is $\Delta V = 33.2$ m/s.

The results of the numerical simulation are summarised in the figures below. First of all, Figure 6.6 shows the evolution of the kinematic variables involved in the control. The angular velocity of target decreases from 10 deg/s to 3 deg/s within 32 days. In addition, the inertial angular velocity of the chaser, the relative distance and the relative pointing of the coil comply with the criteria defined in Section 6.3.1 and therefore, they are successfully controlled during the de-tumbling process.

Figure 6.6: Control parameters during the de-tumbling process.

In addition, Figure 6.7 depicts the evolution of the environmental torques considered throughout the numerical simulation. The interaction of the Earth's magnetic field with the chaser is counteracted thanks to use of the AC current and therefore only the effects of the SRP, air drag and Earth's gravity gradient are illustrated for the chaser spacecraft in the left image of Figure 6.7. The right image in Figure 6.7 depicts the evolution of the SRP, air drag, Earth's gravity gradient and Earth's magnetic field torques that affect the target object. It may be noted that the major environmental perturbation corresponds to the Earth's gravity gradient for both objects.

Figure 6.7: Chaser's and target's environmental torques.

Moreover, Figure 6.8 depicts the magnetic interactions between the chaser and the target. The
figure includes the magnetic force generated between the two objects and the magnetic torque that
appears on the target and the chaser. It may be observed that the interactions decrease with time
due to the fact that the target's angular velocity also decreases with time.
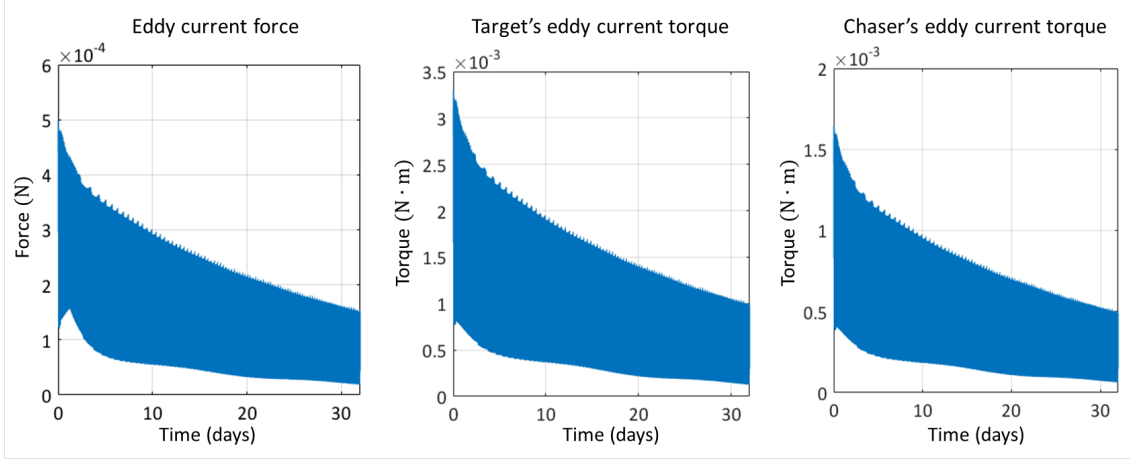
Figure 6.8: Chaser's and target's magnetic interactions.

Furthermore, Figure 6.9 shows the evolution of the control manoeuvres defined in Section 6.2.4.
These manoeuvres need to counteract both the environmental forces and torques and the mag-
netic interactions. The force manoeuvres are in the order of tens of milliNewtons and the torque
manoeuvres are in the order of milliNewtons metres.

Figure 6.9: Manoeuvres executed by the chaser during the de-tumbling process.

In addition, Figures 6.10 and 6.11 depict the evolution of the semimajor axis, eccentricity, inclina-
tion and right ascension of the ascending node (RAAN) of the target and the chaser respectively.
The eccentricity of the chaser's and target's orbits is in the order of 10^{-3} which are almost circular
orbits and this is why the argument of the perigee is not analysed.
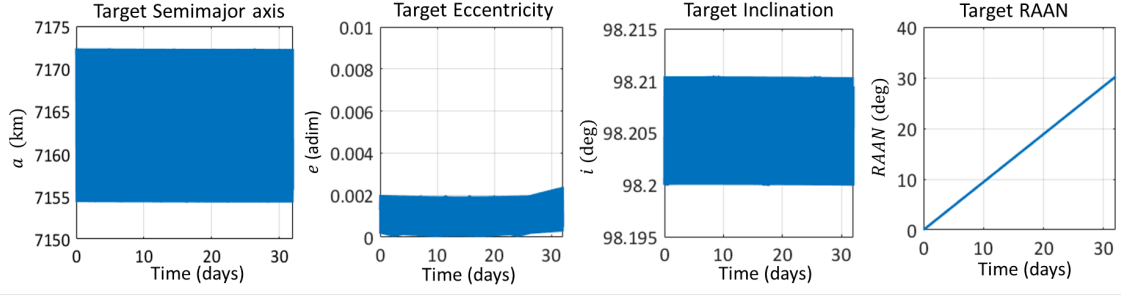
Figure 6.10: Target's orbital parameters.
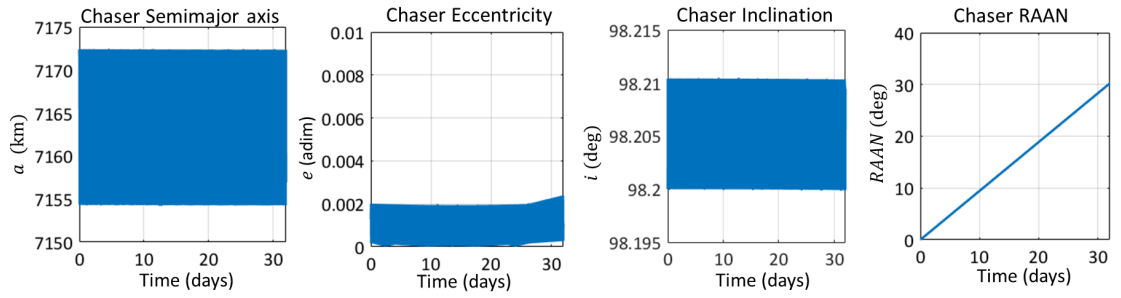
Figure 6.11: Chaser's orbital parameters.

The RAAN exhibits a secular evolution caused primarily by the term J_2 of the Earth's potential gravity field shown in Equation (6.36),

$$RAAN_{J2} = -1.5nJ_2(\frac{R_E}{a})^2 \cos i(1-e^2)^{-2}, \tag{6.36}$$

where n is the mean motion in deg/day, J_2 is equal to 0.00108263, R_E is the Earth's equatorial radius, a is the semimajor axis, i is the inclination, e the eccentricity and $RAAN_{J2}$ is the rate of change of the right ascension of the ascending node in degrees per day.

The mean value of $RAAN_{J2}$ during the simulations is equal to, $RAAN_{J2,t} = 0.94721531$ deg/day for the target and $RAAN_{J2,c} = 0.94721528$ deg/day for the chaser. These values approximate the secular change observed in Figures 6.10 and 6.11 which are $RAAN_{J2,plot,t} = 0.94446703561$ deg/day for the target and $RAAN_{J2,plot,c} = 0.94446703567$ deg/day for the chaser.

6.3.5 Case 2: Ariane-4 in GTO

This second case study analyses the de-tumbling process of an Ariane-4 H10 upper stage in GTO. The target's NORAD ID is 23637 which has the following initial osculating orbital parameters for the propagation:

- Perigee $h_p = 620$ km

- Apogee $h_a = 36784.2$ km

- Inclination $i = 4$ deg

- Argument of perigee $\omega = 0$ deg

- Right ascension of the ascending node $RAAN = 0$ deg

- True anomaly $\nu = 180.0000133$ deg

- Initial date 01/06/2016

As selected in the previous case study, the target's initial angular velocity between its body reference frame and the ECI frame is equal to $\vec{\omega}_0 = [5.8, 5.8, 5.8]$ deg/s ($|\vec{\omega}_0| = 10$ deg/s). The de-tumbling process is carried out until the angular velocity of the target is below 3 deg/s which is an acceptable threshold for many robotic manipulators within ADR processes [8, 45, 58].

The control strategy selected for this case study is the following. A DC current is employed for the chaser's coil above 3000 km of altitude in order to maximise the target's dissipative effect. Below this altitude, the coil's current is changed to AC current in order to cancel out the Earth's magnetic torques on the chaser.

The characteristic times of the control manoeuvres derived from the optimisation process are $\tau_{m1} = 5$ s, $\tau_{m2} = 0.3$ s, $\tau_{m3} = 1e - 3$ s, $\tau_{m4} = 1200$ s, $\tau_{m5} = 50$ s. The total ΔV based on the control forces implemented by the chaser is $\Delta V = 41.29$ m/s.

The results of the numerical simulation are summarised subsequently. First of all, Figure 6.12 shows the evolution of the kinematic variables involved in the control. The angular velocity of target decreases from 10 deg/s to 3 deg/s within 25 days. The de-tumbling process is faster than the previous case study due to the fact that a DC current is applied during a portion of the orbit. In addition, the inertial angular velocity of the chaser, the relative distance and the relative pointing of the coil comply with the criteria defined in Section 6.3.1 and therefore, they are successfully controlled during the de-tumbling process.
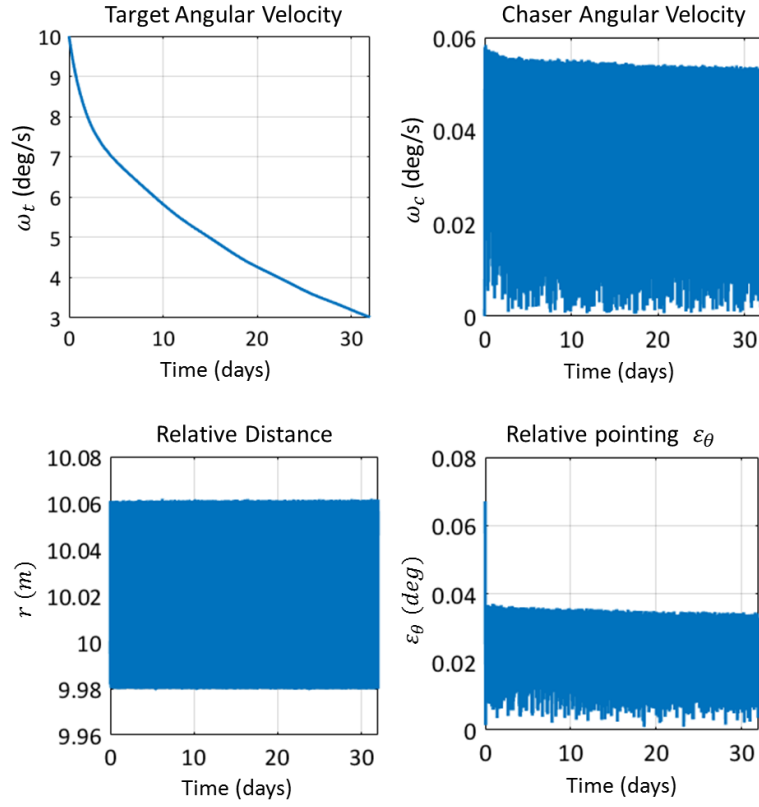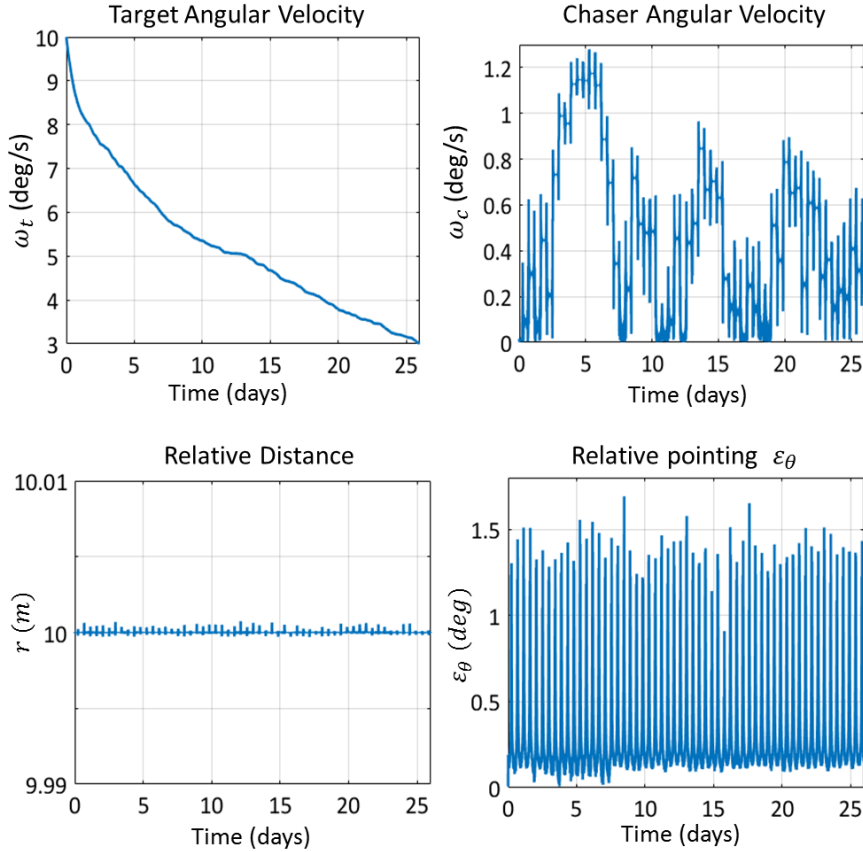

Figure 6.12: Control parameters during the de-tumbling process.

It should be highlighted that the behaviour of the control variables, r, ϵ_θ and ω_c, obtained for this case study and the previous one (shown in Figure 6.6) is somewhat different. For the GTO orbit,

the errors obtained in the relative distance are smaller while the errors in the relative pointing and chaser's angular velocity are bigger. This optimisation problem of 5 parameters τ_{mi} $(i = 1, 5)$ in a highly non-linear dynamical set of equations is a complex problem. It has been identified that the optimisation process increases in difficulty in a GTO orbit due to the fact that the chaser and the target objects are subject to highly variable environmental perturbations throughout each orbit. This issue hampered the convergence of the optimisation problem and the compliance of the constraints imposed (defined in Section 6.3.1). For these reasons, it may be concluded that the proposed PD control strategy is adequate for orbits with low eccentricity while more sophisticated control strategies should be investigated for highly eccentric orbits. One possible solution to tackle this problem is to allow the characteristic times of the control manoeuvres vary with time $\tau_{mi}(t)$ to better adapt to highly variable external perturbations.

In addition, Figure 6.13 depicts the evolution of the environmental torques considered throughout the numerical simulation. The interaction of the Earth's magnetic field with the chaser is only depicted for altitudes above 3000 km when the DC current is applied. It may be observed that this environmental torque is several orders of magnitude higher than the rest of the perturbations for all altitudes. This is due to the fact that the magnetic moment created by the chaser's coil is quite high. This result underscores the fact that the use of an AC current throughout the whole de-tumbling process may be a more optimal control strategy rather than the combination of a DC and AC currents. The rest of the environmental perturbations exhibit big fluctuations due to the altitude variations throughout the GTO orbit. When the target passes through the perigee, the Earth's gravity torque is dominant and when the target passes through the perigee, the SRP torque is the mainstream torque.
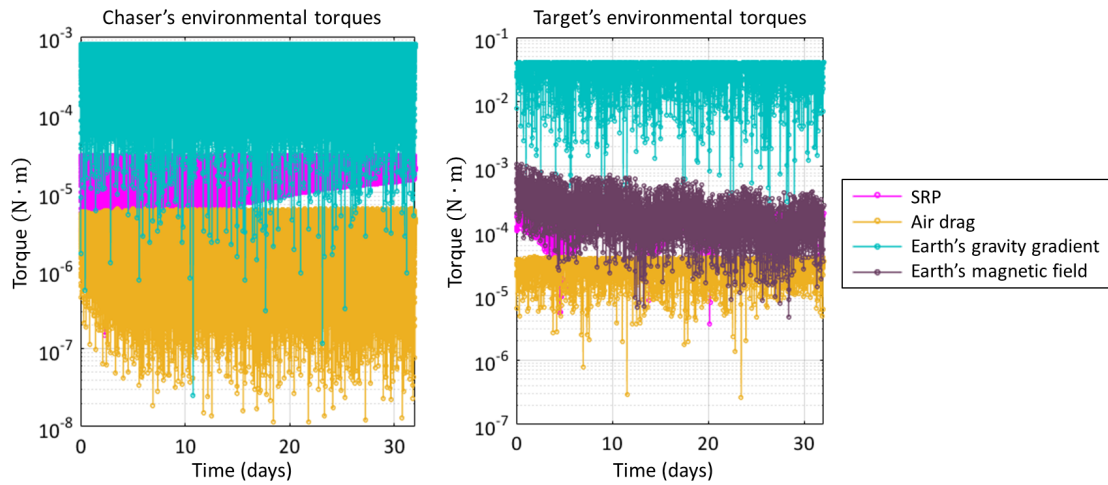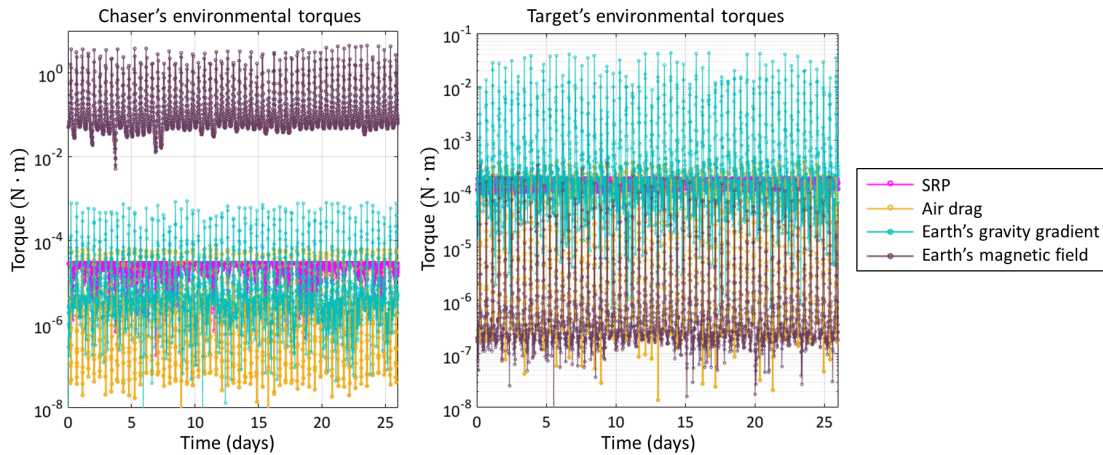

Figure 6.13: Chaser's and target's environmental torques.

Figure 6.14 depicts the magnetic interactions between the chaser and the target. The figure includes the magnetic force generated between the two objects and the magnetic torque that appears on the target and the chaser. It may be observed that the interactions decrease with time due to the fact that the target's angular velocity also decreases with time. In addition, the eddy current forces and torques exhibit period fluctuations. This effect appears due to the periodic changes between DC and AC current.
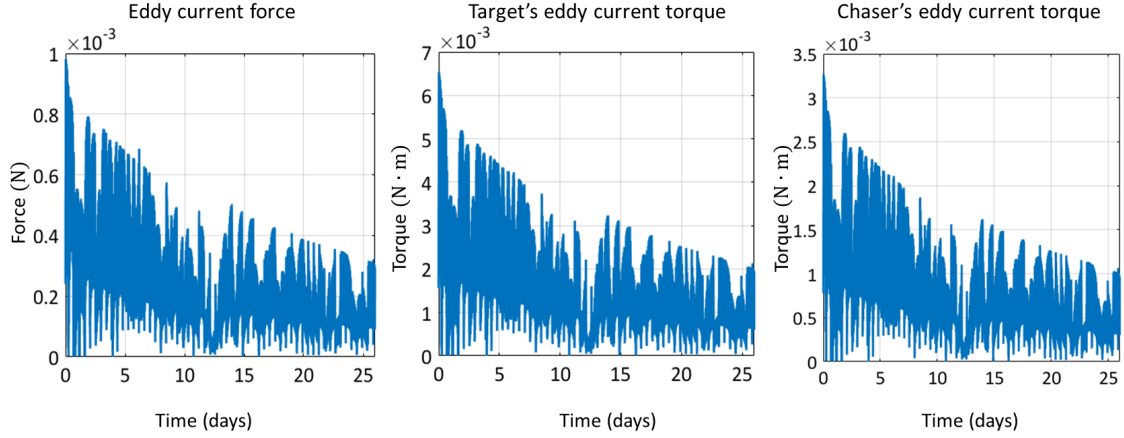
Figure 6.14: Chaser's and target's magnetic interactions.

Furthermore, Figure 6.15 shows the evolution of the control manoeuvres defined in Section 6.2.4.
These manoeuvres need to counteract both the environmental forces and torques and the magnetic interactions. The force manoeuvres are in the order of tens of milliNewtons and the torque
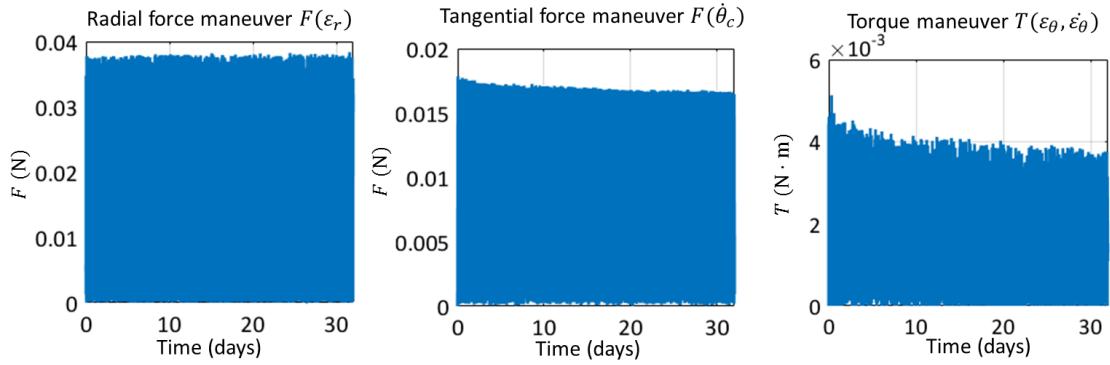manoeuvres are in the order of milliNewtons metres.
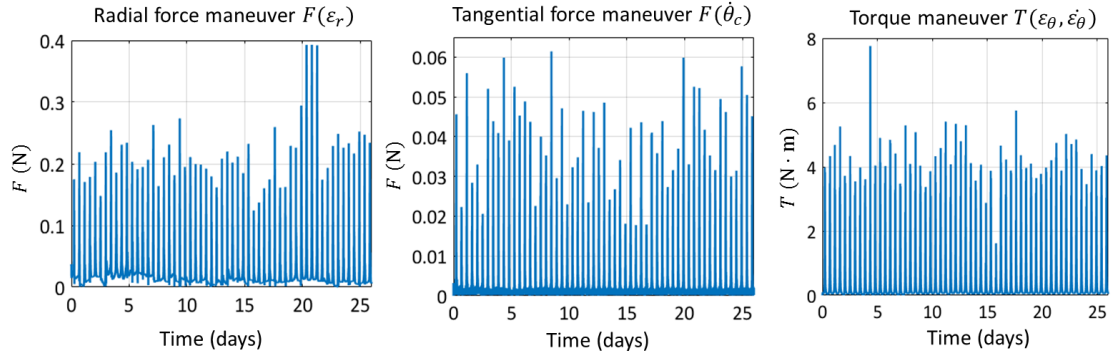
Figure 6.15: Manoeuvres executed by the chaser during the de-tumbling process.

Finally, Figures 6.16 and 6.17 depict the evolution of the semimajor axis, eccentricity, inclination,
argument of the perigee and right ascension of the ascending node (RAAN) of the target and the
chaser respectively. The argument of the perigee and the RAAN exhibit a secular evolution
caused primarily by the term J_2 of the Earth's potential gravity field shown in Equations (6.37),

$$
\begin{aligned}
\omega_{J2} &= 0.75 n J_2 (\frac{R_E}{a})^2 (4 - 5\sin^2 i)(1 - e^2)^{-2}, \\
RAAN_{J2} &= -1.5 n J_2 (\frac{R_E}{a})^2 \cos i (1 - e^2)^{-2},
\end{aligned}
\tag{6.37}
$$

where n is the mean motion in deg/day, J_2 is equal to 0.00108263, R_E is the Earth's equatorial
radius, a is the semimajor axis, i is the inclination, e the eccentricity and $RAAN_{J2}$ is the rate of
change of the right ascension of the ascending node in degrees per day.

The mean rate of change of the RAAN during the simulations is equal to, $RAAN_{J2,t} = -0.35823754$
deg/day for the target and $RAAN_{J2,c} = -0.35823733$ deg/day for the chaser. These values
approximate the secular change observed in Figures 6.16 and 6.17 which are $RAAN_{J2,plot,t} = -0.35986045$ deg/day for the target and $RAAN_{J2,plot,c} = -0.35986072$ deg/day for the chaser.
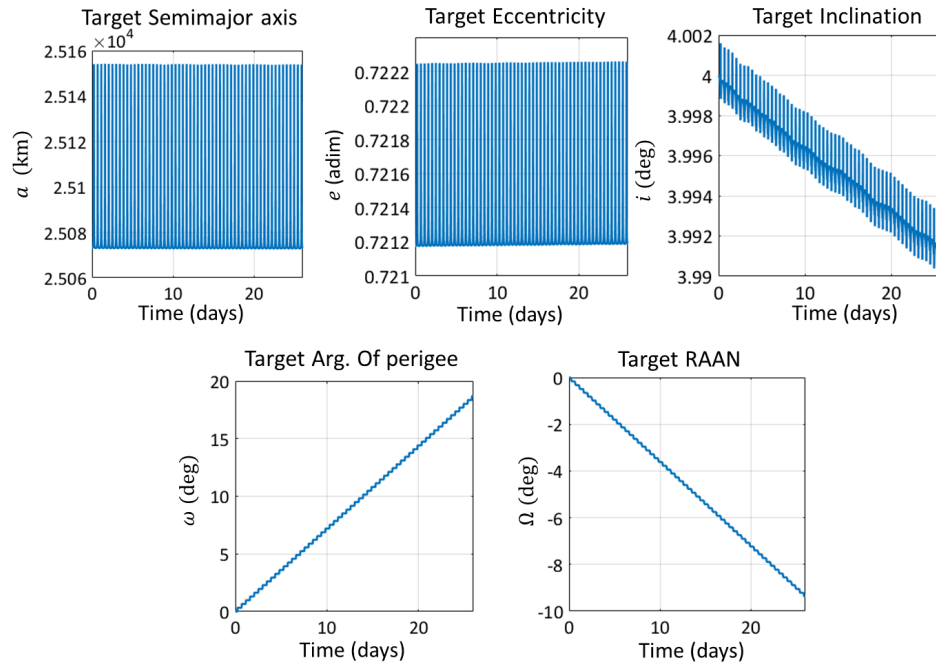
Figure 6.16: Target's orbital parameters.
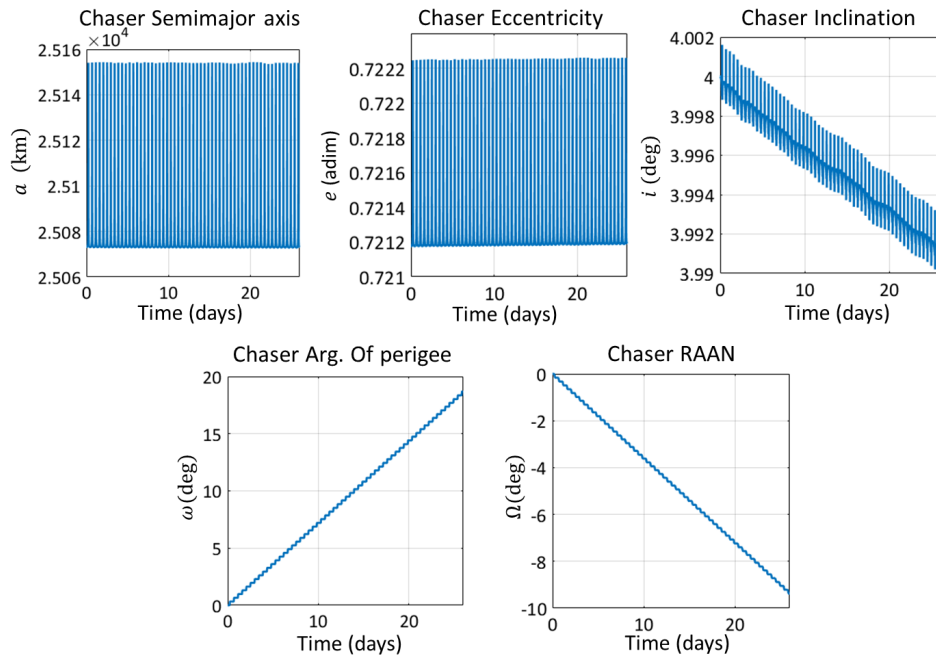
Figure 6.17: Chaser's orbital parameters.

In addition, the mean mean rate of change of the argument of the perigee during the simulations is equal to, $\omega_{J2,t} = 0.71386275$ deg/day for the target and $\omega_{J2,c} = 0.71386233$ deg/day for the chaser. These values approximate the secular change observed in Figures 6.16 and 6.17 which are $RAAN_{J2,plot,t} = 0.71668694$ deg/day for the target and $RAAN_{J2,plot,c} = 0.71668739$ deg/day for the chaser.

6.4 Experimental tests

To explore the practical challenges of in orbit proximity operations, a set of experimental tests were conducted at the Robotics Innovation Centre, DFKI GmbH, (Bremen, Germany). The DFKI is a renowned research institute in the area of robotics for space applications and planetary exploration, able to develop innovative solutions that combine the artificial intelligence with customised robotic hardware.

These tests were conducted during a three-month secondment (from September 2015 until November 2015) at the test facility INVERITAS (innovative technologies for relative navigation and capture of mobile autonomous systems). This facility was developed as a joint project between Airbus Defence & Space (former Astrium GmbH), as a project coordinator, Jena-Optronik and DFKI RIC [203]. The facility contains the following equipment:

- An industrial robot KUKA KR60-3 (Referred to as target or client)

- A spidercam cable robot (Referred to as chaser or servicer)

- A motion tracking system

- A lighting system

- Protection mechanisms

- A control system

This facility is typically used to simulate proximity operations between two objects (chaser-target system) and test sensors on-board the chaser spacecraft (e.g. sensors for pose estimation of the target). The robotic arm that moves the target is capable of providing full 6 degrees of freedom (DOF) and the servicer has three translational DOF and one rotational DOF around its vertical axis. The illumination conditions can be adjusted to simulate a similar environmental conditions to the ones found in orbit. This facility was also used in the past to carry out hardware-in-the-loop simulations for rendezvous and capture manoeuvres [203]. Figure 6.18 shows some photographs of the facility where the chaser and the target objects can be identified.
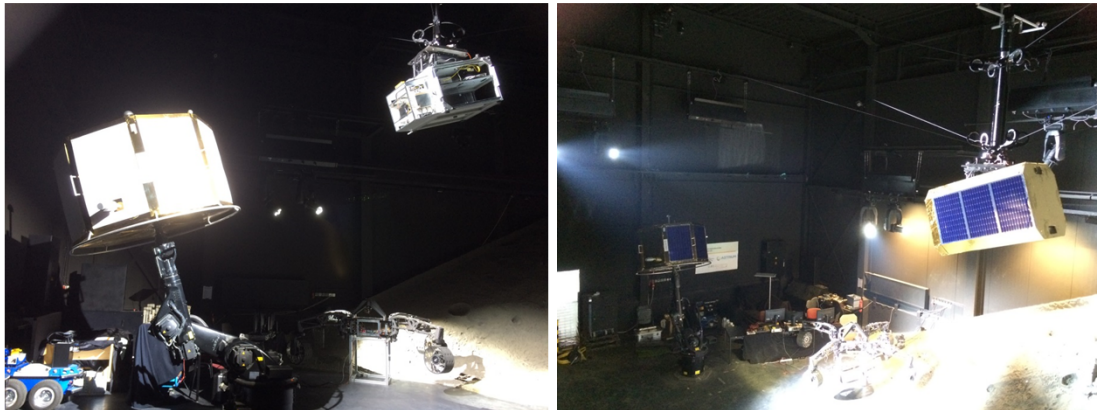
Figure 6.18: DFKI INVERITAS facility.

The main goals of the conducted experimental tests at this site were,

- to get acquainted with the INVERITAS facility, hardware in the loop simulations and pose estimation processes,

- to test open-loop controlled trajectories obtained with the control implemented for the eddy brake at different relative distances,

- to obtain real data of the target with the Bumblebee2 stereo camera mounted on the chaser with different illumination conditions and surface finishes and

- to obtain a 3D reconstruction of the target from the data derived from the stereo camera.

6.4.1 Target and chaser models

The target, illustrated in Figure 6.19, is an octagonal prism 1 metre in height. Moreover, two different external surface materials were tested; a white surface finish and a blue and silver surface finish which are shown in Figure 6.19.

In order to compute its magnetic tensor, it was assumed that the target was fully metallic, made of aluminium with a thickness of 0.0003 m. The right image in Figure 6.19 depicts the grid employed to compute the Magnetic tensor of the object. Under these hypotheses, the mass computed for the object is equal to 65 kg, the principal inertia along the Z axis is equal to 30 kg·m^2 and the magnetic tensor obtained using the frame model is given by Equation (6.38),

$$\mathbf{M_{target}} = \begin{bmatrix} 5.1152 & 0 & 0 \\ 0 & 5.1152 & 0 \\ 0 & 0 & 6.2927 \end{bmatrix} \cdot 10^4 \mathrm{S} \cdot \mathrm{m}^4. \tag{6.38}$$

White surface finish   Blue and silver surface finish   MATLAB frame model
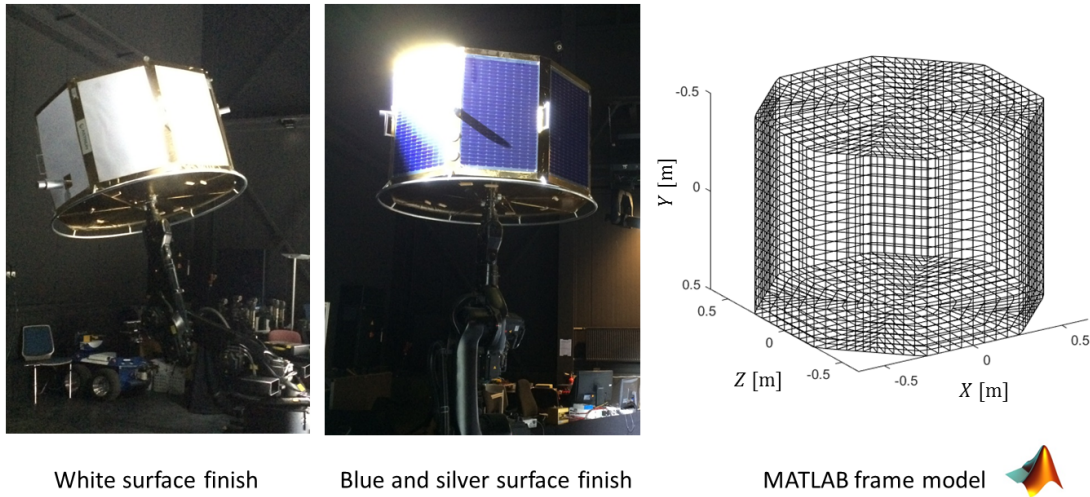
Figure 6.19: Photographs of the INVERITAS target.

The INVERITAS servicer is shown in Figure 6.20. The chaser was assumed to have a fictitious coil on-board based on the baseline parameters defined in 5.7.

A Bumblebee2 stereo camera [21] was located at the chaser for the pose estimation during the de-tumbling process together with a desktop computer to read and store the data generated by the camera (see Figures 6.20 and 6.21). A stereo camera typically has two lenses which allows the camera to simulate human binocular vision and therefore, obtain three-dimensional information [22]. Stereo cameras have been widely used for satellite proximity operations due to their low

weight, volume and power requirements. However, these sensors are strongly affected by the illumination conditions [204].
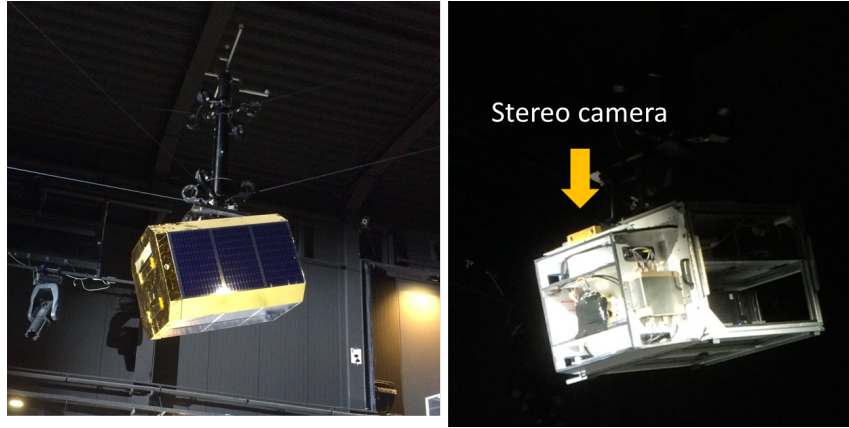
Figure 6.20: Photograph of the INVERITAS servicer.

Figure 6.21: Bumblebee2 stereo camera [21].

6.4.2 Camera calibration

The first step in the pose estimation process is to calibrate the stereo camera. The images have been obtained using the 'FlyCapture Software' [205] and then processed using the MATLAB Image Processing Toolbox [206].

This process includes the estimation of the intrinsic and the extrinsic parameters of the camera. The *extrinsic parameters* refer to the translation and rotation from the 3D world coordinate system, (X_w, Y_w, Z_w), to the 3D camera coordinate system [22]. The extrinsic parameters are typically represented by a 3D rotation matrix, R, and a translation vector, t between the two aforementioned coordinate systems. The *intrinsic parameters* refer to the physical properties of the camera such as its focal length, its skew coefficient and its distortion parameters. The intrinsic parameters are typically gathered in a matrix referred to as 'camera intrinsic matrix', K. The intrinsic parameters are used to transform the 3D camera's coordinates into a 2D image coordinates, (X_{2D}, Y_{2D}), [22].

The transformation between world coordinates and 2D image coordinates used by the MATLAB Image Processing Toolbox is based on Equation (6.39),

$$w \begin{bmatrix} X_{2D} & Y_{2D} & 1 \end{bmatrix} = \begin{bmatrix} X_w & Y_w & Z_w & 1 \end{bmatrix} \begin{bmatrix} R \\ t \end{bmatrix} K, \tag{6.39}$$

where R and t are the extrinsic parameters, K is the camera intrinsic matrix and w is an arbitrary scale factor.

For the calibration process, an asymmetric chessboard was employed as the calibration pattern. The size of the squares in the chessboard were 0.036×0.036 m. This information is important in order to derive afterwards the relative distances from the camera itself. A total of 26 pairs of images of were taken with different relative positions and orientations of the chessboard. Figure 6.22 illustrates all the relative positions and orientations of the images taken by the camera used to derive the extrinsics parameters.
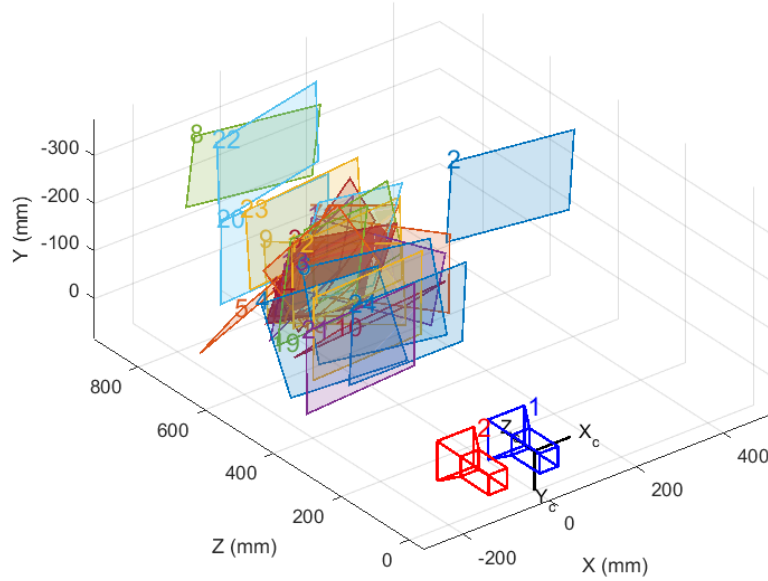
Figure 6.22: Relative positions and orientations of the chessboard with respect to the stereo camera.

Subsequently, the squares within the chessboard must be detected by the image processing toolbox as shown in Figure 6.23.
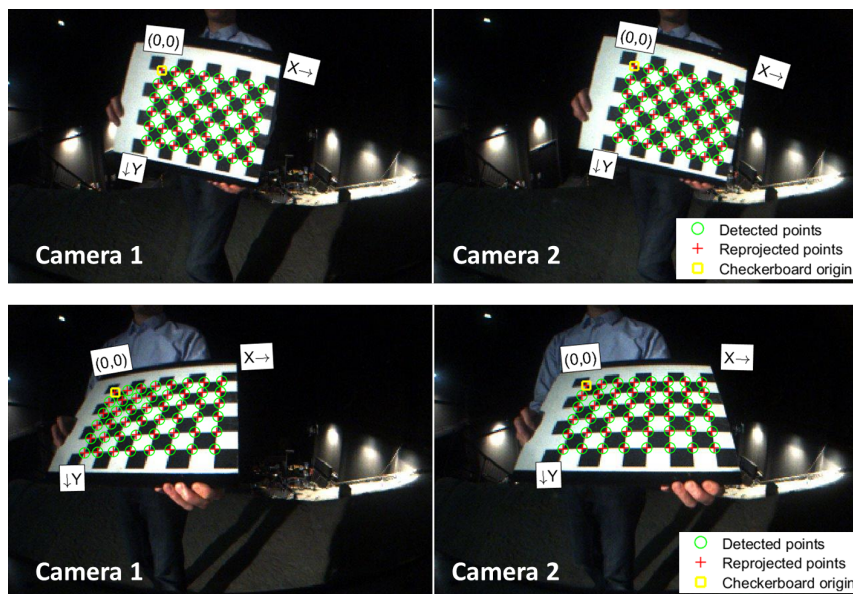
Figure 6.23: Detection of the chessboard pattern in all stereo pairs of images.

Moreover, the *mean reprojection errors* per image obtained are shown in Figure 6.25. This parameter evaluates the accuracy of the calibration process. A reprojection error, depicted in Figure 6.24, is the distance in pixels between a pattern keypoint detected in a calibration image, and the corresponding 3D world point projected into the same image, referred to as reprojected point [207]. The Mathworks Image Processing Toolbox calculates the reprojection errors by projecting the chessboard points from world coordinates into image coordinates. The toolbox then compares the reprojected points to the corresponding detected points. Figure 6.25 displays a bar graph with the reprojection error per image and the overall mean value. It indicates the accuracy achieved for the calibration and the overall mean error was equal to 0.23 pixels.
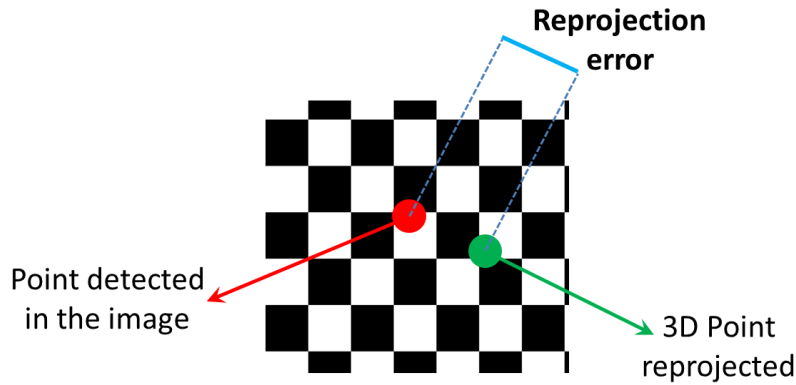
Figure 6.24: Reprojection error sketch.
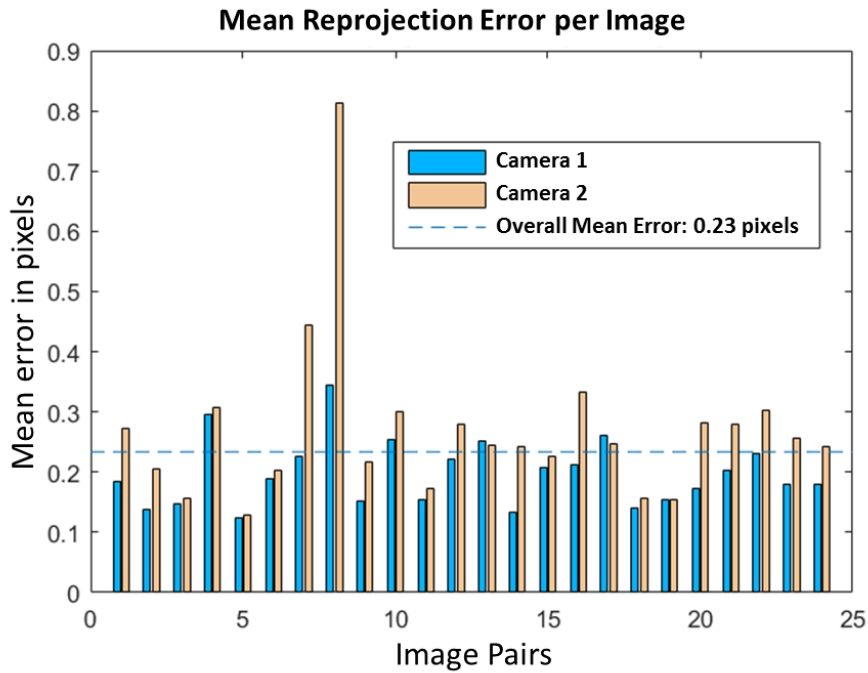
Figure 6.25: Mean reprojection errors.

6.4.3 Tests results

An open loop controlled trajectory was tested in the INVERITAS facility. This means that the sensor data obtained was not fed into the trajectory and the trajectory tested is not modified throughout the experiment.

Figure 6.26 shows the initial configuration for the experimental tests. The selected phase angle (i.e. target-Sun-chaser angle) is equal to 45 degrees. These illumination conditions are quite benign for an optical sensor such as the Bumblebee2 stereo camera [21] which allows for a fine detection of the target object. Finally, two surface finishes were tested on-board the target; a white surface finish and a blue and silver surface finish as previously illustrated in Figure 6.19.
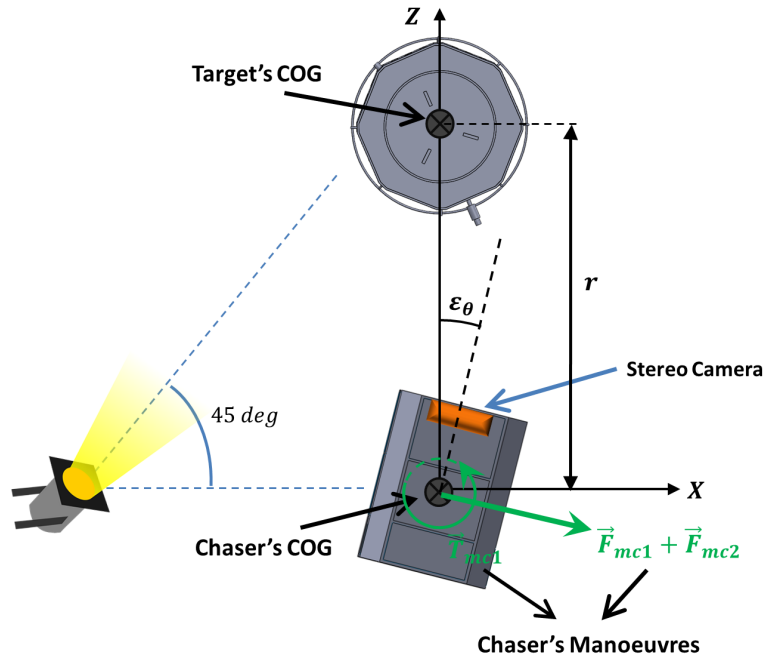
Figure 6.26: Configuration of the chaser-target system in the INVERITAS facility.

The relative distance between the fictitious coil on-board the chaser and the target's COG was four metres and the target is initially rotating at 10 deg/s along the vertical axis of the octagonal prism (Z axis in Figure 6.19). Figures 6.27 and 6.28 illustrate the evolution of the control variables and control manoeuvres as defined in Subsection 6.2.4. First of all, Figure 6.27 displays the evolution of the relative distance, r, relative pointing, ϵ_θ and angular velocities of chaser, ω_c, and target, ω_t. Furthermore, Figure 6.28 indicates the manoeuvres that must be executed by the chaser, $\vec{F}_{mc1}$, $\vec{F}_{mc2}$ and $\vec{T}_{mc1}$, as previously defined in Equations (6.21, 6.22 and 6.23) to achieve a controlled de-tumbling process. This data was fed into the INVERITAS software in order to reproduce a real controlled de-tumbling process by the INVERITAS hardware.

Given the fact that the relative distance between the two objects is small and that the target is assumed to be fully metallic, the de-tumbling process occurs very rapidly. The target is initially rotating at 10 deg/s and its angular velocity decreases to 3 deg/s in 2.5 minutes. This trajectory was selected in order to be able to visualise the full de-tumbling process in the INVERITAS facility within a short period of time.
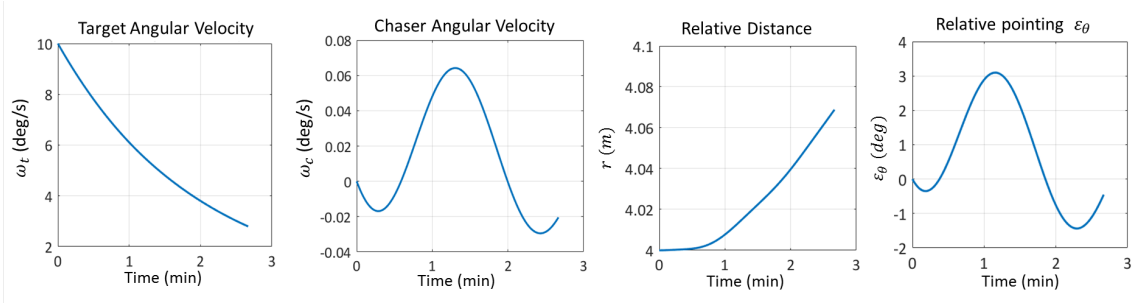
Figure 6.27: Evolution of relative distance, relative pointing and angular velocities of chaser and the target objects.
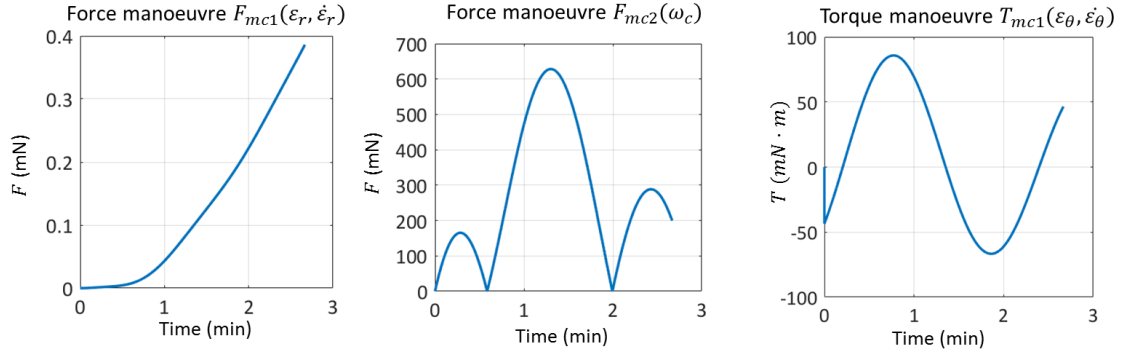
Figure 6.28: Evolution of the control manoeuvres F_{mc1}, F_{mc2} and T_{mc}.

6.4.3.1   White surface finish

The first set of experimental tests was done for a target with a white surface finish. The octagonal object is initially rotating at 10 deg/s and it is subject to the illumination conditions described in Figure 6.26. The de-tumbling process was recorded by the Bumblebee camera. Figure 6.29 shows some examples of the stereo images taken by the sensor throughout the test.

Now, one stereo image pair, shown in Figure 6.30, is selected to describe the process that results in the 3D reconstruction of the scene This process must then be repeated for each stereo image by the image processing toolbox.
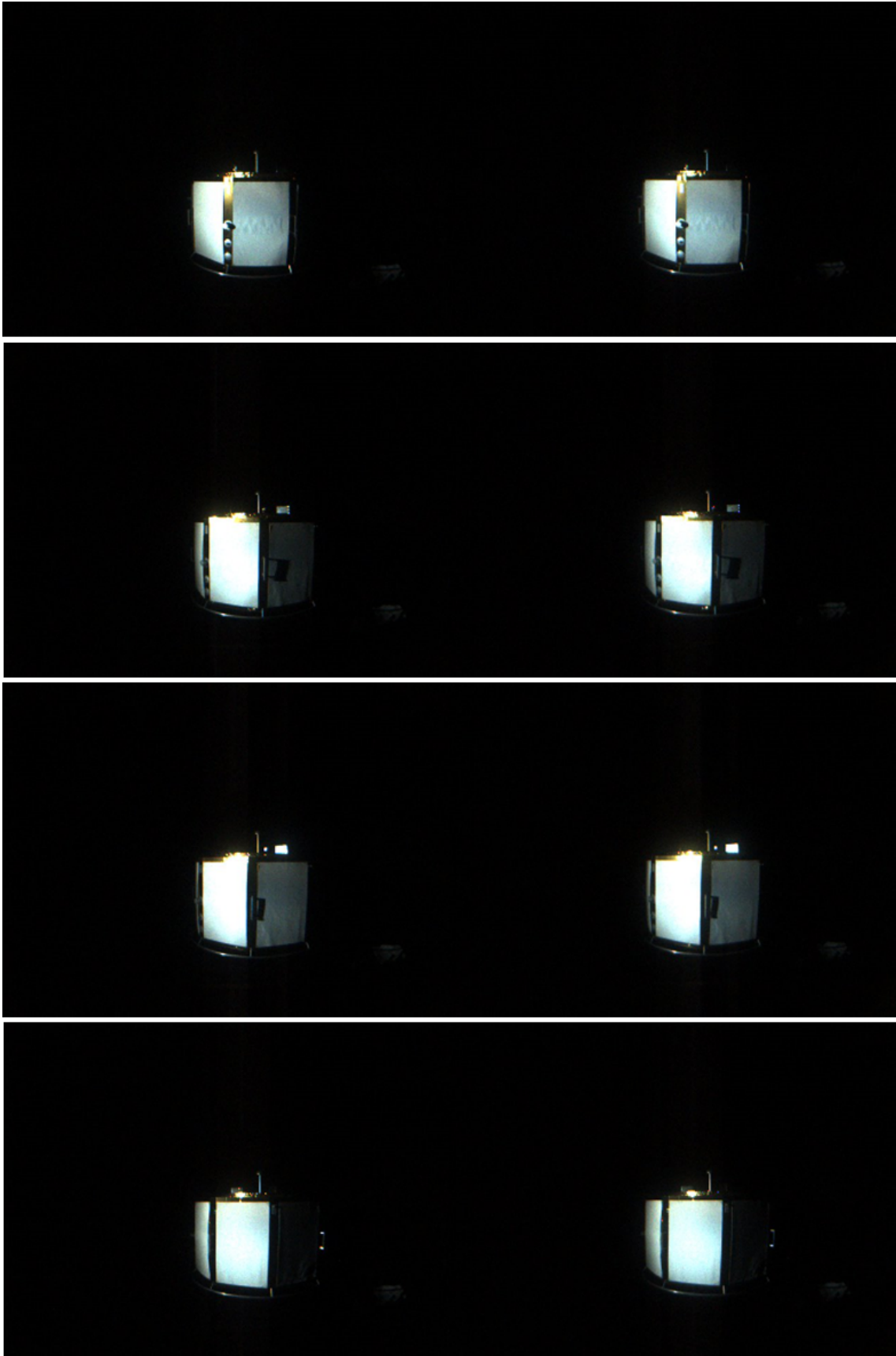
Figure 6.29: Images obtained by the bumblebee camera during the de-tumbling process.

Left Camera   **Right Camera**
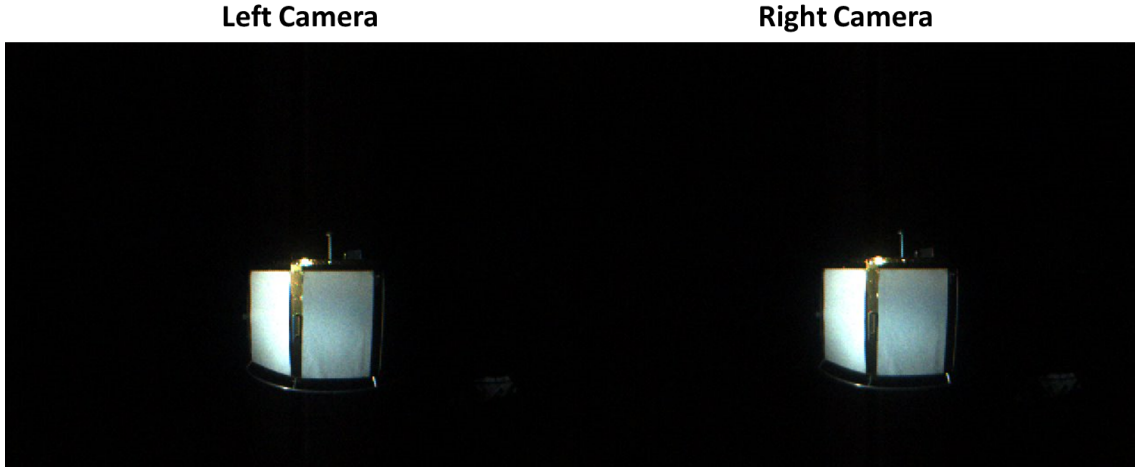
Figure 6.30: Raw data taken by the stereo Bumblebee camera.

The first step is to *rectify* the stereo pair of images. This reduces the 2D stereo correspondence problem to a 1D problem which means that for each point in an image taken with the left camera, its corresponding point in the right camera lies along the same row. Figure 6.31 shows the rectified image [22].

Before Rectification   **After Rectification**
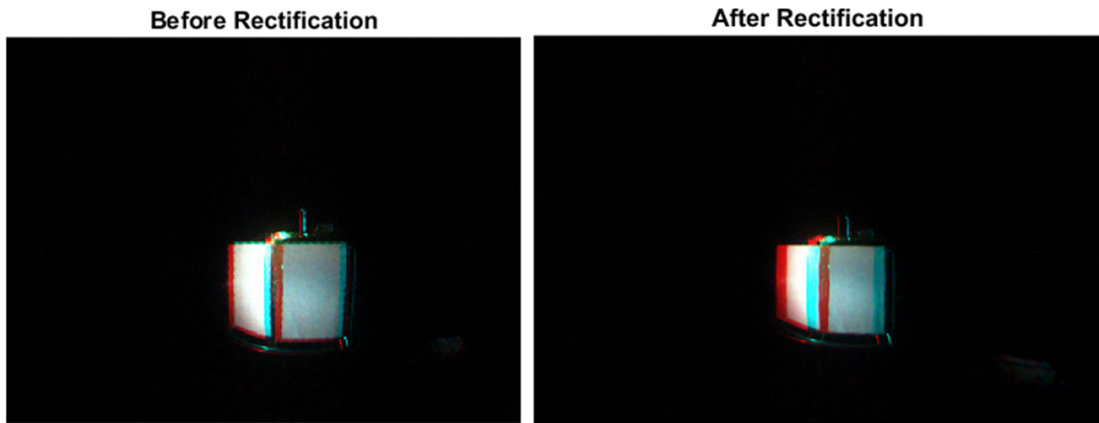
Figure 6.31: Rectification process.

The next step is the computation of the *disparity map*. Disparity refers to the difference in location of an object in the corresponding images seen by the left and right cameras [22]. Since the two cameras are separated by a distance b called baseline, each camera will visualise the same world point P in a different location on the two-dimensional images acquired (see Figure 6.32). The distance between the two projected points is called disparity d. For each pixel in the left image, the disparity map shows the distance to the corresponding pixel in the right image. The disparity is proportional to the depth distance, Z, of the corresponding world point from the camera. The relationship between the depth of a point and the disparity between corresponding points is given by Equation (6.40),

$$Z = f \cdot \frac{b}{d}, \tag{6.40}$$

where f is the focal length of the camera, b is the baseline of the camera and d is the disparity.
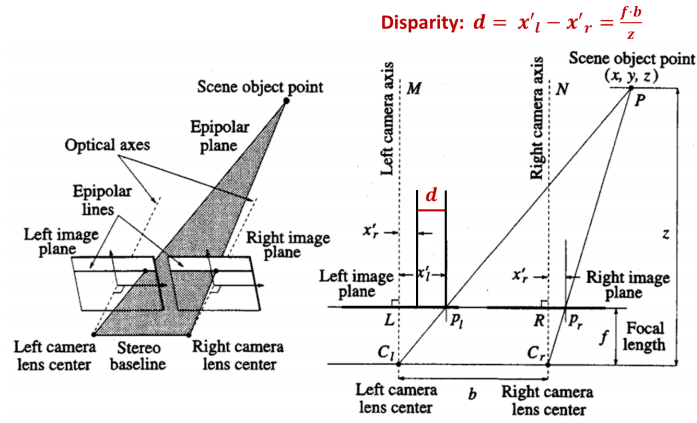
Figure 6.32: Sketch of the stereo vision [22].

Figure 6.33 depicts the disparity map.
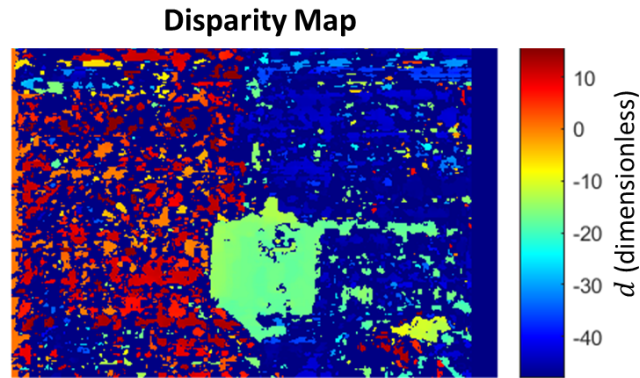
Figure 6.33: Disparity map.

Finally, using the data obtained from the disparity map and the calibration parameters of the stereo camera, a 3D point cloud can be obtained. Figure 6.34 shows the reconstructed 3D scene. The shape of the object can be identified very accurately as well as several markers on the surface.
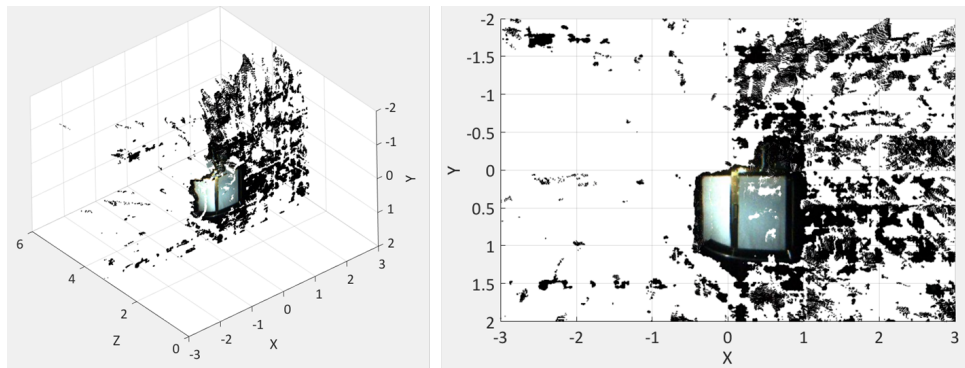
Figure 6.34: Point Cloud.

Some of the images processed show some black spots on the surface. These are due to reflections

of the incident light which are not well characterised by the camera. These effects can be better observed in the set of images depicted in Figure 6.35 that compare one of the original images from the stereo pair with the reconstructed 3D scene done by the image processor.
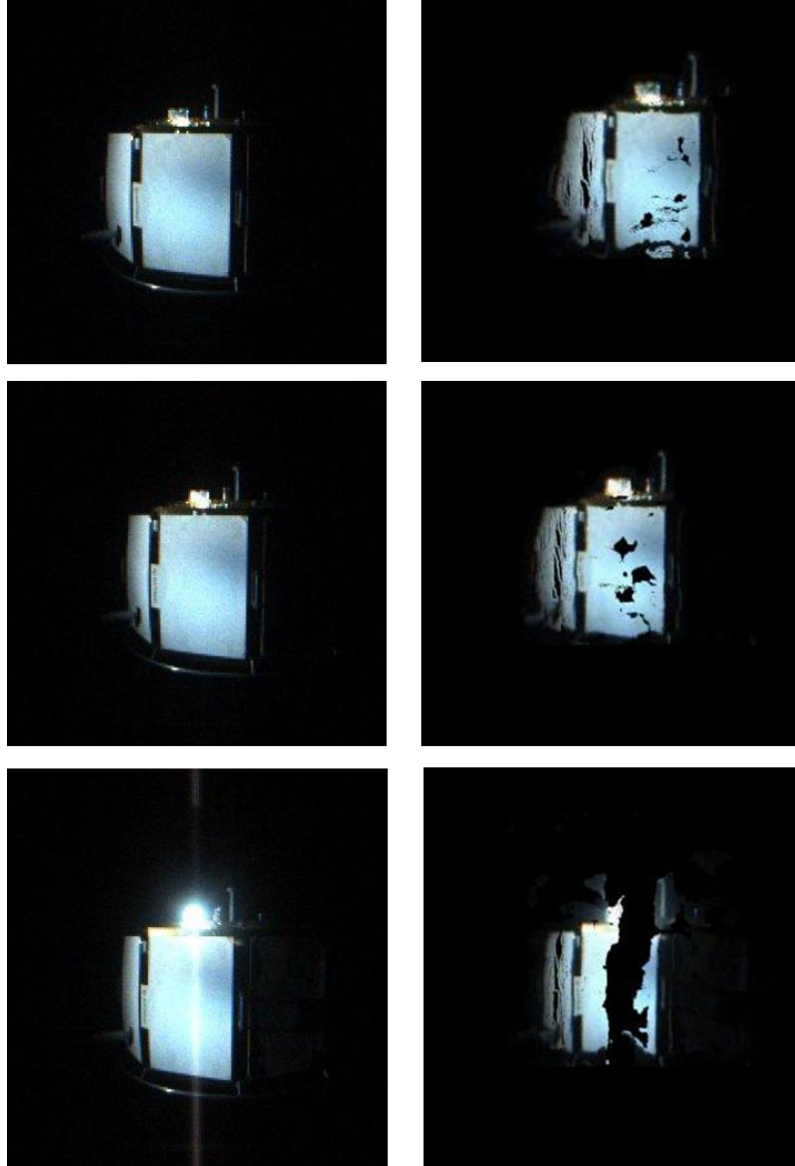
Figure 6.35: Test 1: Original image taken by the camera (left image) and reconstructed image (right image).

6.4.3.2 Blue and silver surface finish

An analogous process to the one described in the previous section was done for a target with a different finish surface. In this second test a blue and silver finish was employed which resembles spacecraft solar cells.

Figure 6.36 compares one of the original images from the stereo pair with respect to the 3D reconstruction carried out by the image processing toolbox. The lighting conditions make the object quite dark which makes it difficult to be fully seen in the images. Nonetheless, various edges and markers can be identified in the reconstructed image with great detail.

However, in some cases, some strong reflections occurred as seen in Figure 6.36 which prevented

the image processor from identifying correctly the whole shape of the object. This effect highlights the importance of not only the illumination conditions for passive optical cameras but also the importance of the surface materials of the target object as very distinct responses may be obtained depending on the materials.
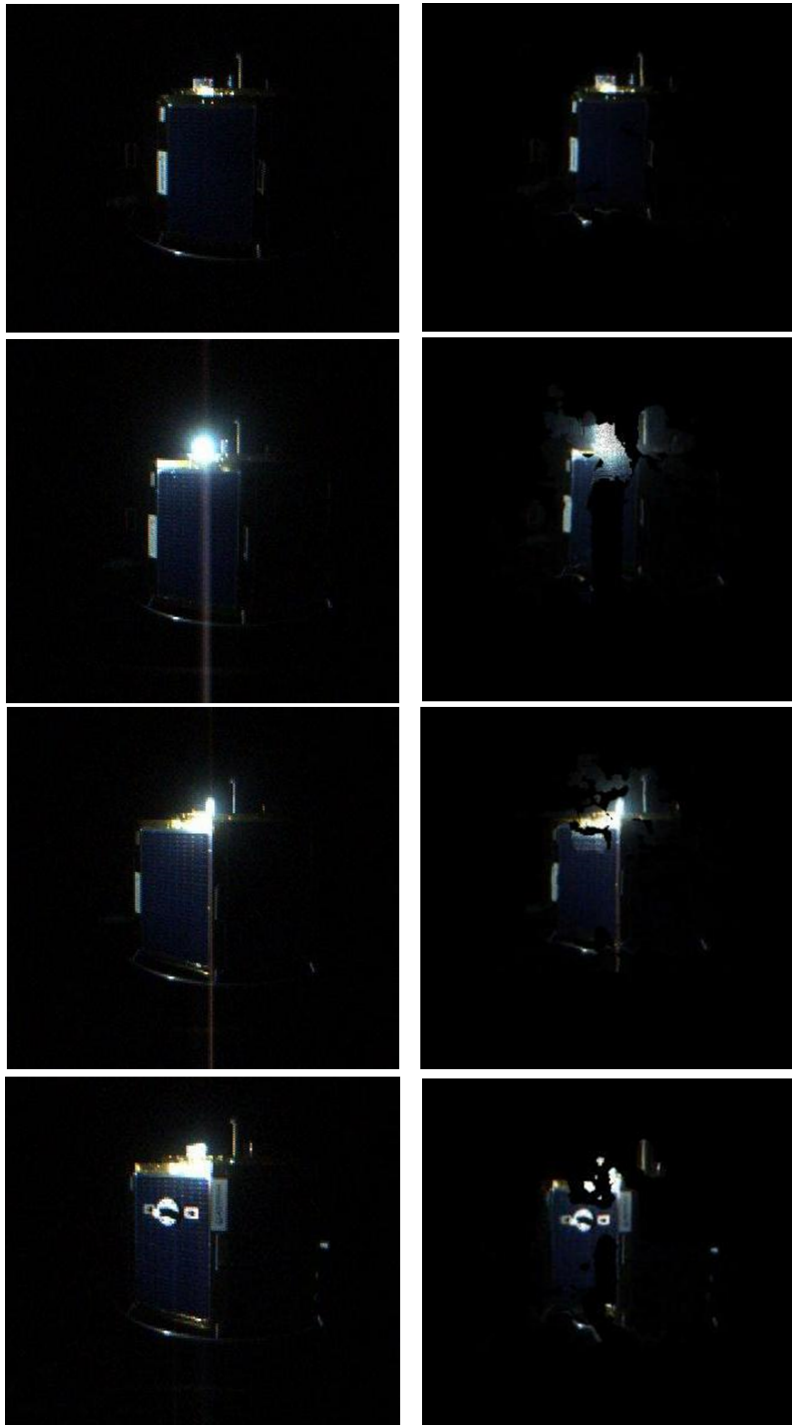
Figure 6.36: Test 2: Original image taken by the camera (left image) and reconstructed image (right image).

6.5 Chapter summary

This chapter has investigated various relevant aspects related to the guidance, navigation and control of the eddy brake method.

First of all, the magnetic interactions of the chaser-target system were formulated based on the magnetic tensor theory in Subsection 6.2.1. In addition, two relevant pointing configurations were highlighted in Subsection 6.2.2. The first one, configuration ($\parallel$), maximises the magnetic field inside the target object and, therefore, minimises the time of the de-tumbling process and the second one, configuration ($\perp$), cancels out the induced magnetic forces between the two objects, which could potentially reduce the overall ΔV. However, it was found out that this last configuration is dependent on the angular velocity of the target and the magnetic tensor of the target which would lead to very complex operations for longer periods of time, making this configuration less appealing than configuration ($\parallel$).

Subsequently, the set of generalised 3D differential equations that describe the de-tumbling process were derived in Subsection 6.2.3. The numerical integration process of the chaser-target system is a complex problem as it includes a set of non-linear differential equations where the translational and rotational dynamics of the two objects are coupled. Moreover, four control variables are identified, the error in the relative distance, the error in the relative pointing, the relative angular velocity of the target and the inertial angular velocity of the chaser. A set of manoeuvres executed by the chaser, based on a proportional-derivative (PD) control, were presented in Subsection 6.2.4. The characteristic times of the manoeuvres need to be calibrated in order to achieve a stable control and an efficient criterion to select these parameters is based on the minimization of the total ΔV of the de-tumbling process. Furthermore, a model to include the possible inaccuracies derived from sensors and actuators was presented by treating the characteristic times as functions of time. The 3D dynamical equations for the de-tumbling process were then generalised including the effect of inaccuracies and delays in Subsection 6.2.4.1.

However, the large amount of possible combinations between the variables τ_{mi} leads to a complicated optimisation process. A simplified 2D analytical study in the vicinity of the final equilibrium state was also included in the Appendix A.9 and it sheds some light over the effect of the characteristic times of the control manoeuvres on the stability of the system. Although the conclusions of the linear analysis can not be exported to the full dynamical problem, it has been shown that it can be a useful tool to make an educated initial guess of the variables τ_{mi} in the optimisation process.

In addition, the generalised 3D control strategy based on a proportional-derivative control was tested and validated for two different case studies; the de-tumbling of an Ariane-4 in a LEO and GTO orbits. These results showed a successful control of the chaser-target system throughout the full dynamical process.

Finally, Section 6.4 focused on the experimental tests carried out at the Robotics Innovation Centre, DFKI, in Bremen (Germany). The tests were carried out at the INVERITAS facility, a test facility typically used to simulate proximity operations between two objects (chaser-target system) and test sensors on-board the chaser spacecraft (e.g. sensors for pose estimation). An open-loop controlled trajectory of the de-tumbling process was fed into the software and a Bumblebee2 stereo camera was located on-board the chaser to record the process. The stereo images were then processed to obtain a 3D reconstruction of the scene. Moreover, two different surface materials were used on the target. The target could be successfully identified in the 3D reconstruction obtained from the image post-processing. However, while the images obtained with the white surfaces exhibited a good resolution, the images obtained with the blue and silver surface were quite dark which made more difficult the target identification. In addition, strong reflections of the incident light on the panels took place at specific moments during the target's rotation which blinded the camera. These results highlighted the importance of not only the illumination conditions for passive optical cameras but also the importance of the surface materials of the target object as very distinct responses were obtained for the two tested materials.

All in all, this chapter has shown that the control for the eddy brake is challenging but achievable.

SEVEN

CONCLUSIONS

7.1 Project summary and key research results

The presented work can be divided into two main areas of research: the development of the *magnetic tensor theory* in Chapters 3 and 4 and the *eddy brake method* in Chapters 5 and 6.

The first part of the project focused on the development of a new mathematical approach that generalises the existing analytical models and simplifies the numerical methods typically employed to analyse the eddy current phenomenon for space debris objects.

The second part of the dissertation investigated the practical application of using this compelling contactless de-tumbling method based on the generation of eddy currents which can serve as a stepping stone for future active debris removal missions.

7.1.1 Project background

The project background was introduced in Chapters 1 and 2 outlining the current status of the space debris population as well as the various mitigation procedures that have been proposed to tackle this problem. Special attention was given to active debris removal processes and the various challenges that still need to be addressed before ADR can become a reality. Among these challenges, the difficulties derived from the capture of non-cooperative rotating objects were presented.

Subsequently, a comprehensive summary of past space debris attitude observations and current attitude models was provided in order to facilitate a concise understanding of the current knowledge of space debris rotational dynamics.

The chapter finalises with a thorough description and comparison of the existing de-tumbling methods highlighting the advantages and disadvantages of each of them. Every method has its restrictions and limitations and therefore, there isn't a unique solution that can tackle all the existing targets within the space debris population. Moreover, the TRL of these methods is still very low and their feasibility in a real ADR mission is still not guaranteed.

7.1.2 The magnetic tensor theory

Chapter 3 focuses on the development of a new mathematical approach, referred to as the *magnetic tensor theory*, which analyses the generation of eddy currents on rotating metallic objects subject to a homogeneous and constant magnetic field. This theory is based on the discovery of a tensor

named the *magnetic tensor*. The existence of this tensor is proved as well as all its major properties which include the fact that it is a symmetric Cartesian tensor of second order with no negative eigenvalues. These properties are in line with the fact that the eddy currents phenomenon is a dissipative effect and they lead to a quadratic form of the dissipated energy from which the magnetic tensor can be derived.

A method to evaluate this tensor based on a generic finite element method was provided as well as a particularization for a specific FEM, called the *frame model*, which leads to a direct formula to evaluate this tensor. This way, the eddy current torque solution may be found without the necessity to solve the classical Poisson equation with Neumann boundary conditions in each time step of the integration process of Euler's equation. This breakthrough greatly reduces the complexity and computational time of the classical approach commonly adopted in the past. In addition, the analytical formulation of the eddy current torque is generalised for any type of body and relative orientation between its angular velocity and the external magnetic field vectors.

In addition, the analytical solutions of the magnetic tensor for a spherical shell, a cylindrical shell with open ends and flat plates were provided. The analytical solution of these canonical shapes together with the use of the frame model for other more complex shapes provides a means to accurately model a generic space debris object in an efficient and fast way.

Furthermore, the effects produced by the non-uniformity of the magnetic field were analysed based on the introduction of an effective magnetic tensor. While this effect can be neglected for the Earth's magnetic field, it becomes noticeable in the proposed eddy brake de-tumbling method. The conducted analysis for non-uniform magnetic fields is only valid for quasi-spherical objects. The non-uniformity of the field results in a loss of efficiency of the magnetic tensor which depends on the dimensions of the target object and the magnetic source (e.g. magnetic coil) and their relative distance. In addition, an explicit formula to evaluate the net force that appears due to the non-uniformity of the field was obtained which is proportional to the magnetic tensor.

Moreover, the magnetic tensor theory was generalised for a time-varying homogeneous magnetic field and objects with relative linear and angular velocity with respect to the magnetic source. An exact solution can be reached based on the magnetic tensor thanks to the fact that the linearity in $\vec{\Omega}$ of the differential equations for the electric current density vector is kept.

Some additional considerations on the introduction of ferromagnetic materials were included and a simplified solution on the target's magnetic moment was provided assuming that the contribution of the ferromagnetic components is small compared to the overall object's volume. These materials are typically avoided in spacecraft design due to their detrimental impact on the total weight and the residual magnetic moment. Therefore, the assumption made is acceptable for most space debris objects. A comprehensive reasoning on the aforementioned statement may also be found in this chapter.

The theoretical analysis of Chapter 3 is concluded with a case study for the Envisat spacecraft. The measurements carried out from 2013 until 2015 showed a gradual decrease in the angular velocity whose cause is attributed to the Earth's magnetic field. The goal of this case study is to validate this hypothesis by comparing the numerical spin rate change obtained with the magnetic tensor theory and the past observations. The numerical results showed a secular decrease in the spin rate of Envisat equal to 0.00149 deg/s per day which is very similar to the result from the measurements, equal to 0.00156 deg/s per day. This result again highlights the effectiveness of the theory developed in providing reliable results.

Then, Chapter 4 gathered a thorough description of the experimental tests carried out at Airbus Defence & Space. The goal of these experimental tests was to empirically validate the magnetic tensor theory. Note that the theory was already numerically validated through the comparison of the magnetic torque provided by the MTT and available results from previous authors in the previous chapter. Nevertheless, experimental tests were conducted seeking to provide empirical validation in order to further consolidate this theory.

The tests consisted in measuring the evolution of the rotation rate of several metallic objects subject to a constant and homogeneous magnetic field. The pieces were suspended from a strut

with a torsion wire in order to generate a uniaxial oscillatory rotation and they were placed at the centre of a Helmholtz coil. Different values of the magnetic fields were analysed in order to obtain the characteristic time of decay of the spin rate of the objects. The experiments allowed for the visualization of the decay rates for different magnetic fields as well as different spin axes. The measurements obtained closely matched the expected numerical results. The deviation between the empirical results and the analytical values ranged from 0.7% to 12.3%. Among the possible causes of the observed deviations, it was concluded that the most probable sources of error could be the registered fluctuations in the magnetic field together with inaccuracies associated with the optical measurements.

Moreover, the empirical results unveiled that the eddy current phenomenon was noticeable for the spherical and cylindrical shells while it was imperceptible for the aluminium honeycomb panels. This difference of behaviour highlights the importance of the amount of metallic material for the eddy current generation. While the spherical and the cylindrical shells were fully metallic components, the aluminium panels only contain very thin aluminium skins. In addition, the panels were not electrically connected which reduces the eddy current effect. Thus, it may be concluded that the most noticeable dissipative effects on spacecraft will appear on fully metallic components, such as propellant tanks.

All in all, the magnetic tensor theory constitutes a breakthrough in the modelling of the eddy currents which generalises and simplifies the analytical and numerical methods used so far. The present document provides the mathematical and physical basis as well as the necessary tools to understand and implement this theory.

7.1.3 The eddy brake method

Chapters 5 and 6 focus on the design of a contactless de-tumbling method based on the generation of eddy currents named the *eddy brake* method. The idea presented here is to subject a space debris object to an enhanced magnetic field in order to damp its rotation and allow for its capture and subsequent controlled de-orbiting phase. This idea was first introduced by Kadaba and Naishadham in 1995 but little work has been carried out since then. The advances in high temperature superconducting materials as well as spacecraft sensors and actuators has allowed for a compelling new design to be reached within this research which may serve as a stepping stone for future ADR missions.

This method has several advantages with respect to other proposed de-tumbling methods. Firstly, the superconducting materials employed allow the chaser to be placed several metres away from the target and still generate a noticeable magnetic field inside the space debris object. This way the de-tumbling process is contactless and thus, eliminates the hazards associated with complicated proximity operations and docking/grabbing of non-cooperative rotating objects. Secondly, it is a non-invasive technique and the risk of generating new debris is very low. The decrease of the angular velocity occurs gradually thanks to Joule's effect which dissipates the kinetic energy of the object into heat. Therefore, this method is less aggressive for the target than other de-tumbling methods which generate impulsive forces that can damage the object or that are based on the sublimation of the surface material. Finally, the eddy brake allows the reduction of the target's angular velocity to be easily controlled. The induced torques will always oppose the target's angular velocity, thus, there is no risk of increasing its spin rate.

First of all, Chapter 5 concentrates on the systems engineering design of the eddy brake. This analysis identified the key drivers and main requirements of the eddy brake, analysed its integration into the chaser and its interactions with the target. The de-tumbling process is carried out actively by the chaser which has an electromagnetic coil on-board based on second generation high temperature superconducting wires (2G HTS).

The design process started with an analysis of the electromagnetic coil. HTS and conventional coil materials were first compared and a thorough parametric analysis was provided for both options. HTS wires greatly reduce the mass and volume compared to conventional wires and they dissipate no power when operating in the superconducting regime, which makes them a far more attractive

option. A baseline design for the coil was reached taking into account the volume and mass limitations of current European launchers.

The two most relevant subsystems to support the operation of the eddy brake are the *thermal* and the *guidance, navigation and control* (GNC) subsystems. Firstly, the thermal subsystem needs to guarantee that the coil will always work below its critical temperature. HTS wires have proved to be superconducting up to temperatures of 100 K or even higher. However, the system will be more stable when working at lower temperatures and a working temperature in the range of 65K-77K is typically recommended. The major sources of heat were analysed concluding that the Sun and the Earth are the two most important ones. Under these conditions a thermal analysis of the coil was carried out including passive insulation techniques. The results from this analysis revealed that the coil was well above its critical temperature both during eclipse and out of eclipse periods which drove the necessity to include active thermal control techniques. Among the various techniques that were assessed, two possible solutions were found; a loop heat pipe plus two cryocoolers or a dewar-based system. The cryocooler option is more advantageous in terms of mass and volume and it does not limit the operational lifetime of the coil. However, these benefits are achieved at the expense of high power consumption by the cryocooler which would be avoided otherwise by the dewar-based system. Hence, the dewar-based system is the preferred option for short de-tumbling operations (i.e. in the order of days) while the cryocooler option is more favourable for longer de-tumbling operations.

Moreover, the major requirements and technological assessment of the GNC subsystem were addressed in Chapter 6. This subsystem has to ensure an adequate chaser-target configuration for the de-tumbling process to be effective, in terms of relative pointing of the coil and relative distance between the two objects. The pose estimation phase is of paramount importance for the eddy brake in order to achieve an effective de-tumbling process. Two possible ways to infer the pose of the target were analysed; from direct measurements taken by sensors on-board the chaser or indirectly from the magnetic interactions between the two objects. However, it was found out that this latter option was very challenging due to the fact that the eddy current forces and torques on the chaser are expected to be of the order of milliNewtons and milliNewtons metres which would be easily covered up by other external perturbations. Then, among the available pose estimation sensors in the market, the flash LIDAR was identified as the most adequate option. This is due to the procured sensor range and field of view, its range and attitude accuracies, its robustness with respect to the illumination conditions, its capacity to capture rapid changing scenes and its reliability. Furthermore, the necessary actuators for the eddy brake were evaluated.

With respect to the attitude control, it was determined that the Earth's magnetic torque was the dominant perturbation which drove the need to include control moment gyros for LEO and reaction wheels for GEO. A solution was found which cancels out the magnetic torque based on the use of an AC electric current of low frequency instead of a direct current. This way the chaser's attitude control is greatly simplified but it increases the characteristic time of the de-tumbling process by a factor of 2.

Additional design drivers were discussed within this chapter such as the possible magnetic interferences with the equipment on-board and possible design configurations of the coil. The trade-offs conducted concluded that the most convenient option would be to have a fixed coil mounted on the main body of the chaser. A list of sensitive equipment to magnetic fields was provided as well as some general guidelines which should be adopted in order to avoid any performance degradation of the on-board equipment.

Chapter 5 concludes with a brief description of the phase 0 study conducted for the Agora mission (Active Grabbing & Orbital Removal of Ariane). This study was performed in the frame of the Stardust programme in collaboration with additional universities and private companies and it enabled the opportunity to analyse the eddy brake as part of an overall ADR mission system design. The de-tumbling phase turned out to be the most power consuming phase and this drove the sizing of the power subsystem. Moreover, a set of in-orbit experimental tests were defined which would prove the correct performance of the eddy brake method in space and raise its TRL.

Then, Chapter 6 presented a comprehensive analysis on the dynamics of the chaser-target system

based on the magnetic tensor theory and the necessary control throughout the de-tumbling process. The generalised 3D differential equations were derived including the magnetic interactions between the two objects, additional external perturbations, the control manoeuvres of the chaser and inaccuracies and delays derived from the on-board sensors and actuators. The generalised problem exhibits a great complexity as it involves the numerical integration of twelve second order differential equations where the linear and rotational dynamics of the two objects are coupled.

Moreover, four control variables were identified: the error in the relative distance, the error in the relative pointing, the relative angular velocity of the target and the inertial angular velocity of the chaser. A set of manoeuvres based on a proportional-derivative controller were presented which include some characteristic times of the manoeuvres, τ_{mi}, that need to be calibrated in order to achieve a stable control. It was also identified that an efficient criterion to select these parameters is based on the minimization of the total ΔV of the de-tumbling process. However, the large amount of possible combinations between the variables τ_{mi} leads to a complicated optimisation process. A simplified 2D analytical study in the vicinity of the final equilibrium state was also included which helped to understand the effect of the different parameters involved in the problem before dealing with the general 3D cases in numerical simulations. Although the conclusions of the linear analysis can not be exported to the full dynamical problem, it was shown that it can be a useful tool to make an educated initial guess of the variables τ_{mi} in the optimisation process.

The generalised 3D control strategy was tested and numerically validated for two different case studies. The selected target is an Ariane-4 H10 upper stage which resides in a LEO orbit for the first case study and a GTO orbit for the second case study. The results of these simulations showed a successful control of the chaser-target system throughout the full dynamical process.

Chapter 6 finalises with some experimental tests conducted at the Robotics Innovation Centre, DFKI, in Germany. The tests were carried out at the INVERITAS facility which contains a system demonstrator of a tumbling target and a servicer. An open-loop controlled trajectory of the de-tumbling process was fed into the software and a Bumblebee2 stereo camera was mounted on the chaser to record the process. The stereo images were then processed to obtain a 3D reconstruction of the scene. Moreover, two different surface materials were used on the target. The target could be successfully identified in the 3D reconstruction obtained from the image post-processing. However, while the images obtained with the white surfaces exhibited a good resolution, the images obtained with the blue and silver surface were quite dark which made the target's identification more difficult. In addition, strong reflections of the incident light on the panels took place at specific moments during the target's rotation which blinded the camera. These results highlighted the importance of not only the illumination conditions for passive optical cameras but also the importance of the surface materials of the target object as very distinct responses were obtained for the two tested materials.

It may be concluded from the systems engineering design together with the numerical and experimental validations that the eddy brake is a promising solution to reduce the rotation of metallic space debris and allow for their subsequent capture. No major impediments were identified which make the eddy brake unfeasible, neither from a physical perspective related to the eddy current phenomenon nor from a technological perspective related to the execution of this method.

However, many of the proposed subsystems are quite novel and still have a low technology readiness level which leads to the necessity for additional on-ground validation and testing. For example, this is the case of HTS wires which have been flown in a few in-orbit demonstration missions but still require further investigation and in-orbit testing to prove their performance in space. Additionally, the thermal subsystem for the coil based on a loop heat pipe and cryocoolers has gone through extensive ground testing at MIT for the EMFF study but it has never been used in space. Finally, various guidelines and recommendations have been provided to avoid electromagnetic interferences. However, all the electronic equipment on-board must go through thorough test campaigns in order to guarantee that their performance will not be affected by the generated magnetic field.

In spite of the fact that additional validation and testing is needed for the eddy brake to become a reality, the present document lays the foundation for subsequent work and points towards the critical technologies and system design areas that need special attention.

7.2 Major contributions

7.2.1 Chapter 3: MTT fundamental theory.

The development of the magnetic tensor theory entails a meaningful progress in the study of the eddy current phenomena and, in particular, in the analysis of the attitude dynamics of man-made objects in orbit. This theory generalises the previously existing analytical solutions of the eddy current torque and greatly simplifies the numerical methods employed so far. The major contributions are listed below:

- Proof of existence of the magnetic tensor and its various properties:

    - The magnetic tensor is a Cartesian second order tensor.

    - The magnetic tensor is symmetric.

    - The magnetic tensor has no negative eigenvalues.

    - If a rigid body is composed of N metallic bodies not electrically connected, the magnetic tensor of the rigid body is equal to the sum of the magnetic tensor of each body.

    - The magnetic tensor does not depend on the origin of the coordinate system.

- General solution to evaluate the magnetic tensor based on a generic FEM and a particularization for a specific FEM (frame model) which leads to a direct formula to evaluate this tensor.

- Establishment of explicit analytical formulae for the eddy current torque and the dissipating energy per unit time based on the MTT.

- Theoretical validation of the MTT with existing solutions of the eddy current torque for certain canonical bodies.

- Analytical solutions of the magnetic tensor for a spherical shell, a cylindrical shell with open ends and flat plates.

- Direct formula for the eddy current force in the case of a non-homogeneous magnetic field.

- Generalisation of the MTT for time-varying magnetic fields, relative linear and rotational velocity of the body with respect to the external magnetic field and ferromagnetic materials.

- Development of a numerical simulator in MATLAB including 3D linear and rotational dynamics of an Earth-orbiting object. The following perturbations were included in the propagator:

    - Earth's gravity field based on JGM-3 gravitational model including 4 zonal harmonic coefficients.

    - Atmospheric drag. The atmospheric density was computed using the Jacchia 1970 model.

    - Solar radiation.

    - Earth's magnetic field based on the IGRF-11 model, magnetic tensor theory to model the eddy current torques and magnetic torques caused by a residual magnetic dipole.

- Successful explanation based on the MTT of the observed behaviour of the rotational dynamics of the Envisat spacecraft. The results showed an outstanding agreement between the observations made by SRL Graz in 2013 and the numerical predictions provided by the MTT, which reinforces the effectiveness of this method.

7.2.2 Chapter 4: MTT experimental validation.

The experimental tests conducted at Airbus Defence & Space showed a noticeably good agreement between the empirical data and the theoretical predicted values by the magnetic tensor theory with deviations ranging from 0.7% to 12.3%. These results enhance the robustness of the MTT.

The tests conducted pursued the following objectives which were successfully met:

- Analyse the characteristic time of decay for different magnetic field intensities.

- Analyse the characteristic time of decay for different shapes.

- Analyse the characteristic time of decay for different orientations.

A significantly different behaviour was observed between the fully metallic objects (i.e. spherical shell and cylindrical shell) and the aluminium honeycomb panels. While the fully metallic components were quickly de-spun, the eddy current effect on the honeycomb panel was imperceptible for the maximum allowable magnetic field within the facility. This result highlights the importance of the amount of metallic material and their electrical connectivity in order to generate eddy current loops. An important conclusion of these tests is that fully metallic components inside space debris such as propellant tanks or electronic boxes are likely to be the most noticeable contributors to the generation of eddy currents.

7.2.3 Chapter 5: Systems engineering design of the eddy brake.

The recent advances in HTS materials have made it possible to design a compelling de-tumbling method which can serve as a stepping stone for future ADR missions. The following accomplishments in the system's engineering design were made:

- Materials and coil design: A thorough parametric analysis was carried out in order to compare conventional coil materials (i.e. aluminium, copper) and HTS materials. A baseline design based on HTS wires was reached which copes with the baseline requirements of the de-tumbling process.

- Thermal subsystem: A thermal analysis was carried out to assess the necessity for passive and/or active thermal control subsystems. Various thermal control subsystems were evaluated and compared reaching two possible solutions. The dewar-based system is the preferred option for short de-tumbling operations (i.e. in the order of days) while the LHP+cryocooler option is more favourable in terms of mass and volume for longer de-tumbling operations. The mass, volume and power requirements for each option were detailed as well as COTS equipment that could be employed.

- GNC subsystem: The main requirements of this subsystem were outlined as well as suitable sensors and actuators needed for the eddy brake. A trade-off analysis of pose estimation sensors was included, indicating expected inaccuracies and delays of the pose estimation phase which may affect the control. Special attention was paid to the Earth's magnetic field because it is the dominant perturbation in LEO. A solution based on the use of an AC current was proposed to cancel out the Earth's magnetic torque on the coil.

- Coil's configuration and electromagnetic interferences: Various trade-offs were performed in order to choose the optimal configuration of the coil. A fixed coil to the main body of the chaser was identified as the most reasonable option in terms of mass, risk, TRL and complexity of the operations. As a consequence of this choice, special attention must be paid to the possible electromagnetic interferences with the on-board instruments. Several design guidelines were presented, including a list of sensitive equipment which should be avoided.

- Agora phase 0: the major results of phase 0 study were provided, including an overview of the mission phases, chaser's design and mission budgets (mass and power budgets). Moreover, a detailed description of the in-orbit experimental tests envisaged for the eddy brake was included.

7.2.4 Chapter 6: Dynamics chaser-target and experimental tests.

The generalised 3D dynamics of the chaser-target system is a complex problem and a successful control strategy was found which can guarantee a stable de-tumbling process. The following accomplishments were made:

- Provision of the generalised dynamical equations that govern the de-tumbling process.

- Assessment of the possible relative configurations of the coil with respect to the target.

- Assessment of the minimum number of control variables and specifications of a control strategy based on a PD controller.

- Stability analysis for a 2D simplified configuration to better understand the local stability around the equilibrium position and the effect of the parameters involved.

- Development of a numerical simulator in MATLAB including the environmental perturbations listed in 7.2.1, the magnetic interactions between the chaser and the target and the proposed control strategy including inaccuracies and delays derived from the chaser's sensors and actuators.

- Numerical simulations for the de-tumbling of Ariane upper stages in LEO and GTO to validate the control strategy throughout the full dynamical problem.

- Experimental tests conducted at the INVERITAS facility at DFKI to test open-loop controlled trajectory of the de-tumbling process, obtain stereo images of the target from a chaser's on-board camera and process them to achieve a 3D reconstruction of the target.

7.3   Secondments

Throughout my research, I carried out two secondments, each lasting three months, outlined below:

- Secondment at Airbus Defence & Space (Oct-Dec 2014, Stevenage, UK): During this secondment I performed experimental tests that have helped to validate the 'Magnetic Tensor Theory'. These tests involved the generation of eddy currents in several rotating metallic objects subject to a homogeneous magnetic field. The experimental and theoretical characteristic time of decay caused by the eddy currents phenomenon showed a very good agreement. This secondment also allowed me to further develop the systems engineering design of the 'Eddy Brake' thanks to the applied knowledge and experience of various experts at the site.

- Secondment at the DFKI Robotics Innovation Centre (Sept-Nov 2015, Bremen, Germany): During this secondment I carried out experimental tests in the INVERITAS facility to test open loop trajectories for the Eddy Brake. The tested trajectories reproduced the relative motion between a mock-up chaser and target during the de-tumbling process. A Bumbleebee2 stereo camera was placed on-board the chaser to obtain stereo images of the target. These images were also processed to analyse the pose of the target. This secondment allowed me to better understand the difficulties derived from image processing in space, to get acquainted with sensors for pose estimation processes and to analyse the effect of delays and inaccuracies in the GNC loop.

7.4   Publications and awards

7.4.1   Journal paper and book publications

The following journal papers have been published:

- N. Ortiz Gómez and S.J. Walker, *'Earth's Gravity Gradient and Eddy Currents Effects on the Rotational Dynamics of Space Debris Objects: Envisat Case Study'*, Advances in Space Research, January 2015, doi:10.1016/j.asr.2014.12.031,

- N. Ortiz Gómez and S.J. Walker, *'Eddy Currents applied to De-tumbling of Space Debris: Analysis and Validation of Approximate Proposed Methods'*, volume 114, pages 34-53, Acta Astronautica, April 2015, doi: 10.1016/j.actaastro.2015.04.012,

- N. Ortiz Gómez and S.J. Walker, *'Guidance, navigation and control for the Eddy Brake method'*, volume 40, issue 1, pages 52-68, Journal of Guidance, Control, and Dynamics, December 2016, doi:10.2514/1.G002081,

In addition, I am co-author of the following chapter of the book *'Asteroid and Space Debris Manipulation'*:

- S. Walker and N. Ortiz Gómez, *'Rotational Dynamics and Attitude Control for Space Debris Rendezvous and Capture'*, chapter 17, Asteroid and Space Debris Manipulation, AIAA 2016.

7.4.2 Conferences and public talks

This research has been presented at the following conferences:

- N. Ortiz Gómez and S.J. Walker, *'Tumbling of space debris and eddy currents applied to de-tumbling of space debris'*, Stardust 1st Global Virtual Workshop on Asteroids and Space Debris, Glasgow, May 2014. Oral presentation.

- N. Ortiz Gómez and S.J. Walker, *'Eddy currents applied to de-tumbling of space debris: feasibility analysis, design and optimization aspects'*, Proceedings of the 40th COSPAR Scientific Assembly PEDAS.1-0030-14, Moscow, August 2014. Oral presentation.

- N. Ortiz Gómez and S.J. Walker, *'High temperature superconducting wires applied to the de-tumbling of space debris with eddy currents'*, Stardust Second Training School on astrodynamics of NEO and space debris, Rome, September 2014. Oral presentation.

- N. Ortiz Gómez and S.J. Walker, *'Eddy currents applied to de-tumbling of space debris: analysis and validation of approximate proposed methods'*, Proceedings of the 65th International Astronautical Congress IAC-14,A6,6,2x22528, Toronto, September 2014. Oral presentation and conference paper.

- M. Jankovic, K. Kumar, N. Ortiz Gómez, J. Romero Martín, F. Kirchner, F. Topputo, S. Walker and M. Vasile, *'Spacecraft concept for active de-tumbling and robotic capture of Ariane rocket bodies'*, 13th Symposium on Advanced Space Technologies in Robotics and Automation (ASTRA), ESTEC The Netherlands, May 2015. Poster presentation.

- N. Ortiz Gómez and S.J. Walker, *'The eddy brake. Experimental validation'*, Stardust 3rd Training School, Universidad Internacional Menéndez Pelayo, Santander, Spain, July 2015. Oral presentation.

- Jankovic, M., Kumar, K., Romero Martín, J., Ortiz Gómez, N., Kirchner, F., Topputo, F., Vasile, M., Walker, S., *'Autonomous robotic system for active debris removal: requirements, state-of-the-art and concept architecture of the rendezvous and capture (RVC) control system'*, 5th CEAS Air & Space Conference (Council of European Aerospace Societies), The Netherlands, September 2015. Oral presentation by M. Jankovic and conference paper.

- K. Kumar, N. Ortiz Gómez, M. Jankovic, J. Romero Martín, F. Topputo, S.J. Walker, F. Kirchner and M. Vasile, *'Agora: Mission to demonstrate technologies to actively remove Ariane rocket bodies'*, 66th International Astronautical Congress IAC-15,A6,6,1,x28851, Jerusalem, October 2015. Oral presentation by K. Kumar and conference paper.

- N. Ortiz Gómez and S.J. Walker, M. Jankovic, J. Romero Martín, F. Kirchner and M. Vasile, *'Control analysis for a contactless de-tumbling method based on eddy currents: problem definition and approximate proposed solutions'*, AIAA Guidance, Navigation, and Control

Conference, AIAA SciTech, San Diego, CA, January 2016. Oral presentation and conference paper.

- N. Ortiz Gómez and S.J. Walker, M. Jankovic and J. Paul, *'Pose estimation and control for the eddy brake de-tumbling method'*, Stardust 2nd Global Virtual Workshop on asteroids and space debris, Southampton, UK, January 2016. Oral presentation and extended abstract.

- N. Ortiz Gómez and S.J. Walker, *'The eddy brake method. A contactless de-tumbling method for space debris objects'*, Final Stardust Conference, European Space Agency (ESTEC), The Netherlands, November 2016. Oral presentation and extended abstract.

The following dissemination talks have been carried out as part of the research:

- N. Ortiz Gómez, *'De-tumbling method based on eddy currents for space debris objects'*, Brown Bag talk at DFKI Robotics Innovation Centre, Germany, 16th September 2015.

- N. Ortiz Gómez, *'Stardust - The Asteroid and Space Debris Network'*, Talk at the Newbury Astronomy Society, UK, 6th May 2016.

7.4.3 Awards

Furthermore, I received the following awards in recognition of the work developed during this research:

- 2015 **Amelia Earhart fellowship**, Zonta International. Zonta International, through its foundation, awards each year Amelia Earhart Fellowships to 35 women pursuing Ph.D./doctoral degrees in aerospace-related sciences and engineering, chosen from applicants worldwide.

- 2016 Committee on Space Research (COSPAR) award. **Outstanding Paper Award for Young Scientists** for the manuscript entitled *'Earth's Gravity Gradient and Eddy Currents Effects on the Rotational Dynamics of Space Debris Objects: Envisat Case Study'*, Advances in Space Research, January 2015, doi:10.1016/j.asr.2014.12.031.

- 2016 **AIAA GNC Best Presentation** in session. Award for the best presentation in session GNC-07 Spacecraft Attitude Control II at the AIAA Science and Technology Forum and Exposition in January 2016. The manuscript presented was *'Control analysis for a contactless de-tumbling method based on eddy currents: problem definition and approximate proposed solutions.'*, AIAA SciTech, San Diego, CA, January 2016.

7.5 Future Work

As a result of the novelty and low TRL of the two main research topics addressed in this thesis, areas for future work can easily be identified.

7.5.1 Magnetic tensor theory

1. Fundamental theory:
   - The mathematical analysis conducted to study the effect produced by a non-uniform magnetic field is only valid for quasi-spherical objects and further in-depth analysis is needed to extend it for other geometries.
   - The mathematical analysis done to study the effect produced by ferromagnetic materials took as a hypothesis that the volume of ferromagnetic material was small compared to the total volume and that the hysteresis effects were negligible. Additional research is required in this area in order to generalise the magnetic tensor theory to all types of magnetic materials.

2. Experimental tests:

- The results obtained for aluminium honeycomb panels were non-conclusive because the eddy current effects could not be observed. Additional experimental tests are needed which foster measurable and observable eddy current effects. This may be achieved by employing higher magnetic fields than the ones used here or by conducting the test inside a vacuum chamber where the effect of the air drag would be avoided.

- Additional tests should be carried out for COTS spacecraft components which usually contain metallic materials such as batteries, power control and distribution units, propellant tanks, etc. in order to accurately characterise their contribution to the generation of eddy currents.

- Additional experimental tests should be done in a vacuum chamber in order to eliminate the effect of the air drag and also for temperatures similar to those expected in orbit. The electrical conductivity is expected to increase when the temperature decreases with the consequent improvement in the generation of the eddy currents.

7.5.2 Eddy brake

- Further research with regard to the electromagnetic interferences is needed in order to evaluate more accurately the maximum magnetic field values that the on-board equipment can tolerate without suffering any performance degradation (e.g. saturation of ferromagnetic components).

- The spacecraft body heating source was neglected in the thermal analysis of the coil assuming a perfect isolation system for the coil. However, the thermal coupling between the coil and the spacecraft body may be strong and a more in-depth analysis will be needed in the future.

- The results of the preliminary study of the plasma drag addressed in Section A.10 of the annex show that this is a non-negligible perturbation for the chaser spacecraft that should be taken into account in future studies. It should be highlighted that the study carried out within this research is just a preliminary study and more detailed analyses of the interaction between the coil and the space plasma will be needed in the future.

- The control strategy can be improved and, therefore, the total ΔV reduced by using time-varying characteristic times of the control manoeuvres, τ_{mi}, which are adjusted and optimised throughout the de-tumbling process.

- Additional effects should be included in the numerical simulations such as non-rigid body motion due to the existence of flexible structures or propellant slosh.

There is, as for any complex engineering problem like this, a significant amount of practical effort required to increase the TRL level and turn this concept into a reality.

This work has taken the spark of the idea previously suggested by by Kadaba and Naishadham in 1995 [11] and has shown it to be a very advantageous solution to the problem. It is hoped that a company or agency in the future will put the necessary time in to make this concept become a reality.

APPENDIX

A.1 Reference frames

Three different reference frames are used throughout this dissertation:

- Inertial Reference Frame: This reference frame has its origin at the Earth's centre. The X axis points at the vernal equinox and the Z axis points in the direction of the North Pole [208]. The nomenclature for this reference system is (X_i, Y_i, Z_i).

- Orbital Reference Frame: This reference frame has its origin in the centre of gravity (COG) of the body in orbit. The Y_0 axis points in the along track direction, parallel to the velocity of the body ($\vec{j}_0 = \frac{\vec{v}}{|\vec{v}|}$) and the Z_0 axis is perpendicular to the orbital plane, parallel to the orbital angular momentum. Finally, the X_0 axis completes the reference frame ($\vec{i}_0 = \vec{j}_0 \times \vec{k}_0$). In the case of a circular orbit, the X_0 axis coincides with the nadir direction.

- Body Frame: This reference frame has its origin in the COG of the body and coincides with the principal axes of inertia of the object. The nomenclature for this reference system is (X_b, Y_b, Z_b).

A.2 Equipment used for the empirical validation of the MTT

Section 4 describes the experimental tests carried out in order to empirically validate the magnetic tensor theory. Table A.1 lists the equipment that was purchased including the supplier and overall budget.

Supplier	Item	Series No	# Pieces	Price (£)
RS Components Ltd	Bosch Rexroth Aluminium Strut, 2m L, 45×45mm profile	390-0032	15	437
RS Components Ltd	Bosch Rexroth Strut Profile Angle Bracket, 10mm	390-1805	32	128
RS Components Ltd	Bosch Rexroth Strut Profile Angle Bracket, 10mm	390-1811	5	47
Advent Research Mat.	Tungsten Wire, ⌀ 0.4mm, 5m	W558211	1	77
GoPro	Camera GoPro Hero		1	98
Harting	Han 2Mod-Housing bulkhead mounted	09140020301	1	12
Harting	Han 70A axial module, female 6-16 mm^2	09140022741	1	14
Harting	Han 70A axial module, female 14-22 mm^2	09140022742	1	14
Harting	Han 40A axial module, female 2,5-8 mm^2	09140022701	1	8
Harting	Han 40A axial module, female 6-10 mm^2	09140022702	1	9
SGWebb	Spherical Shell		1	760
SGWebb	Cylindrical Shell		1	745
				2350

Table A.1: Equipment used for the empirical validation of the MTT.

A.3   2G HTS wire specifications

The second generation HTS wires are based on Rare Earth-Barium-Copper-Oxide (ReBCO). The manufacturing process includes the deposition of the HTS material on flexible metal tapes (substrate) coated with buffering metal oxides. A surrounding stabiliser is usually applied to completely encase the wire. The superconducting layer is very thin (usually about 1μm thickness) in comparison with the wire dimensions. The total thickness of the wire is usually between 100-300 μm and the width is usually between 4 mm and 10 mm. An example of an HTS wire manufactured by the company SuperPower is shown in Figure A.1 where the main parts that make up the wire are indicated.
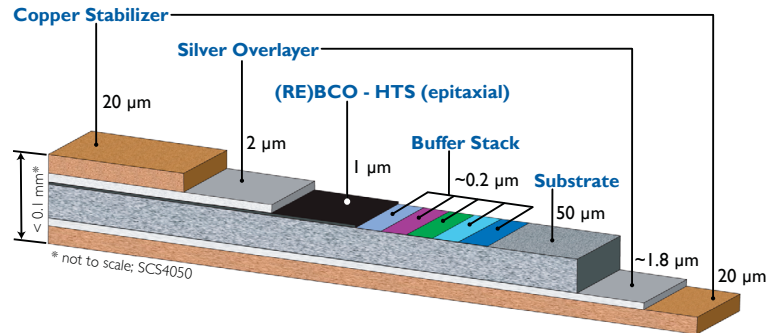
Figure A.1: Example of a 2G HTS wire manufactured by SuperPower Inc.

Table A.2 indicates the characteristics of the HTS second generation wires manufactured by the company SuperPower.

SuperPower® 2G HTS Wire Specifications

Spec SF = Stabilizer Free SCS = Surround Copper Stabilizer	SCS3050	SF4050	SCS4050	SF6050	SCS6050	SF12050	SCS12050	SF12100	Unit
Minimum I$_c$	75	100	100	150	150	300	300	300	amp
Widths	3	4	4	6	6	12	12	12	mm
Total Wire Thickness	0.1	0.055	0.1	0.055	0.1	0.055	0.1	0.105	mm
Standard Copper Stabilizer Thickness	0.04	n/a	0.04	n/a	0.04	n/a	0.04	n/a	mm
Critical Tensile Stress	> 550		> 550		> 550		> 550		MPa
Critical Axial Tensile Strain	0.45%	0.45%	0.45%	0.45%	0.45%	0.45%	0.45%	0.4%	
Critical Bend Diameter in Tension	11	11	11	11	11	11	11	25	mm
Critical Bend Diameter in Compression	11	11	11	11	11	11	11	25	mm

Figure A.2: 2G HTS wire specifications manufactured by SuperPower Inc.

Some of the world-wide manufacturers are listed in Table A.2.

Manufacturer	Country	Substrate	Buffers
AMSC	USA	NiW	Y_2O_3/YSZ/CeO_2
Bruker	Germany	SUS	YSZ/CeO_2
Deutsche Nano	Germany	NiW	LZO/CeO_2
Fujikura	Japan	Hastelloy	AL_2O_3/Y_2O_3/MgO/CeO_2
SJTU/Shanghai SC	China	Hastelloy/SUS	AL_2O_3/Y_2O_3/MgO/CeO_2
SWCC	Japan	Hastelloy	GZO/CeO_2
STI	USA	Hastelloy/SUS	Y_2O_3/MgO
SuNAM	Korea	Hastelloy/SUS	AL_2O_3/Y_2O_3/MgO/LMO
SuperOx	Russia/Japan	Hastelloy	AL_2O_3/Y_2O_3/MgO/LMO/CeO_2
SuperPower	USA	Hastelloy	AL_2O_3/Y_2O_3/MgO/LMO
Theva	Germany	Hastelloy	MgO

Table A.2: Worldwide manufacturers of 2nd Generation HTS wires.

A.4   Material properties

Table A.3 gathers some of the most common metallic materials employed in space indicating useful physical properties.

Name	Composition	Density	Electrical conductivity 20ºC	Permeability
Pure aluminium	Al (100%)	2700 kg/m^3	$3.5 \cdot 10^7$ S/m	1.000022
Pure copper	Cu (100%)	8960 kg/m^3	$5.95 \cdot 10^7$ S/m	0.999
Aluminium 7020	Al (91.2-94.8%), Zn (4.5%), Mg (1%)	2780 kg/m^3	$2.2 \cdot 10^7$ S/m	≈ 1
Aluminium 7075-T6	Al (87.1-91.4%), Cr (0.18-0.28 %), Cu (1.2-2%)	2810 kg/m^3	$1.94 \cdot 10^7$ S/m	≈ 1
Aluminium AA2219	Al (91.5-93.8%), Cu (5.8-6.8 %), Fe (0.3% max)	2840 kg/m^3	$1.72 \cdot 10^7$ S/m	≈ 1
Titanium Ti6Al4V	Ti, Al (6%), V (4%)	4430 kg/m^3	$5.6 \cdot 10^5$ S/m	1.00005
Inconel 600	Ni (70%), Cr (14-17%), Fe (6-10%)	8470 kg/m^3	$9.7 \cdot 10^5$ S/m	1.01

Table A.3: Metallic alloys properties [31, 32].

A.5 Hydrazine tanks 31/0 and 01/0 specifications

Both hydrazine tanks, 31/0 and 01/0 models are manufactured by Airbus Defence & Space. Tables A.4 and A.5 gather the specifications of each tank and Figures A.3 and A.4 show their dimensions.

Hydrazine tank OST 31/0 specifications	
Tank Net Volume	104 to 177 Litres
Propellant	Hydrazine (N_2H_4)
Materials	Ti6AI4V
Mass	6.85 kg
Mean Radius	m
Density Ti6AI4V	4430 kg·m^{-3}
Electrical conductivity Ti6AI4V	$5.62 \cdot 10^5$ S/m

Table A.4: Hydrazine tank OST 31/0 specifications provided by Airbus Defence & Space.

Hydrazine tank OST 01/0 specifications	
Tank Net Volume	58 Litres
Max. Propellant Volume	39 Litres
Propellant	Hydrazine (N_2H_4)
Materials	Ti6AI4V
Mass	8.5 kg
Mean Radius	0.240 m
Density Ti6AI4V	4430 kg·m^{-3}
Electrical conductivity Ti6AI4V	$5.62 \cdot 10^5$ S/m

Table A.5: Hydrazine tank OST 01/0 specifications provided by Airbus Defence & Space.
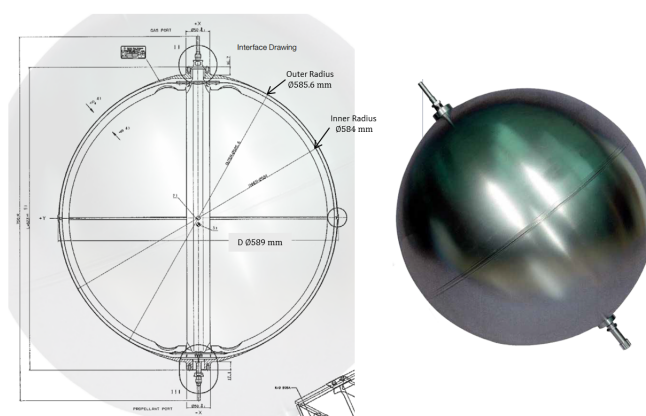
Figure A.3: Hydrazine Propellant Tank 31/0.
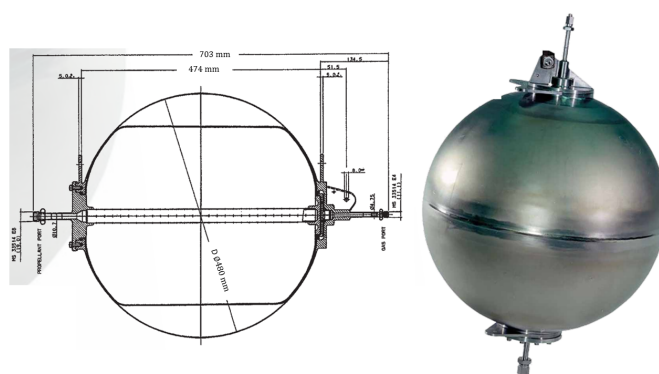
Figure A.4: Hydrazine Propellant Tank 01/0.

A.6 CMG specifications

At present, two companies in Europe manufacture CMGs for agile satellites: Airbus/Teldix which manufactures the model CMG 15-45S for satellites in the one ton class and SSTL which manufacture mini-CMGs for smaller SC. The CMG 15-45S system consists of 4 actuators positioned in a pyramid configuration for singularity avoidance and/or redundancy. Figure A.5 shows a picture of one CMG and its main specifications are outlined in Table A.6.

Figure A.5: CMG 15-45S.

CMG 15-45S Specifications	
Manufacturer	Airbus Defence & Space
Standard Angular momentum	15 [N·m·s] per CMG
Standard Torque	45 [N·m]
Pointing Performance	<10 mrad
Mass per CMG	18 kg
Power	25 W @15 Nms per CMG
Volume	Mechanism diameter= 270mm, height= 350mm. Electronics 310×300×150 mm^3 (1 box for 4 CMG)
Life time	5 years
Past missions	SPOT 6, SPOT 7, Pléiades HR.

Table A.6: CMG 15-45S Specifications.

A.7 Cryocooler K353 specifications

The cryocooler K353 is manufactured by the company RICOR. Figure A.6 shows the dimensions of the cryocooler, Figure A.7 shows the power specifications and Table A.7 contains all the specifications of the device.

Figure A.6: K535 cryocooler manufactured by RICOR.

Figure A.7: K535 cryocooler cooling power.

K535 Specifications	
Manufacturer	RICOR
Cooling Power	7W, @23C, 65K
Weight (cooler+controller)	9.5 Kg
Input Voltage	220V/110V
Maximum Power	300 Wdc
Steady State	200Wdc, @5W, 65K
Cold finger diameter	25.4 mm
Operation Temperature Range	-20°C-71°C
Non-Operational Temperature Range	-56°C-85°C

Table A.7: K535 cryocooler specifications.

A.8 Spacecraft charging effects

Plasma is defined as an electrically neutral medium of ions and electrons of low density. This gas surrounds the Earth planet with different densities depending on the altitude, latitude, day of time and sunspot cycle [209]. In GEO the ambient plasma is characterised by having a low density ($0.1 - 10$ cm^{-3}) and high energy (1-50 keV) while in LEO the plasma environment is more dense ($10^2 - 10^6$) and less energetic (0.1-0.3 eV) [210, 211]. Charge build-up appears on spacecraft moving in this medium as a result of nature's attempt to bring current and charge balance. The difference of potential between the spacecraft and the plasma environment originates because of the current balance, whereas the arcing phenomenon (rapid release of the electrostatically stored charge) occurs because of the charge balance. Except for transients caused by fluxes of energetic charged particles or by changing solar illumination, there can be no net flux of charge to an isolated body in a partially ionised plasma. Therefore, the arcing events are occasional events and the steady state of a space vehicle in a plasma environment will be a current balance state [211].

Regarding the charging, the space environment may cause two different charging effects on the spacecraft: absolute and differential charging. Absolute charging means that the space vehicle charges as a whole and there is an electric potential difference between the space vehicle and the ambient plasma that surrounds it. Differential charging occurs when parts of the spacecraft have different potentials relative to each other. The steady state, in which the sum of all currents is zero, is usually achieved in the order of milliseconds for the overall spacecraft but it can take up to hours between the different surfaces of the spacecraft [212]. Design guidelines have been developed in order to reduce the differential charging and the risk of electrostatic discharge which can damage the equipment on board. These guidelines recommend the use of specific materials and coatings as well as special cabling and grounding [3]. In addition, the spacecraft can incorporate an active charge control device that holds the spacecraft potential close to the space plasma potential. The most important region of surface charging occurs at geosynchronous altitudes where potential differences between the spacecraft and the surrounding plasma can go up to a few tens of kV ($\Delta V \sim 20$ kV). In LEO, the charging level is usually not of concern as it ranges from a few volts up to a few hundreds of volts ($\Delta V \sim 1 - 400$ V). However, in LEO orbits of 55 degrees of inclination and above (auroral latitudes), the spacecraft may be immersed in a high energy electron environment and reach potential differences of the order of a few kVs [209].

If a charged particle is moving with respect to an external magnetic field, a force appears on the particle called Lorentz force [112]. This phenomenon can generate perturbing forces and torques on a charged target which may interfere with the de-tumbling process. For this reason, the following effects must be analysed,

- Charged target subject to a magnetic field generated by the chaser's coil: The target is rotating with respect to this field and therefore, perturbing forces and torques may appear. In this case, the relative linear velocity between the chaser and the target object is assumed to be negligible.

- Charged target subject to the Earth's magnetic field: The target object will have a high relative velocity with respect to the Earth's magnetic field and therefore, perturbing forces and torques may appear.

- Charged chaser subject to the Earth's magnetic field: This effect would also generate perturbing forces and torques on the chaser spacecraft as this object is moving with respect to the Earth's magnetic field. However, as the chaser is an active object, it will be assumed that it has been properly designed in order to cope with any charging events.

An object in orbit will perturb the surrounding plasma over a distance over called 'Debye Length' which is denoted by the parameter λ_D. This length is of the order of millimetres in LEO ($\lambda_D \sim$ 0.001 m) and it can be of the order of hundreds of metres in GEO ($\lambda_D \sim 100$ m). In order to assess this phenomenon, the target is modelled as a capacitor with a static charge Q. The charging process is depicted in Figure A.8. The target exposed to the plasma may have positive surfaces that will collect electrons and/or negative surfaces that will collect ions generating a potential difference between the spacecraft and the ambient medium $\Delta V = V_{SC} - V_{plasma}$. The spacecraft's charge is distributed in a volume V_q and it has a charging density ρ_q given by Equation (A.1),

$$Q = \int_{V_q} \rho_q dV_q. \tag{A.1}$$
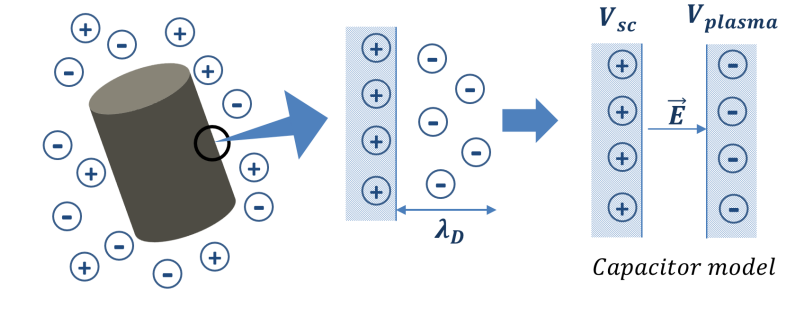
Figure A.8: Interaction between the spacecraft and the plasma environment.

In addition, this static charge may be computed as the product of the capacitance of the spacecraft C and the potential difference ($V_{SC} - V_{plasma}$) (see Eq. A.2). Typical spacecraft capacitances range between $100 - 500$ pF [212].

$$Q = C \cdot (V_{SC} - V_{plasma}). \tag{A.2}$$

The Lorentz force that appears on the charged target object, given by Equation (A.3), can be split into a force generated by the coil on board the chaser ($\vec{F}_q^{coil}$) and a force generated by the Earth's magnetic field ($\vec{F}_q^{Earth}$). The force generated by the chaser's coil appears due to the fact that the target is rotating with an angular velocity $\vec{\omega}$ with respect to the field generated by the coil, $\vec{B}_{coil}$, while the force generated by the Earth's magnetic field appears due to the relative linear orbital velocity $\vec{v}$ with respect to the field $\vec{B}_{Earth}$.

$$\vec{F}_q = \int_{V_q} \vec{v} \times \vec{B} \rho_q dV_q = \overbrace{\int_{V_q} (\vec{\omega} \times \vec{r}) \times \vec{B}_{coil} \rho_q dV_q}^{\vec{F}_q^{coil}} + \overbrace{\int_{V_q} \vec{v} \times \vec{B}_{Earth} \rho_q dV_q}^{\vec{F}_q^{Earth}}. \tag{A.3}$$

Furthermore, the corresponding torque is given by Equation (A.4) and it can also be divided into

two terms,

$$\vec{T}_q = \int_{V_q} \vec{r} \times (\vec{v} \times \vec{B})\rho_q dV_q = \overbrace{\int_{V_q} \vec{r} \times ((\vec{\omega} \times \vec{r}) \times \vec{B}_{coil})\rho_q dV_q}^{\vec{T}_q^{coil}} + \overbrace{\int_{V_q} \vec{r} \times (\vec{v} \times \vec{B}_{Earth})\rho_q dV_q}^{\vec{T}_q^{Earth}}. \quad (A.4)$$

In order to evaluate this effect, a cylindrical target is considered of 2 metres of radius, 8 metres of height and 1 millimetre of thickness, depicted in Figure A.9. A worst case scenario will be analysed by taking into account high values of the capacitance and the potential difference with respect to the surrounding plasma. The target is assumed to be uniformly charged with a capacitance of 500 pF and a potential difference of 20 kV. The target is located at an orbital altitude of 700 km and it is assumed to be rotating at 50 deg/s along the axis of symmetry of the cylinder. In addition, the coil defined in Section 5.7 is employed and it is assumed to be located at a distance of 10 metres with respect to the COG of the target. The magnetic field generated by the coil is assumed to non-uniform inside the target while the Earth's magnetic field is assumed to be homogeneous inside the target.
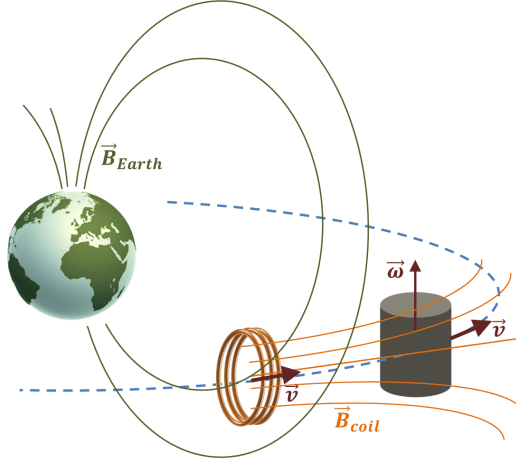
Figure A.9: Charged cylindrical target subject to the Earth's magnetic field and the magnetic field generated by the chaser's coil.

Now, Equations A.3 and A.4 are numerically integrated, leading to the following results. The force and torque generated by the chaser's coil are equal to,

$$\vec{F}_q^{coil} = 1.6 \cdot 10^{-4} \ \mu N, \quad (A.5)$$

$$\vec{T}_q^{coil} = 0.0012 \ \mu N \cdot m, \quad (A.6)$$

while the force and the torque caused by the Earth's magnetic field are equal to,

$$\vec{F}_q^{Earth} = 3.1 \ \mu N, \quad (A.7)$$

$$\vec{T}_q^{Earth} = 0.1 \ \mu N \cdot m. \quad (A.8)$$

It can be observed that the Lorentz force and torque exerted by the Earth's magnetic field is several orders of magnitude higher that the perturbations caused by the chaser's coil. Nonetheless, both results lead to very small effects compared to other environmental perturbations (see the examples presented in Section 6.3). Therefore, it can be concluded that the influence of the environmental plasma on a charged target can be neglected during the de-tumbling process.

A.9   Dynamics of the chaser-target system for a 2D simplified configuration

Within this section, a stability analysis is developed in the vicinity of a stable asymptotic state for a simplified 2D configuration where an analytical approach is viable. The approximate theoretical approach developed in this section is a useful tool to further understand the local behaviour of the system, before dealing with costly and time consuming 3D numerical simulations presented in the following section.

For this purpose, the target and the chaser are assumed to move in coplanar orbits $(X, Y$ plane) and to be able to rotate about an axis perpendicular to the orbital plane (Z axis) (see Figure A.10). Furthermore, the perturbations taken into account are the Earth modelled as a point mass and the magnetic interactions between the two objects. In addition, in order to further simplify the problem, the considered target is a spherical shell. These simplifications are necessary to facilitate an analytical study. Therefore, the conclusions derived here are only theoretical and they must be confirmed by numerical simulations like the ones provided in Section 6.3.

Figure A.10 depicts the kinematic and control variables of a simplified 2D configuration that helps to visualise the problem. In this simplified version of the 3D full dynamical problem, both bodies are assumed to move in coplanar orbits $((X, Y)$ plane) and to rotate about an axis perpendicular to the orbit (Z axis).
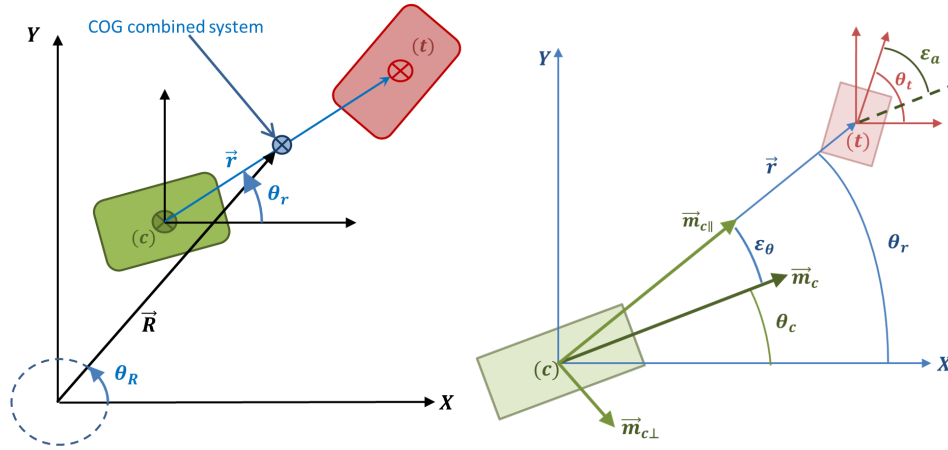
Figure A.10: Diagram of the chaser-target 2D configuration.

A.9.0.1   Earth modelled as a point mass and magnetic interactions

Within this section, the relative motion between the chaser and the target is analysed considering only the gravity of the Earth modelled as a point mass, the magnetic interactions between the two objects and the orbital manoeuvres executed by the chaser.

It should be noted that it has been decided not to employ classical solutions for the relative motion, such as the Clohessy-Wiltshire equations [46] but to instead derive the equations from the basic Newton's Second Law of motion in an inertial reference frame. The classical Clohessy-Wiltshire equations are typically expressed in the rotating target local orbital frame and the inclusion of the magnetic interactions in these equations is not straightforward. Under these conditions, the general equations specified in Subsection 6.2.3 are simplified,

$$m_t \ddot{\vec{r}}_t = \vec{F}_{ct} + \vec{F}_{gt}, \tag{A.9}$$

$$m_c \ddot{\vec{r}}_c = -\vec{F}_{ct} + \vec{F}_{gc} + \sum_i \vec{F}_{mi,c}, \tag{A.10}$$

$$\mathbf{I_t} \dot{\vec{\omega}}_t + \vec{\omega}_t \times \mathbf{I_t} \vec{\omega}_t = \vec{T}_{ct}, \tag{A.11}$$

$$\mathbf{I_c} \dot{\vec{\omega}}_c + \vec{\omega}_c \times \mathbf{I_c} \vec{\omega}_c = \vec{T}_{tc} + \sum_i \vec{T}_{mi,c}, \tag{A.12}$$

where $\vec{F}_{gi}$ $(i = (t, c))$ is the gravitational force at the COG of each object given by

$$\vec{F}_{gi} = -\mu_\oplus \frac{m_i \vec{r}_i}{r_i^3}, \quad i = (t, c) \tag{A.13}$$

and $\mu_\oplus = 398600.44$ km^{3}s^{-2} is the standard Earth's gravitational parameter. Moreover, the COG of the chaser-target system is described by the inertial state vector $\vec{R}$,

$$m\vec{R} = m_t \vec{r}_t + m_c \vec{r}_c, \quad m = m_t + m_c \tag{A.14}$$

and the position vectors $\vec{r}_i$ $(i = t, c)$ may also be expressed as,

$$\vec{r}_t = \vec{R} + \frac{m_c}{m} \vec{r} = \vec{R} + \vec{\rho}_t \tag{A.15}$$

and

$$\vec{r}_c = \vec{R} - \frac{m_t}{m} \vec{r} = \vec{R} + \vec{\rho}_c, \tag{A.16}$$

where $\vec{\rho}_i$ $(i = t, c)$ are position vectors of the target and chaser w.r.t. the COG of the system and it holds that $|\vec{\rho}_i| << \left| \vec{R} \right|$. By expanding $\frac{\vec{r}_i}{r_i^3}$ in a Taylor series with respect to variable $\vec{\rho}_i$ up to the first linear term, the following expression is obtained for $\vec{F}_{gi}$,

$$\frac{\vec{r}_i}{r_i^3} \approx \frac{\vec{R}}{R^3} + \mathbf{P} \frac{\vec{\rho}_i}{R^3} \rightarrow \vec{F}_{gi} \approx -\mu_\oplus m_i (\frac{\vec{R}}{R^3} + \mathbf{P} \frac{\vec{\rho}_i}{R^3}), \tag{A.17}$$

where the matrix $\mathbf{P}$ is equal to [46],

$$\mathbf{P} = \mathbf{I} - 3\vec{u}_R \vec{u}_R^T, \quad \vec{u}_R = \frac{\vec{R}}{R}. \tag{A.18}$$

The motion of the COG of the system can be decoupled from the interaction between the chaser and the target, assuming the gravity force at the COG of the system, $\vec{F}_g$, dominates over the manoeuvring forces exerted by the chaser,

$$m\ddot{\vec{R}} = m_t \ddot{\vec{r}}_t + m_c \ddot{\vec{r}}_c = \vec{F}_g + \sum \vec{F}_{mc} \approx \vec{F}_g \tag{A.19}$$

and $\vec{F}_g$ is equal to,

$$\vec{F}_g = \vec{F}_{gc} + \vec{F}_{gt} \approx -\mu_\oplus m_c \left(\frac{\vec{R}}{R^3} - \frac{m_t}{mR^3} \mathbf{P} \vec{r} \right) - \mu_\oplus m_t \left(\frac{\vec{R}}{R^3} + \frac{m_c}{mR^3} \mathbf{P} \vec{r} \right) = -\mu_\oplus \frac{m}{R^3} \vec{R}. \tag{A.20}$$

Therefore, the differential equation describing the motion of the COG of the system is decoupled from the magnetic interactions between the chaser and target objects and it reduces to Equation (A.21). This result just reflects a virtual object of mass $m = m_t + m_c$ orbiting around the Earth. Although the mathematical process from Equation (A.9) until (A.21) refers to basic space flight dynamics [46], a self-contained development has been included in order to clarify the notation employed and the hypothesis made to reach Equation (A.21). These hypothesis are primarily two:

1. the cancellation of the magnetic interactions as a consequence of the conservation of linear

momentum of the hypothetically isolated chaser-target system; and

2. the dominance of the gravity forces with respect to the chaser's manoeuvres, which are assumed to be small.

The first hypothesis can be derived from the following rationale. The motion of two interacting bodies (the two-body problem) always admits a solution which consists in decomposing the motion of the system into two motions; the motion of the centre of mass and the motion of the two bodies with respect to their centre of mass [94]. In addition, the equation describing the motion of the centre of mass will always reduce to the consideration of the external forces acting on the system (e.g. manoeuvres executed by the chaser) because according to Newton's third law, the forces of interaction between the two bodies are equal in magnitude and opposite in direction and therefore, they will cancel out when summed up.

The validity of the second hypothesis can be inferred from the results obtained in the case studies from Section 6.3. The norm of the gravity force, $\left|\vec{F}_g\right|$, for the combined chaser-target system used in the aforementioned case studies is shown in Figure A.11. It may be observed that the gravitational force ranges between (1-30)kN while the control force manoeuvres obtained are in the order of tens of milliNewtons in the first case study analysed (see Figure 6.9) and in the order of milliNewtons in the second case study analysed (see Figure 6.15). Therefore, it may be concluded that the second hypothesis is physically reasonable for the present 2D simplified analysis.
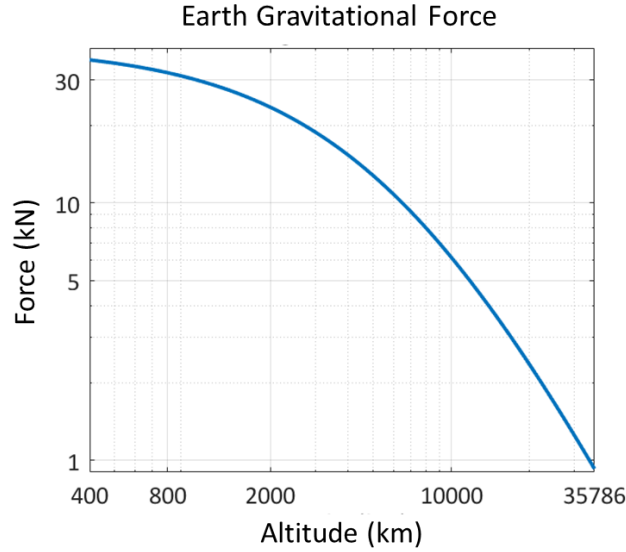
Figure A.11: Earth's gravitational force $\left|\vec{F}_g\right|$ for different orbit altitudes.

$$\ddot{\vec{R}} \approx -\frac{\mu_\oplus}{R^3}\vec{R}. \tag{A.21}$$

Furthermore, an additional differential equation is needed to describe the relative position of the target w.r.t. the chaser. The position vector of the target with respect to the chaser verifies,

$$\ddot{\vec{r}} = \ddot{\vec{r}}_t - \ddot{\vec{r}}_c = \frac{\vec{F}_{ct}}{m_{red}} - \frac{1}{m_c}\sum\vec{F}_{mc} + \vec{a}_{gr}, \tag{A.22}$$

where the reduced mass is $m_{red} = \frac{m_t m_c}{m_t + m_c}$ and the acceleration caused by the Earth's gravity $\vec{a}_{gr}$ is equal to,

$$\vec{a}_{gr} = -\mu_\oplus\frac{\vec{r}_t}{r_t^3} + \mu_\oplus\frac{\vec{r}_c}{r_c^3} \approx -\frac{\mu_\oplus}{R^3}\mathbf{P}\vec{r}. \tag{A.23}$$

Therefore, the set of 3D dynamical equations for this specific reduced problem is,

$$\ddot{\vec{R}} \approx -\frac{\mu_\oplus}{R^3}\vec{R},$$

$$\ddot{\vec{r}} = \frac{\vec{F}_{ct}}{m_{red}} - \frac{\mu_\oplus}{R^3}\mathbf{P}\vec{r} - \frac{1}{m_c}\sum_i \vec{F}_{mi,c},$$

$$\mathbf{I_t}\dot{\vec{\omega}}_t + \vec{\omega}_t \times \mathbf{I_t}\vec{\omega}_t = \vec{T}_{ct},$$

$$\mathbf{I_c}\dot{\vec{\omega}}_c + \vec{\omega}_c \times \mathbf{I_c}\vec{\omega}_c = \vec{T}_{tc} + \sum_i \vec{T}_{mi,c},$$

(A.24)

where the degrees of freedom are the vectors $\vec{R}$, $\vec{r}$, $\vec{\theta}_t$ and $\vec{\theta}_c$.

A.9.0.2 Magnetic interactions between a chaser and a metallic spherical shell in the 2D dynamical problem

In the 2D configuration, the chaser and the spherical target are assumed to move in coplanar orbits and be able to rotate about an axis perpendicular to the orbit. The following reference frame is used here, the origin of the frame is located at the COG of the chaser, the X axis goes along the $\vec{u}_r$ direction, the Z axis is parallel to the angular momentum of the orbital plane and the Y axis goes along the direction $\vec{u}_{r\perp} = \vec{k} \times \vec{u}_r = \mathbf{G}\vec{u}_r$.

Under these assumptions, the number of degrees of freedom is reduced to six,

$$\vec{R} = R\vec{u}_R = R[\cos\theta_R, \sin\theta_R, 0], \tag{A.25}$$

$$\vec{r} = r\vec{u}_r = r[\cos\theta_r, \sin\theta_r, 0], \tag{A.26}$$

$$\vec{\theta}_t = [0, 0, \theta_t], \tag{A.27}$$

$$\vec{\theta}_c = [0, 0, \theta_c], \tag{A.28}$$

where θ_R is the angle used to locate the COG of the system in the ECI frame, θ_r is the angle used to locate the orientation of the relative position vector with respect to the ECI frame and θ_t and θ_c are the attitude angles of each body of their body-fixed reference frames with respect to the ECI frame.

Moreover, in this 2D problem, the error in the relative pointing ϵ_θ and the relative attitude of the target with respect to the chaser ϵ_a (see Figure A.10) may be formulated in a simpler way than the general 3D formulas as expressed in Equations (A.29) and (A.30),

$$\epsilon_\theta = \theta_r - \theta_c, \tag{A.29}$$

$$\epsilon_a = \theta_t - \theta_c. \tag{A.30}$$

Furthermore, the magnetic moment vector of the coil $\vec{m}_c$ on-board the chaser is,

$$\vec{m}_c = |\vec{m}_c|\left(\cos(\epsilon_\theta)\vec{u}_r + \sin(\epsilon_\theta)\mathbf{G}\vec{u}_r\right). \tag{A.31}$$

Introducing Equation (A.31) in (3.188), the magnetic field generated by the coil is,

$$\vec{B} = \frac{\mu_0|\vec{m}_c|}{4\pi r^3}(2\cos(\epsilon_\theta)\vec{u}_r - \sin(\epsilon_\theta)\mathbf{G}\vec{u}_r). \tag{A.32}$$

Furthermore, the magnetic moment of a rotating metallic spherical shell is obtained based on the

analytical formulation of Section 3.3.5.1,

$$\vec{m}_t = \mathbf{M_{eff}}(\dot{\epsilon}_a \vec{k} \times \vec{B}_{Gt}) = \frac{2\pi}{3}\mu_{\text{eff}}\sigma_t R_t^4 e_t(\dot{\epsilon}_a \vec{k} \times \vec{B}_{Gt}), \qquad (A.33)$$

where μ_{eff} is an efficiency factor included due to the fact that the field inside the target is non-uniform, σ_t is the conductivity of the spherical shell, R_t and e_t are the radius and thickness of the target, $\dot{\epsilon}_a \vec{k}$ is the relative angular velocity of the target with respect to the chaser and $\vec{B}_{Gt}$ is the magnetic field at the COG of the target object.

Introducing Equation (A.31) in (6.1), the following formula for the eddy current torque is obtained,

$$\vec{T}_{ct} = -\frac{I_{tz}}{\tau_t}\dot{\epsilon}_a \frac{1 - \frac{3}{4}\sin^2\epsilon_\theta}{(1+\epsilon_r)^6}\vec{k}, \qquad (A.34)$$

where I_{tz} is the principal inertia of the target along the Z axis (which is equal for all axis in a spherical shell) and the characteristic time τ_t is equal to,

$$\tau_t = \frac{6d^6\pi I_{tz}}{\mu_0^2\mu_{\text{eff}}\sigma_t R_t^4 e_t \left|\vec{m}_c\right|^2}. \qquad (A.35)$$

Moreover, introducing Equations (A.31, A.32, A.33) in Equation (3.189), the force that appears at the COG of the target object is evaluated,

$$\vec{F}_{ct} = \frac{m_{red}d}{\tau_r}\dot{\epsilon}_a \frac{(1 - \frac{\sin^2\epsilon_\theta}{2})}{(1+\epsilon_r)^7}\mathbf{G}\vec{u}_r, \qquad (A.36)$$

where the characteristic time of the force τ_r is equal to,

$$\tau_r = m_{red}\frac{4\pi d^8}{\mu_0^2\mu_{\text{eff}}\sigma_t R_t^4 e_t \left|\vec{m}_c\right|^2}. \qquad (A.37)$$

The reactions on the chaser are given by Equations (6.3, 6.8) and for this specific problem, they acquire the form,

$$\vec{F}_{tc} = -\frac{m_{red}d}{\tau_r}\dot{\epsilon}_a(1 - \frac{\sin^2\epsilon_\theta}{2})\mathbf{G}\vec{u}_r, \qquad (A.38)$$

$$\vec{T}_{tc} = -\frac{I_{cz}}{\tau_c}\frac{\dot{\epsilon}_a}{(1+\epsilon_r)^6}\vec{k}, \qquad (A.39)$$

where the characteristic time of the magnetic torque on the chaser τ_c is equal to,

$$\tau_c = \frac{12\pi d^6 I_{cz}}{\mu_0^2\mu_{\text{eff}}\sigma_t R_t^4 e_t \left|\vec{m}_c\right|^2}. \qquad (A.40)$$

A.9.0.3 2D linearised stability analysis

Introducing theses magnetic forces and torques, Equations (A.36,A.38, A.39), together with the chaser manoeuvres, Equations (6.21,6.22,6.23) in (A.24), the 2D dynamical equations are obtained below. Equation (A.41) describes the translation of the COG of the system, Equation (A.42) describes the relative translation of the system and Equations (A.43, A.44) describe the evolution of the uniaxial rotation of the target and the chaser respectively. Note that in these last two Euler equations the terms $\vec{\omega}_i \times \mathbf{I_i}\vec{\omega}_i$ $(i = t, c)$ from the original Euler's equations (6.12, 6.13) have vanished. The dropping of the gyroscopic term is also due to the simplification to 1-dimensional rotation. In the case of the target, which is modelled as a spherical shell in this section, all axes are principal axis of inertia, so the disappearance of this term is straightforward. In the case of

the chaser, it has been assumed that the Z axis is a principal axis of inertia.

$$\ddot{\vec{R}} \approx -\frac{\mu_\oplus}{R^3}\vec{R}, \tag{A.41}$$

$$\frac{\ddot{\vec{r}}}{d} = (\frac{\dot{\epsilon}_a}{\tau_r(1+\epsilon_r)^7}(1 - \frac{\sin^2 \epsilon_\theta}{2})\mathbf{G} - \frac{\mu_\oplus(1+\epsilon_r)}{R^3}\mathbf{P} - (\frac{\epsilon_r}{\tau_{m1}^2} + \frac{\dot{\epsilon}_r}{\tau_{m2}})\mathbf{I} - \frac{\dot{\theta}_c}{\tau_{m3}}\mathbf{G})\vec{u}_r, \tag{A.42}$$

$$\ddot{\theta}_t = -\frac{\dot{\epsilon}_a}{\tau_t}\frac{1 - \frac{3}{4}\sin^2 \epsilon_\theta}{(1+\epsilon_r)^6}, \tag{A.43}$$

$$\ddot{\theta}_c = -\frac{1}{\tau_c}\frac{\dot{\epsilon}_a}{(1+\epsilon_r)^6} + \frac{\epsilon_\theta}{\tau_{m4}^2} + \frac{\dot{\epsilon}_\theta}{\tau_{m5}}, \tag{A.44}$$

where the matrix $\mathbf{P}$ and the matrix $\mathbf{G}$ are equal to,

$$\mathbf{P} = \begin{bmatrix} 1 - 3\cos^2\theta_R & -3\cos\theta_R\sin\theta_R \\ -3\cos\theta_R\sin\theta_R & 1 - 3\sin^2\theta_R \end{bmatrix}, \quad \mathbf{G} = \begin{bmatrix} 0 & -1 \\ 1 & 0 \end{bmatrix}, \tag{A.45}$$

and the characteristic times τ_r, τ_c, τ_t given by Equations (A.37, A.40, A.35) depend on the physical properties of the chaser and the target.

In order to analyse the stability of the system, a hypothetical stable asymptotic state is assumed with $\epsilon_r \to 0$, $\epsilon_\theta \to 0$, $\epsilon_a \to 0$ and $\dot{\theta}_c \to 0$. The variable ϵ_a will tend to zero when the de-tumbling process is close to its end.

Equations (A.42, A.43, A.44) depend on the control variables and they are linearised as follows. First of all, combining Equations (A.43) and (A.44) and neglecting infinitesimals of second order, the linearised equation in ϵ_a is obtained,

$$\ddot{\epsilon}_a = \ddot{\theta}_t - \ddot{\theta}_c = (\frac{1}{\tau_c} - \frac{1}{\tau_t})\dot{\epsilon}_a - \frac{\epsilon_\theta}{\tau_{m4}^2} - \frac{\dot{\epsilon}_\theta}{\tau_{m5}}. \tag{A.46}$$

Secondly, in order to find the differential equation for ϵ_r and ϵ_θ, the following relationship is used,

$$\frac{\vec{r}}{d} = \mathbf{R_c}\vec{\epsilon} + \begin{bmatrix} \cos\theta_c \\ \sin\theta_c \end{bmatrix}, \tag{A.47}$$

where the variables ϵ_r and ϵ_θ have been grouped in a single vector $\epsilon = \begin{bmatrix} \epsilon_r \\ \epsilon_\theta \end{bmatrix}$ and where $\mathbf{R_c}$ is equal to $\mathbf{R_c} = \begin{bmatrix} \cos\theta_c & -\sin\theta_c \\ \sin\theta_c & \cos\theta_c \end{bmatrix}$.

Taking second derivatives with respect to time of both sides of Equation (A.47) results in

$$\frac{\ddot{\vec{r}}}{d} = \mathbf{R_c}\ddot{\vec{\epsilon}} + 2\dot{\theta}_c\mathbf{R_c'}\dot{\epsilon} + (\ddot{\theta}_c\mathbf{R_c'} - \dot{\theta}_c^2\mathbf{R_c})\vec{\epsilon} - \begin{bmatrix} \ddot{\theta}_c\sin\theta_c + \dot{\theta}_c^2\cos\theta_c \\ -\ddot{\theta}_c\cos\theta_c + \dot{\theta}_c^2\sin\theta_c \end{bmatrix}, \tag{A.48}$$

where the following time derivatives of $\mathbf{R_c}$ have been used,

$$\dot{\mathbf{R}}_\mathbf{c} = \dot{\theta}_c\mathbf{R_c'} = \dot{\theta}_c\begin{bmatrix} -\sin\theta_c & -\cos\theta_c \\ \cos\theta_c & -\sin\theta_c \end{bmatrix}, \quad \ddot{\mathbf{R}}_\mathbf{c} = \ddot{\theta}_c\mathbf{R_c'} + \dot{\theta}_c^2\mathbf{R_c''} = \ddot{\theta}_c\mathbf{R_c'} - \dot{\theta}_c^2\mathbf{R_c}. \tag{A.49}$$

Neglecting infinitesimals of second order, Equation (A.48) is equal to,

$$\frac{\ddot{\vec{r}}}{d} = \mathbf{R_c}\ddot{\vec{\epsilon}} + \ddot{\theta}_c\begin{bmatrix} -\sin\theta_c \\ \cos\theta_c \end{bmatrix} \rightarrow \ddot{\vec{\epsilon}} - \mathbf{R_c^{-1}}\frac{\ddot{\vec{r}}}{d} + \ddot{\theta}_c\mathbf{R_c^{-1}}\begin{bmatrix} -\sin\theta_c \\ \cos\theta_c \end{bmatrix} = \vec{0}, \tag{A.50}$$

where the following relationships have been used,

$$\mathbf{R_c^{-1}}\vec{u}_r = \begin{bmatrix} 1 \\ 0 \end{bmatrix}, \quad \mathbf{R_c^{-1}}\mathbf{G}\vec{u}_r = \begin{bmatrix} 0 \\ 1 \end{bmatrix}. \tag{A.51}$$

Now combining Equations (A.42) and (A.50), the following differential equation in $\vec{\epsilon}$ is derived,

$$\ddot{\vec{\epsilon}} + \begin{bmatrix} \frac{\epsilon_r}{\tau_{m1}^2} + \frac{\dot{\epsilon}_r}{\tau_{m2}} + P_1\epsilon_r + P_2\epsilon_\theta \\ -\dot{\epsilon}_a\left(\frac{1}{\tau_r} + \frac{1}{\tau_c}\right) + \frac{\epsilon_\theta}{\tau_{m4}^2} + \frac{\dot{\epsilon}_\theta}{\tau_{m5}} + \frac{\dot{\theta}_c}{\tau_{m3}} + P_2\epsilon_r + P_3\epsilon_\theta \end{bmatrix} = -\frac{\mu_\oplus}{R^3}\begin{bmatrix} P_1 \\ P_2 \end{bmatrix}, \tag{A.52}$$

where,

$$P_1 = \frac{\mu_\oplus}{R^3}(1 - 3\cos^2(\theta_c - \theta_R)), \quad P_2 = \frac{3}{2}\frac{\mu_\oplus}{R^3}\sin 2(\theta_c - \theta_R), \quad P_3 = \frac{\mu_\oplus}{R^3}(1 - 3\sin^2(\theta_c - \theta_R)). \tag{A.53}$$

Finally, the linearised differential equations for the control variables can be expressed in the matrix form $\mathbf{A}\ddot{\vec{Z}} + \mathbf{B}\dot{\vec{Z}} + \mathbf{C}\vec{Z} = \mathbf{D}$,

$$\begin{bmatrix} 1 & 0 & 0 & 0 \\ 0 & 1 & 0 & 0 \\ 0 & 0 & 1 & 0 \\ 0 & 0 & 0 & 0 \end{bmatrix}\ddot{\vec{Z}} + \begin{bmatrix} \frac{1}{\tau_{m2}} & 0 & 0 & 0 \\ 0 & \frac{1}{\tau_{m5}} & -\left(\frac{1}{\tau_r} + \frac{1}{\tau_c}\right) & 0 \\ 0 & \frac{1}{\tau_{m5}} & \frac{1}{\tau_t} - \frac{1}{\tau_c} & 0 \\ 0 & -\frac{1}{\tau_{m3}} & \frac{1}{\tau_c} & 1 \end{bmatrix}\dot{\vec{Z}} + \begin{bmatrix} \frac{1}{\tau_{m1}^2} + P_1 & P_2 & 0 & 0 \\ P_2 & \frac{1}{\tau_{m4}^2} + P_3 & 0 & \frac{1}{\tau_{m3}} \\ 0 & \frac{1}{\tau_{m4}^2} & 0 & 0 \\ 0 & -\frac{1}{\tau_{m4}^2} & 0 & 0 \end{bmatrix}\vec{Z} = -\frac{\mu_\oplus}{R^3}\begin{bmatrix} P_1 \\ P_2 \\ 0 \\ 0 \end{bmatrix}. \tag{A.54}$$

In order to apply the Laplace transformation, the four matrices should be constant; however the parameters $R(t)$ and $P_i(\theta_R, \theta_c)$ vary with time. As a first approximation, this time variation can be neglected. The orbital period $\tau_\oplus = \frac{2\pi R^3}{\mu_\oplus}$ is of the order of one hour in LEO and 1 day in GEO, while the period of the angular rotation of the target object is of the order of seconds. Therefore, the evolution of the COG of the system, given by $R(t), \theta_R(t)$, is slow compared to the angular velocity of the target object. In addition, the control will guarantee that $\dot{\theta}_c \to 0$ and therefore, $\theta_c \approx constant$ in the vicinity of the equilibrium state.

Assuming null initial conditions, the Laplace transformation is now used to derive the characteristic equation $|\boldsymbol{\Delta}(s)| = 0$ as the condition for existence of solutions $\delta\vec{Z} \neq \vec{0}$ around a hypothetical equilibrium state $\vec{Z}$ that verifies Equation (A.54) with $\mathbf{A}, \mathbf{B}, \mathbf{C}, \mathbf{D} \approx constants$ [213],

$$\boldsymbol{\Delta}(s) = s^2\mathbf{A} + s\mathbf{B} + \mathbf{C}. \tag{A.55}$$

The roots of the determinant $|\boldsymbol{\Delta}(s)|$ will indicate the stability of the system in the vicinity of the equilibrium position defined. If the roots have any real positive parts, this may lead to an instability in the control process [214]. In general, the inverses of the characteristic times for the manoeuvres will dominate over the rest of the characteristic times that appear in the problem $\tau_{mi} << \tau_r, \tau_c, \tau_t, \tau_\oplus$. One conclusion derived from this analysis is that the selection of the τ_{mi} is of paramount importance in order to guarantee, at least, local stability.

Introducing the following hypothesis $\tau_{mi} << \tau_r, \tau_c, \tau_t, \tau_\oplus$ in Equation (A.54), the following differential equations are reached:

$$\ddot{Z}_1 + \frac{1}{\tau_{m2}}\dot{Z}_1 + \frac{1}{\tau_{m1}}Z_1 = 0, \tag{A.56}$$

$$\ddot{Z}_2 + \frac{1}{\tau_{m5}}\dot{Z}_2 + \frac{1}{\tau_{m4}^2}Z_2 + \frac{1}{\tau_{m3}}Z_4 = 0, \tag{A.57}$$

$$\ddot{Z}_3 + \frac{1}{\tau_{m5}}\dot{Z}_2 + \frac{1}{\tau_{m4}^2}Z_2 = 0, \tag{A.58}$$

$$-\frac{1}{\tau_{m3}}\dot{Z}_2 + \dot{Z}_4 - \frac{1}{\tau_{m4}^2}Z_2 = 0. \tag{A.59}$$

Now, combining Equations (A.57) and (A.59) an ordinary differential equation (ODE) is found for

the variable Z_2,

$$\dddot{Z}_2 + \frac{1}{\tau_{m5}}\ddot{Z}_2 + (\frac{1}{\tau_{m3}^2} + \frac{1}{\tau_{m4}^2})\dot{Z}_2 + \frac{1}{\tau_{m3}\tau_{m4}^2}Z_2 = 0. \qquad (A.60)$$

Therefore, the variables Z_1 and Z_2 are determined by Equations (A.56) and (A.60) respectively. Once the variable Z_2 is known, the variables Z_3 and Z_4 are determined by Equations (A.58) and (A.57) respectively.

In addition, the ODEs (A.56) and (A.60) may be stabilised in an optimal way by choosing the characteristic times τ_{mi} so that the system is critically damped (i.e. the system returns to equilibrium as quickly as possible without oscillating). This situation is reached if the Laplace transformation of Equation (A.56) is reduced to,

$$s^2 + \frac{1}{\tau_{m2}}s + \frac{1}{\tau_{m1}} = 0 \rightarrow (s + \frac{1}{2\tau_{m2}})^2 = 0 \leftrightarrow \tau_{m1} = 2\tau_{m2}, \qquad (A.61)$$

and Equation (A.57) is reduced to,

$$s^3 + \frac{1}{\tau_{m5}}s^2 + (\frac{1}{\tau_{m3}^2} + \frac{1}{\tau_{m4}^2})s + \frac{1}{\tau_{m3}\tau_{m4}^2} = 0 \rightarrow (s + \frac{1}{3\tau_{m5}})^3 \leftrightarrow \begin{cases} \tau_{m3} = 1.958\tau_{m5}, \tau_{m4} = 3.713\tau_{m5} \\ \tau_{m3} = 8.846\tau_{m5}, \tau_{m4} = 1.767\tau_{m5} \end{cases}.$$
$$\qquad (A.62)$$

These results highlight the fact that the characteristic times of the manoeuvres can be divided into two different groups which will help in the search of solutions during the optimisation process. It should also be noted that the constraints found which link these parameters only apply to this specific problem and they should not be extrapolated as a general conclusion. However, the following grouping conditions should be borne in mind for the 3D optimisation process;

- $\tau_{m2} > \tau_{m1}$,

- $\tau_{m5} < \tau_{m3} < \tau_{m4}$ or $\tau_{m5} < \tau_{m4} < \tau_{m3}$.

Furthermore, as it has been stated above, the characteristic times that appear in the problem will typically comply with the assumption $\tau_{mi} << \tau_r, \tau_c, \tau_t, \tau_\oplus$. However, if special attention is paid to the original set of linearised equations determined by (A.54), it may be observed that the term $(\frac{1}{\tau_t} - \frac{1}{\tau_c})$, which was discarded as a consequence of this assumption, may introduce a change of sign in the linearised equations and therefore, it may lead to an instability. This term appears in Equation (A.58) as follows,

$$\ddot{Z}_3 + \frac{1}{\tau_{m5}}\dot{Z}_2 + (\frac{1}{\tau_t} - \frac{1}{\tau_c})\dot{Z}_3 + \frac{1}{\tau_{m4}^2}Z_2 = 0 \rightarrow \ddot{Z}_3 + (\frac{1}{\tau_t} - \frac{1}{\tau_c})\dot{Z}_3 = f(t), \qquad (A.63)$$

where $f(t)$ is an external excitation. The stability of this Equation around the equilibrium position only depends on the homogeneous part of Equation (A.63) and it leads to an instability when,

$$\tau_c < \tau_t. \qquad (A.64)$$

Now, introducing Equations (A.35) and (A.40) in (A.64), it is found out that the system becomes unstable when the inertia of the chaser is below half the inertia of the target.

$$I_{cz} < \frac{I_{tz}}{2}. \qquad (A.65)$$

It should be noted that this conclusion can not be extrapolated to other cases other than the problem analysed here. However, it makes sense that the chaser will find more difficulties to control the target if the chaser's inertia is well below the one of the target. This aspect should be taken into account in the systems engineering design of the eddy brake due to the fact that instabilities may appear in the control.

Moreover, an example is presented which shows that the results derived from the linear stability analysis may not be conclusive. The target analysed is a metallic spherical shell, made of alu-

minium, which has a radius of 1 metre and a thickness of 3 millimetres. Its magnetic tensor, assuming an efficiency loss of 5%, is equal to,

$$\mathbf{M_{sphere}} = \begin{bmatrix} 3.343 & 0 & 0 \\ 0 & 3.343 & 0 \\ 0 & 0 & 3.343 \end{bmatrix} \cdot 10^6 \ \mathrm{S \cdot m^4}. \tag{A.66}$$

The chaser that carries the de-tumbling subsystem is the spacecraft described for the Agora mission defined in Section 5.8. Both objects are located in a circular orbit at an altitude and inclination of 800 km and 0 degrees respectively, and the relative distance between the coil and the COG of the target object is 10 metres (see Figure A.12). Moreover, the chaser points the magnetic moment of the coil towards the target object to maximise the magnetic field ($\epsilon_\theta = 0$). In addition, the initial angular velocity of the target with respect to the ECI frame is equal to $\vec{\omega} = [0, 0, 10]$ deg/s.
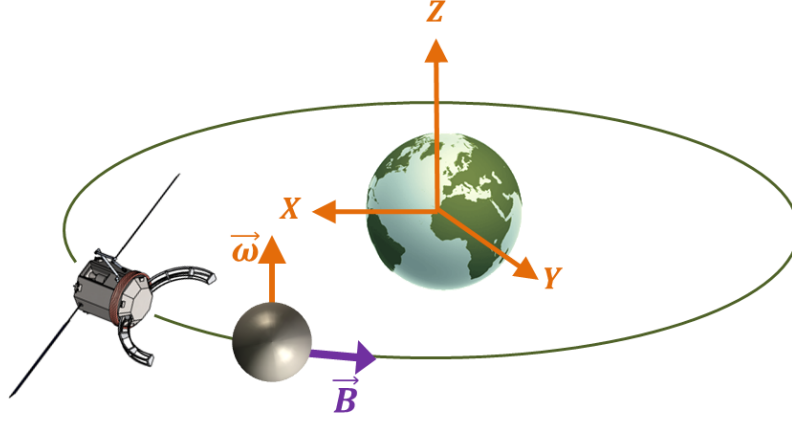

Figure A.12: Initial configuration for de-tumbling process of a spherical shell.

Using the following characteristic times $\tau_{m1} = 5$s, $\tau_{m2} = 1000$s, $\tau_{m3} = 500$s, $\tau_{m4} = 0.1$s, $\tau_{m5} = 0.1$s, the roots of the determinant $|\mathbf{\Delta}(s)|$ are equal to,

$$s_1 = 0, \ s_{2,3} = -4.9 \pm 8.7i, \ s_{4,5} = -0.0005 \pm 0.2i, \ s_6 = -0.002, \ s_7 = -0.00002. \tag{A.67}$$

In this particular case, the stability analysis indicates that the system is locally marginally stable as there is one pole with a zero real part which is a simple root and the rest of the poles have a negative real part. Here, it is impossible to know by inspection whether the full dynamical process will become unstable or not.

Now the dynamical Equations (6.29) are numerically integrated in order to assess the global stability of the system. The numerical simulation includes the Earth modelled as a point mass, the magnetic interactions between the two objects and the control manoeuvres. In addition, it is assumed that there are neither delays nor inaccuracies in the control process.

The evolution of the control parameters; angular velocity of the target and the chaser, the relative distance between the two objects and the relative pointing of the coil, are depicted in Figure A.13. The results show that the selected τ_{mi} lead to a stable control throughout the whole de-tumbling process.
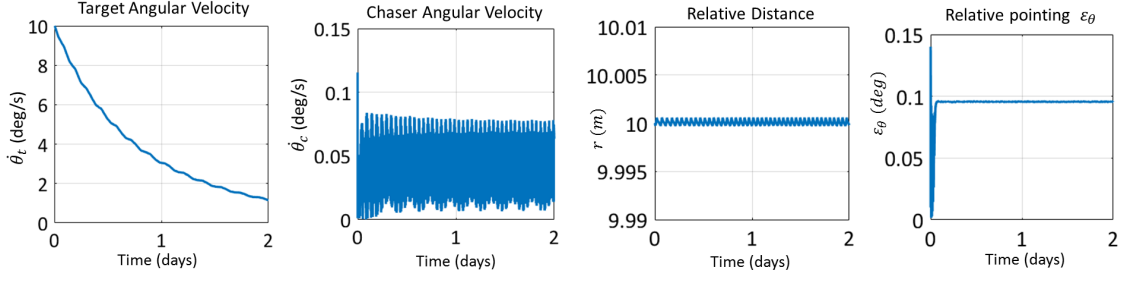
Figure A.13: Kinematics of the chaser-target system.

All in all, the linear stability analysis sheds some light over the local behaviour of the system but it does not ensure that the conclusions derived are valid for the whole dynamical process and the linear analysis must always be complemented by numerical simulations. Therefore, the presented linear analysis is a heuristic tool but it is not conclusive for practical purposes.

Moreover, an optimisation criteria based on the minimisation of the total ΔV is identified as an efficient way to find adequate values of the τ_{mi}. However, the large amount of possible combinations between the 5 variables τ_{mi} leads to a complicated optimisation process. In this case, the stability analysis can be a useful tool in order to make an educated initial guess of the variables τ_{mi}.

A.10 Interaction of the environmental plasma with the coil

This section focuses on the analysis of the interaction of the environmental plasma with the chaser's coil. The charged particles that compose the space plasma in LEO will be deflected by the magnetic field generated by the chaser's coil based on Lorentz force (see Equation 3.10). In turn, the coil will be subject to a reaction force which results in a drag force for the chaser spacecraft [215].

At the boundary, referred to as the magnetopause, on which the charged particles impinge (see Figure A.14), there is a balance between the internal magnetic pressure generated by the coil and the external plasma pressure [23, 215];

$$nm_iv_p^2 = \frac{(2B_{mp})^2}{2\mu_0},$$ (A.68)

where n is the plasma number density in m^{-3}, m_i is the ion mass, v_p is plasma velocity with respect to the coil, B_{mp} is the magnetic field at the boundary and $\mu_0 = 4\pi \cdot 10^{-7}$ N·A^{-2} is the vacuum permeability.

In our case, the norm of the velocity of the plasma with respect to the coil is equal to the norm of the chaser's velocity in orbit, $|\vec{v}_p| = |\vec{v}_{chaser}|$. For this analysis, it will be assumed that the chaser is located at a circular orbit with a mean orbital speed equal to;

$$v_{chaser} = \sqrt{\frac{\mu_\oplus}{(R_{Earth} + H)}},$$ (A.69)

where $\mu_\oplus = 398600.44$ km^{3}s^{-2} is the standard Earth's gravitational parameter, $R_{Earth} = 6371$ km is the mean equatorial radius of the Earth and H is the altitude of the orbit.
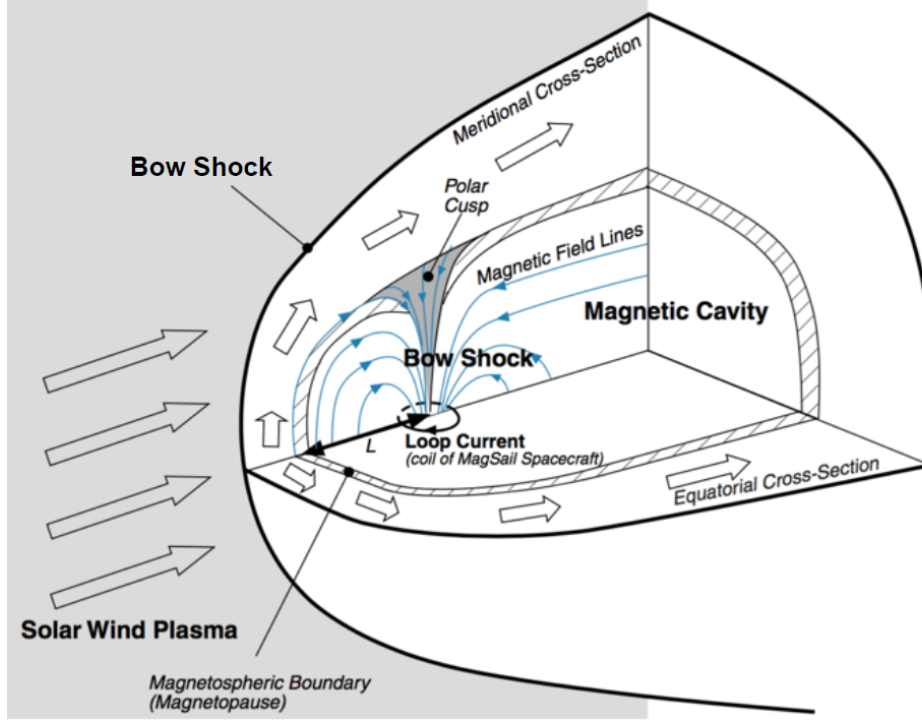
Figure A.14: Plasma flow around a current loop [23].

Assuming that the boundary is located at a certain distance L from the centre of the coil, the magnetic field at the boundary is equal to [23, 215];

$$B_{mp} = \frac{\mu_0 |\vec{m}_{coil}|}{4\pi L^3}, \tag{A.70}$$

where $\vec{m}_{coil}$ is the magnetic moment of the chaser's coil. For the reference coil defined in Table 5.1, the magnetic moment is equal to 502654.8 A·m^2.

Combining Equations (A.68) and (A.70), the distance between the centre of the coil and the magnetopause boundary is expressed as;

$$L = \left(\frac{\mu_0 |\vec{m}_{coil}|^2}{8\pi^2 n m_i v_{chaser}^2}\right)^{1/6}, \tag{A.71}$$

The drag force exerted on the coil depends on the area blocking the plasma flow, πL^2, and it may be formulated as [23, 215];

$$F_p = \frac{1}{2} C_D \rho_p v_{chaser}^2 \pi L^2, \tag{A.72}$$

where ρ_p is the plasma density and C_D is the drag coefficient which will be assumed to be equal to $C_D = 2$ [23].

Based on the assumption that the in-orbit plasma is quasi-neutral, it is assumed that the number density of the plasma, n, is equal to the electron number density [23, 215]. The electron density has been obtained by means of the International Reference Ionosphere (IRI) model [125] for 1st January 2017 during daytime and nighttime. The results are depicted in Figure A.15. The number densities vary significantly for the two cases analysed due to the fact that the molecules in orbit are ionized by the Sun during the daytime [215].
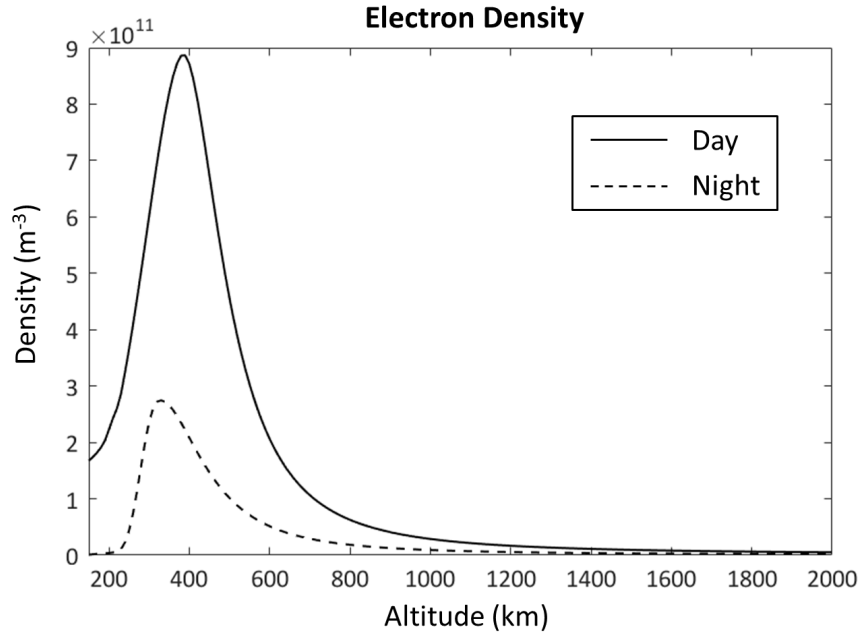
Figure A.15: Electron density calculated by the IRI 2012 model for 1st January 2017.

Moreover, the composition of the in-orbit space plasma for different altitudes has been obtained by means of the IRI model for the same date as before. Figure A.16 depicts the ion composition percentage for different altitudes (left image) and the combined ion mass (right image). It may be observed that the major component is O^+ for low altitudes and H^+ for high altitudes in the LEO region.
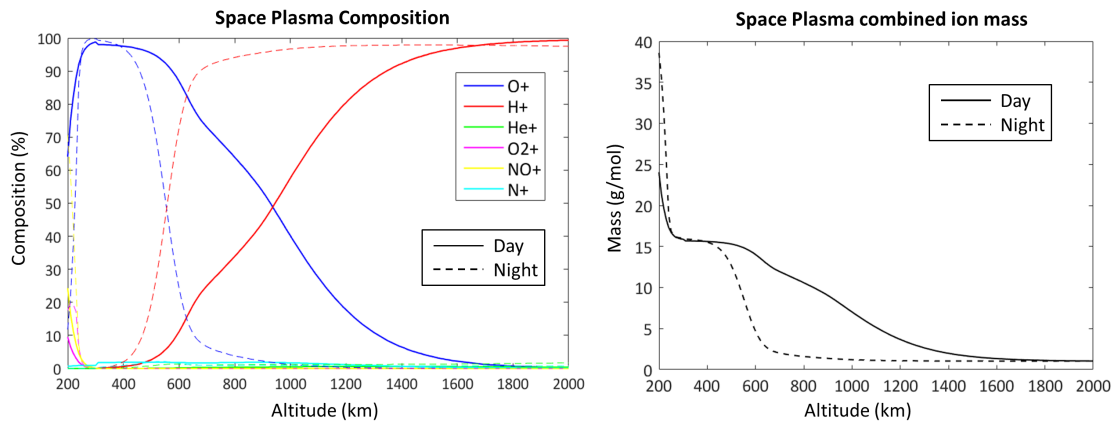
Figure A.16: Composition of the in-orbit space plasma calculated by the IRI 2012 model for 1st January 2017 (left image) and combined ion mass (right image).

Now, using Equation (A.72), the plasma drag is obtained and depicted in the right image of Figure A.17. The force reaches a maximum value around 400 km altitude where it ranges between 3-6 milliNewtons between daytime and nighttime. The right image in Figure A.17 depicts the detachment distance of the boundary from the centre of the coil for various altitudes obtained by means of Equation (A.71).
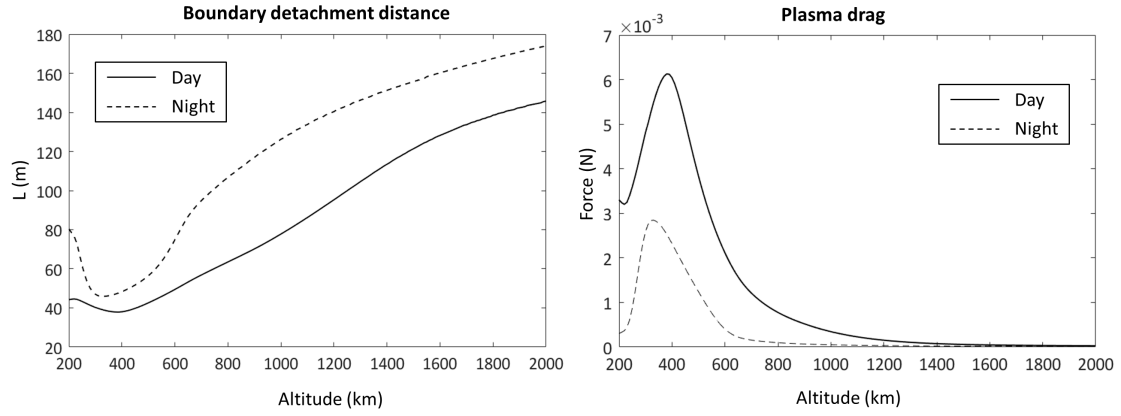
Figure A.17: Detachment distance of the magnetopause (left image) and plasma drag force (right image).

Finally, Figure A.18 compares some of the environmental accelerations acting on the chaser spacecraft. The figure shows the first term (Kepler model) and second term (J2) of the Earth's gravity acceleration, the air drag acceleration for high and low solar activity, the plasma drag acceleration during daytime and nighttime and the SRP acceleration. The purpose of this graphic is to get a first insight of the order of magnitude of the plasma drag with respect to other perturbations. Nevertheless, it should be noted that there are additional environmental perturbations acting on the chaser spacecraft such as the lunisolar perturbations or the Earth's tidal perturbations that are not shown in the present figure. It may be derived from the results that the plasma drag is a non-negligible acceleration which outcomes both the air drag and the SRP at certain altitudes in the LEO region. Therefore, as pointed out in Section 7.5.2, this perturbation should be studied further in future analysis of the eddy brake.
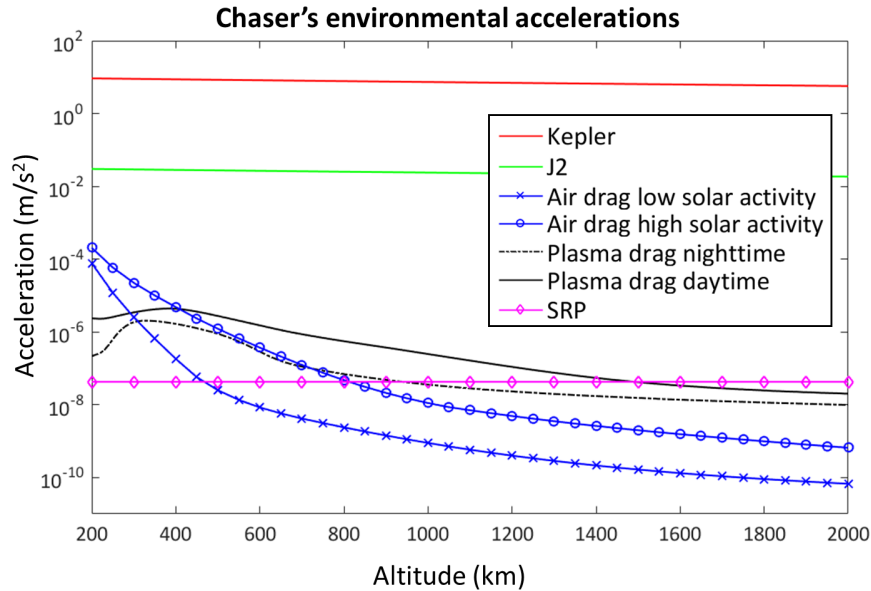
Figure A.18: Comparison of the plasma drag acceleration with other environmental accelerations.

BIBLIOGRAPHY

[1] IADC, "IADC Space Debris Mitigation Guidelines," Tech. Rep. IADC-02-01, Rev. 1, Inter-Agency Space Debris Coordination Committee, Sept. 2007.

[2] T. Schildknecht, E. Linder, J. Silha, and M. Hager, "Photometric monitoring of non-resolved space debris and data-bases of optical light curves," in *Advanced Maui Optical and Space Surveillance Technologies Conference*, 2015.

[3] W. J. Larson and J. R. Wertz, *Space mission analysis and design*. Kluwer Academic Publishers, 2005.

[4] NASA, "Spacecraft Aerodynamic Torques," Tech. Rep. NASA SP-8058, Jan. 1971.

[5] CDF, "e.Deorbit Study Report," Tech. Rep. CDF-135 (A), ESA, 9 2012.

[6] CNES, "Dossier de définition troisième étage h10 iii," Tech. Rep. A4-DF-1300000-D, Centre national d'études spatiales, 1994.

[7] G. Koppenwallner, B. Fritsche, T. Lips, and H. Klinkrad, "SCARAB - A multi-disciplinary code for destruction analysis of spacecraft during re-entry," in *5th European Symposium on Aerothermodynamics for Space Vehicles*, November 2004. ESA, Cologne (Germany).

[8] S. Nishida and S. Kawamoto, "Strategy for Capturing of a Tumbling Space Debris," *Acta Astronautica*, vol. 68, pp. 113–120, 2011. Doi:10.1016/j.actaastro.2010.06.045.

[9] P. Brun, "GNC Challenges for heavy active debris removal using blow effect to proces or de-tumble debris," in *5th International Conference on Spacecraft Formation Flying Missions and Technologies*, 2013.

[10] T. Bennett, D. Stevenson, E. Hogan, and H. Schaub, "Prospects and challenges of touchless electrostatic detumbling of small bodies," *Advances in Space Research*, vol. 56, Aug. 2015. Doi:10.1016/j.asr.2015.03.037.

[11] P. K. Kadaba and K. Naishadham, "Feasibility of Noncontacting Electromagnetic Despinning of a Satellite by Inducing Eddy Currents in Its Skin-Part I: Analytical Considerations," *IEEE Transactions on Magnetics*, vol. 31, July 1995. Doi:10.1109/20.390159.

[12] F. Sugai, S. Abiko, T. Tsujita, X. Jiang, and M. Uchiyama, "Detumbling an uncontrolled satellite with contactless force by using an eddy current brake," in *IEEE/RSJ International Conference on Intelligent Robots and Systems, Japan*, 2013.

[13] D. W. Kwon and R. J. Sedwick, *Cryogenic Heat Pipe for Cooling High Temperature Superconductors with Application to Electromagnetic Formayion Flying satellites*. PhD thesis, Massachusetts Institute of Technology, 2009.

[14] P. A. Lightsey, C. Atkinson, M. Clampin, and L. D. Feinberg, "James Webb Space Telescope: large deployable cryogenic telescope in space," *Optical Engineering*, vol. 51, 2012. Doi:10.1117/1.OE.51.1.011003.

[15] B. F. Kutter, F. C. Zegler, and M. R. Ragab, "Cryogenic propellant depot and integral sunshield," Tech. Rep. US Patent 8196868 B2, 06 2012.

[16] D. G. Gilmore, *Spacecraft Thermal Control Handbook. Vol. I: fundamental technologies.* The Aerospace Press, 2002.

[17] B. Zohuri, *Heat Pipe Design and Technology.* CRC Press, 2011.

[18] R. Votel and D. Sinclair, "Comparison of Control Moment Gyros and Reaction Wheels for Small Earth-Observing Satellites," in *26th Annual AIAA/USU Conference on Small Satellites, Logan, Utah,*, 2012.

[19] K. Kumar, N. Ortiz Gómez, M. Jankovic, J. Romero Martín, F. Topputo, S. Walker, F. Kirchner, and M. Vasile, "Agora: Mission to demonstrate technologies to actively remove Ariane rocket bodies," in *66th International Astronautical Congress. IAC-15,A6,6,1*, Oct. 2015. Jerusalem.

[20] Arianespace, "Ariane 5 data related to flight va205," tech. rep., March 2012.

[21] FLIR Integrated Imaging Solutions Inc, "Bumblebee2 Stereo Camera." URL: https://www.ptgrey.com/bumblebee2-firewire-stereo-vision-camera-systems/. Accessed: 15/08/2017.

[22] R. Jain, R. Kasturi, and B. Schunck, *Machine Vision.* McGraw-Hill, 1995.

[23] I. Funaki, H. Kojima, H. Yamakawa, Y. Nakayama, and Y. Shimizu, "Laboratory Experiment of Plasma Flow Around Magnetic Sail," *Astrophysics and Space Science*, vol. 112, pp. 63–68, Jan. 2007. Doi:10.1007/s10509-006-9251-4.

[24] N. Ida, *Engineering Electromagnetics.* Springer, 3rd Edition, 2015.

[25] P. Fortescue, J. Stark, and G. Swinerd, *Spacecraft Systems Engineering.* John Wiley & Sons, 2003.

[26] RICOR, "Cryocoolers for scientific instruments." URL: http://www.ricor.com/. Accessed: 11/05/2015.

[27] Janis Research Company, "Liquid Nitrogen Storage Dewars." URL: http://www.janis.com/. Accessed: 11/05/2015.

[28] ASC, "DragonEye 3D." URL: http://www.advancedscientificconcepts.com/. Accessed: 01/07/2016.

[29] Astro- und Feinwerktechnik Adlershof GmbH, "Reaction Wheels." URL: http://www.astrofein.com/. Accessed: 01/07/2016.

[30] Airbus Defence & Space, "Control Moment Gyro." URL: http://www.space-airbusds.com/. Accessed: 01/07/2016.

[31] B. Dunn, *Materials and Processes for spacecraft and high reliability applications.* Springer, 2016.

[32] A. . Duval, "Metallic materials properties." URL: http://www.aubertduval.com/. Accessed: 1–07–2015.

[33] D. J. Kessler, N. L. Johnson, J. Liou, and M. Matney, "The Kessler Syndrome: Implications to Future Space Operations," in *33rd Annual AAS Guidance and Control Conference*, 2010. Paper no. AAS 10-016.

[34] H. Klinkrad, *Space Debris. Models and Risk Analysis.* Springer, 2006.

[35] F. La Porte and E. Sasot, "Operational management of collision risks for LEO satellites at CNES," in *AIAA SpaceOps Conference*, 2008. AIAA 2008-3409.

[36] R. Biesbroek, *Active Debris Removal in Space.* Amazon UK, 2015.

[37] COPUOS, "Space Debris Mitigation Guidelines," tech. rep., Committee on the Peaceful Uses of Outer Space, United Nations, 2010.

[38] ESA, "Position Paper on Space Debris Mitigation. Implementing Zero Debris Creation Zones," Tech. Rep. The Netherlands, SP-1301, Oct. 2005.

[39] H. Klinkrad, P. Beltrami, S. Hauptmann, C. Martin, H. Sdunnus, H. Stokes, R. Walker, and J. Wilkinson, "The ESA Space Debris Mitigation Handbook 2002," *Advances in Space Research*, vol. 34, pp. 1251–1259, 2004. Doi:10.1016/j.asr.2003.01.018.

[40] N. L. Johnson and E. G. Stansbery, "The new NASA orbital debris mitigation procedural requirements and standards," *Acta Astronautica*, vol. 66, pp. 362–367, 2010. Doi:10.1016/j.actaastro.2009.07.009.

[41] IADC, "Stability of the Future LEO Environment," Tech. Rep. IADC-12-08, Rev. 1, Inter-Agency Space Debris Coordination Committee, Jan. 2013.

[42] J. C. Liou, "An active debris removal parametric study for LEO environment remediation," *Advances in Space Research*, vol. 47, pp. 1865–1876, June 2011. Doi:10.1016/j.asr.2011.02.003.

[43] J. C. Liou, N. Johnson, and N. Hill, "Controlling the growth of future LEO debris populations with active debris removal," *Acta Astronautica*, vol. 66, pp. 648–653, 2010. Doi:10.1016/j.actaastro.2009.08.005.

[44] M. Shan, J. Guo, and E. Gill, "Review and comparison of active space debris capturing and removal methods," *Progress in Aerospace Sciences*, vol. 80, pp. 18–32, Jan. 2016. Doi:10.1016/j.paerosci.2015.11.001.

[45] C. Bonnal, J.-M. Ruault, and M.-C. Desjean, "Active debris removal: Recent progress and current trends," *Acta Astronautica*, vol. 85, pp. 51–60, 2013. Doi:10.1016/j.actaastro.2012.11.009.

[46] W. Fehse, "Rendezvous with and capture/removal of non-cooperative bodies in orbit: the technical challenges," *Journal of Space Safety Engineering*, vol. 1, no. 1, pp. 17–27, 2014.

[47] IADC, "Key Definitions of the Inter-Agency Space Debris Coordination Committee," Tech. Rep. IADC-13-02, Inter-Agency Space Debris Coordination Committee, Apr. 2013.

[48] NASA, "Orbital Debris Quarterly News," *Orbital Debris Program Office*, vol. 21, Feb. 2017.

[49] NASA, "Orbital Debris Program Office." URL: http://orbitaldebris.jsc.nasa.gov/, 2014. Accessed: 11–08–2014.

[50] NASA, "Orbital Debris Quarterly News," *Orbital Debris Program Office*, vol. 20, Jan. 2016.

[51] NASA, "Orbital Debris Quarterly News," *Orbital Debris Program Office*, vol. 19, 2015.

[52] C. Pardini and L. Anselmo, "Review of past on-orbit collisions among cataloged objects and examination of the catastrophic fragmentation concept," *Acta Astronautica*, vol. 100, pp. 30–39, 2014. Doi:10.1016/j.actaastro.2014.03.013.

[53] NASA, "Process for Limiting Orbital Debris," Tech. Rep. Washington DC, NASA-STD-8719.14A, Dec. 2011.

[54] UNOOSA, "Active Debris Removal - An Essential Mechanism for Ensuring the Safety and Sustainability of Outer Space," Tech. Rep. Vienna, A/AC.105/C.1/2012/CRP.16, COPUOS, United Nations Office for Outer Space Affairs, Feb. 2012.

[55] A. White and H. Lewis, "The many futures of active debris removal," *Acta Astronautica*, vol. 95, pp. 189–197, 2014. Doi:10.1016/j.actaastro.2013.11.009.

[56] A. White and H. Lewis, "An adaptive strategy for active debris removal," *Advances in Space Research*, vol. 53, pp. 1195–1206, 2014. Doi:10.1016/j.asr.2014.01.021.

[57] W. Fehse, *Automated Rendezvous and Docking of Spacecraft*. Cambridge Univ.Press, 2003.

[58] M. M. Castronuovo, "Active space debris removal A preliminary mission analysis and design," *Acta Astronautica*, vol. 69, pp. 848–859, 2011. Doi:10.1016/j.actaastro.2011.04.017.

[59] Committee on Space Debris, *Orbital Debris. A technical Assessment.* National Academy Press, 1995.

[60] B. E. Tweddle, T. P. Settereld, A. Saenz-Otero, and D. W. Miller, "An Open Research Facility for Vision-Based Navigation Onboard the International Space Station," *Journal of Field Robotics*, vol. 33, pp. 157–186, Oct. 2015. Doi:10.1002/rob.21622.

[61] S. Ruel, T. Luu, and A. Berube, "Space Shuttle Testing of the TriDAR 3D Rendezvous and Docking Sensor," *Journal of Field Robotics*, vol. 29, July 2012. Doi:10.1002/rob.20420.

[62] X. Du, B. Liang, X. Wenfu, and Y. Qiu, "Pose measurement of large non-cooperative satellite based on collaborative cameras," *Acta Astronautica*, vol. 68, pp. 2047–2065, June 2011. Doi:10.1016/j.actaastro.2010.10.021.

[63] J.-F. Shi, S. Ulrich, S. Ruel, and M. Anctil, "Uncooperative Spacecraft Pose Estimation Using an Infrared Camera During Proximity Operations," in *AIAA Space Conference and Exposition*, Aug. 2015. Paper no. AIAA 2015-4429.

[64] R. Opromolla, G. Fasano, G. Rufino, and M. Grassi, "Uncooperative pose estimation with LIDAR-based system," *Acta Astronautica*, vol. 110, pp. 287–297, May 2015. Doi:10.1016/j.actaastro.2014.11.003.

[65] D. Fourie, B. E. Tweddle, S. Ulrich, and A. Saenz-Otero, "Flight Results of Vision-Based Navigation for Autonomous Spacecraft Inspection of Unknown Objects," *Journal of spacecraft and rockets*, vol. 51, Dec. 2014. Doi:10.2514/1.A32813.

[66] R. Benvenuto, S. Salvi, and M. Lavagna, "Dynamics analysis and GNC design of flexible systems for space debris active removal," *Acta Astronautica*, vol. 110, pp. 247–265, May 2015. Doi:10.1016/j.actaastro.2015.01.014.

[67] R. Dudziaka, S. Tuttlea, and S. Barraclough, "Harpoon technology development for the active removal of space debris," *Advances in Space Research*, vol. 56, pp. 509–527, Aug. 2015. Doi:10.1016/j.asr.2015.04.012.

[68] S. Ferraris, S. Perero, G. Gautier di Conengo, A. Chiesa, A. Messidoro, and M. Ferraris, "Friction, mechanical and ageing properties of surface modied materials for space debris capture," *Advances in Space Research*, vol. 57, pp. 1177–1188, 2016. Doi:10.1016/j.asr.2015.12.034.

[69] C. Bombardelli and J. Pelaez, "Ion Beam Shepard for Contactless Space Debris Removal," *Journal of Guidance, Control and Dynamics*, vol. 34, May 2011. Doi:10.2514/1.51832.

[70] T. Vincent-Peters, A. Pellacani, P. Attina, M. Lavagna, R. Benvenuto, and E. Luraschi, "COBRA Active Debris Removal Concept," in *64th International Astronautical Congress, Beijing, China*, 2013. Paper no. IAC-13-A6.6.6.

[71] W. Schall, "Laser Radiation for Cleaning Space Debris from Lower Earth Orbits," *Journal of Spacecraft and Rockets*, vol. 39, Jan. 2002. Doi:10.2514/2.3785.

[72] M. Andrenucci, P. Pergola, and A. Ruggiero, "Active Removal of Space Debris Expanding foam application for active debris removal," Tech. Rep. Ariadna ID: 10-6411, ESA, Feb. 2011.

[73] E. A. Hogan and H. Schaub, "General High-Altitude Orbit Corrections Using Electrostatic Tugging with Charge Control," *Journal of Guidance, Control and Dynamics*, vol. 38, Apr. 2015. Doi:10.2514/1.G000092.

[74] J. Beck, P. V. Hauwaert, S. Hobbs, D. Evans, F. Robinson, I. Holbrough, and J. Virgili, "Bodies under connected elastic dynamics: A theoretical grounded assessment of elastic tether dynamics for active debris removal missions," Tech. Rep. The Netherlands, GSP-13-090, ESA, Apr. 2015. Doi:10.13140/RG.2.1.5050.6001.

[75] J. Deloo and E. Mooij, "Active debris removal: Aspects of trajectories, communication and illumination during final approach," *Acta Astronautica*, vol. 117, pp. 277–295, Dec. 2015. Doi:10.1016/j.actaastro.2015.08.001.

[76] H. Schaub and J. L. Junkins, *Analytical Mechanics of Space Systems*. AIAA Education Series, Reston, VA, 2003.

[77] W. Cheng, L. Tianxi, and Z. Yang, "Grasping Strategy in Space Robot Capturing Floating Target," *Chinese Journal of Aeronautics*, vol. 23, pp. 591–598, 2010. Doi:10.1016/S1000-9361(09)60259-4.

[78] M. Wilde, M. Ciarci, A. Grompone, and M. Romano, "Experimental Characterization of Inverse Dynamics Guidance in Docking with a Rotating Target," *Journal of Guidance, Control and Dynamics*, vol. 0, Feb. 2016. Doi:10.2514/1.G001631.

[79] G. Boyarko, O. Yakimenko, and M. Romano, "Optimal Rendezvous Trajectories of a Controlled Spacecraft and a Tumbling Object," *Journal of Guidance, Control and Dynamics*, vol. 34, July 2011. Doi:10.2514/1.47645.

[80] L. Jaspera and H. Schaub, "Input Shaped Large Thrust Maneuver with a Tethered Debris Object," *Acta Astronautica*, 2013. Doi:10.1016/j.actaastro.2013.11.005.

[81] E. Linder, J. Silha, T. Schildknecht, and M. Hager, "Extraction of Spin Periods of Space Debris from Optical Light Curves," in *66th International Astronautical Congress, IAC-15-A6.1.2*, 2015.

[82] F. Santoni, E. Cordelli, and F. Piergentili, "Determination of Disposed-Upper-Stage Attitude Motion by Ground-Based Optical Observations," *Journal of Spacecraft and Rockets*, vol. 50, no. 3, 2013. Doi:10.2514/1.A32372.

[83] R. Cognion, "Rotation rates of inactive satellites near geosynchronous earth orbit," in *Advanced Maui Optical and Space Surveillance Technologies Conference*, 2014.

[84] W. H. Ryan and E. V. Ryan, "Photometric Studies of Rapidly Spinning Decommissioned GEO Satellites," in *Advanced Maui Optical and Space Surveillance Technologies Conference*, 2015.

[85] P. Papushev, Y. Karavaev, and M. Mishina, "Investigations of the evolution of optical characterisics and dynamics of proper rotation of uncontrolled geostationary articial satellites," *Advances in Space Research*, vol. 43, pp. 1416–1422, 2009. Doi:10.1016/j.asr.2009.02.007.

[86] Y. Karavaev, R. Kopyatkevich, and M. Mishina, "Astrophotometrical Observation of Artificial Satellites and Study of the Technical Status of Parental Bodies of Space Debris at Geostationary Ring," in *4th European Conference on Space Debris Darmstadt*, 2005.

[87] C. Binz, M. Davis, B. Kelm, and C. Moore, "Optical Survey of the Tumble Rates of Retired GEO Satellites," in *Advanced Maui Optical and Space Surveillance Technologies Conference*, 2014.

[88] V. Williams and A. J. Meadows, "Eddy current torques, air torques, and the spin decay of cylindrical rocket bodies in orbit," *Planetary and Space Science*, vol. 26, pp. 721–726, 1978. Doi:10.1016/0032-0633(78)90003-X.

[89] H. Boehnhardt, H. Koehnhke, and A. Seidel, "The acceleration and the deceleration of the tumbling period of Rocket Intercosmos 11 during the first two years after launch," *Astrophysics and Space Science*, vol. 162, no. 2, pp. 297–313, 1989. Doi:10.1007/BF00640745.

[90] B. De Pontieu, "Database of Photometric Periods of Artificial Satellites," *Advances in Space Research*, vol. 19, pp. 229–232, 1997. Doi:10.1016/S0273-1177(97)00005-7.

[91] T. Yanagisawa and H. Kurosaki, "Shape and motion estimate of LEO debris using light curves," *Advances in Space Research*, vol. 50, pp. 136–145, 2012. Doi:10.1016/j.asr.2012.03.021.

[92] J. Silha, E. Linder, M. Hager, and T. Schildknecht, "Optical Light Curve Observations to Determine Attitude States of Space Debris," in *30th International Symposium on Space Technology and Science. Kobe, Japan*, 2015.

[93] D. Kucharski, G. Kirchner, F. Koidl, F. Cunbo, R. Carman, C. Moore, A. Dmytrotsa, M. Ploner, G. Bianco, M. Medvedskij, A. Makeyev, G. Appleby, M. Suzuki, J.-M. Torre, Z. Zhongping, L. Grunwaldt, and Q. Feng, "Attitude and Spin Period of Space Debris Envisat Measured by Satellite Laser Ranging," *Geoscience and Remote Sensing, IEEE Transactions*, vol. 52, pp. 7651 – 7657, 2014. Doi:10.1109/TGRS.2014.2316138.

[94] L. D. Landau and E. M. Lifshitz, *Mechanics. Course of Theoretical Physics, vol. 1, 3rd Edition*. Reed Educational and Professional Publishing Ltd, 1976.

[95] P. C. Hughes, *Spacecraft Attitude Dynamics*. Dover Publications, 2004.

[96] F. L. Janssens and J. C. Van der Ha, "Flat-spin recovery of spinning satellites by an equatorial torque," *Acta Astronautica*, vol. 116, pp. 355–367, November 2015. Doi:10.1016/j.actaastro.2015.05.011.

[97] B. Pattan, *Satellite Systems. Principles and Technologies*. Springer, 1993.

[98] J. A. J. Angelo, *Encyclopedia of Space and Astronomy*. Facts on File, 2006.

[99] E. J. Routh, *The advanced part of treatise in the dynamics of system of rigid bodies*. The Macmillan Co., London and New York, 1982.

[100] V. N. Koshlyakov, "On some special cases of integration of the Euler dynamical equations associated with the motion of a gyroscope in a resisting medium," *Prikl. Mat. Mekh*, vol. 17, no. 2, pp. 137–148, 1953.

[101] D. P. A.-M. Dr. Gregory W Ojakangas and D. H. Cowardin, "Probable Rotation States of Rocket Bodies in Low Earth Orbit," in *14th annual Maui Optical and Space and Surveillance Technologies Conference*, 2012.

[102] NASA, "Spacecraft Gravitational Torques," Tech. Rep. NASA SP-8024, May 1969.

[103] J. R. Wertz, *Attitude Determination and Control*. Kluwer Academic Publishers, 1978.

[104] N. Ortiz Gómez and S. Walker, "Earth's Gravity Gradient and Eddy Currents Effects on the Rotational Dynamics of Space Debris Objects: Envisat Case Study," *Advances in Space Research*, 2015. Doi:10.1016/j.asr.2014.12.031.

[105] T. Bak and R. Wisniewski, "Passive Aerodynamic Stabilisation of Low Earth Orbit Satellite," in *3rd ESA International Conference*, November 1996. ESTEC The Netherlands.

[106] E. Canuto, "Drag-free and attitude control for the GOCE satellite," *Automatica*, vol. 44, pp. 1766–1780, 2008. Doi:10.1016/j.automatica.2007.11.023.

[107] NASA, "Spacecraft Radiation Torques," Tech. Rep. NASA SP-8027, Oct. 1969.

[108] G. W. Ojakangas, H. Cowardin, and N. Hill, "Toward realistic dynamics of rotating orbital debris, and implications for lightcurve interpretation," in *Advanced Maui Optical and Space Surveillance Technologies Conference*, 2011.

[109] W. F. Bottke, D. Vokrouhlický, D. P. Rubincam, and M. Broz, "The effect of Yarkovsky thermal forces on the dynamical evolution of asteroids and meteoroids," *Asteroids III*, vol. 395, 2002.

[110] A. A. Albuja, D. J. Scheeres, and J. W. McMahon, "Evolution of angular velocity for defunct satellites as a result of YORP: An initial study," *Advances in Space Research*, vol. 56, pp. 237–251, July 2015. Doi:10.1016/j.asr.2015.04.013.

[111] L. D. Landau and E. M. Lifshitz, *Electrodynamics of continuous media, Course of Theoretical Physics, Vol. 8*. Pergamon Press, 1984.

[112] J. Vanderlinde, *Classical Electromagnetic Theory, 2nd Edition*. Kluwer Academic Publishers, 2004.

[113] NASA, "Assessment and control of spacecraft magnetic fields," Tech. Rep. SP-8037, 1970.

[114] J. F. A. Ormsby, "Eddy Current Torques and Motion Decay on Rotating Shells," Tech. Rep. Project 8051, US Air Force, 1967.

[115] E. Y. YU, "Spin Decay, Spin-Precession Damping, and Spin-Axis Drift of the Telstar Satellite," *Bell System Technical*, pp. 2169–2193, 1963. Doi:10.1002/j.1538-7305.1963.tb00963.x.

[116] H. B. Rosenstock, "The effect of the Earth's Magnetic Field on the Spin of a Satellite," *Astronautica Acta*, vol. 3, no. 3, pp. 215–221, 1956.

[117] J. P. Vinti, "Theory of The Spin of a Conducting Satellite in the Magnetic Field of the Earth," Tech. Rep. Rep. Number 1020, Ballistic Res. Labs., Aberdeen Proving Groung, 1967.

[118] L. Smith, "A Theoretical Study of the Torques induced by a Magnetic Field on Rotating Cylinders and Spinning Thin-wall Cones, Cone Frustums, and General Body of Revolution," Tech. Rep. Rep. Number R-129, NASA, 1962.

[119] L. Smith, "Effects of Magnetically induced Eddy-current Torques on Spin Motions of an Earth Satellite," Tech. Rep. NASA TN D-2198, NASA, 1965.

[120] N. Praly, M. Hillion, C. Bonnal, J. Laurent-Varin, and N. Petit, "Study on the eddy current damping of the spin dynamics of space debris from the Ariane launcher upper stages," *Acta Astronautica*, vol. 76, pp. 145–153, 2012. Doi:10.1016/j.actaastro.2012.03.004.

[121] Arianespace, "Ariane 5 user's manual," Tech. Rep. issue 5 revision 1, July 2011.

[122] Arianespace, "Ariane 4 user's manual," tech. rep., Feb. 1999.

[123] B. Bastida Virgili, S. Lemmens, and H. Krag, "Investigation on Envisat Attitude Motion," in *e.Deorbit Workshop, ESA, The Netherlands*, May 2014.

[124] ECSS, "Space Engineering. Space Environment," Tech. Rep. ECSS-E-ST-10-04C, ESA, November 2008.

[125] M. Mandea and M. Korte, *Geomagnetic Observations and Models*. Springer, 2011.

[126] S. Kawamoto, S. Kitagawa, and K. Matsumoto, "Angular Momentum Reduction Using Mechanical Impulse for Uncontrollable Satellite Capturing," *Journal of Space Technology and Science*, vol. 18, no. 2, pp. 25–31, 2002.

[127] S. Kawamoto, K. Matsumoto, and S. Wakabayashi, "Ground Experiment of Mechanical Impulse Method for Uncontrollable Satellite Capturing," in *6th International Symposium on Artificial Intelligence and Robotics and Automation in Space*, 2001.

[128] D. McKnight, F. Pentino, A. Kaczmarek, and S. Knowles, "Detumbling Rocket Bodies in Preparation for Active Debris Removal," in *6th European Conference on Space Debris, European Space Operations Centre, Darmstadt, Germany*, 2013.

[129] A. Caubet and J. D. Biggs, "Design of an Attitude Stabilization Electromagnetic Module for Detumbling Uncooperative Targets," in *IEEE Aerospace Conference*, 2014.

[130] L. DeLuca, F. Bernelli, F. Maggi, P. Tadini, C. Pardini, and L. Anselmo, "Active space debris removal by a hybrid propulsion module," *Acta Astronautica*, vol. 91, no. 2, pp. 20–33, 2013. Doi:10.1016/j.actaastro.2013.04.025.

[131] F. Ferrari, R. Benvenuto, and M. Lavagna, "Gas Plume Impingement Technique for Space Debris De-tumbling," in *9th International ESA Conference on Guidance, Navigation and Control Systems, Portugal*, 2014.

[132] T. Peters and D. Escorial, "Applicability of COBRA concept to de-tumbling space debris objects," in *6th International Conference on Astrodynamics Tools and Techniques (ICATT), Germany*, Mar. 2016.

[133] D. Stevenson and H. Schaub, "Multi-sphere method for modeling spacecraft electrostatic forces and torques," *Advances in Space Research*, vol. 51, pp. 10–20, Jan. 2013. Doi:10.1016/j.asr.2012.08.014.

[134] H. Schaub, "Stabilization of Satellite Motion Relativeto a Coulomb Spacecraft Formation," *Journal of Guidance, Control and Dynamics*, vol. 28, November 2005. Doi:10.2514/1.8577.

[135] M. Vetrisano, C. Colombo, and M. Vasile, "Asteroid rotation and orbit control via laser ablation," *Advances in Space Research*, vol. 57, pp. 1762–1782, Apr. 2016. Doi:10.1016/j.asr.2015.06.035.

[136] M. Vetrisano, N. Thiry, and M. Vasile, "Detumbling Large Space Debris via Laser Ablation," in *IEEE Aerospace Conference*, 2015.

[137] T. Voirin, S. Kowaltschek, and O. Dubois-Matra, "NoMAD: a contactless technique for active large debris removal," in *63rd International Astronautical Congress, Italy, IAC-12-A6,7,3.x14126*, 2012.

[138] P. K. Kadaba and K. Naishadham, "Feasibility of Noncontacting Electromagnetic Despinning of a Satellite by Inducing Eddy Currents in Its Skin-Part II: Design Implementation," *IEEE Transactions on Magnetics*, vol. 31, July 1995. Doi:10.1109/20.390160.

[139] F. Sugai, S. Abiko, T. Tsujita, X. Jiang, and M. Uchiyama, "Development of an eddy current brake system for detumbling malfunctional satellites," in *IEEE/SICE International Symposium on System Integration (SII) Japan*, 2012.

[140] K. Fitzpatrick, *Maxwell's Equations and the Principles of Electromagnetism*. Physics Series, 2008.

[141] D. Griffiths, *Introduction to Electrodynamics*. Prentice Hall, 1999.

[142] A. E. Seaver, "An Equation For Charge Decay Valid in Both Conductors and Insulators," in *ESA-IEJ Joint Meeting, Northwestern University, Chicago, IL*, pp. 349–360, 2002.

[143] H. Weinberger, *A first course in Partial Differential Equations with Complex Variables and Transform Methods*. Dover Publications, 1995.

[144] R. Ash, *A Prime of Abstract Mathematics*. The Mathematical Association of America, 1998.

[145] J. D. Jackson, *Classical Electrodynamics*. John Wiley & Sons, NY, 3rd Edition, 1999.

[146] F. Reif, *Fundamentals of Statistical and Thermal Physics*. McGraw-Hill, 1965.

[147] N. Pottier, *Nonequilibrium Statistical Physics. Linear Irreversible Processes*. Oxford Univ. Press, 2010.

[148] O. C. Zienkiewicz, *The Finite Element Method, 3rd Edition*. McGraw-Hill, 1978.

[149] A. Ben-Israel and T. Greville, *Generalized Inverses*. Springer, 2003.

[150] H. T. Boyer, "The force on a magnetic dipole," *American Journal of Physics*, vol. 56, pp. 688–692, 1988. Doi:10.1119/1.15501.

[151] S. Timoshenko and J. Goodier, *Theory of Elasticity*. McGraw-Hill, 1934.

[152] A. Farrahi and A. Sanz-Andrés, "Efficiency of Hysteresis Rods in Small Spacecraft Attitude Stabilization," *The Scientific World Journal*, 2013. Doi:10.1155/2013/459573.

[153] N. Koshkin, E. Korobeynikova, L. Shakun, S. Strakhova, and Z. Tang, "Remote Sensing of the EnviSat and Cbers-2B satellites rotation around the centre of mass by photometry," *Advances in Space Research*, 2016. Doi:10.1016/j.asr.2016.04.024.

[154] H. Wirnsberger, O. Baur, and G. Kirchner, "Space debris orbit prediction errors using bistatic laser observations. Case study: ENVISAT," *Advances in Space Research*, vol. 55, pp. 2607–2615, 2015. Doi:10.1016/j.asr.2015.02.018.

[155] S. Lemmens, H. Krag, J. Rosebrock, , and I. Carnelli, "Radar Mappings for Attitude Analysis of Objects in Orbit," in *6th European Conference on Space Debris, Darmstadt*, 2013.

[156] R. Biesbroek, T. Soares, J. Huesing, and L. Innocenti, "The e.Deorbit CDF Study: A design study for the safe removal of a large space debris," in *64rd IAC conference Beijing*, 2013.

[157] D. Vallado, *Fundamentals of Astrodynamics and Applications*. Kluwer Academic Publishers, 2004.

[158] J. D. Faires and R. Burde, *Numerical methods*. Thomson, 3rd Edition, 2004.

[159] ESA, "Envisat-1. Mission and System Summary," Tech. Rep. ESA Brochure, Issue 2, The Netherlands, Mar. 1998.

[160] Y. M. Griffiths, "Polar Platform Propulsion Subsystem," in *2nd European Spacecraft Propulsion Conference. ESA, The Netherlands*, 1997.

[161] NASA, "Spacecraft solar cells arrays," Tech. Rep. NASA SP-8074, May 1971.

[162] S. Timoshenko, *Strength of Materials, Part II. Advanced Theory and Problems*. D. Van Nostrand Company. 3rd Edition, 1956.

[163] Advent Research Material, "Torsion Wire." URL: http://www.advent-rm.com/. Accessed: 15/07/2016.

[164] J. Wijker, *Spacecraft Structures*. The Netherlands, Springer, 2008.

[165] Anixter, *Wire and Cable Technical Information Handbook*. Anixter, 2013.

[166] W. Yuan, *Second Generation High Temperature Superconducting Coils and Their Applications for Energy Storage*. Springer, 2011.

[167] E. Polturak, G. Koren, I. Flohr, R. Waller, and M. Guelman, "IEEE Transactions on Microwave Theory and Techniques," *Cryogenics*, vol. 48, pp. 1289–1291, Jul. 2000. Doi:10.1109/22.853476.

[168] T. Kawecki, S. Chappie, and D. Mahony, "High Temperature Superconducting Space Experiment II (HTSSE II) cryogenic design," *Cryogenics*, vol. 36, pp. 741–752, Oct. 1996. Doi:10.1016/0011-2275(96)00036-7.

[169] D. W. Kwon and D. W. Miller, *Electromagnetic Formation Flight of Satellite Arrays*. PhD thesis, Massachusetts Institute of Technology, 2005.

[170] D. Kwon and R. Sedwick, "Cryogenic heat pipe for cooling high temperature superconductors," *Cryogenics*, vol. 49, pp. 514–523, Sept. 2009. Doi:10.1016/j.cryogenics.2009.07.005.

[171] Y. Iwasa, *Case Studies in Superconducting Magnets. Design and Operational Issues*. Springer, 2009.

[172] E. A. Young, J. Pelegrin, I. Falorio, J. Archer, L. L. Jarvis, and Y. Yang, "Temperature and Background Field Dependence of a Compact React and Wind MgB2 Solenoid Coil," *IEEE Transactions on Applied Superconductivity*, vol. 25, June 2015. Doi:10.1109/TASC.2014.2361095.

[173] B. Collaudin and N. Rando, "Cryogenics in space: a review of the missions and of the technologies," *Cryogenics*, vol. 40, pp. 797–819, Feb. 2001. Doi:10.1016/S0011-2275(01)00035-2.

[174] D. W. Kwon, R. J. Sedwick, and D. W. Miller, "Method of both cooling and maintaining the uniform temperature of an extended object," Tech. Rep. US Patent 20120036870 A1, Feb. 2012.

[175] TWP Inc, "Stainless Steel Mesh." URL: http://www.twpinc.com/. Accessed: 01/06/2016.

[176] R. Bonsignori, A. Coradini, P. Drossart, and G. Arnold, "VIRTIS Visual and Infrared Imaging Spectrometer for the Rosetta Mission," in *International Astronautical Federation*, 1997.

[177] M. Donabedian, *Spacecraft Thermal Control Handbook. Vol. II: cryogenics.* The Aerospace Press, 2003.

[178] J. A. Christian and S. Cryan, "A Survey of LIDAR Technology and its Use in Spacecraft Relative Navigation," in *AIAA Guidance, Navigation, and Control Conference, Honolulu, HI, USA*, Aug. 2008. Paper no. AIAA 2013-4641.

[179] T. W. Lim, "Point cloud modeling using the homogeneous transformation for non-cooperative pose estimation," *Acta Astronautica*, vol. 111, pp. 61–67, July 2015. Doi:10.1016/j.actaastro.2015.02.002.

[180] M. Nazari, E. Butcher, and H. Schaub, "Spacecraft Attitude Stabilization using Nonlinear Delayed Multi-Actuator Control and Inverse Dynamics," *Journal of Guidance, Control, and Dynamics*, vol. 36, pp. 1440–1452, Sept. 2013. Doi:10.2514/1.58249.

[181] M. Sidi, *Spacecraft Dynamics and Control.* Cambridge university Press, 1997.

[182] A. Chunodkar and M. Akella, "Attitude Stabilization with Unknown Bounded Delay in Feedback Control Implementation," *Journal of Guidance, Control and Dynamics*, vol. 34, pp. 535–542, Mar. 2011. Doi:10.2514/1.50352.

[183] M. P. Oomen, *AC loss in superconducting tapes and cables.* PhD thesis, Universiteit Twente, The Netherlands, 2000.

[184] G. Alberti, *Interfacing with the NASA data system: the case of the AMS02 experiment on board the International Space Station.* PhD thesis, Universita degli studi di Perugia, Italy, 2012.

[185] S. Ahlen, V. M. Balebanov, R. Battiston, U. Becker, J. Burger, M. Capell, and et al., "An antimatter spectrometer in space," *Nuclear Instruments and Methods in Physics Research Section A*, vol. 350, pp. 351–367, 1994. Doi:10.1016/0168-9002(94)91184-3.

[186] G. Gettliffe, N. Inamdar, R. Masterson, and D. W. Miller, "High-Temperature Superconductors as Electromagnetic Deployment and Support Structures in Spacecraft," Tech. Rep. NASA NIAC Phase I, Final Report, MIT Space Systems Lab, 01 2012.

[187] R. Battison, W. Burguer, V. Calvalli, and R. Musenich, "Active Magnetic Shielding for Long Duration Manned Space Missions," in *6th IAASS International Space Safety Conference, Montreal*, May 2013.

[188] M. Jankovic, K. Kumar, N. Ortiz Gómez, J. Romero Martín, F. Kirchner, F. Topputo, S. Walker, and M. Vasile, "Spacecraft concept for active de-tumbling and robotic capture of Ariane rocket bodies," in *13th Symposium on Advanced Space Technologies in Robotics and Automation (ASTRA)*, May 2015. ESTEC The Netherlands.

[189] FP7 Marie-Curie ITN, "Stardust Programme." URL: http://www.stardust2013.eu/. Accessed: 15/07/2016.

[190] D-Orbit Srl, "Decommissioning device." URL: http://www.deorbitaldevices.com/. Accessed: 01/08/2016.

[191] K. Wormnes, R. Le Letty, , L. Summerer, R. O. Schonenborg, Dubois-Matra, E. Luraschi, A. Cropp, H. Krag, and J. Delaval, "ESA Technologies for Space Debris Remediation," in *6th Conference Space Debris ESOC*, 2013.

[192] C. LeFèvre, H. Fraysse, V. Morand, A. Lamy, C. Cazaux, P. Mercier, C. Dental, F. Deleflie, and D. Handschuh, "Compliance of disposal orbits with the French Space Operations Act:The Good Practices and the STELA tool," *Acta Astronautica*, vol. 94, pp. 234–245, 2014. Doi:10.1016/j.actaastro.2013.07.038.

[193] H. Holsten, "Development of the Ariane 5 Upper Stage," *Acta Astronautica*, vol. 29, pp. 117–120, 1993. Doi:10.1016/0094-5765(93)90029-V.

[194] C. Bonnal and W. Naumann, "Ariane debris mitigation measures - Past and future," *Acta Astronautica*, vol. 40, pp. 275–282, 1997. Doi:10.1016/S0094-5765(97)00141-0.

[195] S. Schmidt, S. Beyer, H. Knabe, H. Immich, R. Meistring, and A. Gessler, "Advanced ceramic matrix composite materials for current and future propulsion technology applications," *Acta Astronautica*, vol. 55, pp. 409–420, 2004. Doi:10.1016/j.actaastro.2004.05.052.

[196] L. Ravet, "The ARIANE 5 launcher improvements," *Air & Space Europe*, vol. 2, pp. 68–72, 2000. Doi:10.1016/S1290-0958(00)80045-3.

[197] P. Amadieu, G. Beckwith, B. Dore, J. Bouchery, and V. Pery, "Automated transfer vehicle (atv) structural and thermal model testing at estec," Tech. Rep. Bulletin 111, ESA, Aug. 2002.

[198] DISCOS, "ESA Database and Information System Characterization Objects in Space." URL: http://discosweb.esoc.esa.int. Accessed: 1–07–2015.

[199] Scitor, "Space-Track.Org." URL: http://www.space-track.org/. Accessed: 1–07–2015.

[200] Air Liquide, "Ariane-4 H10 Cryogenic Tank." URL:http://www.airliquideadvancedtechnologies.com/. Accessed: 14/07/2016.

[201] A. Teissier, "Ariane 4 Third Stage Tanks with Stiffened Shells," in *28th Joint Propulsion Conference and Exhibit, TN, USA*, 1992. AIAA-92-3181.

[202] ECSS, "Space engineering structural materials handbook: Load transfer and design of joints and design of structures," Tech. Rep. ECSS-E-HB-32-20 Part 3A, ESA, Mar. 2011.

[203] J. Paul, A. Dettmann, B. Girault, J. Hilljegerdes, F. Kirchner, I. Ahrns, and J. Sommer, "INVERITAS: A facility for hardware-in-the-loop long distance movement simulation for rendezvous and capture of satellites and other autonomous objects," *Acta Astronautica*, vol. 116, pp. 1–24, Nov. 2015. Doi:10.1016/j.actaastro.2015.06.003.

[204] N. Oumer, G. Panin, Q. Mulbaer, and A. Tseneklidou, "Vision-based localization for on-orbit servicing of a partially cooperative satellite," *Acta Astronautica*, vol. 117, pp. 19–37, Dec. 2015. Doi:10.1016/j.actaastro.2015.07.025.

[205] Point Grey Research, "Fly capture sdk." URL:http://www.ptgrey.com/flycapture-sdk, 2015.

[206] Mathworks, "Matlab image processing toolbox." URL:http://de.mathworks.com/products/image/, 2015.

[207] R. Hartley and A. Zisserman, *Multiple view geometry in computer vision*. Cambridge University Press, 2003.

[208] V. A. Chobotov, *Orbital Mechanics*. AIAA, Education Series, 3rd Edition, 2002.

[209] S. T. Lai, *Spacecraft Charging*. AIAA, 2011.

[210] NASA, "Low Earth Orbit Spacecraft Charging Design Handbook," Tech. Rep. NASA HDBK 4006, 3 2007.

[211] H. B. Garrett and C. P. Pike, *Space Systems and Their Interactions with Earth's Space Environment*. AIAA, 1980.

[212] H. B. Garrett and A. C. Whittlesey, *Guide to Mitigating Spacecraft Charging Effects*. John Wiley & Sons, 2012.

[213] R. Stengel, *Optimal control and estimation*. Dover Publications, 1994.

[214] A. Oppenheim, A. Willsky, and S. H. Nawab, *Signals and Systems (2nd Edition)*. Prentice-Hall, Inc. Upper Saddle River, NJ, USA, 1996.

[215] T. Inamori, K. R., P. Saisutjarit, N. Sako, and O. H., "Magnetic plasma deorbit system for nano- and micro- satellites using magnetic torquer interference with space

plasma in low Earth orbit," *Acta Astronautica*, vol. 112, pp. 192–199, July 2015. Doi:10.1016/j.actaastro.2015.02.025.